

AL SUBEH, ZEINAB Y., PHD. Preclinical Development of Fungal Secondary Metabolites and The Discovery of New Metabolites with Cytotoxic Properties. (2021)

Directed by Dr. Nicholas Oberlies. 330 pp.

Cancer is still the second leading cause of deaths worldwide and responsible for nearly 10.0 million deaths in 2020. In addition to the high morbidity and mortality rate, cancer results in a significant economic burden on the healthcare systems and countries all over the world. The discovery and development of new anticancer leads is essential with the continuous emergence of anticancer resistance. Secondary metabolites from natural resources played a major role in the discovery of chemotherapy drugs, particularly those from plant and microbial origins. Although fungi represent a valuable source of promising cytotoxic molecules, none of the fungal secondary metabolites or any of their derivatives have been successfully approved for cancer management in the clinical settings. As part of a multidisciplinary project to identify and develop anticancer leads from fungal origin, my research work involved the development of a local prolonged-release drug delivery system of eupenifeldin, a fungal secondary metabolite with potent cytotoxic properties. This delivery system significantly reduced the reoccurrence of lung cancer in *in vitro* and *in vivo* models. In addition, various fermentation conditions were investigated to enhance the obtained yield of the two main *cis*-enone RALs (hypothemycin and 5Z-7-oxozeaenol) from fungal strains MSX78495 and MSX63935, and the photoactivated perylenequinones (mainly *ent*-shiraiachrome A) from *Shiraia*-like sp. (strain MSX60519). These studies allowed for the isolation and purification of 1043 mg of hypothemycin, 760 mg of 5Z-7-oxozeaenol, and over 700 mg of *ent*-shiraiachrome A. In addition, the redox behavior of fungal perylenequinones were investigated and allowed for better understanding the biosynthesis of these fungal secondary metabolites. Overall, this work allowed the identification of 34 fungal secondary metabolites, of which 26 are known and eight are new.

PRECLINICAL DEVELOPMENT OF FUNGAL SECONDARY METABOLITES AND  
THE DISCOVERY OF NEW METABOLITES WITH CYTOTOXIC PROPERTIES

by

Zeinab Y. A Subeh

A DISSERTATION

Submitted to

the Faculty of The Graduate School at

The University of North Carolina at Greensboro

in Partial Fulfillment

of the Requirements for the Degree

Doctor of Philosophy

Greensboro

2021

Approved by

Dr. Nicholas Oberlies

Committee Chair

APPROVAL PAGE

This dissertation written by Zeinab Y. Al Subeh has been approved by the following committee of the Faculty of The Graduate School at The University of North Carolina at Greensboro.

Committee Chair      Dr. Nicholas Oberlies

Committee Members      Dr. Mitchell Croatt

Dr. Shabnam Hematian

Dr. Nadja Cech

Dr. Aaron Colby

5/26/2021

Date of Acceptance by Committee

5/26/2021

Date of Final Oral Examination

## ACKNOWLEDGEMENTS

I am grateful to God (Alhamdulillah) who gave me the strength to keep going through this four-year journey in the biochemistry PhD program at University of North Carolina at Greensboro (UNCG). This would not become true without all the great professors, colleagues, and friends who surrounded me with their guidance and caring. I was fortunate to have the opportunity to know you all and learn from you. I will always be thankful that I got the chance to pursue my PhD under the mentorship of Prof. Nicholas Oberlies. His tremendous support, encouragement, patience, and guidance is what made me a good chemist and a better scientist. I cannot imagine having a better advisor and I will forever remember his appreciable advices. I would also like to thank my committee members: Dr. Mitchell Croatt, Dr. Shabnam Hematian, Prof. Nadja Cech, and Dr. Aaron Colby. I am glad I had the opportunity to work on various projects under your guidance and mentoring. My PhD experience was enriched with what I learned from you, starting from local drug delivery with Dr. Aaron Colby, to semisynthesis with Dr. Mitchell Croatt, to redox activity with Dr. Shabnam Hematian, and quantitative analysis with Prof. Nadja Cech.

I truly want to thank my colleagues and lab mates in Oberlies research group who helped training me throughout the PhD program. I especially would like to thank Dr. Tamam El-Elimat, Dr. José Rivera-Chávez, and Dr. Laura Flores-Bocanegra for helping me mastering the isolation, purification, and structural elucidation of fungal secondary metabolites, Mr. Tyler Graf for his continuous guidance and making the work going smoothly in the lab, and Dr. Huzefa Raja for his support and for help growing and identifying the wonderful fungi I worked on. Special thank you goes to Jennifer Obike, the undergraduate who helped me isolating gram quantities of priceless secondary metabolites. I also appreciate the collaboration opportunities I had with other scientists and PhD students. I particularly mention, Dr. Sherri McFarland, Dr. Mark Grinstaff, Dr. Joanna Burdette, Dr. James Fuchs, Tian Li, Ngoc-Quynh Chu, and Jeremy Korunes-Miller.

I want to thank all the individuals who I met throughout this journey and became good friends, particularly Soumia Amrine, Diana Kao, and Laura Bocanegra. Special thank you goes to Herma Pierre for always being there for me. You were a great support and help, and we really had unforgettable time and laughs together.

The last but not the least, exceptional thank you goes to my Mom and Dad who believed in me and surrounded with their love and prayers over the days and nights. Thank you to my brothers, sisters, uncles, and aunts.

## TABLE OF CONTENTS

LIST OF TABLES .....	viii
LIST OF FIGURES .....	x
CHAPTER I: Introduction .....	1
CHAPTER II: Delivery of Eupenifeldin via Polymer-Coated Surgical Buttresses Prevents Local Lung Cancer Recurrence.....	8
Introduction.....	8
Materials and Methods.....	11
Results and Discussion .....	16
Conclusion .....	27
Funding .....	27
Supplementary Data.....	28
CHAPTER III: Media and Strain Studies for the Scaled Production of <i>cis</i> -Enone Resorcylic Acid Lactones as Feedstocks for Semisynthesis .....	42
Introduction.....	42
Results and Discussion .....	44
Discussion.....	54
Conclusion .....	56
Material and Methods .....	56
Funding .....	60
Supplementary Data.....	61
CHAPTER IV: Enhanced Production and Anticancer Properties of Photoactivated Perylenequinones .....	111
Introduction.....	111

Results and Discussion .....	114
Conclusion .....	127
Materials and Methods.....	128
Funding .....	134
Supplementary Data.....	135
CHAPTER V: Thielavins: Tuned Biosynthesis and LR-HSQMBC for Structure Elucidation..	166
Introduction.....	166
Results and Discussion .....	167
Conclusion .....	174
Materials and Methods.....	175
Funding .....	177
Supplementary Data.....	178
CHAPTER VI: Redox Behaviors of Perylenequinones Drive their Structural Diversity .....	198
Introduction.....	198
Results and Discussion .....	201
Conclusion .....	215
Materials and Methods.....	215
Supplementary Data.....	221
CHAPTER VII: Three diketomorpholines from a <i>Penicillium</i> sp. (strain G1071) .....	262
Introduction.....	262
Results and Discussion .....	263
Conclusion .....	271
Materials and Methods.....	272
Funding .....	278

Supplementary Data.....	278
REFERENCES .....	312

## LIST OF TABLES

Table 2.1. The number of layers and the composition of formulations <b>1-6</b> of eupenifeldin-loaded butters ..... 30	30
Table 2.2. Precision (RSD%) and accuracy (RE%) of eupenifeldin calibration curves .....34	34
Table 2.3. <i>In vivo</i> dose titration study of “free” eupenifeldin dissolved in 50/50 Cremophor EL/ethanol. The MTD was not reached and is < 20 $\mu\text{g}$ .....38	38
Table 3.1. $^1\text{H}$ and $^{13}\text{C}$ NMR spectroscopic data for <b>19</b> and <b>20</b> in $\text{DMSO-}d_6$ .....54	54
Table 3.2. The calibration curve parameters used for the quantitative analysis of hypothemycin ( <b>1</b> ) and (5 <i>Z</i> )-7-oxozeaenol ( <b>2</b> ) .....67	67
Table 3.3. Comparison between the application of reverse-phase HPLC vs. resuspension/centrifugation techniques in the purification process of hypothemycin and (5 <i>Z</i> )-7-oxozeaenol .....109	109
Table 4.1. NMR Spectroscopic Data for <b>5</b> and <b>8</b> in $\text{CDCl}_3$ (500 MHz for $^1\text{H}$ and 125 MHz for $^{13}\text{C}$ , $\delta$ in ppm) .....120	120
Table 4.2. $\text{EC}_{50}$ Values of Compounds <b>1</b> , <b>3</b> , and <b>5-8</b> against SK-MEL-28 Cancer Cells .....126	126
Table 4.3. Summary of the nomenclature that has been used for the key members of the hypocrellin family of perylenequinones .....135	135
Table 4.4. NMR Spectroscopic Data for <b>1</b> , <b>3</b> , and <b>6-7</b> in $\text{CDCl}_3$ ( $\delta$ in ppm) .....164	164
Table 5.1. $^1\text{H}$ and $^{13}\text{C}$ NMR data of <b>4</b> in $\text{CDCl}_3$ .....172	172
Table 5.2. $\text{IC}_{50}$ ( $\mu\text{M}$ ) values of <b>1-4</b> against three human cancer cell lines .....174	174
Table 5.3. $^1\text{H}$ and $^{13}\text{C}$ NMR data of compounds <b>1-3</b> .....195	195
Table 5.4. Collected $^1\text{H}$ and $^{13}\text{C}$ NMR data of <b>1</b> as compared to the literature .....196	196
Table 5.5. Collected $^1\text{H}$ and $^{13}\text{C}$ NMR data of <b>2</b> as compared to the literature .....197	197
Table 6.1. NMR Spectroscopic Data for <b>7</b> in $\text{CDCl}_3$ (700 MHz for $^1\text{H}$ and 175 MHz for $^{13}\text{C}$ , $\delta$ in ppm). .....200	200

Table 6.2. $E_{1/2}$ , $\Delta E_{1/2}$ , and $i_{pa}/i_{pc}$ values for the cyclic voltammograms of <b>1-6</b> in MeCN with 100mM of [(nBu) <sub>4</sub> N][PF <sub>6</sub> ] as the supporting electrolyte.....	227
Table 6.3. NMR Spectroscopic Data for <b>8-10</b> in CDCl <sub>3</sub> ( $\delta$ in ppm) .....	231
Table 6.4. NMR Spectroscopic Data for <b>11-12</b> in CDCl <sub>3</sub> ( $\delta$ in ppm) .....	257
Table 7.1. <sup>1</sup> H and <sup>13</sup> C NMR data in CDCl <sub>3</sub> for <b>1</b> and CD <sub>3</sub> CN for <b>2</b> and <b>3</b> . .....	265
Table 7.2. Collected <sup>1</sup> H and <sup>13</sup> C NMR data of <b>1</b> in CDCl <sub>3</sub> as compared to the literature .....	285
Table 7.3. Collected <sup>1</sup> H and <sup>13</sup> C NMR data of <b>4</b> in CDCl <sub>3</sub> as compared to the literature .....	288
Table 7.4. Cytotoxic activities of compounds <b>1</b> & <b>2</b> (IC <sub>50</sub> in $\mu$ M) against three cancer cell lines .....	310
Table 7.5. Minimal Inhibitory Concentrations (MICs) in $\mu$ g/mL for compounds <b>1-3</b> against a series of pathogenic microorganisms .....	310

## LIST OF FIGURES

Figure 2.1. Paradigms of treatment for early stage non-small cell lung cancer (NSCLC) patients .....	10
Figure 2.2. Kinetics of eupenifeldin release .....	18
Figure 2.3. <i>In vitro</i> cytotoxicity of eupenifeldin-loaded buttresses .....	20
Figure 2.4. Local recurrence-free survival ( <b>A.</b> ), disease-specific survival ( <b>B.</b> ), and overall survival ( <b>C.</b> ) after surgical resection of tumors .....	23
Figure 2.5. Tissue necrosis surrounding eupenifeldin-loaded buttress ( <b>A.</b> ) .....	24
Figure 2.6. <sup>1</sup> H NMR spectrum of eupenifeldin [500 MHz, CDCl <sub>3</sub> ] .....	28
Figure 2.7. UPLC chromatograms of eupenifeldin (UV detection), demonstrating >97% purity .....	29
Figure 2.8. Eupenifeldin solubility in PBS solutions with various concentrations of Tween 80 .....	31
Figure 2.9. The amount of eupenifeldin released in 20, 50, and 100 mL solutions of PBS (2% Tween 80).....	32
Figure 2.10. SEM images of uncoated PGA buttress (A) and eupenifeldin-loaded formulations <b>1-6</b> (B-G) .....	33
Figure 2.11. Timeline of the <i>in vitro</i> release study .....	33
Figure 2.12. Calibration curves for evaluating the concentration of eupenifeldin .....	35
Figure 2.13. Eupenifeldin growth inhibition effect in disease-oriented human tumor cell line panel .....	36
Figure 2.14. IC <sub>50</sub> values of eupenifeldin against Lewis lung carcinoma (A) and human lung carcinoma A549 (B) cell lines .....	37
Figure 2.15. <i>In vivo</i> dose titration study of eupenifeldin-loaded buttresses demonstrated that 100 μg was the maximum tolerated dose.....	39
Figure 2.16. Stability of PGA buttress in dichloromethane vs hexafluoro-2-propanol .....	40

Figure 2.17. Panel A: PGA buttress coated with alternating layers of phycocyanobilin-polymer layer ( <b>1</b> & <b>3</b> , blue color) and <i>ent</i> -shiraiachrome A-polymer layer ( <b>2</b> & <b>4</b> , red color). Panel B: representative diagram for the coated buttress in panel A .....	41
Figure 3.1. Structures of hypothemycin ( <b>1</b> ) and (5Z)-7-oxozeaenol ( <b>2</b> ).....	45
Figure 3.2. Panels A and B show the relative percentages and the absolute amounts of hypothemycin ( <b>1</b> ), respectively, across cultures grown on rice, oatmeal, and Cheerios media. Panels C and D show the relative percentages and the absolute amounts of (5Z)-7-oxozeaenol ( <b>2</b> ), respectively, across cultures grown on the same three media.....	47
Figure 3.3. Illustration of the isolation and purification protocol of hypothemycin ( <b>1</b> ) showing how <b>1</b> can be generated both from a column fraction and via centrifugation .....	49
Figure 3.4. Illustration of the isolation and purification protocol of (5Z)-7-oxozeaenol.....	50
Figure 3.5. Fungal secondary metabolites produced by strains MSX78495 and MSX63935.....	52
Figure 3.6. HRESIMS data (base peak chromatograms) for the extracts of strains MSX78495, MSX63935, and MSX45109, where the presence of hypothemycin ( <b>1</b> ) and (5Z)-7-oxozeaenol ( <b>2</b> ) were identified via dereplication .....	61
Figure 3.7. The three <i>cis</i> -enone RALs-producing fungi grown in triplicates on three different media: rice, oatmeal, and Cheerios.....	62
Figure 3.8. Representative images of the three fungal strains MSX78495, MSX63935, and MSX45109 grown on three different media (i.e. rice, oatmeal, and Cheerios) .....	63
Figure 3.9. The extract amounts produced by the fungal strains MSX78495, MSX63935, and MSX45109 grown on rice, oatmeal, and Cheerios .....	64
Figure 3.10. UPLC-HRESIMS chromatograms of the extracts of the cultures from Fig. 3.9, all prepared at a concentration of 0.3 mg/mL.....	65
Figure 3.11. Calibration curves for hypothemycin (A) and (5Z)-7-oxozeaenol (B) developed to measure the absolute amounts for these two compounds across various extracts.....	66
Figure 3.12. First round of fractionation for the fungal extracts of MSX78495 via normal-phase flash chromatography to obtain six fractions (F.1-F.6).....	68

Figure 3.13. <b>A:</b> $^1\text{H}$ NMR spectrum of fraction 4 from the flash chromatography shown in Fig. 3.12, demonstrating the purity of hypothemycin [400 MHz, $\text{CDCl}_3$ ]. <b>B:</b> UPLC chromatogram (PDA detection) of fraction 4 from the flash chromatography shown in Fig. 3.12, demonstrating >97% purity .....	69
Figure 3.14. <b>A:</b> $^1\text{H}$ NMR spectrum of fraction 3 from the flash chromatography shown in Fig. 3.12, demonstrating the purity of hypothemycin [400 MHz, $\text{CDCl}_3$ ]. <b>B:</b> UPLC chromatogram (PDA detection) of fraction 3 from the flash chromatography shown in Fig. 3.12, demonstrating ~68% hypothemycin content .....	70
Figure 3.15. <b>A:</b> $^1\text{H}$ NMR spectrum of the hypothemycin precipitate after two cycles of reconstitution and centrifugation in MeOH [400 MHz, $\text{CDCl}_3$ ]. <b>B:</b> UPLC chromatograms (PDA detection) of the hypothemycin precipitate after two cycles of reconstitution and centrifugation in MeOH, demonstrating > 94% purity .....	71
Figure 3.16. $^1\text{H}$ NMR spectrum of the supernatants as compared to the precipitate after two cycles of reconstitution and centrifugation in MeOH [400 MHz, $\text{CDCl}_3$ ].....	72
Figure 3.17. Fractionation via normal-phase flash chromatography for the fungal extract MSX63935 grown on rice .....	73
Figure 3.18. <b>A:</b> $^1\text{H}$ NMR spectrum of fraction 3 from the flash chromatography shown in Fig. 3.17, demonstrating the purity of (5 <i>Z</i> )-7-oxozeaenol [400 MHz, $\text{CDCl}_3$ ]. <b>B:</b> UPLC chromatogram (PDA detection) of fraction 3 from the flash chromatography shown in Fig. 3.17, ~68% (5 <i>Z</i> )-7-oxozeaenol content .....	74
Figure 3.19. <b>A:</b> $^1\text{H}$ NMR spectrum of the (5 <i>Z</i> )-7-oxozeaenol precipitate after four cycles of reconstitution and centrifugation in MeOH and $\text{CH}_3\text{CN}$ [400 MHz, $\text{CDCl}_3$ ]. <b>B:</b> UPLC chromatograms (PDA detection) of the (5 <i>Z</i> )-7-oxozeaenol precipitate after four cycles of reconstitution and centrifugation, demonstrating > 94% purity.....	75
Figure 3.20. $^1\text{H}$ NMR spectrum of the MSX63935 supernatants collected after each cycle of the reconstitution and centrifugation process [400 MHz, $\text{CDCl}_3$ ].....	76
Figure 3.21. $^1\text{H}$ and $^{13}\text{C}$ NMR spectra of hypothemycin ( <b>1</b> ) [400 MHz for $^1\text{H}$ and 100 MHz for $^{13}\text{C}$ , $\text{CDCl}_3$ ].....	77
Figure 3.22. $^1\text{H}$ and $^{13}\text{C}$ NMR spectra of (5 <i>Z</i> )-7-oxozeaenol ( <b>2</b> ) [400 MHz for $^1\text{H}$ and 100 MHz for $^{13}\text{C}$ , $\text{CDCl}_3$ ].....	78
Figure 3.23. $^1\text{H}$ and $^{13}\text{C}$ NMR spectra of dihydrohypothemycin ( <b>3</b> ) [400 MHz for $^1\text{H}$ and 100 MHz for $^{13}\text{C}$ , $\text{CDCl}_3$ ].....	79

Figure 3.24. $^1\text{H}$ and $^{13}\text{C}$ NMR spectra of aigialomycin A ( <b>4</b> ) [400 MHz for $^1\text{H}$ and 100 MHz for $^{13}\text{C}$ , $\text{CDCl}_3$ ]	80
Figure 3.25. $^1\text{H}$ and $^{13}\text{C}$ NMR spectra of paecilomycin A ( <b>5</b> ) [400 MHz for $^1\text{H}$ and 100 MHz for $^{13}\text{C}$ , $\text{DMSO}-d_6$ ]	81
Figure 3.26. $^1\text{H}$ NMR spectrum of 4-O-demethylhypothemycin ( <b>6</b> ) [400 MHz, $\text{DMSO}-d_6$ ]	82
Figure 3.27. $^1\text{H}$ and $^{13}\text{C}$ NMR spectra of (5 <i>E</i> )-7-oxozeaenol ( <b>7</b> ) [400 MHz for $^1\text{H}$ and 100 MHz for $^{13}\text{C}$ , $\text{DMSO}-d_6$ ]	83
Figure 3.28. $^1\text{H}$ and $^{13}\text{C}$ NMR spectra of LL-Z1640-1 ( <b>8</b> ) [500 MHz for $^1\text{H}$ and 125 MHz for $^{13}\text{C}$ , $\text{CDCl}_3$ ]	84
Figure 3.29. $^1\text{H}$ and $^{13}\text{C}$ NMR spectra of zeaenol ( <b>9</b> ) [400 MHz for $^1\text{H}$ and 100 MHz for $^{13}\text{C}$ , $\text{CDCl}_3$ ]	85
Figure 3.30. $^1\text{H}$ and $^{13}\text{C}$ NMR spectra of 7- <i>epi</i> -zeaenol ( <b>10</b> ) [400 MHz for $^1\text{H}$ and 100 MHz for $^{13}\text{C}$ , $\text{DMSO}-d_6$ ]	86
Figure 3.31. $^1\text{H}$ and $^{13}\text{C}$ NMR spectra of aigialomycin B ( <b>11</b> ) [400 MHz for $^1\text{H}$ and 100 MHz for $^{13}\text{C}$ , $\text{CDCl}_3$ ]	87
Figure 3.32. $^1\text{H}$ and $^{13}\text{C}$ NMR spectra of cochliomycin F ( <b>12</b> ) [400 MHz for $^1\text{H}$ and 100 MHz for $^{13}\text{C}$ , $\text{DMSO}-d_6$ ]	88
Figure 3.33. $^1\text{H}$ and $^{13}\text{C}$ NMR spectra of radicinin ( <b>13</b> ) [500 MHz for $^1\text{H}$ and 125 MHz for $^{13}\text{C}$ , $\text{CDCl}_3$ ]	89
Figure 3.34. $^1\text{H}$ and $^{13}\text{C}$ NMR spectra of dihydroradicinin ( <b>14</b> ) [400 MHz for $^1\text{H}$ and 100 MHz for $^{13}\text{C}$ , $\text{CDCl}_3$ ]	90
Figure 3.35. $^1\text{H}$ and $^{13}\text{C}$ NMR spectra of alternariol ( <b>15</b> ) [500 MHz for $^1\text{H}$ and 125 MHz for $^{13}\text{C}$ , $\text{DMSO}-d_6$ ]	91
Figure 3.36. $^1\text{H}$ and $^{13}\text{C}$ NMR spectra of alternariol 9-methyl ether ( <b>16</b> ) [500 MHz for $^1\text{H}$ and 125 MHz for $^{13}\text{C}$ , $\text{DMSO}-d_6$ ]	92
Figure 3.37. $^1\text{H}$ and $^{13}\text{C}$ NMR spectra of rhizopycnin D ( <b>17</b> ) [500 MHz for $^1\text{H}$ and 125 MHz for $^{13}\text{C}$ , $\text{DMSO}-d_6$ ]	93
Figure 3.38. $^1\text{H}$ and $^{13}\text{C}$ NMR spectra of palmariol B ( <b>18</b> ) [500 MHz for $^1\text{H}$ and 125 MHz for $^{13}\text{C}$ , $\text{DMSO}-d_6$ ]	94
Figure 3.39. Mass spectrum of palmariol C ( <b>19</b> ) collected via an LTQ-Orbitrap XL mass spectrometer	95

Figure 3.40. $^1\text{H}$ and $^{13}\text{C}$ NMR spectra of palmariol C ( <b>19</b> ) [400 MHz for $^1\text{H}$ and 100 MHz for $^{13}\text{C}$ , DMSO- $d_6$ ] .....	96
Figure 3.41. Edited-HSQC NMR spectrum of palmariol C ( <b>19</b> ) [400 MHz, DMSO- $d_6$ ].....	97
Figure 3.42. COSY NMR spectrum of palmariol C ( <b>19</b> ) [400 MHz, DMSO- $d_6$ ].....	98
Figure 3.43. HMBC NMR spectrum of palmariol C ( <b>19</b> ) [400 MHz, DMSO- $d_6$ ] .....	99
Figure 3.44. NOESY NMR spectrum of palmariol C ( <b>19</b> ) [400 MHz, DMSO- $d_6$ ].....	100
Figure 3.45. Mass spectrum of palmariol D ( <b>20</b> ) collected via an LTQ-Orbitrap XL mass spectrometer.....	101
Figure 3.46. $^1\text{H}$ and $^{13}\text{C}$ NMR spectra of palmariol D ( <b>20</b> ) [500 MHz for $^1\text{H}$ and 125 MHz for $^{13}\text{C}$ , DMSO- $d_6$ ] .....	102
Figure 3.47. Edited-HSQC NMR spectrum of palmariol D ( <b>20</b> ) [400 MHz, DMSO- $d_6$ ] .....	103
Figure 3.48. HMBC NMR spectrum of palmariol D ( <b>20</b> ) [400 MHz, DMSO- $d_6$ ] .....	104
Figure 3.49. NOESY NMR spectrum of palmariol D ( <b>20</b> ) [400 MHz, DMSO- $d_6$ ].....	105
Figure 3.50. Key COSY and HMBC correlations of compounds <b>19</b> and <b>20</b> .....	106
Figure 3.51. NOESY correlations of compounds <b>19</b> and <b>20</b> .....	106
Figure 3.52. Analytical vs Prep HPLC chromatograms for hypothemycin-containing fraction demonstrating a co-elution of dihydrohypothenycin ( <b>3</b> ) with hypothemycin ( <b>1</b> ) despite the optimization of the analytical method .....	107
Figure 3.53. Analytical vs Prep HPLC chromatograms for a (5Z)-7-oxozeaenol-containing fraction demonstrating a co-elution of LL-Z1640-1 ( <b>8</b> ) with (5Z)-7-oxozeaenol ( <b>2</b> ) despite the optimization of the analytical method .....	108
Figure 3.54. Molecular phylogenetic analysis of fungal ITS sequences reveal MSX63935, MSX78495, and MSX45109 are members of the genus, <i>Setophoma</i> ( <i>Phaeosphaeriaceae</i> , <i>Ascomycota</i> ).....	110
Figure 4.1. Chemical structure of compounds <b>1-5</b> .....	113
Figure 4.2. Panels A and B show the relative percentages of <b>5</b> and <b>1</b> , respectively, across cultures grown on rice, Cheerios, and oatmeal media under 12:12 h light:dark cycles, continuous LED, or in darkness .....	117

Figure 4.3. The atropisomerization process (A) and the tautomerism process (B) of hypocrellins.....	119
Figure 4.4. Panels A-C show the relative percentages of 6-8, respectively, across cultures grown on rice, Cheerios, and oatmeal media under 12:12 h light:dark cycles, continuous LED, or in darkness .....	122
Figure 4.5. Experimental ECD spectrum of <b>6</b> compared with calculated ECD spectra of [ <i>M(R)</i> , 1 <i>S</i> , 2 <i>R</i> , 14 <i>R</i> , 15 <i>S</i> , 17 <i>R</i> ]- configuration and its enantiomer (left frame), and [ <i>M(R)</i> , 1 <i>R</i> , 2 <i>S</i> , 14 <i>S</i> , 15 <i>R</i> , 17 <i>S</i> ]- configuration and its enantiomer (right frame).....	123
Figure 4.6. Experimental VCD (left frame) and IR (right frame) spectra observed for hypomycin A ( <b>6</b> ) compared with calculated VCD and IR spectra of [ <i>M(R)</i> , 1 <i>S</i> , 2 <i>R</i> , 14 <i>R</i> , 15 <i>S</i> , 17 <i>R</i> ]-configuration (0.65 similarity factor to <b>6</b> ) and [ <i>M(R)</i> , 1 <i>R</i> , 2 <i>S</i> , 14 <i>S</i> , 15 <i>R</i> , 17 <i>S</i> ]- configuration (0.11 similarity factor to <b>6</b> ).....	124
Figure 4.7. Key HMBC (A) and NOESY (B) correlations for hypomycin E ( <b>8</b> ).....	125
Figure 4.8. Panel A: photocytotoxic activity plot for compounds 1, 3, and 5-8 against SK-MEL-28 melanoma cells without (black) or with visible- (blue) or red- (red) light irradiation. Panel B: phototherapeutic index (PI) activity plot for compounds <b>1</b> , <b>3</b> , <b>5-8</b> against SK-MEL-28 melanoma cells treated with visible- (blue) or red- light (red) .....	127
Figure 4.9. The extract amounts produced by cultures grown on rice, Cheerios, and oatmeal media under 12:12 h light:dark cycles, continuous LED light, or in complete darkness.....	136
Figure 4.10. UPLC-HRESIMS chromatograms of the extracts of the cultures from Fig. 4.9, all prepared at a concentration of 0.3 mg/mL .....	136
Figure 4.11. <i>In vitro</i> concentration–response curves for extracts obtained from MSX60519 cultures grown under different conditions .....	137
Figure 4.12. Analytical HPLC chromatogram for the second flash chromatography fractions obtained from MSX60519 cultures grown on rice medium and exposed to either light:dark cycles or continuous LED light .....	138
Figure 4.13. (+)-HRESIMS spectra of compounds <b>1</b> , <b>3</b> , and <b>5-8</b> .....	139
Figure 4.14. ECD spectra for compounds <b>1</b> and <b>5-8</b> in CH <sub>3</sub> OH at a concentration of 0.2 mg/mL.....	140

Figure 4.15. $^1\text{H}$ and $^{13}\text{C}$ NMR spectra of <i>ent</i> -shiraiachrome A ( <b>5</b> ) [500 MHz for $^1\text{H}$ and 125 MHz for $^{13}\text{C}$ , $\text{CDCl}_3$ ]	141
Figure 4.16. Edited-HSQC NMR spectrum of <i>ent</i> -shiraiachrome A ( <b>5</b> ) [400 MHz, $\text{CDCl}_3$ ]	142
Figure 4.17. COSY NMR spectrum of <i>ent</i> -shiraiachrome A ( <b>5</b> ) [500 MHz, $\text{CDCl}_3$ ]	143
Figure 4.18. HMBC NMR spectrum of <i>ent</i> -shiraiachrome A ( <b>5</b> ) [500 MHz, $\text{CDCl}_3$ ]	144
Figure 4.19. NOESY NMR spectrum of <i>ent</i> -shiraiachrome A ( <b>5</b> ) [500 MHz, $\text{CDCl}_3$ ]	145
Figure 4.20. $^1\text{H}$ and $^{13}\text{C}$ NMR spectra of hypocrellin ( <b>1</b> ) [400 MHz for $^1\text{H}$ and 100 MHz for $^{13}\text{C}$ , $\text{CDCl}_3$ ]	146
Figure 4.21. $^1\text{H}$ and $^{13}\text{C}$ NMR spectra of hypocrellin B ( <b>3</b> ) [500 MHz for $^1\text{H}$ and 125 MHz for $^{13}\text{C}$ , $\text{CDCl}_3$ ]	147
Figure 4.22. The amounts isolated of compounds <b>6</b> (A), <b>7</b> (B), and <b>8</b> (C) from cultures grown on rice, Cheerios, and oatmeal media under either 12:12 h light:dark cycles or LED light	148
Figure 4.23. $^1\text{H}$ and $^{13}\text{C}$ NMR spectra of hypomycin A ( <b>6</b> ) [400 MHz for $^1\text{H}$ and 100 MHz for $^{13}\text{C}$ , $\text{CDCl}_3$ ]	149
Figure 4.24. $^1\text{H}$ and $^{13}\text{C}$ NMR spectra of hypomycin C ( <b>7</b> ) [400 MHz for $^1\text{H}$ and 100 MHz for $^{13}\text{C}$ , $\text{CDCl}_3$ ]	150
Figure 4.25. NOESY NMR spectrum of hypomycin A ( <b>6</b> ) [500 MHz, $\text{CDCl}_3$ ]	151
Figure 4.26. NOESY NMR spectrum of hypomycin C ( <b>7</b> ) [500 MHz, $\text{CDCl}_3$ ]	152
Figure 4.27. Key NOESY correlations of hypomycin A ( <b>6</b> ) and hypomycin C ( <b>7</b> )	153
Figure 4.28. $^1\text{H}$ and $^{13}\text{C}$ NMR spectra of hypomycin E ( <b>8</b> ) [400 MHz for $^1\text{H}$ and 125 MHz for $^{13}\text{C}$ , $\text{CDCl}_3$ ]	154
Figure 4.29. Edited-HSQC NMR spectrum of hypomycin E ( <b>8</b> ) [500 MHz, $\text{CDCl}_3$ ]	155
Figure 4.30. COSY NMR spectrum of hypomycin E ( <b>8</b> ) [500 MHz, $\text{CDCl}_3$ ]	156
Figure 4.31. HMBC NMR spectrum of hypomycin E ( <b>8</b> ) [500 MHz, $\text{CDCl}_3$ ]	157
Figure 4.32. NOESY NMR spectrum of hypomycin E ( <b>8</b> ) [500 MHz, $\text{CDCl}_3$ ]	158

Figure 4.33. <i>In vitro</i> concentration–response curves for compounds ( <b>1</b> , <b>3</b> , and <b>5-8</b> ) in SK-MEL-28 cells without (black) or with visible (blue) or red (red) light irradiation .....	159
Figure 4.34. Maximum Likelihood analysis of fungi taxon sampled from two studies on hypocrellin-producing strains in the Pleosporales, Dothideomycetes showing Phylogram of the most likely tree (-lnL = 3561.05) from a RAxML analysis of 56 strains based on ITS region sequence data (403 bp) .....	160
Figure 4.35. Pictures of strain MSX60519 cultures grown on three different media and exposed to three different light conditions .....	161
Figure 4.36. The nine growth conditions utilized to grow strain MSX60519 .....	161
Figure 4.37. UPLC chromatograms of compounds <b>1</b> , <b>3</b> , and <b>5-8</b> PDA detection at 254 nm), demonstrating >97% purity .....	162
Figure 4.38. UV spectra of compounds <b>1</b> , <b>3</b> , and <b>5-8</b> analyzed in CH <sub>3</sub> OH at a concentration of 0.0125 mg/mL. ....	163
Figure 5.1. Structures of compounds <b>1-4</b> .....	168
Figure 5.2. Panels A-D show the relative percentages of <b>1-4</b> , respectively, across cultures grown on rice, Cheerios, and oatmeal media under 12:12 h light:dark cycles, continuous LED, or in darkness .....	169
Figure 5.3. Key LR-HSQMBC correlations of compound <b>1</b> .....	171
Figure 5.4. Key HMBC correlations of compound <b>4</b> .....	173
Figure 5.5. Intra- and inter-ring NOESY correlations for <b>3</b> and <b>4</b> .....	174
Figure 5.6. (+)-HRESIMS data of compounds <b>1-4</b> .....	178
Figure 5.7. <sup>1</sup> H and <sup>13</sup> C NMR spectra of compound <b>1</b> [500 MHz for <sup>1</sup> H and 125 MHz for <sup>13</sup> C, Pyridine- <i>d</i> <sub>5</sub> ].....	179
Figure 5.8. HMBC NMR spectrum of compound <b>1</b> [500 MHz, Pyridine- <i>d</i> <sub>5</sub> ] .....	180
Figure 5.9. LR-HSQMBC NMR spectrum of compound <b>1</b> [500 MHz, Pyridine- <i>d</i> <sub>5</sub> ].....	181
Figure 5.10. <sup>1</sup> H and <sup>13</sup> C NMR spectra of compound <b>2</b> [500 MHz for <sup>1</sup> H and 125 MHz for <sup>13</sup> C, CD <sub>3</sub> OD].....	182

Figure 5.11. $^1\text{H}$ and $^{13}\text{C}$ NMR spectra of compound <b>3</b> [700 MHz for $^1\text{H}$ and 175 MHz for $^{13}\text{C}$ , $\text{CDCl}_3$ ].....	183
Figure 5.12. HMBC NMR spectrum of compound <b>3</b> [700 MHz, $\text{CDCl}_3$ ].....	184
Figure 5.13. Key HMBC correlations of compound <b>3</b> .....	185
Figure 5.14. $^1\text{H}$ and $^{13}\text{C}$ NMR spectra of compound <b>4</b> [700 MHz for $^1\text{H}$ and 175 MHz for $^{13}\text{C}$ , $\text{CDCl}_3$ ].....	186
Figure 5.15. Edited-HSQC NMR spectrum of compound <b>4</b> [700 MHz, $\text{CDCl}_3$ ].....	187
Figure 5.16. HMBC NMR spectrum of compound <b>4</b> [700 MHz, $\text{CDCl}_3$ ].....	188
Figure 5.17. LR-HSQMBC NMR spectrum of compound <b>4</b> [400 MHz, $\text{CDCl}_3$ ].....	189
Figure 5.18. Key LR-HSQMBC correlations of compound <b>4</b> .....	190
Figure 5.19. (+)-HRESIMS fragmentation of <b>1-4</b> .....	191
Figure 5.20. NOESY NMR spectrum of compound <b>3</b> [400 MHz, $\text{CDCl}_3$ ].....	192
Figure 5.21. NOESY NMR spectrum of compound <b>4</b> [400 MHz, $\text{CDCl}_3$ ].....	193
Figure 5.22. UV spectra of compounds <b>3</b> and <b>4</b> analyzed in $\text{CH}_3\text{OH}$ (0.0125 mg/mL).....	194
Figure 6.1. Structures of the hypocrellins ( <b>1-3</b> ) and hypomyces ( <b>4-6</b> ) discussed in this study.....	200
Figure 6.2. Structure of compound <b>7</b> (A) as compared to the synthetic precursor used in the total synthesis of hypocrellin A (B) as reported by O'Brien <i>et al.</i> .....	202
Figure 6.3. Compound <b>7</b> as a common precursor for class B perylenequinone derivatives.....	204
Figure 6.4. Normalized cyclic voltammograms of hypocrellins ( <b>1-3</b> ) and hypomyces ( <b>4-6</b> ) in acetonitrile with 100 mM of $[(n\text{Bu}_4)\text{N}][\text{PF}_6]$ as the supporting electrolyte.....	205
Figure 6.5. UV-vis spectroelectrochemistry spectra of the first (semiquinone radical anion form, $\text{SQ}^{\cdot-}$ ) and second (hydroquinone form, $\text{Q}^{2-}$ ) reductions of <i>ent</i> -shiraiachrome A ( <b>1</b> ) (248 $\mu\text{M}$ ) in acetonitrile with 0.1 M $[(n\text{Bu})_4\text{N}][\text{PF}_6]$ as the supporting electrolyte.....	206
Figure 6.6. Generation of <b>8-10</b> via reduction of <i>ent</i> -shiraiachrome A ( <b>1</b> ) under aerobic conditions.....	208

Figure 6.7. UPLC-PDA-HRESIMS chromatogram of anaerobic reduction reaction of A) <i>ent</i> -shiraiachrome A ( <b>1</b> ) and B) hypocrellin ( <b>2</b> ).....	209
Figure 6.8. Derivatives obtained by chemical reduction of <i>ent</i> -shiraiachrome A ( <b>1</b> ) with Na <sub>2</sub> S <sub>2</sub> O <sub>4</sub> under anaerobic condition .....	211
Figure 6.9. X-ray crystallography of hypocrellin B ( <b>3</b> ).....	213
Figure 6.10. Structural similarity between hypocrellin ( <b>2</b> ) and cercosporin. ....	221
Figure 6.11. UPLC-(+)-HRESIMS chromatogram of <b>7</b> .....	221
Figure 6.12. UV spectrum of <b>7</b> in methanol at concentration of 0.0125 mg/mL.....	222
Figure 6.13. <sup>1</sup> H and <sup>13</sup> C NMR spectra of <b>7</b> [700 MHz for <sup>1</sup> H and 175 MHz for <sup>13</sup> C, CDCl <sub>3</sub> ].....	223
Figure 6.14. Edited-HSQC NMR spectrum of <b>7</b> [700 MHz, CDCl <sub>3</sub> ].....	224
Figure 6.15. COSY NMR spectrum of <b>7</b> [700 MHz, CDCl <sub>3</sub> ].....	225
Figure 6.16. HMBC NMR spectrum of <b>7</b> [700 MHz, CDCl <sub>3</sub> ].....	226
Figure 6.17. Key HMBC correlations of <b>7</b> .....	227
Figure 6.18. Small scale reduction reactions of <i>ent</i> -shiraiachrome A ( <b>1</b> ), hypocrellin ( <b>2</b> ), and hypocrellin B ( <b>3</b> ) with Na <sub>2</sub> S <sub>2</sub> O <sub>4</sub> under aerobic condition.....	228
Figure 6.19. UPLC-PDA-HRESIMS chromatogram of <i>ent</i> -shiraiachrome A ( <b>1</b> ) before and after treatment with Na <sub>2</sub> S <sub>2</sub> O <sub>4</sub> as a reducing agent overnight.....	228
Figure 6.20. UPLC-PDA-HRESIMS chromatogram of hypocrellin ( <b>2</b> ) before and after treatment with Na <sub>2</sub> S <sub>2</sub> O <sub>4</sub> as a reducing agent overnight .....	229
Figure 6.21. UPLC-PDA-HRESIMS chromatogram of hypocrellin B ( <b>3</b> ) before and after treatment with Na <sub>2</sub> S <sub>2</sub> O <sub>4</sub> as a reducing agent overnight .....	229
Figure 6.22. UPLC-PDA-HRESIMS chromatograms for the four replicates aerobic reduction reactions of <i>ent</i> -shiraiachrome A ( <b>1</b> ) with Na <sub>2</sub> S <sub>2</sub> O <sub>4</sub> (10 mg of <b>1</b> was used in each reaction) .....	230
Figure 6.23. <sup>1</sup> H and <sup>13</sup> C NMR spectra of <b>8</b> [400 MHz for <sup>1</sup> H and 100 MHz for <sup>13</sup> C, CDCl <sub>3</sub> ].....	233
Figure 6.24. <sup>1</sup> H and <sup>13</sup> C NMR spectra of <b>9</b> [500 MHz for <sup>1</sup> H and 125 MHz for <sup>13</sup> C, CDCl <sub>3</sub> ].....	234
Figure 6.25. <sup>1</sup> H and <sup>13</sup> C NMR spectra of <b>10</b> [700 MHz for <sup>1</sup> H and 175 MHz for <sup>13</sup> C, CDCl <sub>3</sub> ]...	235

Figure 6.26. Key HMBC correlations for compounds <b>8-10</b> .....	236
Figure 6.27. UV spectrum of compounds <b>8-10</b> in methanol at concentration of 0.0125 mg/mL as compared to <i>ent</i> -shiraiachrome A ( <b>1</b> ) .....	237
Figure 6.28. ECD spectra for compounds <b>8-10</b> as compared to <i>ent</i> -shiraiachrome A ( <b>1</b> ) in CH <sub>3</sub> OH at a concentration of 0.2 mg/mL .....	238
Figure 6.29. UPLC-PDA-HRESIMS chromatogram of hypomycin A ( <b>4</b> ) before and after treatment with Na <sub>2</sub> S <sub>2</sub> O <sub>4</sub> as a reducing agent overnight .....	239
Figure 6.30. UPLC-PDA-HRESIMS chromatogram of hypomycin C ( <b>5</b> ) before and after treatment with Na <sub>2</sub> S <sub>2</sub> O <sub>4</sub> as a reducing agent overnight .....	239
Figure 6.31. UPLC-PDA-HRESIMS chromatogram of hypomycin E ( <b>6</b> ) before and after treatment with Na <sub>2</sub> S <sub>2</sub> O <sub>4</sub> as a reducing agent overnight.....	240
Figure 6.32. Small scale reduction reactions of hypomycin A ( <b>4</b> ), C ( <b>5</b> ), and E ( <b>6</b> ) with Na <sub>2</sub> S <sub>2</sub> O <sub>4</sub> under aerobic conditions.....	240
Figure 6.33. UPLC-PDA-HRESIMS chromatograms for the triplicate anaerobic reduction reactions of <i>ent</i> -shiraiachrome A ( <b>1</b> ) with Na <sub>2</sub> S <sub>2</sub> O <sub>4</sub> .....	241
Figure 6.34. UPLC-PDA-HRESIMS chromatograms for the anaerobic reduction reactions of <i>ent</i> -shiraiachrome A ( <b>1</b> ) as compared to UPLC-HRESIMS chromatograms of pure standards of <b>2-6</b> .....	242
Figure 6.35. ECD spectra in CH <sub>3</sub> OH for compounds <b>4-6</b> and <b>11</b> which were isolated from the anaerobic reduction reaction of <b>1</b> and <b>2</b> .....	243
Figure 6.36. Hypomycin A ( <b>4</b> ) obtained by chemical reduction of hypocrellin ( <b>2</b> ) with Na <sub>2</sub> S <sub>2</sub> O <sub>4</sub> under anaerobic condition .....	244
Figure 6.37. Intramolecular hydrogen-bonding between HO-14 and the C-17 carbonyl in the 3D structures of <i>ent</i> -shiraiachrome A ( <b>1</b> ) and hypocrellin ( <b>2</b> ).....	245
Figure 6.38. Keto-enol tautomerism of <i>ent</i> -shiraiachrome A ( <b>1</b> ) at C-17 carbonyl intermediates the conversion process of <b>1</b> into <b>2</b> .....	246
Figure 6.39. <sup>1</sup> H NMR of pure <i>ent</i> -shiraiachrome A ( <b>1</b> ) in DMSO- <i>d</i> <sub>6</sub> ( <b>A</b> ) and <sup>1</sup> H NMR of <b>1</b> in CDCl <sub>3</sub> after exposure to DMSO ( <b>B</b> ).....	247
Figure 6.40. <sup>1</sup> H NMR of pure <i>ent</i> -shiraiachrome A ( <b>1</b> ) in CDCl <sub>3</sub> before and after exposure to DMSO vs <sup>1</sup> H NMR of hypocrellin ( <b>2</b> ) in CDCl <sub>3</sub> .....	248

Figure 6.41. <sup>1</sup> H NMR for the anaerobic reduction reaction mixture of <i>ent</i> -shiraiachrome A (1) as compared to hypomycin E (6) in acetonitrile- <i>d</i> <sub>3</sub> .....	249
Figure 6.42. <sup>1</sup> H NMR for the anaerobic reduction reaction mixture of hypocrellin (2) as compared to hypomycin A (4) in acetonitrile- <i>d</i> <sub>3</sub> .....	250
Figure 6.43. Previously reported structures of hypomycin C (5) and E (6) as compared to <i>ent</i> -shiraiachrome A (1) .....	251
Figure 6.44. Key NOESY correlations of hypomycin C (5) and hypomycin E (6).....	252
Figure 6.45. The observed intramolecular hydrogen-bonding of the exchangeable protons in hypomycin A (4), C (5), and E (6).....	252
Figure 6.46. <sup>1</sup> H NMR of hypomycin A (4) [400 MHz, CDCl <sub>3</sub> ] .....	253
Figure 6.47. <sup>1</sup> H NMR of hypomycin C (5) [400 MHz, CDCl <sub>3</sub> ] .....	254
Figure 6.48. <sup>1</sup> H NMR of hypomycin C (5) [400 MHz, DMSO- <i>d</i> <sub>6</sub> ].....	255
Figure 6.49. <sup>1</sup> H NMR of hypomycin E (6) [400 MHz, CDCl <sub>3</sub> ].....	256
Figure 6.50. <sup>1</sup> H and <sup>13</sup> C NMR spectra of 11 [400 MHz for <sup>1</sup> H and 100 MHz for <sup>13</sup> C, CDCl <sub>3</sub> ].....	259
Figure 6.51. <sup>1</sup> H and <sup>13</sup> C NMR spectra of 12 [700 MHz for <sup>1</sup> H and 175 MHz for <sup>13</sup> C, CDCl <sub>3</sub> ].....	260
Figure 6.52. Key HMBC correlations for compounds 11 and 12.....	261
Figure 7.1. Chemical structures of compounds 1-6 .....	264
Figure 7.2. Key COSY and HMBC correlations of 1-3.....	267
Figure 7.3. Key NOESY correlations of compounds 1-3 .....	268
Figure 7.4. ECD spectra of compounds 1-4 in CH <sub>3</sub> CN .....	269
Figure 7.5. (+)-HRESIMS fragmentation patterns of 1-3.....	269
Figure 7.6. Proposed methanolysis products of 1-4. R <sub>1</sub> and R <sub>2</sub> groups for compounds 1-4 are as noted in Fig. 7.5 .....	270
Figure 7.7. UPLC-(+)-HRESIMS spectrum of 1 .....	279

Figure 7.8. $^1\text{H}$ and $^{13}\text{C}$ NMR spectra of <b>1</b> [400 MHz for $^1\text{H}$ and 100 MHz for $^{13}\text{C}$ , $\text{CDCl}_3$ ] .....	280
Figure 7.9. Edited-HSQC NMR spectrum of <b>1</b> [400 MHz, $\text{CDCl}_3$ ] .....	281
Figure 7.10. COSY NMR spectrum of <b>1</b> [400 MHz, $\text{CDCl}_3$ ] .....	282
Figure 7.11. HMBC NMR spectrum of <b>1</b> [400 MHz, $\text{CDCl}_3$ ] .....	283
Figure 7.12. NOESY NMR spectrum of <b>1</b> [500 MHz, $\text{CDCl}_3$ ] .....	284
Figure 7.13. UPLC-(+)-HRESIMS spectrum of <b>4</b> .....	286
Figure 7.14. $^1\text{H}$ and $^{13}\text{C}$ NMR spectra of <b>4</b> [500 MHz for $^1\text{H}$ and 125 MHz for $^{13}\text{C}$ , $\text{CDCl}_3$ ] .....	287
Figure 7.15. UPLC-(+)-HRESIMS spectrum of <b>2</b> .....	289
Figure 7.16. $^1\text{H}$ and $^{13}\text{C}$ NMR spectra of <b>2</b> [400 MHz for $^1\text{H}$ and 100 MHz for $^{13}\text{C}$ , $\text{CD}_3\text{CN}$ ] .....	290
Figure 7.17. Edited-HSQC NMR spectrum of <b>2</b> [400 MHz, $\text{CD}_3\text{CN}$ ] .....	291
Figure 7.18. COSY NMR spectrum of <b>2</b> [400 MHz, $\text{CD}_3\text{CN}$ ] .....	292
Figure 7.19. HMBC NMR spectrum of <b>2</b> [400 MHz, $\text{CD}_3\text{CN}$ ] .....	293
Figure 7.20. NOESY NMR spectrum of <b>2</b> [400 MHz, $\text{CD}_3\text{CN}$ ] .....	294
Figure 7.21. UPLC-HRESIMS chromatograms of the hydrolysate sample of <b>2</b> and standard tryptophan sample showing the release to Trp by acid hydrolysis .....	295
Figure 7.22. UPLC-PDA chromatograms of tryptophan Marfey's derivative of <b>2</b> .....	296
Figure 7.23. UPLC-(+)-HRESIMS spectrum of <b>3</b> .....	297
Figure 7.24. $^1\text{H}$ and $^{13}\text{C}$ NMR spectra of <b>3</b> [700 MHz for $^1\text{H}$ and 175 MHz for $^{13}\text{C}$ , $\text{CD}_3\text{CN}$ ] .....	298
Figure 7.25. Edited-HSQC NMR spectrum of <b>3</b> [700 MHz, $\text{CD}_3\text{CN}$ ] .....	299
Figure 7.26. COSY NMR spectrum of <b>3</b> [700 MHz, $\text{CD}_3\text{CN}$ ] .....	300
Figure 7.27. HMBC NMR spectrum of <b>3</b> [700 MHz, $\text{CD}_3\text{CN}$ ] .....	301
Figure. 7.28. NOESY NMR spectrum of <b>3</b> [500 MHz, $\text{CD}_3\text{CN}$ ] .....	302

Figure 7.29. MS2 fragmentation patterns of compounds <b>1-3</b> .....	303
Figure 7.30. UPLC-PDA chromatograms of compounds <b>1-4</b> after exposure to methanol for 48 hours at a concentration of 0.2 mg/mL .....	304
Figure 7.31. UPLC-(+)-HRESIMS spectrum of <b>5</b> .....	305
Figure 7.32. <sup>1</sup> H and <sup>13</sup> C NMR spectra of <b>5</b> [400 MHz for <sup>1</sup> H and 100 MHz for <sup>13</sup> C, DMSO-d <sub>6</sub> ].....	306
Figure 7.33. <sup>1</sup> H and <sup>13</sup> C NMR spectra of <b>5:5a</b> mixture [400 MHz for <sup>1</sup> H and 100 MHz for <sup>13</sup> C, DMSO-d <sub>6</sub> ] .....	307
Figure 7.34. UPLC-(+)-HRESIMS spectrum of <b>6</b> .....	308
Figure 7.35. <sup>1</sup> H and <sup>13</sup> C NMR spectra of <b>6</b> [500 MHz for <sup>1</sup> H and 125 MHz for <sup>13</sup> C, DMSO-d <sub>6</sub> ].....	309
Figure 7.36. Phylogram of the most likely tree (-lnL = 5734.34) from a RAxML analysis of 22 taxa based on <i>RPB2</i> sequences (974 bp) from several <i>Penicillium</i> strains belonging to the section <i>Sclerotiora</i> .....	311

## CHAPTER I: INTRODUCTION

Cancer is a generic name given to a large group of diseases caused when cells start to divide uncontrollably and spread into surrounding tissues and/or organs.<sup>1,2</sup> Cancer has captured the attention of a number of scientists and researchers in the healthcare field, as it is still the second leading cause of deaths worldwide.<sup>2</sup> In 2020, cancer was responsible for nearly 10 million deaths with more than 19 million cancer cases diagnosed that year.<sup>3</sup> In the United States, an estimated 1.9 million new cancer cases and 608,570 cancer deaths were projected to occur in 2021.<sup>4</sup> In addition to the high morbidity and mortality rate, cancer care results in a significant economic burden on the healthcare systems of countries all over the world.<sup>5,6</sup> The projected global cost of cancer in 2010 was approximately \$1.16 trillion (US).<sup>7</sup> In the United States, the estimated total cost of cancer care in 2020 was \$173 billion, a 39% increase from 2010.<sup>8</sup> Additionally, while the development of new techniques for cancer detection, diagnosis, and treatment has improved the survival rate among cancer patients, these new developments also translate to further increases in the cost of cancer care.<sup>8</sup>

Various therapeutic modalities are now available for cancer management, and they are usually ascribed to patients based on the type of cancer they have and how advanced it is. These mainly include surgical removal of the primary tumor, chemotherapy, and/or radiotherapy.<sup>9</sup> Chemotherapy represents a powerful tool for cancer treatment and secondary prevention. For instance, neoadjuvant chemotherapy is administered pre-operatively to shrink tumor size to be surgically operable, while adjuvant chemotherapy plays a vital role in the elimination of remaining cancer cells after surgery.<sup>10</sup> Despite the advanced treatment approaches of cancer, the development of new therapeutic agents is still essential with the continuous emergence of drug resistance. During the course of cancer progression, cancer cells tend to differentiate into various heterogeneous forms with diverse molecular features.<sup>11</sup> This heterogeneity in cancer tumor is responsible, at least in part, for the increased prevalence of cancer resistance toward the available chemotherapeutic agents.<sup>12</sup> The ability of cancer cells to manipulate their genomes and metabolism to resist the effect of chemotherapy usually results in cancer relapse or recurrence.<sup>13</sup>

Secondary metabolites from natural resources played a major role in the discovery of chemotherapy drugs, particularly those from plant and microbial origins.<sup>14</sup> According to Newman and Cragg,<sup>15</sup> a total of 185 small-molecules were approved for cancer management in the period between 1981 to 2019. Of these, only 15% were made by total chemical synthesis, while 75% were either natural products, derived from natural products, or inspired by natural products.<sup>15</sup> Plants, in particular, were the source for the majority of anticancer drugs approved by the Food and Drug Administration (FDA). For instance, plant-derived alkaloids in their natural forms, or synthetically modified derivatives, were some of the firstly discovered and approved drugs for cancer treatment, and still used in many of the standard chemotherapeutic regimens.<sup>14</sup><sup>16</sup> Vinca alkaloids, like vincristine, vinblastine, vinorelbine, vindesine and vinflunine, were originally obtained from the pink periwinkle plant, *Catharanthus roseus* G. Don.<sup>17</sup> Taxol (paclitaxel) and its analogue, docetaxel, were discovered from the bark of the Pacific yew, *Taxus brevifolia* Nutt.<sup>18</sup> Plants were also the source of approved topoisomerase I and II inhibitors, such as camptothecin analogs (irinotecan and topotecan) and podophyllotoxins (etoposide and teniposide) that were produced by *Camptotheca acuminata* and *Podophyllum peltatum* L., respectively.<sup>19, 20</sup>

Secondary metabolites from bacteria were the second leading source of the naturally derived anticancer drugs. Among the approved derivatives of microbial metabolites that deserve attention are anthracyclines (daunorubicin, doxorubicin, epirubicin, pirarubicin, and valrubicin) from *Streptomyces peuceitius*, bleomycin from *Streptomyces verticillus*, mitosanes (mitomycin C) from *Streptomyces caespitosus*, anthracenones (mithramycin, streptozotocin and pentostatin) from various *Streptomyces* species, enediynes (calcheamycin) from *Micromonospora echinospora*, and epothilones from *Sorangium cellulosum*.<sup>21</sup> Anthracyclines, in particular, are some of the most commonly used anticancer agents as they exhibit activity against more types of cancer than any other class of chemotherapy agents.<sup>22</sup>

Overall, plants and bacterium were the main sources of naturally-derived anticancer drugs approved by the FDA, while none of the fungal secondary metabolites or any of their derivatives have been successfully approved for cancer management in the clinical settings.<sup>23</sup> However, many of the FDA-approved medicines for various life-threatening conditions were obtained or derived from fungal secondary metabolites. For instance, statins for hypercholesterolemia and

cardiovascular diseases,<sup>24</sup> penicillins and cephalosporins for bacterial infections,<sup>25</sup> fingolimod for multiple sclerosis,<sup>26</sup> caspofungin and griseofulvin for fungal infections,<sup>27, 28</sup> cyclosporin A and mycophenolic acid as immunosuppressants for organ transplantation,<sup>29, 30</sup> and ergotamine for migraine headache<sup>31</sup> are approved drugs that were discovered or synthetically modified from fungal secondary metabolites.

The absence of any chemotherapy drug of fungal origin does not refute that fungi are still a promising reservoir for anticancer leads with novel chemical and biological properties. Fungal secondary metabolites tend to cover a more extensive chemical diversity than compounds produced by synthesis or by combinatorial chemistry.<sup>32</sup> Diverse structural classes were obtained from fungi such as alkaloids, terpenoids, polyketides, steroids, quinones, phenols, cytochalasans, macrolides, naphthalenones, pyrones, coumarins, peptides, and others.<sup>33, 34</sup> A large number of fungal metabolites were reported to exhibit potent cytotoxic activity against cancer cells in *in vitro* and *in vivo* studies.<sup>35-37</sup> In addition to the chemical diversity of fungal-derived cytotoxic agents, they tend to exert a wide variety of mode of actions through different pathways, including pro-apoptotic, anti-angiogenic, antiproliferative, and anti-migratory effects.<sup>35</sup>

Several fungal species have been shown to also produce compounds that have become FDA-approved anticancer agents.<sup>38</sup> For instance, the discovery of taxol represented a breakthrough in cancer chemotherapy for its unique mode of action as enhancer of tubulin polymerization.<sup>39, 40</sup> Taxol usually described as a plant-derived anticancer drug, however, taxol and its precursor (baccatin III) were later obtained from two fungal species, *Taxomyces andreanae* and *Penicillium raistrickii*.<sup>38, 41</sup> Podophyllotoxin is another plant-derived anticancer agent that was later isolated from various fungal strains.<sup>42-44</sup> Uzma et. al. reported more than 40 taxol-producing, 12 podophyllotoxin-producing, nine camptothecin-producing, and five vinca alkaloids-producing endophytic fungi.<sup>45</sup> Therefore, fungi are as valuable resource as plants for the discovery of potential anticancer compounds.

From the perspective of anticancer drug discovery, fungi offer various advantages over other natural resources. First, fungi represent an inexhaustible supply of their secondary metabolites, where fungal cultures can be easily collected, cultivated, and manipulated in laboratory settings. Second, the incubation period for fungal cultures is relatively short and range between 1-6

weeks. Moreover, large-scale fungal fermentation is a well-known technique that allows for large supply of many pharmaceutical compounds.<sup>46, 47</sup> Unlike fungi, plant materials need to be collected from their natural habitats and might need years to decades for full growth and developments. Commercial drug supply was a major concern for many plant-derived medicines due to their low abundance, as was the case with taxol and podophyllotoxin.<sup>48, 49</sup> Searching for fungal producers is an established strategy to provide alternative resources of plant-derived anticancer drugs.<sup>38, 45</sup>

Despite the growing interest in fungi as a source of promising cytotoxic molecules, the Fungal Kingdom is largely understudied and only little is known about its biodiversity. Of the nearly 250,000 bioactive natural products described in the literature, only 8600 (3.5%) of these were obtained from fungi.<sup>50, 51</sup> Fungal Kingdom is estimated to include between 2.2 to 3.8 million species.<sup>52</sup> Of these, only 120,000 species were named in the literature, which represent 3-8% of the total estimated number.<sup>52</sup> A small percentage were investigated for their bioactive secondary metabolites, and much less were studied for cytotoxic activity.<sup>50</sup> Therefore, many fungal secondary metabolites are still to be discovered.

The development of anticancer drugs of fungal origin is not without its own challenges. First of all, it is essential for future anticancer leads to overcome the limitations of the existing chemotherapies, which usually exhibit serious side effects caused by their detrimental impact on rapidly dividing healthy cells in the human body; like hair follicle cells, gastrointestinal tract cells, and bone marrow cells.<sup>53</sup> Future anticancer leads need to selectively eliminate cancer cells while having minimal effect over normal human cells and organs functions. Moreover, potential anticancer medicine should have sufficient efficacy, tolerable side effects, and proper pharmacokinetics properties that allow for acceptable absorption, stability, and tissue penetration.<sup>54</sup>

The development of local drug delivery systems is one way to achieve a high therapeutic concentration of chemotherapy at tumor sites while minimizing its systemic toxicity.<sup>55</sup> Previously described systems differed in their mode of administration and mechanism of action. Some were designed for systemic delivery where the drug vehicles find their way to the targeted solid tumor via different mechanisms to release the loaded chemotherapeutic agent locally at the

tumor site. These usually consist of nano-materials such as polymer nanoparticles, liposomes, and dendrimers. Locally implanted drug delivery systems with controlled release properties, such as drug-eluting films, gels, wafers, rods, and particles, were also developed for the purpose of locally delivering the loaded anticancer agent over a prolonged period of time to eliminate cancerous cells.<sup>55</sup>

In an attempt to develop a suitable drug delivery system for eupenifeldin, which is a fungal secondary metabolite with potent cytotoxic properties, a drug-loaded polymeric buttress was developed and characterized to provide local and sustained release of eupenifeldin over 90 days (Chapter II).<sup>56</sup> Eupenifeldin-loaded buttresses were shown to prevent the local reoccurrence of non-small cell lung cancer (NSCLC) in *in vitro* and *in vivo* models, overcome the poor solubility of eupenifeldin, minimize its systemic side effects, and avoid the frequent administration of anticancer agent.<sup>56</sup> As the systemic administration of eupenifeldin is associated with high toxicity and challenged by the poor solubility of eupenifeldin, this unique drug delivery system is the first step toward the development of eupenifeldin as an anticancer drug.

Fungal secondary metabolites as a source of anticancer leads is also challenged by the low yields that are naturally achieved in most microbes.<sup>57</sup> Unfortunately, the biosynthesis of secondary metabolites is usually favored under suboptimal growth conditions. Accordingly, growth optimization and fermentation characterization to secure more materials of the targeted secondary metabolite is a prerequisite step for its drug development process. The anticancer drug discovery and development process – from concept through preclinical testing in the laboratory to clinical trial development, including Phase I–III trials – is a long process that requires the availability of sufficient quantities of the potential anticancer lead.

This dissertation includes chapters devoted to the enhanced production of various fungal secondary metabolites to facilitate investigating their biological activities, structure-activity relationship, and secure feedstocks for semi-synthesis studies. Chapter III represents a selected example of such studies, where media and strain studies were conducted to scale up the production of *cis*-enone resorcylic acid lactones (RALs), mainly hypothemycin and (5*Z*)-7-oxozeaenol. These fungal secondary metabolites show promise as future cancer treatments because of their potent and irreversible inhibitory activity against transforming growth factor

beta-activated kinase 1 (TAK1). Identification of the best producing fungal strain, modifying fungal growth conditions to enhance their biosynthesis, and the implementation of practical and time efficient purification techniques allowed for the isolation of gram quantities of hypothemycin and (5Z)-7-oxozeaenol. In addition, twenty fungal secondary metabolites, two of which were new, were isolated and identified.

Enhancing the production of photoactivated perylenequinones and investigating their anticancer properties were the main focus of Chapter IV.<sup>58</sup> The effects of culture medium and light exposure on the production of hypocrellins and hypomyces from *Shiraia-like* sp. (strain MSX60519) were investigated and resulted in the enhanced biosynthesis of hypocrellins and hypomyces on rice and oatmeal mediums, respectively. In both cases, light exposure was an essential factor for the enhanced biosynthesis of these perylenequinones. Moreover, two new perylenequinones, *ent*-shiraiachrome A and hypomyces E, were described for the first time and the photocytotoxic effects of both classes of compounds were evaluated against human skin melanoma, with EC<sub>50</sub> values at nanomolar levels for hypocrellins and micromolar levels for hypomyces.

Considering the growing interest in hypocrellins and hypomyces as naturally-occurring photosensitizers, more studies were conducted to better understand the biosynthesis of these two unique subclasses of fungal perylenequinones (Chapter VI). This was achieved by the isolation and identification of the immediate biosynthetic precursor of hypocrellins, followed by the use of cyclic voltammetry (CV), UV-vis spectroelectrochemistry, aerobic chemical reduction, and anaerobic chemical reduction to investigate the redox behaviors of hypocrellins and hypomyces. Accordingly, hypomyces were shown to derive from hypocrellins upon exposure to chemical reduction under anaerobic condition, which, in other words, provided evidence for the ability of hypocrellins-producing fungi to reduce these compounds. We believe that hypocrellin-producing fungi adapted this mechanism to defend themselves against these photosensitizers.

Chapter V represents a continued investigation of the chemical diversity exhibited by *Shiraia-like* sp. (strain MSX60519) upon exposure to different culture media and light exposure.<sup>59</sup> In this study, four compounds belonging to the thielavin class, of which one is new, were described and shown to exhibit cytotoxic activity at the micromolar level. Oatmeal medium and exposure to

white LED light were shown to negatively affect the biosynthesis of these thielavins. Moreover, the utility of LR-HSQMBC and NOESY NMR experiments in the structural elucidation of these hydrogen-deficient natural products was demonstrated.

In the course of our continuous effort to explore the chemical diversity of freshwater fungi, which is an under-investigated ecological niche of microorganisms,<sup>60</sup> the secondary metabolites produced by a fungal culture collected from submerged wood in a stream in Connecticut, USA [*Penicillium* sp. (strain G1071)] were investigated (Chapter VII). This project expanded the natural diketomorpholines family with the identification of three new fungal metabolites, along with two known phenalenones. NMR spectroscopy, mass spectrometry fragmentation patterns, ECD spectra, and Marfey's analysis were used to determine the absolute configuration of these compounds.

In summary, this dissertation involves multidisciplinary research projects that focused on the preclinical development of cytotoxic fungal secondary metabolites with potential anticancer activities (Chapters II and III). This is in addition to investigating the effect of fermentation conditions and/or other environmental factors, i.e., light exposure, on the chemical diversity of various fungal strains (MSX78495, MSX63935, and MSX60519) (Chapters III-V), studying the redox behavior of the naturally-occurring perylenequinones (Chapter VI), and expanding the relatively rare diketomorpholines class by studying the chemical profile of *Penicillium* sp. (strain G1071) (Chapter VII). Overall, this work allowed for the development of local prolonged-release drug delivery system of eupenifeldin, scaling-up the production of three fungal secondary metabolites with potential anticancer activity from milligram to gram scale, and the identification of 36 fungal secondary metabolites, of which eight were new.

## CHAPTER II: DELIVERY OF EUPENIFELDIN VIA POLYMER-COATED SURGICAL BUTTRESSES PREVENTS LOCAL LUNG CANCER RECURRENCE

Zeinab Y. Al Subeh, Ngoc-Quynh Chu, Jeremy T. Korunes-Miller, Lillian L. Tsai, Tyler N. Graf, Yin P. Hung, Cedric J. Pearce, Mark W. Grinstaff, Aaron H. Colby, Yolonda L. Colson, and Nicholas H. Oberlies. *Journal of Controlled Release* 2021, 331, 260-269.

Lung cancer is the leading cause of cancer deaths worldwide. Unfortunately, high recurrence rates and poor survival remain despite surgical resection and conventional chemotherapy. Local drug delivery systems are a promising intervention for lung cancer treatment with the potential for improved efficacy with reduced systemic toxicity. Here, we describe the development of a chemotherapy-loaded polymer buttress, to be implanted along the surgical margin at the time of tumor resection, for achieving local and prolonged release of a new anticancer agent, eupenifeldin. We prepared five different formulations of buttresses with varying amounts of eupenifeldin, and additional external empty polymer coating layers (or thicknesses) to modulate drug release. The *in vitro* eupenifeldin release profile depends on the number of external coating layers with the formulation of the greatest thickness demonstrating a prolonged release approaching 90 days. Similarly, the long-term cytotoxicity of eupenifeldin-loaded buttress formulations against murine Lewis lung carcinoma (LLC) and human lung carcinoma (A549) cell lines mirrors the eupenifeldin release profiles and shows a prolonged cytotoxic effect. *In vivo*, eupenifeldin-loaded buttresses significantly decrease local tumor recurrence and increase disease-free survival in a resection model.

### **Introduction**

Lung cancer is the most common cancer in the world with a projected 1.9 million new cases in 2020.<sup>61, 62</sup> Despite improvements in prevention, diagnosis, and treatment, lung cancer still has the highest incidence and mortality rate, with nearly 1.8 million deaths in 2018, accounting for more than those reported for breast, colon, and prostate cancers combined.<sup>63</sup> Unfortunately, the overall 5-year relative survival rate for patients with lung cancer is less than 20%.<sup>64</sup>

Treatment of lung cancer is usually based on its histological type (non-small cell vs small cell) and stage of the disease, and includes surgical intervention, chemotherapy and radiation, or a combination of these modalities.<sup>65</sup> Surgical resection of primary non-small cell lung cancer (NSCLC) is done with curative intent for stage I-III. Unfortunately, cure decreases as a function of increasing stage with 5-year survival following surgical resection remaining as low as 68% for clinical stage I, 53-60% for stage II, and 13-36% for stage III.<sup>66</sup> Recurrence is attributed, at least in part, to microscopic cancerous cells remaining after tumor resection.<sup>67</sup> The presence of positive surgical margins is a known risk factor for poor prognosis and reduced survival as evidenced by a significant reduction in the 5-year disease-free survival rate among lung cancer patients with positive surgical margins compared to those with clean margins (30.8% vs. 82.6%,  $P = 0.001$ ; Fig. 2.1A, bottom path).<sup>68, 69</sup>

The high recurrence rate of lung cancer remains a major clinical challenge, and current attempts to prevent potential recurrence with adjuvant systemic chemotherapy are not justified given the associated toxicity.<sup>70</sup> For example, the International Adjuvant Lung Cancer Trial (IALT) showed that adjuvant cisplatin-based chemotherapy following complete resection of NSCLC lead to a 4% increase in 5-year survival and a 5% higher disease-free survival rate in patients but, similar to other trials, did not significantly prevent nodal or local recurrence.<sup>71-74</sup> Furthermore, systemic administration of chemotherapies carries the potential for both off-target toxicities and side effects that are typically not justified by the limited efficacy.<sup>75</sup> Consequently, there is a need for innovative approaches for eliminating residual cancer cells after surgery, particularly approaches with reduced toxicity, and with a particular emphasis on treating NSCLC.

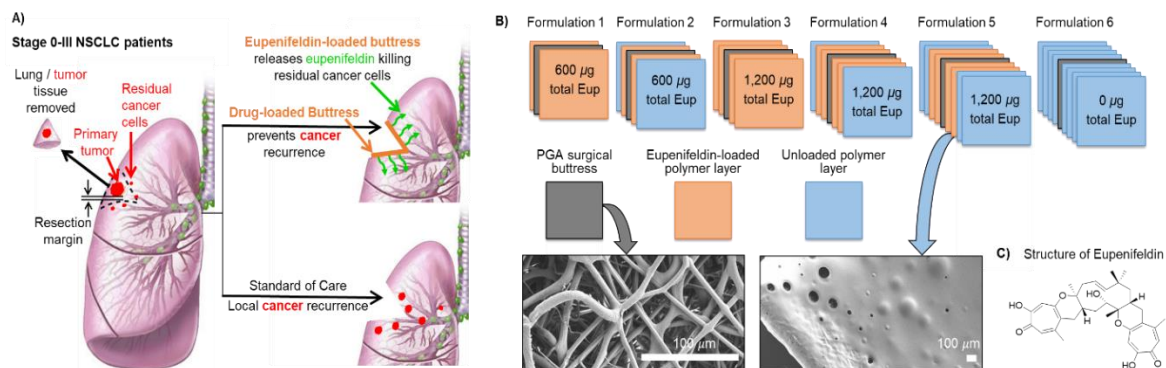


**Figure 2.1.** Paradigms of treatment for early stage non-small cell lung cancer (NSCLC) patients. **A.** *Bottom path:* unresected residual disease leads to cancer recurrence. *Top path:* drug-loaded surgical buttresses implanted at the resection margin locally deliver drug thereby eliminating residual tumor cells and preventing recurrence. **B.** Schematic illustration of five different eupenifeldin-loaded buttress formulations. Formulation **1**: loaded with 300  $\mu\text{g}$  of eupenifeldin on each face (total of  $\sim 600 \mu\text{g}$ ); Formulation **2**: same as **1** with an extra single layer of unloaded polymer on each face (total of  $\sim 600 \mu\text{g}$  of eupenifeldin); Formulation **3**: loaded with 600  $\mu\text{g}$  of eupenifeldin on each face (total of  $\sim 1200 \mu\text{g}$ ); Formulation **4**: same as **3** with an extra single layer of unloaded polymer on each face (total of  $\sim 1200 \mu\text{g}$  of eupenifeldin); Formulation **5**: same as **3** with extra two layers of unloaded polymer on each face (total of  $\sim 1200 \mu\text{g}$  of eupenifeldin); and, Formulation **6**: with four unloaded layers of polymer on each face (no eupenifeldin loaded). *Insert:* SEM images of PGA surgical buttress and representative polymer-coated PGA buttress). **C.** Chemical structure of eupenifeldin.

Successful approaches to address these challenges require the development of drug delivery systems that target cancerous cells in the lung with minimal effects on normal tissues. One strategy to achieve this goal is to use nanoscale drug carriers synthesized from versatile materials, such as polymers,<sup>55, 76-79</sup> lipids,<sup>80, 81</sup> or inorganic carriers,<sup>82</sup> to selectively deliver an anticancer agent to the tumor site. However, these strategies suffer from a lack of tumoral accumulation and drug delivery in much the same way as systemic chemotherapy. As an alternative strategy, we are investigating the delivery of therapeutics via surgical buttresses that are implanted at the resection margin at the time of surgery, providing a locally high dose of chemotherapy for a prolonged period while averting systemic toxicity (Fig. 2.1A, top path). Coating a standard surgical buttress with polymer-drug formulations yields a flexible, conformal, biocompatible device that is easily handled and implanted. Various types of “unloaded” buttresses are clinically available and can be employed to reinforce the lung tissue at the resection margin in order to prevent air leaks from the lung parenchyma.<sup>83</sup> Leveraging this strategy for drug delivery offers several advantages over traditional chemotherapeutic regimens, including local drug release at the target site, improved therapeutic efficacy and minimized systemic toxicity, enhanced bioavailability and tissue penetration, and 100% patient compliance (Fig. 2.1). Additionally, drug release occurs over a prolonged period of time and avoids the requirement of frequent chemotherapy dosing protocols.

Similar strategies show some benefit, either in *in vivo* models and/or in the clinic. For example, Gliadel<sup>®</sup> wafers of carmustine increase survivability in patients with malignant gliomas from 11.6 to 13.9 months.<sup>84</sup> Intracranial implants of paclitaxel afford higher survival in a rat model of

malignant glioma.<sup>85</sup> More recently, hyaluronate-based films loaded with cisplatin prevent tumor recurrence in pleural mesothelioma,<sup>86</sup> while cisplatin-loaded superhydrophobic polymer meshes increase recurrence-free survival *in vivo*.<sup>87</sup>

Here, we are investigating polymer-coated buttresses to deliver eupenifeldin – a novel anticancer agent (Fig. 2.1C). Eupenifeldin is a fungal metabolite, first reported in 1993 by researchers at Bristol-Myers Squibb from cultures of *Eupenicillium brefeldianum*. It exhibits potent cytotoxic activity at the nanomolar level against, for example, human MDA-MB-231 breast, MSTO-211H mesothelioma, and OVCAR-3 and OVCAR-8 ovarian cancer cell lines, and *in vivo* activity against a murine model of leukemia.<sup>88,89</sup> However, eupenifeldin's physical properties, particularly its poor water solubility, handicap its use as a standalone chemotherapeutic agent. To overcome the poor solubility of eupenifeldin and investigate its potential as a cancer therapeutic against an *in vivo* solid tumor, we report eupenifeldin-loaded polymer-coated surgical buttresses as an extended drug release formulation (Fig. 2.1B). The prolonged cytotoxic activity of this formulation was evaluated using long-term cell culture assays, and the efficacy in reducing the recurrence rate of NSCLC was evaluated using a murine model of lung cancer recurrence.

## Materials and Methods

**Materials and Instrumentations.** Eupenifeldin was isolated and characterized from *Neosetophoma* sp. (strain MSX50044) as reported recently in detail.<sup>89</sup> The purity of eupenifeldin was > 97% as determined by <sup>1</sup>H NMR and UPLC analyses (Figs. 2.6 & 2.7). Poly(glycerol monostearate co- $\epsilon$ -caprolactone) polymer (PGC-C<sub>18</sub>) was synthesized as previously described.<sup>90</sup>

Phosphate buffered saline (PBS) solution was prepared using 137 mmol/L NaCl (Fisher Scientific), 2.7 mmol/L KCl (Macron Fine Chemicals), 1.8 mmol/L KH<sub>2</sub>PO<sub>4</sub> (EMD Millipore Corporation), and 10 mmol/L Na<sub>2</sub>HPO<sub>4</sub> (Fisher Scientific). This PBS solution was supplemented with 2% Tween 80 (VWR International) to improve the solubility of eupenifeldin (Fig. 2.8), and 0.02% of sodium azide (Sigma-Aldrich) to prevent microbial growth. The pH was buffered to 7.35-7.45.

The UV absorbances of standard solutions and PBS samples were measured using an Agilent Cary Ultraviolet-Visible (UV-Vis) Spectrophotometer at a wavelength of 364 nm, which is the  $\lambda_{\text{max}}$  of eupenifeldin in PBS solution.

**Preparation of Polyglycolic Acid (PGA) Buttress.** Fibrous meshes of polyglycolic acid (PGA) were used as a buttress onto which PGC-C<sub>18</sub> was coated with or without eupenifeldin. PGA polymer was selected to develop the buttress based upon its unique properties, where PGA polymer is insoluble in most organic solvents, including dichloromethane (Fig. 2.16).<sup>91</sup> A large mesh was used for the buttress stock, formed via electrospinning of a 20% wt/v solution of PGA dissolved in hexafluoro-2-propanol, pumped at 25 mL/hr at ~13 kV, and with a tip-to-collector distance of 9 inches. The resulting mesh were ~140  $\mu\text{m}$  in thickness with a mass density of 5.84 g/cm<sup>2</sup>. Electrospun PGA buttress exhibited a mean fiber diameter of 3.63 micron and a porosity of 38.05% as determined via image analysis with the ImageJ plugin, DiameterJ. While this is an in-house generated PGA-based buttress, PGA is a biodegradable polymer commonly used in FDA-approved sutures and buttresses (e.g., ~140  $\mu\text{m}$  thickness, 5.84 g/cm<sup>2</sup> basis weight (i.e., density), and 38.05% porosity) as well as drug delivery carriers due to its fast degradation (~ 3 months).<sup>92</sup>

**Preparation of Eupenifeldin-Polymer Loaded Buttresses.** A sheet of PGA polymer was cut into 1 cm<sup>2</sup> buttresses. These were used to prepare six different formulations of eupenifeldin-loaded buttresses (formulations **1-6**). Briefly, PGC-C<sub>18</sub> polymer (10% w/v) and eupenifeldin (1.0% w/v) were dissolved in dichloromethane to produce a clear eupenifeldin-polymer solution. A second solution of blank polymer (10% w/v) dissolved in dichloromethane was prepared to cover the eupenifeldin-polymer layers in formulations **2, 4** and **5**, as described below. Unloaded or eupenifeldin-polymer solutions were uniformly coated layer by layer over the upper and lower face of each buttress. Each layer was created by applying 30  $\mu\text{L}$  of blank polymer solution (~3 mg of PGC-C<sub>18</sub> polymer) or 30  $\mu\text{L}$  of eupenifeldin-polymer solution (~3 mg of PGC-C<sub>18</sub> polymer with 300  $\mu\text{g}$  of eupenifeldin) using a Hamilton syringe and spread over the buttress face. Each layer was allowed to dry for at least one hour before adding any subsequent layers. Formulations **1-6** differ in the number and types of loaded layers as follows (Fig. 2.1B): formulation **1** were loaded with a single layer of eupenifeldin-polymer on each face (total of 600  $\mu\text{g}$  of eupenifeldin), formulation **2** was the same as **1** with an additional single layer of unloaded

polymer on each face (total of 600  $\mu\text{g}$  of eupenifeldin), formulation **3** was loaded with two layers of eupenifeldin-polymer on each face (total of 1200  $\mu\text{g}$  of eupenifeldin for each), formulations **4** and **5** were the same as **3** with an additional single layer and two layers of unloaded polymer on each face, respectively (total of 1200 $\mu\text{g}$  of eupenifeldin). Formulation **6** was four layers of unloaded polymer on each face. These were used as a vehicle control in the *in vitro* and *in vivo* testing. All formulations were placed on glass cover slips and left overnight under nitrogen lines to dry completely. SEM images were taken for unloaded PGA buttress and eupenifeldin-loaded buttresses (formulations **1-6**). Once coated and dried, formulations **1-6** had a smooth, uniform topology with no exposed PGA fibers (Fig. 2.10). Table 2.1 summarizes the number of layers and the composition of eupenifeldin and PGC-C<sub>18</sub> across formulations **1-6**. To further illustrate the layering concept and ensure that formulations **1-6** maintain the layered structure as envisioned in Fig. 2.1, we coated a 1-cm<sup>2</sup> PGA buttress from one side with phycocyanobilin-polymer solution (blue-colored) to create the first and the third layers and ent-shiraiachrome A-polymer solution (red-colored) to build the second and the fourth layers (Fig. 2.17). Each subsequent layer does not entirely cover the previous layer thereby allowing visualization of all four layers under a microscope (Fig. 2.17). Phycocyanobilin and ent-shiraiachrome A are colored secondary metabolite with high solubility in DCM (similar to eupenifeldin). The alternate blue/red layers demonstrate that the layers stay intact upon coating and any mixing between them is minimal.

**Release Study of Eupenifeldin-Loaded Buttress Formulations 1-5.** Given the low solubility of eupenifeldin in aqueous media, various steps were taken to ensure the continuous release of eupenifeldin and the accurate measurement of its release profile. These include measuring the solubility of eupenifeldin in phosphate buffer saline (PBS) across a suite of percentages of Tween 80 (Fig. 2.8). Eupenifeldin solubility greatly increased with the addition of Tween 80 (e.g., 1.7  $\mu\text{g}/\text{mL}$  without Tween 80 v. 50  $\mu\text{g}/\text{mL}$  with 2% v/v Tween 80; Fig. 2.8). Moreover, we identified the optimal buffer volume of 50 mL by conducting a volume-saturation study (Fig. 2.9) in which five buttresses, each loaded with 600  $\mu\text{g}$  of eupenifeldin, were submerged in 20, 50, and 100 mL of release buffer (PBS with 2% v/v Tween 80). Eupenifeldin release was measured for 25 days without changing the buffer. Total eupenifeldin released increased with time and, over 25 days, exceeded 1200  $\mu\text{g}$  in the 100- and 50-mL release buffers (Fig. 2.9). In contrast, the 20 mL PBS solution was saturated within a week, demonstrating the inadequate

solvation capacity of this volume of release buffer. Accordingly, 50 mL of PBS with 2% Tween 80 was used as a release media with an estimated solvation capacity of 2500  $\mu\text{g}$  of eupenifeldin.

Each formulation (i.e., **1-5**, Fig. 2.1B) was submerged in 50 mL PBS containing Tween 80 (2% v/v) with a pH range of 7.35-7.45 and incubated at 37 °C for 90 days. At specific time intervals (Fig. 2.11), the entire PBS solution was collected and replaced with the same volume of fresh buffer to ensure the continuous monitoring of eupenifeldin release. Collected buffer samples were refrigerated at 4 °C until analysis (~2-3 weeks); a day before analysis, buffer samples were incubated overnight at 37 °C with shaking to ensure homogeneity and that eupenifeldin was fully dissolved. The concentration of eupenifeldin in collected PBS samples was measured by UV-Vis at 364 nm.

**Standards Preparation and Method Validation.** Six standard samples of PBS with known eupenifeldin concentration (ranging from 80 ng/mL to 2.56  $\mu\text{g/mL}$ ) were prepared to build a calibration curve using a UV-Vis spectrophotometer ( $\lambda = 364 \text{ nm}$ ). All measurements were performed in triplicate ( $n=3$ ), and a new calibration curve was created each time the PBS samples were analyzed, which was every 2 to 3 weeks (a total of five calibration curves were obtained, Fig. 2.12). These standard curves were used to determine the amount of eupenifeldin in PBS samples collected from the *in vitro* release study. The linearity of each calibration curve was assessed using linear least squares regression analysis. The correlation coefficient ( $R^2$ ) in all calibration curves was  $0.998 \pm 0.001$ , and the linearity range was 0.08-2.56  $\mu\text{g/mL}$ . The relative error (RE) remained less than or equal to 15.5% over a concentration range of 160 ng/mL to 2.56  $\mu\text{g/mL}$ . The limit of quantitation (LOQ) was  $152.0 \pm 50.0 \text{ ng/mL}$ , which is the lowest amount of analyte that can be quantitatively determined with suitable precision and accuracy. LOQ was defined as  $10 S_a / b$ , where  $S_a$  is the standard deviation of the y-intercept, and b is the slope of the calibration curve. Relative standard deviation (RSD) and relative error (RE) percentages were calculated to evaluate the precision and accuracy of the calibration curves, as summarized in Table 2.2 and Fig. 2.12.

**Extraction of Eupenifeldin-Loaded Buttress Formulations 1-5.** The amount of eupenifeldin remaining on formulations **1-5** was measured by extracting three of the eupenifeldin-loaded buttresses of each formulation, both before being exposed to PBS solution and after 30, 60, and

90 days of being submerged in PBS. At the designated time point, each formulation was dissolved in 1 mL dichloromethane. The polymer was then precipitated from eupenifeldin by adding a 50:50 mixture of water and acetonitrile. After vortexing, the organic layer was separated from the aqueous layer and evaporated to dryness. The remaining eupenifeldin from the dried organic layer was re-dissolved in dimethyl sulfoxide and quantified by UV-Vis.

#### **Long-term *In vitro* Cytotoxicity Assay of Eupenifeldin-Loaded Buttress Formulations 1-6.**

Each buttress in formulations **1-6** was placed in a Transwell insert of a 12-well plate and co-incubated with adherent LLC, murine Lewis lung carcinoma, and A549, human lung carcinoma, cells 24 h after plating. Cells were maintained in complete media containing 10% fetal bovine serum and 1% penicillin/streptomycin in DMEM and F-12K media for LLC and A549 cells, respectively. After 24 h of co-incubation, the buttress was transferred into the elution sink (2% v/v Tween 80 in PBS) to allow for continuous eupenifeldin release for 6 days before a second cycle of co-incubation with another aliquot of freshly plated cancer cells. Eupenifeldin-loaded buttresses were washed in two 50 mL PBS baths prior to placement into the Transwell inserts to remove residual Tween 80. These cycles of co-incubation (24 h) and elution (6 days) were conducted for a total of 10 weeks. The viability of tumor cells was assessed three days after each co-incubation period and compared to those exposed to blank polymer-loaded buttresses (i.e., formulation **6**), which acted as a vehicle control, and a non-treated control with no film. Cell viability was assessed using a tetrazolium-based colorimetric assay of 3-(4,5-dimethylthiazol-2-yl)-5-(3-carboxymethoxyphenyl)-2-(4-sulfophenyl)-2H-tetrazolium (MTS; CellTiter 96® Aqueous One Solution Cell Proliferation Assay).

***In vivo* Maximum Tolerated Dose Study.** Animal studies were approved by the Institutional Animal Care and Use Committee at Massachusetts General Hospital (IACUC approval number is 2019N000085). To determine the maximum tolerated dose (MTD) of “free” eupenifeldin (i.e., not loaded into a buttress), eupenifeldin was solubilized in 50/50 Cremophor EL/ethanol, the excipient used clinically to delivery paclitaxel, due to eupenifeldin’s poor aqueous solubility. Intraperitoneal injections of eupenifeldin were systemically administered to 6- to 8-week old C57Bl/6 mice with predetermined doses of 20  $\mu\text{g}$ , 40  $\mu\text{g}$ , 60  $\mu\text{g}$ , 120  $\mu\text{g}$ , 180  $\mu\text{g}$  and 540  $\mu\text{g}$  of eupenifeldin (Table 2.3). Animals were monitored daily for clinical deterioration manifested by significant weight loss, lethargy, and/or respiratory distress.

To determine the MTD of eupenifeldin-loaded buttresses, five different doses were employed, all of which used the structure of formulation **5** (Fig. 2.1B). The amount of eupenifeldin loaded into the 1 cm<sup>2</sup> buttress was titrated to five doses: 1200 µg, 600 µg, 300 µg, 200 µg, or 100 µg. These eupenifeldin-loaded buttresses were implanted subcutaneously on the dorsum of non-tumor-bearing animals. Animal weight (as a corollary of morbidity) and mortality were followed over 14-days. A greater than 20% drop in body weight or severe clinical deterioration (respiratory distress, lethargy, decreased activity) necessitated humane euthanasia.

***In vivo* Murine Model of Local Cancer Recurrence.** Six-to-eight-week-old female C57Bl/6 mice were injected subcutaneously at the interscapular space of the upper dorsum with 750,000 LLC cells. Tumors were allowed to grow for approximately two weeks and resected after reaching at least 500 mm<sup>3</sup>. Using sterile technique and under isoflurane anesthesia, visible tumor was removed leaving behind adjacent tissue, such that residual microscopic disease leads to recurrent tumor growth. Animals were immediately randomized into treatment groups: (1) surgery only (no treatment implanted), (2) implantation of blank unloaded formulation, and (3) implantation of 100 µg eupenifeldin-loaded formulation. Eupenifeldin formulation was applied directly over the resection bed and secured with suture at the corners. The incision was closed with wound clips. Mice were monitored post-operatively for clinical deterioration, freedom from local recurrence, and survival. Recurrence was determined by the presence of tumor re-growth at the surgical site. Animals were euthanized when tumor size had reached greater than 2 cm, appeared systemically ill, or had nonhealing skin ulcers. A log-rank (Mantel-Cox) test was used to assess efficacy of the treatments for statistical significance in prolonging tumor-free survival and overall survival.

**Histological Analysis.** After euthanasia, autopsy was conducted on the animals. Organs and tissue surrounding the buttress implants were harvested and stored in 10% formalin. Tissues were sent to the core facilities for paraffin embedding, sectioning, and H&E staining.

## **Results and Discussion**

Given the limited knowledge on the anticancer activity of eupenifeldin, we submitted eupenifeldin for evaluation against the NCI cell line panel representing a total of 60 human tumor cell lines.<sup>93</sup> Eupenifeldin showed the greatest activity against melanoma, leukemia, and

lung cancer cell lines (Fig. 2.13). We are keenly interested in treatments to prevent lung cancer recurrence after a surgical resection and, thus, the broad activity of eupenifeldin drew our interest. However, eupenifeldin is hydrophobic with negligible solubility in water and therefore requires a traditional excipient or drug delivery device to enable *in vivo* delivery. Therefore, to assess the ability of eupenifeldin to eliminate residual malignant disease following tumor resection via a local-delivery system, we developed eupenifeldin-loaded buttresses of various formulations to achieve a sustained, tunable therapeutic dose over a prolonged period. We initially characterized drug release and evaluated the cytotoxicity of the buttresses *in vitro* against two NSCLC cell lines over 70 days. Finally, we determined the maximum tolerated dose *in vivo* and characterized the buttress' ability to prevent local tumor recurrence in a murine model of lung cancer recurrence.

**Kinetics of Eupenifeldin Release from Polyglycolide Buttresses.** Preventing local lung cancer recurrence following surgical resection of the primary tumor requires a drug-delivery system that can maintain a therapeutic, though non-toxic, dose of the anticancer agent for a prolonged period of time. In particular, the local drug-delivery system should minimize the intensity of initial burst release that usually occurs within the first 24-48 h, so as to avoid interfering with post-surgical healing. To achieve these requirements, PGA buttress was manufactured in-house, and it was coated with five different eupenifeldin-loaded buttresses formulations (**1-5**, Fig. 2.1B) whose drug-release characteristics were then evaluated. Specifically, we varied the amount of eupenifeldin between 600 and 1200  $\mu\text{g}/\text{cm}^2$  and the number of unloaded polymer layers covering the eupenifeldin layer. The goal of this study was to evaluate the impact of both total drug loading as well as polymer layering or thickness (e.g., multiple drug loaded- or unloaded polymer-layers) upon eupenifeldin release kinetics. Due to eupenifeldin's hydrophobic character, we selected a biodegradable, biocompatible, hydrophobic polymer, poly(glycerol monostearate co- $\epsilon$ -caprolactone) (PGC-C<sub>18</sub>)<sup>90</sup>, as the coating/encapsulating polymer to entrap eupenifeldin.

**Kinetics of Eupenifeldin Release.** We characterized eupenifeldin release profiles over 90 days (Fig. 2.2). In formulation **1**, eupenifeldin was loaded directly into a single PGC-C<sub>18</sub> polymer layered on each face of the buttress (Fig. 2.1B). In formulation **2**, an additional layer of unloaded PGC-C<sub>18</sub> polymer was added on each side of the buttress. We hypothesized that this additional polymer layer would slow the release rate of eupenifeldin. Indeed, the initial release of

eupenifeldin in the first 4 h was lower in formulation 2 ( $17.6 \pm 2.8\%$ ) than in formulation 1 ( $34.0 \pm 2.2\%$ ). We attributed this reduction in release to the extra polymer layer on formulation 2, which provided an additional barrier to the release of eupenifeldin to the surrounding release medium. After 24 h, the release profiles were similar for both formulation 1 and 2 (Fig. 2.2A). Over 90 days,  $86.5 \pm 2.3\%$  of the eupenifeldin payload was released from formulation 1, while  $78.9 \pm 1.4\%$  was released from formulation 2 (Fig. 2.2B). These data correlated well with the mass-balance of eupenifeldin performed by extracting unreleased eupenifeldin from each formulation after 90 days (Fig. 2.2D).

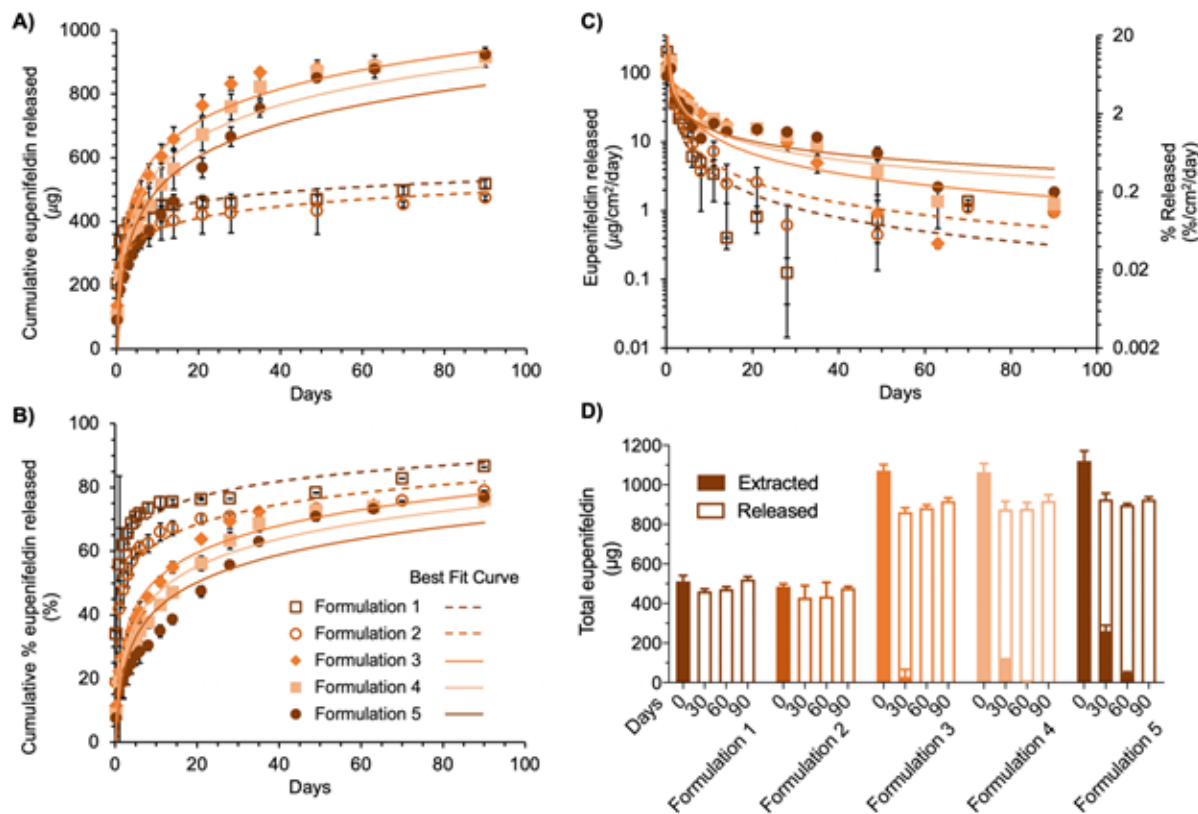


**Figure 2.2.** Kinetics of eupenifeldin release. Cumulative release of eupenifeldin from formulations 1 - 5 over 90 days plotted as mass of eupenifeldin ( $\mu\text{g}$ , **A.**) and percent (% , **B.**) of total loaded eupenifeldin in the buttress. **C.** Daily release rate of eupenifeldin normalized by surface area. **D.** Mass-balance of eupenifeldin. Total eupenifeldin is equal to that released plus that remaining (extracted) at each of four time points throughout the release study. For all plots, each time point represents 4-10 experimental replicates. Error bars represent standard deviation.

**Impact of Layering on Kinetics of Eupenifeldin Release.** Based upon the result that formulation 2 experienced a delay in burst release compared to formulation 1, we next

interrogated our ability to further tune the release profile through the incorporation of additional loaded- and unloaded polymer layers. We prepared formulations **3-5** with 1200  $\mu\text{g}$  of eupenifeldin total per buttress. Formulation **3** mimicked formulation **1** but doubled the total drug through addition of a second layer of eupenifeldin/ PGC-C<sub>18</sub> on each side (Fig. 2.1B). Formulation **4** mimicked formulation **3** with one layer of unloaded PGC-C<sub>18</sub> polymer on each face, while formulation **5** included two layers of empty polymer on each face. These additional layers of empty polymer were added to increase the distance eupenifeldin would have to diffuse through the polymer in order to release, thereby reducing the burst release (i.e., amount of released agent over 24 hr). The initial burst release was highest for formulation **3** ( $22.2 \pm 3.2\%$ ), lower in formulation **4** ( $19.1 \pm 5.2\%$ ), and the lowest in formulation **5** ( $15.5 \pm 0.7\%$ ). As anticipated, formulation **5** exhibited the slowest release rate for the first three weeks as compared to formulations **3** and **4** (Fig. 2.2A-C). Interestingly, after day 21, formulation **5** maintained a *higher* daily release of eupenifeldin, which is attributed to a generally more moderated and sustained release profile (Fig. 2.2C). As shown in the cumulative release profiles (Fig. 2.2B), formulation **3** maintained a considerable release rate of eupenifeldin for approximately 35 days before reaching a plateau. Formulations **4** and **5** showed a more prolonged release of eupenifeldin, up to 50 days for formulation **4** and approaching 90 days for formulation **5**. The total amount of released eupenifeldin during the study was similar among formulations **3**, **4**, and **5** at 70 - 80% of the total eupenifeldin payload over the course of the study. As with formulations **1** and **2**, these data correlated well with the mass-balance of eupenifeldin extracted from the buttresses after 90 days (Fig. 2.2D).

**Mass-Balance of Eupenifeldin-Loaded Buttress Formulations 1-5.** To investigate the mass-balance of eupenifeldin during the release study (i.e., released drug + un-released drug = total drug), we extracted and quantified the eupenifeldin remaining in each formulation at predesignated timepoints over the course of the study (Fig. 2.2D). These results correlated well with the previous eupenifeldin-release data confirming the kinetics of release. By 30 days, formulations **1** and **2** contained no detectable eupenifeldin. Formulation **5** showed the highest amount of remaining eupenifeldin at 30 and 60 days, indicating the slowest release rate amongst formulations **3-5**. Overall, only formulations **3-5** maintained a measurable eupenifeldin payload after the first 30 days and only formulation **5** contained a measurable amount of eupenifeldin by 60 days (approximately 50  $\mu\text{g}$ ). This remaining drug was released over the final 30 days and no

eupenifeldin was detected at the end of the release study. Of note, the recovered eupenifeldin at 0 day accounted for 81-88% of the theoretical loading, which may be attributed to partial loss through the processes of weighing, loading, and extraction. Furthermore, the cumulative released amount of eupenifeldin at 90 days accounted for more than 82% of the originally extracted amount at 0 day of formulations **1-5**. The handling of eupenifeldin-loaded buttresses over a period of 90 days may also contribute to this minor loss of mass.

**Long-term Cytotoxicity of Formulations 1-5 Against Lung Cancer Cell Lines.** Eupenifeldin showed cytotoxicity against murine Lewis lung carcinoma (LLC) and human lung carcinoma (A549) cell lines with  $IC_{50}$  values of 8.5 and 123.9 ng/mL, respectively (Fig. 2.14). We next determined the long-term cytotoxicity of formulations **1-5** against lung cancer cells.

Formulations **1-5** that were co-incubated with cells in a Transwell insert for 24 h exhibited a prolonged cytotoxic effect against LLC cells over various durations (Fig. 2.3A). Formulations **1** and **2** maintained potent cytotoxic activity over four weeks, while formulations **3-5** maintained cytotoxicity for eight weeks, with formulation **5** being the longest lasting (i.e., 10 weeks).

Against A549 cells (Fig. 2.3B), the cytotoxic activity of formulations **1** and **2** diminished after the third week, while formulations **3** and **4** performed well until week 6 and formulation **5** showed prolonged cytotoxicity over seven weeks.

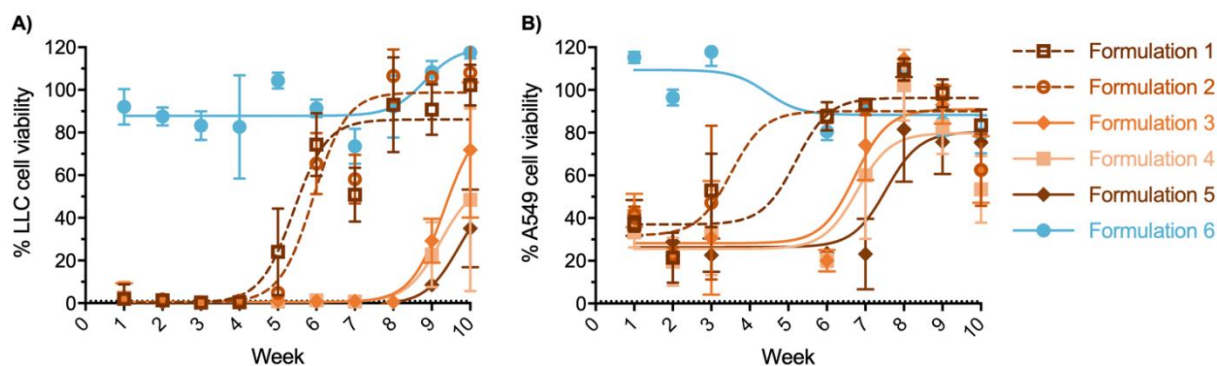


**Figure 2.3.** *In vitro* cytotoxicity of eupenifeldin-loaded buttresses. Cytotoxicity of formulations **1-5** against Lewis lung carcinoma (A.) and human lung carcinoma A549 (B.). Each time point represents five culture replicates. Error bars represent standard deviations.

***In vivo* Efficacy and Toxicity of Eupenifeldin-Loaded Buttresses.** To determine the optimal tolerable dose of eupenifeldin, we first performed two dose-escalation studies in C57Bl/6 mice. To determine the maximum tolerated dose (MTD) of “free” eupenifeldin (i.e., not loaded into a

buttruss), intraperitoneal injections of 20  $\mu\text{g}$ , 40  $\mu\text{g}$ , 60  $\mu\text{g}$ , 120  $\mu\text{g}$ , 180  $\mu\text{g}$  and 540  $\mu\text{g}$  of eupenifeldin were administered (Table 2.3). All animals in the 60  $\mu\text{g}$  dose group or higher died within 24 hours of injection of acute toxicity. Only in the group receiving 20  $\mu\text{g}$  did more than 50% of the animals survive to one-week post injection. The NCI definition of MTD requires <10% mortality and, therefore, even a dose as low as 20  $\mu\text{g}$  of eupenifeldin in Cremophor EL/ethanol did not meet the requirements for MTD.

To determine the MTD of eupenifeldin-loaded buttrusses, five different doses were employed, all of which used the structure of formulation **5** (Fig. 2.1B). The structure of formulation **5** was selected as it provided the most extended release profile *in vitro*. The amount of eupenifeldin loaded into the 1  $\text{cm}^2$  buttruss was titrated to five doses: 1200  $\mu\text{g}$ , 600  $\mu\text{g}$ , 300  $\mu\text{g}$ , 200  $\mu\text{g}$ , or 100  $\mu\text{g}$ . The 1200  $\mu\text{g}$  (n= 5), 600  $\mu\text{g}$  (n= 3) and 300  $\mu\text{g}$  (n= 4) loaded formulations resulted in the most acute and significant decrease in body weight, leading to rapid mortality with a median overall survival (OS) of 2-3 days (Fig. 2.15). The majority of animals (3 out of 4) receiving 200  $\mu\text{g}$  loaded formulation also experienced early mortality (median OS of 6 days). However, all mice in the 100  $\mu\text{g}$  group maintained stable body weights and survived to at least 14 days. Therefore, we determined the MTD of eupenifeldin loaded buttrusses to be 100  $\mu\text{g}$  and proceeded with this loading for the subsequent efficacy study.

The difference in MTD between the buttruss-loaded and “free” (i.e., Cremophor EL/ethanol) versions of eupenifeldin (100  $\mu\text{g}$  vs. <20  $\mu\text{g}$ , respectively) clearly demonstrates the benefits of extended or slow-release drug delivery systems over simple bolus systemic delivery. Due to the fact that the dose of drug in the buttruss-loaded group would be at least 5X+ higher than that of the “free” drug control, the Cremophor EL/ethanol control was excluded from the following animal studies as the equivalent 100  $\mu\text{g}$  systemic dose was lethal.

To evaluate the *in vivo* efficacy of eupenifeldin-loaded buttrusses in preventing local cancer recurrence, we employed a previously developed and published heterotopic murine model of lung cancer recurrence following surgical resection.<sup>94</sup> Tumors were established by subcutaneous injection of LLC cells on the dorsum of C57Bl/6 mice. Tumors were surgically removed once they reached a size threshold of 500  $\text{mm}^3$ . Immediately following resection the mice were randomized, and we applied the following treatments at the resection site: (1) no treatment (i.e.

surgery alone, control), (2) unloaded-buttresses (i.e., formulation **6** in Fig. 2.1B, vehicle control), or (3) 100  $\mu\text{g}$  eupenifeldin-loaded buttresses (experimental) which equates to a dose of  $\sim 5$  mg/kg. Given the toxicity of eupenifeldin, we chose to not perform an equivalent drug alone control in this study.

Animals receiving surgery alone (n=9) exhibited early recurrence (median recurrence day 8) and mortality [median overall survival (OS)=11 days]. Animals treated with control unloaded-buttress following surgery (n=9) had similar recurrence-free and overall survival rates with a median of 6 days to recurrence and a median OS of 9 days, with animals being sacrificed due to progression of malignant disease. In contrast, tumor recurrence was delayed in animals treated with eupenifeldin-loaded buttresses (n=10) following surgery with a median time to recurrence of 16 days (Fig. 2.4A) and a median disease-specific survival of 30 days (Fig. 2.4B). However, 60% of the animals treated with eupenifeldin-loaded buttresses developed skin ulcerations, many of which required euthanasia due to their nonhealing nature and thus overall survival, though statistically significant, decreased (median OS=17 days) (Fig. 2.4C). Given the absence of ulceration with the unloaded buttresses, we investigated the tissues surrounding the eupenifeldin-loaded buttresses. Histological analysis showed local fat and skin necrosis around the eupenifeldin-loaded buttresses (Fig. 2.5A). Furthermore, animals receiving buttresses loaded with high-dose eupenifeldin (i.e., 1200  $\mu\text{g}$ ) exhibited evidence of cardiac and hepatic toxicity, which likely accounts for the mortality of mice receiving eupenifeldin-loaded buttress of higher doses in the MTD study. This toxicity is absent with implantation of the 100  $\mu\text{g}$  eupenifeldin-loaded buttresses (Figs. 2.5B-C).

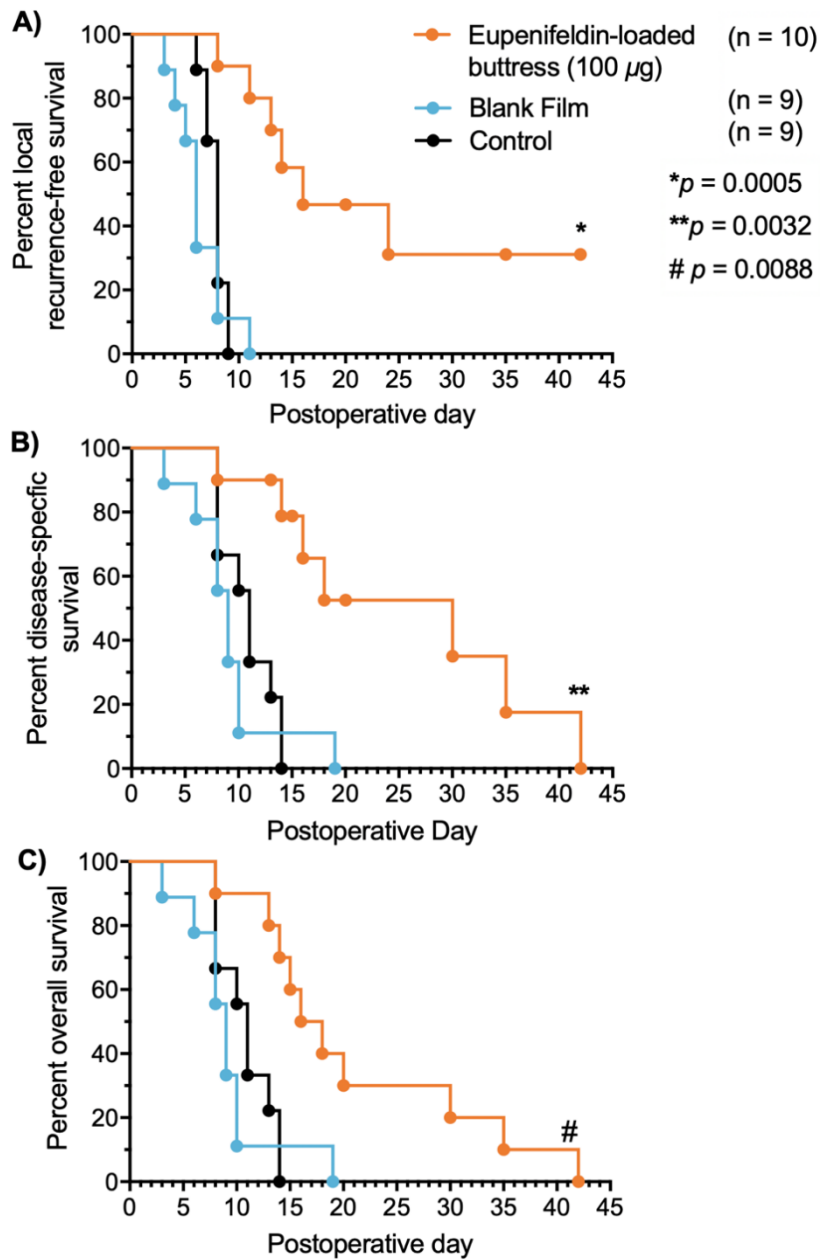


**Figure 2.4.** Local recurrence-free survival (A.), disease-specific survival (B.), and overall survival (C.) after surgical resection of tumors. Disease-specific survival represents animals that died of disease-related reasons only, excluding those that required euthanasia due to reasons unrelated to tumor i.e. nonhealing skin ulcerations.  $p$  values represent a statistically significant difference between animal group treated with eupenifeldin-loaded buttress and untreated groups.

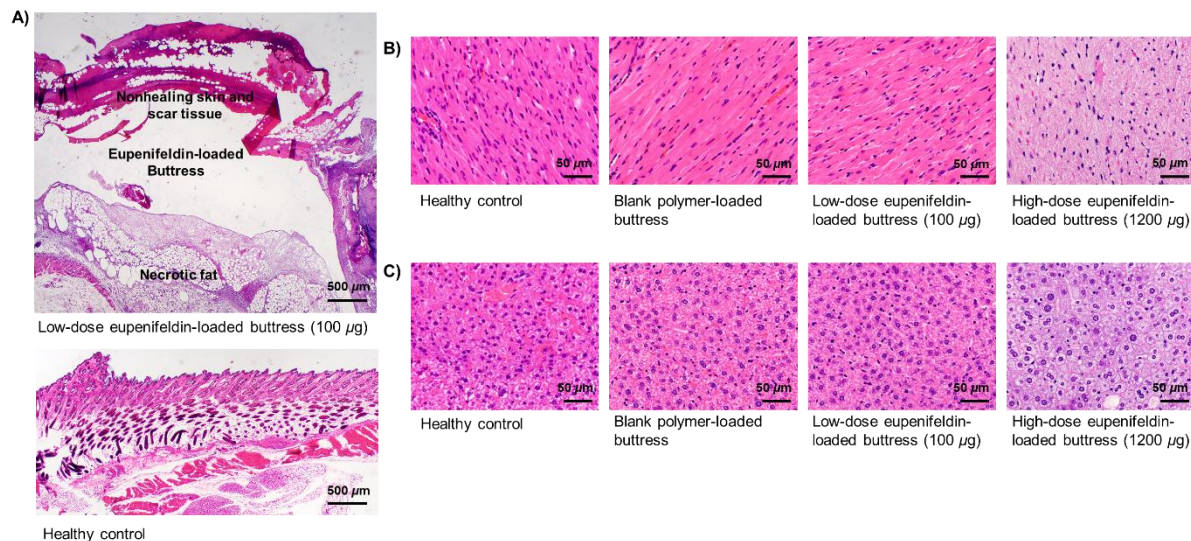


**Figure 2.5.** Tissue necrosis surrounding eugenifeldin-loaded buttress (A.). Cardiac (B.) and hepatic (C.) cells appear vacuolated with irregular appearing cytoplasm in animals treated with high-dose eugenifeldin-loaded buttresses (i.e., 1200  $\mu\text{g}$ ), indicative of toxicity.

Surgical resection offers the best chance for cure in most early stage cancers.<sup>95, 96</sup> The success of surgical cure relies on achieving negative margins to ensure that all disease, including microscopic tumor, is removed to minimize the risk of recurrence. This procedure is not always feasible for either anatomic or physiologic reasons. In lung cancer, for example, the high-incidence of co-morbidities and compromised lung function often limit the amount of removable lung tissue.<sup>97</sup> Less aggressive surgical approaches, such as wedge- or sublobar-resection, are associated with a higher risk of local and loco-regional cancer recurrence due to the presence of positive surgical margins that can grow after the removal of the primary tumor.<sup>98, 99</sup> Unfortunately, lung cancer patients with local recurrence are often ineligible for a second resection, leaving only less curative options, such as radiotherapy and/or chemotherapy.<sup>100, 101</sup>

There is an ongoing effort to develop new treatment approaches to successfully prevent the local recurrence of lung cancer while averting the toxicity, morbidity, and mortality associated with systemic adjuvant chemotherapy.<sup>102</sup> Drug-loaded surgical buttresses, implanted at the site of resection, are one solution to achieve this goal of maintaining a locally therapeutic concentration of the anticancer agent at the resection margin for an extended period of time while averting systemic toxicity. A significant advantage of this polymer-coated buttress system is its ability to encapsulate and deliver a wide range of therapeutic cargoes, including small molecule natural

products with poor solubility that cannot be overcome through traditional (e.g., excipient) or nano-based (e.g., particle or liposomal) formulations. Polymer-coated buttresses can often address these challenges through solvent evaporation casting, heat-melt casting or even microparticulate suspension of the agent, in cases where there is no method to co-solvate the drug and polymer.<sup>103, 104</sup> The hydrophobicity of the loaded anticancer agent, along with the hydrophobicity of polymers used to fabricate the coating on the buttress, both play critical roles in determining the drug release profile from these systems. In previous studies, paclitaxel-loaded PGC-C<sub>18</sub> delivery systems exhibited a prolonged release behavior for 50 days.<sup>105, 106</sup> Poor water solubility of both paclitaxel and PGC-C<sub>18</sub> polymer allowed this extended release property. Moreover, a sustained release profile of cisplatin was observed for 90 days by loading cisplatin over superhydrophobic nanofiber meshes.<sup>87</sup> On the other hand, short release behavior was reported for cisplatin when loaded over a non-superhydrophobic polycaprolactone film, where cytotoxic efficacy was noticeable only for the first day of exposure.<sup>87</sup>

Polyglycolide (PGA) is a linear aliphatic polyester, known since 1954, used to fabricate synthetic bioresorbable sutures.<sup>107</sup> PGA is readily available, non-toxic, biodegradable, and a thermoplastic polymer, all of which are favorable characteristics for a surgical buttress. We chose to use PGA-based surgical buttresses since the PGA-polymer is insoluble in the hydrophobic organic solvents (e.g., dichloromethane) used to dissolve and apply the eupenifeldin- PGC-C<sub>18</sub> coatings. PGC-C<sub>18</sub> is a novel biodegradable polymer which has successfully passed FDA 10999 biocompatibility studies.<sup>86, 87</sup> Cast films of PGC-C<sub>18</sub> are compliant, and the casting procedure is amenable to varied surfaces, including the soft and flexible cloth-like surgical PGA buttresses.<sup>90</sup> Given the design requirements, the toxicity of the eupenifeldin and its hydrophobicity, we prepared eupenifeldin-loaded buttresses of varying PGC-C<sub>18</sub> and eupenifeldin/ PGC-C<sub>18</sub> layers to control and extend the release to greater than 30 days. Adding unloaded layers of PGC-C<sub>18</sub> on top of the eupenifeldin-loaded layers, as in formulation **5**, effectively slows and extends the release profile to 90 days. Multiple factors are likely responsible for the slower release profile achieved in formulation **5**, including the layer-by-layer loading technique used to develop these eupenifeldin-loaded buttresses, the increased thickness of this formulation, and the higher PGC-C<sub>18</sub> polymer:drug ratio represented by the external blank polymer layers added to each face.

We employed LLC and A549 cell lines for the *in vitro* cytotoxicity studies, as these cells are representative of an aggressive pro-metastatic murine lung tumor cell line of epidermoid histology and a cell line derived from a human lung adenocarcinoma.<sup>108</sup> Eupenifeldin-loaded buttresses exhibit a more potent and prolonged cytotoxic activity against the LLC cell line than the A549 cell line (8.5 vs. 123.9 ng/mL, respectively). This result may be related to the mode of action of eupenifeldin rather than the release characteristics of the buttresses. We are currently further investigating this finding given the stark difference in the IC<sub>50</sub> values.

We evaluated the *in vivo* efficacy of the eupenifeldin-loaded buttresses in a murine model of lung cancer recurrence following surgical resection. Even very low doses (20  $\mu$ g) of “free” eupenifeldin administered via Cremophor EL/ethanol are lethal and the MTD of free eupenifeldin is likely 10  $\mu$ g or lower; this toxicity is an obvious concern that is being probed via ongoing studies to modify the structure to enhance potency and/or minimize toxicity. Loading eupenifeldin into buttresses reduces the toxicity, though high doses of (200  $\mu$ g or greater) are still lethal, leading to acute death in mice. Histological analysis revealed cardiac and hepatic toxicity of the drug at the highest dose tested. Loading of only 100  $\mu$ g eupenifeldin within the polymer buttress avoided systemic toxicity and afforded a modest, but statistically significant, delay in the time to tumor recurrence and a significant improvement in disease-specific survival. However, the eupenifeldin-loaded buttresses impaired local tissue healing, suggesting another challenge that must be explored in the future. Additional studies focused on the kinetics of delivery and mechanism of action are underway to address this concern. *In vivo* reduction in post-surgical local recurrence of various types of cancer were previously reported using chemotherapy-loaded drug delivery systems, such as cisplatin-loaded polymeric films for pleural mesothelioma,<sup>109, 110</sup> paclitaxel-loaded polymer films for NSCLC and sarcoma,<sup>105, 106</sup> and doxorubicin-loaded film for neuroblastoma.<sup>111</sup> However, this is the first application of a natural product that is still in the pre-clinical stages of investigations in such a prolonged local delivery system for cancer treatment. This has the added benefit of demonstrating the value of such delivery systems for testing the efficacy of cytotoxic agents that may still have poor physical properties (i.e., prior to further development). Although the translation of such promising *in vitro* and *in vivo* efficacy into clinical settings is highly challenging, investigating optimal delivery platforms is important for clinical applications, both to maximize efficacy and to minimize toxicity. Many major anticancer agents, such as paclitaxel and camptothecin, were fraught with toxicity and solubility challenges

early in their development,<sup>112</sup> and yet today, they are used as front line chemotherapeutic agents. Notwithstanding the challenges observed with eupenifeldin, given the need for new anticancer agents and the efficacy observed in this murine model of lung cancer when delivered as a eupenifeldin-loaded buttress, further studies are warranted, both to enhance efficacy and minimize toxicity.

## **Conclusion**

Systemic chemotherapy is not recommended for early stage patients with non-small cell lung cancer due to the unfavorable risk:benefit ratio. Drug-loaded buttresses are a promising drug delivery strategy with significant potential to prevent local tumor recurrence following surgery. Eupenifeldin-loaded buttresses are efficacious *in vitro* for 70 days and delay tumor recurrence and improved disease-specific overall survival in a murine model of resection. From a drug delivery perspective, we describe: 1) the first use of eupenifeldin against any solid tumor; 2) a delivery system which enables controlled and extended release of an active agent via a layering method; and, 3) long-term *in vitro* cytotoxic activity and *in vivo* decreased local tumor recurrence and increased disease-free survival in a murine lung cancer model. The use of a buttress also offers a strategy to evaluate the *in vivo* efficacy of natural-product derived drug leads at an early stage, as many such compounds, including those that eventually became life-saving chemotherapeutic agents, such as paclitaxel and the camptothecins (among many others), often suffer from solubility issues. Clinically speaking, chemotherapy-loaded buttresses are an attractive therapeutic approach for reducing tumor recurrence and improving the patient risk to benefit ratio. We envision the use of such buttresses offers a “plus” treatment as its implementation does not require a change in the standard of care or surgical procedure except the replacement of a non-drug loaded buttress with a drug-loaded buttress.

## **Funding**

This work was supported by the National Institutes of Health (NIH)/National Cancer Institute [No. P01 CA125066, R01 CA227433, and R01 CA232708] as well as the NIH Small Business Innovation Research (SBIR) program [No. R43 CA213538, R43 CA224739 and R44 CA189215].

Supplementary Data

28

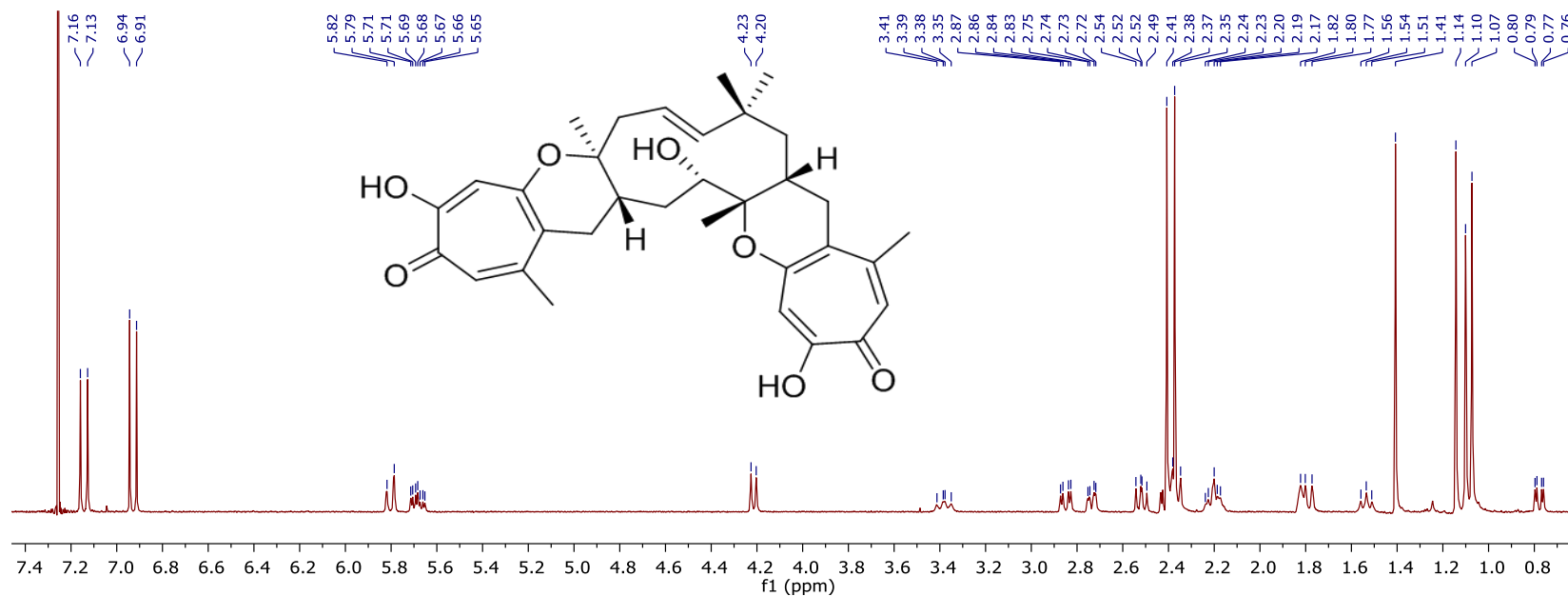
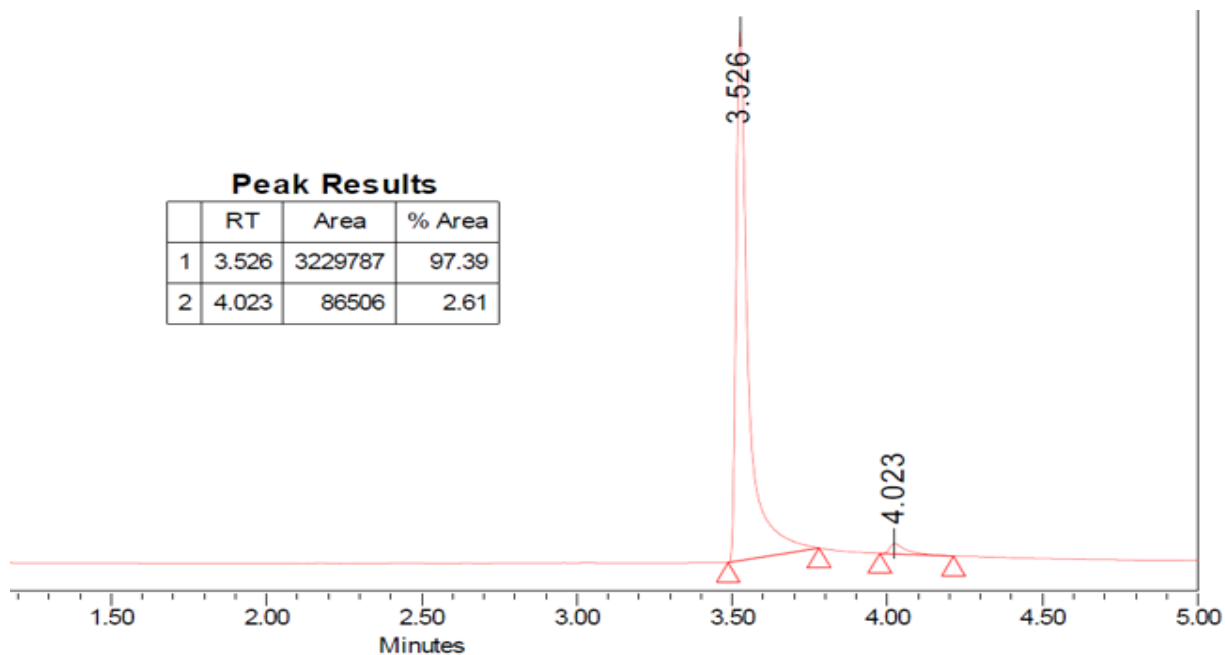


Figure 2.6. <sup>1</sup>H NMR spectrum of eupenifeldin [500 MHz, CDCl<sub>3</sub>].



**Figure 2.7.** UPLC chromatograms of eupenifeldin (UV detection), demonstrating >97% purity. Data were acquired via an Acquity UPLC system with a BEH C18 (1.7  $\mu\text{m}$ , 2.1  $\times$  50 mm) column and a  $\text{CH}_3\text{CN-H}_2\text{O}$  (0.1% formic acid) gradient that increased linearly from 20 to 100 %  $\text{CH}_3\text{CN}$  over 4.5 min.

**Table 2.1.** The number of layers and the composition of formulations **1-6** of eupenifeldin-loaded buttress.

<b>Formulation</b>	<b>1</b>	<b>2</b>	<b>3</b>	<b>4</b>	<b>5</b>	<b>6</b>
Number of eupenifeldin-polymer layers on each face	one	one	two	two	two	-
Total amount of loaded eupenifeldin ( $\mu\text{g}$ )	600	600	1200	1200	1200	0
Number of blank PGC-C <sub>18</sub> polymer layers on each side	-	one	-	one	two	Four
Total amount of loaded polymer (mg)	6	12	12	18	24	24
Representative image						

**The Effect of Tween 80 on the Solubility of Eupenifeldin in PBS.** To determine the best buffer solution to use, the extent of eupenifeldin solubility was evaluated in phosphate buffer saline (PBS) solutions with various concentrations of Tween 80 (VWR International). Eupenifeldin (0.5 mg) was dissolved in each 0.5 mL solution of PBS with 0, 0.25, 0.5, 1.0, and 2.0% (v/v) of Tween 80. The solutions were evaluated in Eppendorf tubes and incubated overnight at 37 °C with vigorous shaking. These solutions were then centrifuged for 10 mins to precipitate the undissolved eupenifeldin. The concentration of eupenifeldin in the supernatants, which represent the solubility limit, was measured by UV-Vis at 364 nm.

Eupenifeldin solubility in PBS was greatly improved with increasing concentrations of Tween 80 (50 µg/mL with 2% Tween 80 vs. 1.7 µg/mL without adding Tween), Fig. 2.8. The buffer media used in the *in vitro* release studies should be able to dissolve eupenifeldin in an amount equivalent to at least the total amount loaded on eupenifeldin-loaded buttresses (~1200 µg). Accordingly, adding 2% Tween to PBS increased eupenifeldin solvation capacity to approximately 2.5 mg in 50 mL PBS with 2% Tween 80.

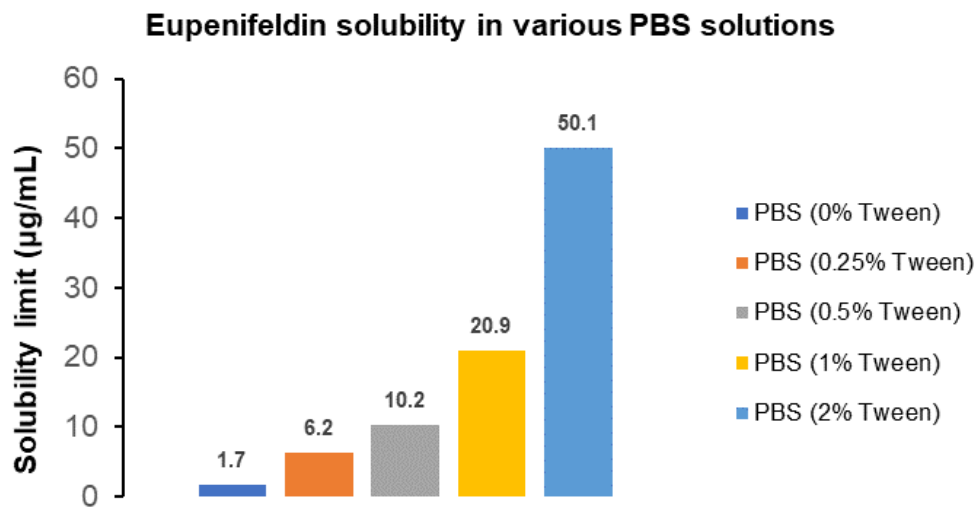


**Figure 2.8.** Eupenifeldin solubility in PBS solutions with various concentrations of Tween 80.

**PBS Volume-Saturation Study.** To determine the optimum volume of PBS for the *in vitro* release study, 15 eupenifeldin-loaded buttresses identical to those described for formulation **1** were prepared (600  $\mu\text{g}$  of eupenifeldin per buttress). Five of these eupenifeldin-loaded buttresses were submerged in each of 20, 50, and 100 mL solutions of PBS (2% Tween 80). The released amount of eupenifeldin in each solution was followed for 25 days without changing the buffer at any point. The total amount of released eupenifeldin increased with time, and over 25 days, it exceeded 1200  $\mu\text{g}$  in the 100- and 50-mL PBS solutions (Fig. 2.9). In contrast, the 20 mL PBS solution was saturated after a few days, demonstrating the limited eupenifeldin solvation capacity of this buffer volume.

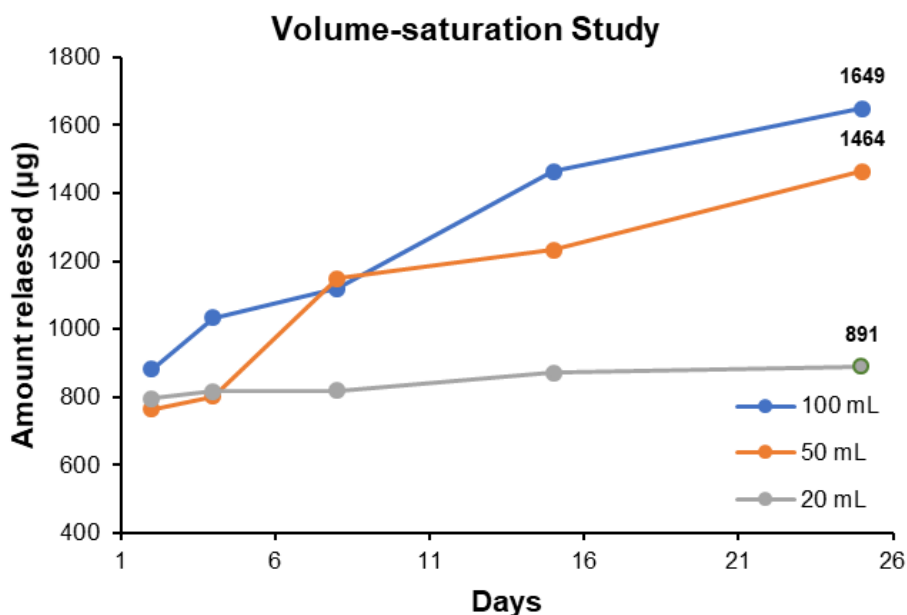


**Figure 2.9.** The amount of eupenifeldin released in 20, 50, and 100 mL solutions of PBS (2% Tween 80).

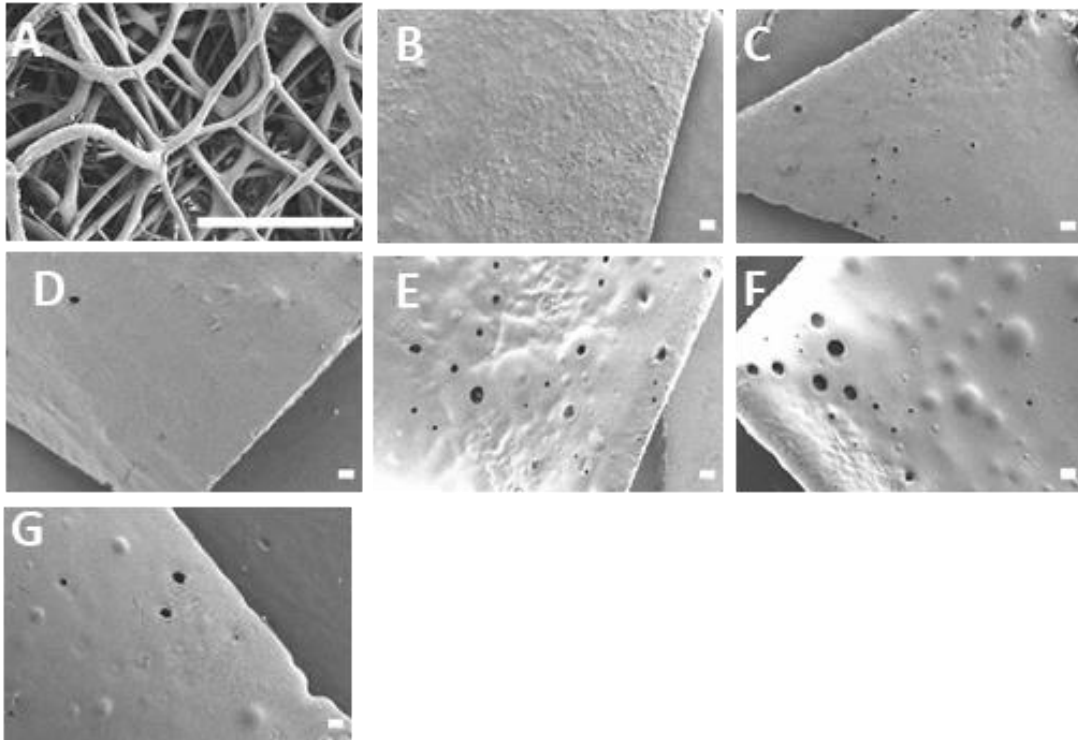


**Figure 2.10.** SEM images of uncoated PGA buttress (A) and eupenifeldin-loaded formulations 1-6 (B-G). Buttress were sputter coated with a gold-palladium target prior to imaging. SEM micrographs were taken on a Zeiss Supra 55 at 3 kV, 30 micron aperture, and a working distance of 6 mm. Scale = 100  $\mu\text{m}$ .

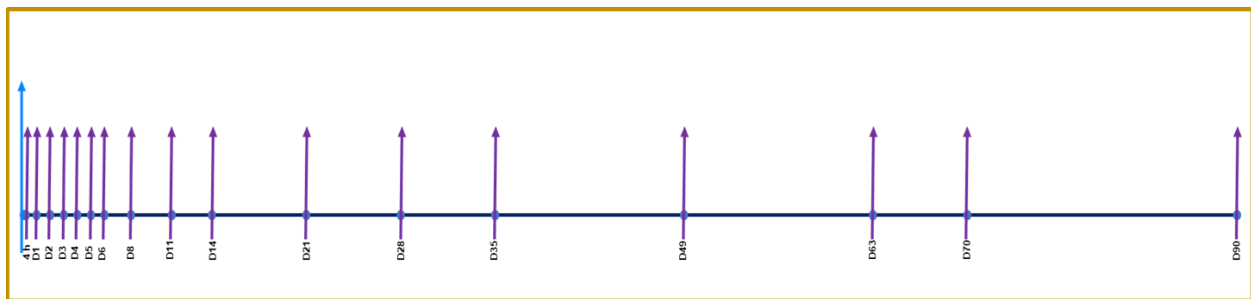


**Figure 2.11.** Timeline of the *in vitro* release study. Arrows represent the time points for replacing the buffer solutions and evaluating the concentration of eupenifeldin.

**Table 2.2.** Precision (RSD%) and accuracy (RE%) of the eupenifeldin calibration curves.

<b>no.</b>	<b>Concentration of standard solutions (ng/mL)</b>	<b>RSD (%)</b>	<b>RE (%)</b>
<b>1</b>	80	8.80	46.7
	160	2.60	7.5
	320	4.14	0.3
	640	2.43	-7.5
	1280	0.55	-1.9
	2560	0.88	0.9
<b>2</b>	80	9.67	20.8
	160	7.69	0.8
	320	4.49	3.2
	640	1.80	-3.0
	1280	0.53	-1.8
	2560	0.32	0.6
<b>3</b>	80	8.06	36.8
	160	3.24	15.5
	320	2.54	-3.5
	640	3.37	-5.1
	1280	1.91	-2.8
	2560	0.91	1.0
<b>4</b>	80	6.93	23.4
	160	7.00	6.9
	320	1.23	-9.5
	640	0.85	-0.1
	1280	1.35	-0.2
	2560	1.52	0.2
<b>5</b>	80	6.25	51.9
	160	7.56	5.9
	320	5.01	-11.0
	640	1.82	-9.2
	1280	1.23	-4.1
	2560	0.76	1.7

RSD%: Relative standard deviation percentage.

RE%: Relative error percentage.

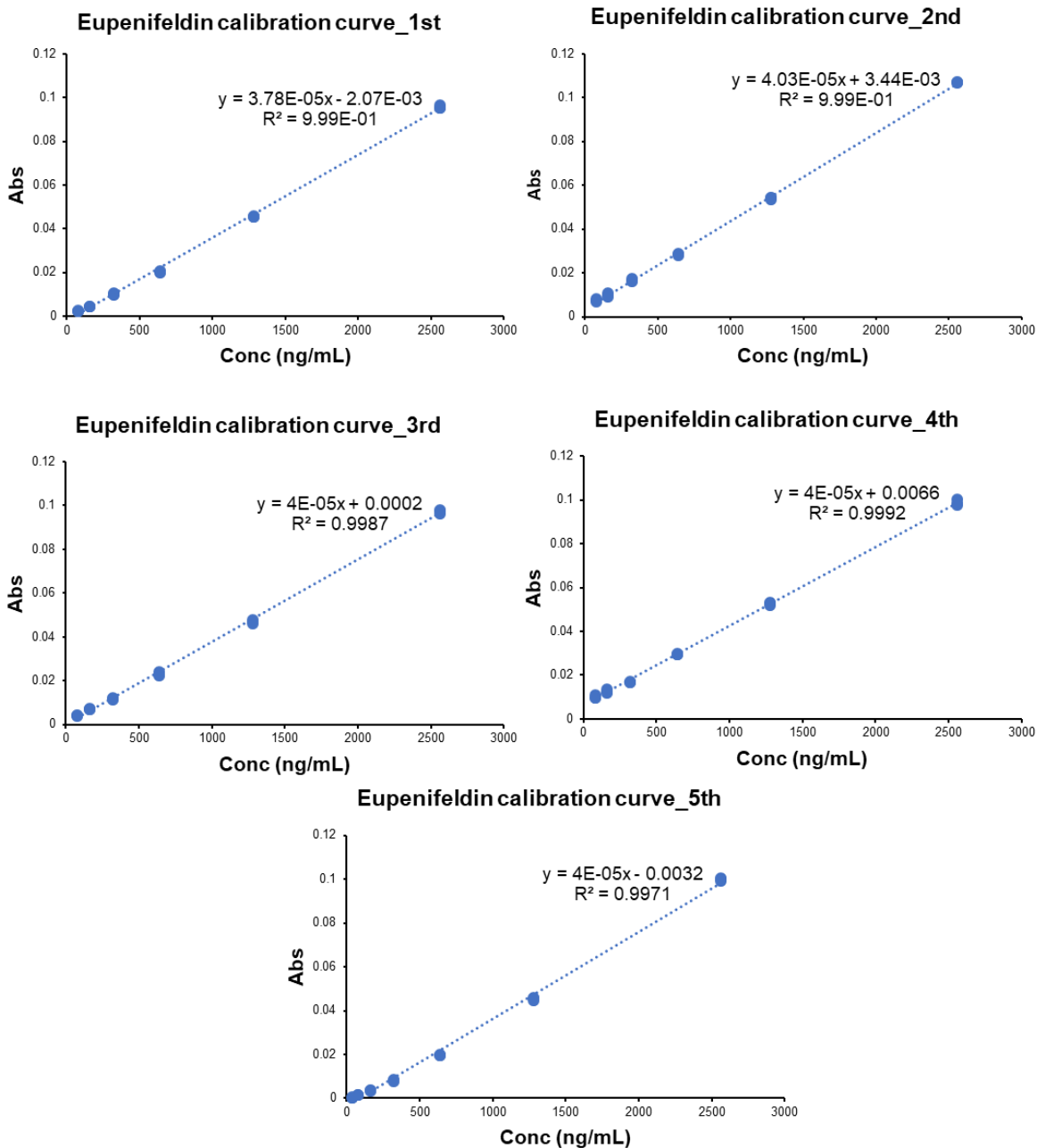


**Figure 2.12.** Calibration curves for evaluating the concentration of eupenifeldin. Each standard was evaluated thrice via UV-Vis spectrophotometry at a wavelength of 364 nm.

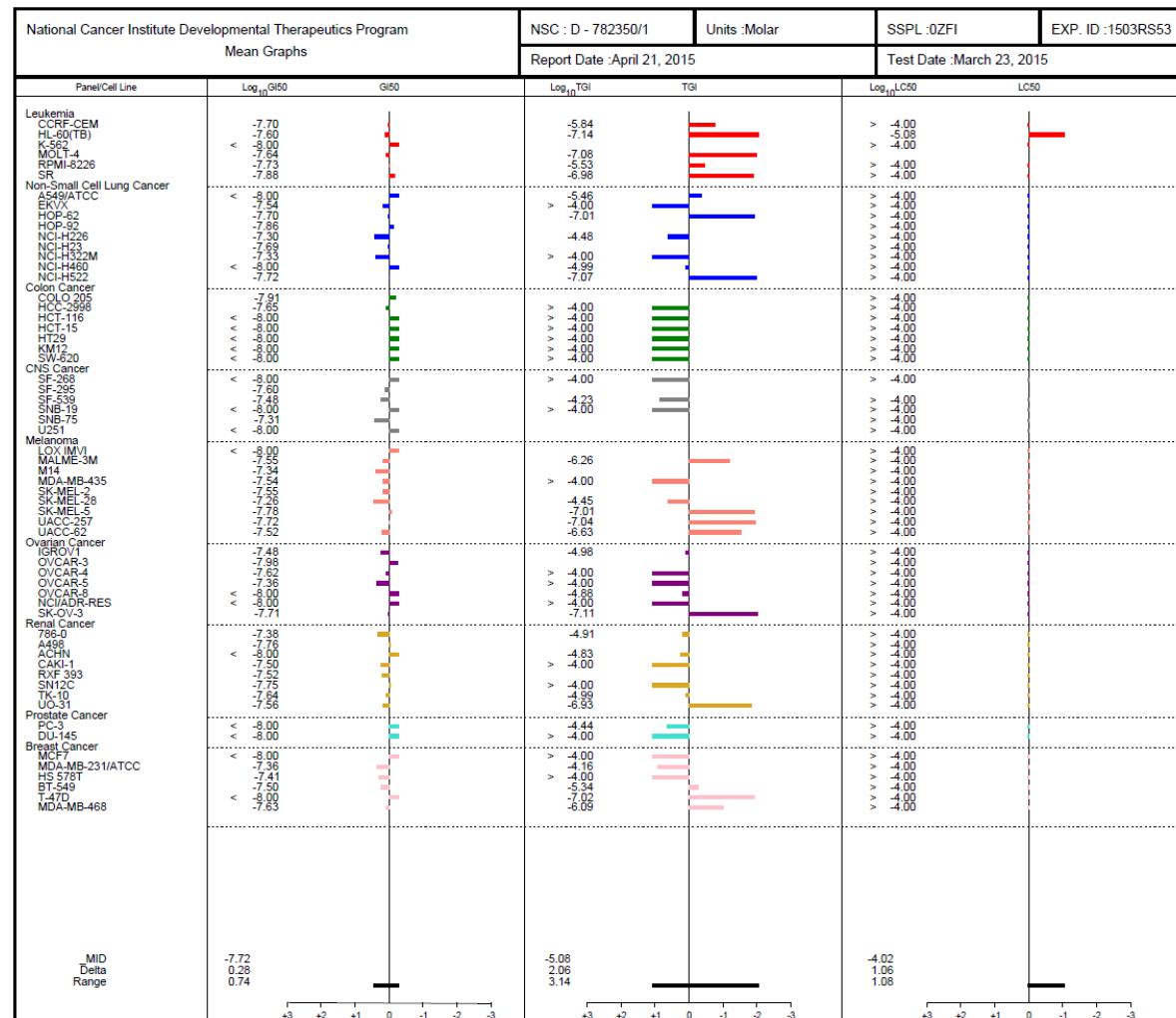
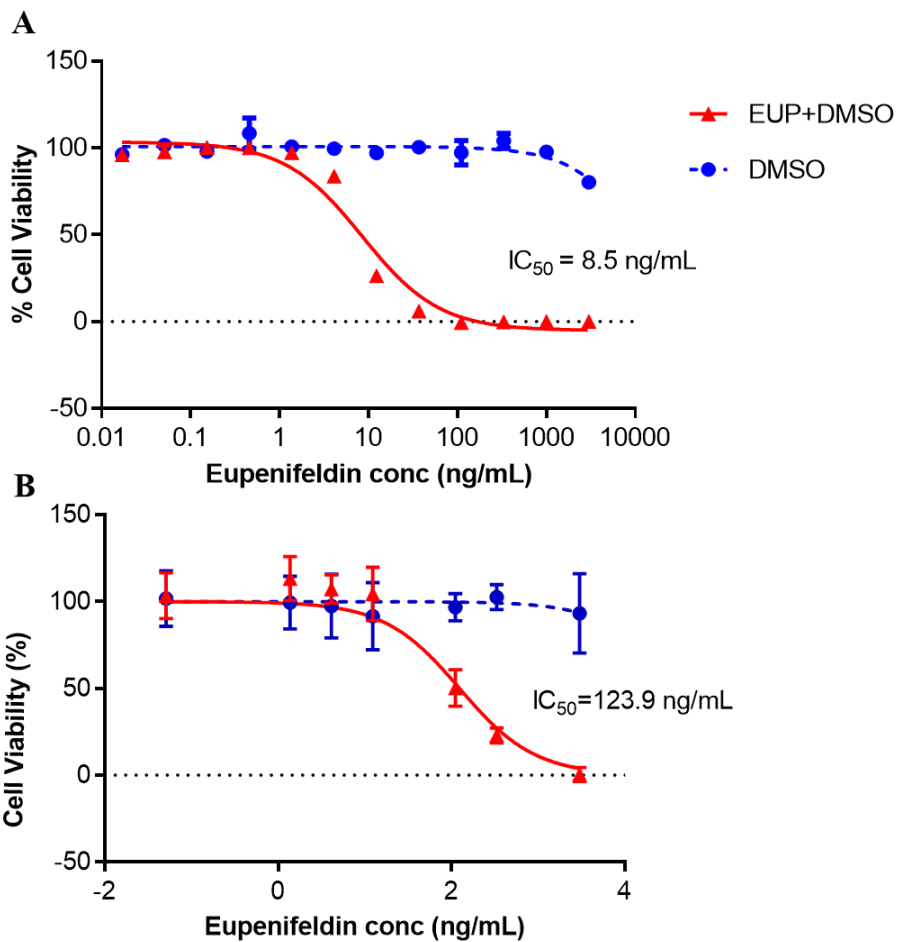


Figure 2.13. Eupenifeldin growth inhibition effect in disease-oriented human tumor cell line panel.



**Figure 2.14.**  $IC_{50}$  values of eupenifeldin against Lewis lung carcinoma (A) and human lung carcinoma A549 (B) cell lines.

***In vivo* Dose Titration Study of Eupenifeldin.** To determine the optimal tolerable dose of eupenifeldin, an initial *in vivo* maximum tolerated dose (MTD) study was conducted. To determine the dosing for “free” eupenifeldin as a comparative control (i.e., injected intraperitoneally rather than implanted in a buttress), eupenifeldin had to be dissolved in an excipient as it is not water soluble. A 50/50 combination of Cremophor EL/ethanol was selected as the excipient as this is used widely to deliver paclitaxel (i.e., Taxol) and has a long history of safe use in humans. Mice received intraperitoneal doses of eupenifeldin dissolved in Cremophor EL/ethanol to mimic systemic delivery. A prospectively determined dose escalation of 20  $\mu\text{g}$ , 40  $\mu\text{g}$ , 60  $\mu\text{g}$ , 120  $\mu\text{g}$ , 180  $\mu\text{g}$  and 540  $\mu\text{g}$  was carried out with animal’s body weight recorded and observed for signs of morbidity. Unfortunately, even at a dose as low as 20  $\mu\text{g}$ , a “tolerated” dose was not achieved. The NCI defined MTD requires < 10% deaths. Based on these results, the MTD is likely ~10  $\mu\text{g}$ .

**Table 2.3.** *In vivo* dose titration study of “free” eupenifeldin dissolved in 50/50 Cremophor EL/ethanol. The MTD was not reached and is < 20  $\mu\text{g}$ .

<b>Eupenifeldin dose</b>	<b>% of animals alive 7 days post-injection</b>	<b>Reason of death</b>
20 $\mu\text{g}$	60%	Body weight loss or moribund
40 $\mu\text{g}$	25%	Acute toxicity, body weight loss or moribund
60 $\mu\text{g}$	20%	Acute toxicity
120 $\mu\text{g}$	0%	Acute toxicity
180 $\mu\text{g}$	0%	Acute toxicity
540 $\mu\text{g}$	0%	Acute toxicity

To determine the impact of loading eupenifeldin into the buttress on MTD, doses of 600  $\mu\text{g}$ , 300  $\mu\text{g}$ , 200  $\mu\text{g}$ , and 100  $\mu\text{g}$  were loaded into PGA buttresses mimicking formulation 5’s design with two extra layers of blank polymer on each face. These were implanted subcutaneously on the upper backs of non-tumor-bearing animals. Animal weights (as a corollary of morbidity) and mortality were followed over a 14-day time period. The 600  $\mu\text{g}$  (n=3) and 300  $\mu\text{g}$  (n=4) loaded

formulations resulted in the most acute and significant decrease in body weights resulting in early mortality with median overall survival (OS) of 2-3 days. The majority of animals (3 out of 4 mice) receiving 200  $\mu\text{g}$  loaded formulation also experienced early mortality (median OS of 6 days). However, all mice in the 100  $\mu\text{g}$  group maintained stable body weights and survived to at least 14 days.

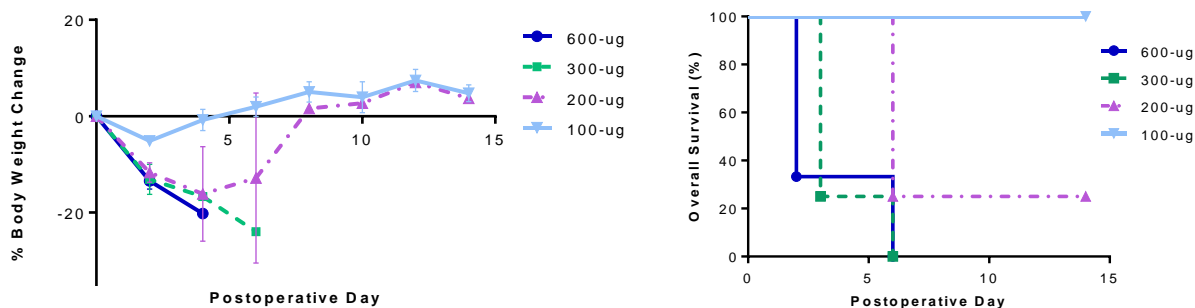


**Figure 2.15.** *In vivo* dose titration study of eupenifeldin-loaded buttresses demonstrated that 100  $\mu\text{g}$  was the maximum tolerated dose. Higher doses of 200  $\mu\text{g}$ , 300  $\mu\text{g}$ , and 600  $\mu\text{g}$  caused significant weight loss (left) and early mortality with the majority of animals unable to survive beyond a median 6 days (right).

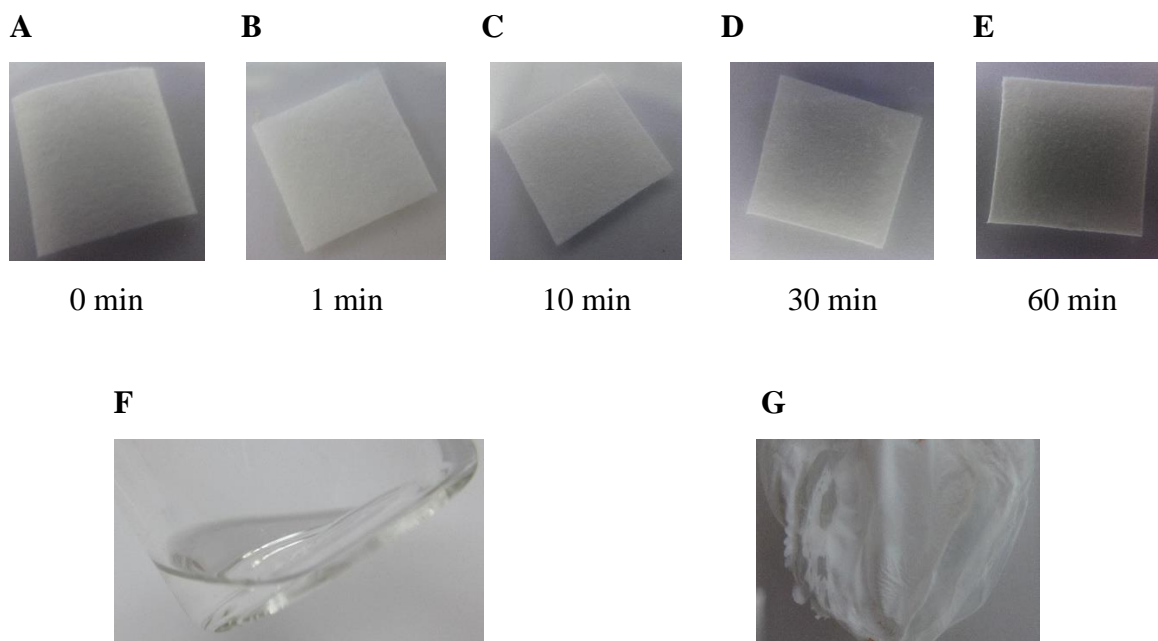


**Figure 2.16.** Stability of PGA buttress in dichloromethane vs hexafluoro-2-propanol. **A:** PGA buttress before solvent exposure, **B-E:** PGA buttress after 1, 10, 30, and 60 min of exposure to dichloromethane, **F:** PGA buttress fully dissolved in 1 mL hexafluoro-2-propanol, and **G:** PGA buttress recovered after 30 seconds of exposure to 1 mL hexafluoro-2-propanol.

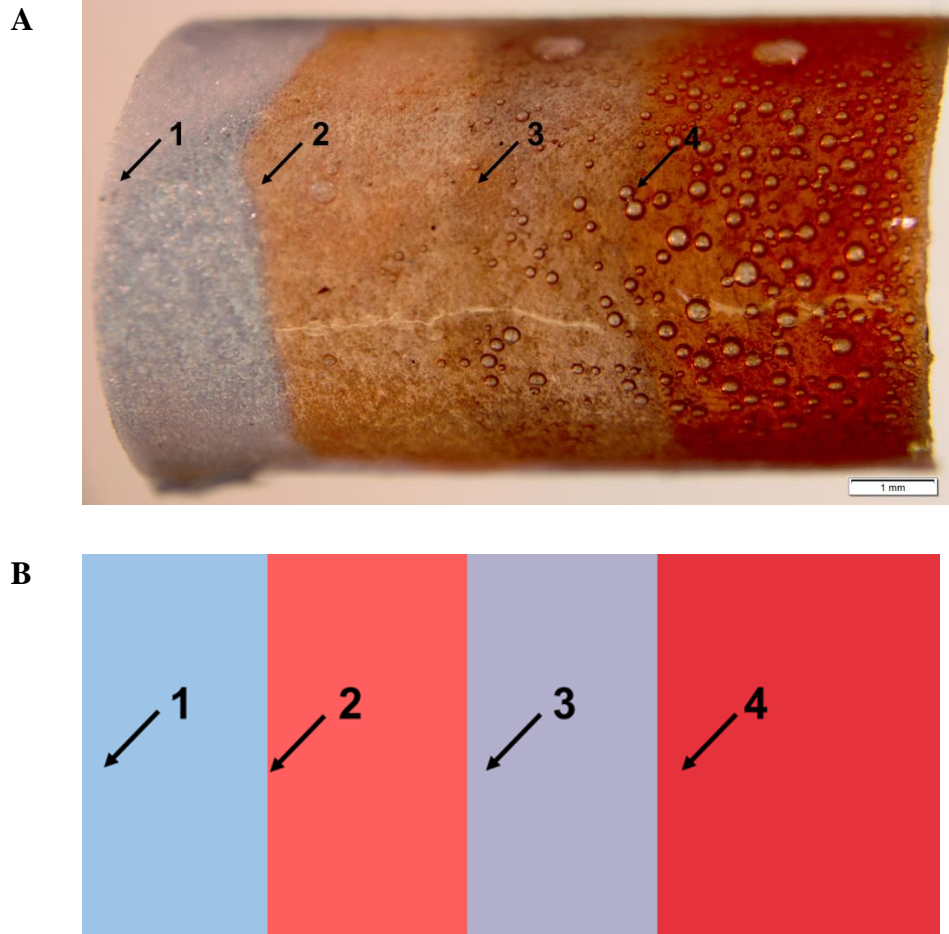


**Figure 2.17.** Panel **A**: PGA buttress coated with alternating layers of phycocyanobilin-polymer layer (**1** & **3**, blue color) and *ent*-shiraiachrome A-polymer layer (**2** & **4**, red color). Panel **B**: representative diagram for the coated buttress in panel A.

## CHAPTER III: MEDIA AND STRAIN STUDIES FOR THE SCALED PRODUCTION OF *CIS*-ENONE RESORCYLIC ACID LACTONES AS FEEDSTOCKS FOR SEMISYNTHESIS

Zeinab Y. Al Subeh, Huzefa A. Raja, Jennifer C. Obike, Cedric J. Pearce, Mitchell P. Croatt, and Nicholas H. Oberlies. *Journal of Antibiotics*, 2021. DOI.org/10.1038/s41429-021-00432-3.

Resorcylic acid lactones (RALs) with a *cis*-enone moiety, represented by hypothemycin (**1**) and (5*Z*)-7-oxozeaenol (**2**), are fungal secondary metabolites with irreversible inhibitory activity against protein kinases, with particularly selective activity for inhibition of TAK1 (transforming growth factor beta-activated kinase 1). With the goal of synthesizing RAL-analogues to explore their structure-activity relationship in a step-economical manner, starting with the isolated natural product would be the ideal approach. However, this requires a scalable isolation procedure to access sufficient quantities of these RALs. This study had three primary goals: identify fungi that biosynthesized **1** and **2**, enhance their production by optimizing the fermentation conditions on the lab scale, and develop straight forward purification processes. After evaluating 536 fungal extracts via an in-house dereplication protocol, three strains were identified as producing *cis*-enone RALs (i.e., MSX78495, MSX63935, MSX45109). Screening these fungal strains on three grain-based media revealed enhanced production of **1** by strain MSX78495 on oatmeal medium, while rice medium increased the biosynthesis of **2** by strain MSX63935. Furthermore, the purification processes were improved, moving away from HPLC purification to utilizing two to four cycles of resuspension and centrifugation in small volumes of organic solvents, generating gram-scale quantities of these metabolites readily. In addition, studying the chemistry profiles of strains MSX78495 and MSX63935 resulted in the isolation of ten other RALs (**3-12**), two radicinin analogues (**13-14**), and six benzopyranones (**15-20**), with **19** and **20** being newly described chlorinated benzopyranones.

### Introduction

The fungal kingdom, which is estimated to include between 2.2 to 5.1 million species represents a large reservoir for a variety of bioactive compounds.<sup>52, 113</sup> It is well known that growth conditions and fermentation media have a significant impact on the fungal biosynthetic machinery.<sup>114</sup> Both the yield and the composition of fungal secondary metabolites are affected by

environmental factors.<sup>58, 59, 115-119</sup> The “One-Strain-Many Compounds” approach (OSMAC) was popularized by Bode et al.<sup>120</sup> as a powerful strategy to increase the number of secondary metabolites available from one microbial source, and this involves the alteration of easily accessible cultivation parameters, i.e., media composition. We have recently used the OSMAC approach to produce verticillins as a feedstock for the generation of semisynthetic analogues.<sup>116,</sup>  
121

Resorcylic acid lactones (RALs) are a class of fungal macrolactone polyketides that have received significant attention due to a wide range of pharmacological properties, including antibiotic, antifungal, antimalarial, antiparasitic, antiviral, anabolic, cytotoxic, estrogenic, immunosuppressive, nematocidal, and sedative activities.<sup>122-125</sup> More specifically, interest in RALs has increased since the discovery of their potent inhibitory activity against several oncogenic protein kinases.<sup>126</sup> In particular, *cis*-enone containing RALs, represented by hypothemycin (**1**) and (5*Z*)-7-oxozeaenol (**2**), act as irreversible inhibitors of a select few protein kinases by forming stable Michael addition products with cysteine residues in the ATP-binding pocket.<sup>127, 128</sup> Given the vital role of protein kinases in the development, progression, and aggressiveness of cancer,<sup>129</sup> these natural products have promise for cancer drug discovery. Accordingly, we and others<sup>130-134</sup> have probed analogues of hypothemycin (**1**) and (5*Z*)-7-oxozeaenol (**2**) for their kinase inhibitory activities.

A goal of the current study was to leverage our experience in natural products chemistry with expertise in synthetic chemistry.<sup>130, 135-137</sup> Building from our knowledge of mycology and fungal metabolites, we strove to develop methods to generate the RALs on a scale that facilitates synthetic chemistry efforts. We have previously characterized a suite of RALs from various fungal species, such as *Halenospora* sp., *Phoma* sp., and *Setophoma* sp.<sup>138-140</sup> For example, (5*Z*)-7-oxozeaenol and its derivatives were isolated from a *Phoma* sp. (now identified as *Setophoma* sp., strain MSX63935) and evaluated for effects on cancer cells.<sup>139, 141, 142</sup> Using those RALs as starting materials, seven semisynthetic analogues of (5*Z*)-7-oxozeaenol were synthesized and investigated for transforming growth factor beta-activated kinase 1 (TAK1)-inhibitory activities, where the novel nonaromatic difluoro-derivative of (5*Z*)-7-oxozeaenol inhibited TAK1 at the nanomolar level.<sup>130</sup>

The development of *cis*-enone RAL analogues that retain TAK1 inhibitory activity can be achieved through two main pathways: total synthesis from simple starting materials or semisynthesis via altering the compounds isolated from nature. While total synthesis of a variety of RALs has been disclosed,<sup>123</sup> total synthesis of *cis*-enone RALs is often challenged by the high number of the reactions involved, the low overall yields, and the need to install the *cis*-enone at a late stage to avoid isomerization to the more stable *trans*-isomer,<sup>143, 144</sup> which lacks activity against TAK1.<sup>130</sup> Comparatively, it is attractive to use the naturally occurring *cis*-enone RALs as starting points to perform chemical modifications. This semisynthetic approach could facilitate the generation of a large number of analogues in very few synthetic operations, i.e. a more step-economical approach.<sup>145-149</sup> Semisynthesis is not without its own set of challenges, and the limited supply of the naturally occurring RALs is paramount, as evidenced by the high cost of the two main *cis*-enone RALs (e.g., \$569 for 1 mg of **1** and \$185 for 1 mg of **2** from Sigma-Aldrich).<sup>150</sup> Thus, the generation of gram-scale quantities of **1** and **2** was approached via three interrelated goals. First, fungi known to biosynthesize *cis*-enone RALs were identified. Next, the fermentation conditions were probed, with the goal of developing cost-efficient methods that could be implemented on the gram-scale. Finally, the techniques to purify **1** and **2** from fungal extracts were optimized. In addition, a benefit of scaling up the fermentation procedures was the identification of new compounds that are minor constituents.

## Results and Discussion

**Identifying Fungal Strains that Biosynthesize *cis*-enone RALs.** Over the past decade, our research team has built an in-house library of secondary metabolites isolated from filamentous fungi<sup>151, 152</sup>. This database, which includes over 625 compounds, is used to probe the metabolite profile of fungal extracts, and to date, at least 536 fungal cultures have been screened with our dereplication protocol. Among these, seven fungal strains were identified as biosynthesizing RALs (data not shown), and three of those produced *cis*-enone RALs (i.e., hypothemycin (**1**) and (5*Z*)-7-oxozeaenol (**2**)) (Figs. 3.1 and 3.6). Accordingly, fungal strains MSX78495, MSX63935, and MSX45109 were chosen to investigate their potential for yielding gram-scale amounts of **1** and **2**. Interestingly, while two of the strains (i.e., MSX78495 and MSX63935) produced both compounds, strain MSX45109 seemed to only generate **1**, albeit at a very low level (Fig. 3.6).

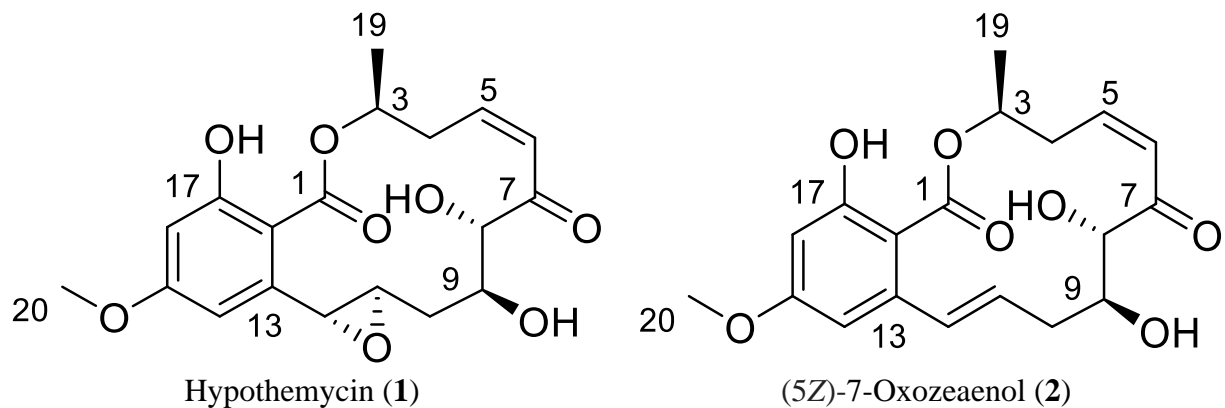


**Figure 3.1.** Structures of hypothemycin (**1**) and (5Z)-7-oxozeaenol (**2**).

**Media Studies to Enhance the Production of *Cis*-enone RALs.** To enhance the production of hypothemycin (**1**) and (5Z)-7-oxozeaenol (**2**) on the gram- scale, solid-state fermentation cultures of the three *cis*-enone RAL-producing fungi were examined on rice, oatmeal, and Cheerios (Figs. 3.7 and 3.8), due to previous experience with these media as a starting point for enhanced biosynthesis of fungal metabolites;<sup>58, 116</sup> each of those conditions were studied as biological triplicates. While we have employed scores of other media, both defined and rich, we find that these three are a cost effective way to begin the process, turning to other media only if necessary.<sup>119</sup> Subsequently, the cultures were extracted and subjected to UPLC-HRESIMS to confirm the production of the targeted compounds (i.e., **1** and/or **2**), to measure their relative abundance among the various growth conditions, and to determine the preferred fungal strain and culture medium for the highest yields (Fig. 3.9).

Based on the UPLC-HRESIMS chromatograms (Fig. 3.10), hypothemycin (**1**) was detected in the extracts of strains MSX78495, MSX63935, and MSX45109, while (5Z)-7-oxozeaenol (**2**) was detected only in the former two strains. Since the growth medium is known to affect the secondary metabolite profile of fungal cultures,<sup>114</sup> the relative abundance of both **1** and **2** were measured across the three strains and three different culture media. For **1**, strain MSX78495 showed the highest production, with oatmeal delivering the most robust results, relative to rice and Cheerios (Fig. 3.2A). Interestingly, while **1** could be detected under at least one growth condition for all three strains (Fig. 3.10), the biosynthesis by strain MSX78495 was far superior. On the other hand, the highest biosynthesis of **2** was observed with fungal strain MSX63935

fermented on rice medium (Fig. 3.2C). In contrast to each other, strain MSX78495 biosynthesized **1** on all three media, with a preference for oatmeal, whereas with strain MSX63935, the production of **2** was by far the best on rice medium; with nearly zero production when fermenting with Cheerios. Studies are warranted to investigate how the biosynthesis of two structurally-related compounds could be so different. During our study, one of the three biological replicates of strain MSX63935 grown on rice medium did not show optimal growth as compared to the other two cultures. This caused the manifestation of large error bars in Figs. 3.2C and D for the relative and absolute amount of **2** from strain MSX63935 (Fig. 3.9). We, therefore, excluded this culture from all further isolation and purification processes as discussed below.

The absolute amounts of **1** and **2** among the various extracts were measured by developing calibration curves for these two RALs (Fig. 3.11 and Table 3.2). Accordingly, the amount of **1** produced by the fungal strain MSX78495 was  $87.9 \pm 13.6$  mg/flask,  $141.3 \pm 7.8$  mg/flask, and  $121.8 \pm 17.0$  mg/flask using rice (10 g/flask), oatmeal (10g/flask), and Cheerios (7g/flask) media, respectively (Fig. 3.2B). Strain MSX78495 was a superb producer of **1**, with a slight, although not statistically significant, preference for oatmeal media. Growing fungal strain MSX63935 on rice allowed for the production of  $337.9 \pm 227.9$  mg per flask of (5Z)-7-oxozeaenol (**2**) as compared to  $80.0 \pm 61.8$  mg per flask of oatmeal medium (Fig. 3.2D). While the error bars for these latter measurements were somewhat large (Fig. 3.2), the general trend was approximately a 4-fold improvement in biosynthesis of **2** when fermenting strain MSX63935 on rice vs. oatmeal.

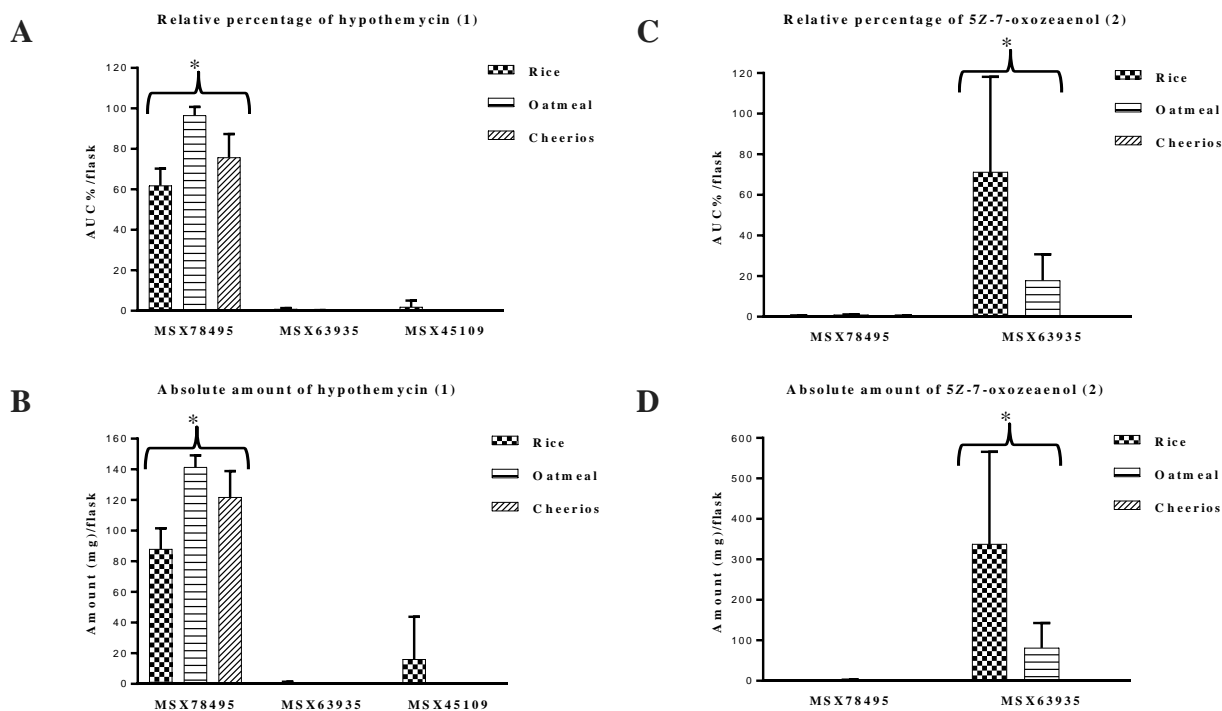


**Figure 3.2.** Panels A and B show the relative percentages and the absolute amounts of hypothemycin (**1**), respectively, across cultures grown on rice, oatmeal, and Cheerios media. Panels C and D show the relative percentages and the absolute amounts of (5Z)-7-oxozeaenol (**2**), respectively, across cultures grown on the same three media. The relative percentages were measured by LC-HRESIMS in three biological replicates and multiplied by the extract weight, and then normalized according to the extract with highest abundance. \* Indicates significantly higher productions of hypothemycin (**1**) by strain MSX78495 in panels A-B or (5Z)-7-oxozeaenol (**2**) by strain MSX63935 in panels C-D, as compared to other fungal strains ( $p < 0.05$ ). Data are presented as mean  $\pm$  SD. One of the three biological replicates of strain MSX63935 on rice medium did not show optimal growth, which caused the large error bars in panels C and D for the relative and absolute amount of **2** from strain MSX63935 grown on rice.

**Improved Procedures for the Isolation and Purification of Hypothemycin.** With enhanced fermentation procedures in hand via strain MSX78495, we sought to next optimize the isolation and purification of **1**. To do so, the extracts obtained from strain MSX78495 grown on the three different culture media were combined and subjected to a first round of fractionation via normal phase flash chromatography to obtain six fractions (Figs. 3.3 and 3.12). The fourth fraction (643 mg) was found to be over 97% pure hypothemycin (**1**) as noted by  $^1\text{H}$  NMR and UPLC-PDA data (Fig. 3.13). In addition, the adjacent fraction (i.e., fraction 3; 650 mg) was approximately

68% **1** as indicated by analogous  $^1\text{H}$  NMR and UPLC-PDA data (Fig. 3.14). To further purify fraction 3, a second round of flash chromatography was performed using nearly identical procedures (data not shown) to obtain a fraction (~500 mg) that was enriched in **1** (~89% pure). This sample was subjected to two cycles of resuspension in small volumes of HPLC-grade MeOH (6 mL for the 1<sup>st</sup> cycle and 3 mL for the 2<sup>nd</sup> cycle) followed each time by centrifugation for 5 min at 14000 RPM (g force of ~15340) to yield a pelleted sample of **1** (>94% pure; 400 mg; Fig. 3.15). The supernatants from the 1<sup>st</sup> and the 2<sup>nd</sup> cycle of centrifugations were collected (64 mg and 33 mg, respectively), and their  $^1\text{H}$  NMR spectra were compared to that of the precipitate (Fig. 3.16). While hypothemycin (**1**) was a major component in the supernatant samples, most of the impurities and/or other secondary metabolites were efficiently removed into the supernatant, leaving a >94% pure precipitate of **1**. Following this simplified purification procedure, more than 1 g of hypothemycin (**1**) was obtained rapidly, without the use of HPLC, and at a level of purity that was suitable feedstock for semi-synthetic chemistry efforts. Moreover, the amount of **1** “lost” in the supernatant was relatively low as compared to the total recovered amount of pure hypothemycin (i.e., ~60 mg of **1** recovered from supernatant samples vs. 1040 mg of **1** obtained in the precipitate).

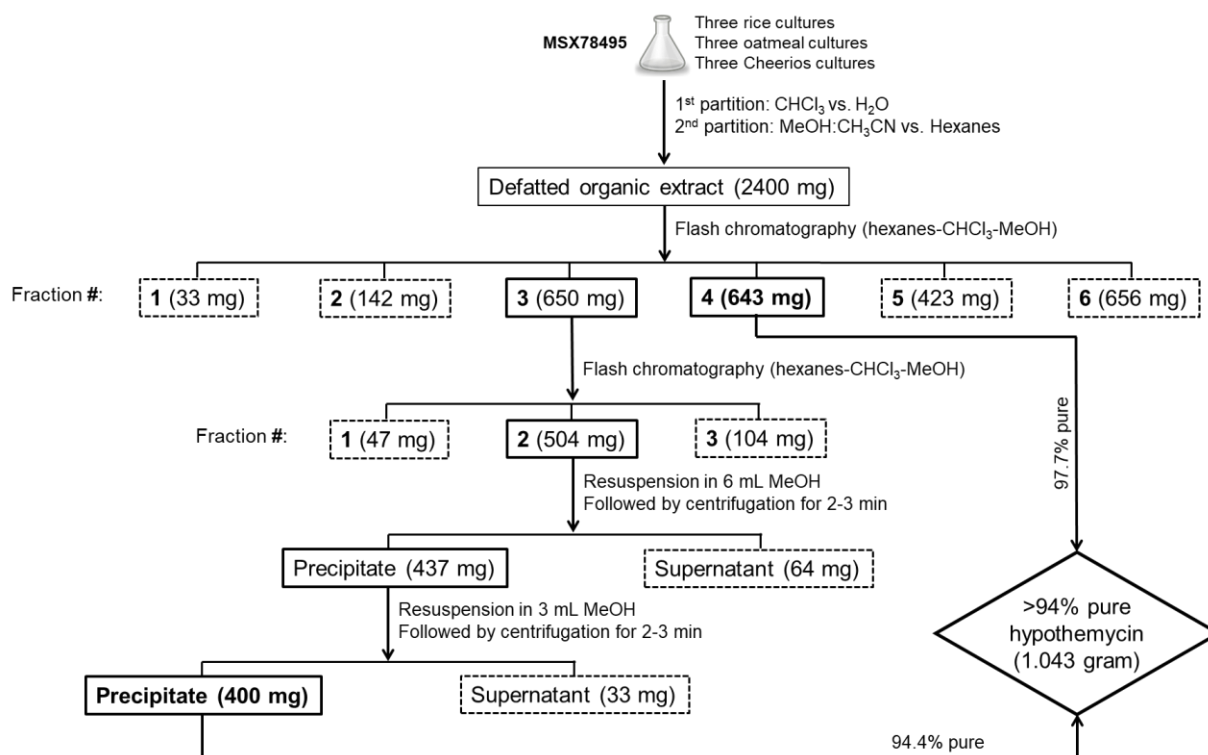


**Figure 3.3.** Illustration of the isolation and purification protocol of hypothemycin (**1**), showing how **1** can be generated both from a column fraction and via centrifugation. Over a gram of **1** was generated from nine flasks: three fermented on rice, three fermented on oatmeal, and three fermented on Cheerios. We predict that the yield would be even higher by approximately 20% if all nine flasks were grown on oatmeal.

**Improved isolation and purification of (5Z)-7-oxozeaenol.** Extracts from the fungal strain MSX63935 grown on rice showed the highest abundance of (5Z)-7-oxozeaenol (**2**) (Fig. 3.2) and therefore were used for the isolation process. By investigating the three biological replicates grown on rice, the second culture did not grow well as evidenced by a lower amount of extract, and thus less of **2**, as compared to the other two cultures (Fig. 3.9). While this resulted in a large error bar, we felt it was important to be transparent about this fact. Accordingly, the spurious extract was excluded from the purification process. The other two extracts were combined and subjected to flash chromatography to obtain 1,080 mg of the third fraction (Figs. 3.4 and 3.17), which was enriched for (5Z)-7-oxozeaenol (**2**) as noted in the <sup>1</sup>H NMR spectrum and UPLC-PDA chromatogram (Fig. 3.18; ~68% **2**). Further purification of this fraction was performed by following the resuspension/centrifugation technique described above for **1** with some modifications. In this case, instead of pursuing another round of flash chromatography, two cycles of resuspension and centrifugation in HPLC-grade MeOH (12 mL for the 1<sup>st</sup> cycle and 6

mL for the 2<sup>nd</sup> cycle) were followed by another two cycles of resuspension and centrifugation in HPLC-grade CH<sub>3</sub>CN (6 mL per cycle); each time, the centrifuge time and force was the same as noted for **1**. In each case, the precipitates were collected, with a final yield of 760 mg of **2** (> 94% pure; Fig. 3.19). The supernatants from the four cycles of centrifugations were collected (i.e., 118 mg, 57 mg, 39 mg, and 75 mg, respectively), and their <sup>1</sup>H NMR spectra were compared to that of the precipitate (Fig. 3.20). As expected, and despite the presence of **2** as a main constituent in the supernatant samples, the amount of other secondary metabolites was high. Similar to our experience with **1**, the streamlined procedure, which did not require HPLC, was used to generate more than 750 mg of **2**, which are now being used as feedstock in semi-synthetic chemistry studies, similar to those reported previously.<sup>130</sup> Again, any amount of **2** that was “lost” in the supernatant samples were relatively low (i.e., ~138 mg) and can be recovered by 1-2 injections via prep-HPLC, as described below.

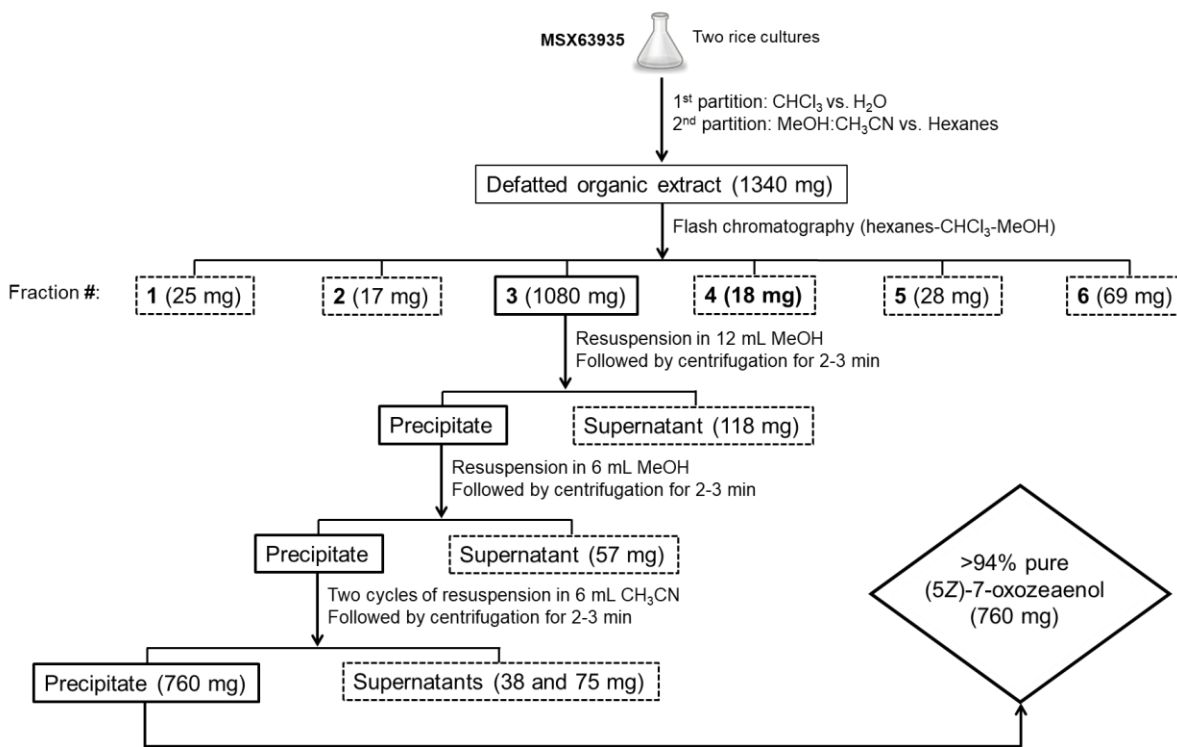


**Figure 3.4.** Schematic illustrating the improved isolation and purification process of (5Z)-7-oxozeaenol. Illustration of the isolation and purification protocol of (5Z)-7-oxozeaenol (**2**), showing how **2** can be generated both from a column fraction and via centrifugation. 760 mg of **2** were generated from two flasks fermented on rice. We predict that over a gram of **2** could be generated with this procedure from three flasks of strain MSX63935 grown on rice.

**Chemical Profile of Hypothemycin-producing Fungal Strain (MSX78495).** Purification of hypothemycin (**1**) from cultures of strain MSX78495 required its separation from other metabolites produced by this fungus. To study the other minor constituents, the supernatants were subjected to preparative high-performance liquid chromatography (HPLC) to obtain nine RALs. In addition to **1**<sup>153</sup> and **2**,<sup>139, 154</sup> dihydrohypothemycin (**3**),<sup>155</sup> aigialomycin A (**4**),<sup>155</sup> paecilomycin A (**5**),<sup>156</sup> and 4-O-demethylhypothemycin (**6**)<sup>157</sup> were isolated, and their NMR data compared favorably to literature values (see Figs. 3.21-3.26 for <sup>1</sup>H and <sup>13</sup>C NMR spectra of **1-6**).

**Chemical Profile of (5Z)-7-Oxozeaenol-producing Fungal Strain (MSX63935).** The fungal strain MSX63935 exhibited more chemical diversity and higher sensitivity to culture medium as compared to strain MSX78495 (Fig. 3.10). Investigating the content of the collected supernatant via preparative HPLC showed that strain MSX63935 was producing three classes of fungal secondary metabolites. In addition to the RALs (**1-2** and **7-12**), two radicinin analogues (**13-14**) and six benzopyranones (**15-20**) were isolated. <sup>1</sup>H and <sup>13</sup>C NMR data were used for identifying these compounds as hypothemycin (**1**), (5Z)-7-oxozeaenol (**2**), (5E)-7-oxozeaenol (**7**),<sup>139</sup> LL-Z1640-1 (**8**),<sup>158</sup> zeaenol (**9**),<sup>159</sup> 7-*epi*-zeaenol (**10**), aigialomycin B (**11**),<sup>155</sup> cochliomycin F (**12**),<sup>160</sup> radicinin (**13**),<sup>161</sup> dihydroradicinin (**14**),<sup>162</sup> alternariol (**15**),<sup>163</sup> alternariol 9-methyl ether (**16**),<sup>164</sup> rhizopycnin D (**17**),<sup>165</sup> palmariol B (**18**),<sup>164</sup> and the two new benzopyranones (**19-20**). <sup>1</sup>H and <sup>13</sup>C NMR spectra of **7-18** are presented in Figs. 3.27-3.38.

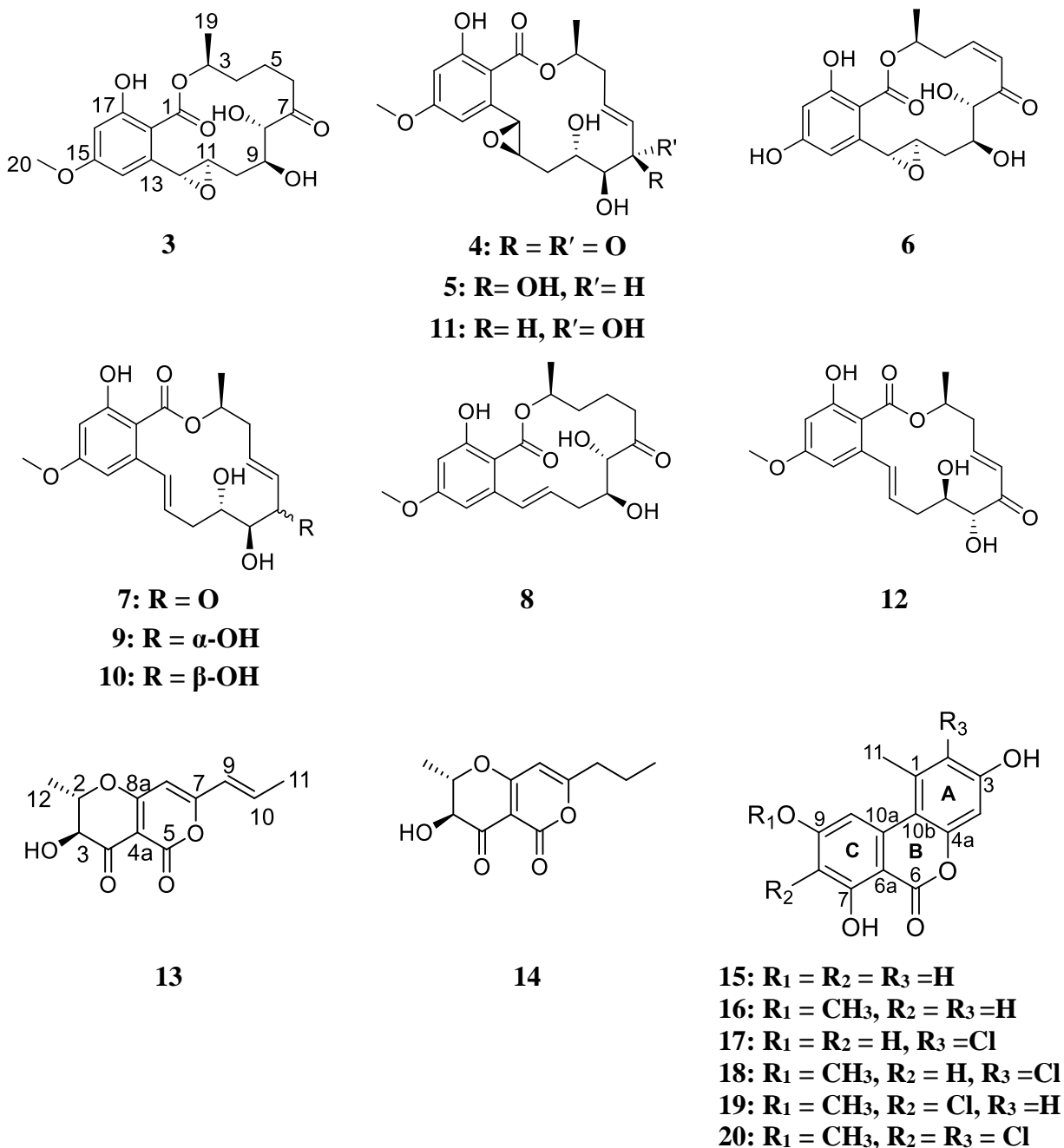


**Figure 3.5.** Fungal secondary metabolites produced by strains MSX78495 and MSX63935.

Compound **19** was obtained as a white amorphous powder with HRESIMS data matching that observed for palmariol A and B (**18**).<sup>164, 166</sup> The isotopic pattern in the mass spectrum indicated the presence of one chlorine atom in **19**, i.e., molecular ion peaks  $[M + H]^+$  of  $m/z$  307 and 309 in a 3 to 1 ratio (Fig. 3.39). The NMR data indicated the presence of twelve aromatic carbons, one carbonyl, an aromatic methyl, a methoxy group, and three aromatic protons (Table 3.1 and Fig.

3.40). Two of the aromatic protons (i.e., H-2 and H-4) showed meta-coupling with a  $J$  value of 2.3 Hz indicating their presence on a tetrasubstituted aromatic ring (Table 3.1 and Fig. 3.42). The HMBC correlations of H-2 with C-3, C-4, C-10b, and C-11 and H-4 with C-2, C-3, C-4a, and C-10b confirmed the structure of ring A (Figs. 3.43 and 3.50). The third singlet aromatic signal at  $\delta_{\text{H}}$  7.23 (H-10) indicated the presence of a pentasubstituted aromatic ring. The HMBC correlations of H-10 with C-10a and C-10b established the connections between ring A and C through ring B. The HMBC correlations of the methoxy protons with C-9 and C-10 confirmed its position at C-9 (Figs. 3.43 and 3.50). The position of the chlorine atom at C-8 was suggested by the HMBC correlation of H-10 with C-8, in addition to the chemical shift of C-8 ( $\delta_{\text{C}}$  105.8).

In a similar fashion, the molecular formula of **20** was deduced by HRESIMS data as  $\text{C}_{15}\text{H}_{10}\text{Cl}_2\text{O}_5$  (Fig. 3.45). The molecular ion peaks  $[\text{M} + \text{H}]^+$  of  $m/z$  341, 343, and 345 at a 9:6:1 ratio confirmed the presence of two chlorine atoms in **20**. The NMR data indicated the presence of two singlet aromatic protons, instead of the three observed in **19** (Table 3.1 and Fig. 3.46). The absence of meta-coupling between these two aromatic protons suggested the position of the second chlorine atom at either C-2 or C-4, and the HMBC correlation of H<sub>3</sub>-11 with C-2 confirmed the position of the second chlorine atom at C-2 (Figs. 3.48 and 3.50).

The relatively small molecular weight of these two benzopyranones (**19** and **20**), their low hydrogen to carbon ratio, and the sparsity of  $^1\text{H}$ - $^1\text{H}$  coupling imparts difficulty in confirming the positions of the aromatic substituents. Therefore, NOESY experiments were used to further facilitate the structure elucidation of these compounds, and this approach has been implemented for other hydrogen-deficient natural products<sup>59</sup>. The NOESY correlations between H-2/CH<sub>3</sub>-11, CH<sub>3</sub>-11/H-10, H-10/CH<sub>3</sub>O-9 confirmed the structure of **19** (Figs. 3.44 and 3.51). Similarly, compound **20** showed NOESY correlations between CH<sub>3</sub>-11/H-10, H-10/CH<sub>3</sub>O-9, CH<sub>3</sub>O-9/CH<sub>3</sub>-11 suggesting the replacement of the aromatic proton at C-2 with a second chlorine atom (Figs. 3.49 and 3.51). The structures of **19** and **20** were similar to palmariol A and B, which are monochlorinated benzopyranones isolated from *Lachnum palmae* and *Hyalodendriella* sp.<sup>164, 166</sup> Palmariol A has a chlorine attached to C-4, while palmariol B has a chlorine attached to C-2. Thus, compounds **19** and **20** were ascribed the trivial names palmariol C and palmariol D, respectively.

**Table 3.1.**  $^1\text{H}$  and  $^{13}\text{C}$  NMR spectroscopic data for **19** and **20** in  $\text{DMSO-}d_6$ .

Position	<b>19</b> <sup>a</sup>		<b>20</b> <sup>b</sup>	
	$\delta_{\text{C}}$ , type	$\delta_{\text{H}}$ (J, Hz)	$\delta_{\text{C}}$ , type	$\delta_{\text{H}}$ (J, Hz)
1	138.3, C		135.5, C	
2	118.0, CH	6.71, d (2.3)	120.3, C	
3	158.9, C		155.2, C	
4	101.6, CH	6.59, d (2.3)	101.9, CH	6.89, s
4a	152.5, C		150.2, C	
6	164.4, C		164.2, C	
6a	99.5, C		100.3, C	
7	158.3, C		158.1, C	
8	105.8, C		106.4, C	
9	160.7, C		160.7, C	
10	99.7, CH	7.23, s	101.2, CH	7.38, s
10a	136.1, C		135.5, C	
10b	108.4, C		110.1, C	
11	24.9, CH <sub>3</sub>	2.73, s	20.9, CH <sub>3</sub>	2.92, s
CH <sub>3</sub> O-9	56.5, CH <sub>3</sub>	4.01, s	56.9, CH <sub>3</sub>	4.09, s

<sup>a</sup>Recorded at 400 MHz for  $^1\text{H}$  and 100 MHz for  $^{13}\text{C}$ .

<sup>b</sup>Recorded at 500 MHz for  $^1\text{H}$  and 125 MHz for  $^{13}\text{C}$ .

## Discussion

Herein, the OSMAC approach was used to enhance the biosynthesis of *cis*-enone RALs from three different fungal strains. Interestingly, the effect of fermentation media, i.e., rice, oatmeal, and Cheerios, on the production of these compounds was different across the three fungal strains. Hypothemycin (**1**) was detected in the extracts of the three fungal strains (MSX78495, MSX63935, and MSX45109), which agreed with the previously reported isolation of **1** from MSX63935 and MSX45109.<sup>139, 140</sup> However, the yield of **1** was significantly higher in fungal strain MSX78495 as compared to the latter two strains (Fig. 3.2), and while growth media did not have a large impact on the chemical profile, oatmeal medium allowed for the highest yield of **1**. Despite the structural similarity between (5*Z*)-7-oxozeaenol (**2**) and **1** (i.e., its epoxide derivative), fungal strain MSX63935 was the main producer of **2** as compared to strain MSX78495 (Fig. 3.2). Moreover, culture media had a significant impact on the biosynthesis of **2**, where rice medium allowed for a higher yield as compared to oatmeal, while production was nearly eliminated in Cheerios. The effect of fermentation medium on the production of **1** from

*Aigialus parvus* was reported previously, where culture medium and its initial pH were the most important factors that affect the production of **1**.<sup>167</sup> However, that study was for growth in liquid media, which yielded 13.6 mg per g of biomass. In addition, no studies have been reported that optimized the production of **2** on the lab scale or compared the production of **1** vs **2**.

The isolation of **1** and **2** and their separation from other secondary metabolites in the culture extracts was another aspect addressed in scaling-up the biosynthesis of these compounds. Our usual isolation protocol involves the fractionation of the defatted culture extract via flash chromatography to obtain three to five fractions, followed by one to three rounds of purification using reverse-phase HPLC.<sup>138, 139</sup> As is well known to this audience, preparative HPLC has become the main isolation tool of natural products in the last several decades,<sup>168</sup> and this obviously works quite well for milligram quantities of secondary metabolites. However, its application in gram-scale isolation can be challenging and resource intensive, and with **1** and **2**, scaling their purification via HPLC is limited by the low solubility of these compounds. For example, HPLC can be used to isolate **1** and **2**, but the co-elution of dihydrohypothemycin (**3**) with **1** and LL-Z1640-1 (**8**) with **2** became problematic when injecting a 50-100 mg sample (Figs. 3.52 and 3.53). Accordingly, using a reverse-phase HPLC system for the purification of gram quantities of **1** and **2** would require 10 to 15 repeated cycles of prep-HPLC, which would consume large quantities of organic solvents and produce larger amounts of mixed solvent waste. This is in addition to the long extract-to-purification period, personnel and instrumentation time, and the associated high cost of this procedure (Table 3.3). A simplified purification process was achieved by optimizing the separation method at an early stage via flash chromatography and applying the concept of resuspension and precipitate collection from small solvent volumes. The facts that **1** and **2** were the main constituents in the original extracts, and that both exhibit relatively low solubility in solvents like MeOH and CH<sub>3</sub>CN, allowed for the enrichment of these two compounds by sedimentation in a sub-gram to gram quantity. As evidenced by the composition of the secondary metabolites isolated from the collected supernatants (Fig. 3.5), two to four cycles of resuspension/precipitate collection were efficient for purifying the targeted two *cis*-enone RALs from a mixture that includes compounds from the same structural class and/or other different classes. Table 3.3 compares the application of reverse-phase HPLC vs. the resuspension/centrifugation technique in the purification of **1** and **2**. Moreover, the ultimate goal is to use **1** and **2** as feedstock for semi-synthetic efforts, as will be reported in the future, and

thus, having a larger quantity (i.e., gram-scale) was more important than the final purity, since synthesis products will be purified in the final step.

## Conclusion

In conclusion, *cis*-enone RALs are promising fungal metabolites with potent anticancer activity. Scaling up the production of these compounds from the milligram to gram scale required the identification of the best producing fungal strain, modifying fungal growth conditions to enhance their biosynthesis, and the implementation of practical and time efficient purification techniques. Applying the above three-pronged approach allowed for the isolation of 1043 mg of hypothemycin (**1**), 760 mg of (5*Z*)-7-oxozeaenol (**2**), and the identification of 18 (**1-18**) known and two new (**19-20**) secondary metabolites.

## Material and Methods

**General Experimental Procedures.** Ultraviolet (UV) spectra were measured using a Varian Cary 100 Bio UV–Vis spectrophotometer (Varian Inc.). 1D and 2D NMR data were obtained using a JEOL ECA-500 spectrometer operating at 500 MHz or a JEOL ECS-400 spectrometer operating at 400 MHz that is equipped with a high sensitivity JEOL Royal probe and a 24-slot autosampler (both from JEOL Ltd.). Residual solvent signals were utilized for referencing (For CDCl<sub>3</sub>  $\delta_{\text{H}}$ /  $\delta_{\text{C}}$  7.26/ 77.16 and for DMSO-*d*<sub>6</sub>  $\delta_{\text{H}}$ /  $\delta_{\text{C}}$  2.50/ 39.52). UPLC-HRESIMS data were collected via an LTQ-Orbitrap XL mass spectrometer (Thermo Finnigan, San Jose, CA, USA) equipped with an electrospray ionization source (ESI) and connected to a Waters Acquity UPLC system. A BEH Shield RP18 column (Waters, 1.7  $\mu\text{m}$ ; 50  $\times$  2.1 mm) was used and heated to 40°C. The flow rate of the mobile phase was 0.3 mL/min and consisted of a gradient system of 15:85 to 100:0 of CH<sub>3</sub>CN-H<sub>2</sub>O (0.1% formic acid) over 10 min. MS data were collected from *m/z* 150 to 2000 in the positive mode. A Varian Prostar HPLC system, equipped with ProStar 210 pumps and a Prostar 335 photodiode array detector (PDA), was used to conduct all analytical and preparative HPLC experiments, with data collected and analyzed using Galaxie Chromatography Workstation software (version 1.9.3.2, Varian Inc.). Flash chromatography was performed on a Teledyne ISCO CombiFlash Rf 200 using Silica Gold columns (from Teledyne Isco) and monitored by UV and evaporative light–scattering detectors. An Eppendorf 5415

centrifuge, equipped with rotor F-45-18-11, was used for the resuspension/centrifugation of fractions enriched in hypothemycin (**1**) and (5Z)-7-oxozeaenol (**2**).

**Fungal Strains Identification.** Mycosynthetix fungal strain MSX45109 was isolated from leaf litter collected in a mangrove habitat in 1989;<sup>140</sup> MSX63935 was isolated in 1992 from leaf litter collected at an agricultural farm;<sup>139</sup> and MSX78495 was collected on terrestrial leaf litter in 1993. Molecular techniques were used to identify the three MSX strains by sequencing the internal transcribed spacer regions 1 & 2 and 5.8S nrDNA (ITS)<sup>169, 170</sup> with primers ITS1F and ITS4<sup>171, 172</sup>. As MSX45109 was identified in a previous study as *Setophoma terrestris*,<sup>140</sup> we hypothesized that the two other RAL producing strains may have phylogenetic affinities to *Setophoma*. A BLAST search using the RefSeq Database in NCBI GenBank showed MSX63935 and MSX78495 had  $\geq 90\%$  sequence homology with members of *Setophoma* spp.<sup>173</sup> Hence, we downloaded all previously described species of *Setophoma* from recently published literature<sup>174-178</sup> and constructed a multiple sequence alignment in MUSCLE using the program Seaview.<sup>179</sup> The alignment was trimmed to remove ambiguous characters using GBLOCKS.<sup>180</sup> ModelFinder was used to select the best-fit model using Akaike Information Criterion.<sup>181</sup> The best fitting substitution model: transversion model with empirical base frequencies, allowing for a proportion of invariable sites, and a discrete Gamma model with four rate categories (TVM+F+I+G4) was determined by AIC. The trimmed alignment was then used to infer the Maximum Likelihood of ITS sequence data using IQ-TREE implemented in PhyloSuite.<sup>182</sup> Ultrafast bootstrapping was done with 5000 replicates<sup>183</sup>. Nodes with UFBoot  $\geq 90\%$  are shown on the clades but only nodes  $\geq 95$  were considered strongly supported. Based on results of the Maximum Likelihood analysis using IQ-Tree, the MSX strains showed phylogenetic affinities with *Setophoma* and were nested within the *Setophoma* clade (Fig. 3.54), but we could not assign a species name to MSX63935 and MSX78495. It is likely these two strains represent putative new isolates; however additional phenotypic data along with multigene data from LSU, *tub2*, *tef-1 $\alpha$*  and *gapdh* (polyphasic approach) needs to be undertaken to determine their exact identities. Herein, we identify the two strains as *Setophoma* spp. (*Phaeosphaeriaceae*, *Pleosporales* *Ascomycota*). The ITS sequences of the two new strains are deposited in the GenBank (accession numbers: MSX63935: MW881143, MW881144; MSX78495: MW881145, MW881146).

**Media and Fermentations.** The cultures of fungal strains MSX78495, MSX63935, and MSX45109 were maintained on potato dextrose agar (PDA; Difco) and were transferred periodically to fresh PDA plates. An agar plug from the leading edge of the PDA culture was transferred to a sterile tube with 10 mL of YESD (2% soy peptone, 2% dextrose, and 1% yeast extract). The YESD culture was grown for 7 days on an orbital shaker (100 rpm) at room temperature (~23°C) and then used to inoculate three types of solid fermentation media.

As previously described,<sup>58</sup> cultures of each fungal strain were grown in three different grain-based media in triplicate: rice, breakfast oatmeal, and Cheerios breakfast cereal<sup>184</sup> for a total of 27 cultures (Fig. 3.7 and 3.8). Solid-state fermentations were carried out in 250 mL Erlenmeyer flasks. To prepare rice medium, 10 g of rice was added to each flask with 20 mL of deionized water (DI H<sub>2</sub>O). For the oatmeal medium, the same amount was used in each flask with 17 mL of DI H<sub>2</sub>O. For Cheerios medium, 7 g of Cheerios were used in each flask without water. After autoclaving these samples at 120 °C for 20 min, the flasks were inoculated with YESD seed cultures (described above) and incubated at room temperature for two weeks. Over the incubation period, the fungal cultures grew normally with no sign of growth retardation, except for the MSX63935 cultures growing on Cheerios medium, which were dried out by the time of extraction (Fig. 3.8).

**Extraction, Fractionation, and Isolation.** The extraction procedure was described previously.<sup>58</sup> Briefly, each flask of solid culture was extracted with 90 mL of 1:2 CH<sub>3</sub>OH-CHCl<sub>3</sub> and vacuum filtered. To the filtrate, 90 mL of CHCl<sub>3</sub> and 100 mL of DI H<sub>2</sub>O were added, and the mixture was stirred for 30 min and then transferred into a separatory funnel. The bottom layer was drawn off and evaporated to dryness. The dried organic extract was re-constituted in 100 mL of 1:1 CH<sub>3</sub>OH-CH<sub>3</sub>CN and 100 mL of hexanes. The CH<sub>3</sub>OH/CH<sub>3</sub>CN layer was drawn off and evaporated to dryness under vacuum. The extract amounts that were produced by each culture are shown in Fig. 3.9. Before performing further fractionation, quantitative UPLC-HRESIMS data were collected. After that, the extracts of MSX78495 grown on various media were combined to give a total of 2.4 g of extract material, while the extracts of MSX63935 grown on rice were combined to provide 1.34 g of extract material. Both extracts from the fungal strains MSX78495 and MSX63935 were subjected to normal-phase flash chromatography to obtain six fractions each using a gradient solvent system of hexanes-CHCl<sub>3</sub>-CH<sub>3</sub>OH at a 35 mL/min flow

rate. The hypothemycin-containing fraction (from MSX78495) and the (5Z)-7-oxozeaenol-containing fraction (from MSX63935) were identified via UPLC-HRESIMS. Further purification of **1** and **2** was achieved by following the outlined work-flows (Figs. 3.3 and 3.4, respectively). The supernatant collected from the resuspension/centrifugation process of the hypothemycin-containing fraction (Fig. 3.3) was subjected to preparative HPLC over a Phenomenex Synergi-Max C<sub>12</sub> preparative column using an isocratic system of 35:65 of CH<sub>3</sub>CN-H<sub>2</sub>O (0.1% formic acid) for 30 min at a flow rate of 21.2 mL/min to yield compounds **1** (60 mg), **2** (2.4 mg), **3** (6.0 mg), **4** (5.6 mg), **5** (5.2 mg), **6** (1.6 mg). The supernatant collected from the resuspension/centrifugation of the (5Z)-7-oxozeaenol-containing fraction (Fig. 3.4) was subjected to preparative HPLC over a Phenomenex Synergi-Max C<sub>12</sub> preparative column using an isocratic system of 35:65 of CH<sub>3</sub>CN-H<sub>2</sub>O (0.1% formic acid) for 28 min, then to 80:20 of CH<sub>3</sub>CN-H<sub>2</sub>O (0.1% formic acid) over 5 min at a flow rate of 21.2 mL/min to yield compounds **1** (1.1 mg), **2** (137.9 mg), **7** (27.2 mg), **8** (10.0 mg), **9** (7.7 mg), **10** (2.1 mg), **11** (2.45 mg), **12** (1.9 mg), **13** (3.0 mg), **14** (1.4 mg), **15** (8.2 mg), **16** (4.0 mg), **17** (2.4 mg), **18** (2.0 mg), **19** (13.7 mg), **20** (1.9 mg).

*Palmarinol C (19)*: Compound **19** was isolated as a white amorphous powder, UV (CH<sub>3</sub>OH)  $\lambda_{max}$  (log  $\epsilon$ ) 205 (4.2), 257 (4.5), 291 (3.9), 302 (3.9), 342 (3.9) nm; <sup>1</sup>H NMR (DMSO-*d*<sub>6</sub>, 400 MHz) and <sup>13</sup>C NMR (DMSO-*d*<sub>6</sub>, 100 MHz) (see Table 3.1); HRESIMS *m/z* 307.0364 [M + H]<sup>+</sup> (calcd. for C<sub>15</sub>H<sub>12</sub>ClO<sub>5</sub>, 307.0373).

*Palmarinol D (20)*: Compound **20** was isolated as a white amorphous powder, UV (CH<sub>3</sub>OH)  $\lambda_{max}$  (log  $\epsilon$ ) 212 (4.0), 299 (3.7), 258 (4.0), 347 (4.0) nm; <sup>1</sup>H NMR (DMSO-*d*<sub>6</sub>, 500 MHz) and <sup>13</sup>C NMR (DMSO-*d*<sub>6</sub>, 125 MHz) (see Table 3.1); HRESIMS *m/z* 340.9974 [M + H]<sup>+</sup> (calcd. for C<sub>15</sub>H<sub>11</sub>Cl<sub>2</sub>O<sub>5</sub>, 340.9984).

**Quantification of Hypothemycin (1) and (5Z)-7-Oxozeaenol (2).** Calibration curves of hypothemycin (**1**) and (5Z)-7-oxozeaenol (**2**) were developed using pure standards isolated from fungal strains MSX78495 and MSX63935, respectively. Ten standard solutions were prepared in CH<sub>3</sub>CN at a concentration range of 3-1536 ng/mL. HRESIMS data was collected in triplicate via a UPLC-HRESIMS (Thermo LTQ Orbitrap XL) system using the area under the curve (AUC) to generate the calibration curves. A BEH Shield RP18 column (Waters, 1.7  $\mu$ m; 50  $\times$  2.1 mm)

heated to 40 °C was utilized to generate the calibration curves. The flow rate of the mobile phase was 0.3 mL/min and consisted of a gradient system of 15:85 to 100:0 of CH<sub>3</sub>CN-H<sub>2</sub>O (0.1% formic acid) over 10 min. MS data were collected from *m/z* 150 to 2000 in the positive mode. The linearity of each calibration curve, relative error (RE), and limit of quantitation (LOQ), which is the lowest amount of analyte that can be quantitatively determined with suitable precision and accuracy, were calculated and summarized (Fig. 3.11 and Table 3.2). Extracts from the fungal strains MSX78495, MSX63935, and MSX45109 were analyzed in triplicate, the areas were averaged, and the concentrations of **1** and **2** were extrapolated from the corresponding calibration curve. Statistical analysis was carried out using GraphPad Prism (GraphPad Software, La Jolla, CA), and comparisons were made using one-way ANOVA followed by Tukey post hoc test.

## **Funding**

This research was supported in part by the National Institutes of Health/National Cancer Institute via grants P01 CA125066 and R15 CA246491.

## Supplementary Data

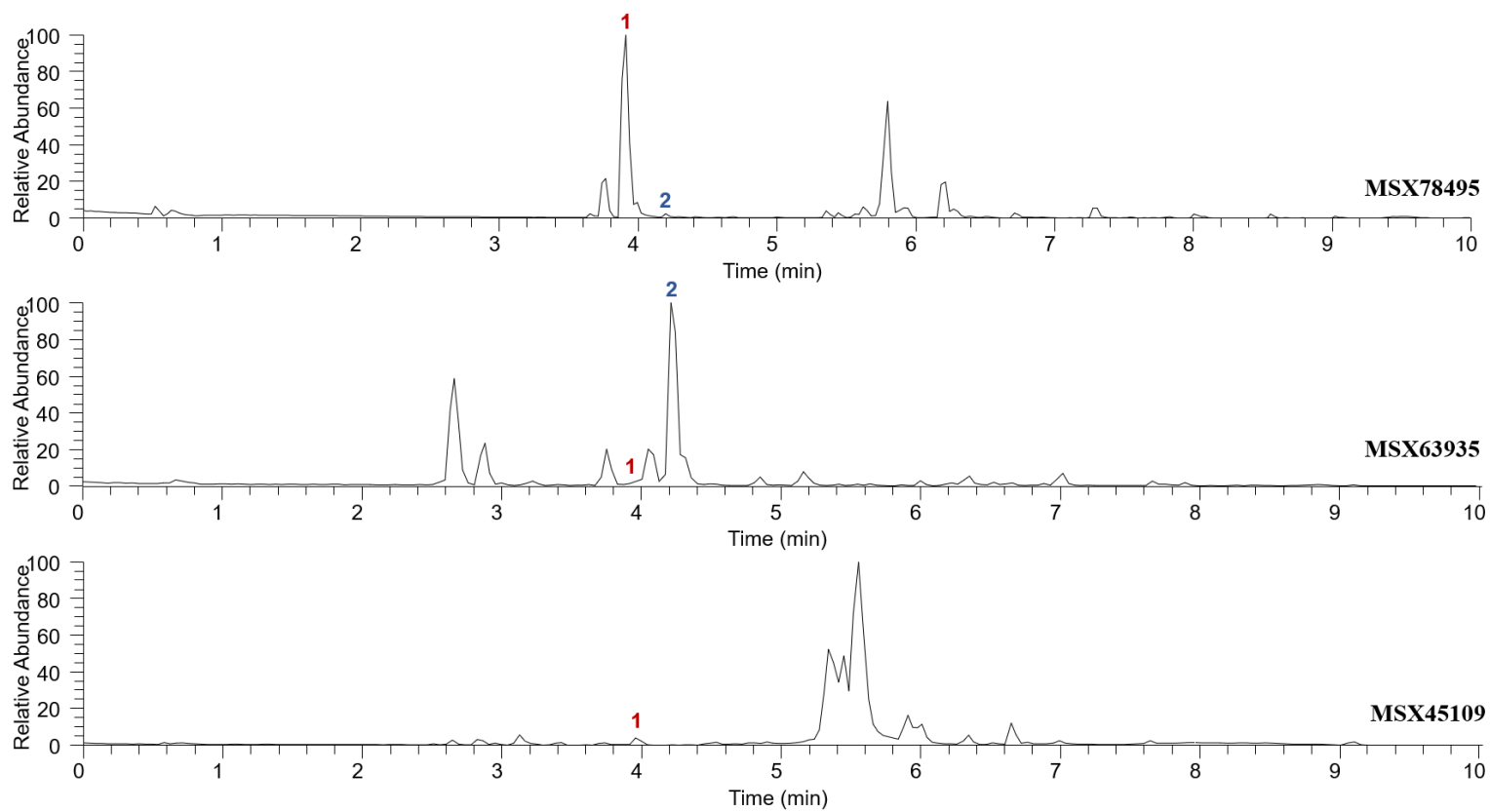


**Figure 3.6.** HRESIMS data (base peak chromatograms) for the extracts of strains MSX78495, MSX63935, and MSX45109, where the presence of hypothemycin (**1**) and (5*Z*)-7-oxozeaenol (**2**) were identified via dereplication.

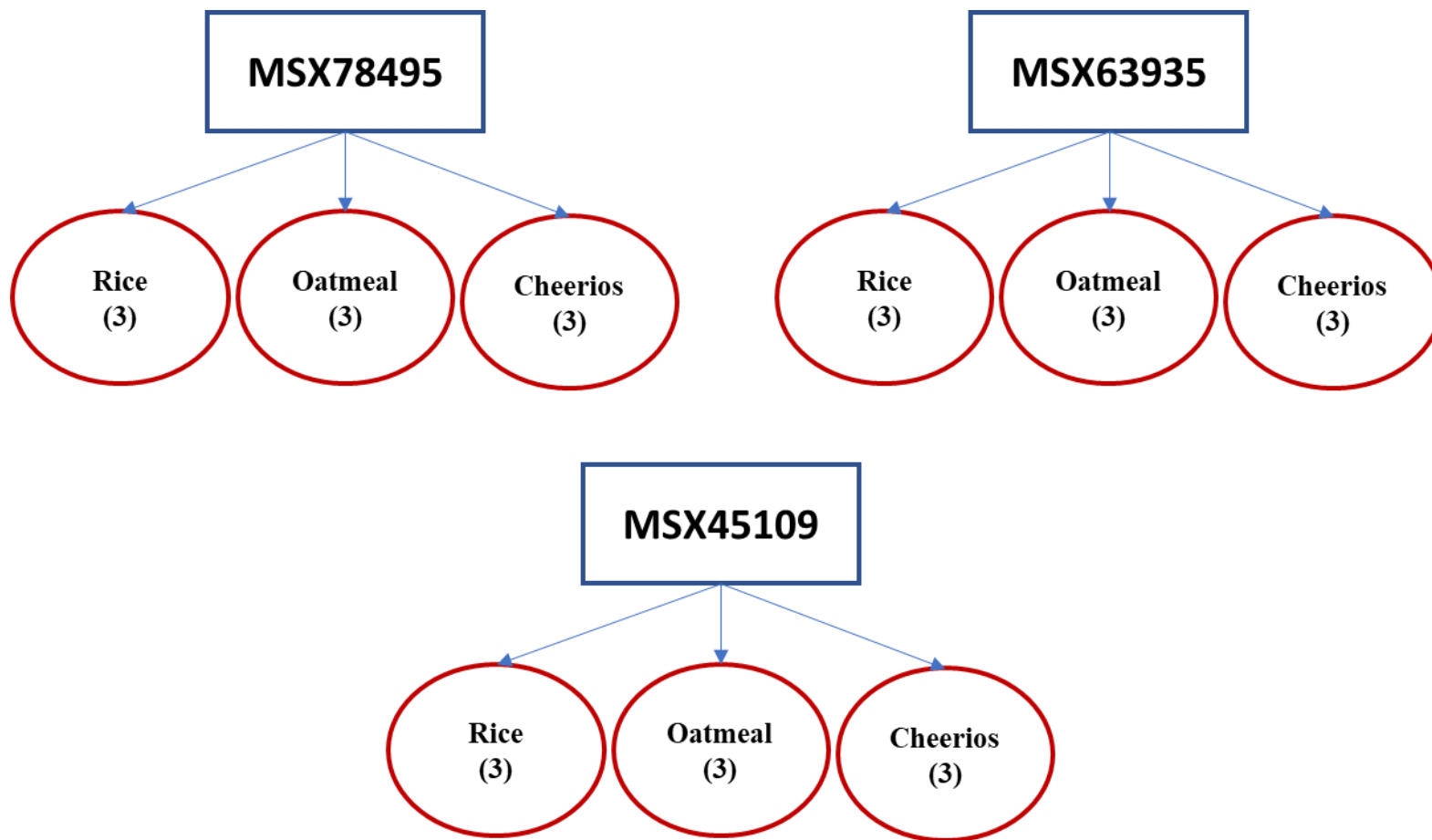


**Figure 3.7.** The three *cis*-enone RALs-producing fungi grown in triplicates on three different media: rice, oatmeal, and Cheerios.

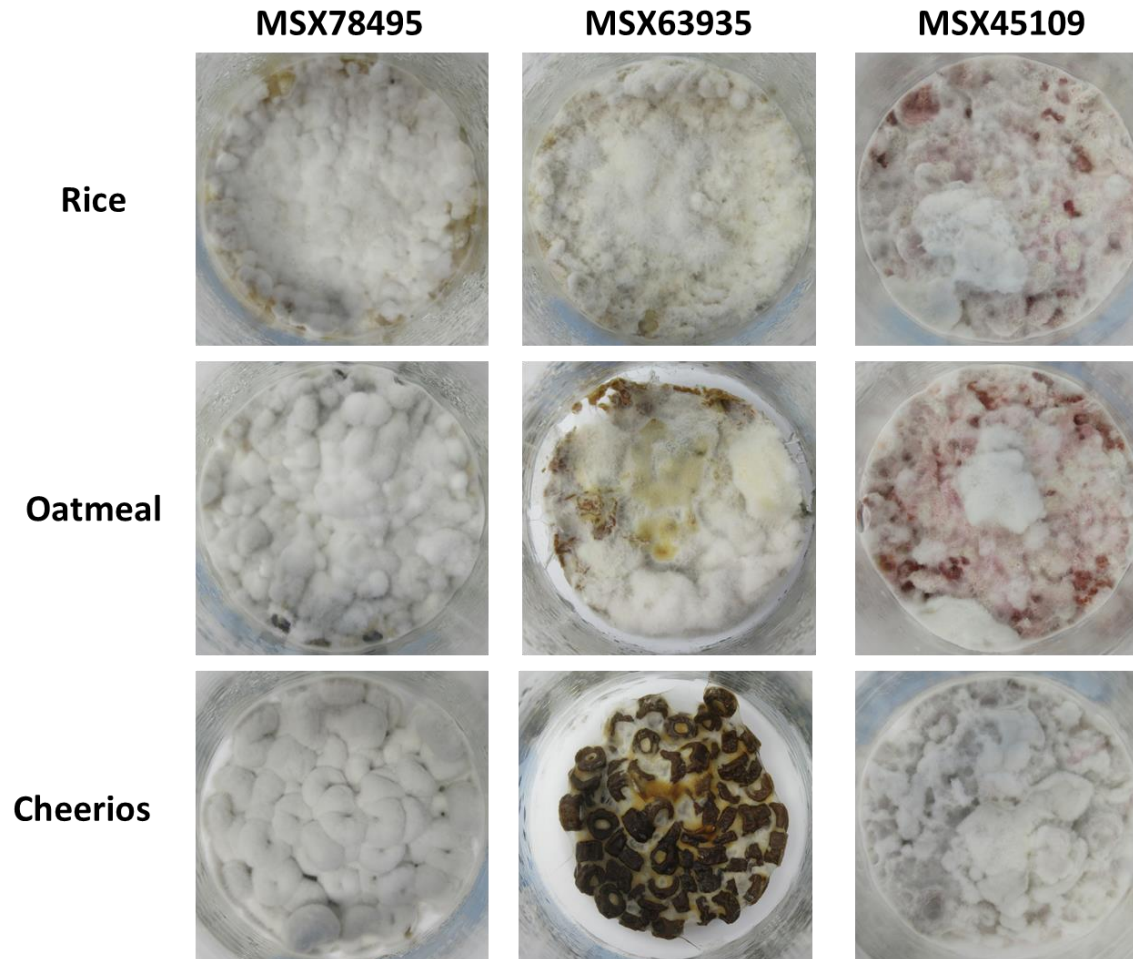
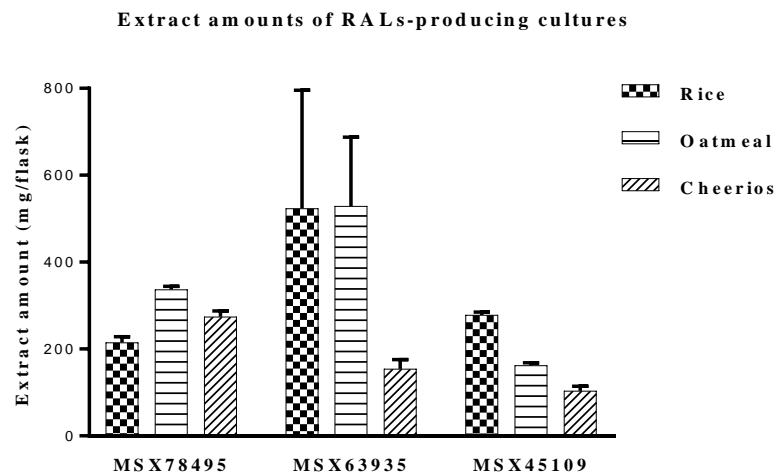


**Figure 3.8.** Representative images of the three fungal strains MSX78495, MSX63935, and MSX45109 grown on three different media (i.e. rice, oatmeal, and Cheerios). These photographs were taken looking down the neck of the Erlenmeyer flasks after the samples had been growing for 14 days.



**Extract amount (mg) obtained from strains MSX78495, MSX63935, and MSX45109 grown on rice, oatmeal, and Cheerios.**

MSX78495			MSX63935			MSX45109		
Rice	Oatmeal	Cheerios	Rice	Oatmeal	Cheerios	Rice	Oatmeal	Cheerios
227.2	329	266	753	650	144	270	167	113
201.7	345	289	222	350	141	283	165	92
216.6	337	268	596	588	179	280	155	107

**Figure 3.9.** The extract amounts produced by the fungal strains MSX78495, MSX63935, and MSX45109 grown on rice, oatmeal, and Cheerios. The error bars are based on three biological replicates, each analyzed in triplicate. The value highlighted in red was considered an outlier and was responsible for the large error bars associated with strain MSX63935. That culture was not used in the purification studies for (5Z)-7-oxozeaenol. Data in the bar graph are presented as mean  $\pm$  SD.

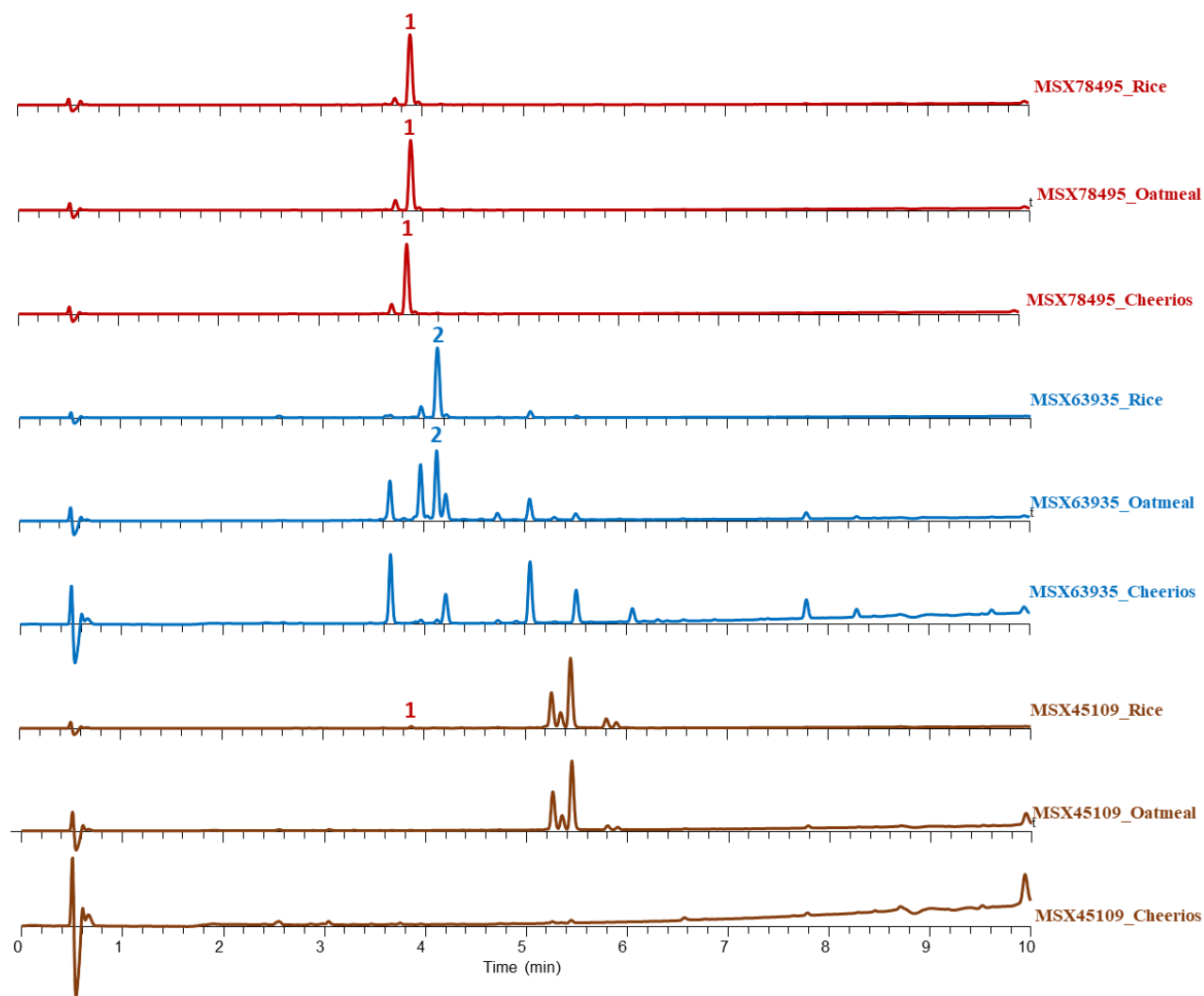


**Figure 3.10.** UPLC-HRESIMS chromatograms of the extracts of the cultures from Fig. 3.9, all prepared at a concentration of 0.3 mg/mL. Each chromatogram represents an average of three biological replicates, and the annotation refers to hypothemycin (**1**) and (5Z)-7-oxozeaenol (**2**) as detected via dereplication.

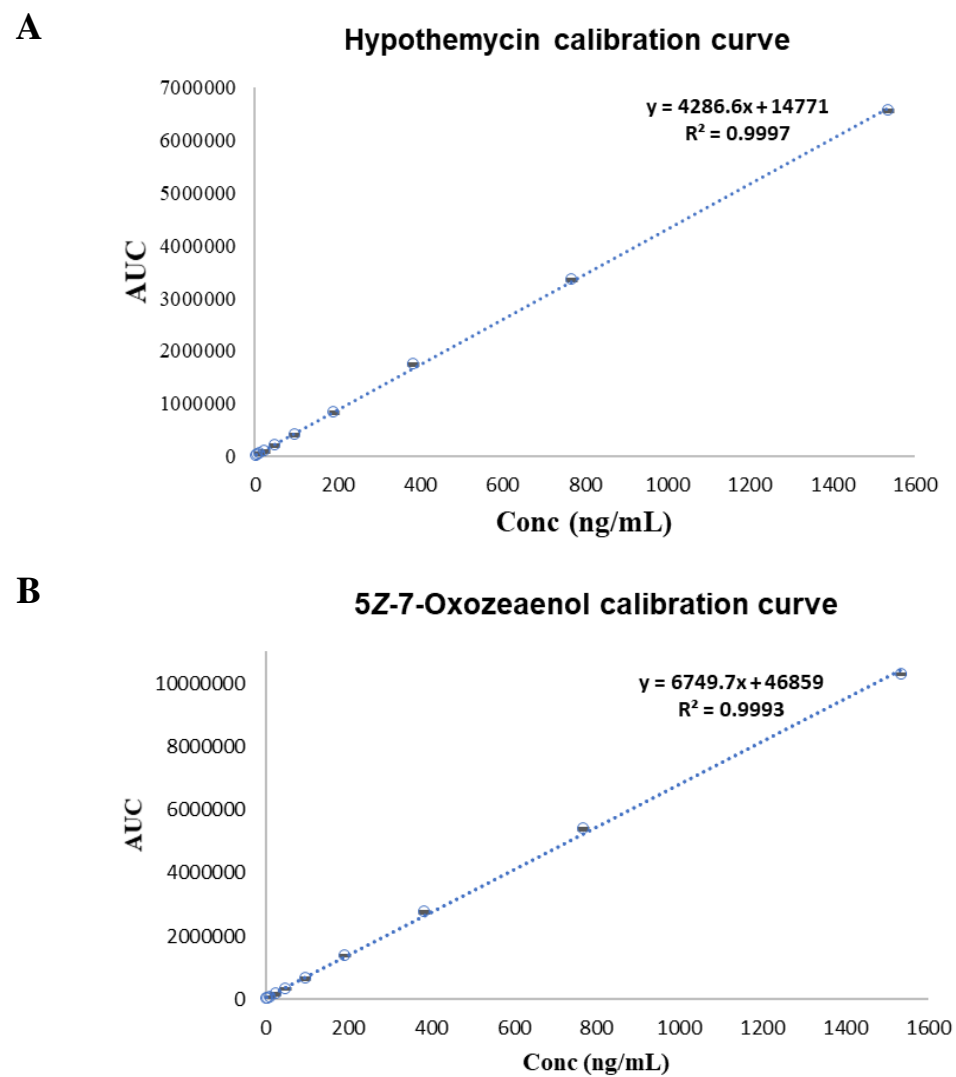


**Figure 3.11.** Calibration curves for hypothemycin (A) and (5Z)-7-oxozeaenol (B) developed to measure the absolute amounts for these two compounds across various extracts. Each standard was subjected thrice to UPLC-HRESIMS to measure the AUC.

**Table 3.2.** The calibration curve parameters used for the quantitative analysis of hypothemycin (**1**) and (5Z)-7-oxozeaenol (**2**).

<b>Parameters</b>	<b>1</b>	<b>2</b>
Retention time (min)	3.89	4.14
Observed mass ( <i>m/z</i> )	379.13773	363.14285
Calculated mass ( <i>m/z</i> )	379.1393	363.1443
Linear equation	$y = 4286.6x + 14771$	$y = 6749.7x + 46859$
R <sup>2</sup>	0.9997	0.9993
Range (ng/mL)	3-1536	3-1536
Relative error (RE)	<15%	<15%
Linearity range (ng/mL)	48-1536	48-1536

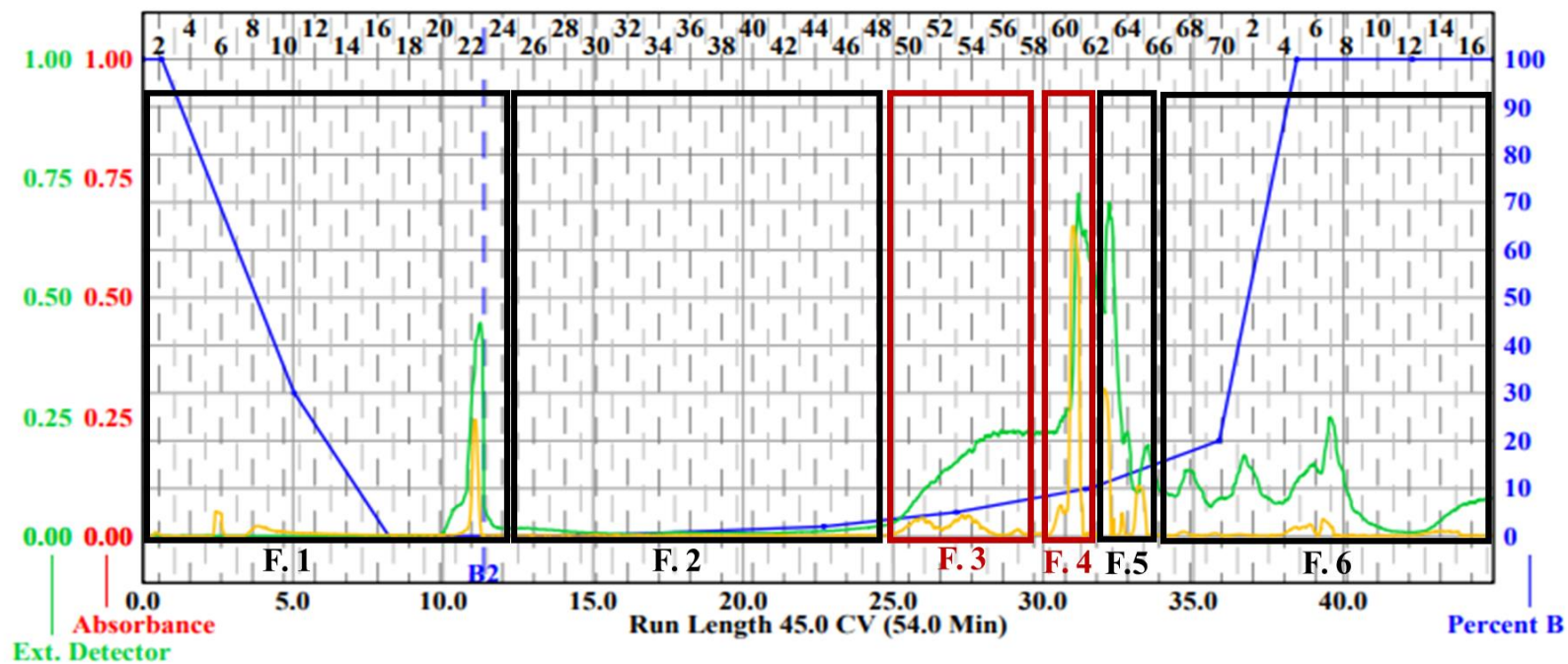


**Figure 3.12.** First round of fractionation for the fungal extracts of MSX78495 via normal-phase flash chromatography to obtain six fractions (F.1-F.6). A gradient solvent system of hexanes- $\text{CHCl}_3$ - $\text{CH}_3\text{OH}$  at a 35 mL/min flow rate was used. The elution of compounds was monitored via ELSD detector (green line) and PDA detector (yellow line).

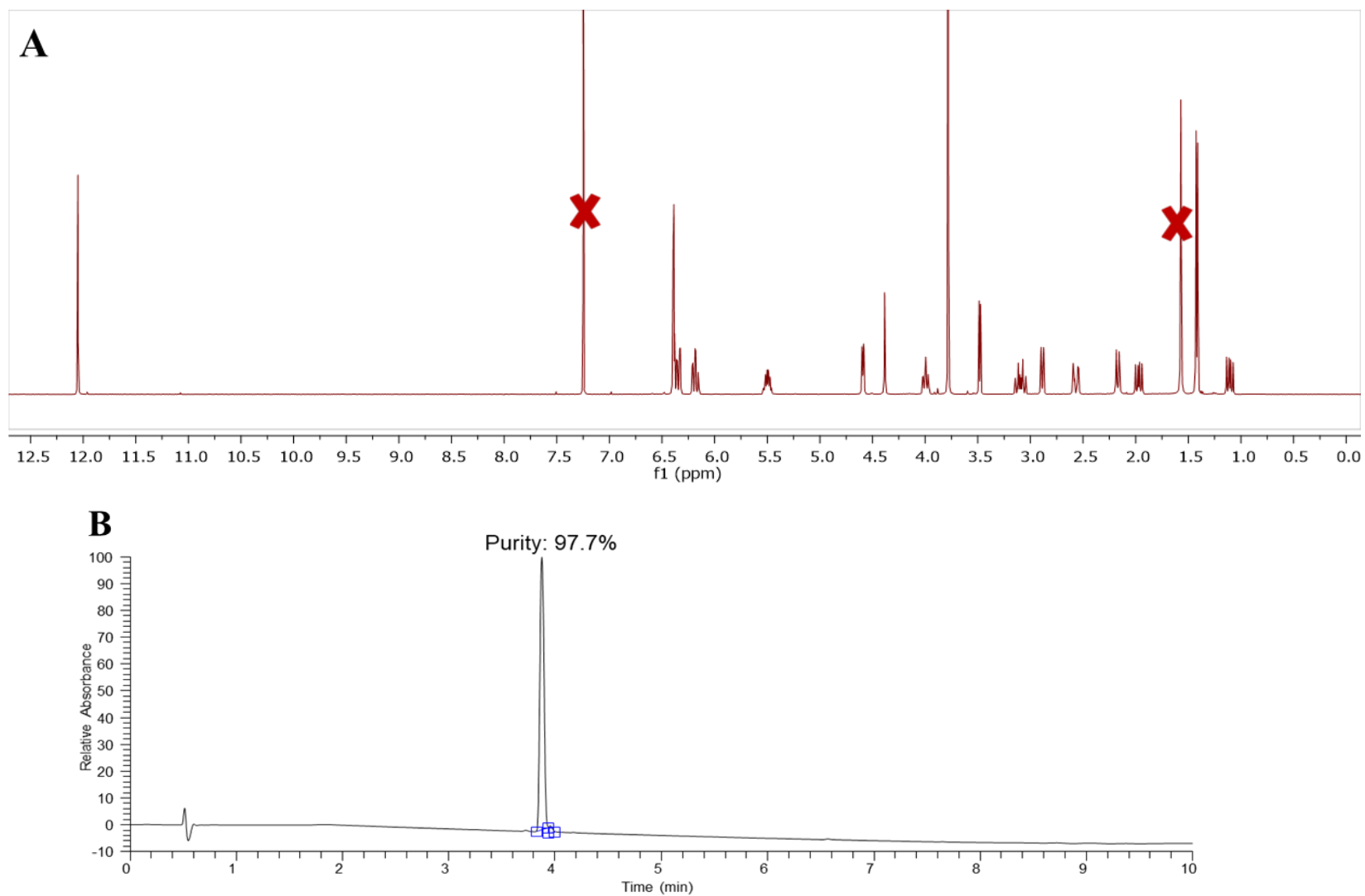


**Figure 3.13. A:**  $^1\text{H}$  NMR spectrum of fraction 4 from the flash chromatography shown in Fig. 3.12, demonstrating the purity of hypothemycin [400 MHz,  $\text{CDCl}_3$ ]. **B:** UPLC chromatogram (PDA detection) of fraction 4 from the flash chromatography shown in Fig. S7, demonstrating >97% purity.

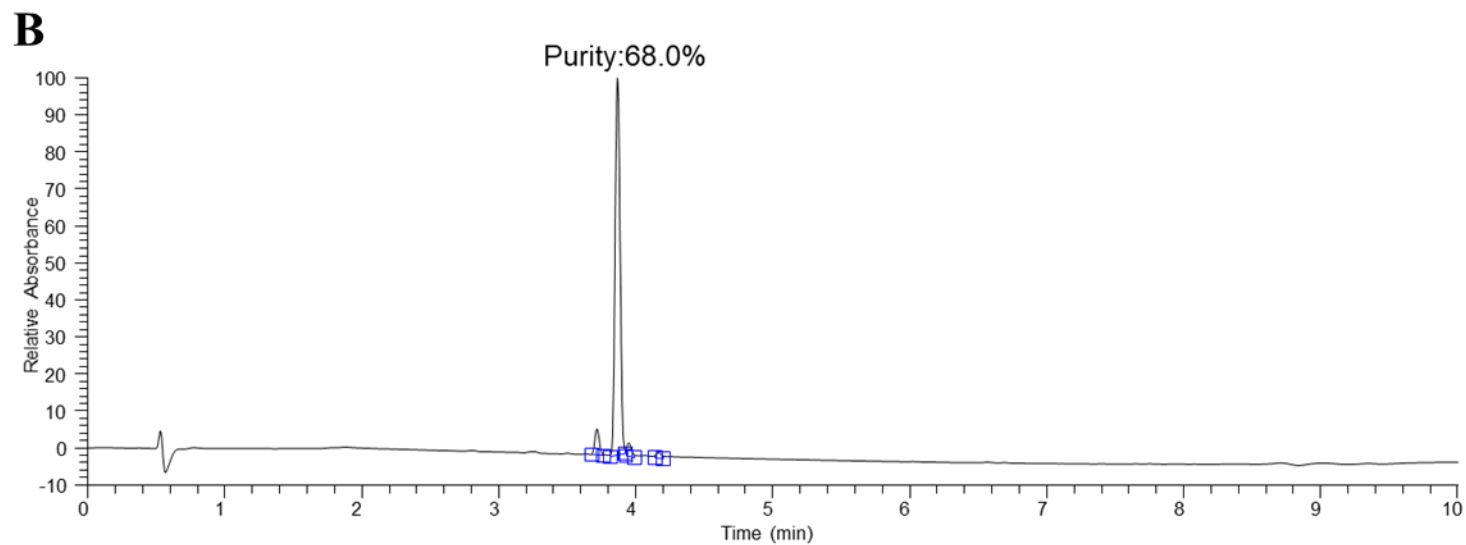
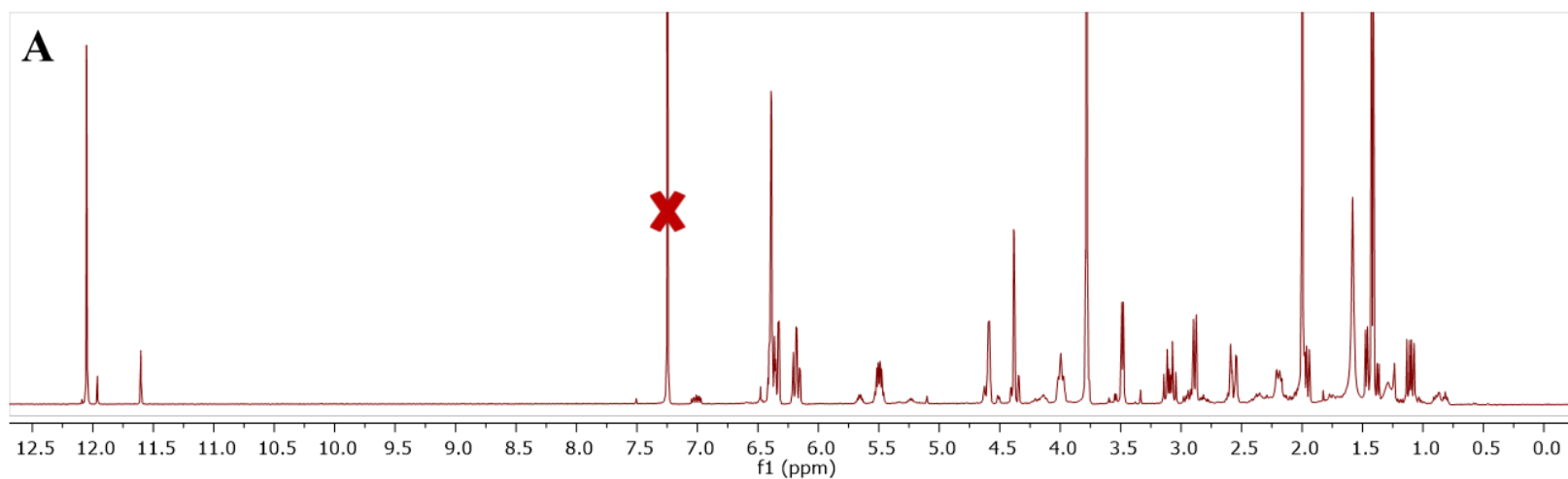


**Figure 3.14. A:**  $^1\text{H}$  NMR spectrum of fraction 3 from the flash chromatography shown in Fig. 3.12, demonstrating the purity of hypothemycin [400 MHz,  $\text{CDCl}_3$ ]. **B:** UPLC chromatogram (PDA detection) of fraction 3 from the flash chromatography shown in Fig. S7, demonstrating ~68% hypothemycin content.

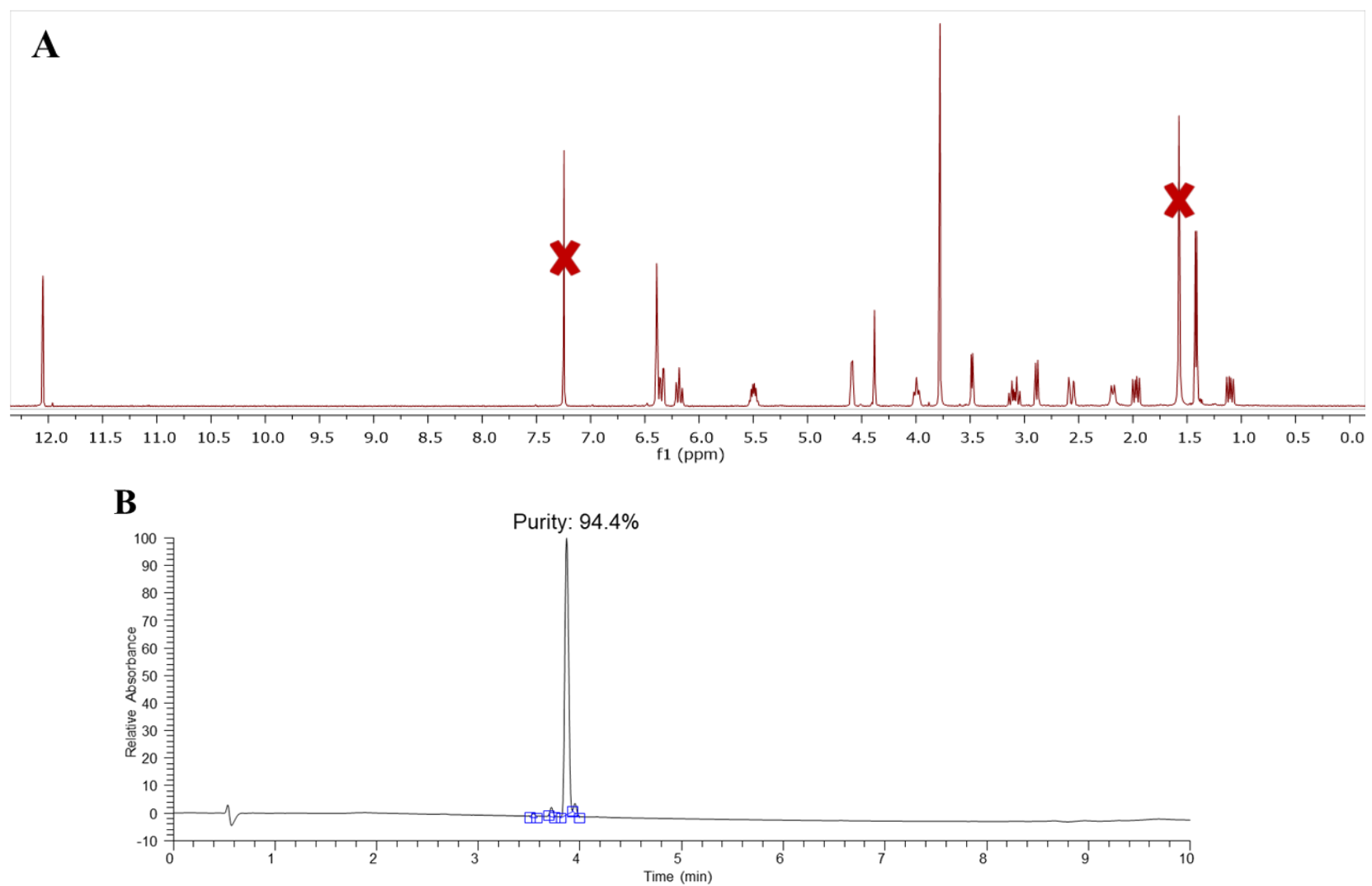


**Figure 3.15.** **A:**  $^1\text{H}$  NMR spectrum of the hypothemycin precipitate after two cycles of reconstitution and centrifugation in MeOH [400 MHz,  $\text{CDCl}_3$ ]. **B:** UPLC chromatograms (PDA detection) of the hypothemycin precipitate after two cycles of reconstitution and centrifugation in MeOH, demonstrating > 94% purity.

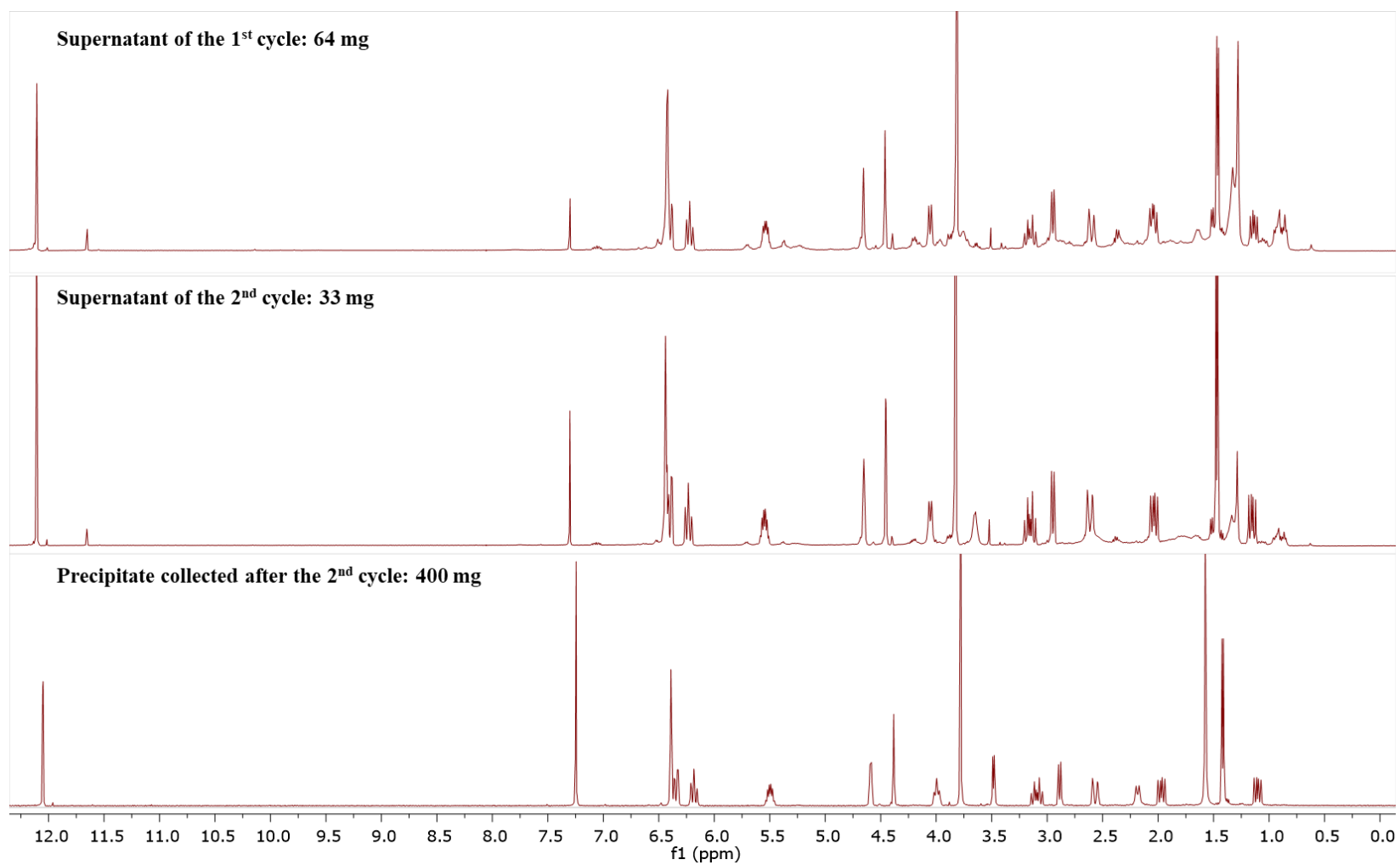


**Figure 3.16.**  $^1\text{H}$  NMR spectrum of the supernatants as compared to the precipitate after two cycles of reconstitution and centrifugation in MeOH [400 MHz,  $\text{CDCl}_3$ ].

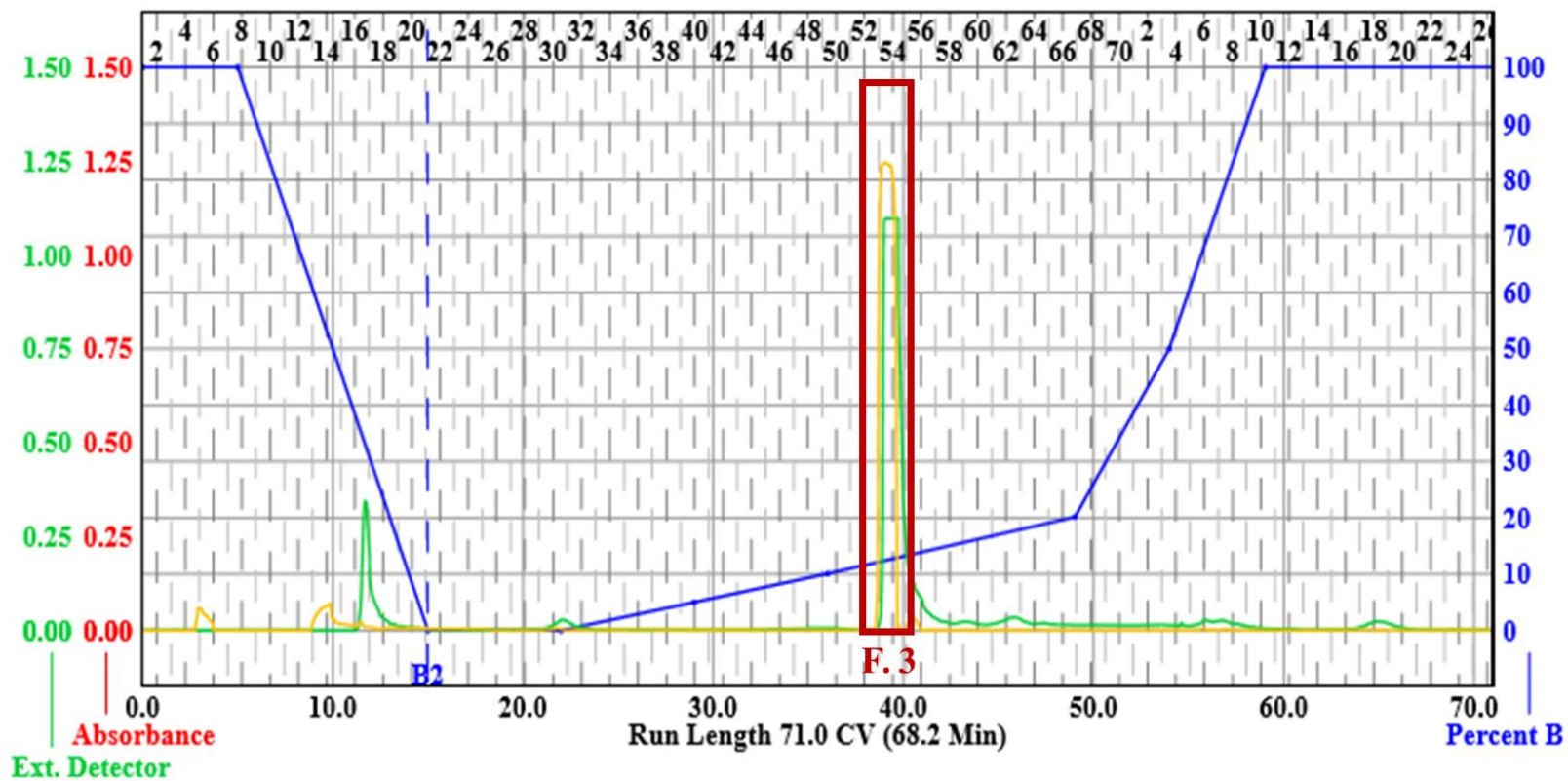


**Figure 3.17.** Fractionation via normal-phase flash chromatography for the fungal extract MSX63935 grown on rice. A gradient solvent system of hexanes- $\text{CHCl}_3$ - $\text{CH}_3\text{OH}$  at a 35 mL/min flow rate was used (blue line). The elution of compounds was monitored via ELSD detector (green line) and PDA detector (yellow line).

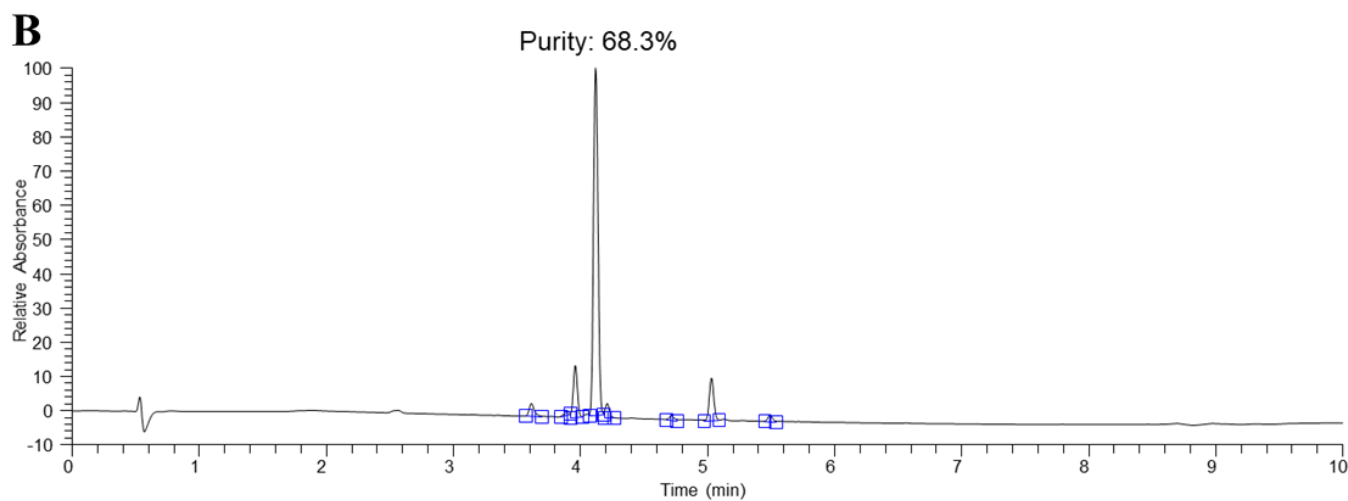
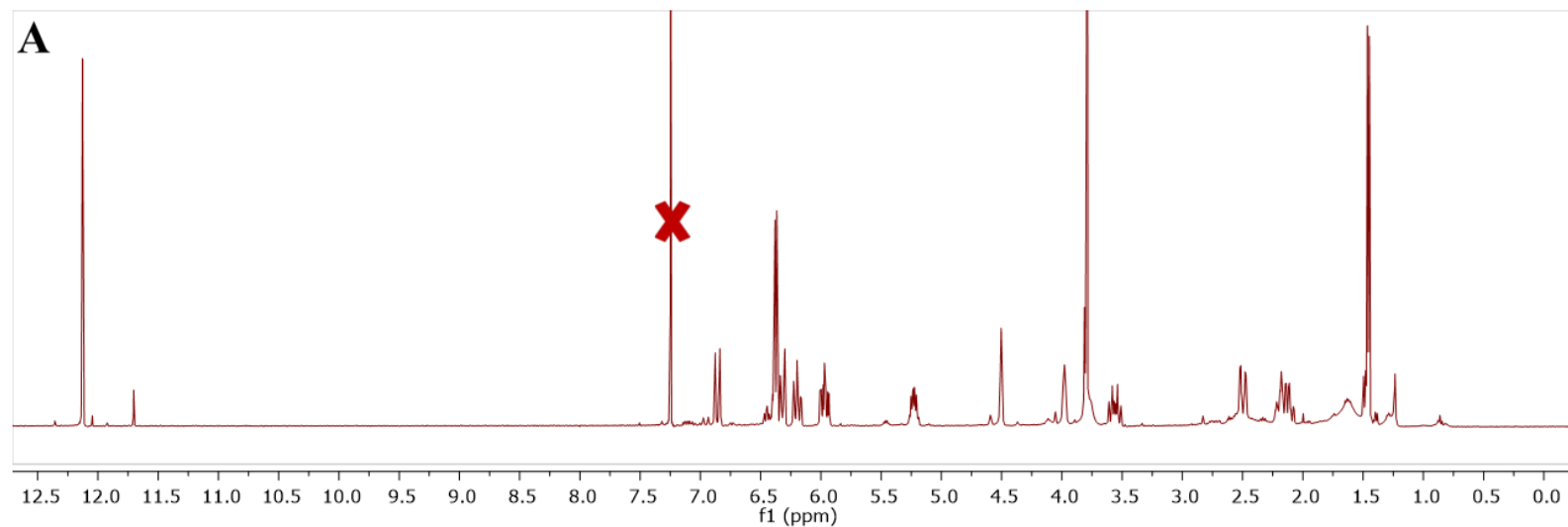


**Figure 3.18.** **A:**  $^1\text{H}$  NMR spectrum of fraction 3 from the flash chromatography shown in Fig. 3.17, demonstrating the purity of (5Z)-7-oxozeaenol [400 MHz,  $\text{CDCl}_3$ ]. **B:** UPLC chromatogram (PDA detection) of fraction 3 from the flash chromatography shown in Fig. 3.17, ~68% (5Z)-7-oxozeaenol content.

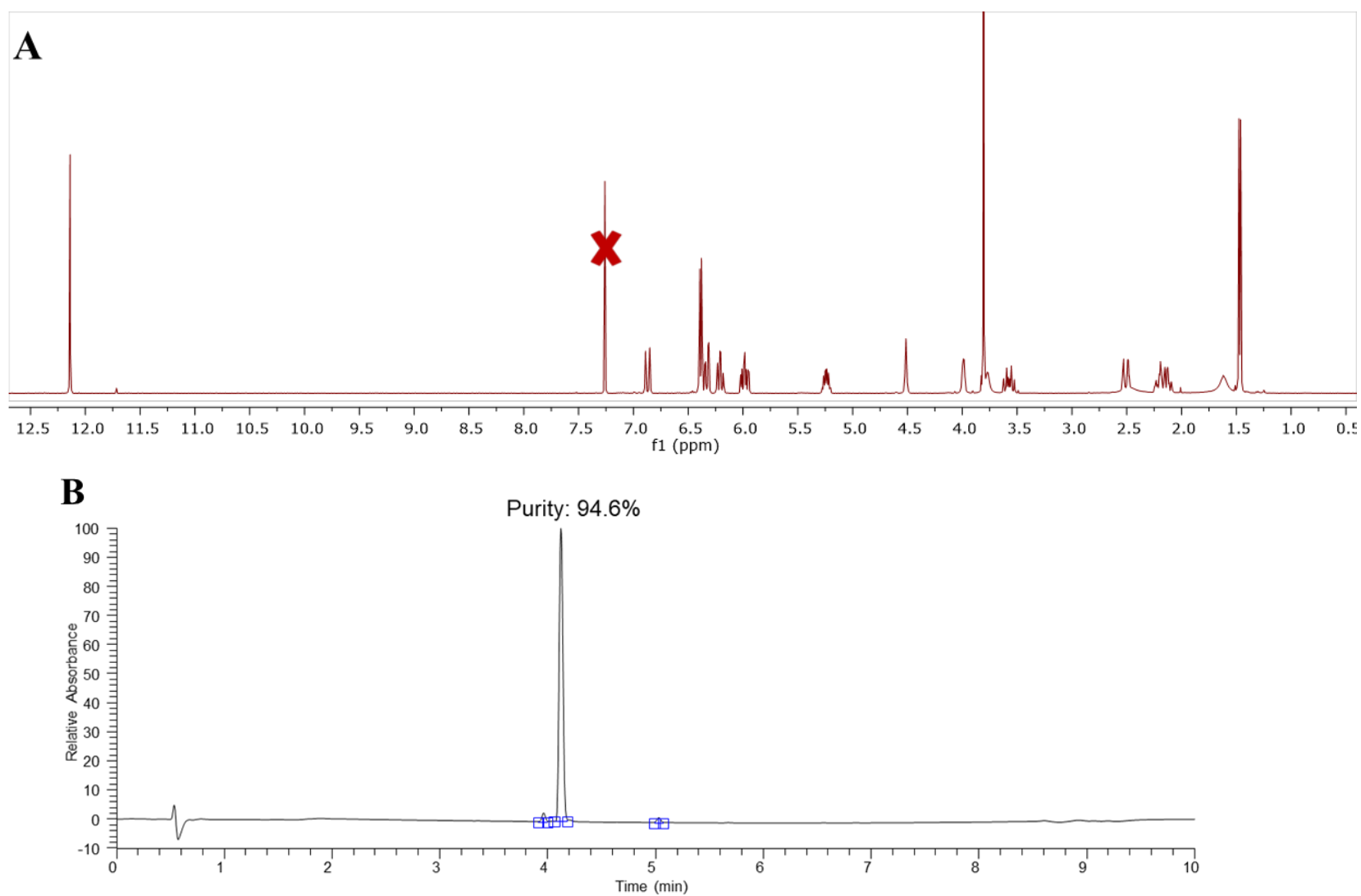


**Figure 3.19.** **A:**  $^1\text{H}$  NMR spectrum of the (5Z)-7-oxozeaenol precipitate after four cycles of reconstitution and centrifugation in MeOH and  $\text{CH}_3\text{CN}$  [400 MHz,  $\text{CDCl}_3$ ]. **B:** UPLC chromatograms (PDA detection) of the (5Z)-7-oxozeaenol precipitate after four cycles of reconstitution and centrifugation, demonstrating > 94% purity.

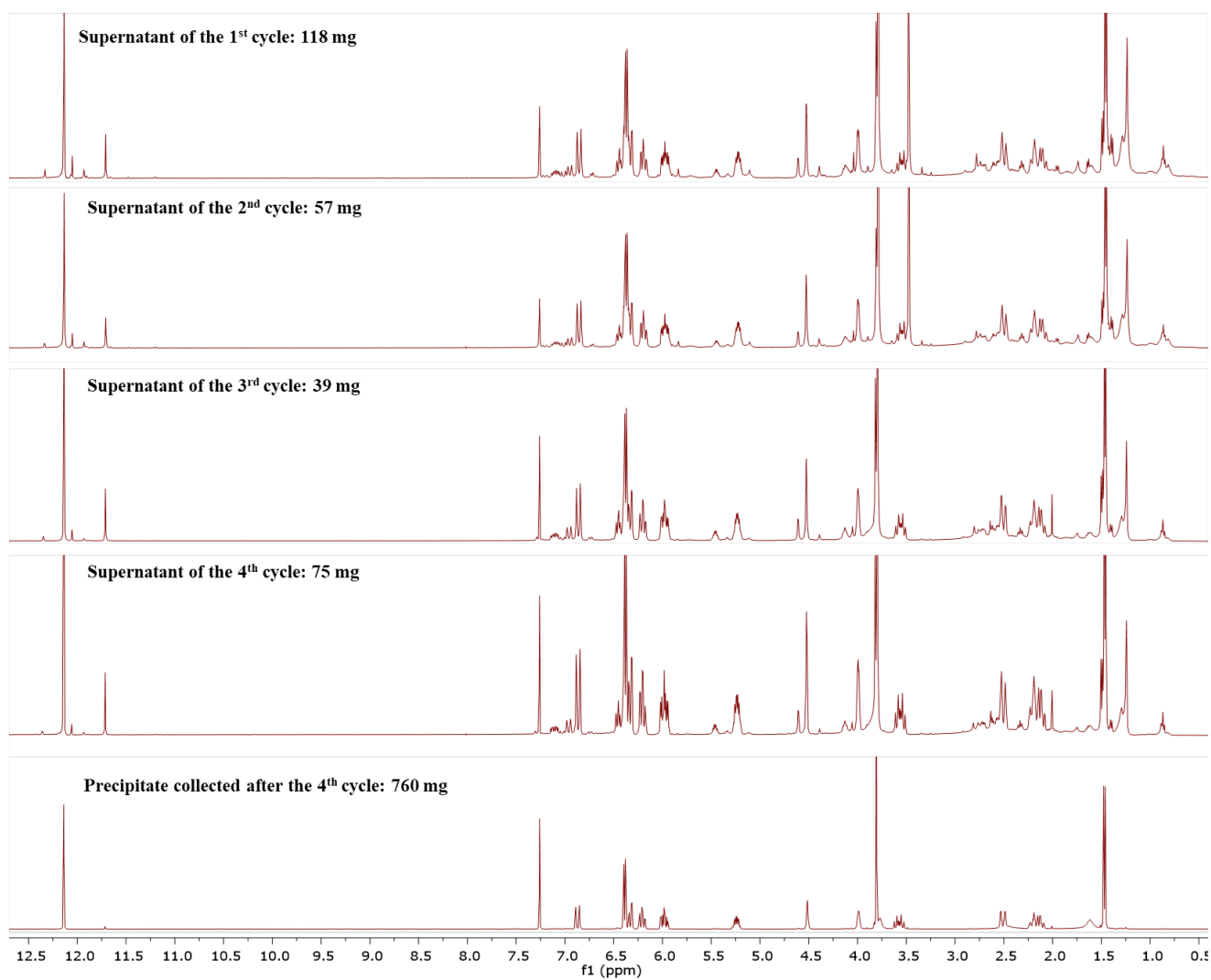


**Figure 3.20.**  $^1\text{H}$  NMR spectrum of the MSX63935 supernatants collected after each cycle of the reconstitution and centrifugation process [400 MHz,  $\text{CDCl}_3$ ]. HPLC-grade MeOH was used in the first two cycles, while HPLC-grade  $\text{CH}_3\text{CN}$  was used in the next two cycles.

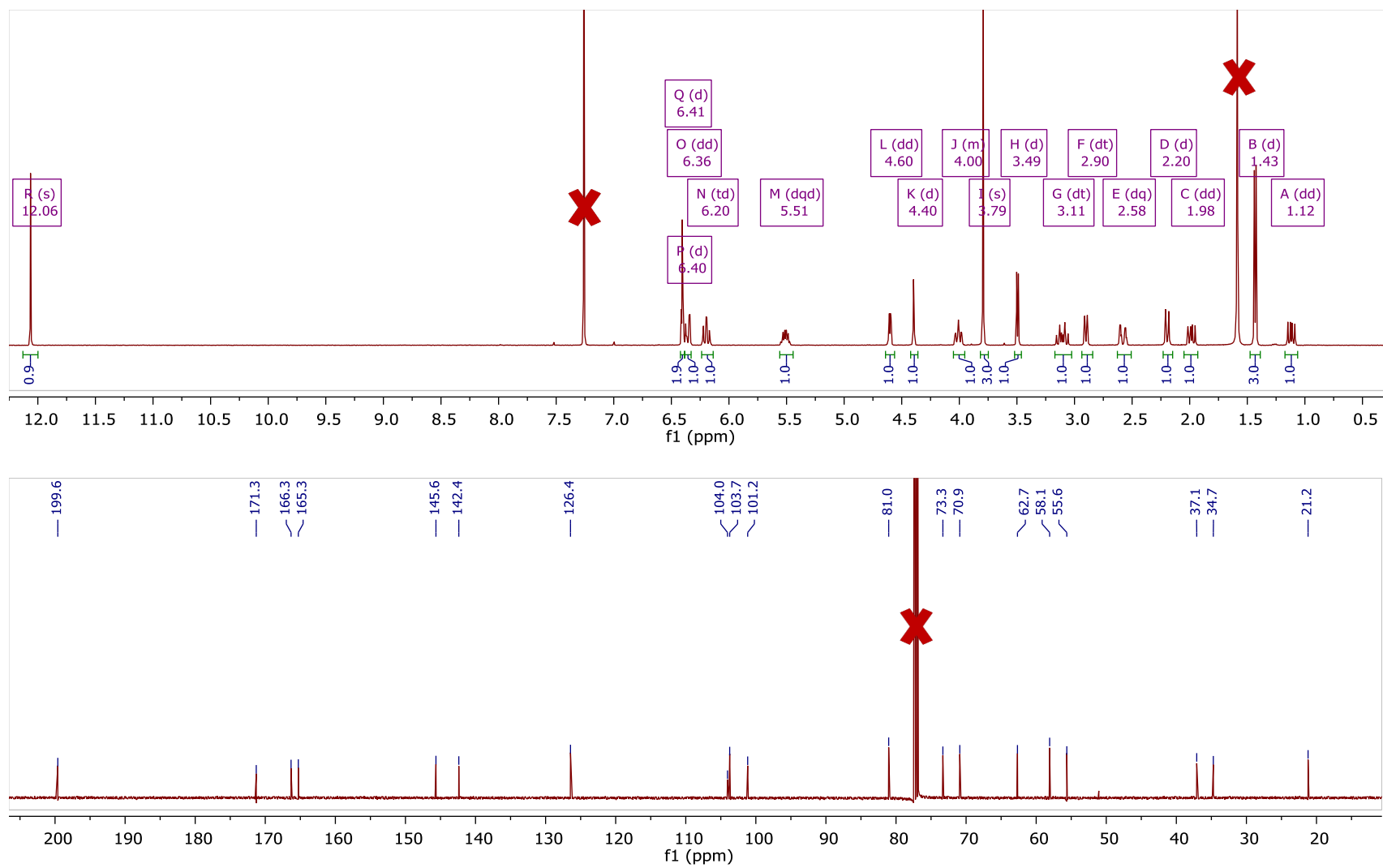


**Figure 3.21.**  $^1\text{H}$  and  $^{13}\text{C}$  NMR spectra of hypothemycin (1) [400 MHz for  $^1\text{H}$  and 100 MHz for  $^{13}\text{C}$ ,  $\text{CDCl}_3$ ].

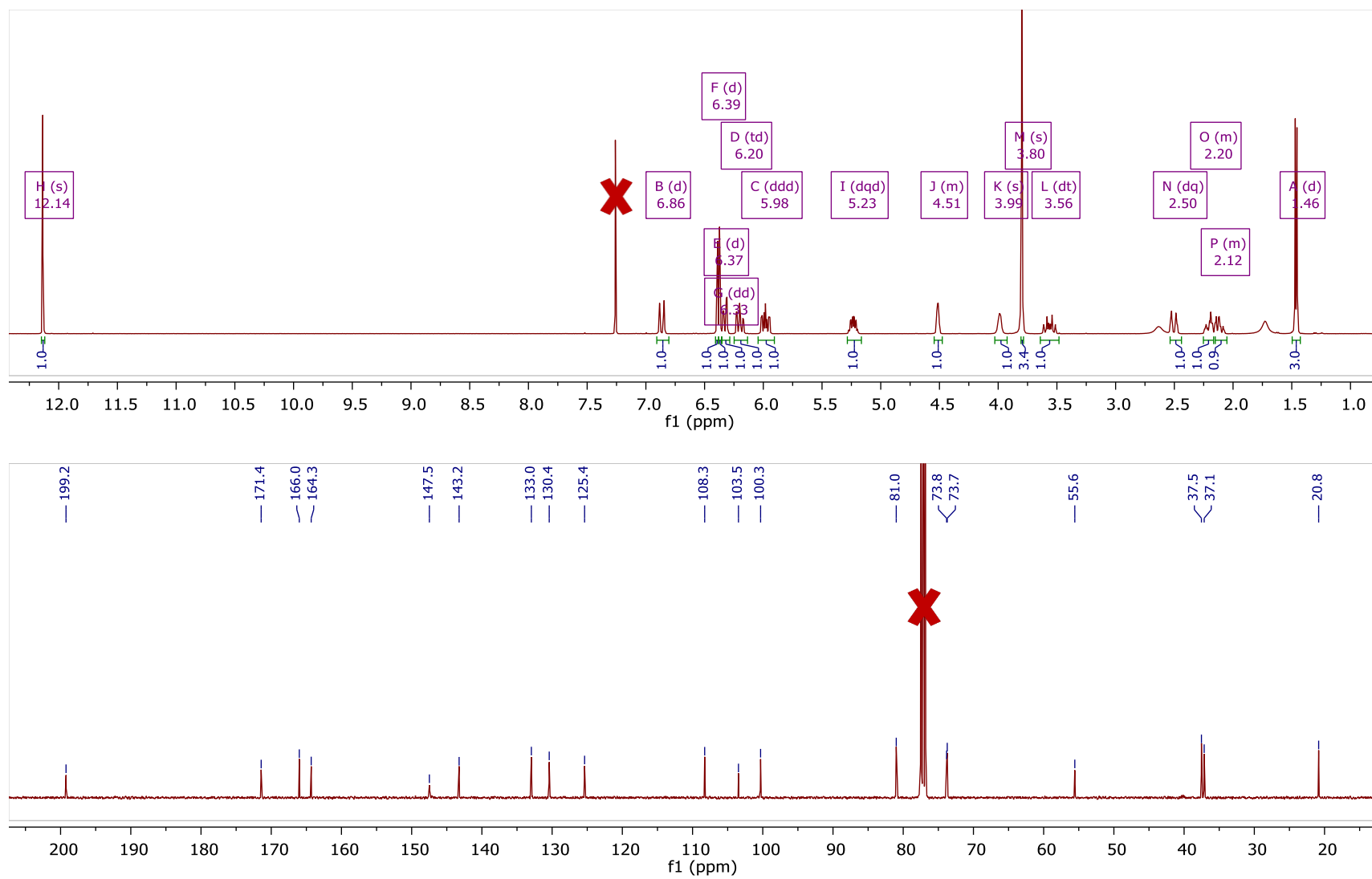


**Figure 3.22.**  $^1\text{H}$  and  $^{13}\text{C}$  NMR spectra of (5Z)-7-oxozeaenol (2) [400 MHz for  $^1\text{H}$  and 100 MHz for  $^{13}\text{C}$ ,  $\text{CDCl}_3$ ].

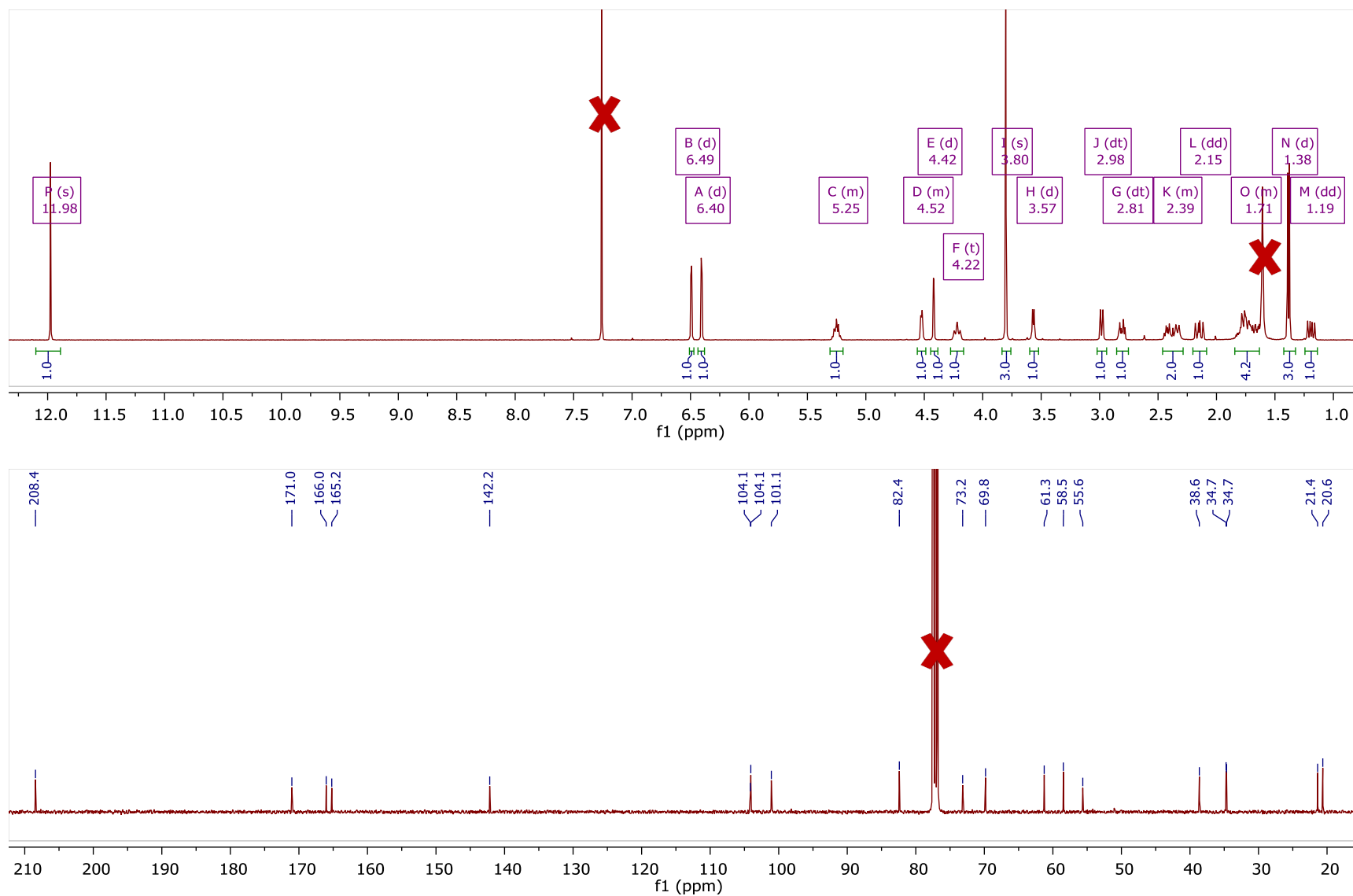


**Figure 3.23.**  $^1\text{H}$  and  $^{13}\text{C}$  NMR spectra of dihydrohypothenycin (3) [400 MHz for  $^1\text{H}$  and 100 MHz for  $^{13}\text{C}$ ,  $\text{CDCl}_3$ ].

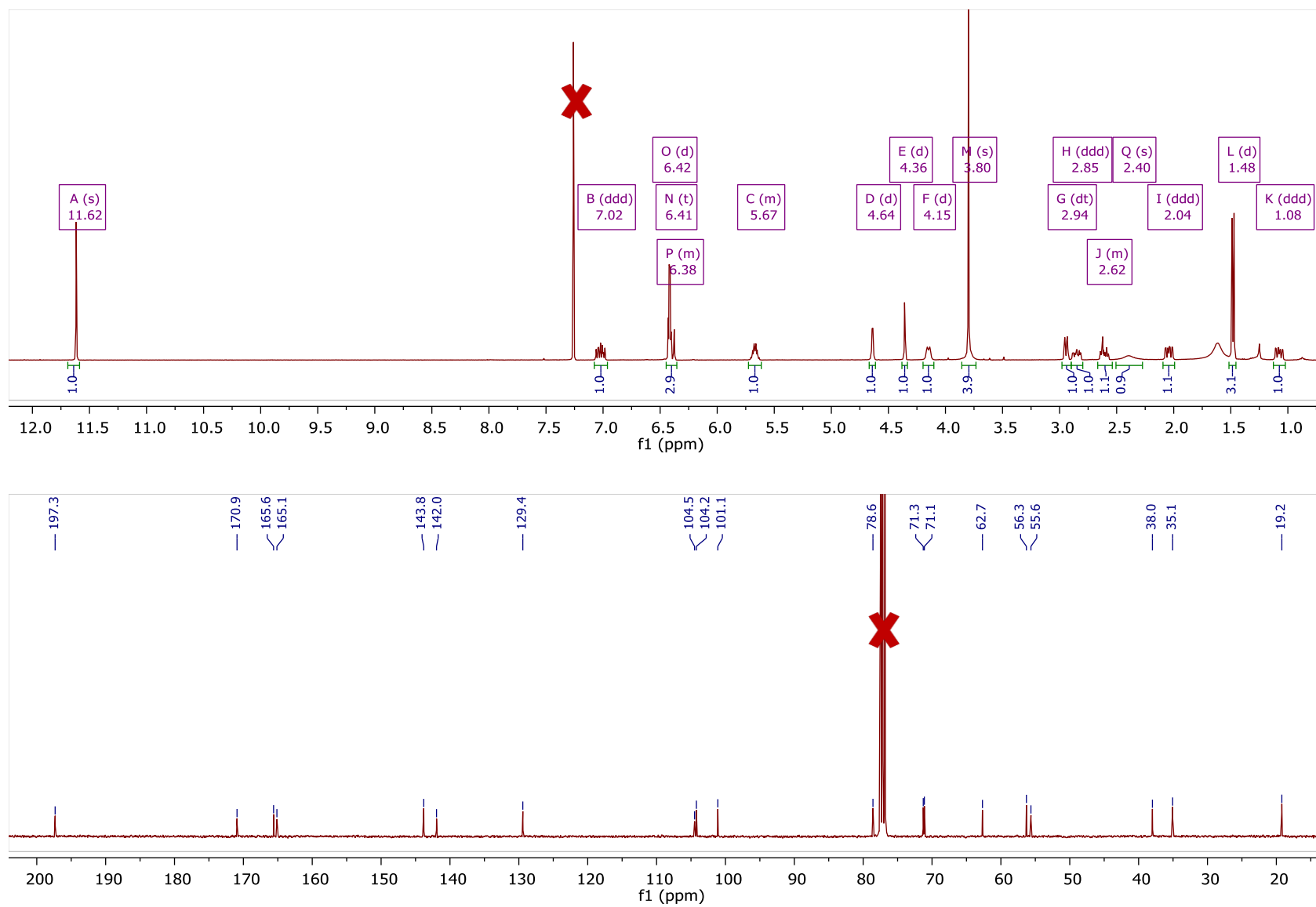


**Figure 3.24.**  $^1\text{H}$  and  $^{13}\text{C}$  NMR spectra of aigialomycin A (4) [400 MHz for  $^1\text{H}$  and 100 MHz for  $^{13}\text{C}$ ,  $\text{CDCl}_3$ ].

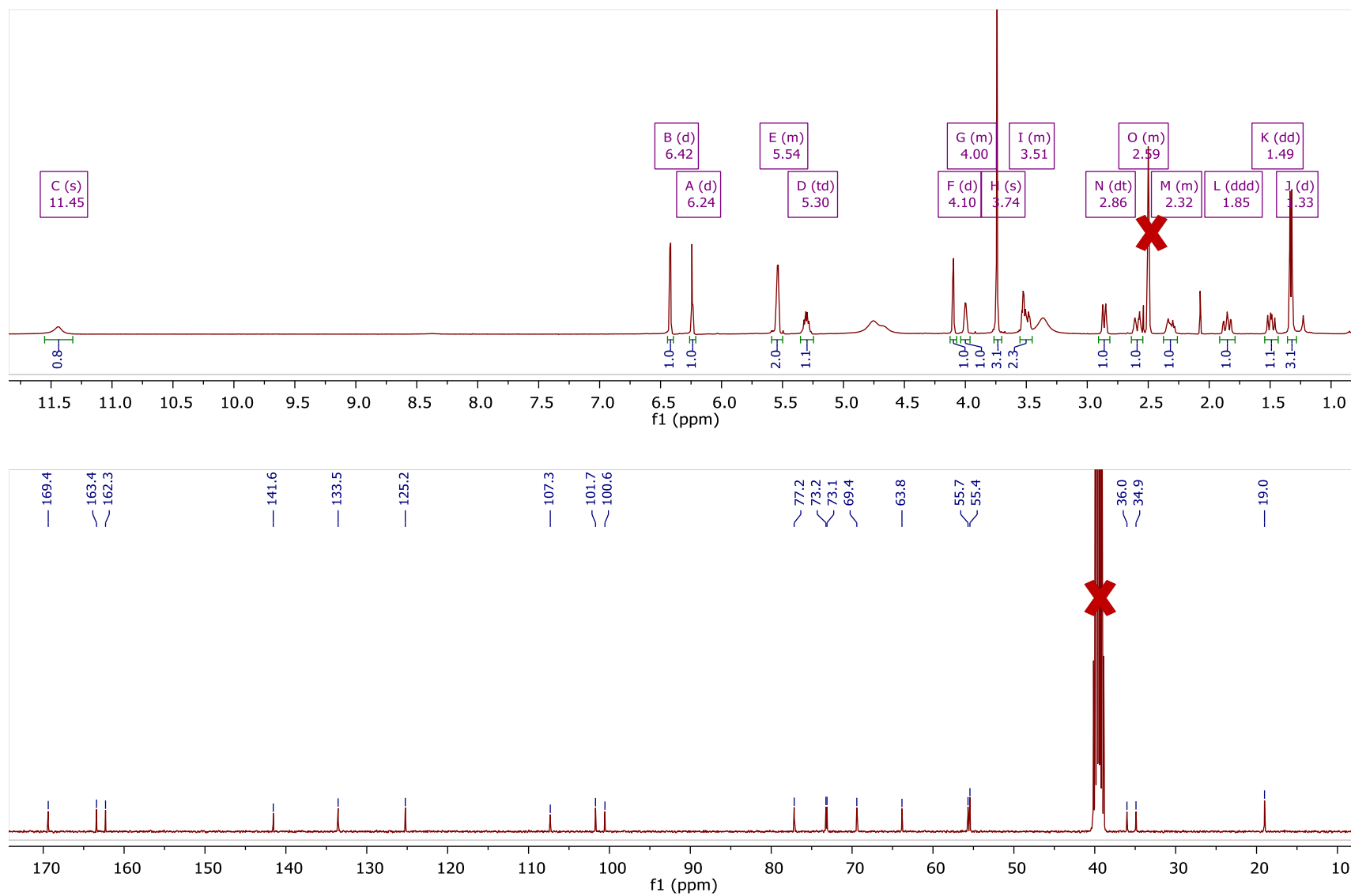


**Figure 3.25.**  $^1\text{H}$  and  $^{13}\text{C}$  NMR spectra of paecilomycin A (5) [400 MHz for  $^1\text{H}$  and 100 MHz for  $^{13}\text{C}$ ,  $\text{DMSO-}d_6$ ].

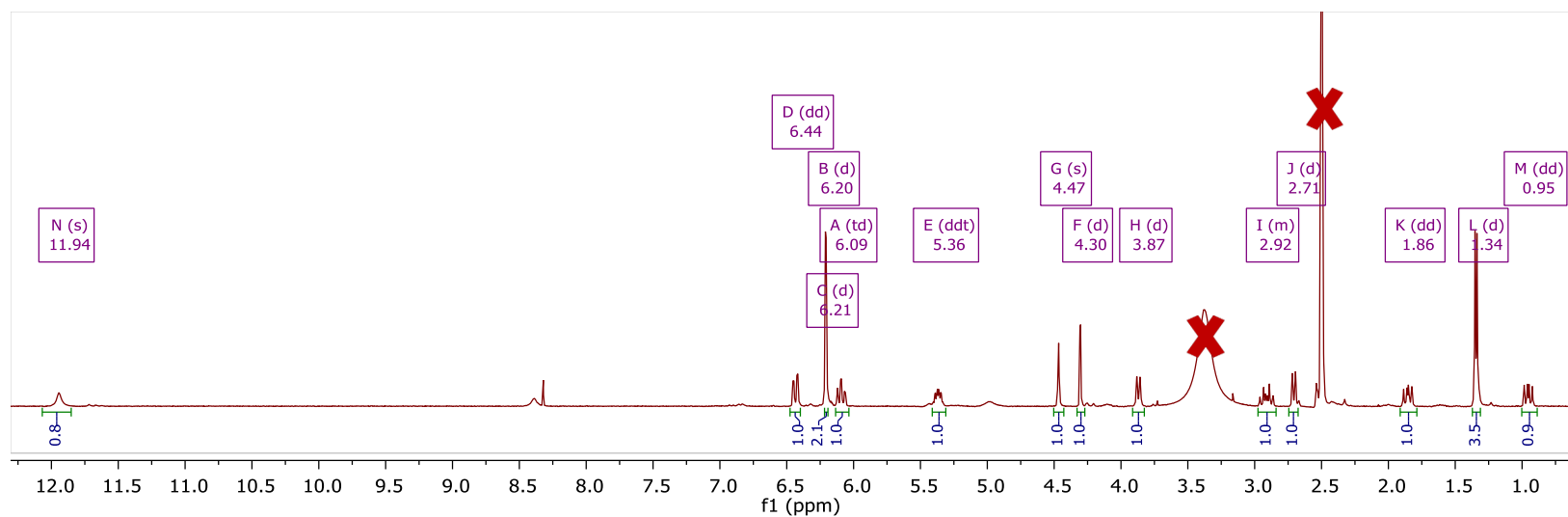


**Figure 3.26.**  $^1\text{H}$  NMR spectrum of 4-O-demethylhypothemycin (**6**) [400 MHz,  $\text{DMSO-}d_6$ ]

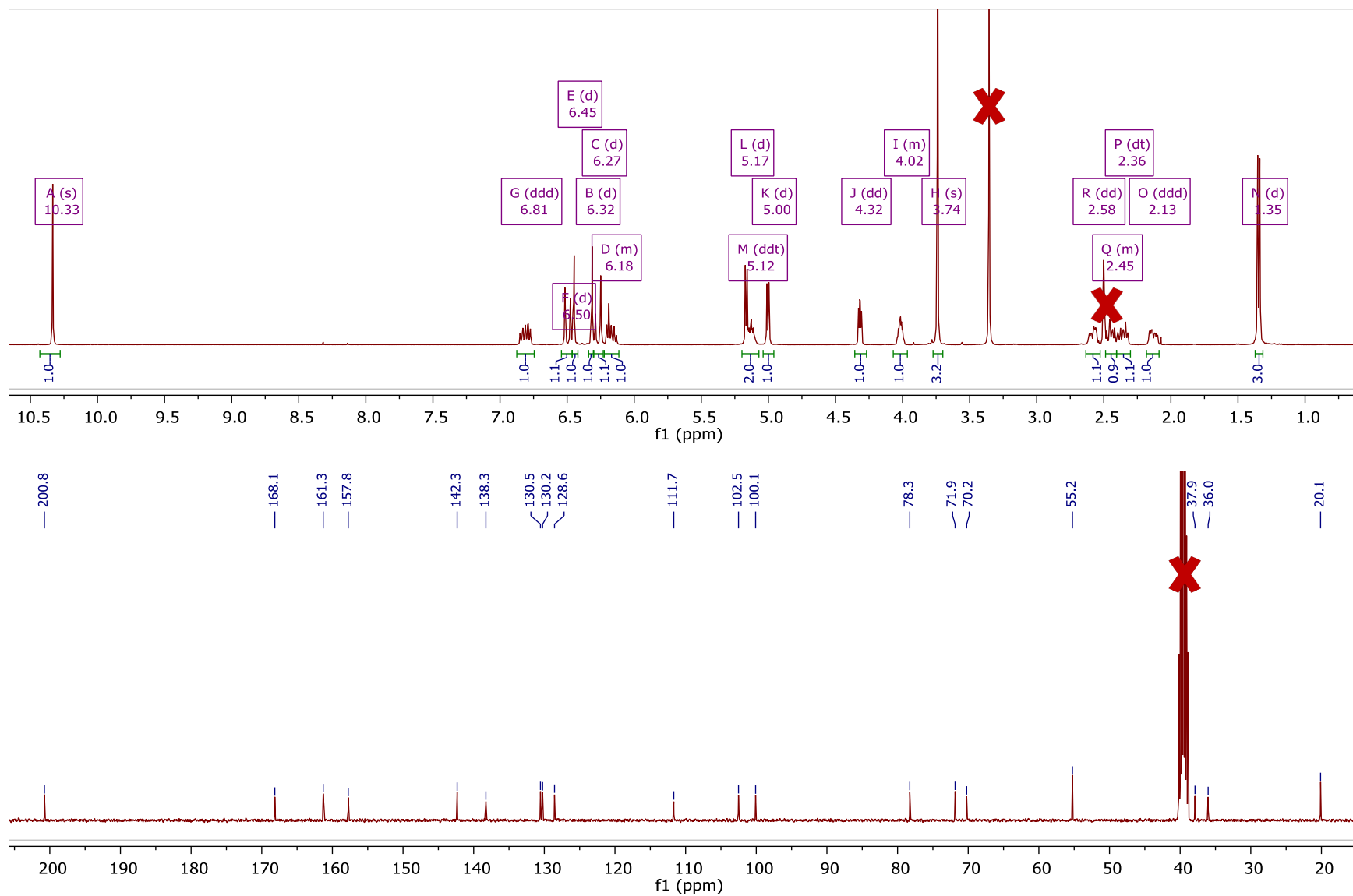


**Figure 3.27.**  $^1\text{H}$  and  $^{13}\text{C}$  NMR spectra of (5E)-7-oxozeaenol (7) [400 MHz for  $^1\text{H}$  and 100 MHz for  $^{13}\text{C}$ , DMSO- $d_6$ ].

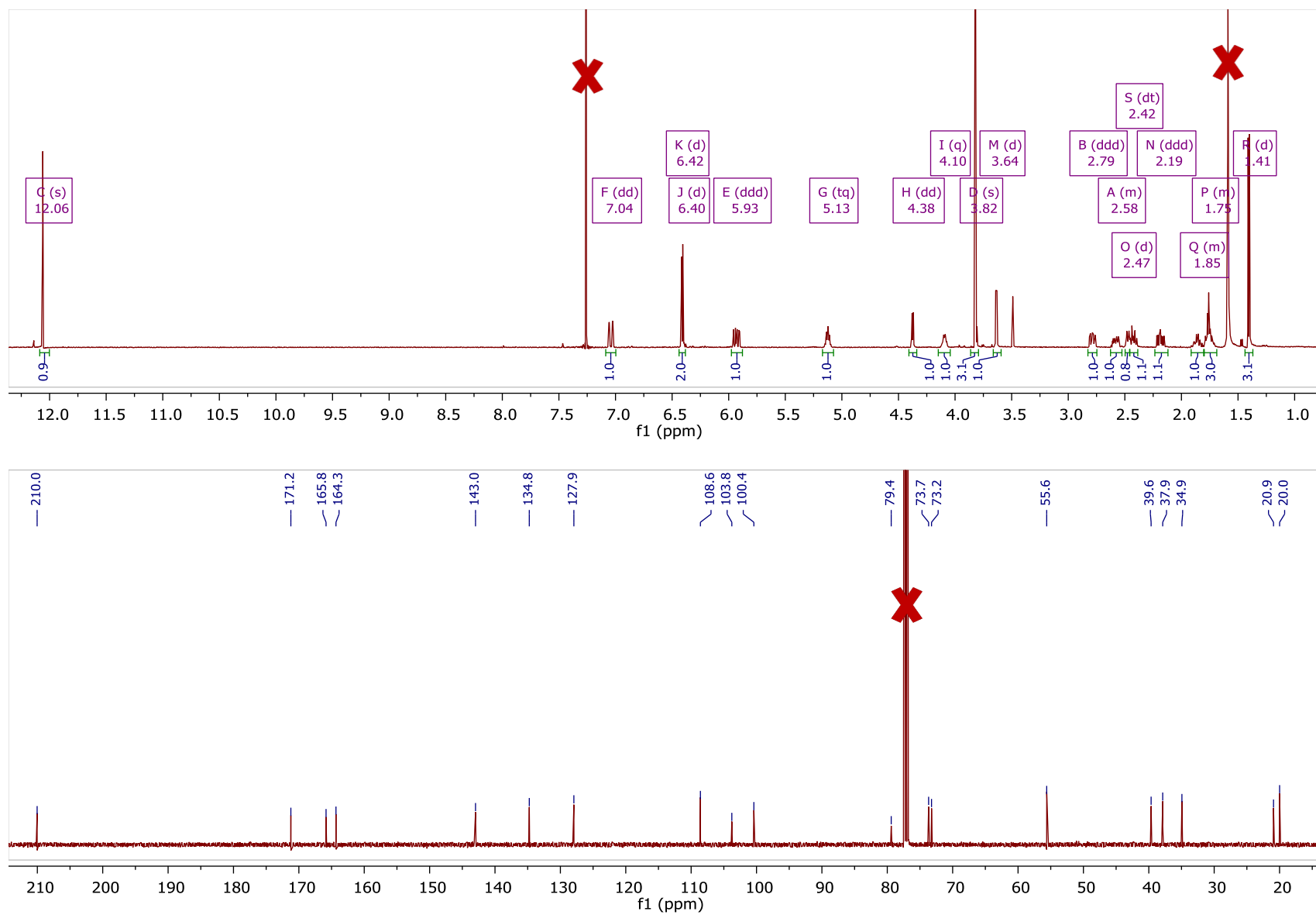


**Figure 3.28.**  $^1\text{H}$  and  $^{13}\text{C}$  NMR spectra of LL-Z1640-1 (**8**) [500 MHz for  $^1\text{H}$  and 125 MHz for  $^{13}\text{C}$ ,  $\text{CDCl}_3$ ].

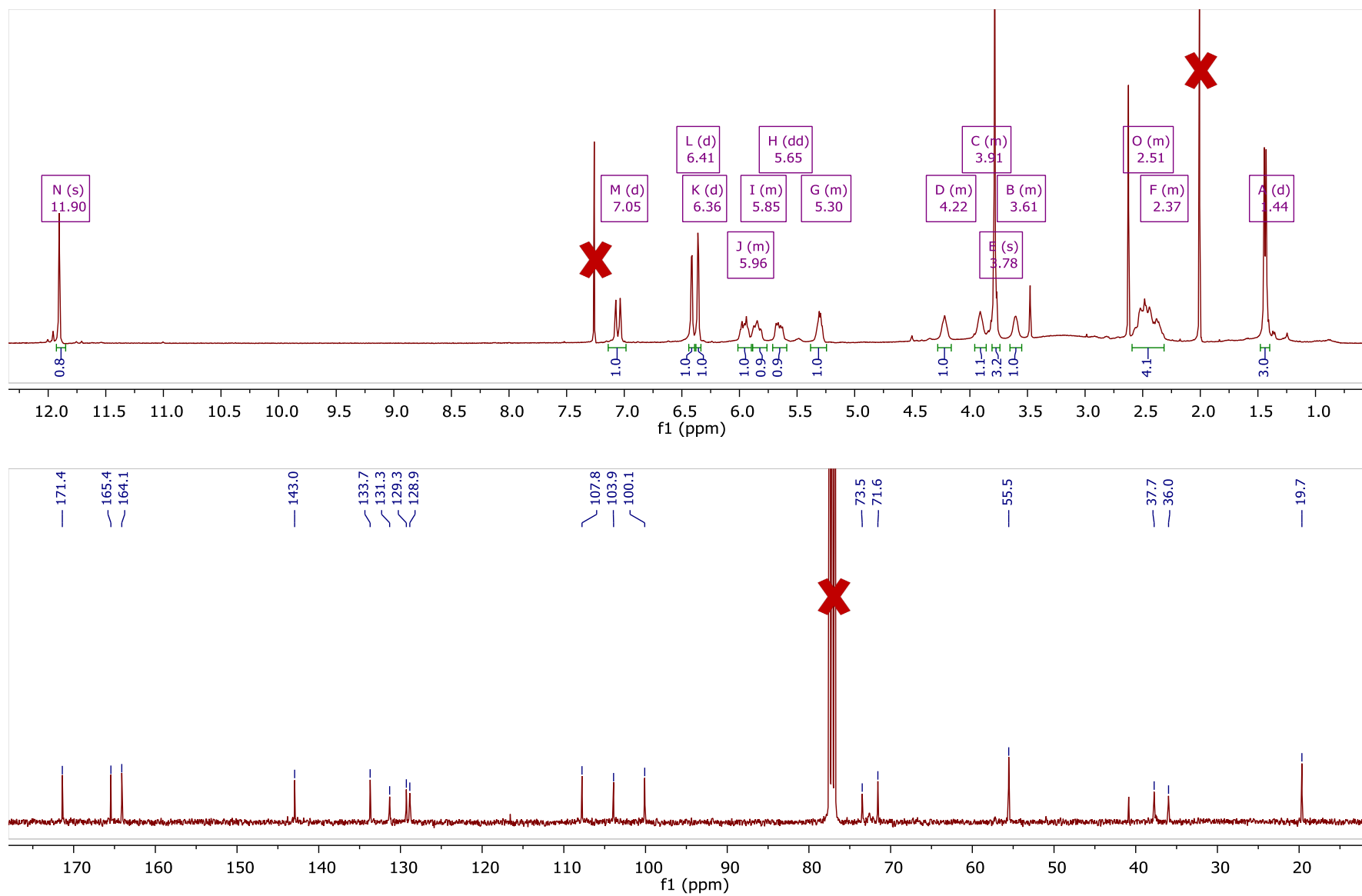


**Figure 3.29.** <sup>1</sup>H and <sup>13</sup>C NMR spectra of zeaenol (**9**) [400 MHz for <sup>1</sup>H and 100 MHz for <sup>13</sup>C, CDCl<sub>3</sub>].

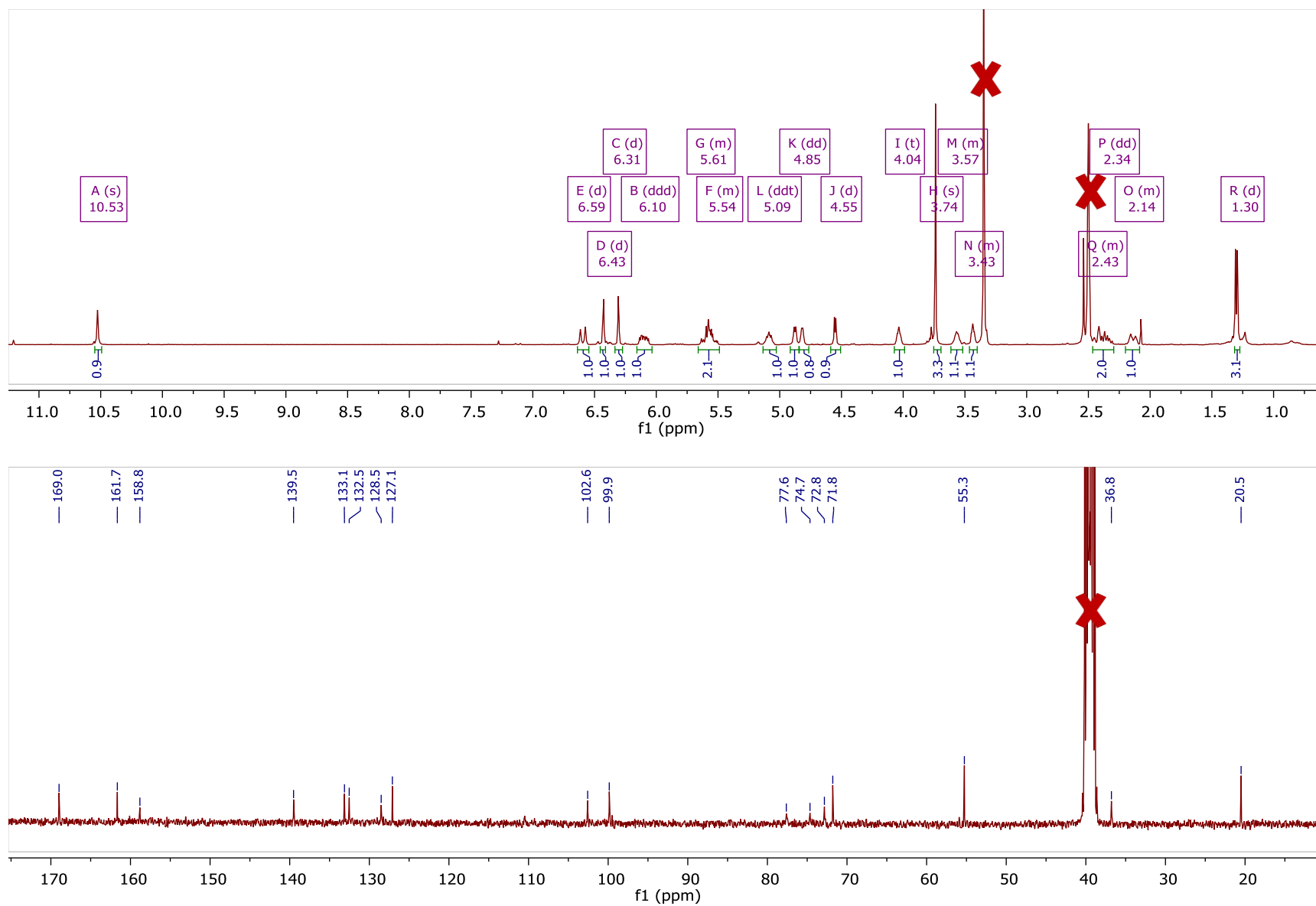


**Figure 3.30.** <sup>1</sup>H and <sup>13</sup>C NMR spectra of 7-*epi*-zeanol (**10**) [400 MHz for <sup>1</sup>H and 100 MHz for <sup>13</sup>C, DMSO-*d*<sub>6</sub>].

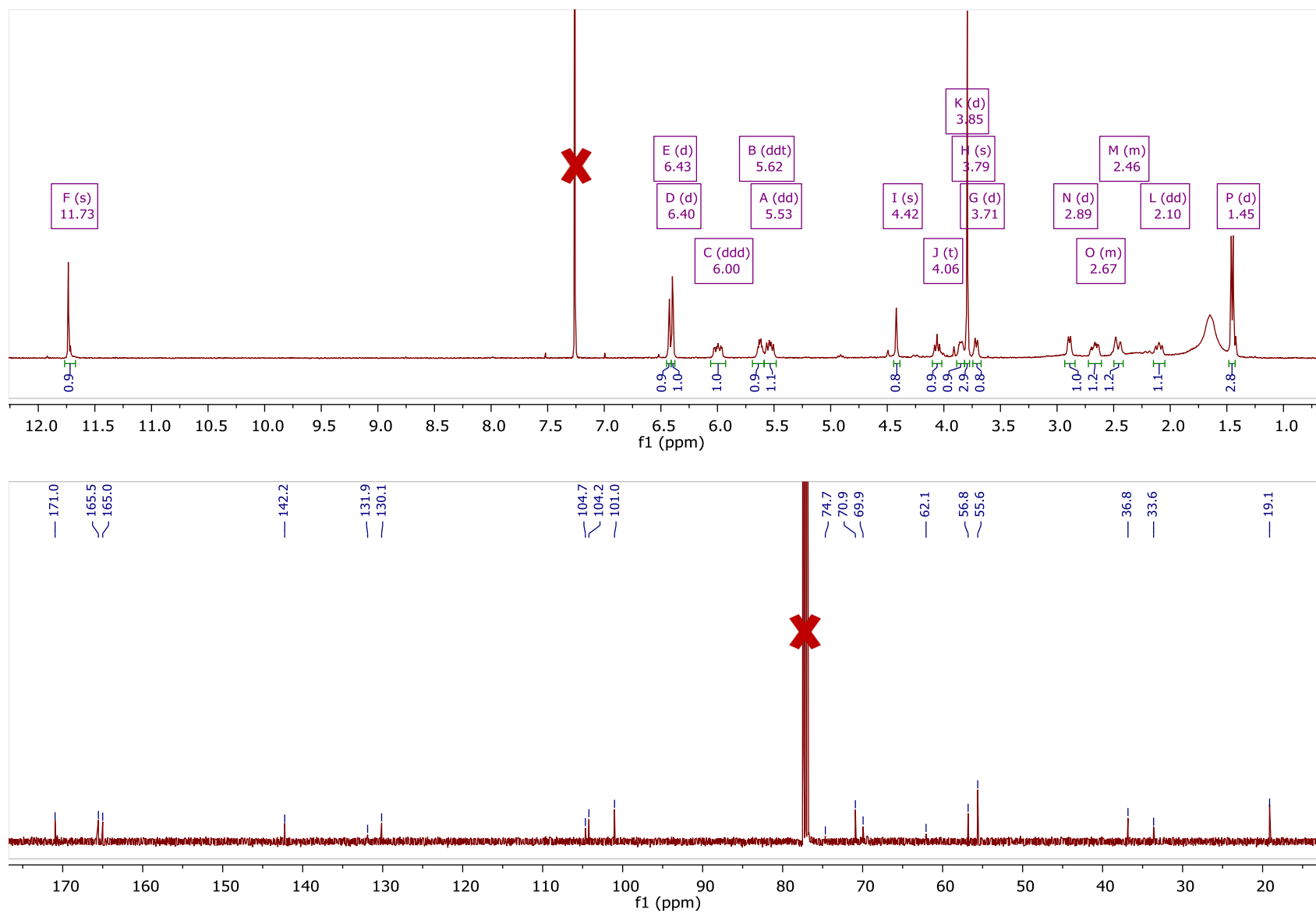


**Figure 3.31.**  $^1\text{H}$  and  $^{13}\text{C}$  NMR spectra of aigialomycin B (**11**) [400 MHz for  $^1\text{H}$  and 100 MHz for  $^{13}\text{C}$ ,  $\text{CDCl}_3$ ].

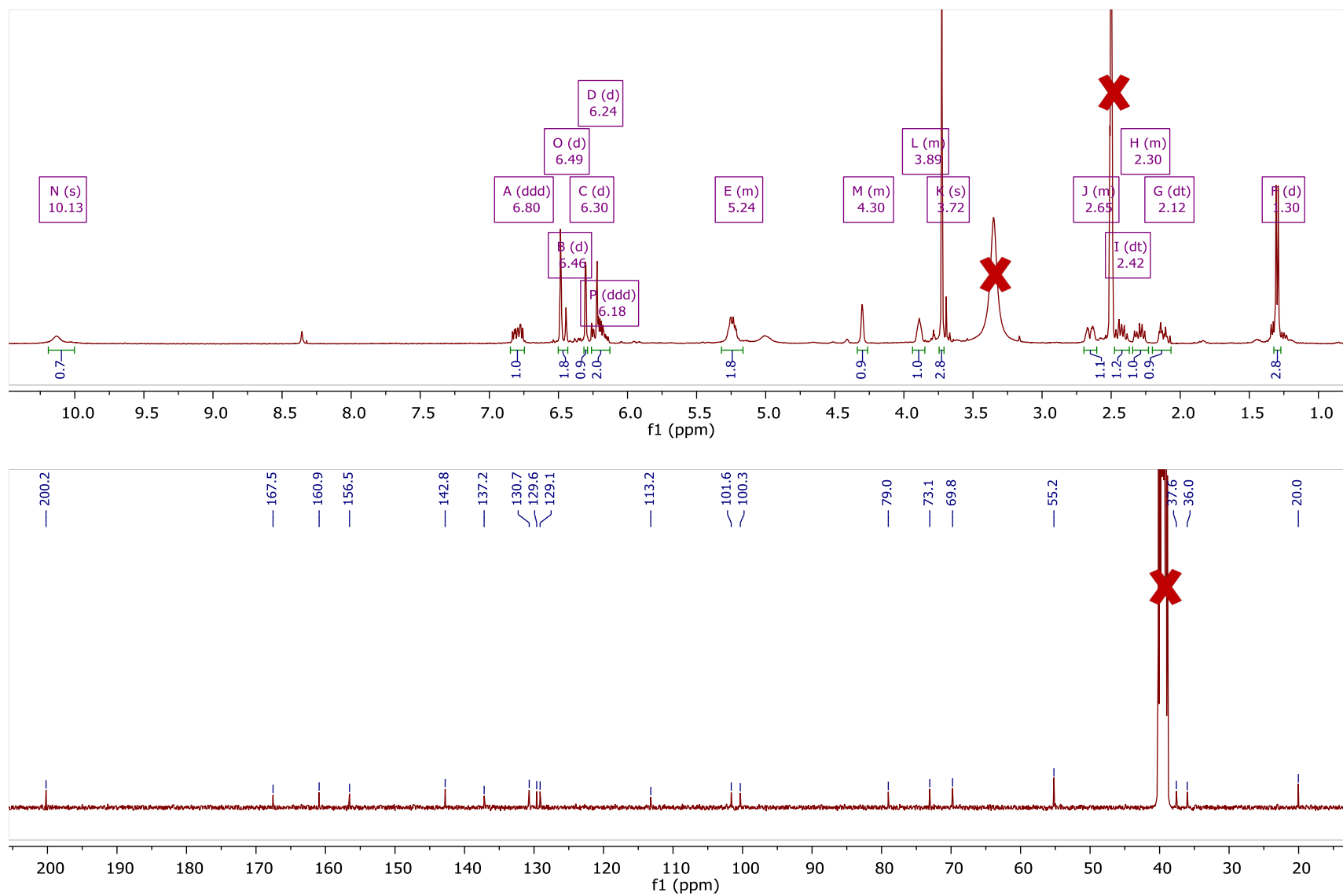


**Figure 3.32.**  $^1\text{H}$  and  $^{13}\text{C}$  NMR spectra of cochliomycin F (**12**) [400 MHz for  $^1\text{H}$  and 100 MHz for  $^{13}\text{C}$ , DMSO- $d_6$ ].

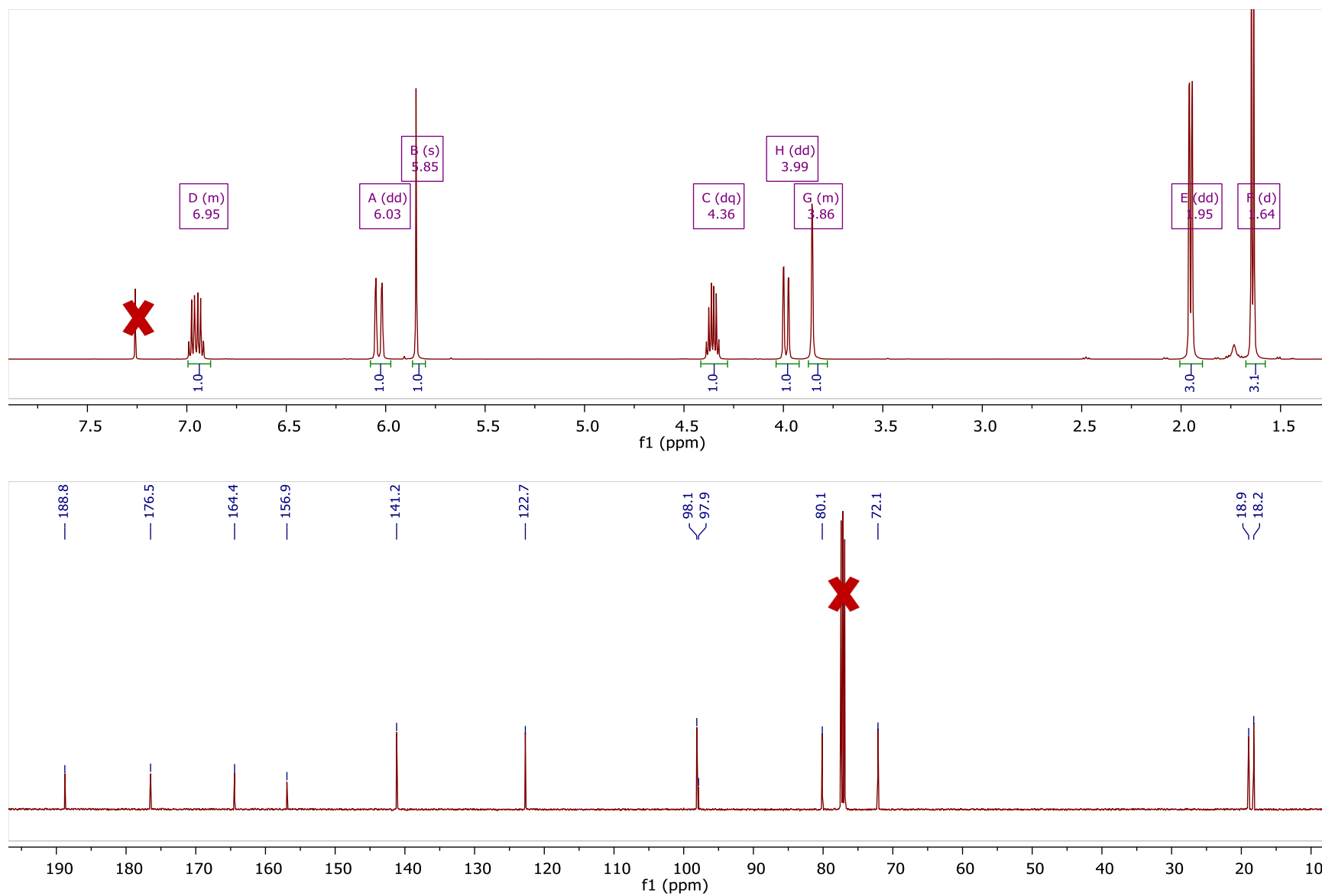


**Figure 3.33.**  $^1\text{H}$  and  $^{13}\text{C}$  NMR spectra of radicinin (**13**) [500 MHz for  $^1\text{H}$  and 125 MHz for  $^{13}\text{C}$ ,  $\text{CDCl}_3$ ].

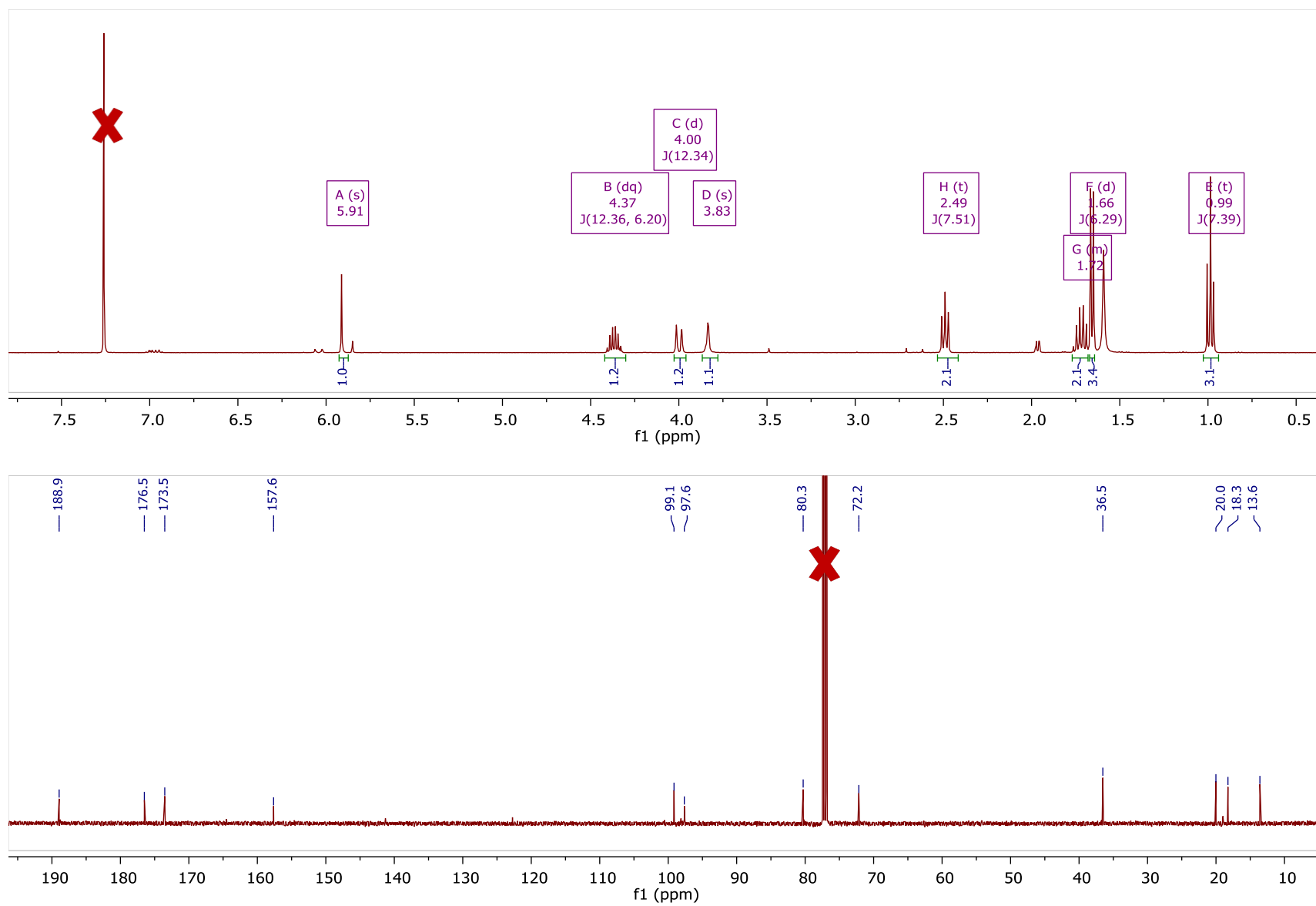


**Figure 3.34.**  $^1\text{H}$  and  $^{13}\text{C}$  NMR spectra of dihydroradicinin (**14**) [400 MHz for  $^1\text{H}$  and 100 MHz for  $^{13}\text{C}$ ,  $\text{CDCl}_3$ ].

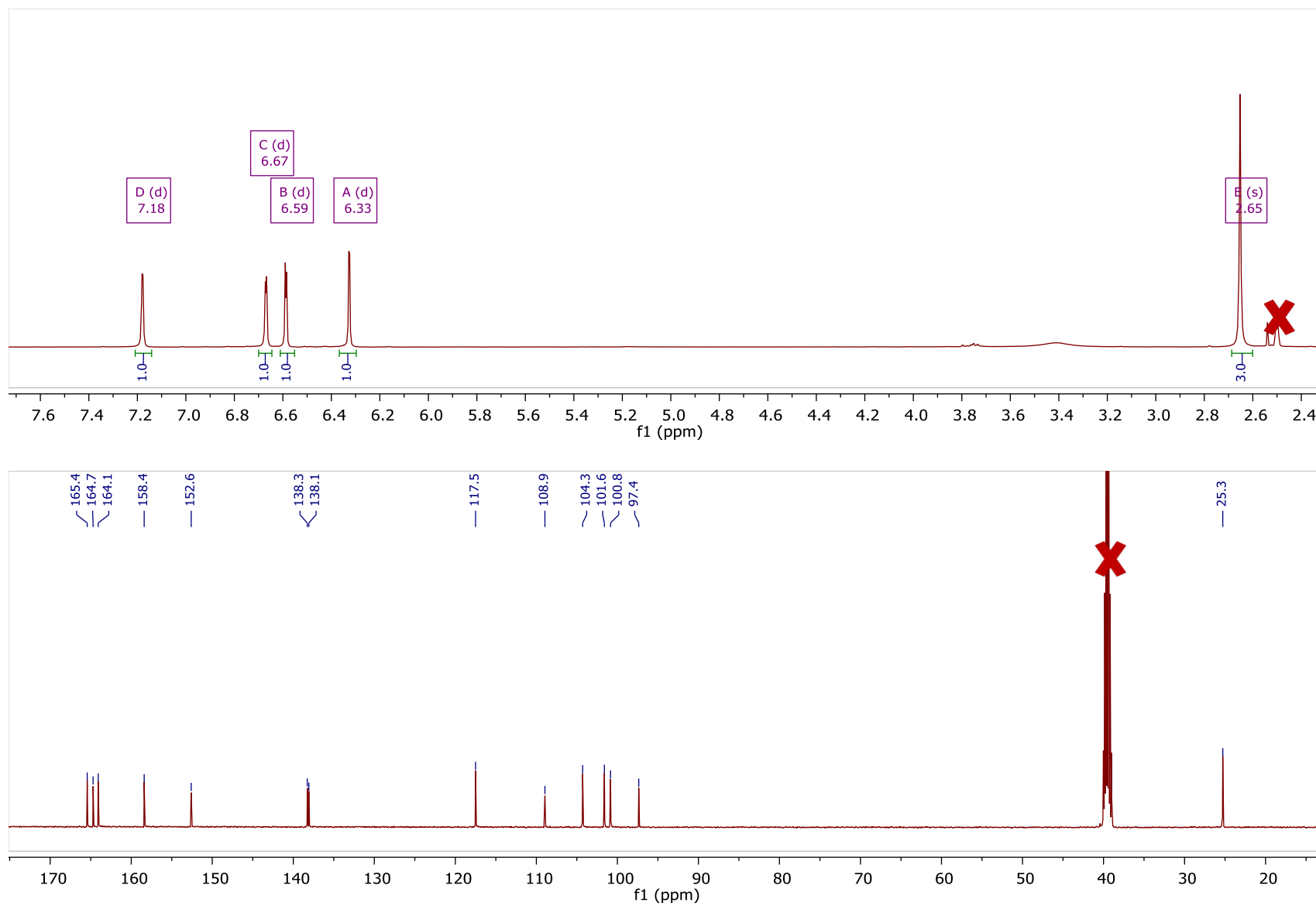


**Figure 3.35.**  $^1\text{H}$  and  $^{13}\text{C}$  NMR spectra of alternariol (15) [500 MHz for  $^1\text{H}$  and 125 MHz for  $^{13}\text{C}$ ,  $\text{DMSO-}d_6$ ].

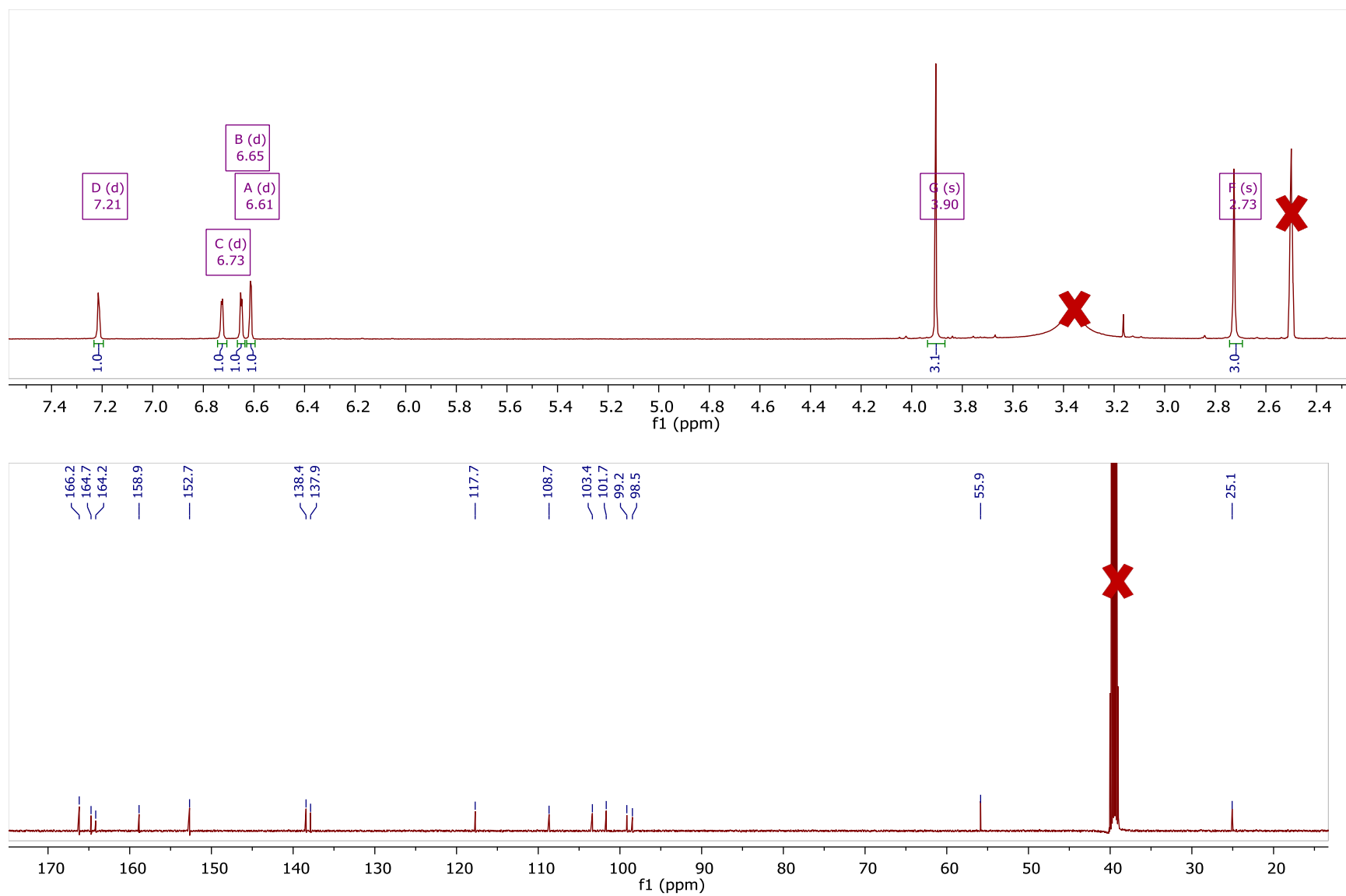


**Figure 3.36.**  $^1\text{H}$  and  $^{13}\text{C}$  NMR spectra of alternariol 9-methyl ether (**16**) [500 MHz for  $^1\text{H}$  and 125 MHz for  $^{13}\text{C}$ ,  $\text{DMSO-}d_6$ ].

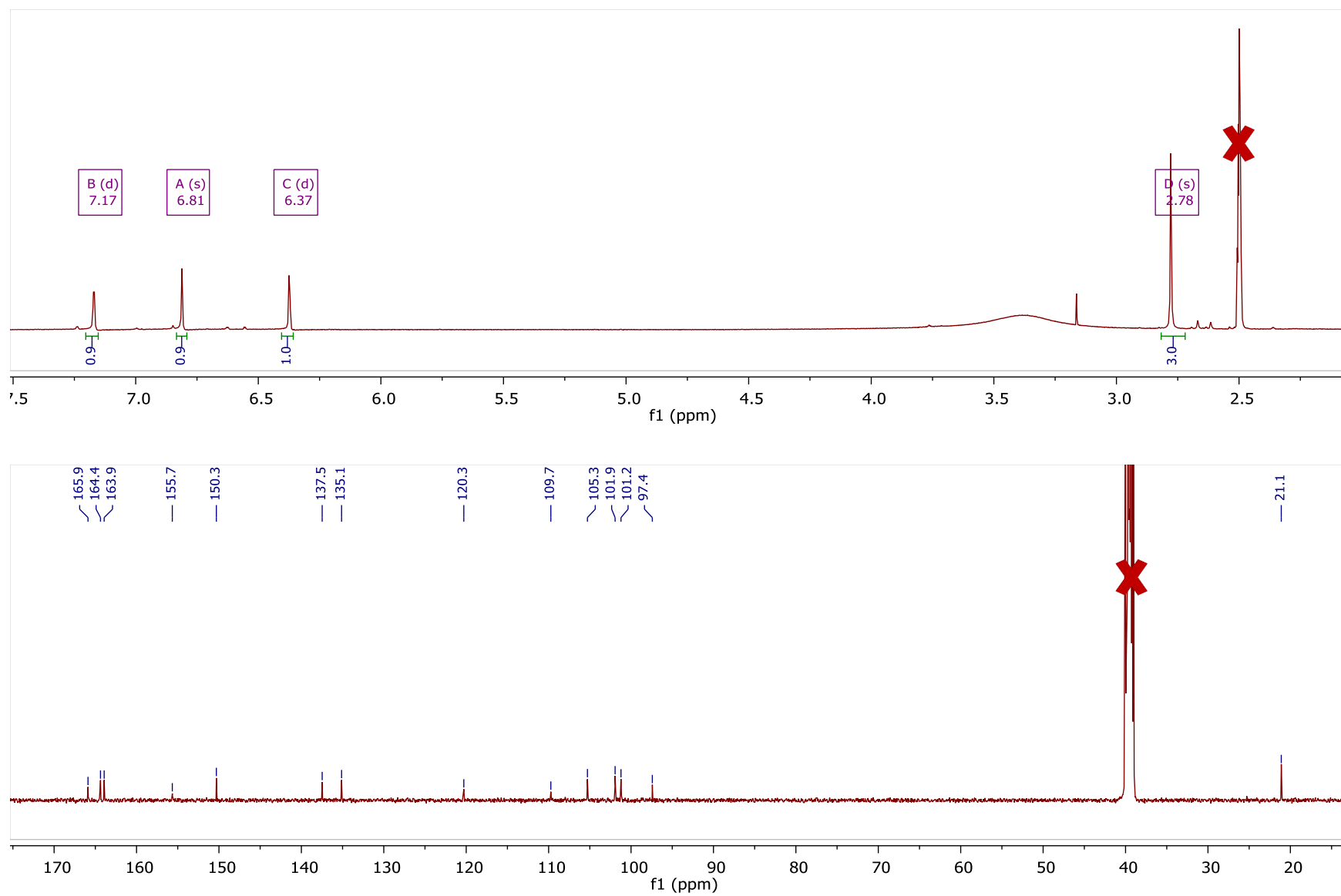


**Figure 3.37.** <sup>1</sup>H and <sup>13</sup>C NMR spectra of rhizopycnin D (**17**) [500 MHz for <sup>1</sup>H and 125 MHz for <sup>13</sup>C, DMSO-*d*<sub>6</sub>].

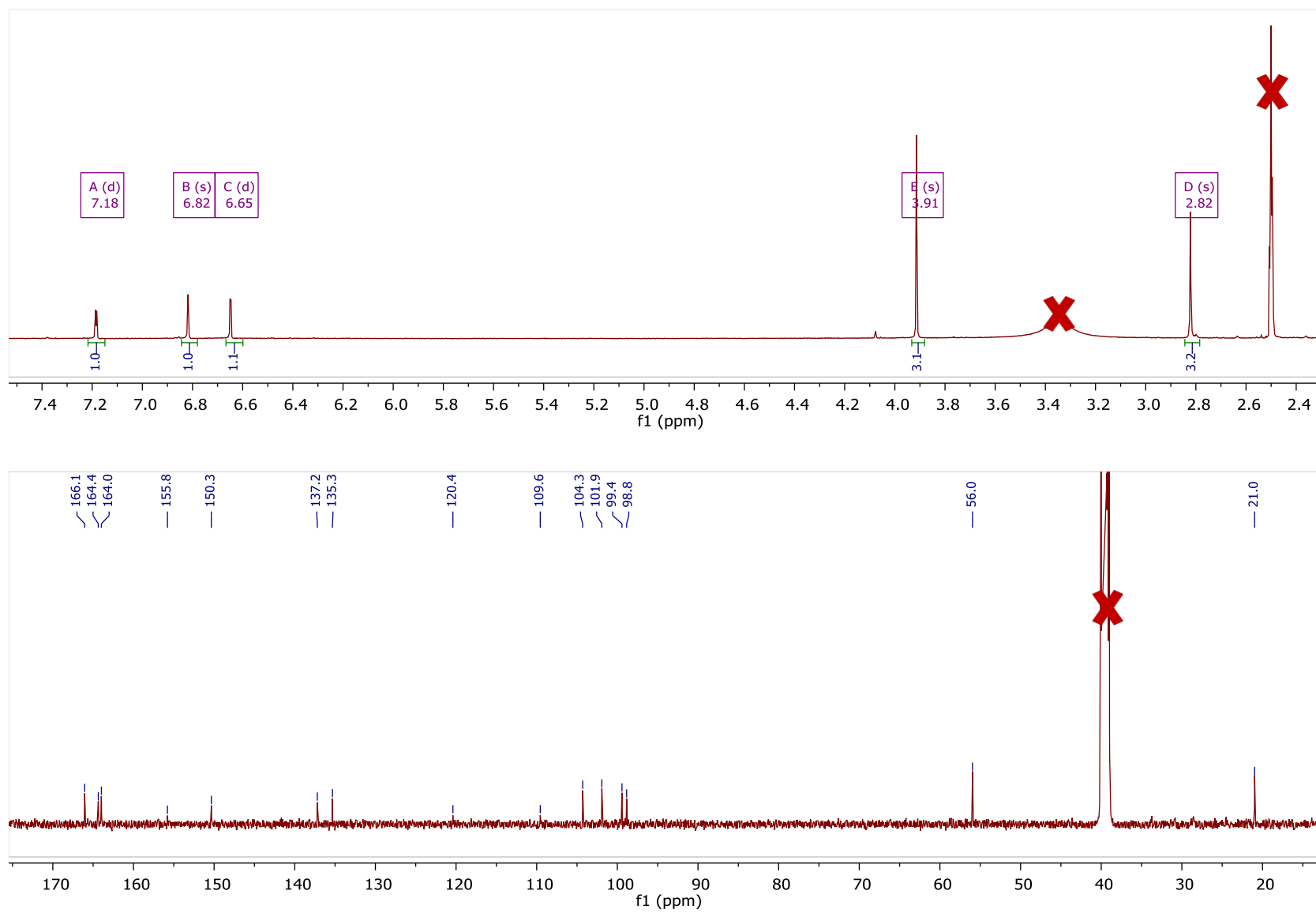


**Figure 3.38.**  $^1\text{H}$  and  $^{13}\text{C}$  NMR spectra of palmariol B (**18**) [500 MHz for  $^1\text{H}$  and 125 MHz for  $^{13}\text{C}$ ,  $\text{DMSO-}d_6$ ].

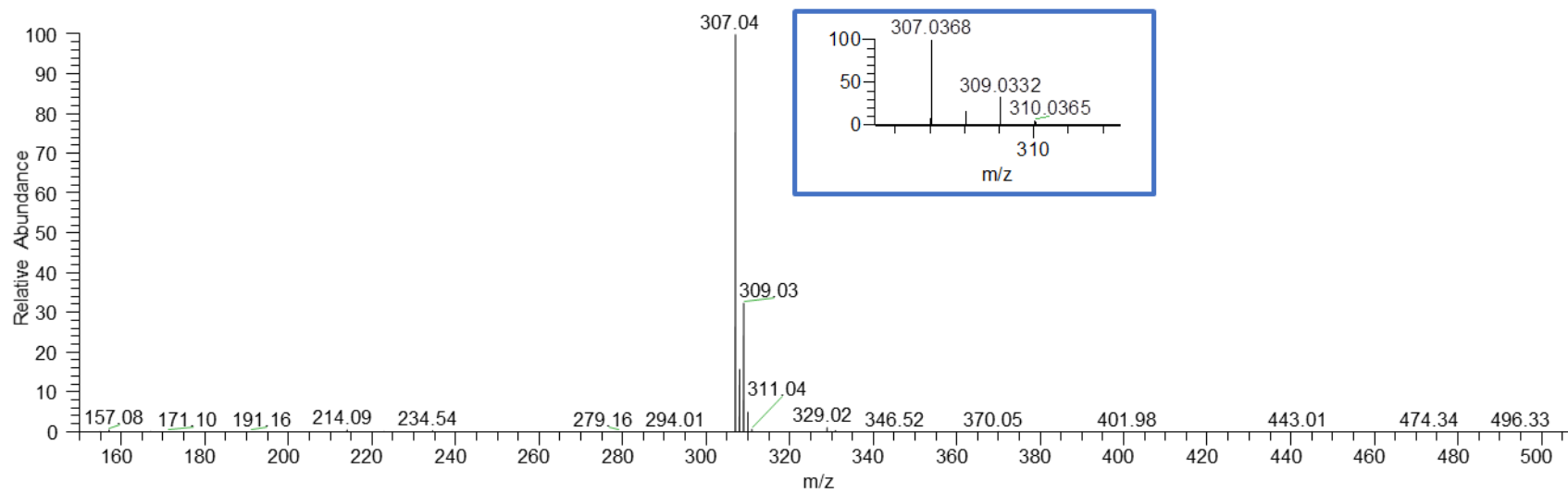


**Figure 3.39.** Mass spectrum of palmariol C (**19**) collected via an LTQ-Orbitrap XL mass spectrometer.

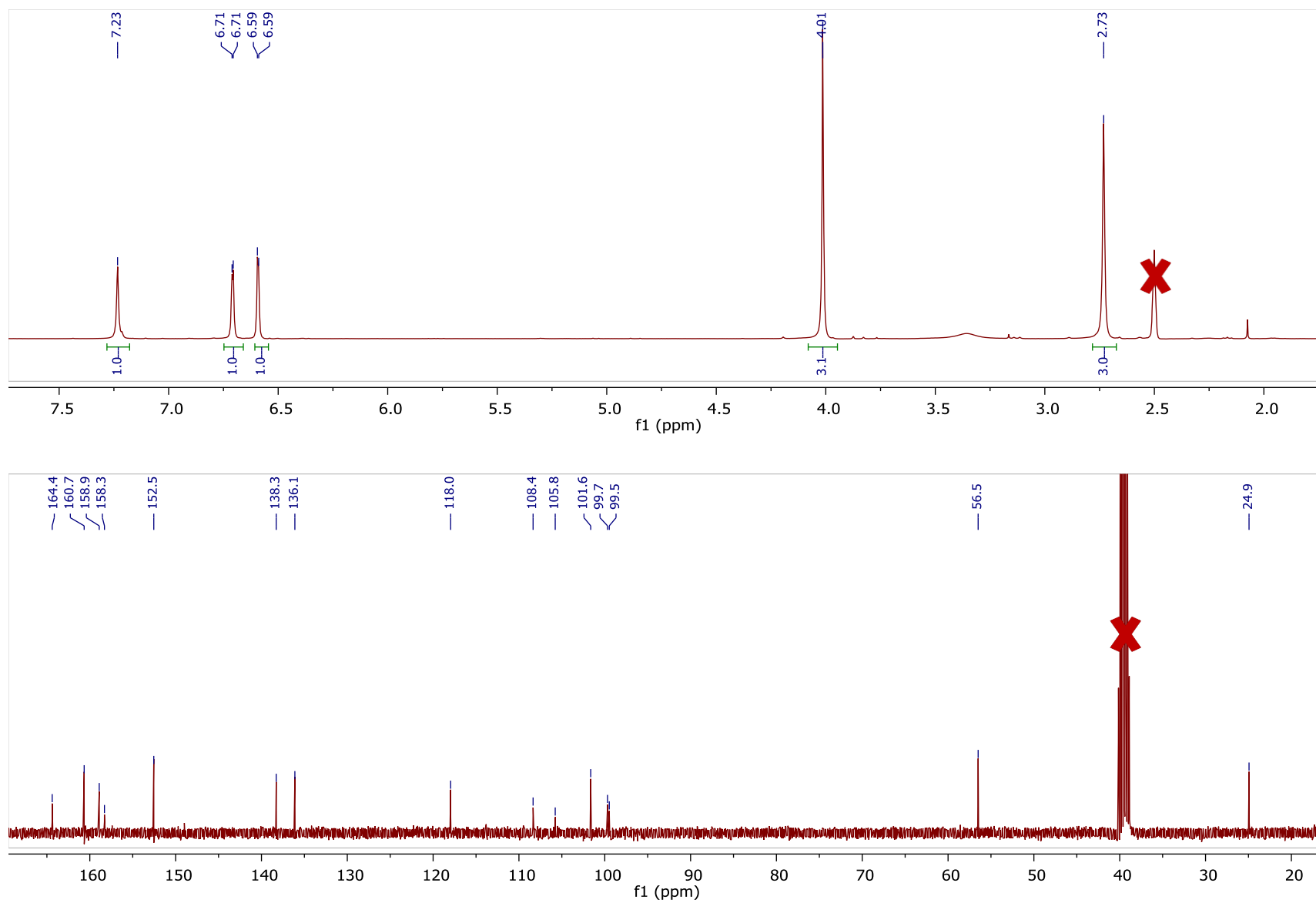


**Figure 3.40.**  $^1\text{H}$  and  $^{13}\text{C}$  NMR spectra of palmariol C (**19**) [400 MHz for  $^1\text{H}$  and 100 MHz for  $^{13}\text{C}$ ,  $\text{DMSO-}d_6$ ].

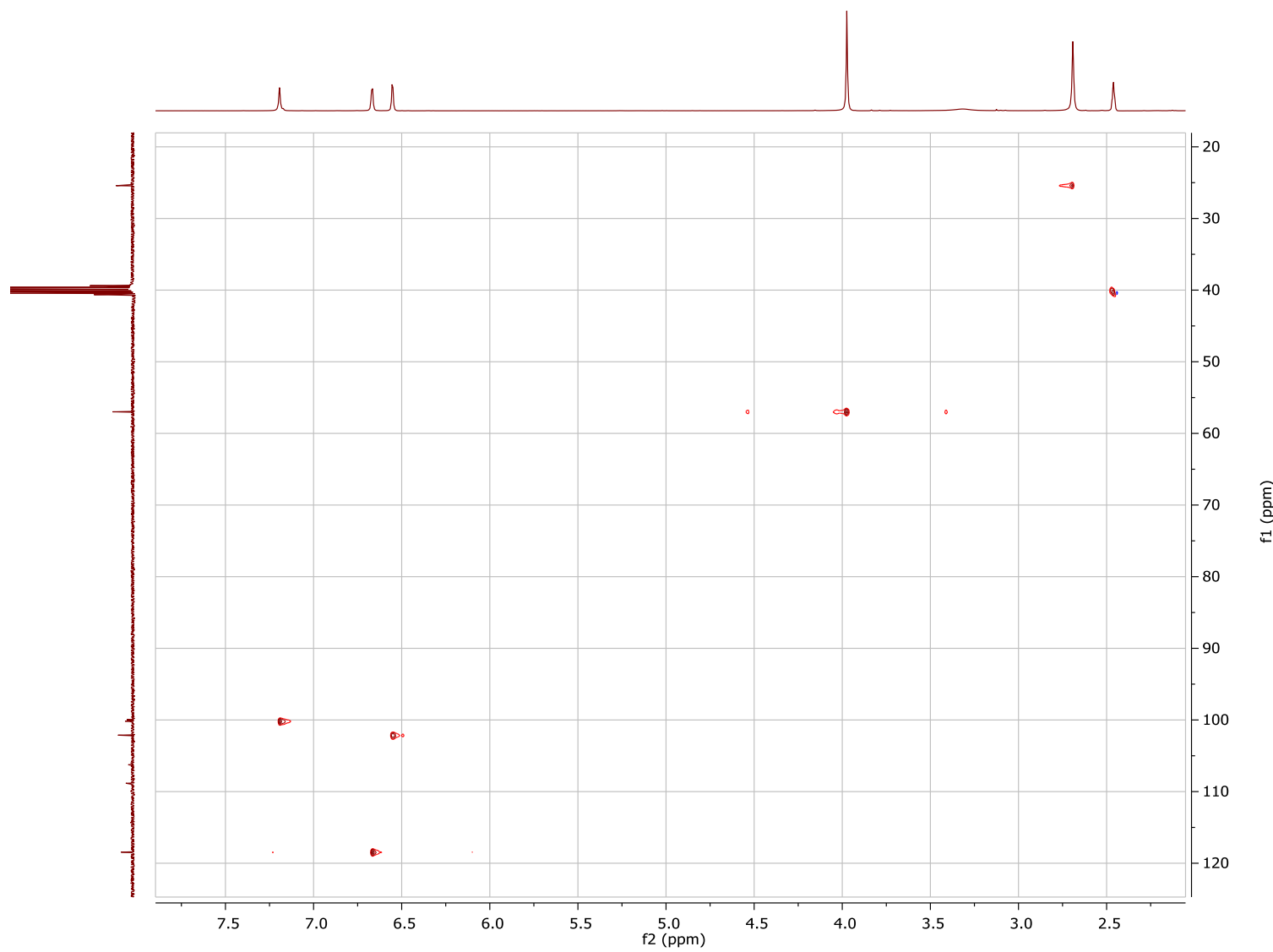


**Figure 3.41.** Edited-HSQC NMR spectrum of palmariol C (19) [400 MHz, DMSO-*d*<sub>6</sub>].

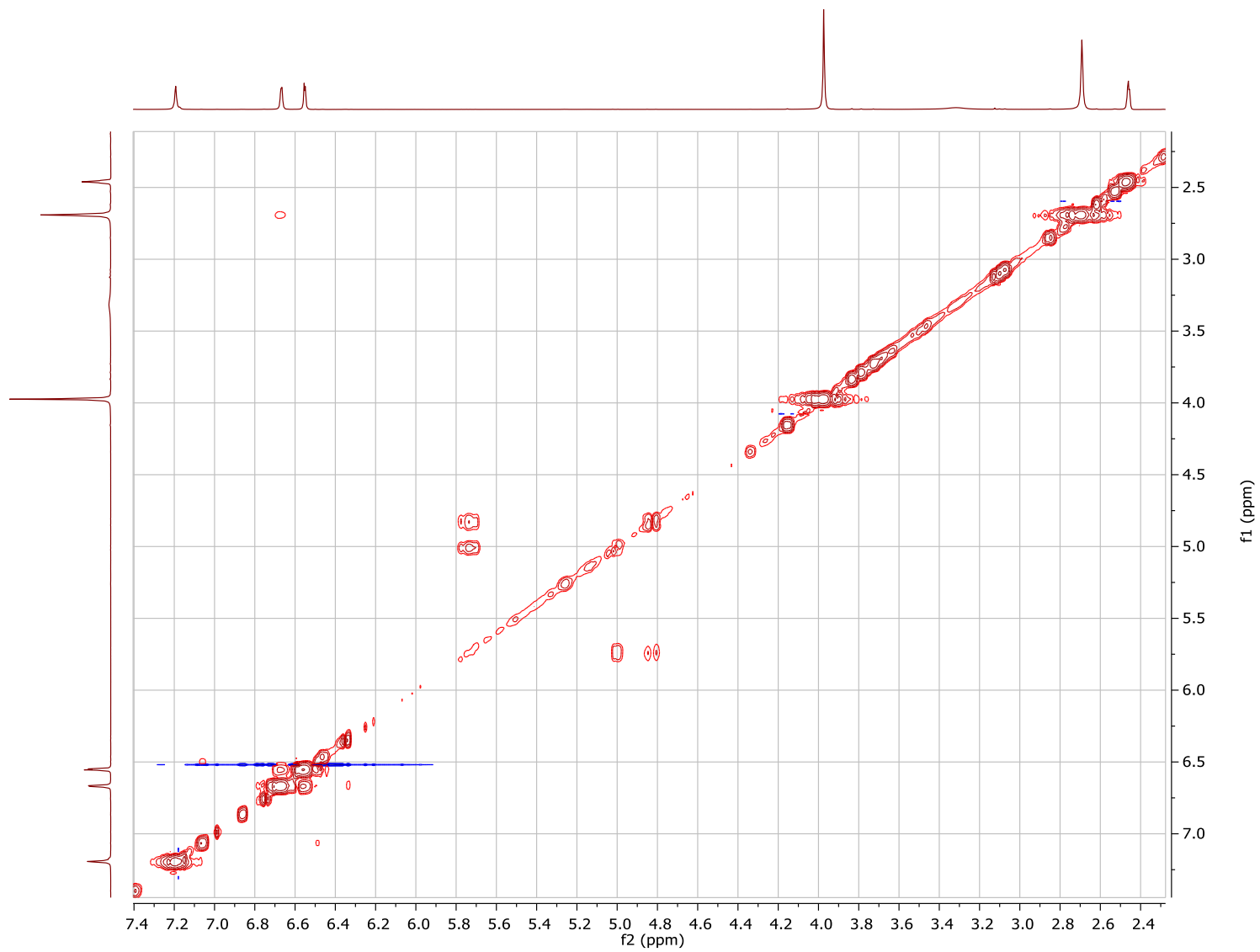


**Figure 3.42.** COSY NMR spectrum of palmariol C (**19**) [400 MHz, DMSO-*d*<sub>6</sub>].

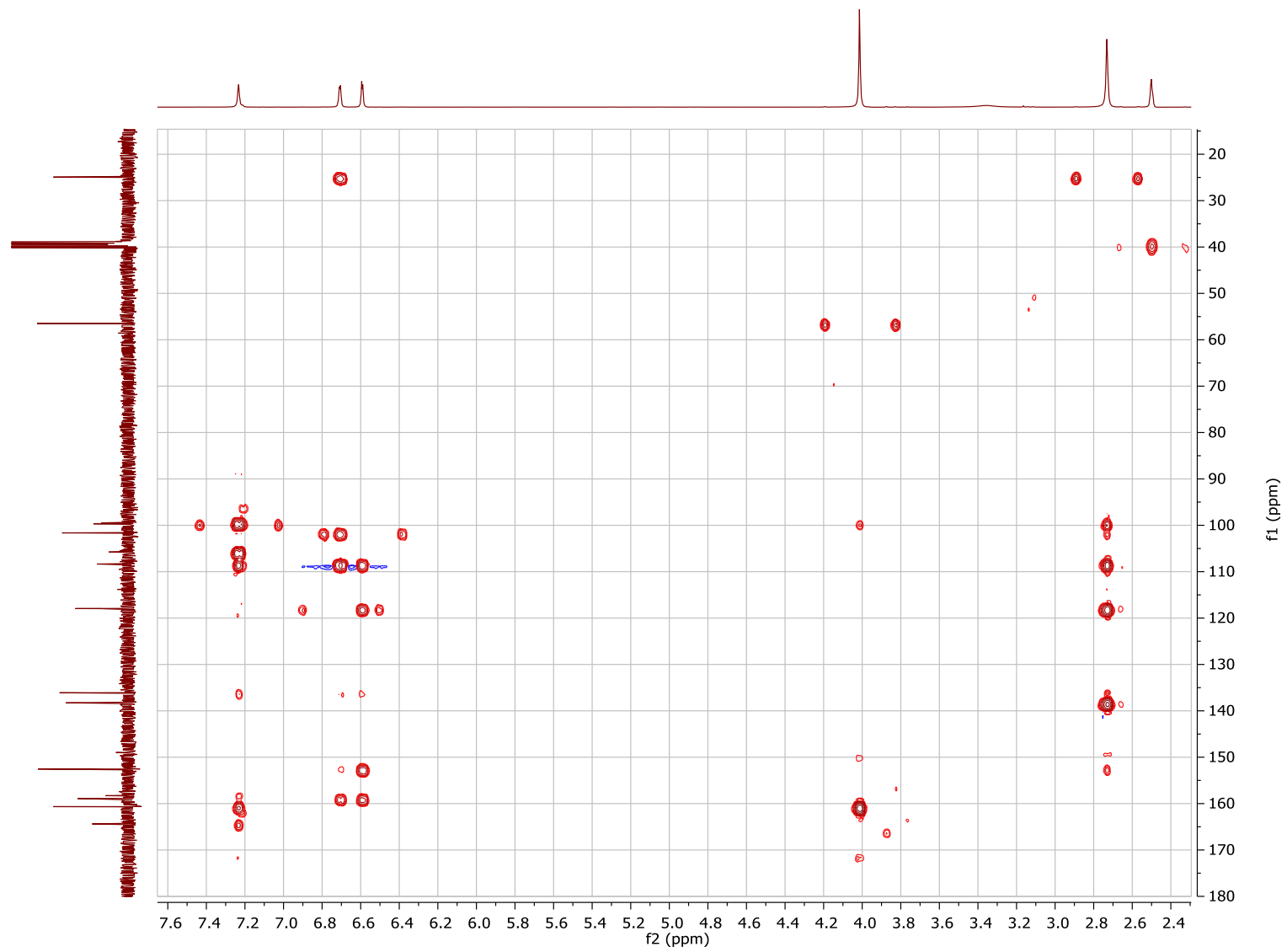


**Figure 3.43.** HMBC NMR spectrum of palmariol C (**19**) [400 MHz, DMSO-*d*<sub>6</sub>].

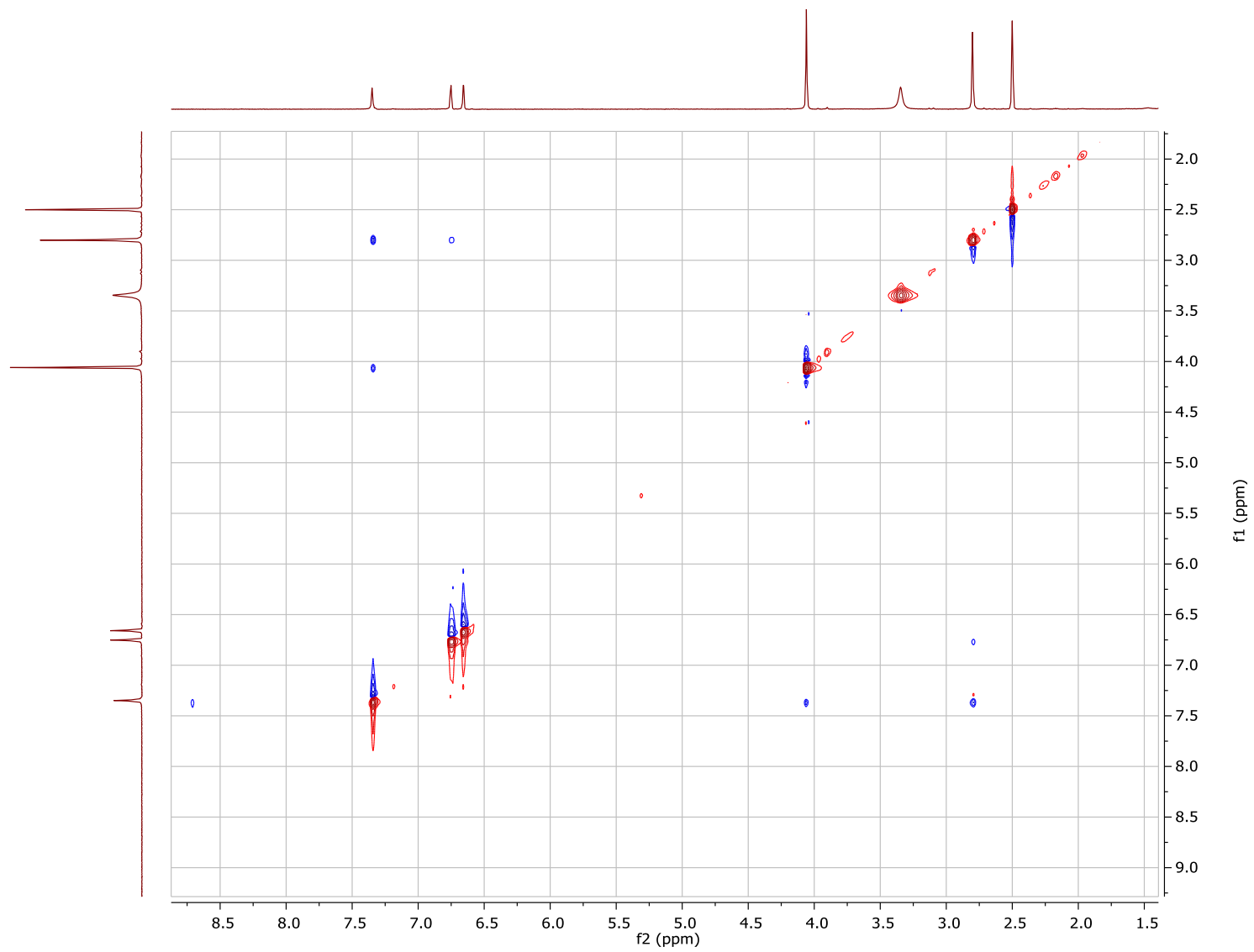


**Figure 3.44.** NOESY NMR spectrum of palmariol C (**19**) [400 MHz, DMSO-*d*<sub>6</sub>].

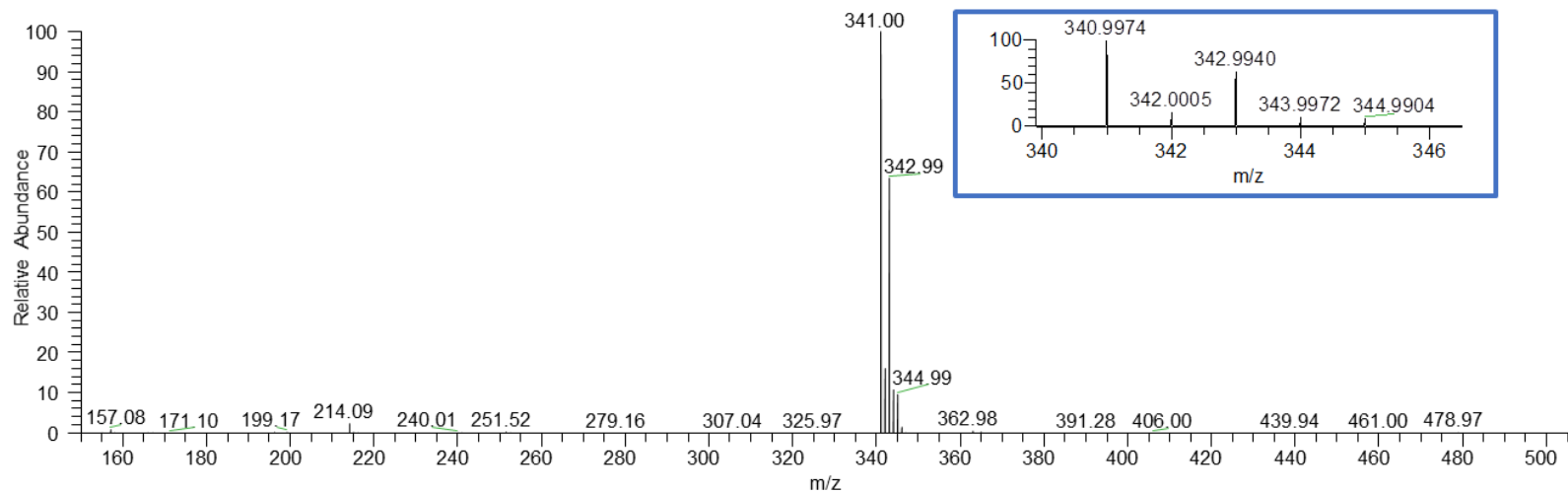


**Figure 3.45.** Mass spectrum of palmariol D (**20**) collected via an LTQ-Orbitrap XL mass spectrometer.

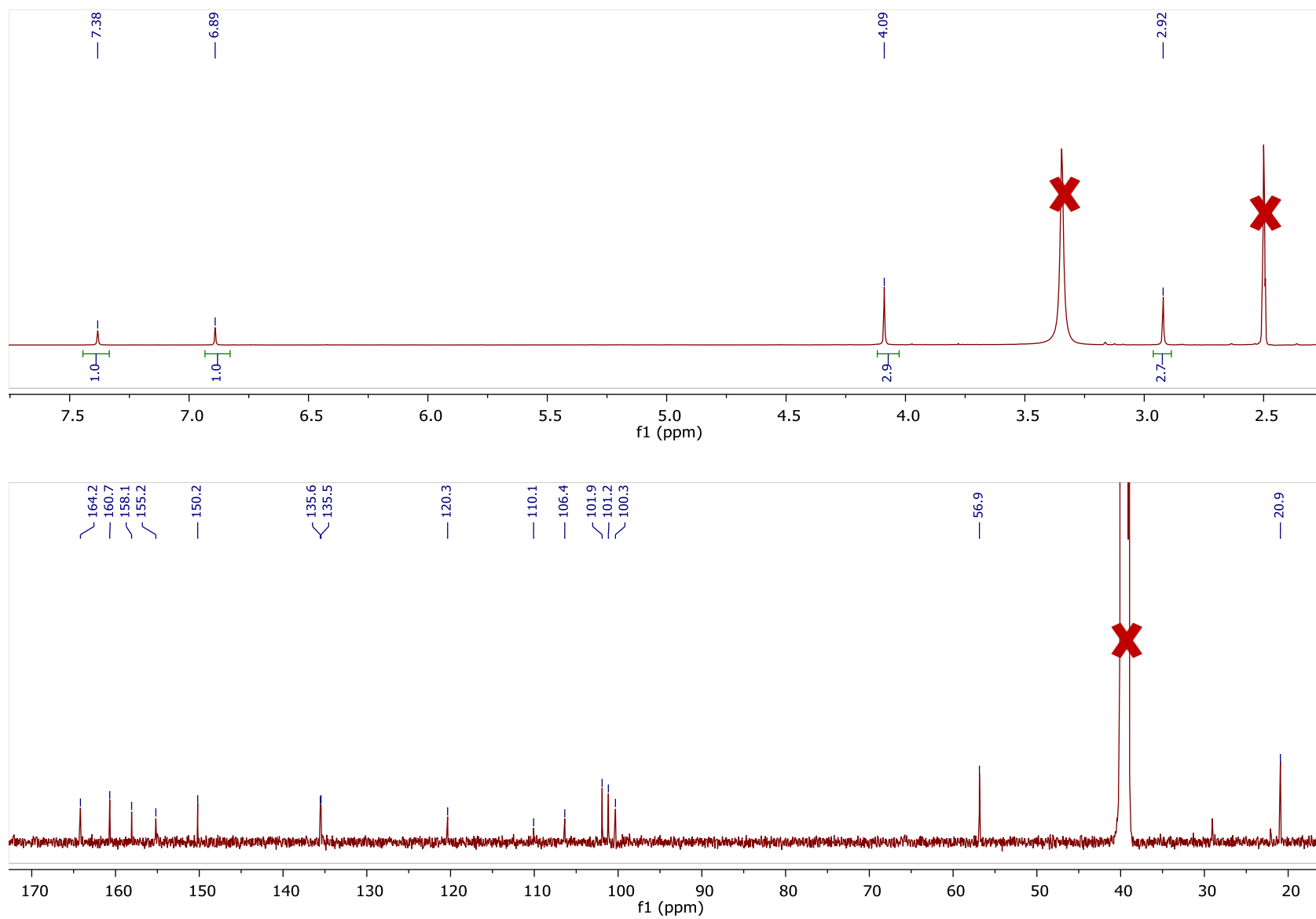


**Figure 3.46.**  $^1\text{H}$  and  $^{13}\text{C}$  NMR spectra of palmariol D (**20**) [500 MHz for  $^1\text{H}$  and 125 MHz for  $^{13}\text{C}$ ,  $\text{DMSO-}d_6$ ].

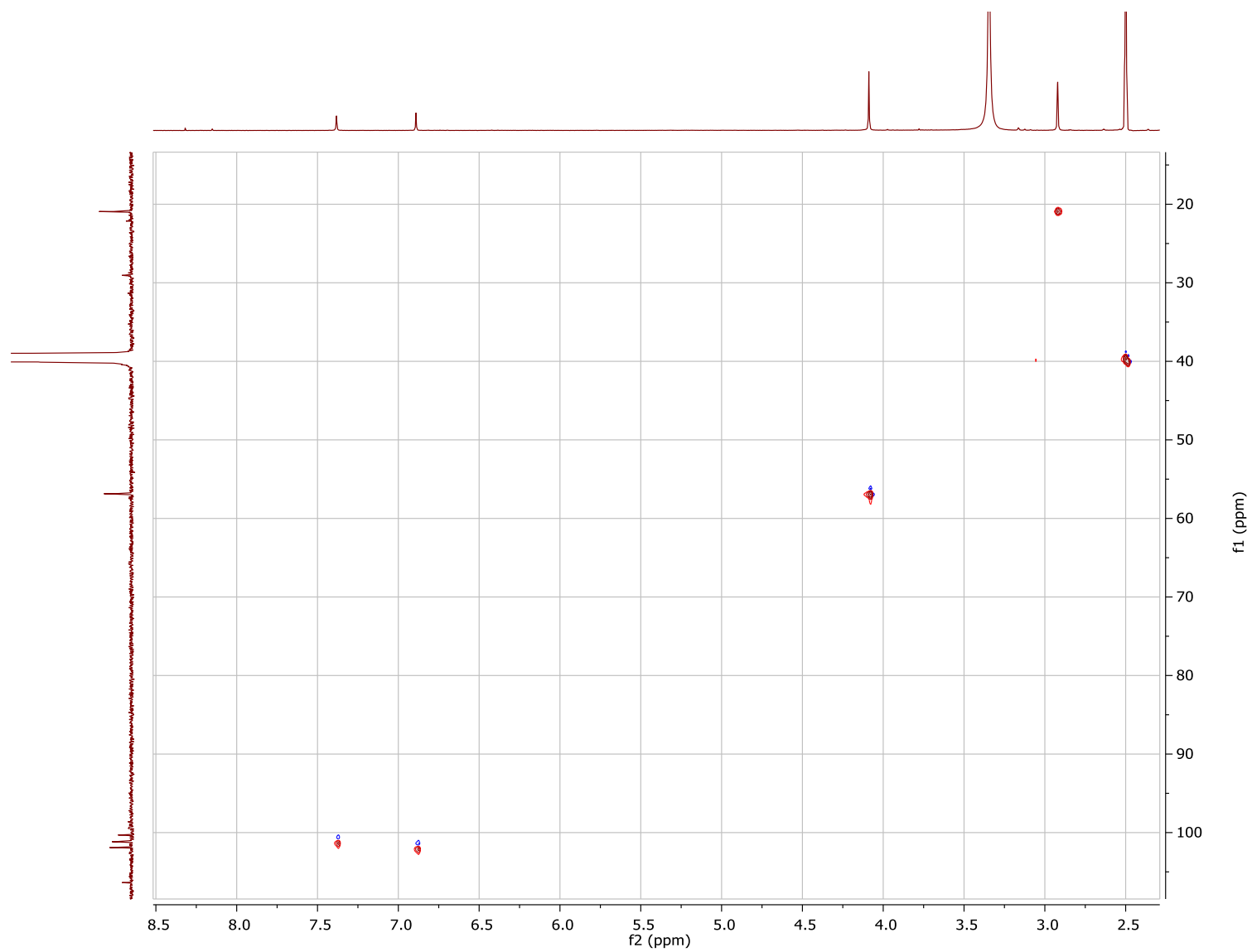


**Figure 3.47.** Edited-HSQC NMR spectrum of palmariol D (**20**) [400 MHz, DMSO-d<sub>6</sub>].

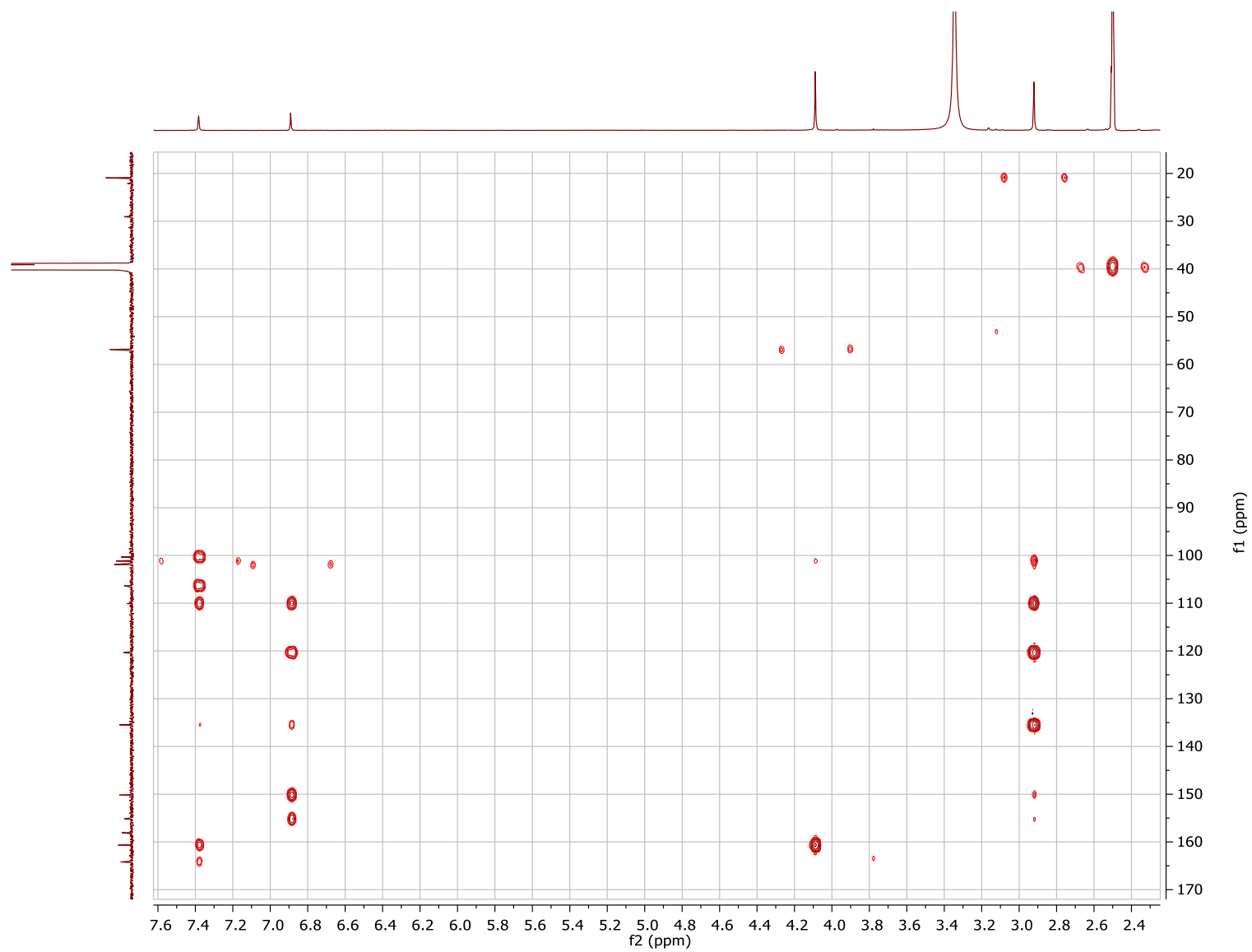


**Figure 3.48.** HMBC NMR spectrum of palmariol D (**20**) [400 MHz, DMSO- $d_6$ ].

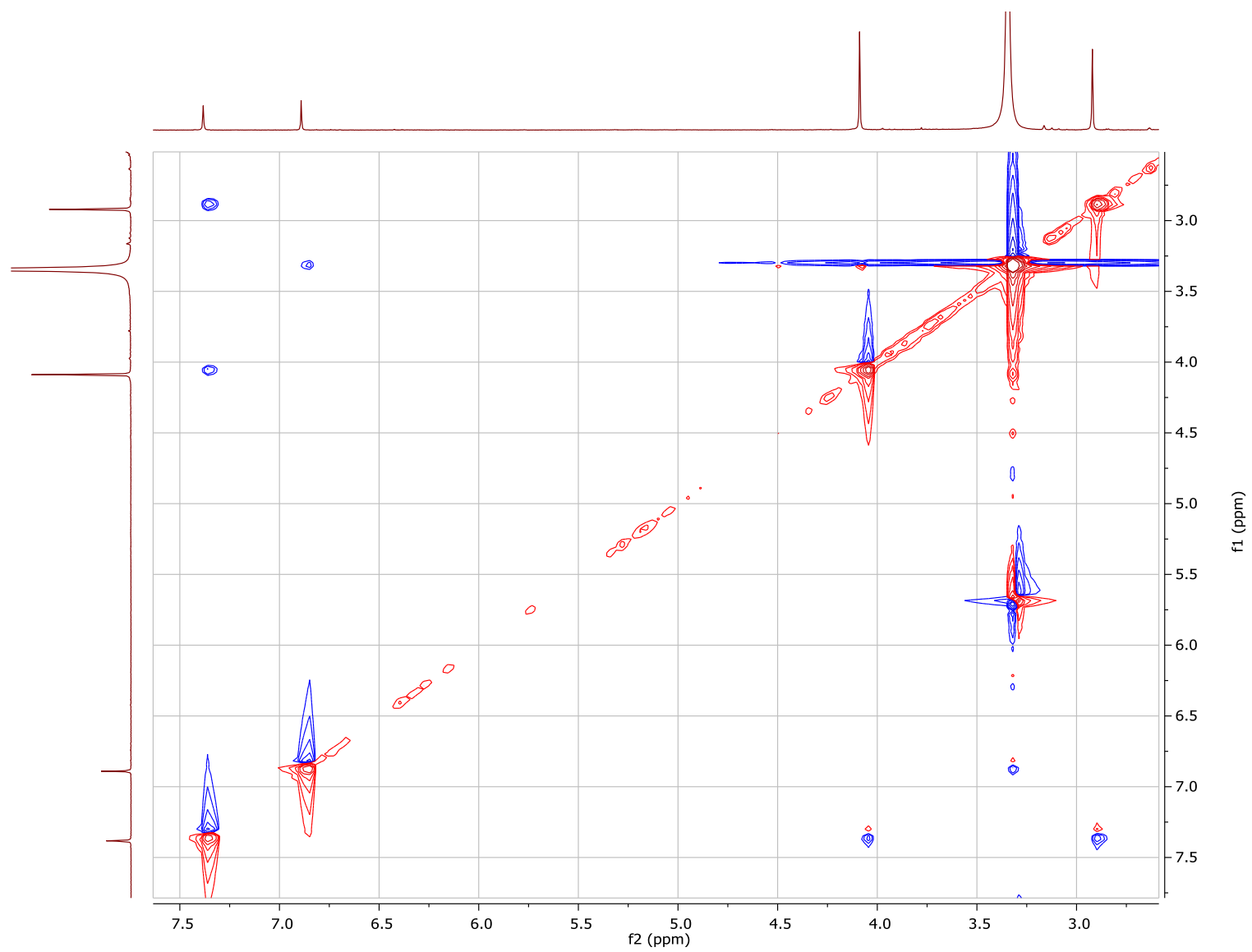


**Figure 3.49.** NOESY NMR spectrum of palmariol D (**20**) [400 MHz, DMSO- $d_6$ ].

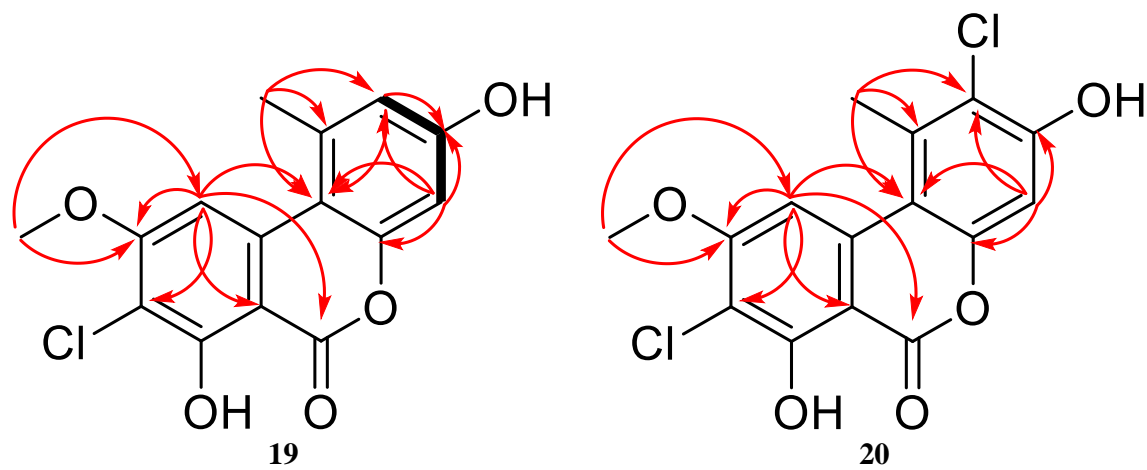


Figure 3.50. Key COSY and HMBC correlations of compounds **19** and **20**.

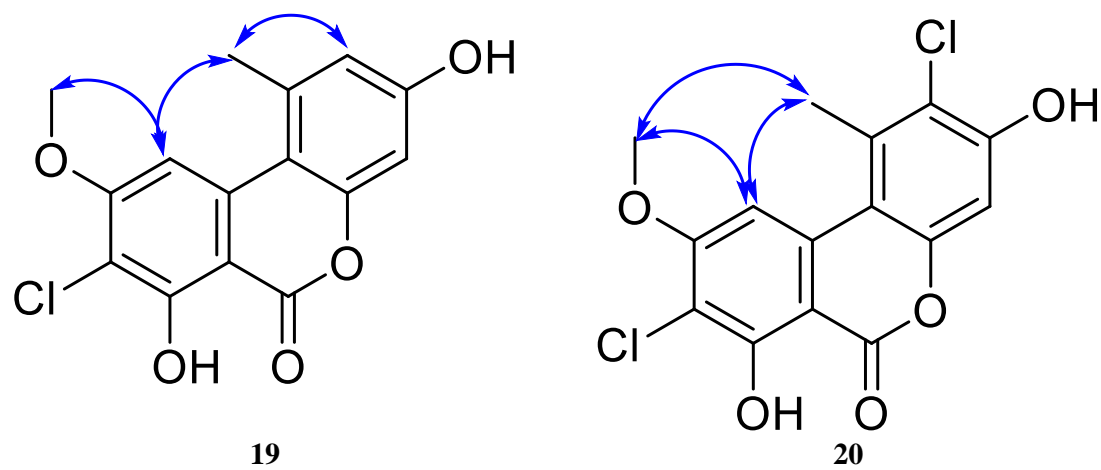
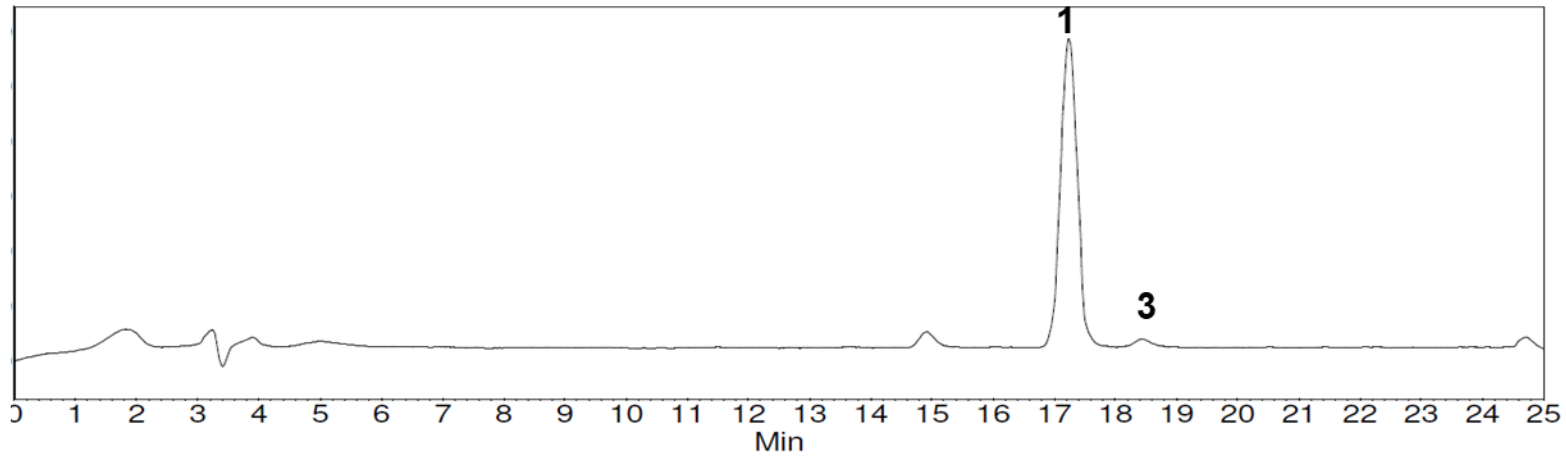
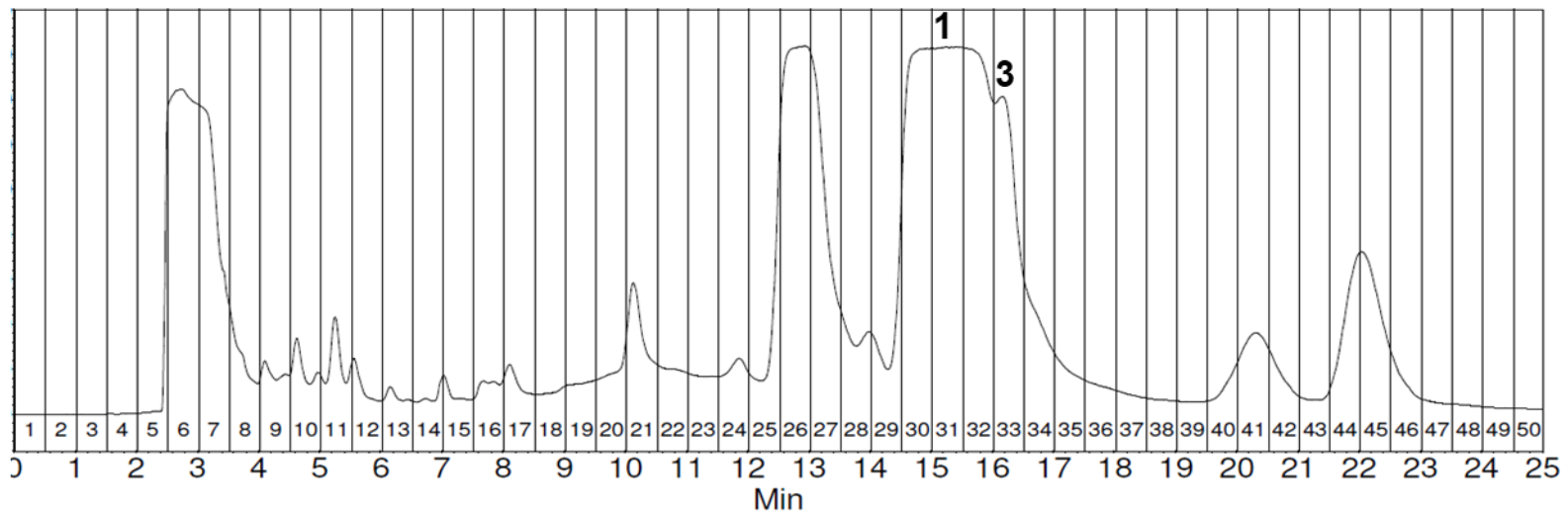


Figure 3.51. NOESY correlations of compounds **19** and **20**.

Analytical HPLC chromatogram for hypothemycin-containing fraction

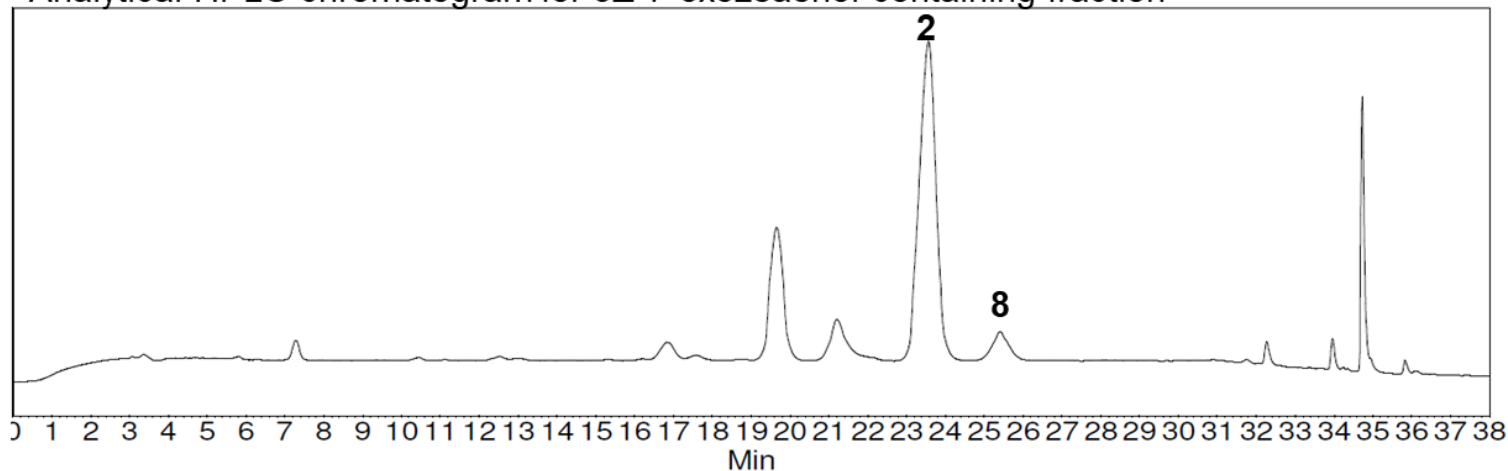


Prep HPLC chromatogram for hypothemycin-containing fraction

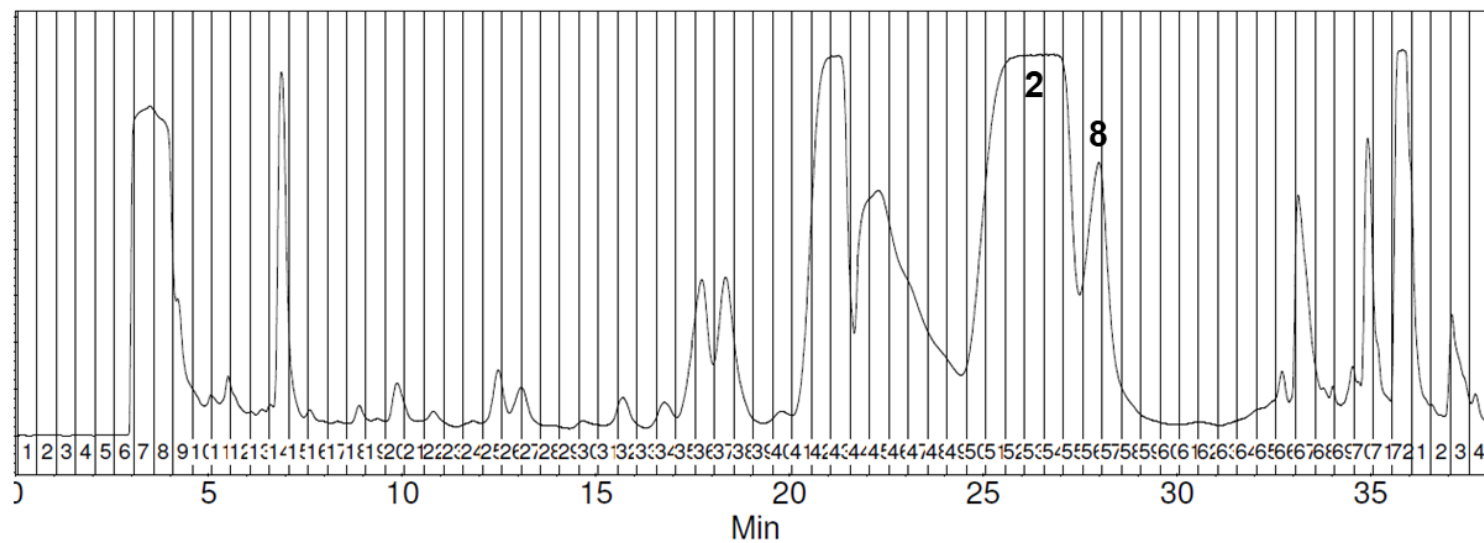


**Figure 3.52.** Analytical vs Prep HPLC chromatograms for hypothemycin-containing fraction demonstrating a co-elution of dihydrohypothemycin (**3**) with hypothemycin (**1**) despite the optimization of the analytical method.

Analytical HPLC chromatogram for 5Z-7-oxozeaenol-containing fraction



Prep HPLC chromatogram for 5Z-7-oxozeaenol-containing fraction



108

**Figure 3.53.** Analytical vs Prep HPLC chromatograms for a (5Z)-7-oxozeaenol-containing fraction demonstrating a co-elution of LL-Z1640-1 (8) with (5Z)-7-oxozeaenol (2) despite the optimization of the analytical method.

**Table 3.3.** Comparison between the application of reverse-phase HPLC vs. resuspension/ centrifugation techniques in the purification process of hypothemycin and (5Z)-7-oxozeaenol.

parameters	Reverse-phase HPLC		Resuspension/centrifugation approach	
	Hypothemycin	(5Z)-7-oxozeaenol	Hypothemycin	(5Z)-7-oxozeaenol
Number of injections	10-15	10-15	--	--
Amount per injection (mg)	50-100 mg	50-100 mg	--	--
Estimated usage of HPLC- grade acetonitrile	2.5-3.5 L	3.5-5.0 L	--	12 mL
Estimated usage of DI H <sub>2</sub> O (0.1% formic acid)	4.1-6.2 L	6.2-9.3 L	--	--
Estimated usage of HPLC-grade methanol	--	--	10 mL	--
Average extraction-to-purification time	2-3 weeks	2-3 weeks	3-4 days	3-4 days
Instrumentation time on the HPLC	7-10 hr	9-14 hr	--	--
Instrumentation time on the rotavap	2-3 days	2-3 days	--	--

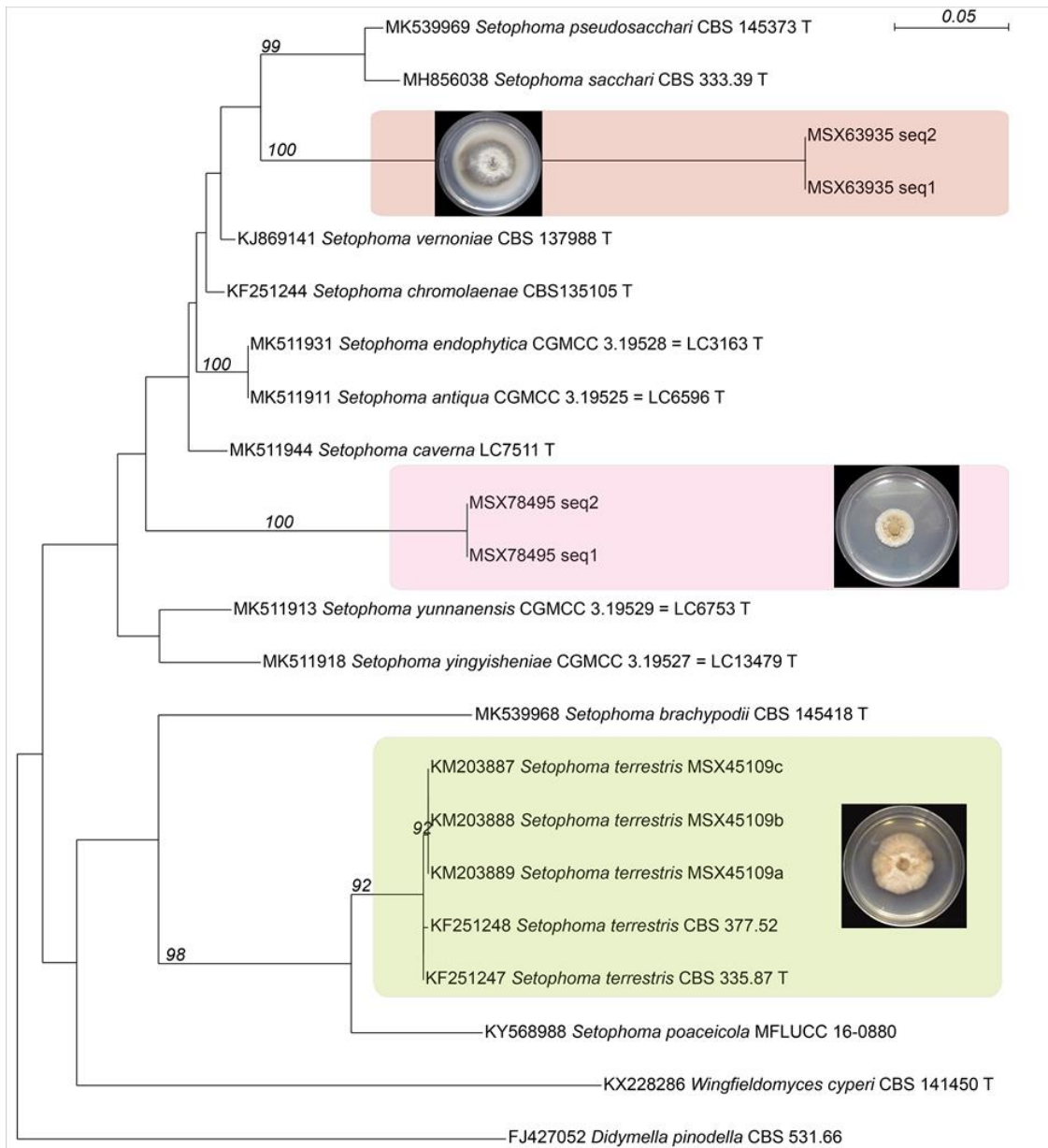


**Figure 3.54.** Molecular phylogenetic analysis of fungal ITS sequences reveal MSX63935, MSX78495, and MSX45109 are members of the genus, *Setophoma* (*Phaeosphaeriaceae*, *Ascomycota*). Phylogram of the most likely tree ( $-\ln L = 2720.466$ ) from a Maximum Likelihood analysis of 22 sequences based on the ITS region (505 bp) using IQ-TREE. Numbers refer to UFBoot support values  $\geq 90\%$  based on 5000 replicates. Nodes  $\geq 95$  are considered strongly supported. Three week old, malt extract agar cultures of MSX63935 and MSX78495 and potato dextrose agar culture of MSX45109 are shown. *Didymella pinodella* CBS 531.66 was used as outgroup. Ex-type isolates are designated by the letter T. Bar indicates nucleotide substitutions per site.

## CHAPTER IV: ENHANCED PRODUCTION AND ANTICANCER PROPERTIES OF PHOTOACTIVATED PERYLENEQUINONES

Zeinab Y. Al Subeh, Huzefa A. Raja, Susan Monro, Laura Flores-Bocanegra, Tamam El-Elimat, Cedric J. Pearce, Sherri A. McFarland, and Nicholas H. Oberlies. *Journal of Natural Products* 2020, 83, 8, 2490-2500.

Hypocrellins and hypomyces are naturally occurring fungal perylenequinones with potential photodynamic activity against cancer and microbial diseases. This project pursued three lines of research. First, the production of perylenequinones was enhanced by investigating the effect of culture medium and light exposure on their biosynthesis. Solid-fermentation cultures on rice medium allowed for enhanced production of hypocrellins as compared to Cheerios or oatmeal medium. Alternatively, increased production of hypomyces, which are structurally related to the hypocrellins, was observed on oatmeal medium. In both cases, light exposure was an essential factor for the enhanced biosynthesis. In addition, this led to the discovery of two new perylenequinones, *ent*-shiraiachrome A (**5**) and hypomycesin E (**8**), which were elucidated based on spectroscopic data. Finally, the photocytotoxic effects of both classes of compounds were evaluated against human skin melanoma, with EC<sub>50</sub> values at nanomolar levels for hypocrellins and micromolar levels for hypomyces. In contrast, both classes of compounds showed reduced dark toxicity (EC<sub>50</sub> values > 100 μM), demonstrating promising phototherapeutic indices.

### Introduction

Hypocrellins are a class of fungal metabolites (perylenequinone) that were first isolated from the fruiting bodies of *Hypocrella bambusae*, *Shiraia bambusicola*, and other *Shiraia*-like fungi.<sup>185-188</sup> Hypocrellin-producing fungi have been used in traditional Chinese medicine for the treatment of rheumatoid arthritis, vertigo, psoriasis, and other diseases.<sup>189</sup> Hypocrellins are known to have an oxidized pentacyclic core, a highly conjugated ring system, and exhibit various pharmacological activities. Recently, hypocrellins have started gaining attention in

photodynamic therapy (PDT) to combat cancer and bacterial, fungal, and viral infections.<sup>190-195</sup> In photodynamic therapy, a non-toxic photosensitizer is irradiated with visible-light at a defined wavelength in the presence of oxygen to induce the production of reactive oxygen species and free radicals that are fatal to cancerous cells and microbial pathogens.<sup>196</sup> Owing to their high quantum yields of singlet oxygen ( $^1\text{O}_2$ ), low general toxicity in the absence of light, and light absorption properties in the red spectral region, hypocrellins are of clinical interest as naturally-derived photosensitizers.<sup>197, 198</sup>

The hypocrellin family consists of four main compounds, hypocrellin (**1**), hypocrellin A (**2**), hypocrellin B (**3**), and shiraiachrome A (**4**) (Fig. 4.1). A great deal of confusion exists in the literature on the naming of these perylenequinones. For instance, hypocrellin (**1**) and hypocrellin A (**2**), which are enantiomers, were isolated from *Hypocrella bambusae* and *Shiraiachroma bambusicola*, respectively.<sup>185, 186</sup> However, several studies on the biological and photodynamic properties of these compounds do not differentiate between their structures.<sup>192, 199, 200</sup> Moreover, hypocrellin A (**2**) was referred by Wu et al.<sup>186</sup> as shiraiachrome B. Similarly, shiraiachrome A (**4**) was also named as hypocrellin B,<sup>201</sup> which is the trivial name that is used most often in the literature to refer to **3**.<sup>202, 203</sup> On the other hand, hypocrellin B (**3**) was named as either shiraiachrome C or hypocrellin C by Wu et al.<sup>186</sup> or Kishi et al.,<sup>201</sup> respectively. Owing to the large number of studies that use the names hypocrellin (**1**), hypocrellin A (**2**), hypocrellin B (**3**), and shiraiachrome A (**4**), we propose that these names should take precedent; Table 4.3 should be examined for an illustration of the varied nomenclature of these compounds.

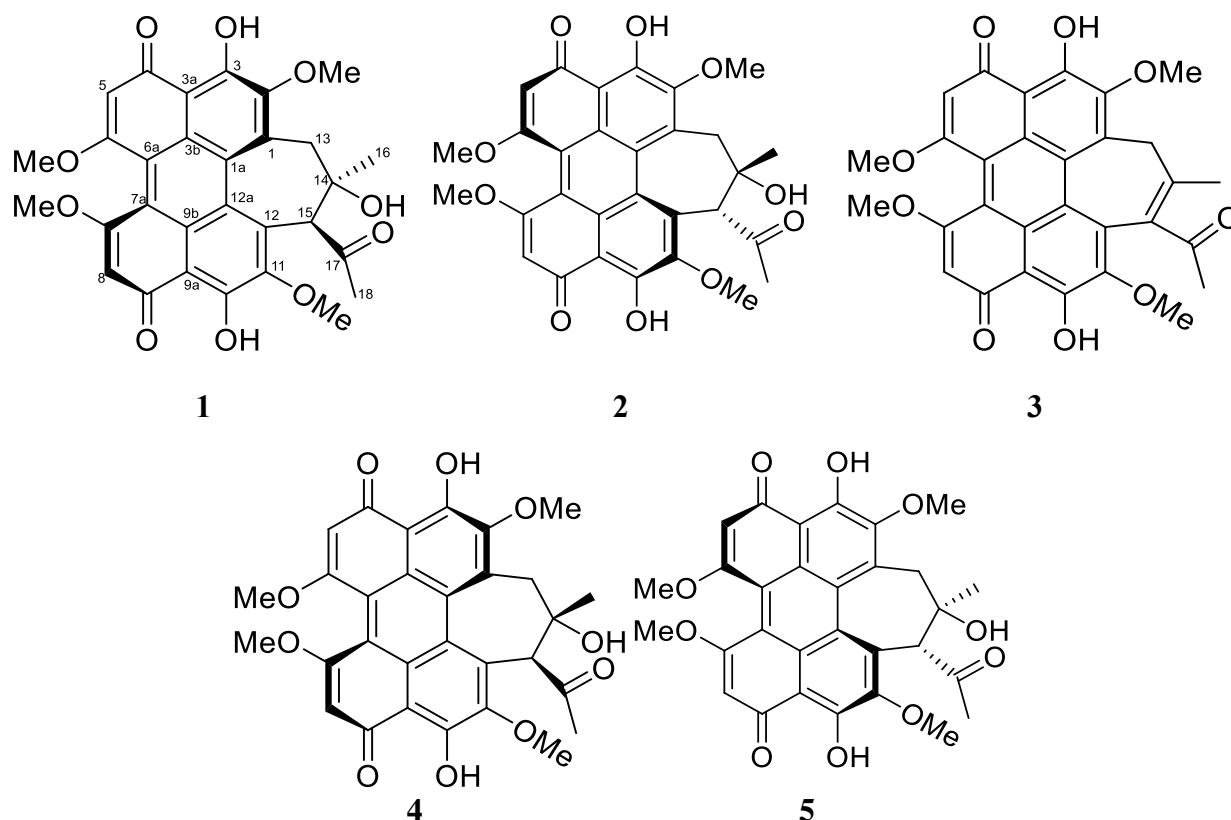


**Figure 4.1.** Chemical structure of compounds 1-5.

There was a need to increase the production of these compounds to facilitate further investigations on their promising photodynamic properties. Moreover, the axial chirality of hypocrellins, along with the atropisomerization (inversion of axial chirality) and tautomerism exhibited by these compounds make the total synthesis of hypocrellins challenging (e.g. 19 steps with a 1.6% overall yield to generate **2**).<sup>204</sup> Fermentation constitutes a viable route to supply these compounds, and several attempts have been made to increase their production. Of these, enhanced production of hypocrellin A (**2**) was observed after the addition of Triton X-100 surfactant to the submerged cultures of *S. bambusicola* (yield ~100 mg/L).<sup>205</sup> Co-cultivation of *Shiraia* sp. with *Pseudomonas fulva* was found to stimulate the production of various perylenequinone compounds, including hypocrellin A (**2**).<sup>206, 207</sup> In another study, solid-state fermentation of *Shiraia* sp. using corn was found to enhance the production of **2** as compared to seven other types of grain.<sup>208</sup> Furthermore, enhanced biosynthesis of hypocrellin A (**2**) along with stimulating its release to the medium was observed after treating the submerged culture of *Shiraia* sp. with low intensity ultrasound irradiation.<sup>209</sup> In general, the literature suggests that

hypocrellin-producing fungi are sensitive to media, growth conditions, available nutrients, and surrounding environmental factors.

Light is a major factor that regulates fungal growth, reproduction, sexual development, and production of secondary metabolites.<sup>210</sup> Strong evidence exists on the impact of light exposure for the production of hypocrellins. Wang et al.<sup>211</sup> investigated the effect of exposing cultures of *Shiraia* sp. to light at various wavelengths and found that a red light emitting diode (LED) maximized the production of **2** to >3 fold that of the dark control. Similarly, growing *Shiraia* sp. cultures under light and dark cycles (12:12 or 24:24 h) was found to increase the production of **2** by 1.7 fold as compared to the dark culture control.<sup>212</sup> High intensity light (i.e. 600-800 lux) negatively affected fungal growth and decreased the production of **2**, while lower intensity light (i.e. 200-400 lux) was shown to up-regulate the biosynthesis of **2**.<sup>212</sup> Although those studies suggested that light exposure might help to increase the production of **2**, Gao et al.<sup>213</sup> found that higher hypocrellin production was observed in *Shiraia* sp. grown under dark conditions, as compared to those grown under light of various wavelengths (i.e. white, red, yellow, green, blue, and purple). Therefore, uncertainty persists with regard to the effect of light on the biosynthesis of secondary metabolites from hypocrellin-producing fungi.

As part of ongoing studies to uncover potential anticancer leads from natural resources,<sup>50</sup> a hypocrellin-producing fungus (i.e. strain MSX60519) was examined. This strain was grown under a suite of growth conditions to investigate the effect of culture medium and light exposure on the production of these compounds (**1-8**),<sup>214</sup> resulting in the discovery of new analogues **5** and **8** and the refinement of the structures of compounds **6** and **7**. In addition, the photodynamic properties were evaluated under both light and dark conditions, revealing light-induced cytotoxicity in the nanomolar range, suggestive of the pharmacological potential of these compounds.

## Results and Discussion

As reported previously, our standard protocol is to first grow fungal cultures on a pilot scale (i.e., using ~ 10 g of rice), and then, if a biologically active sample passes dereplication (i.e., filtering out extracts that contain well studied mycotoxins),<sup>151, 152</sup> it will be scaled for more in depth natural products studies.<sup>119</sup> For strain MSX60519, the major compounds isolated from solid state

fermentation cultures were identified as *ent*-shiraiachrome A (**5**; elucidation discussed below) and hypocrellin (**1**),<sup>185, 204</sup> where the spectroscopic data matched the literature. However, the purified amounts of these two compounds were limited to a few milligrams (~2-3 mg).

To facilitate further investigations on the photodynamic properties of these compounds, larger supplies were necessary. This was initiated by first identifying the strain as a *Shiraiia*-like sp. in the family Shiraiaceae based on maximum likelihood analysis using the ITSr\_DNA region.<sup>170</sup> Solid-state fermentations of this fungus were grown in triplicate under nine conditions to investigate the effect of culture medium and light exposure on the production of perylenequinones. Herein, we report enhanced production of hypocrellins on solid rice medium as compare to Cheerios or oatmeal media. Alternatively, it was found that oatmeal was the ideal medium to enhance the production of hypomyces, which are closely related analogues that have an additional six-membered ring. Interestingly, light exposure was an essential factor for the production of both hypocrellins and hypomyces. In addition, we report two new perylenequinones, compound **5** (which is the enantiomer of **4**), and hypomycesin E (**8**), along with identifying the absolute configuration of hypomycesin A (**6**) and hypomycesin C (**7**) based on analysis of their NOESY spectra and comparing their experimental ECD and VCD data with the calculated spectra.

**The Effect of Growth Medium and Light on the Production of Hypocrellins.** UPLC-HRMS data were collected for extracts and flash chromatography fractions of cultures of strain MSX60519 to confirm the production of *ent*-shiraiachrome A (**5**) and hypocrellin (**1**) across different growth conditions, to measure their relative abundance, and to guide the isolation process of these compounds (Figs. 4.9 and 4.10). Cultures grown under complete darkness exhibited a low abundance of compounds **5** and **1** (Fig. 4.2). *Ent*-shiraiachrome A (**5**) and hypocrellin (**1**) were optimally produced by cultures grown on rice medium and incubated under 12:12 h light:dark cycles, or continuous LED light exposure (Fig. 4.2), supporting that light facilitates the biosynthesis of these compounds, as suggested by Wang et al.<sup>211, 212</sup> Furthermore, the organic extracts were tested for photocytotoxic activity, and cultures grown under complete darkness exhibited significantly reduced photocytotoxic activity as compared to those grown under 12:12 h light:dark cycles or continuous LED light (Fig. 4.11). This further supported a higher production of hypocrellins in cultures that were exposed to light.

Perylenequinones are produced by a variety of fungal species, particularly by plant pathogens that cause damage to plant tissues.<sup>215</sup> Light-activated hypocrellins exhibited a broad-range of toxicities against bacteria, fungi, as well as human tumor cells.<sup>193, 194, 216, 217</sup> As such, obvious questions pertain to how fungi that biosynthesize hypocrellins protect themselves against their own toxins or how light exposure facilitates the biosynthesis of these compounds without a noticeable decrease in fungal growth and development. Although the mechanisms of protection against autotoxicity have not been reported for these fungi, *Cercospora* spp. were suggested to defend themselves against the cercosporin photosensitizer by a transient reduction and detoxification of cercosporin molecules.<sup>218</sup> Reduced cercosporin absorbs less light, and has been shown to be less toxic, than cercosporin itself.<sup>215</sup> Similar mechanisms may be adapted by fungi that biosynthesize hypocrellins, where hypocrellins in contact with fungal hyphae are maintained in a reduced (i.e., non-photoactive) form. Aeration by diffusion out of fungal hyphae (or by extraction) results in oxidation. Furthermore, light exposure was reported to be essential for the biosynthesis of cercosporin, and the spectrum of light required for the induction of cercosporin biosynthesis resembled the absorption spectrum of cercosporin itself.<sup>219, 220</sup> While more studies are needed, the structural similarity between hypocrellins and cercosporin suggests that analogous mechanisms for autoprotection and the stimulation of biosynthesis are at least plausible.

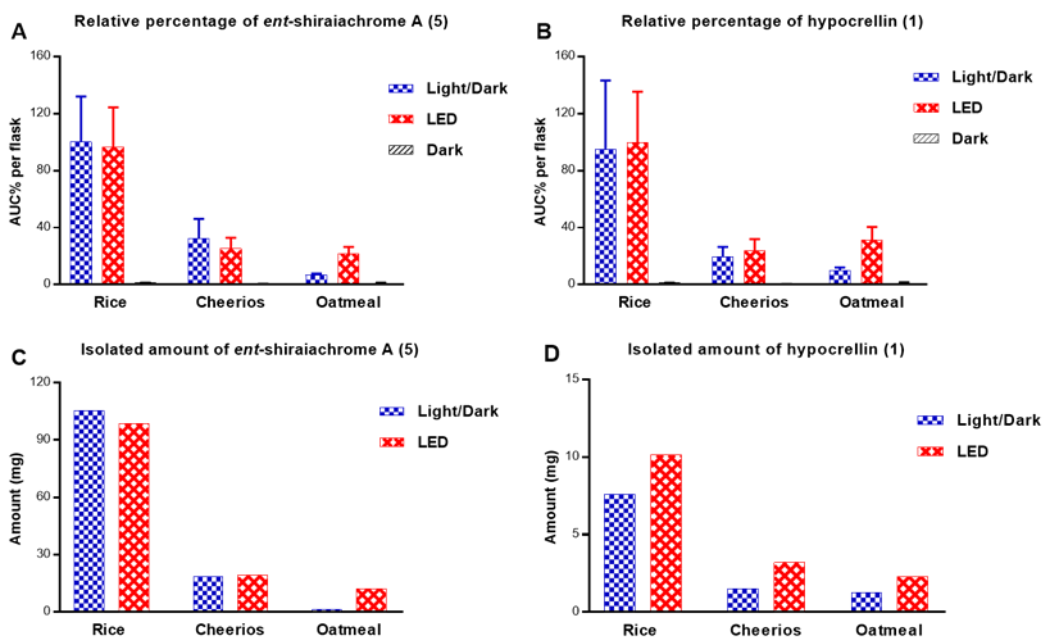


**Figure 4.2.** Panels A and B show the relative percentages of **5** and **1**, respectively, across cultures grown on rice, Cheerios, and oatmeal media under 12:12 h light:dark cycles, continuous LED, or in darkness. The relative percentages were measured by LC-HRESIMS in three biological replicates and multiplied by the extract weight, and then normalized according to the extract with highest abundance. Panels C and D show the amounts isolated of **5** and **1**, respectively, from cultures shown in panels A and B and grown on rice, Cheerios, and oatmeal media under either 12:12 h light:dark cycles or LED conditions.

Based on HRESIMS data, the second fraction from flash chromatography was identified as the hypocrellins-containing fraction. Accordingly, *ent*-shiraiachrome A (**5**) and hypocrellin (**1**) were isolated from this fraction from all cultures grown under either light:dark cycles or continuous LED light. Interestingly, the isolated amounts of **5** and **1** from these cultures nearly matched their relative abundance ratios (Fig. 4.2). The isolated amounts of **5** and **1** from rice cultures that were grown under light:dark cycles were ~100 mg (**5**) and 8-10 mg (**1**); nearly identical results were observed from rice cultures grown under continuous LED light. However, the purification process of these compounds using preparative HPLC was more straightforward from cultures grown under continuous LED light (Fig. 4.12). This was due to the production of other non-hypocrellin compounds by cultures grown under light:dark cycles. In addition, < 1 mg of hypocrellin B (**3**) was isolated from cultures grown on rice exposed to light:dark cycles. To obtain more of this compound, **3** was produced by a dehydration reaction of **5** and **1**, as described below.

**The Structure Elucidation of 5 and 1 and Generation of 3.** Compound **5** was isolated as a deep red amorphous powder. Using HRESIMS data (Fig. 4.13), the molecular formula was determined as C<sub>30</sub>H<sub>26</sub>O<sub>10</sub>, corresponding to an index of hydrogen deficiency of 18. The <sup>1</sup>H and <sup>13</sup>C NMR data (Table 4.1) matched those reported for shiraiachrome A (**4**),<sup>186, 201</sup> and 2D NMR data confirmed that **5** and **4** shared the same 2D structure (Figs. 4.15-4.19). However, the ECD spectrum of **5** (Fig. 4.14) was the opposite of the spectrum reported for **4**,<sup>186, 201</sup> indicating that **5** was the enantiomer of shiraiachrome A (**4**), thereby suggestive of the trivial name, *ent*-shiraiachrome A (**5**). As noted earlier (Table 4.3), there are some inconsistencies in the literature regarding the nomenclature of this class of compounds, and indeed, **4** was reported differently in 1989 and 1991, where those authors referred to this compound as shiraiachrome A and hypocrellin B, respectively.<sup>186, 201</sup> Moreover, the absolute configuration of **4** was later revised to

*M(R)*, 14*S*, 15*S*;<sup>221</sup> therefore, the absolute configuration of *ent*-shiraiachrome A (**5**) was *P(S)*, 14*R*, 15*R*.

Like other hypocrellins, the fused pentacyclic core of *ent*-shiraiachrome A (**5**) is twisted out of plane, thereby establishing axial chirality. The stability of this axial chirality varies among different perylenequinones. In compounds like **5**, the additional seven-membered ring, attached to the pentacyclic core, lowers the barrier of atropisomerization for these compounds, such that it can be observed at room temperature.<sup>221</sup> For some perylenequinones, this process can be observed on the NMR timescale and involves interconversion between the compound and its atropisomer (Fig. 4.3A).<sup>221</sup> Unlike hypocrellin (**1**) and hypocrellin A (**2**), which each exist as an equilibrium mixture of two atropisomers in a ratio of 4:1 as recognized by their <sup>1</sup>H NMR spectra, the atropisomerization of **4** and its enantiomer (**5**) occurs at a slower rate and, hence, it takes longer before the atropisomers are observed by NMR spectroscopy. The <sup>13</sup>C NMR spectrum of **5** (Fig. 4.15), collected shortly after its purification, showed a total of 30 carbons, consistent with its molecular formula. However, the number of carbon signals doubled when **5** was stored for ~two months at room temperature (data not shown), suggesting that **5** existed in equilibrium with its atropisomer.

Another characteristic of perylenequinones is keto-enol tautomerism. All hypocrellins, including **5**, exist in an equilibrium with a 1:1 ratio of the tautomers (Fig. 4.3B). In this case, the tautomerism is too fast to be detected by <sup>1</sup>H or <sup>13</sup>C NMR spectroscopy using standard experiments.<sup>221</sup> However, the HMBC correlations of the HO-3 proton with C-2, C-3, C-3a, C-4, and C-5 (Fig. 4.18) suggested that this proton was in continuous tautomerism with the C-4 carbonyl. Similar HMBC correlations were observed for the HO-10 proton (Fig. 4.18).

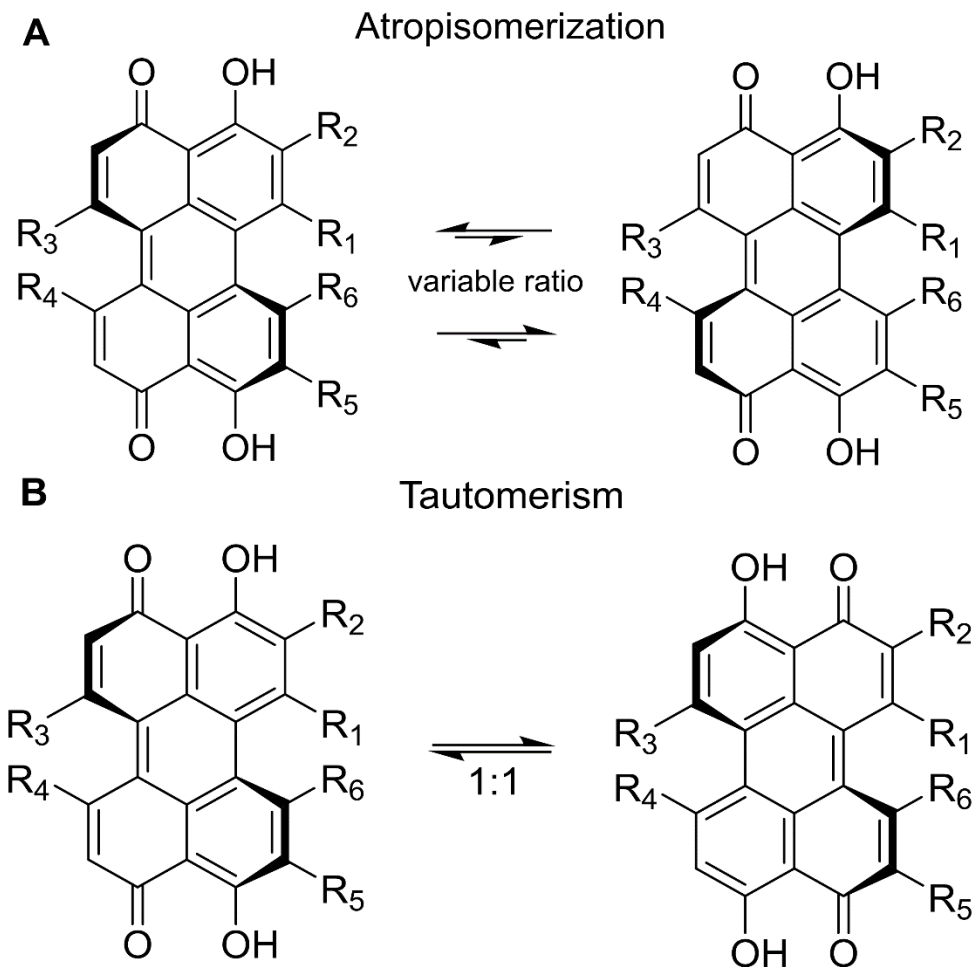


**Figure 4.3.** The atropisomerization process (A) and the tautomerism process (B) of hypocrellins.

The HRESIMS (Fig. 4.13) and NMR data (Table 4.4 and Fig. 4.20) for **1** matched those reported for hypocrellin (**1**) and hypocrellin A (**2**),<sup>185, 204</sup> both of which have a molecular formula of  $C_{30}H_{26}O_{10}$ . However, **1** was identified as hypocrellin and differentiated from its enantiomer (i.e. **2**) based on the ECD spectrum, which compared favorably to the literature (Fig. 4.14).<sup>204</sup>

Hypocrellin was first isolated from *Hypocrella bambusae* in 1981, and the absolute configuration was determined by X-ray crystallographic analysis to be  $M(R)$ ,  $14R$ ,  $15S$ .<sup>185</sup> Hypocrellin (**1**) and hypocrellin A (**2**) are known to exist as an equilibrium mixture of two atropisomers in a ratio of 4:1, favoring the more stable atropisomer with  $M(R)$  axial chirality for **1** and  $P(S)$  for **2**.<sup>221, 222</sup> The two hypocrellin (**1**) atropisomers can be recognized by examining the  $^1H$  NMR spectrum collected immediately after purification (Fig. 4.20). Moreover, each atropisomer is present in equilibrium with its tautomer in a 1:1 ratio.<sup>204, 221</sup>

The molecular formula of **3** was deduced as C<sub>30</sub>H<sub>24</sub>O<sub>9</sub> by HRESIMS data, and the structure was identified as hypocrellin B based on favorable comparisons with the reported <sup>1</sup>H and <sup>13</sup>C NMR data (Table 4.4 and Fig. 4.21).<sup>201</sup> Interestingly, analysis of **3** by ECD spectroscopy produced a baseline spectrum, which has been attributed by Kozłowski et al.<sup>204</sup> to the presence of a racemic mixture of the two atropisomeric enantiomers of **3**. Effectively, compound **3** has a lower barrier of atropisomerization, and as such, the ECD Cotton effects of the *M(R)* and *P(S)* atropisomers cancel each other. The ability to produce **3** via dehydration of either hypocrellin A (**2**) or shiraiachrome A (**4**) has been reported.<sup>186, 201</sup> By analogy, 6.5 mg of **3** were generated by a dehydration reaction of a mixture of **1** and **5**.

**Table 4.1.** NMR Spectroscopic Data for **5** and **8** in CDCl<sub>3</sub> (500 MHz for <sup>1</sup>H and 125 MHz for <sup>13</sup>C,  $\delta$  in ppm).

no.	<b>5</b>		<b>8</b>	
	$\delta_C$ , type	$\delta_H$ (J, Hz)	$\delta_C$ , type	$\delta_H$ (J, Hz)
1	135.2, C		52.8, C	
1a	127.9, C		141.4, C	
2	151.9, C		39.5, CH <sub>2</sub>	2.91, s
3	171.7, C		199.9, C	
3a	106.8, C		104.3, C	
3b	124.5 or 125.4, C		129.2, C	
4	180.1, C		165.0, C	
5	102.2, CH	6.56, s	100.4, CH	6.73, s
6	167.3 or 167.7, C		164.6, C	
6a	118.0, C		115.8, C	
7	167.3 or 167.7, C		165.6, C	
7a	117.6, C		112.4, C	
8	101.8, CH	6.57, s	99.4, CH	6.76, s
9	179.7, C		169.9, C	
9a	107.1, C		107.0, C	
9b	124.5 or 125.4, C		124.7, C	
10	171.8, C		181.4, C	
11	149.2, C		149.6, C	
12	131.3, C		138.6, C	
12a	128.3, C		122.5, C	
13	42.6, CH <sub>2</sub>	H <sub>a</sub> 2.34, dd (13.8, 2.0) H <sub>b</sub> 3.67, d (13.8)	52.9, CH <sub>2</sub>	H <sub>a</sub> 1.97, d (13.2) H <sub>b</sub> 2.61, d (13.2)

14	78.7, C		79.2, C	
15	64.3, CH	3.72, s	59.4, CH	3.86, s
16	24.9, CH <sub>3</sub>	1.78, s	32.3, CH <sub>3</sub>	1.77, s
17	206.8, C		84.1, C	
18	28.6, CH <sub>3</sub>	1.83, s	21.7, CH <sub>3</sub>	1.18, s
CH <sub>3</sub> O-2	62.0	4.18, s	--	
CH <sub>3</sub> O-6	56.6 or 56.7	4.07, s	56.4	4.05, s
CH <sub>3</sub> O-7	56.6 or 56.7	4.07, s	56.4	4.09, s
CH <sub>3</sub> O-11	61.1	4.27, s	61.2	4.05, s
HO-3		15.97, s		
HO-4				13.57, s
HO-9				15.23, s
HO-10		16.07, s		
HO-14		3.80, d (2.0)		

---

**The Effect of Growth Medium and Light on the Production of Hypomycons.** Upon examining the LC-HRESIMS data of the extracts obtained from cultures grown under LED light using oatmeal medium, there were signals for three compounds, other than **1** or **5**, that exhibited the characteristic UV spectrum of perylenequinones (Fig. 4.10). These were identified as hypomycin A (**6**), hypomycin C (**7**), and hypomycin E (**8**), as discussed below. Hypomycons have the same pentacyclic core of perylenequinone; however, the typical conjugated system is disrupted by the absence of the  $\Delta 1(2)$  double bond. In addition, the acetyl group observed in hypocrellins has been rearranged in hypomycons to form an additional six-membered ring. Based on the relative abundance of hypomycons across various growths of strain MSX60519 (Fig. 4.4), it was obvious that both oatmeal medium and light were beneficial for the biosynthesis of these compounds. The isolated amounts of **6-8** were the highest from cultures that were grown in oatmeal medium and exposed to continuous LED light (Fig. 4.22). This is the first report of the production of hypocrellins and hypomycons from the same fungus and represents an additional example of how compound production can be tuned based on varying fermentation conditions, including varying the light source.<sup>223-225</sup>

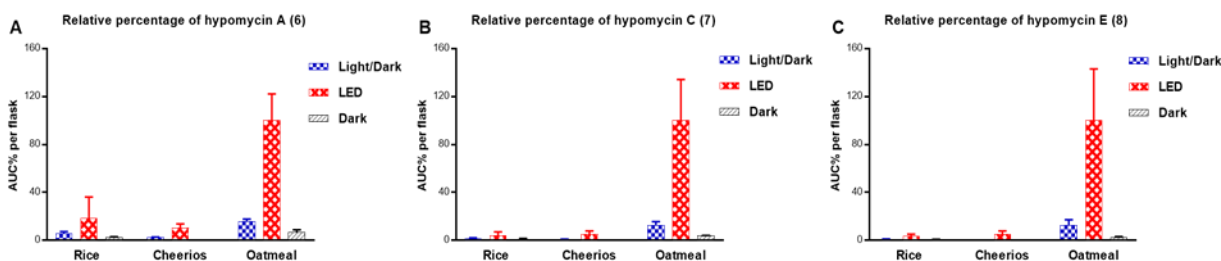
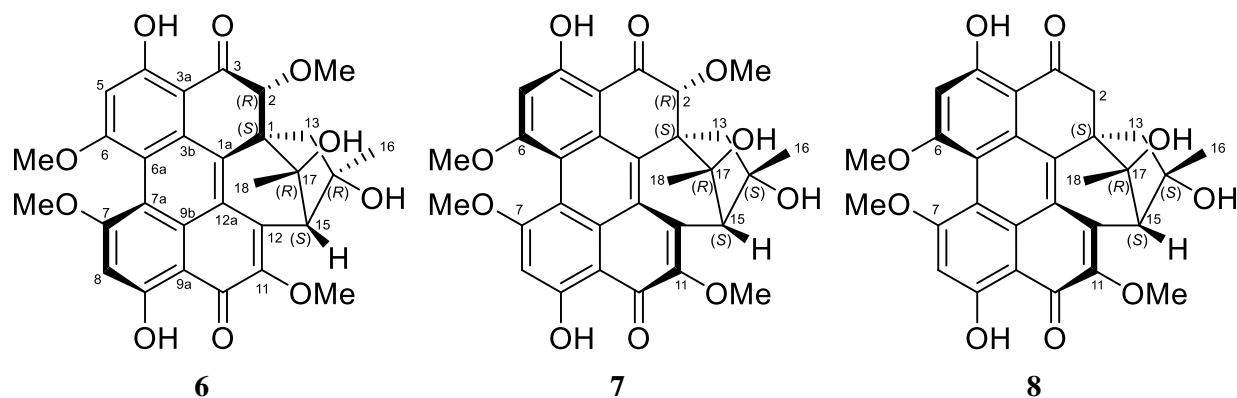


**Figure 4.4.** Panels A-C show the relative percentages of 6-8, respectively, across cultures grown on rice, Cheerios, and oatmeal media under 12:12 h light:dark cycles, continuous LED, or in darkness. The relative percentages were measured by LC-HRMS in three biological replicates and multiplied by the extract weight, and then normalized according to the extract with highest abundance.

**The Structure Elucidation of 6-8.** Hypomycins A (**6**) and C (**7**) had the same molecular formula, as defined by HRESIMS data (Fig. 4.13), and these were identified by  $^1\text{H}$  and  $^{13}\text{C}$  NMR data (Table 4.4 and Figs. 4.23-4.24), which were congruent with the literature.<sup>226, 227</sup> Both compounds were reported previously from the mycelia of *Hypomyces sp.* (Hypocreales, Ascomycota),<sup>226, 227</sup> but only their relative configurations were reported. Updated chemical shift assignments of C-4, C-6, and C-7, for both compounds, based on the HMBC correlations for HO-4, H-5, and H-8 are given in Table 4.4. Unlike hypocrellins, the axial chirality of hypomycins has not been reported, and little is known about their biological effects or light-induced activities. Compounds **6** and **7** exhibited opposite ECD spectra (Fig. 4.14). Moreover, the ECD spectrum of **6** was similar to that exhibited by **1**, while the spectrum of **7** was similar to that of **5**. Since axial chirality is the major factor that generates the Cotton effects observed for perylenequinones,<sup>228</sup> the axial chirality would be  $M(R)$  for **6** and  $P(S)$  for **7**; these assignments were confirmed via calculation of the ECD spectrum of **6**. The calculated ECD spectra for the two possible configurations of **6** with  $M(R)$  axial chirality [ $(M(R), 1S, 2R, 14R, 15S, 17R)$  and

(*M(R)*, 1*R*, 2*S*, 14*S*, 15*R*, 17*S*)] showed good agreement with the experimental ECD spectrum of **6** (Fig. 4.5). However, only the *M(R)*, 1*S*, 2*R*, 14*R*, 15*S*, 17*R*- configuration reproduced the positive Cotton effect at 500 nm (Figure 4.5). Accordingly, the experimental ECD spectra of hypomycin A (**6**) and hypomycin C (**7**) were mainly driven by their axial chirality.

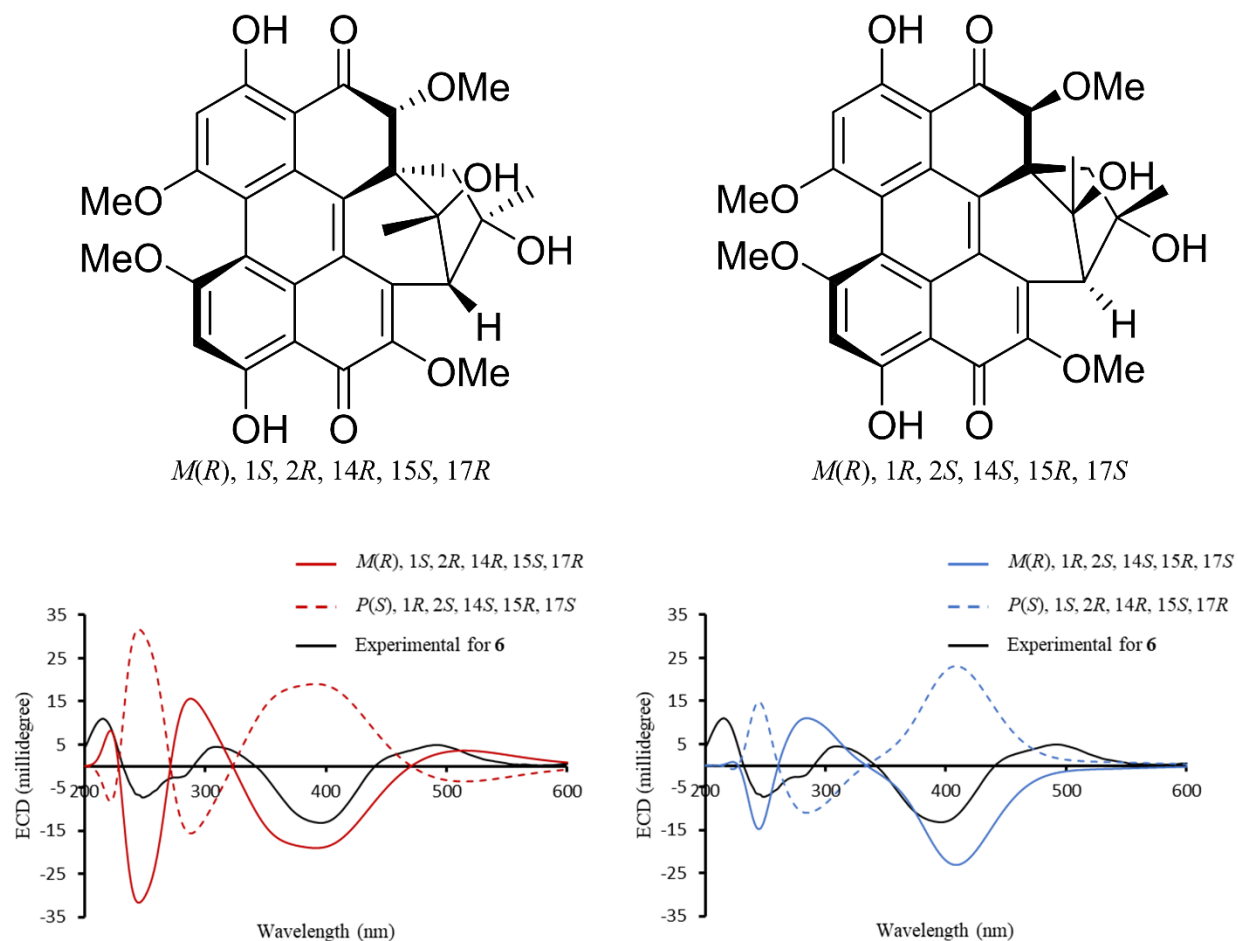


**Figure 4.5.** Experimental ECD spectrum of **6** compared with calculated ECD spectra of [*M(R)*, 1*S*, 2*R*, 14*R*, 15*S*, 17*R*]- configuration and its enantiomer (left frame), and [*M(R)*, 1*R*, 2*S*, 14*S*, 15*R*, 17*S*]- configuration and its enantiomer (right frame).

A series of NOESY correlations were used to differentiate between compounds **6** and **7** (Figs. 4.25-4.26). The NOESY spectrum of **6** showed strong correlations between CH<sub>3</sub>-16/2-OCH<sub>3</sub>, CH<sub>3</sub>-16/11-OCH<sub>3</sub>, and CH<sub>3</sub>-16/H<sub>a</sub>-13, suggesting the same orientation for CH<sub>3</sub>-16, 2-OCH<sub>3</sub>, and H<sub>a</sub>-13 (Fig. 4.27). In addition, CH<sub>3</sub>-18 and H-2 were cofacial, opposite to the correlations noted above, also based on NOESY correlations. The orientation of the six-membered ring was suggested by the NOESY correlations of H<sub>b</sub>-13 with both the HO-14 and HO-17 protons (Fig.

4.27). Alternatively, in hypomycin C (**7**), the NOESY correlations of CH<sub>3</sub>O-11/CH<sub>3</sub>-16, CH<sub>3</sub>-16/H<sub>b</sub>-13, CH<sub>3</sub>O-11/CH<sub>3</sub>-18, CH<sub>3</sub>-18/H-2 suggested the same orientation for CH<sub>3</sub>-16, CH-18, H<sub>b</sub>-13, and H-2 (Fig. 4.26). The correlation of H<sub>b</sub>-13 with CH<sub>3</sub>-16 and HO-17 supported the same orientation of the six-membered ring as in **6**. Therefore, compounds **6** and **7** differed in the configuration of the C-14 stereogenic center and their axial chirality. The absolute configuration of **6** was suggested by comparing the experimental VCD spectrum with the calculated VCD spectra for the two possible configurations of **6**, *M(R)*, 1*S*, 2*R*, 14*R*, 15*S*, 17*R*, or *M(R)*, 1*R*, 2*S*, 14*S*, 15*R*, 17*S*. The experimental VCD of **6** showed the best match with the calculated VCD spectrum of *M(R)*, 1*S*, 2*R*, 14*R*, 15*S*, 17*R* configuration (Fig. 4.6). Accordingly, the absolute configuration of **6** was *M(R)*, 1*S*, 2*R*, 14*R*, 15*S*, 17*R*, while the absolute configuration of **7** was *P(S)*, 1*S*, 2*R*, 14*S*, 15*S*, 17*R*.

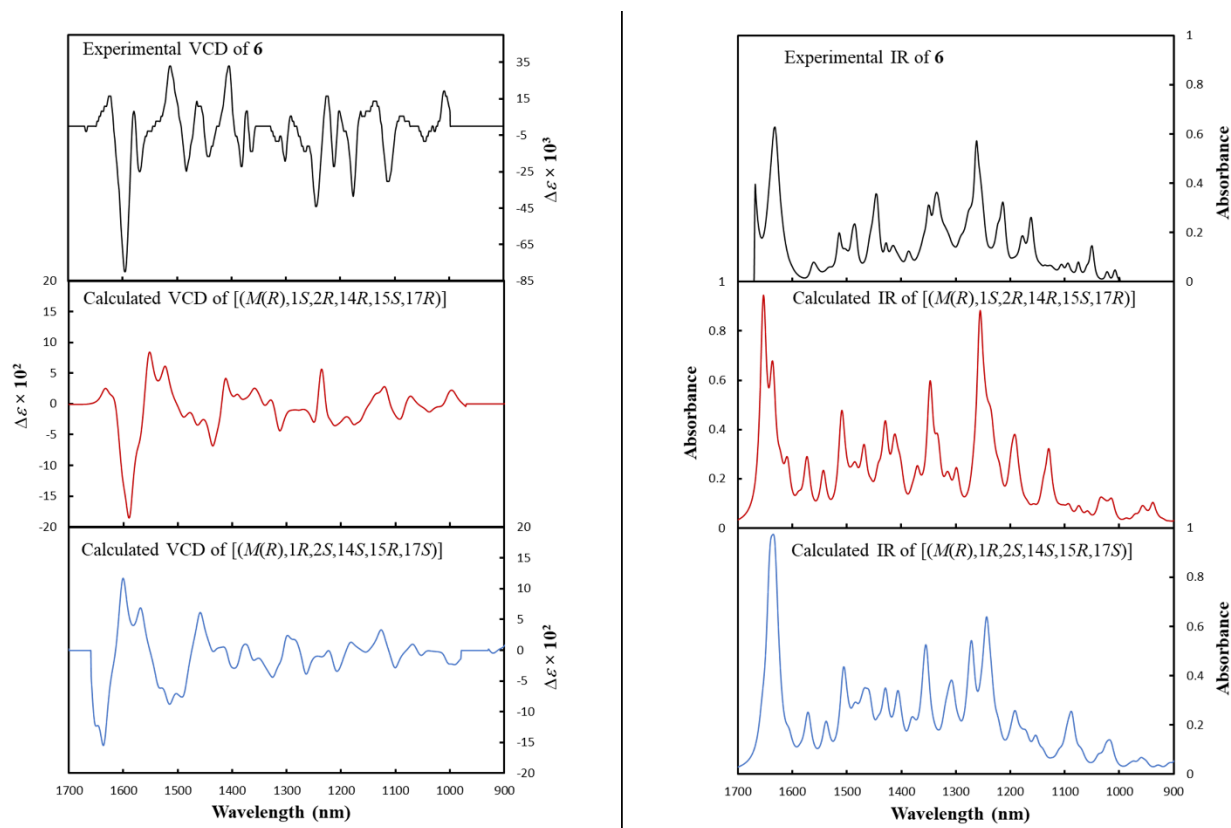


**Figure 4.6.** Experimental VCD (left frame) and IR (right frame) spectra observed for hypomycin A (**6**) compared with calculated VCD and IR spectra of [*M(R)*, 1*S*, 2*R*, 14*R*, 15*S*, 17*R*]-configuration (0.65 similarity factor to **6**) and [*M(R)*, 1*R*, 2*S*, 14*S*, 15*R*, 17*S*]-configuration (0.11 similarity factor to **6**). Specdis software was utilized to calculate the similarity factors.

The molecular formula of **8** was deduced as  $C_{29}H_{26}O_9$  by HRESIMS data (Fig. 4.13), suggesting a loss of a methoxy group relative to **6** and **7**. The 1D and 2D NMR spectra of **8** (Figs. 4.28-4.32) confirmed the presence of methoxy groups attached to C-6, C-7, and C-11, but the absence of the methoxy group at C-2. HMBC correlations of the C-2 methylene protons with C-1, C-1a, C-3, C-3a, and C-17 supported this assignment (Fig. 4.7A). Comparing the NOESY correlations of **8** with those observed for **6** and **7** suggested that **8** exhibited the same relative configuration as hypomycin C (**7**). For example, key NOESY interactions of CH<sub>3</sub>O-11/CH<sub>3</sub>-16, CH<sub>3</sub>O-11/CH<sub>3</sub>-18, and CH<sub>3</sub>-16/H<sub>b</sub>-13 indicated the same orientation for CH<sub>3</sub>-16 and CH<sub>3</sub>-18 (Fig. 4.7B). In addition, H-15 showed strong NOESY correlations with both CH<sub>3</sub>-16 and CH<sub>3</sub>-18. The ECD spectrum of **8** was highly similar to **7** (Fig. 4.14), confirming the *P(S)* axial chirality. Accordingly, the absolute configuration of **8** was defined as [*P(S)*, 1*S*, 14*S*, 15*S*, 17*S*], and this compound was ascribed the trivial name hypomycin E.

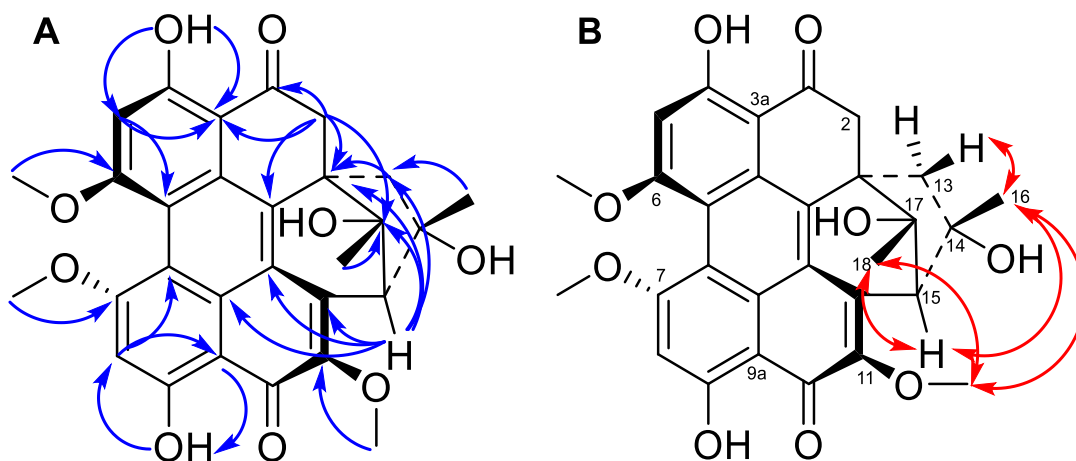


**Figure 4.7.** Key HMBC (A) and NOESY (B) correlations for hypomycin E (**8**).

### **Cytotoxicity and Photocytotoxicity Toward Human Melanoma Cancer Cells (SK-MEL-28).**

Perylenequinones are generally known for their promising light-induced cytotoxicity.<sup>229</sup> The photocytotoxic activity of hypocrellins A (**2**) and B (**3**) was reported previously.<sup>200, 230, 231</sup> However, the limited supply of hypomycins hindered more in depth investigations of their photoactivated cytotoxic properties. As such, the activities of hypocrellins **1**, **3**, and **5** and hypomycins **6-8** were evaluated against a human skin melanoma cancer cell line (SK-MEL-28) for photocytotoxicity. Briefly, melanoma cells were treated with the compound of interest at a

concentration range of 1 nM to 300  $\mu$ M and incubated at 37 °C (5% CO<sub>2</sub>) for 16 h before evaluation under dark, broadband visible-light (100 J/cm<sup>2</sup>), or monochromatic red-light (100 J/cm<sup>2</sup>, 625 nm) treatments, resulting in both EC<sub>50</sub> values and phototherapeutic indices (PIs) (Table 4.2). The phototherapeutic index represents the ratio of the dark to light EC<sub>50</sub> values and indicates the amplification of cytotoxicity with the light treatment. Hypocrellins **1**, **3**, and **5** exhibited potent photocytotoxic activities at the nanomolar level, with *ent*-shiraiachrome A (**5**) and hypocrellin B (**3**) being the most active. Moreover, comparable light-induced cytotoxicity of these compounds was observed with visible- and red-light treatments (Figs. 4.8 and 4.33). On the other hand, hypomyxins **6-8** were less potent photosensitizers with EC<sub>50</sub> values at the micromolar level. This might be attributed to the absence of the  $\Delta 1(2)$  double bond in **6-8**, resulting in reduced conjugation. In contrast to hypocrellins, hypomyxins exhibited reduced cytotoxicity with red-light treatment as compared to visible-light treatment (Fig. 4.8). In both classes of compounds, toxicity without the presence of light was much lower than light-induced cytotoxicity. This allowed for large phototherapeutic index (PI) values for hypocrellins that ranged between 2200-3800 for both visible- and red-light treatments. The low dark toxicity of hypomyxin C (**7**) resulted in a large PI with visible-light treatment (> 2200). In summary, hypocrellins, and potentially hypomyxins, represent promising naturally-derived photosensitizers that compare well with the photodynamic activity of the FDA approved photosensitizer for cancer treatment, photofrin.<sup>232</sup> The compounds in this family with PIs >10<sup>3</sup> are under further investigation to test the robustness of this response in other cell lines and models, including in vivo tumors.

**Table 4.2.** EC<sub>50</sub> Values of Compounds **1**, **3**, and **5-8** Against SK-MEL-28 Cancer Cells.

Compound	Dark ( $\mu$ M)	Vis <sup>a</sup> (nM)	PI <sub>vis</sub> <sup>b</sup>	Red <sup>c</sup> (nM)	PI <sub>red</sub> <sup>d</sup>
<b>1</b>	130.0 $\pm$ 12.0	53.5 $\pm$ 1.0	2430	59.2 $\pm$ 6.0	2196
<b>3</b>	43.7 $\pm$ 5.9	14.7 $\pm$ 8.0	2973	15.7 $\pm$ 6.0	2783
<b>5</b>	39.3 $\pm$ 6.2	10.3 $\pm$ 1.0	3816	15.3 $\pm$ 3.0	2569
<b>6</b>	132.0 $\pm$ 13.0	172.0 $\pm$ 43.0	767	603.0 $\pm$ 41.0	219

<b>7</b>	> 300	135.0 ± 56.0	> 2222	1280 ± 20.0	> 234
<b>8</b>	98.7 ± 1.7	176.0 ± 23.0	561	2550 ± 60.0	39

<sup>a</sup>Vis: 16 hours drug-to-light interval followed by 100 J/cm<sup>2</sup> broadband visible-light irradiation, <sup>b</sup>PI<sub>vis</sub> = phototherapeutic index (ratio of dark EC<sub>50</sub> to visible-light EC<sub>50</sub>), <sup>c</sup>Red: 16 hours drug-to-light interval followed by 100 J/cm<sup>2</sup> light irradiation with 625 nm LEDs, <sup>d</sup>PI<sub>red</sub> = phototherapeutic index (ratio of dark EC<sub>50</sub> to red-light EC<sub>50</sub>).

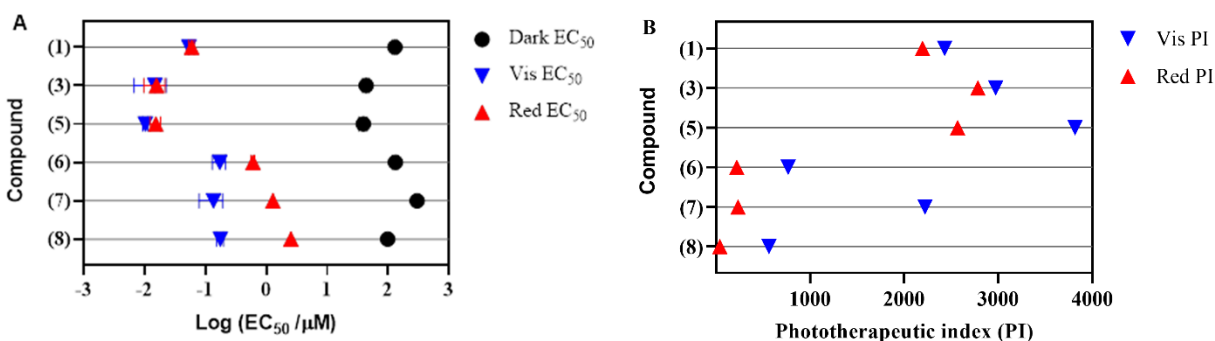


**Figure 4.8.** Panel A: photocytotoxic activity plot for compounds 1, 3, and 5-8 against SK-MEL-28 melanoma cells without (black) or with visible- (blue) or red- (red) light irradiation. Panel B: phototherapeutic index (PI) activity plot for compounds 1, 3, 5-8 against SK-MEL-28 melanoma cells treated with visible- (blue) or red- light (red).

## Conclusion

The present study was carried out to enhance the production of two different classes of perylenequinones, hypocrellins and hypomyces, via fermentation. Interestingly, the biosynthesis of these fungal metabolites could be tuned based on media and light exposure. *Ent-shiraiachrome A* (**5**) and hypomycesin E (**8**) were reported for the first time, and additional studies were carried out to refine the structure elucidation of **6** and **7**, including the combined use of both ECD and VCD data for the former. Both hypocrellins and hypomyces exhibited significant photodynamic activity. Hypocrellins, in particular, showed potent light-induced cytotoxicity at the nanomolar level. Equipotent photodynamic activities with both visible- and red-light treatment renders hypocrellins as suitable candidates for further in vivo photodynamic therapy (PDT) studies.

## Materials and Methods

**General Experimental Procedures.** Ultraviolet (UV) and electronic circular dichroism (ECD) data were measured using a Varian Cary 100 Bio UV–Vis spectrophotometer (Varian Inc.) and an Olis DSM 17 ECD spectrophotometer (Olis, Inc.), respectively. The IR and VCD measurements were performed on a BioTools ChiralIR FT-VCD spectrometer equipped with dual photoelastic modulation (PEM). A sample of 3.0 mg of **6** was dissolved in 150  $\mu\text{L}$   $\text{CDCl}_3$  and placed in a BaF<sub>2</sub> IR cell with a path length of 100  $\mu\text{m}$ , and data were acquired at 4  $\text{cm}^{-1}$  resolution with total measurement time of 12 h and 1400  $\text{cm}^{-1}$  PEM setting. 1D and 2D NMR data were obtained using a JEOL ECA-500 spectrometer operating at 500 MHz or a JEOL ECS-400 spectrometer operating at 400 MHz that is equipped with a high sensitivity JEOL Royal probe and a 24-slot autosampler (both from JEOL Ltd.). Residual solvent signals were utilized for referencing. UPLC-HRMS data were collected via Thermo Fisher Scientific Q Exactive Plus mass spectrometer equipped with an electrospray ionization source (ESI) and connected to a Waters Acquity UPLC system. A BEH Shield RP18 column (Waters, 1.7  $\mu\text{m}$ ; 50  $\times$  2.1 mm) was used and heated to 40°C. The flow rate of the mobile phase was 0.3 mL/min and consisted of a gradient system of 15:85 to 100:0 of  $\text{CH}_3\text{CN}$ - $\text{H}_2\text{O}$  (1% formic acid) over 10 min. MS data were collected from  $m/z$  150 to 2000 while alternating between positive and negative modes. The same UPLC system (Waters Corp.) utilizing the same column was used to measure the purity of compounds **1**, **3**, and **5-8** with data collected and analyzed using Empower 3 software (Fig. 4.37). A Varian Prostar HPLC system, equipped with ProStar 210 pumps and a Prostar 335 photodiode array detector (PDA), was used to conduct all analytical and preparative HPLC experiments, with data collected and analyzed using Galaxie Chromatography Workstation software (version 1.9.3.2, Varian Inc.). Flash chromatography was performed on a Teledyne ISCO CombiFlash Rf 200 using Silica Gold columns (from Teledyne Isco) and monitored by UV and evaporative light–scattering detectors.

**Identification of Fungal Strain.** Fungal strain MSX60519 was isolated from dry leaf litter by A. Abraham on 2/15/1992. Based on growth on potato dextrose agar and malt extract agar, Difco, the fungal strain did not show any characteristics that were useful for morphological identification. The culture only grew as sterile mycelium. Therefore, to identify this strain, genomic DNA extraction, PCR, and sequencing were performed for the nuclear ribosomal

internal transcribed spacers and 5.8s gene (ITS rDNA region) using methods outlined previously.<sup>170</sup> The PCR experiment was performed using primer combination ITS1F and ITS4.<sup>171, 233</sup> The PCR reaction was cleaned up using a Wizard SV Gel and PCR Clean-up System (Promega) followed by Sanger sequencing using the same primer combination ITS1F and ITS4 at Eurofins Scientific, USA. The contig was assembled in Sequencher 5.2.3 (Gene Codes), optimized by eye and BLAST searched in NCBI GenBank to estimate the placement of strain MSX60519. Since hypocrellins-producing strains are produced by fungal genera such as *Hypocrella bambusae* (Sordariomycetes, Ascomycota), *Shiraia bambusicola*, and *Rubroshiraia bambusae* (Dothideomycetes, Ascomycota), we hypothesized that MSX60519 would likely show homology and phylogenetic affinities towards one of these classes of fungi. A BLAST search in NCBI showed that strain MSX60519 shared homology with members of the Pleosporales, Dothideomycetes, Ascomycota with one strain, Pleosporales sp. MX286 (JQ905814), which was isolated as an endophyte from *Hevea brasiliensis* (rubber tree) in Peru showing 99% sequence similarity, while all other strains in the Pleosporales showed  $\geq 90$ -95% sequence similarity. Since the results of the BLAST search were equivocal, further placement of MSX60519 was evaluated by Maximum Likelihood (RAxML) phylogenetic analysis of the ITS region using methods outlined previously.<sup>170</sup> The choice of taxon sampling was based on phylogenetic studies of Pleosporalean taxa, which were known to produce hypocrellins.<sup>187, 188</sup> Interestingly, based on the RAxML analysis using the ITS region, strain MSX60519 was placed basal to *Shiraia bambusicola*, and *Rubroshiraia bambusae* as well as endophytic *Shiraia*-like fungal clade (group A) as defined by Morakatkarn et al.<sup>187</sup> Strain MSX60519 was placed in the family Shiraiaceae (Pleosporales, Dothideomycetes, Ascomycota) with 89% RAxML bootstrap support (Fig. 4.34). Strain MSX60519 showed 100% RAxML bootstrap support with rubber tree endophyte from Peru strain MX286 (JQ905814)<sup>234</sup> (Fig. 4.34). The RAxML analysis indicated that all hypocrellins-producing strains in the Shiraiaceae, Pleosporales are monophyletic (Fig. 4.34). Furthermore, all strains in endophytic *Shiraia*-like fungal clade group A produced pinkish to reddish pigment in potato dextrose media,<sup>187</sup> which was similar to the morphology of strain MSX60519 on both potato dextrose and malt extract agar, including solid-state rice fermentation (Figs. 4.34 and 4.35), which was used to isolate hypocrellins and hypomyces in the present study. Therefore, based on RAxML analysis, strain MSX60519 was identified as a *Shiraia*-like fungus in the family Shiraiaceae, Pleosporales, Dothideomycetes, Ascomycota. The ITS

sequences have been deposited in GenBank under the accession number: MN970609 and MN970610. A live culture of this strain is accessioned at Mycosynthetix, Inc. (Hillsborough, NC, USA).

**Media and Fermentations.** The culture of fungal strain MSX60519 was maintained on potato dextrose agar (PDA; Difco) and was transferred periodically to fresh PDA Petri plates. An agar plug from the leading edge of the PDA culture was transferred to a sterile tube with 10 mL of YESD (2% soy peptone, 2% dextrose, and 1% yeast extract). The YESD culture was grown for 7 days on an orbital shaker (100 rpm) at room temperature (~23°C) and then used to inoculate three types of solid fermentation media.

Nine cultures of strain MSX60519 were grown over three different grain-based media in triplicate: rice, Cheerios breakfast cereal,<sup>184</sup> and breakfast oatmeal (old fashioned Quaker oats) for a total of 27 cultures. Solid-state fermentations were carried out in 250 mL Erlenmeyer flasks. To prepare rice medium, 10 g of rice were added to each flask with 20 mL of deionized water (DI H<sub>2</sub>O). For the oatmeal medium, the same amount was used in each flask with 17 mL of DI H<sub>2</sub>O. For Cheerios medium, 7 g of Cheerios were used in each flask without water. After autoclaving these samples at 120°C for 20 min, the flasks were inoculated with YESD seed cultures (described above) and incubated at room temperature for 15 days under three different conditions.

Out of the nine cultures that were grown on rice medium, three were incubated under usual room light with 12:12 h light:dark cycles to simulate daily light:dark cycles. Three were placed inside a light box (33 cm × 24 cm × 15 cm) that was equipped with light-emitting diode (LED) lamps (Ustellar, flexible LED strip lights; 24 watt) to incubate these cultures under continuous light exposure for 15 days. Finally, three cultures were incubated in complete darkness by covering the flasks with aluminum foil and placing them inside a dark area for 15 days. The same growth parameters were employed for the nine cultures that were grown on Cheerios and oatmeal medium, respectively (Fig. 4.36). Over the incubation period, the fungal cultures grew normally with no sign of growth retardation, except for the cultures growing on oatmeal medium under 12:12 h light:dark cycles, which were dried out by the time of extraction (Fig. 4.35).

**Extraction, Fractionation, and Isolation.** Each flask of solid culture was extracted with 90 mL of 1:2 CH<sub>3</sub>OH-CHCl<sub>3</sub>. Each culture was chopped and shaken for 20 h at ~125 rpm. The extract was vacuum filtered, and the remaining residues were washed with 30 mL of CHCl<sub>3</sub>. To the filtrate, 90 mL of CHCl<sub>3</sub> and 100 mL of DI H<sub>2</sub>O were added, and the mixture was stirred for 30 min and then transferred into a separatory funnel. The bottom layer was drawn off and evaporated to dryness. The dried organic extract was re-constituted in 100 mL of 1:1 CH<sub>3</sub>OH-CH<sub>3</sub>CN and 100 mL of hexanes. The biphasic solution was shaken vigorously and transferred into a separatory funnel. The CH<sub>3</sub>OH/CH<sub>3</sub>CN layer was drawn off and evaporated to dryness under vacuum. The extract amounts that were produced by each culture were not significantly different across cultures grown under the different conditions (Fig. 4.9).

Before performing further purifications, quantitative UPLC-HRMS data were collected. The organic extracts collected from the triplicate cultures, which were grown under the same growth conditions, were combined and dissolved in CHCl<sub>3</sub>, adsorbed onto Celite 545, and subdivided into four fractions via normal-phase flash chromatography using a gradient solvent system of hexanes-CHCl<sub>3</sub>-CH<sub>3</sub>OH at a 30 mL/min flow rate and 75 column volumes over 42 min. The second flash chromatography fraction of each extract was subjected to preparative HPLC over a Phenomenex Synergi C<sub>12</sub> preparative column using an isocratic system of 60:40 of CH<sub>3</sub>CN-H<sub>2</sub>O (0.1% formic acid) over 45 min at a flow rate of 21.24 mL/min to yield *ent*-shiraiachrome A (**5**), hypocrellin (**1**), and hypomyacin A (**6**). The third flash chromatography fraction of each extract was subjected to preparative HPLC using a Phenomenex Synergi preparative column on an isocratic system of 50:50 of CH<sub>3</sub>CN-H<sub>2</sub>O (0.1% formic acid) over 30 min to give hypomyacin C (**7**) and hypomyacin E (**8**). The isolated amounts of **1**, **5** and **6-8**, based on the suite of media and light conditions, are provided in Figs. 4.2 and 4.22. The purity of **1**, **3**, and **5-8** were evaluated using an Acquity UPLC system, which showed > 97% purity (Fig. 4.37).

*Hypocrellin (1)*: Dark red amorphous powder; UV (CH<sub>3</sub>OH)  $\lambda_{\max}$  (log  $\epsilon$ ) 581 (3.96), 540 (3.94), 464 (4.25), 341 (3.62), 285 (4.31), 265 (4.38), 213 (4.56) nm; ECD (c 3.7 × 10<sup>-4</sup> M, CH<sub>3</sub>OH)  $\lambda_{\max}$  ( $\Delta\epsilon$ ) 232 (5.22), 268 (-4.48), 294 (-4.02), 346 (2.66), 446 (-2.72), 532 (2.52), 576 (2.33) nm; <sup>1</sup>H NMR (CDCl<sub>3</sub>, 400 MHz) and <sup>13</sup>C NMR (CDCl<sub>3</sub>, 100 MHz) (see Table 4.4); HRESIMS *m/z* 547.1596 [M + H]<sup>+</sup> (calcd. for C<sub>30</sub>H<sub>27</sub>O<sub>10</sub>, 547.1604).

*Hypocrellin B (3)*: Dark red amorphous powder; UV (CH<sub>3</sub>OH)  $\lambda_{\max}$  (log  $\epsilon$ ) 590 (3.92), 548 (4.12), 460 (4.40), 335 (3.92), 223 (4.71) nm; <sup>1</sup>H NMR (CDCl<sub>3</sub>, 500 MHz) and <sup>13</sup>C NMR (CDCl<sub>3</sub>, 125 MHz) (see Table 4.4); HRESIMS  $m/z$  529.1491 [M + H]<sup>+</sup> (calcd. for C<sub>30</sub>H<sub>25</sub>O<sub>9</sub>, 529.1498).

*Ent-shiraiachrome A (5)*: Dark red amorphous powder; UV (CH<sub>3</sub>OH)  $\lambda_{\max}$  (log  $\epsilon$ ) 581 (4.07), 540 (4.05), 467 (4.34), 343 (3.72), 286 (4.38), 265 (4.48), 214 (4.65) nm; ECD (c 3.7 × 10<sup>-4</sup> M, CH<sub>3</sub>OH)  $\lambda_{\max}$  ( $\Delta\epsilon$ ) 202 (-11.43), 270 (8.79), 352 (-7.00), 460 (9.47), 582 (-4.54) nm; <sup>1</sup>H NMR (CDCl<sub>3</sub>, 500 MHz) and <sup>13</sup>C NMR (CDCl<sub>3</sub>, 125 MHz) (see Table 4.1); HRESIMS  $m/z$  547.1590 [M + H]<sup>+</sup> (calcd. for C<sub>30</sub>H<sub>27</sub>O<sub>10</sub>, 547.1604).

*Hypomycin A (6)*: Orange amorphous powder; UV (CH<sub>3</sub>OH)  $\lambda_{\max}$  (log  $\epsilon$ ) 527 (3.68), 494 (3.03), 465 (3.99), 414 (4.39), 394 (4.03), 276 (4.55), 242 (4.53), 215 (4.58) nm; ECD (c 3.7 × 10<sup>-4</sup> M, CH<sub>3</sub>OH)  $\lambda_{\max}$  ( $\Delta\epsilon$ ) 216 (10.95), 248 (-7.33), 308 (4.45), 396 (-13.22), 490 (4.88) nm; <sup>1</sup>H NMR (CDCl<sub>3</sub>, 400 MHz) and <sup>13</sup>C NMR (CDCl<sub>3</sub>, 100 MHz) (see Table 4.4); HRESIMS  $m/z$  549.1746 [M + H]<sup>+</sup> (calcd. for C<sub>30</sub>H<sub>29</sub>O<sub>10</sub>, 549.1760).

*Hypomycin C (7)*: Orange amorphous powder; UV (CH<sub>3</sub>OH)  $\lambda_{\max}$  (log  $\epsilon$ ) 522 (3.46), 489 (3.82), 462 (3.80), 413 (4.24), 393 (4.16), 274 (3.40), 241 (4.36), 214 (4.44) nm; ECD (c 3.7 × 10<sup>-4</sup> M, CH<sub>3</sub>OH)  $\lambda_{\max}$  ( $\Delta\epsilon$ ) 218 (-11.66), 256 (12.37), 310 (-7.46), 394 (20.39), 492 (-5.28) nm; <sup>1</sup>H NMR (CDCl<sub>3</sub>, 400 MHz) and <sup>13</sup>C NMR (CDCl<sub>3</sub>, 100 MHz) (see Table 4.4); HRESIMS  $m/z$  549.1749 [M + H]<sup>+</sup> (calcd. for C<sub>30</sub>H<sub>29</sub>O<sub>10</sub>, 549.1760).

*Hypomycin E (8)*: Orange amorphous powder; UV (CH<sub>3</sub>OH)  $\lambda_{\max}$  (log  $\epsilon$ ) 489 (3.86), 461 (3.85), 412 (4.29), 394 (4.15), 336 (3.80), 273 (4.44), 243 (4.42), 215 (4.45) nm; ECD (c 3.9 × 10<sup>-4</sup> M, CH<sub>3</sub>OH)  $\lambda_{\max}$  ( $\Delta\epsilon$ ) 216 (-18.56), 252 (20.00), 310 (-6.63), 388 (23.60), 486 (-7.25) nm; <sup>1</sup>H NMR (CDCl<sub>3</sub>, 400 MHz) and <sup>13</sup>C NMR (CDCl<sub>3</sub>, 125 MHz) (see Table 4.1); HRESIMS  $m/z$  519.1646 [M + H]<sup>+</sup> (calcd. for C<sub>29</sub>H<sub>27</sub>O<sub>9</sub>, 519.1655).

**Semi-synthesis of Hypocrellin B.** Hypocrellin B (**3**) was produced from a mixture of **5** and **1** (~11 mg) by a dehydration reaction, as previously described.<sup>186</sup> In brief, the mixture was treated with 7 mL of a 3% KOH solution and left at room temperature for 5 h. The reaction mixture was neutralized with 7 mL of a 10% HCl solution and extracted with 20 mL CHCl<sub>3</sub>. The organic

fraction was evaporated to dryness under vacuum and then subjected to preparative HPLC over a Phenomenex PFP preparative column using an isocratic system of 60:40 of CH<sub>3</sub>CN-H<sub>2</sub>O (0.1% formic acid) over 45 min at a flow rate of 21.24 mL/min to yield 6.5 mg of hypocrellin B (**3**).

**Computational Methods.** Molecular Merck force field (MMFF) and density functional theory (TD-DFT/DFT) calculations were carried out with Spartan'10 (Wavefunction Inc., Irvine, CA, USA) and GaussView 06 software, respectively. The conformers were optimized using DFT calculations at the B3LYP/cc-pVTZ level in CH<sub>3</sub>OH for ECD prediction of **6**, and in CDCl<sub>3</sub> for VCD prediction of **6**. The ECD and VCD spectra were generated using SpecDis 1.71 software.<sup>235</sup>

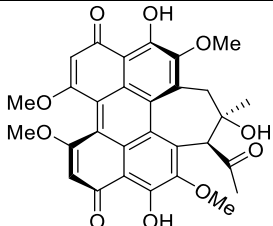
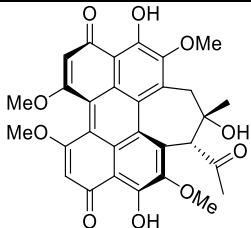
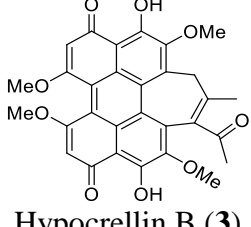
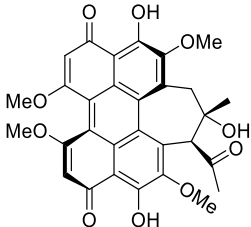
**Cytotoxicity and Photocytotoxicity Assay.** The in vitro cytotoxic and photocytotoxic activities of compounds **1**, **3**, and **5-8** were evaluated against SK-MEL-28 melanoma cells as previously described.<sup>236, 237</sup> In brief, SK-MEL-28 cells (~550,000-600,000 cells/mL) were transferred in 50  $\mu$ L aliquots to the inner wells of a 96-well TC-treated microtiter plates, and then incubated at 37 °C under 5% CO<sub>2</sub> for 3 h. Solutions of compounds **1**, **3**, and **5-8** were serially diluted with DPBS and aliquots of 25  $\mu$ L of the appropriate dilutions were added to cells, and the plates were incubated at 37 °C under 5% CO<sub>2</sub> for 16 h. Dark (control) microplates were kept in the incubator, and light-treated microplates were irradiated for approximately 48 and 60 min under one of the following conditions: visible-light (400–700 nm, 34.7 mW/cm<sup>2</sup>) using a 190 W BenQ MS 510 overhead projector or red-light (625 nm, 27.8 mW/cm<sup>2</sup>) from an LED array. Following the dark or light treatment, the microplates were incubated for 48 h followed by the addition of 10  $\mu$ L of prewarmed alamarBlue reagent (Life Technologies DAL 1025) to all sample wells. The plates were subsequently incubated for another 15-16 h. Cell viability was determined by fluorescence using a Cytofluor 4000 fluorescence microplate reader (excitation = 530  $\pm$  25 nm and emission = 620  $\pm$  40 nm). Cisplatin was used as a positive control for cytotoxicity, yielding an EC<sub>50</sub> value of 3.4  $\mu$ M in the dark, with no significant changes upon illumination with visible or red light. [Ru(bpy)<sub>2</sub>(dppn)Cl<sub>2</sub>] was used as a negative control for cytotoxicity (dark EC<sub>50</sub> >100  $\mu$ M) and a positive control for photocytotoxicity (vis EC<sub>50</sub>=290 nM, red EC<sub>50</sub>=760 nM).

## **Funding**

This research was supported in part by the National Institutes of Health via the National Cancer Institute (P01 CA125066) and by the National Science and Engineering Research Council of Canada (NSERC).

## Supplementary Data

**Table 4.3.** Summary of the various nomenclature that has been used for these key members of the hypocrellin family of perylenequinones.

Compound name	References	Alternative name	References
 <p>Hypocrellin (1)</p>	185, 204, 221	Hypocrellin A	192, 231
 <p>Hypocrellin A (2)</p>	201, 204, 221	Shiraiachrome B	186
 <p>Hypocrellin B (3)</p>	201, 204	Shiraiachrome C	186
 <p>Shiraiachrome A (4)</p>	186, 204, 221	Hypocrellin B	201

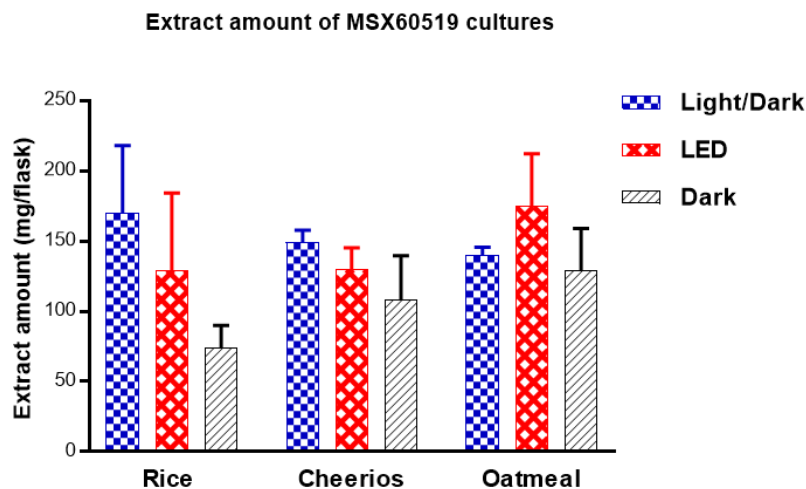


**Figure 4.9.** The extract amounts produced by cultures grown on rice, Cheerios, and oatmeal media under 12:12 h light:dark cycles, continuous LED light, or in complete darkness. The error bars are based on three biological replicates, each analyzed in triplicate.

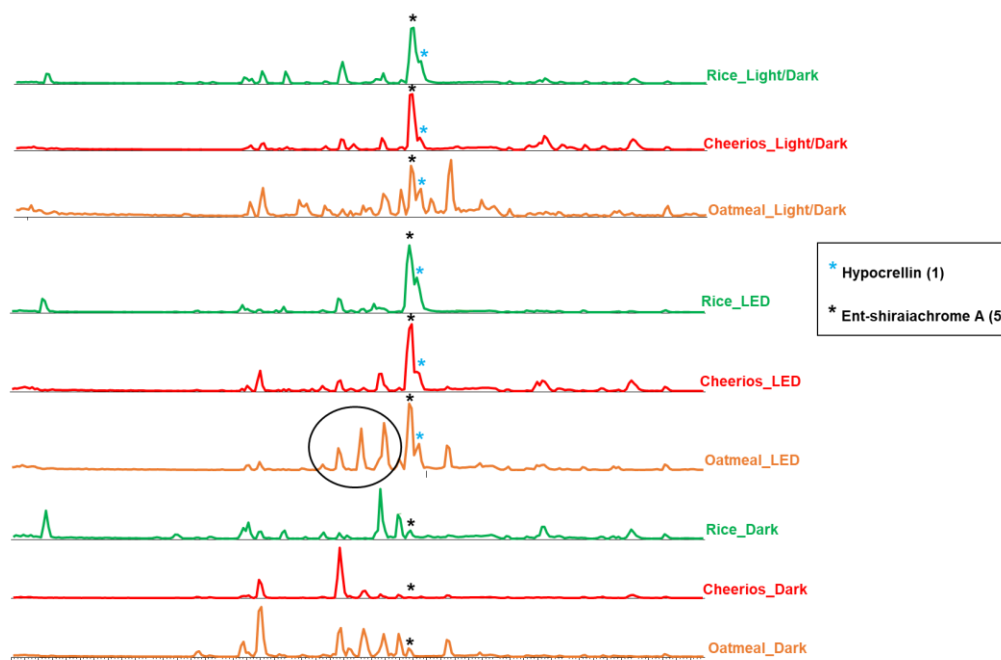


**Figure 4.10.** UPLC-HRESIMS chromatograms of the extracts of the cultures from Fig. 4.9, all prepared at a concentration of 0.3 mg/mL. Each chromatogram represents an average of three biological replicates. The peaks circled under LED light when grown on oatmeal led to the isolation of a series of hypomycins (6-8).

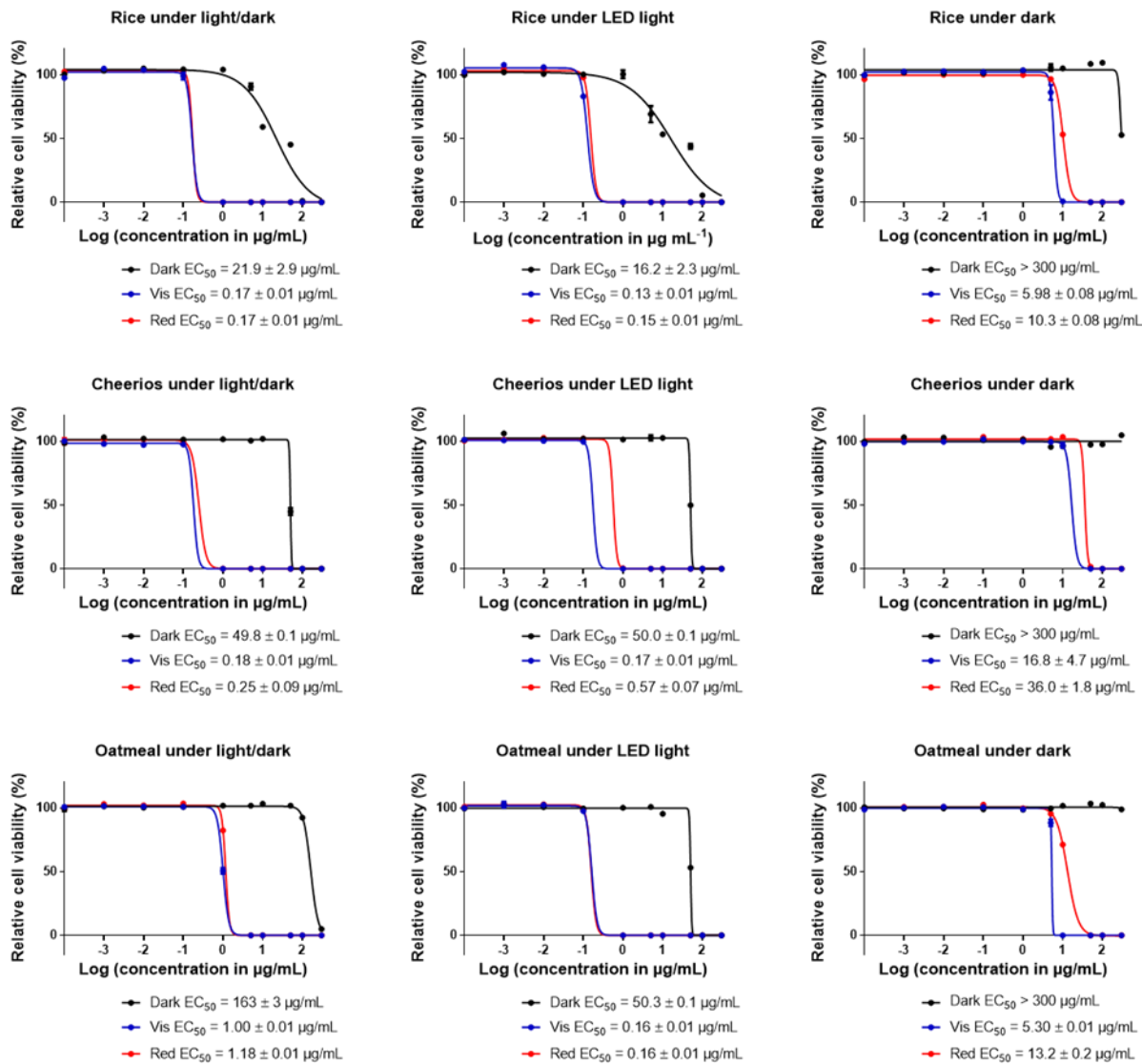
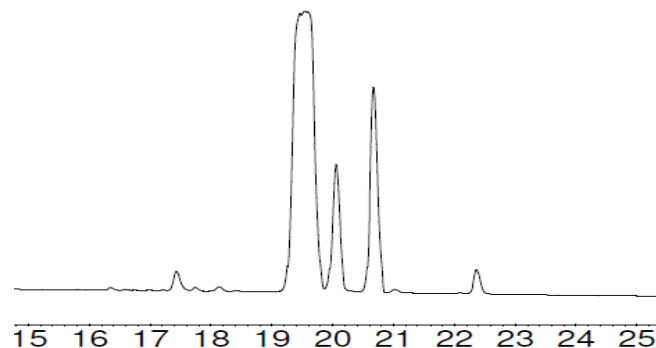


**Figure 4.11.** *In vitro* concentration–response curves for extracts obtained from MSX60519 cultures grown under different conditions.  $EC_{50}$  values are reported against SK-MEL-28 cells without light (black), with visible light (blue), or with red (red) light irradiation.

**2<sup>nd</sup> fraction from extract obtained from cultures grown on rice under light/dark conditions**



**2<sup>nd</sup> fraction from extract obtained from cultures grown on rice under continuous LED light**

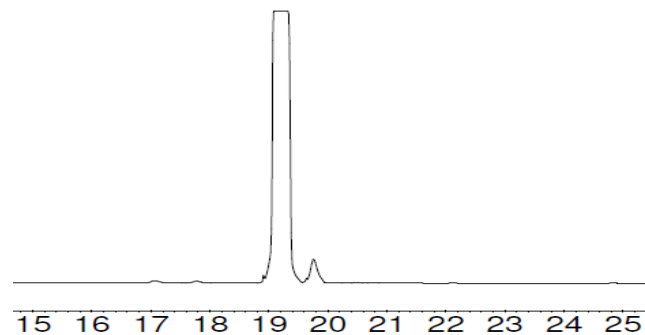


**Figure 4.12.** Analytical HPLC chromatogram for the second flash chromatography fractions obtained from MSX60519 cultures grown on rice medium and exposed to either light:dark cycles or continuous LED light. Compounds eluting at 19 and 20 min are ent-shiraiachrome A (**5**) and hypocrellin (**1**), respectively. The chromatograms were generated using a Varian Prostar HPLC system equipped with a Phenomenex Synergi C12 analytical column using an isocratic system of 60:40 of CH<sub>3</sub>CN-H<sub>2</sub>O (0.1% formic acid) over 30 min at a flow rate of 1 mL/min.

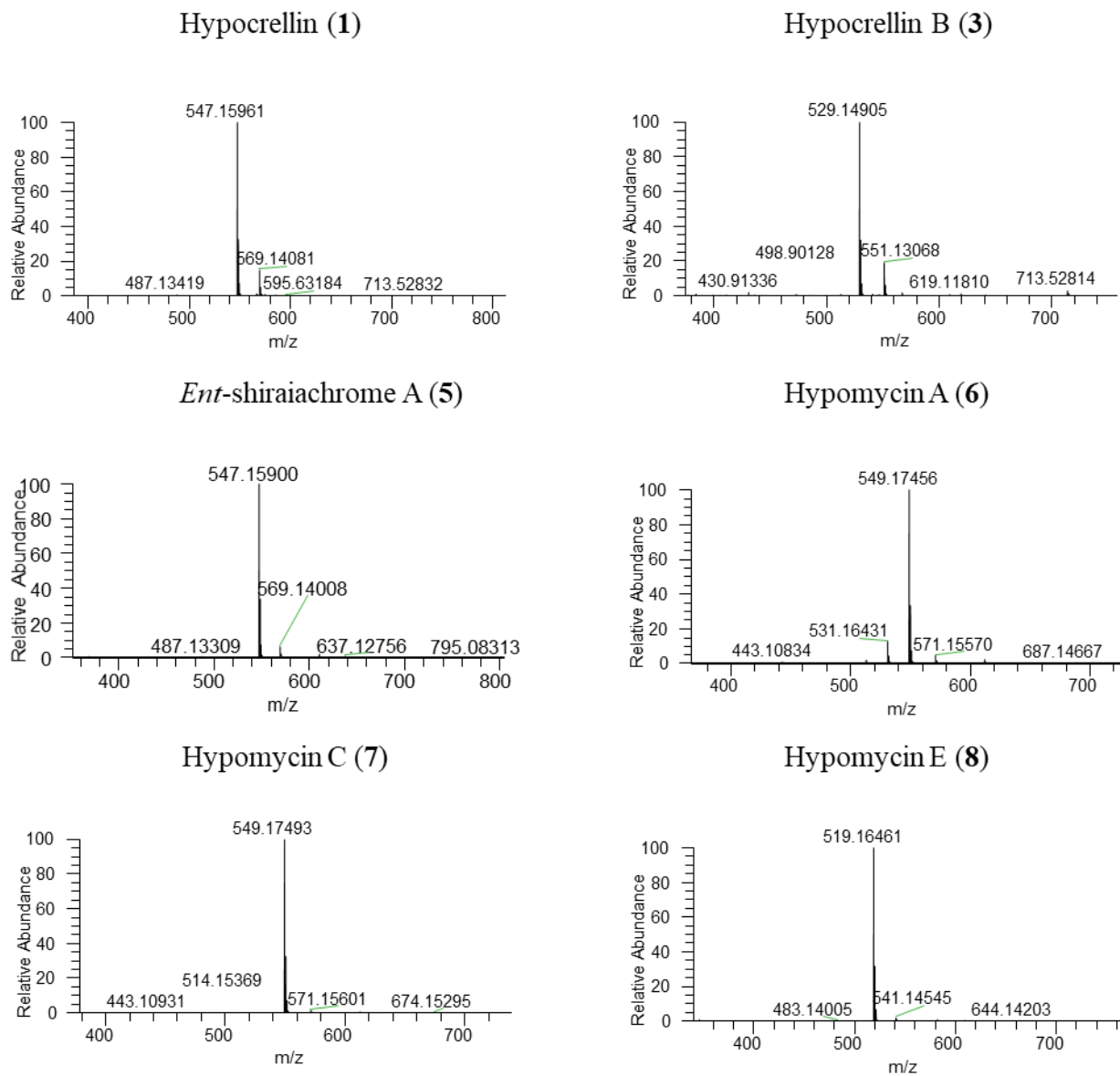


**Figure 4.13.** (+)-HRESIMS spectra of compounds **1**, **3**, and **5-8**.

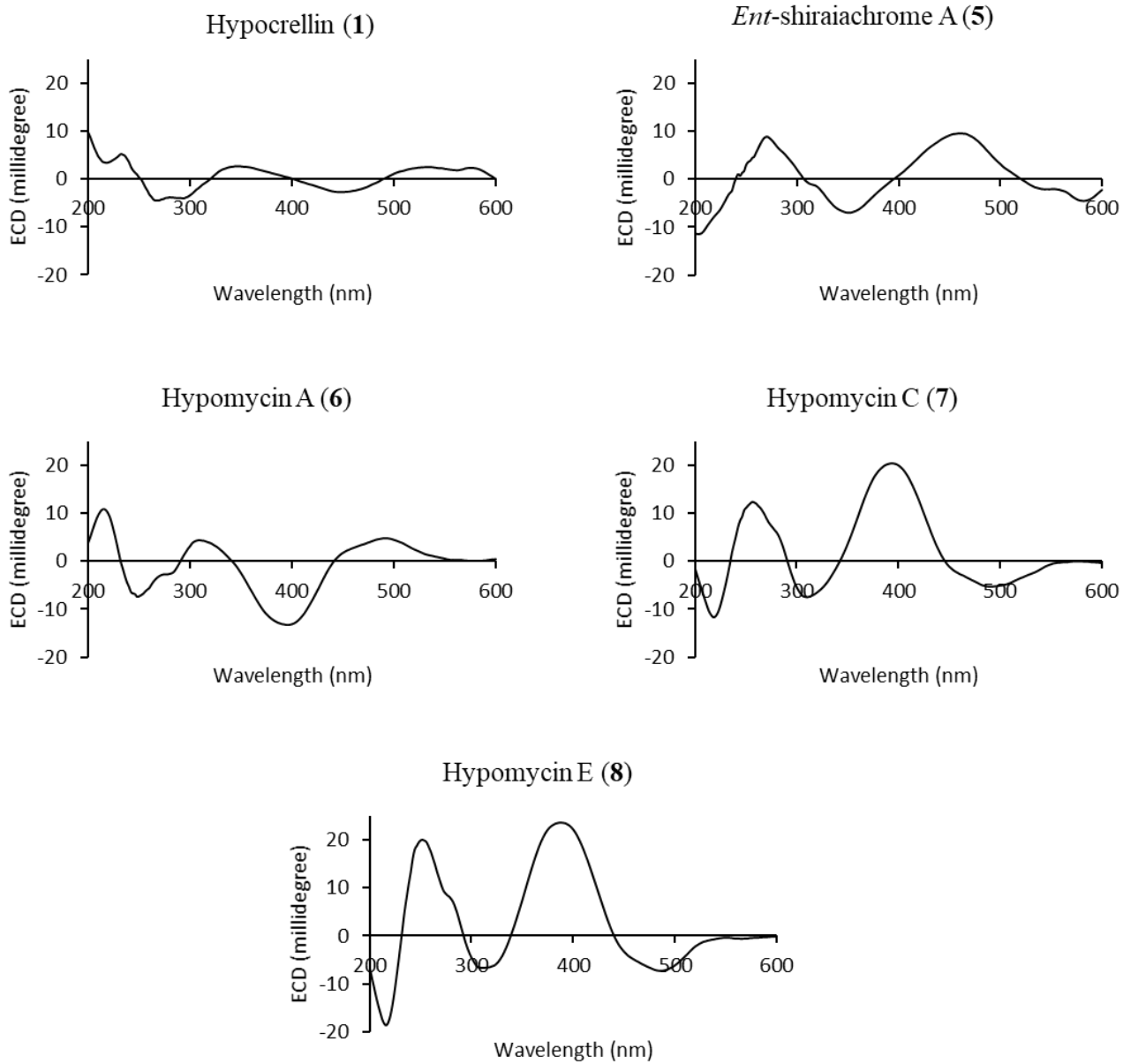


**Figure 4.14.** ECD spectra for compounds **1** and **5-8** in CH<sub>3</sub>OH at a concentration of 0.2 mg/mL.

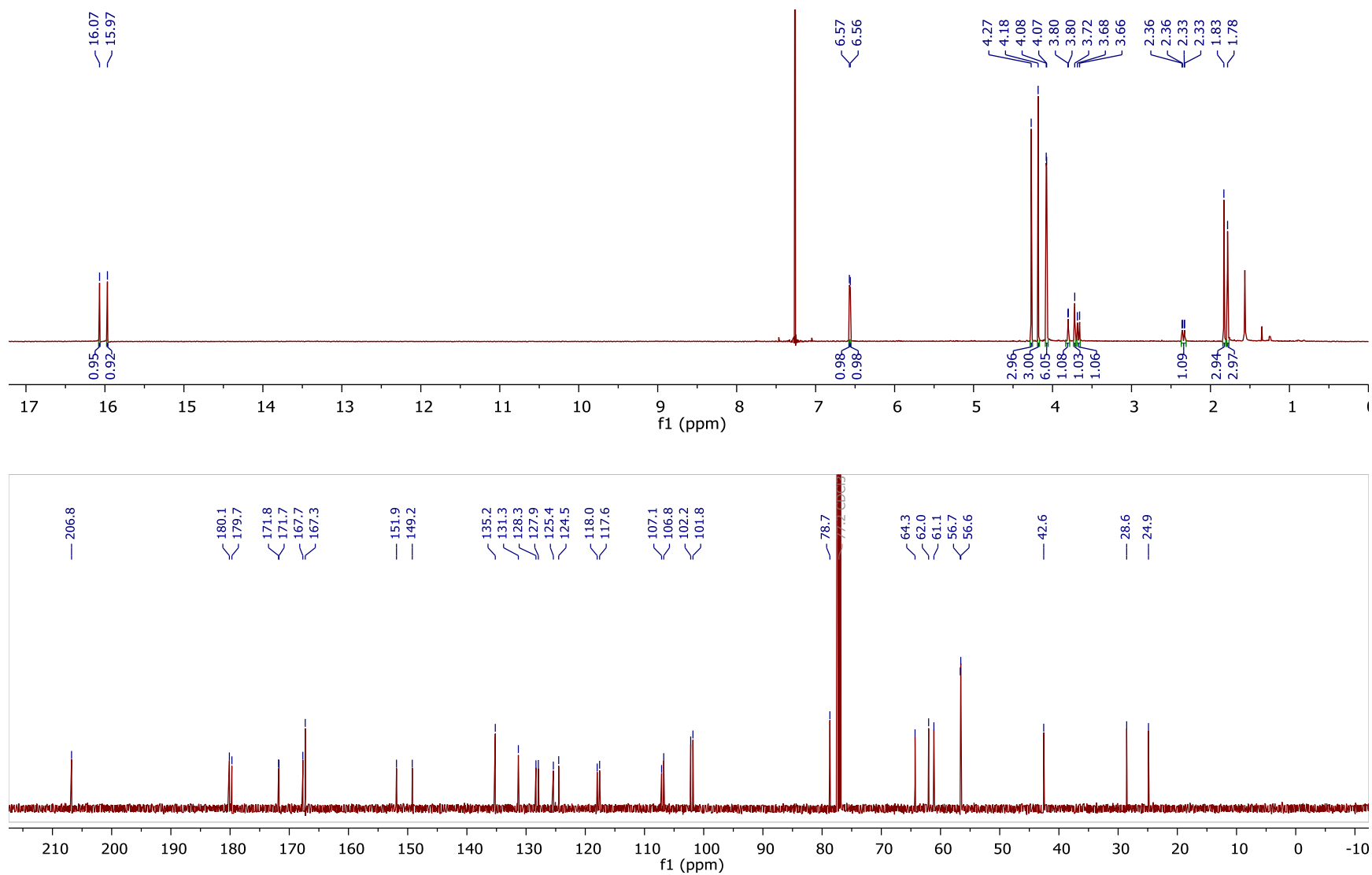


**Figure 4.15.**  $^1\text{H}$  and  $^{13}\text{C}$  NMR spectra of *ent*-shiraiachrome A (5) [500 MHz for  $^1\text{H}$  and 125 MHz for  $^{13}\text{C}$ ,  $\text{CDCl}_3$ ].

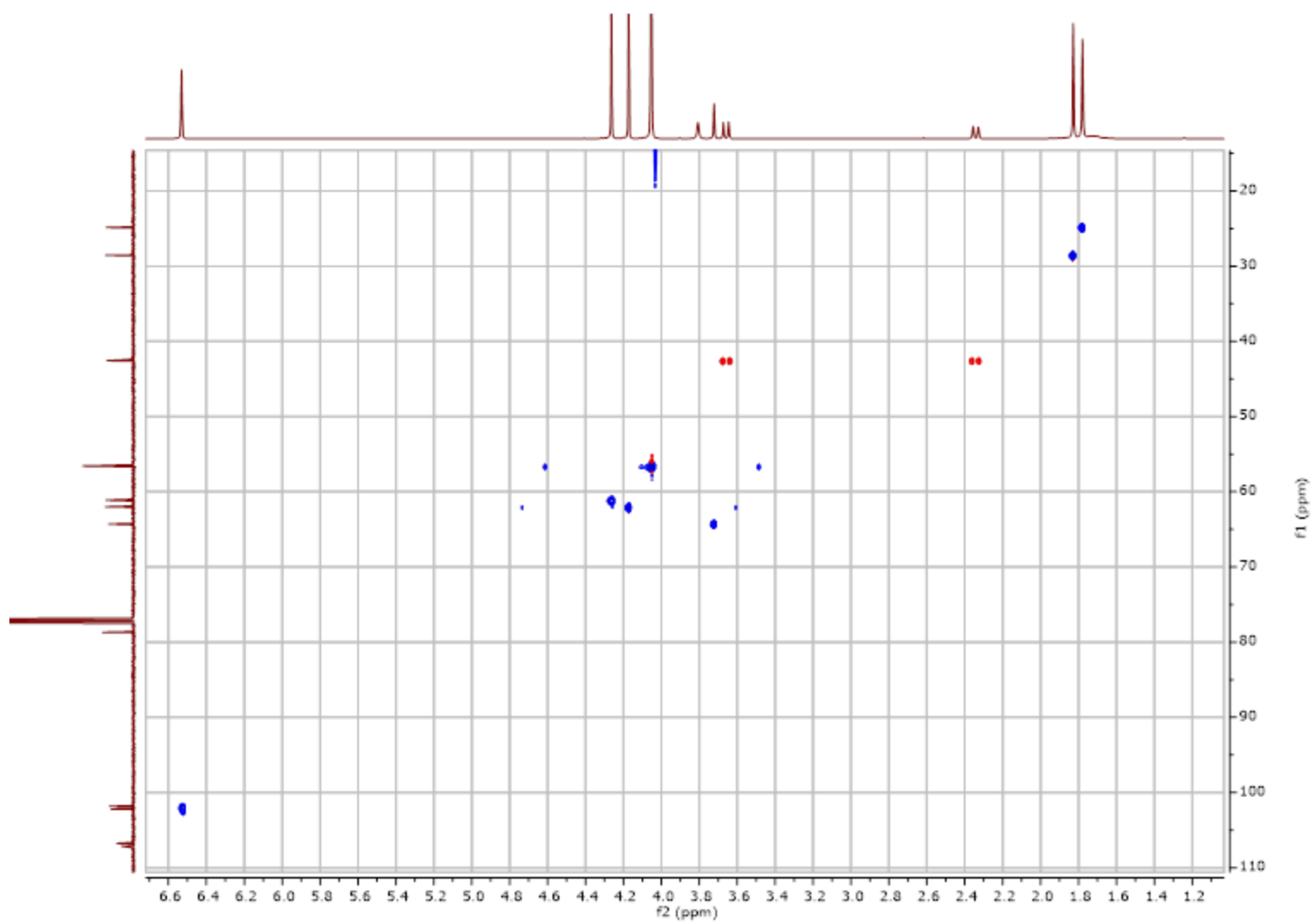


**Figure 4.16.** Edited-HSQC NMR spectrum of *ent*-shiraiachrome A (**5**) [400 MHz, CDCl<sub>3</sub>].

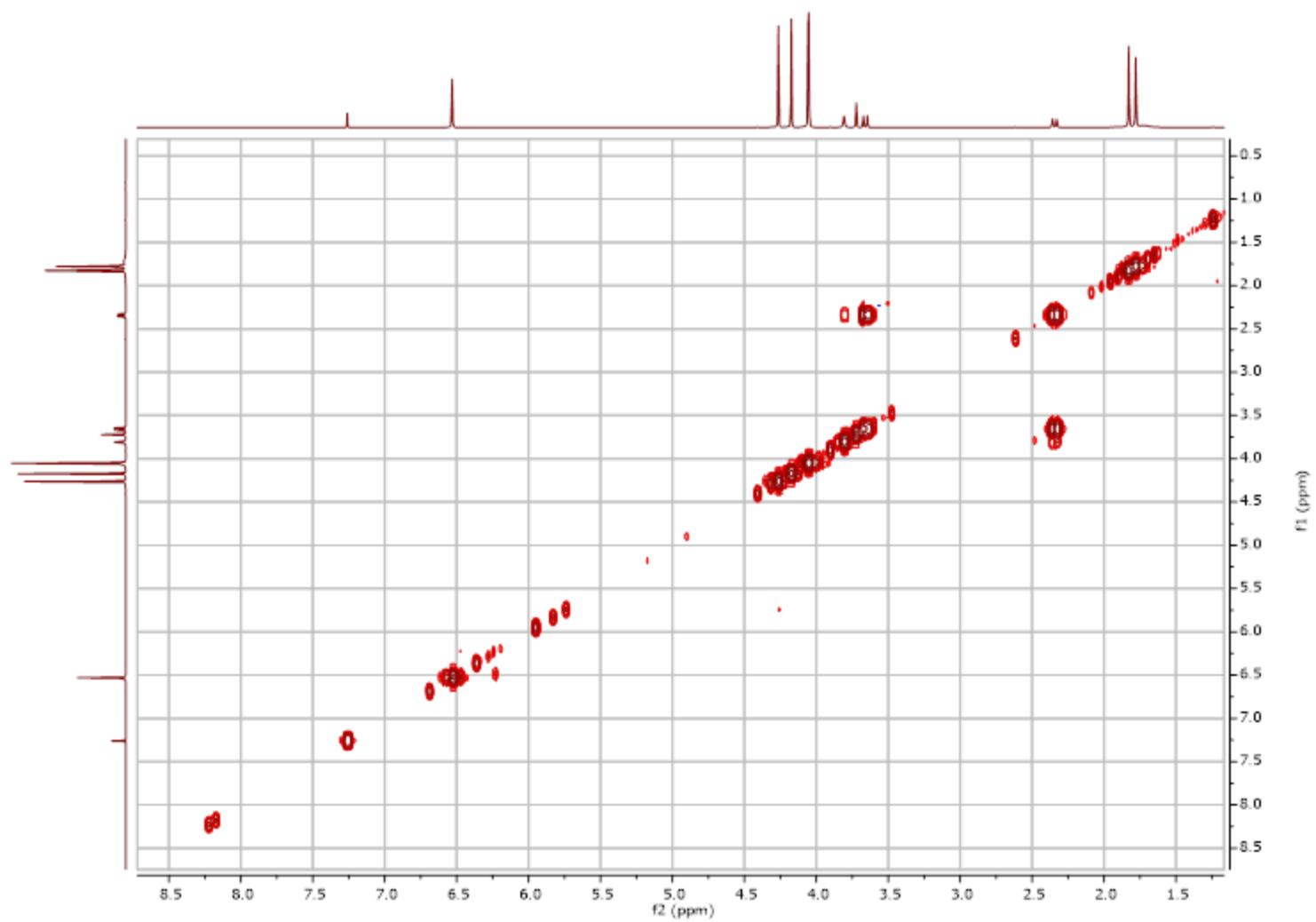


**Figure 4.17.** COSY NMR spectrum of *ent*-shiraiachrome A (**5**) [500 MHz, CDCl<sub>3</sub>].

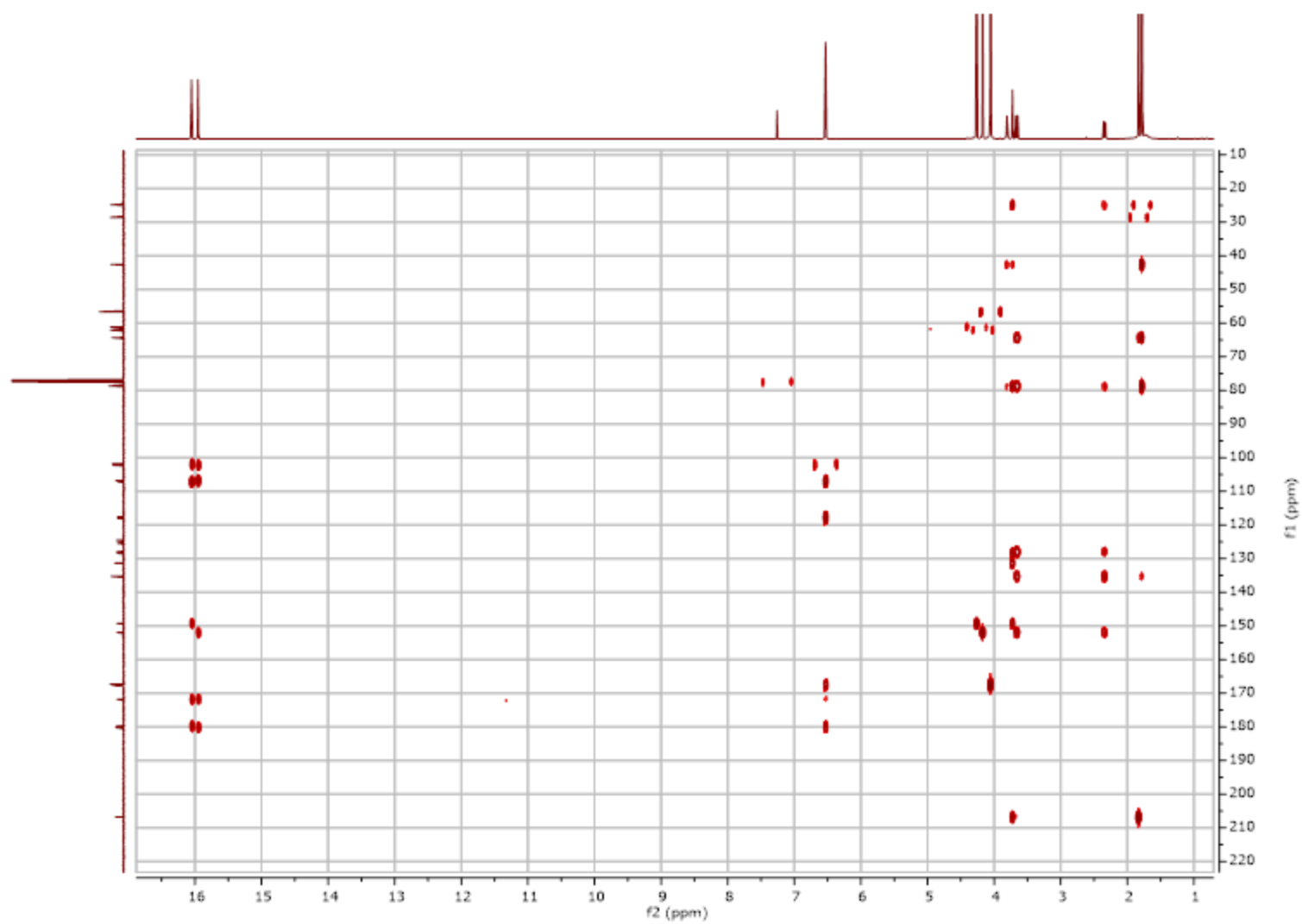


**Figure 4.18.** HMBC NMR spectrum of *ent*-shiraiachrome A (**5**) [500 MHz, CDCl<sub>3</sub>].

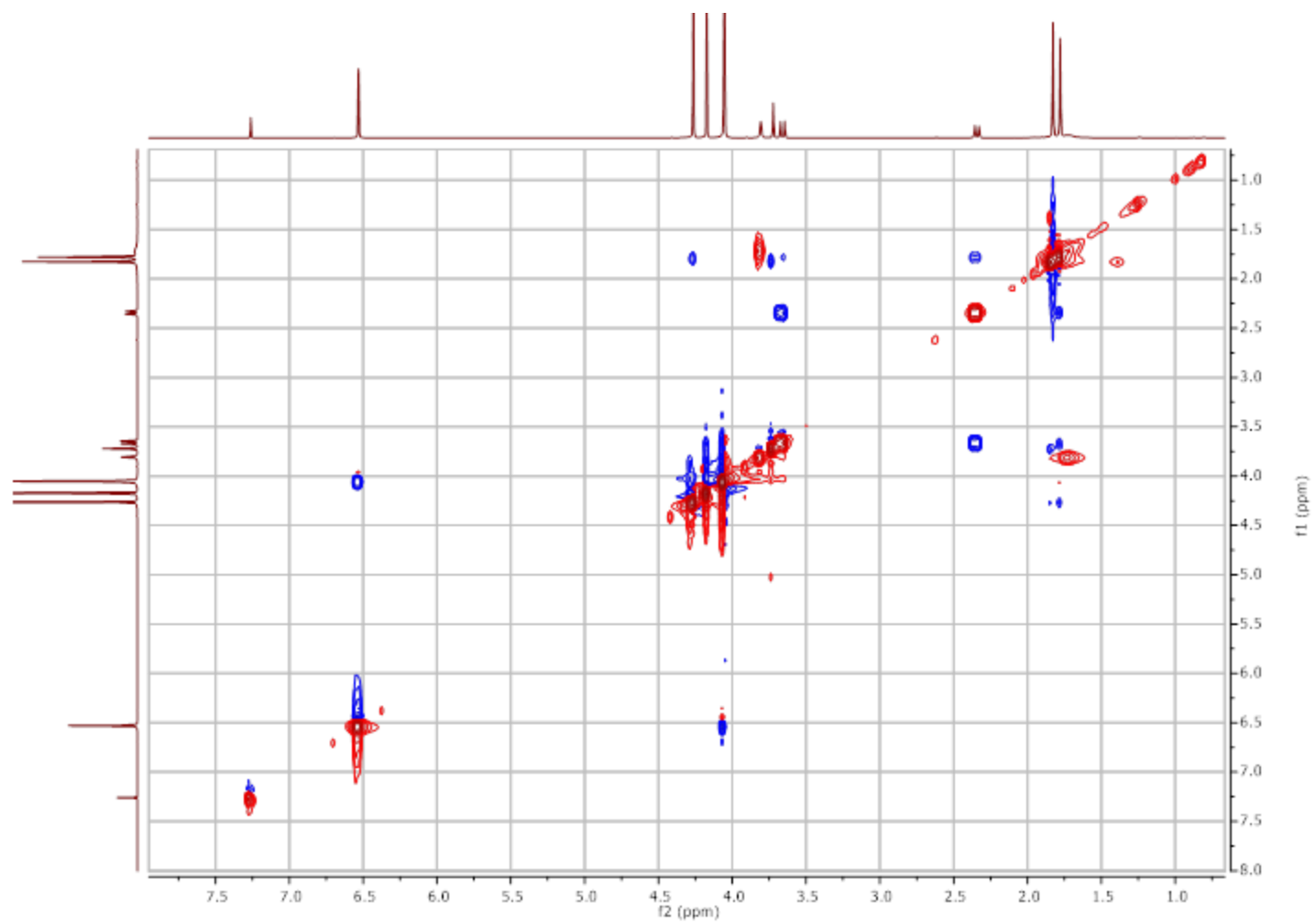


**Figure 4.19.** NOESY NMR spectrum of *ent*-shiraiachrome A (**5**) [500 MHz, CDCl<sub>3</sub>].

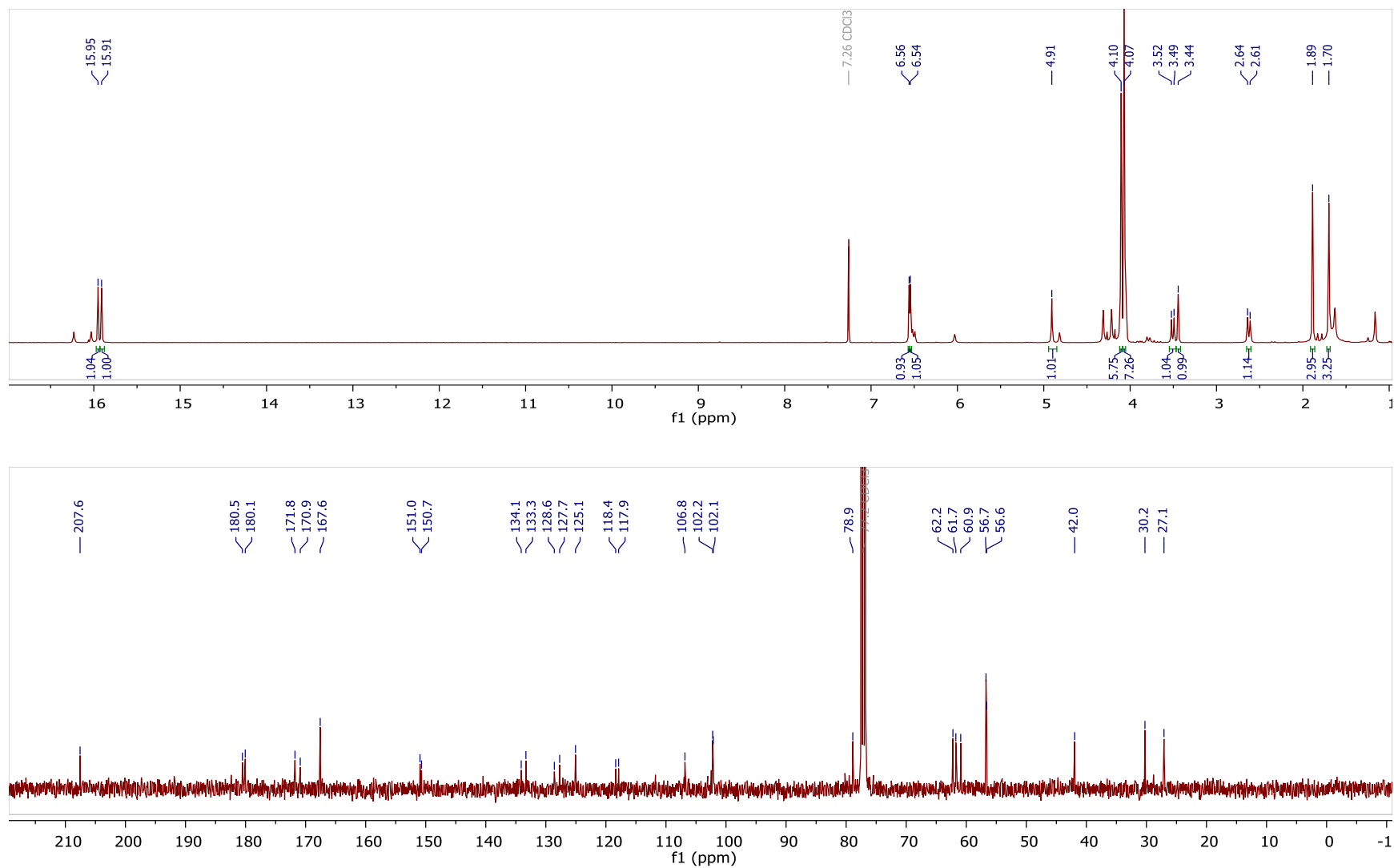


**Figure 4.20.**  $^1\text{H}$  and  $^{13}\text{C}$  NMR spectra of hypocrellin (1) [400 MHz for  $^1\text{H}$  and 100 MHz for  $^{13}\text{C}$ ,  $\text{CDCl}_3$ ].

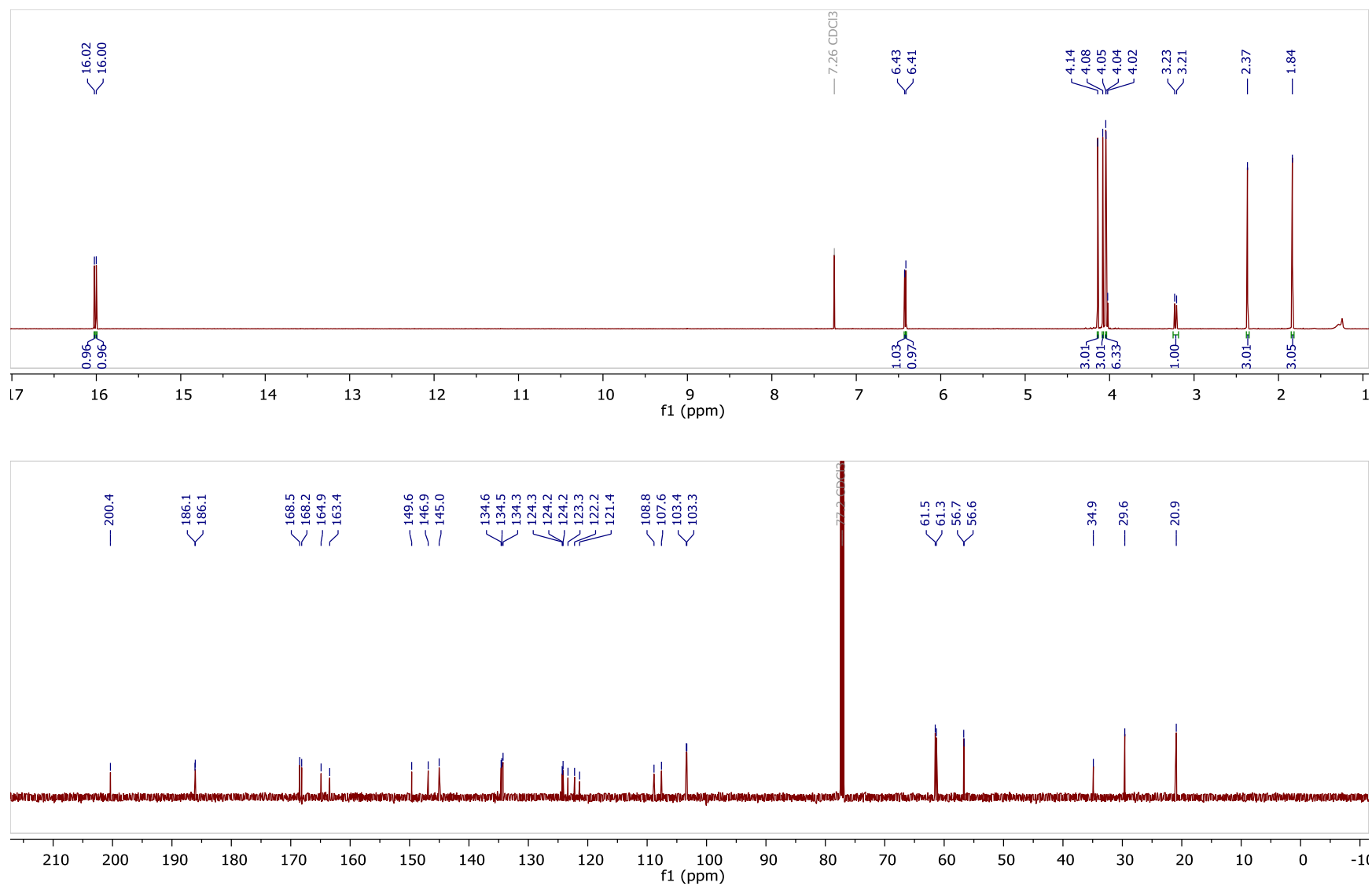


**Figure 4.21.**  $^1\text{H}$  and  $^{13}\text{C}$  NMR spectra of hypocrellin B (**3**) [500 MHz for  $^1\text{H}$  and 125 MHz for  $^{13}\text{C}$ ,  $\text{CDCl}_3$ ].

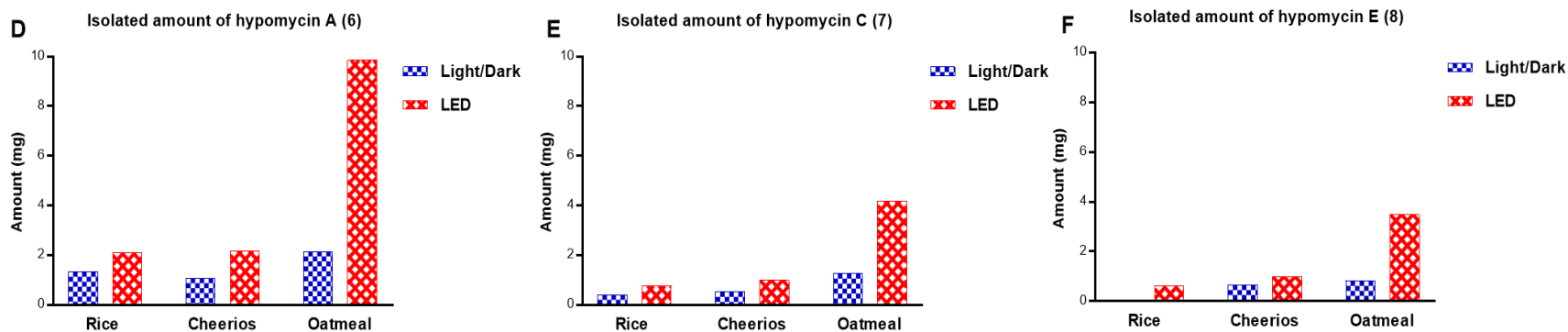


**Figure 4.22.** The amounts isolated of compounds **6** (A), **7** (B), and **8** (C) from cultures grown on rice, Cheerios, and oatmeal media under either 12:12 h light:dark cycles or LED light.

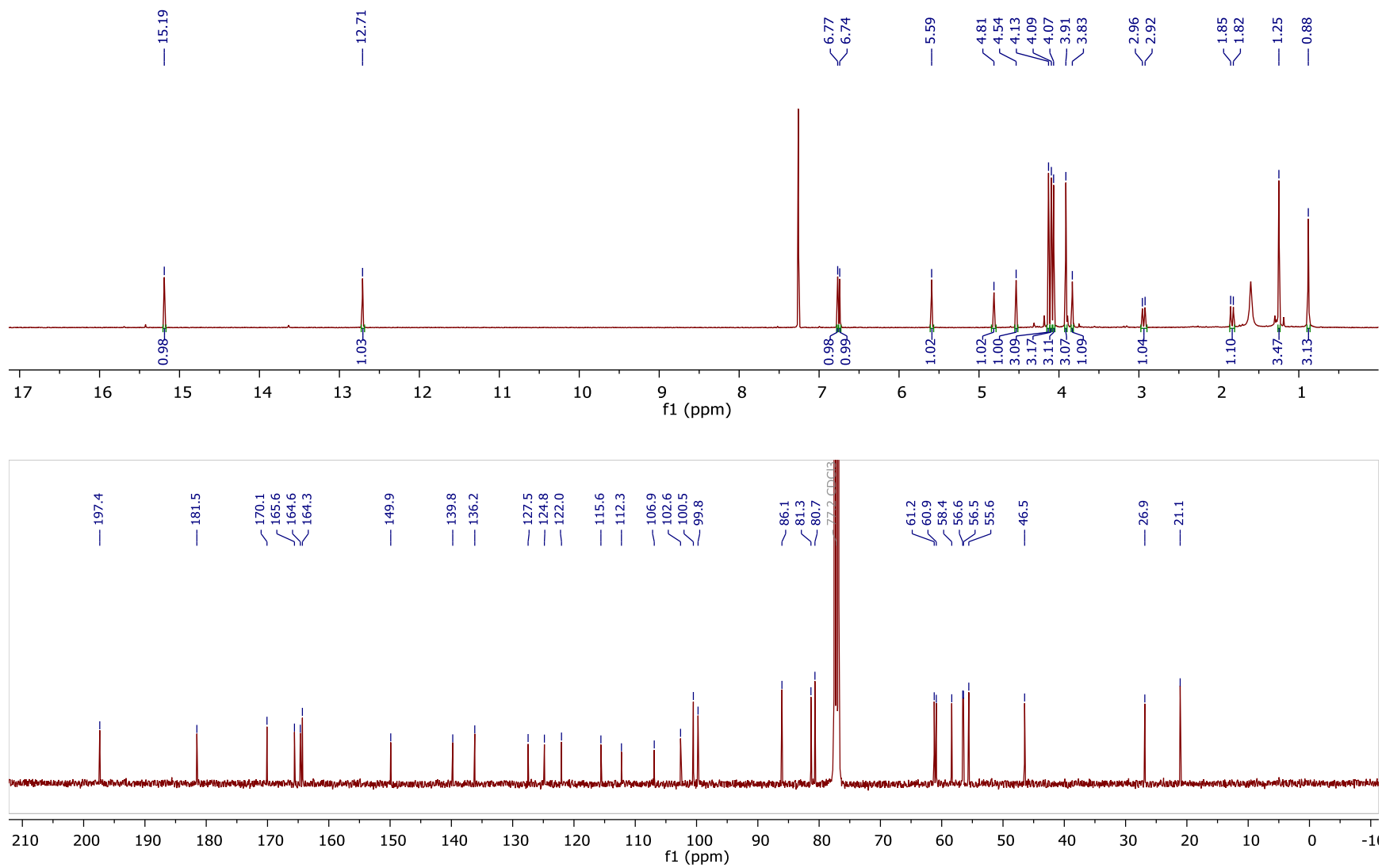
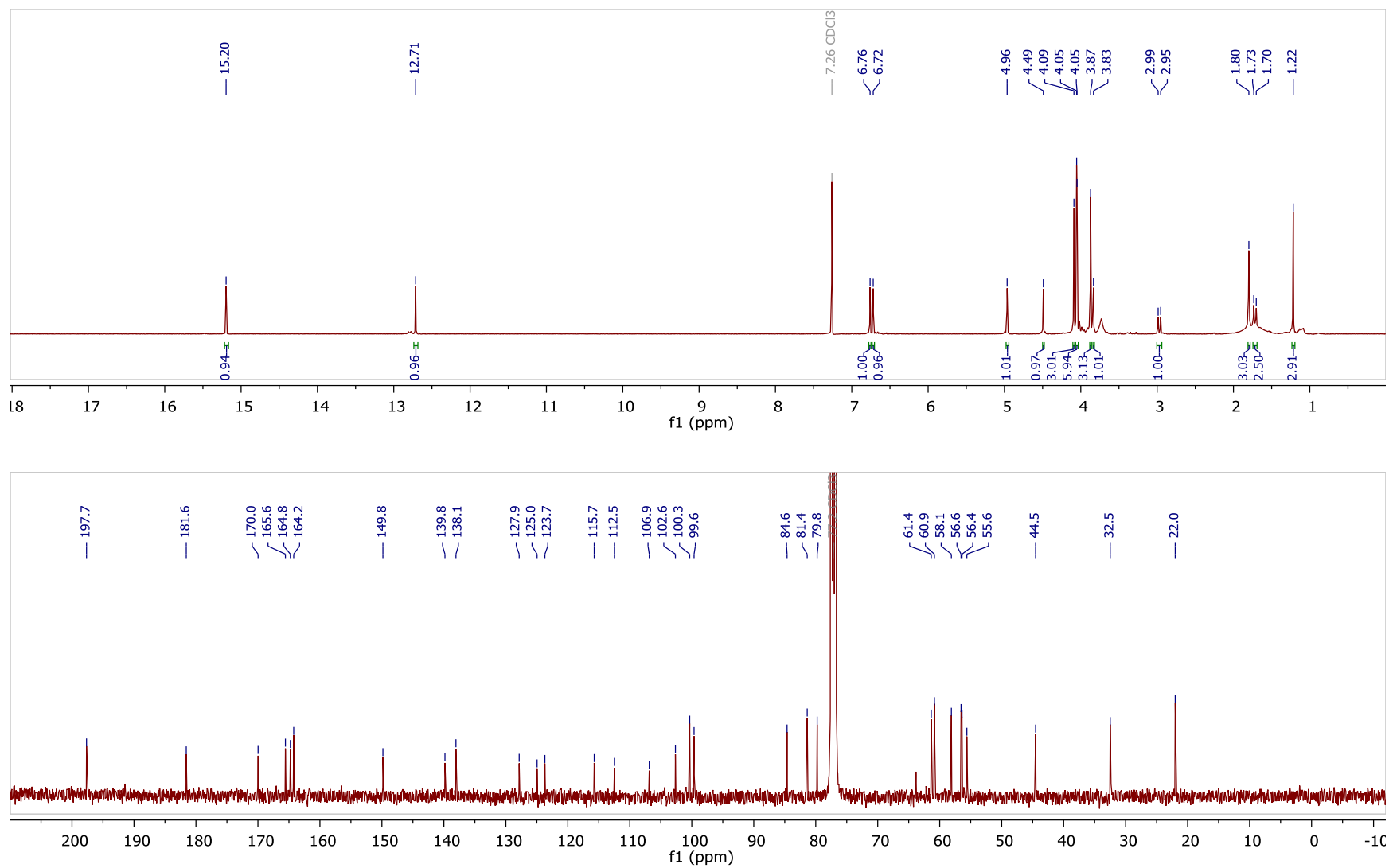
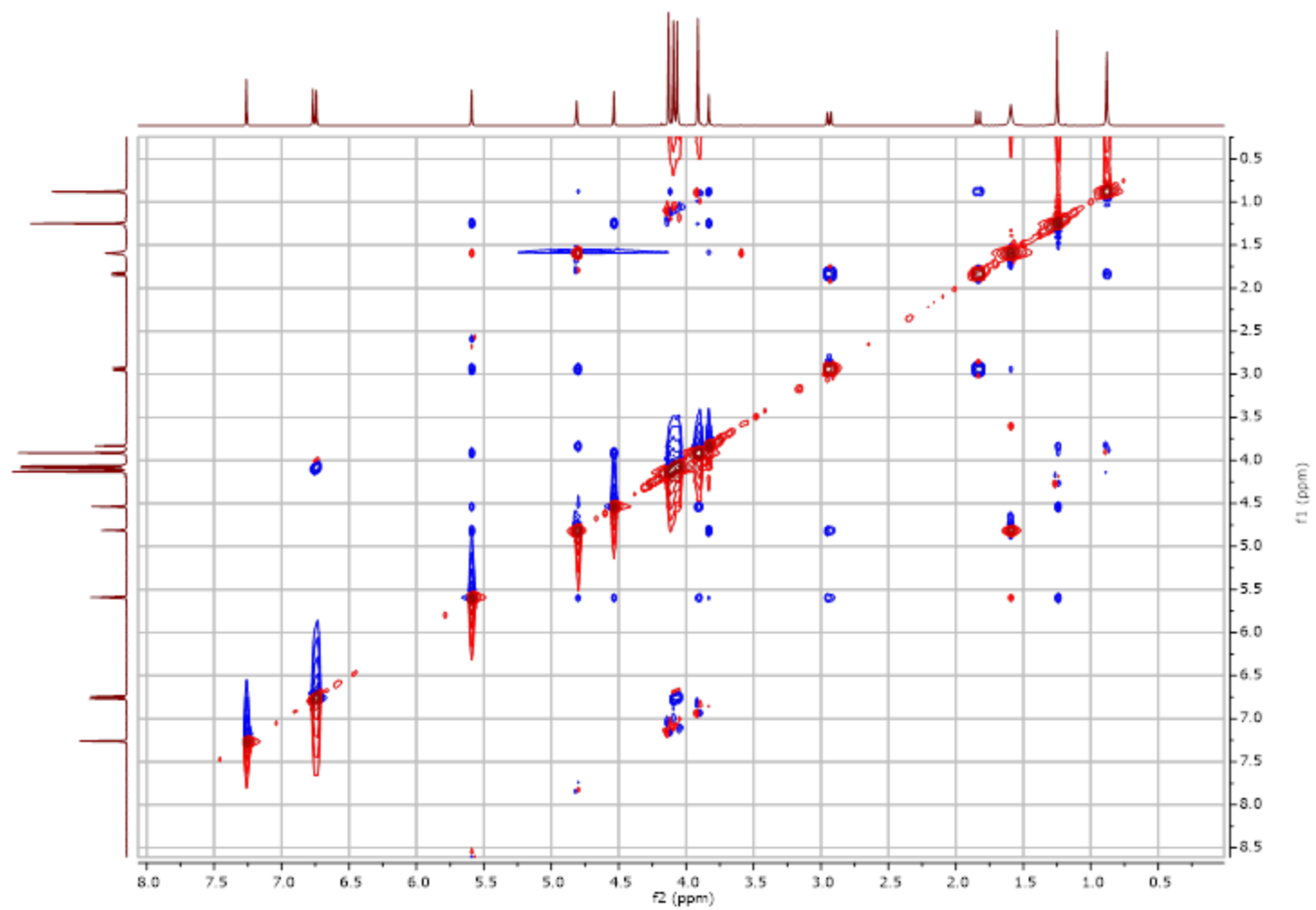


Figure 4.23.  $^1\text{H}$  and  $^{13}\text{C}$  NMR spectra of hypomycin A (6) [400 MHz for  $^1\text{H}$  and 100 MHz for  $^{13}\text{C}$ ,  $\text{CDCl}_3$ ].



**Figure 4.24.**  $^1\text{H}$  and  $^{13}\text{C}$  NMR spectra of hypomycin C (**7**) [400 MHz for  $^1\text{H}$  and 100 MHz for  $^{13}\text{C}$ ,  $\text{CDCl}_3$ ].



**Figure 4.25.** NOESY NMR spectrum of hypomycin A (**6**) [500 MHz, CDCl<sub>3</sub>].

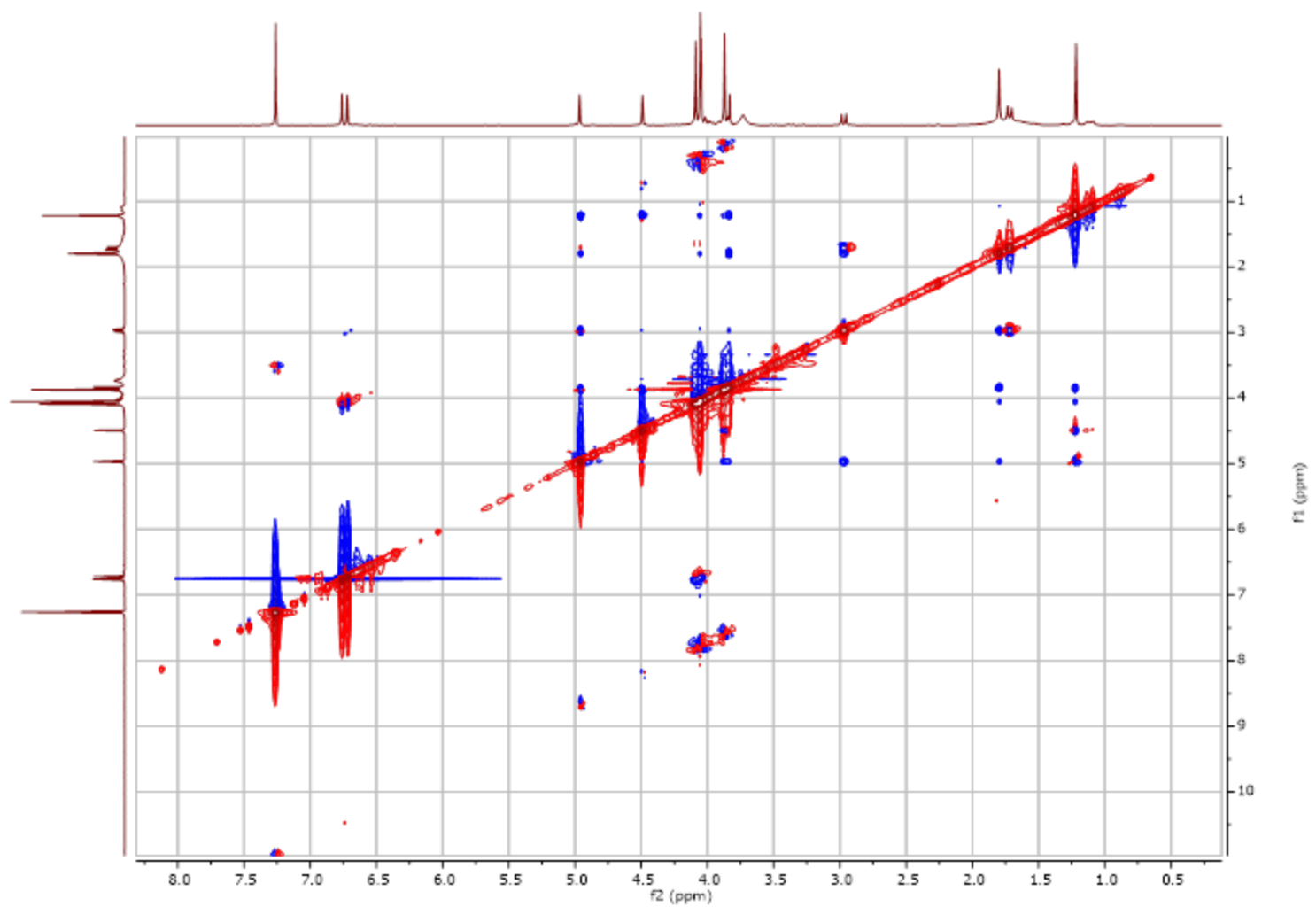


**Figure 4.26.** NOESY NMR spectrum of hypomycin C (7) [500 MHz, CDCl<sub>3</sub>].

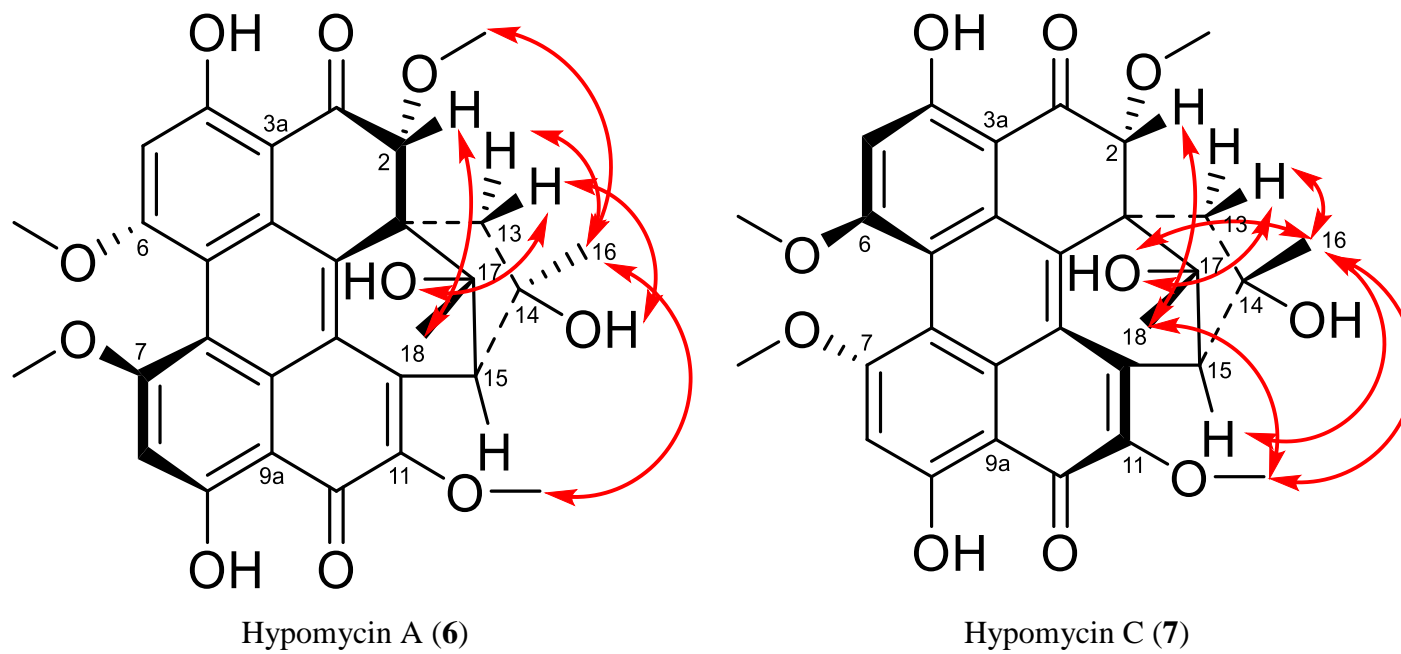


**Figure 4.27.** Key NOESY correlations of hypomycin A (6) and hypomycin C (7).

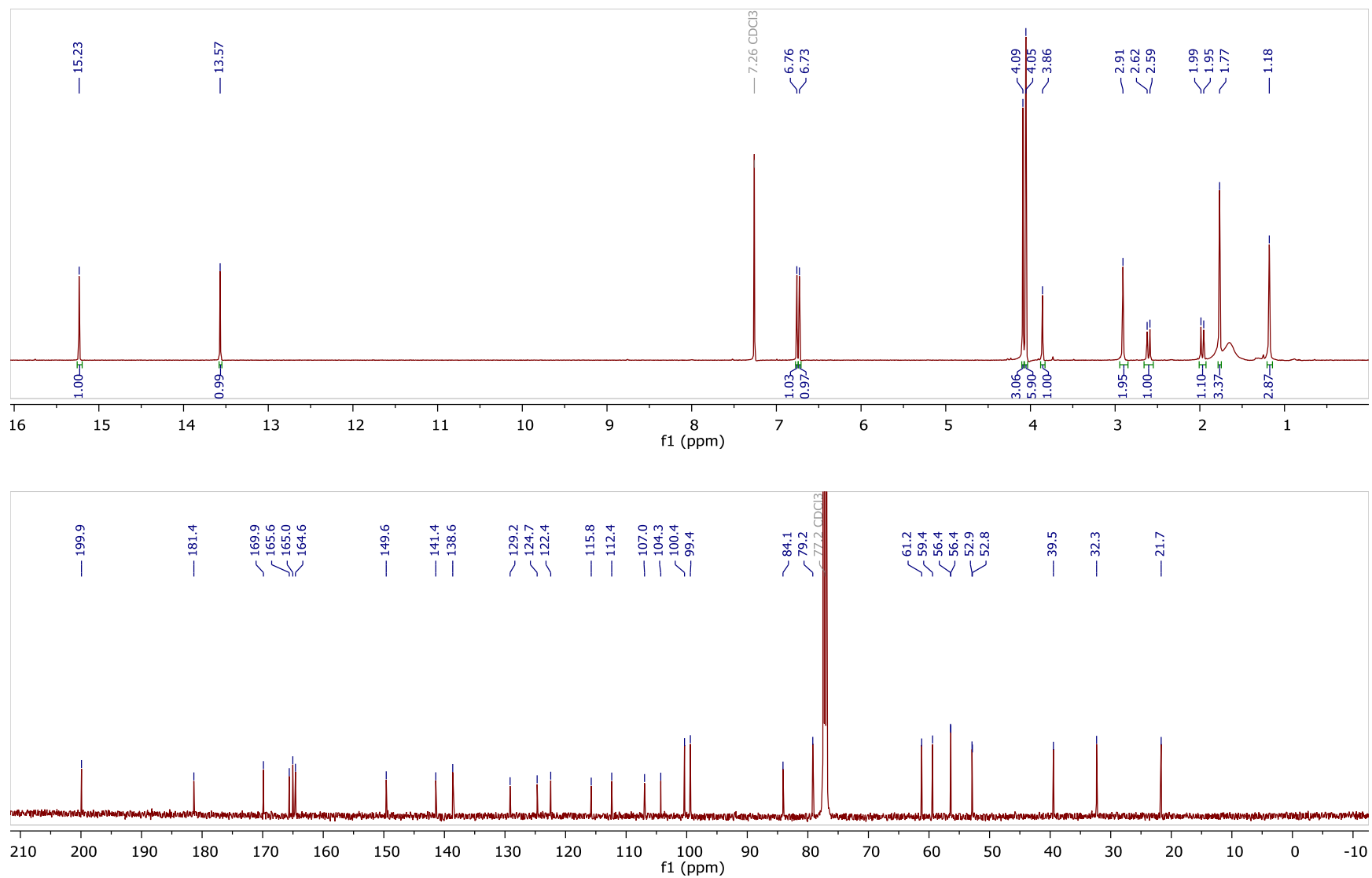


**Figure 4.28.**  $^1\text{H}$  and  $^{13}\text{C}$  NMR spectra of hypomycin E (**8**) [400 MHz for  $^1\text{H}$  and 125 MHz for  $^{13}\text{C}$ ,  $\text{CDCl}_3$ ].

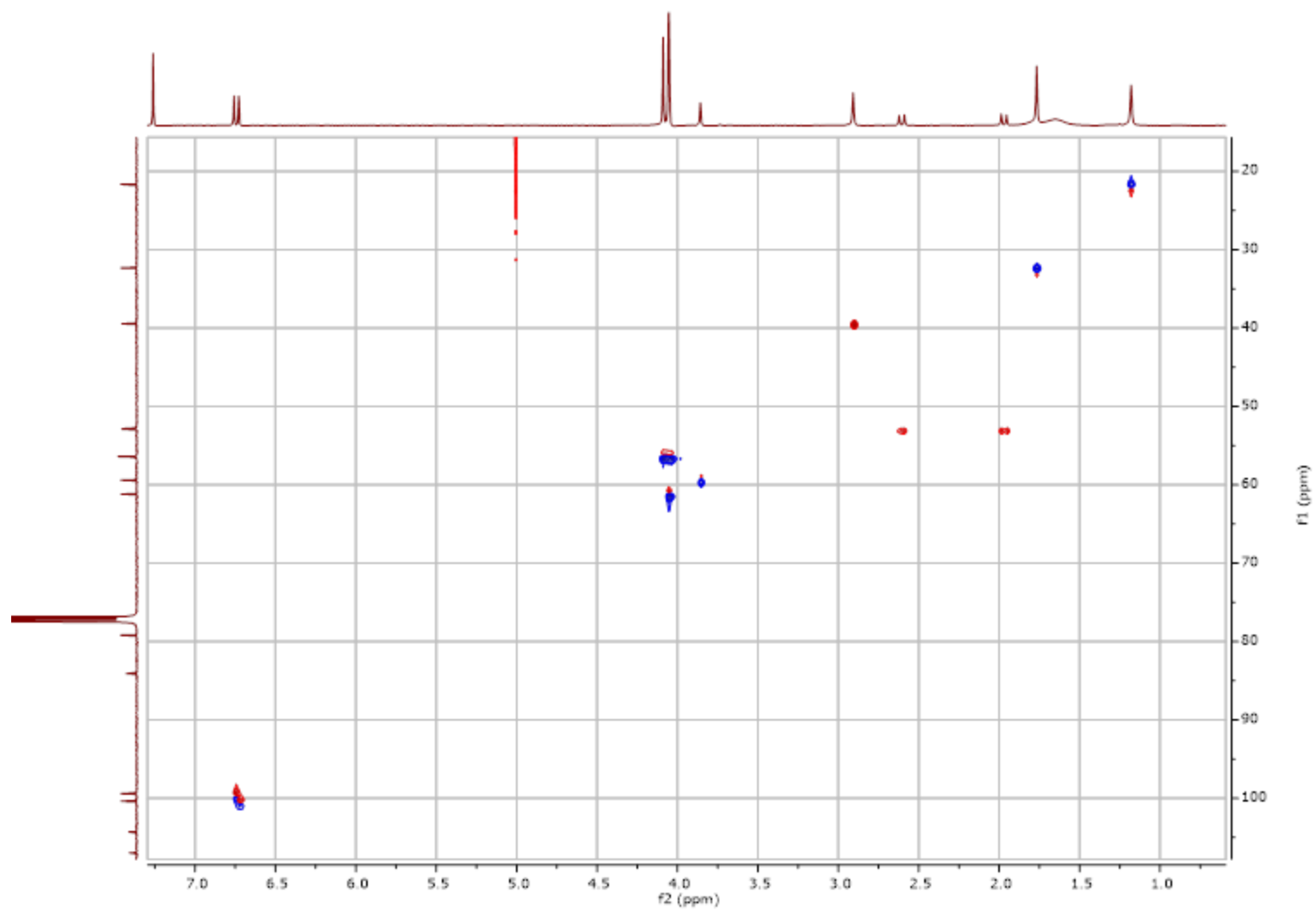


**Figure 4.29.** Edited-HSQC NMR spectrum of hypomycin E (**8**) [500 MHz, CDCl<sub>3</sub>].

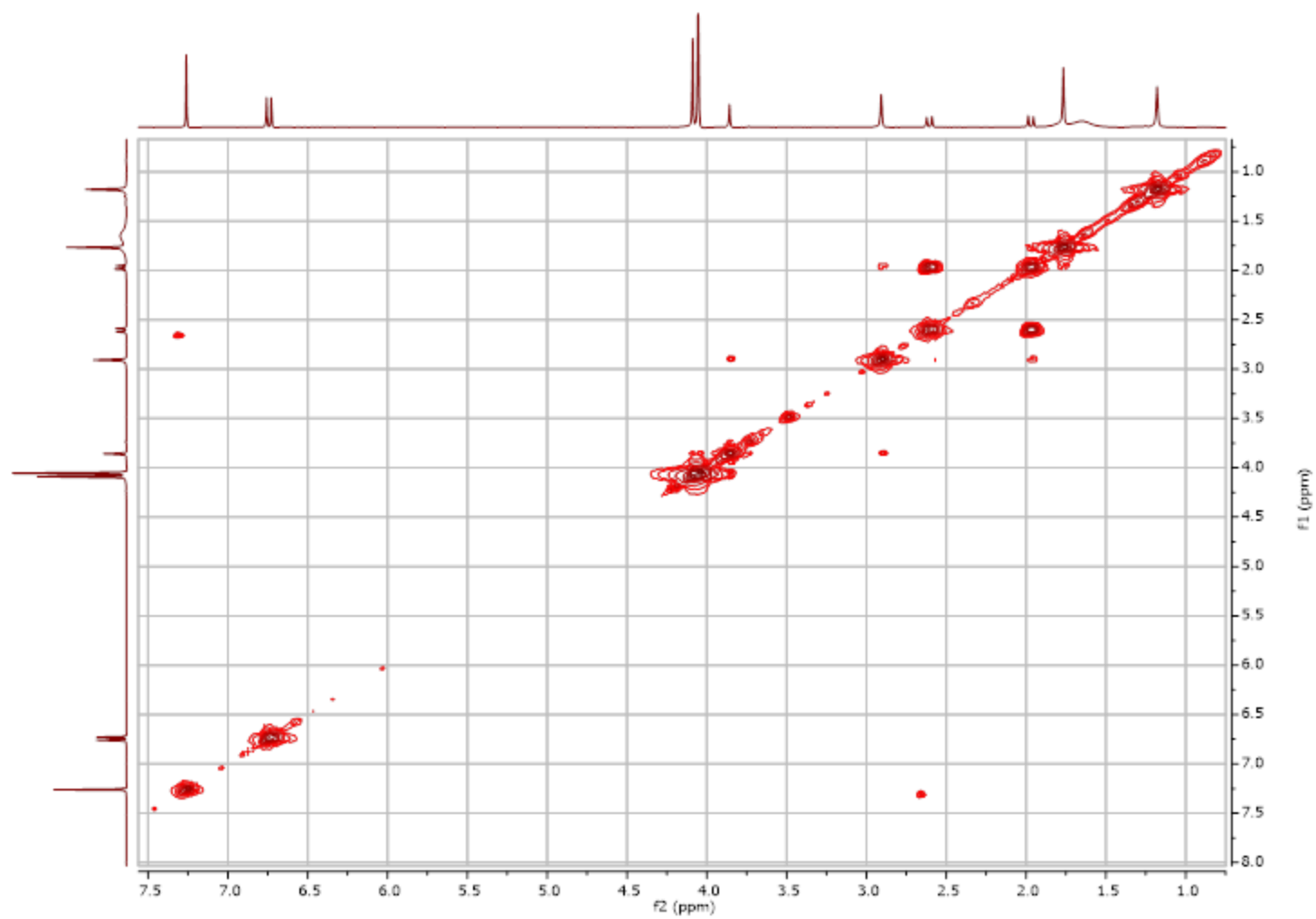


**Figure 4.30.** COSY NMR spectrum of hypomycin E (**8**) [500 MHz, CDCl<sub>3</sub>].

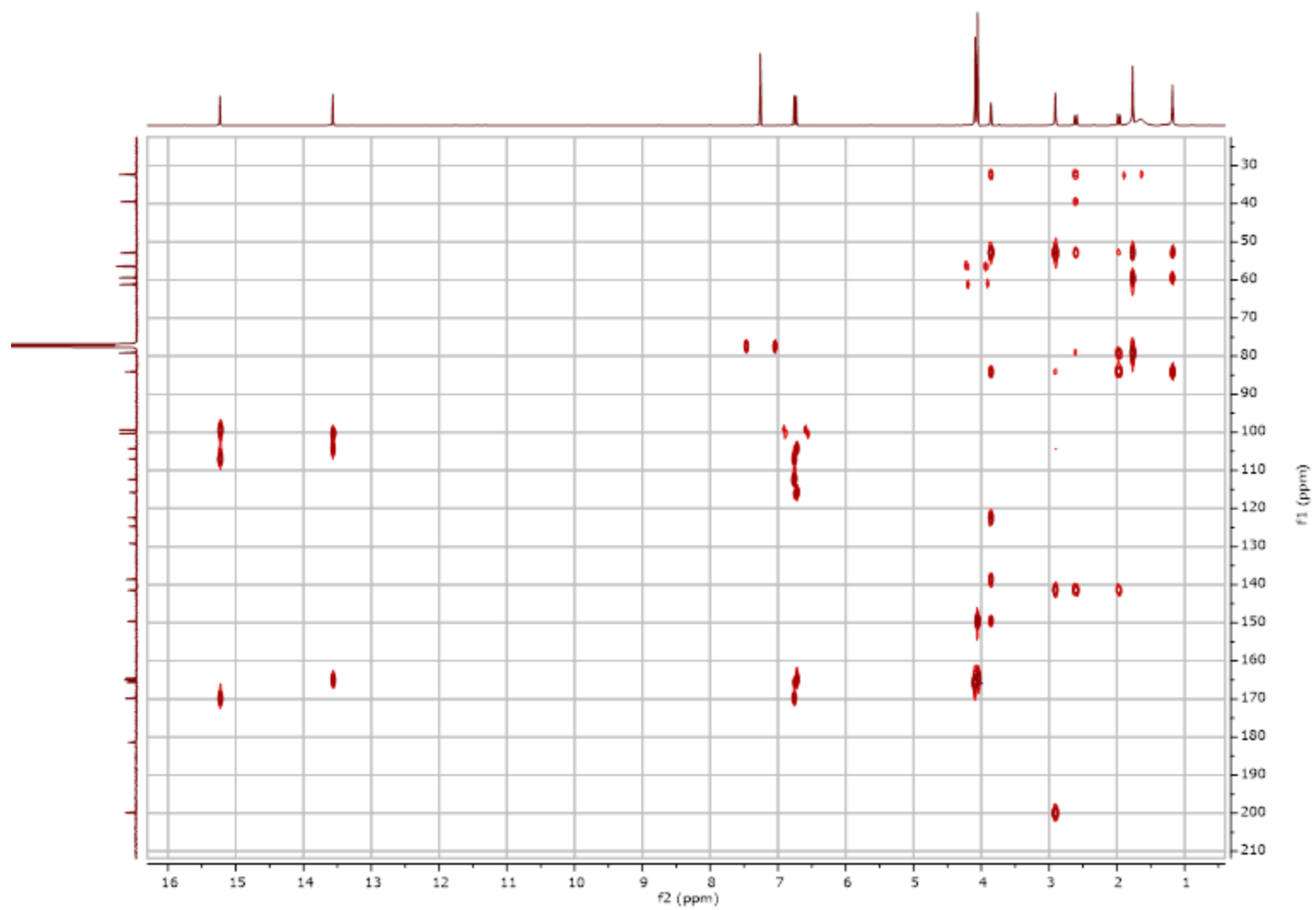


**Figure 4.31.** HMBC NMR spectrum of hypomycin E (**8**) [500 MHz, CDCl<sub>3</sub>].

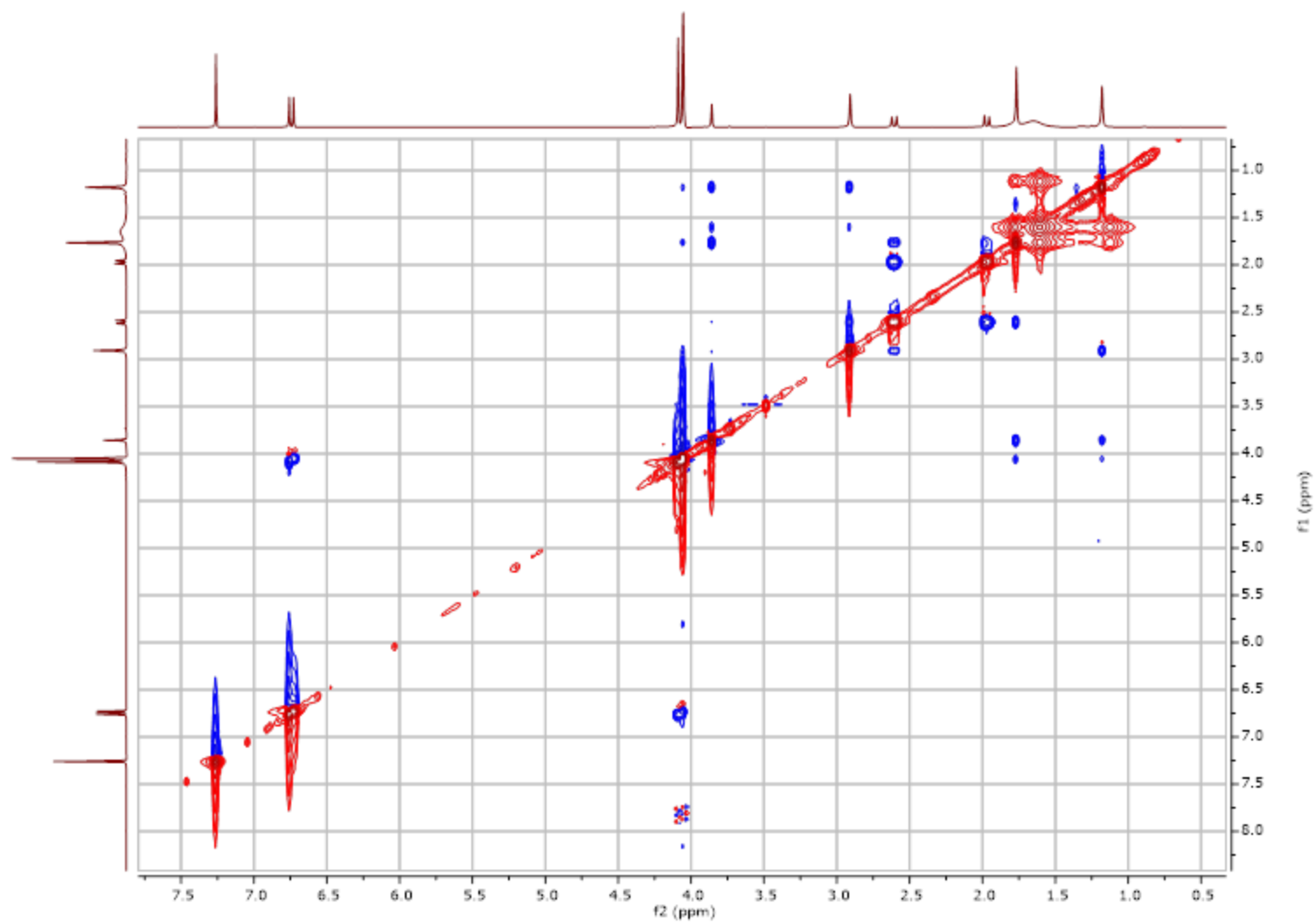


**Figure 4.32.** NOESY NMR spectrum of hypomycin E (**8**) [500 MHz, CDCl<sub>3</sub>].

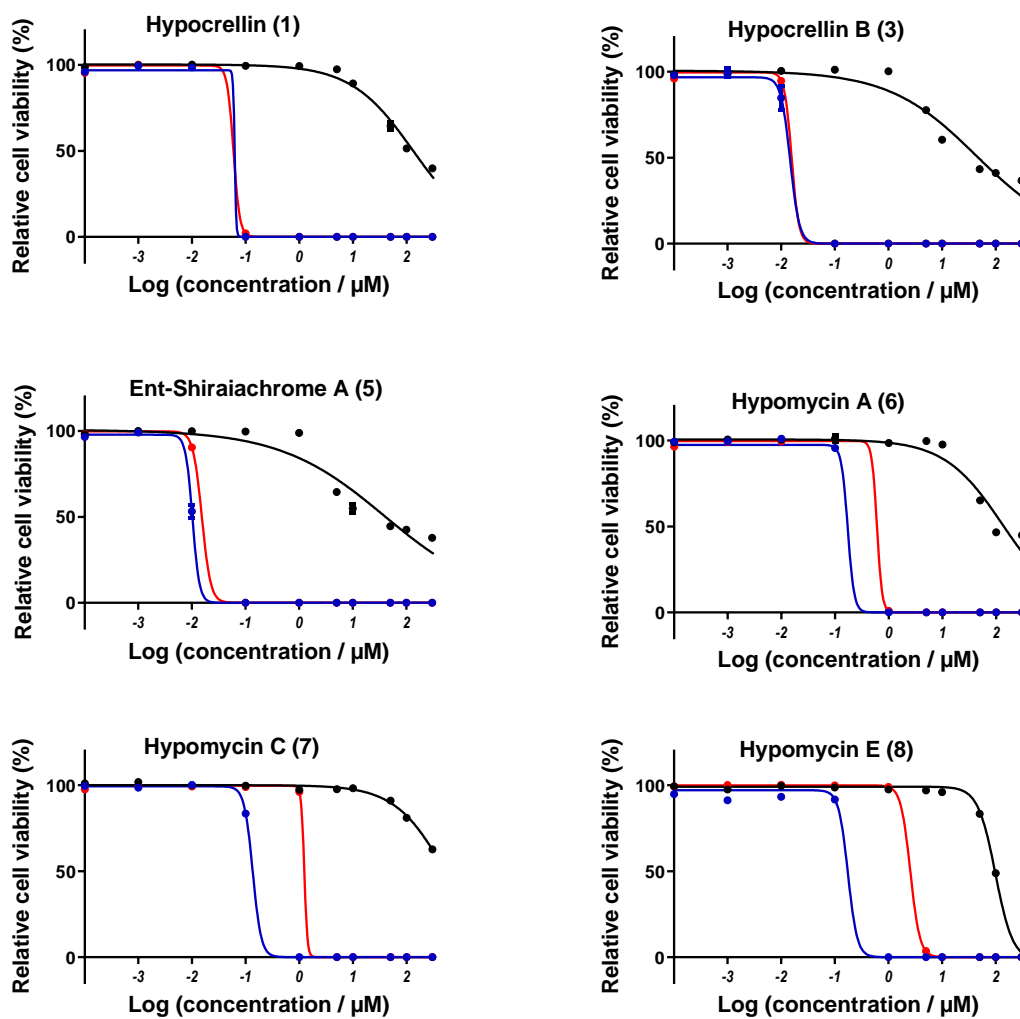


**Figure 4.33.** *In vitro* concentration–response curves for compounds (1, 3, and 5-8) in SK-MEL-28 cells without (black) or with visible (blue) or red (red) light irradiation. These plots were used to generate the data in Table 3.

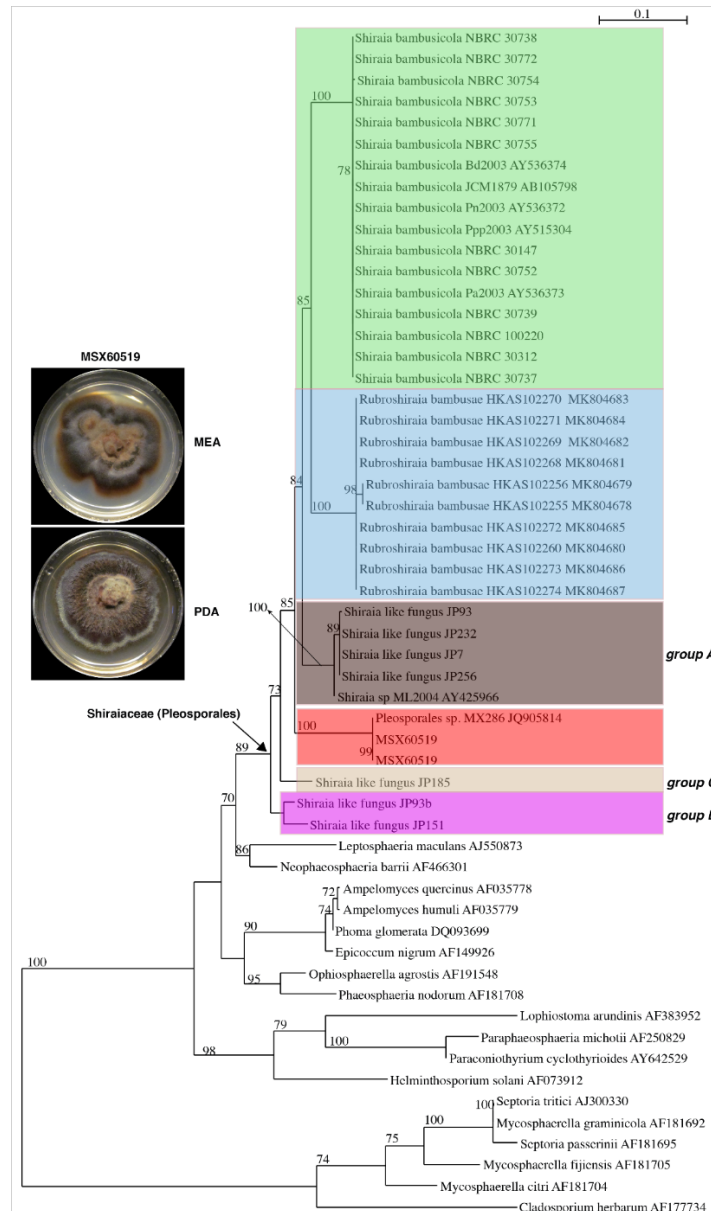


**Figure 4.34.** Maximum Likelihood analysis of fungi taxon sampled from two studies on hypocrellin-producing strains in the Pleosporales, Dothideomycetes<sup>187, 188</sup> showing Phylogram of the most likely tree (-lnL = 3561.05) from a RAxML analysis of 56 strains based on ITS region sequence data (403 bp). Numbers refer to RAxML bootstrap support values  $\geq 70\%$  based on 1000 replicates. Strain MSX60519 was identified as *Shiraia*-like fungus in the family Shiraiaceae, Pleosporales, Dothideomycetes, Ascomycota as it demonstrated 89% bootstrap support with members of Shiraiaceae. Strain MSX60519 is highlighted in a bright orange box and shared 100% bootstrap support with a fungal endophyte isolated from a rubber tree in Peru.<sup>234</sup> Three weeks old cultures on potato dextrose agar and malt extract agar are shown. Bar indicates nucleotide substitutions per site. The tree was rooted with members of the Capnodiales.

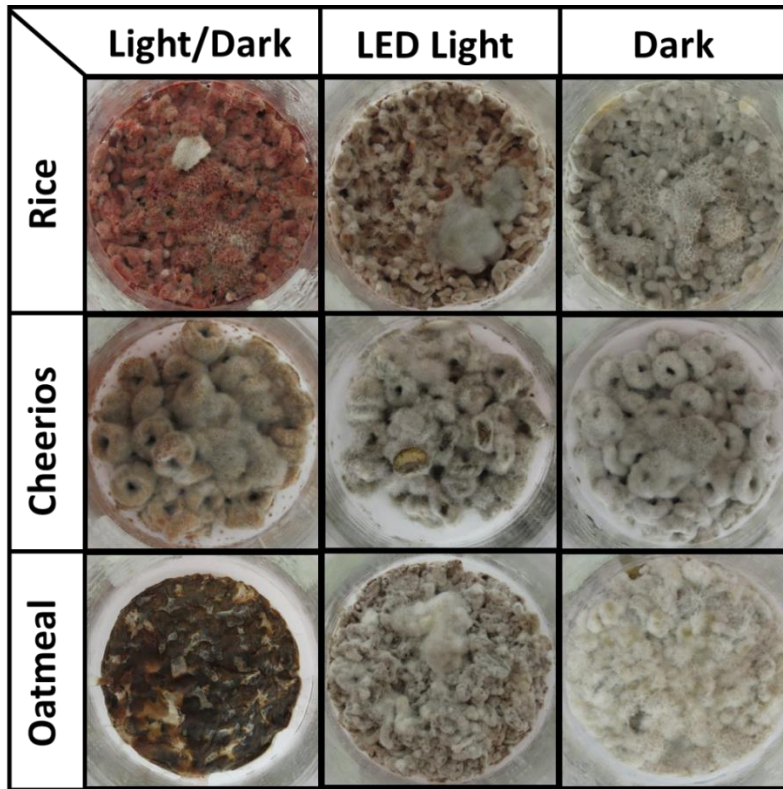


**Figure 4.35.** Pictures of strain MSX60519 cultures grown on three different media and exposed to three different light conditions.

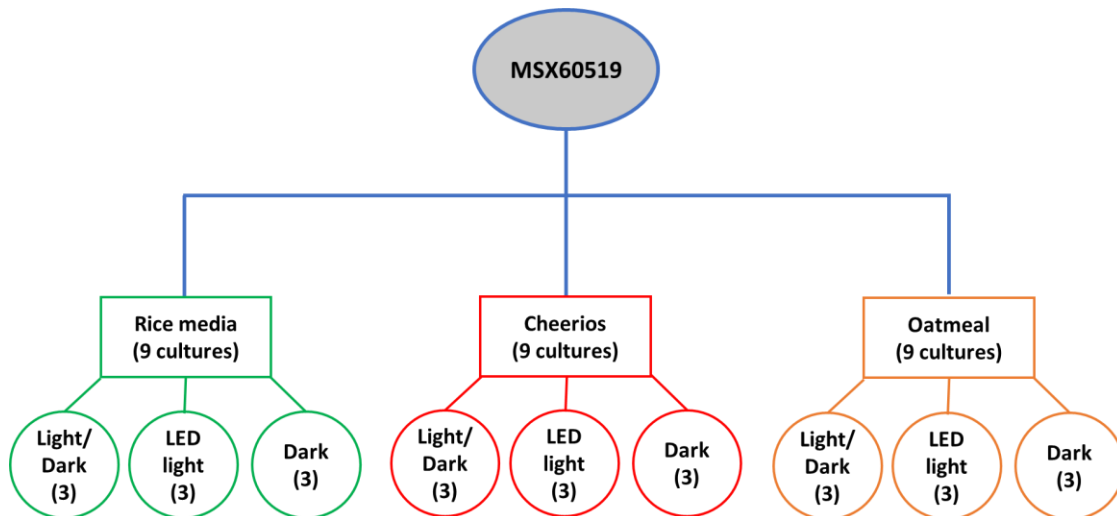


**Figure 4.36.** The nine growth conditions utilized to grow strain MSX60519. Three cultures were grown under each condition to generate biological replicates.

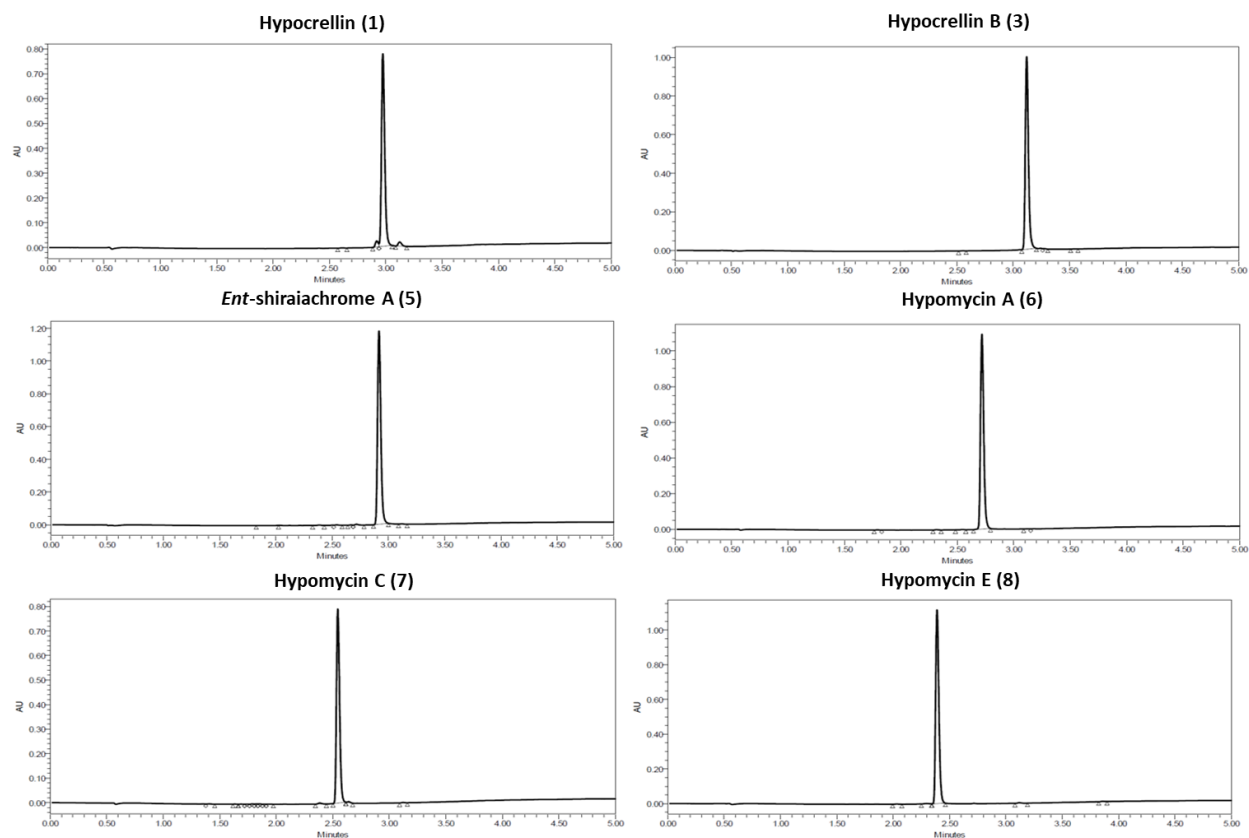


**Figure 4.37.** UPLC chromatograms of compounds **1**, **3**, and **5-8** (PDA detection at 254 nm), demonstrating >97% purity. All data were acquired via an Acquity UPLC system with a BEH Shield RP18 column (Waters, 1.7  $\mu\text{m}$ ; 50  $\times$  2.1 mm) and a  $\text{CH}_3\text{CN-H}_2\text{O}$  gradient that increased linearly from 20 to 100 %  $\text{CH}_3\text{CN}$  over 4.5 min.

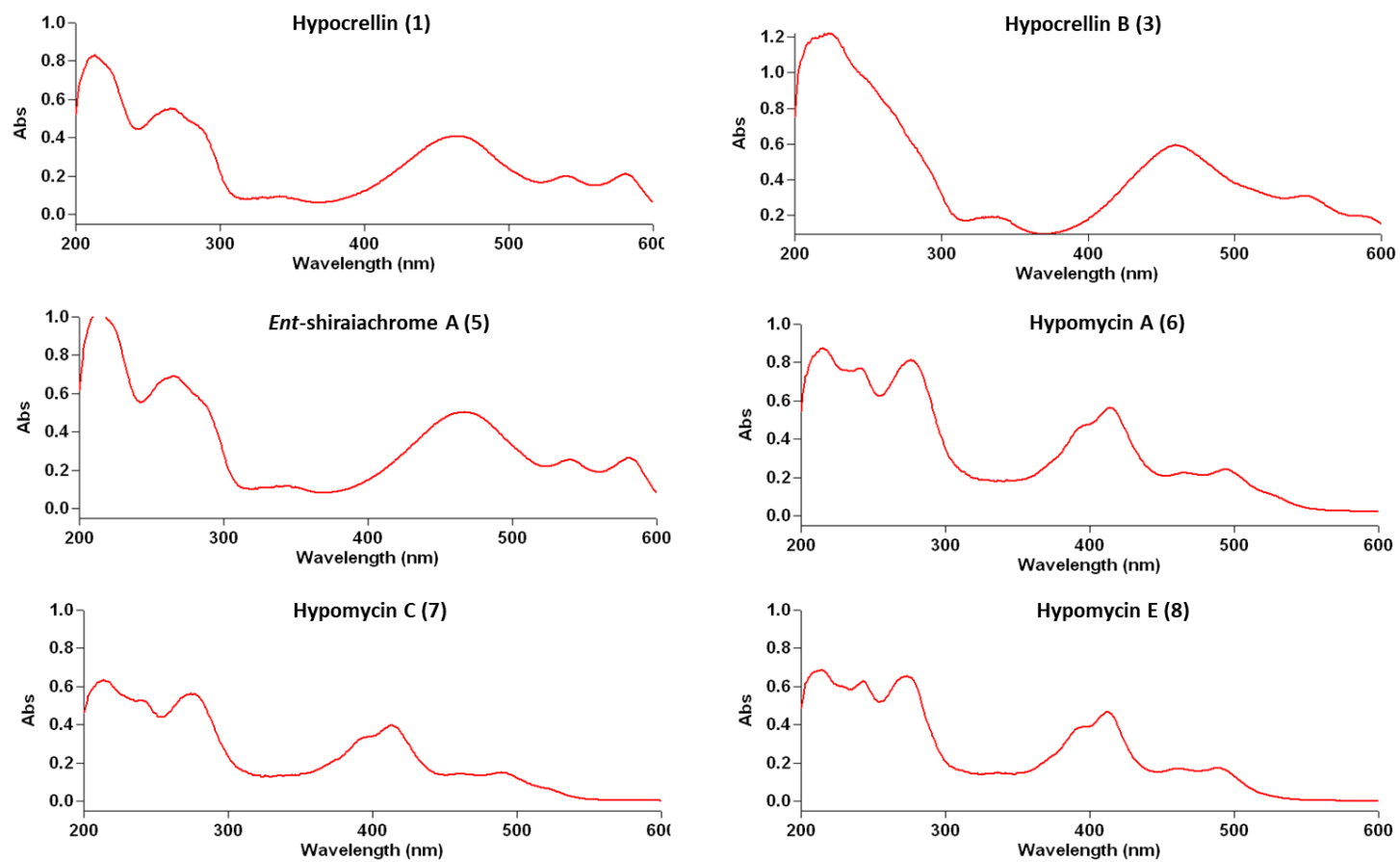


**Figure 4.38.** UV spectra of compounds **1**, **3**, and **5-8** analyzed in CH<sub>3</sub>OH at a concentration of 0.0125 mg/mL.

**Table 4.4.** NMR Spectroscopic Data for **1**, **3**, and **6-7** in CDCl<sub>3</sub> ( $\delta$  in ppm).

no.	<b>1<sup>a</sup></b>		<b>3<sup>b</sup></b>		<b>6<sup>a</sup></b>		<b>7<sup>a</sup></b>	
	$\delta_C$ , type	$\delta_H$ (J, Hz)						
1	133.3, C		134.3, C		55.6, C		55.6, C	
1a	127.7, C		124.2, C		139.8, C		139.8, C	
2	151.0, C		146.9, C		81.3, CH	4.54, s	81.4, CH	4.49, s
3	170.9, C		164.9, C		197.4, C		197.7, C	
3a	106.8, C		107.6, C		102.6, C		102.6, C	
3b	125.1, C		123.3, C*		127.5, C		127.9, C	
4	180.5, C		186.1, C		164.3, C		164.2, C	
5	102.2, CH	6.54, s	103.4, CH	6.41, s	100.5, CH	6.74, s	100.3, CH	6.72, s
6	167.6, C		168.2, C		164.7, C		164.8, C	
6a	118.4, C		122.2, C		115.6, C		115.7, C	
7	167.6, C		168.5, C		165.6, C		165.6, C	
7a	117.9, C		121.4, C		112.3, C		112.5, C	
8	102.1, CH	6.56, s	103.3, CH	6.43, s	99.8, CH	6.77, s	99.6, CH	6.76, s
9	180.1, C		186.1, C		170.1, C		170.0, C	
9a	106.8, C		108.9, C		106.9, C		106.9, C	
9b	125.1, C		124.2, C*		124.8, C		125.0, C	
10	171.8, C		163.4, C		181.5, C		181.6, C	
11	150.7, C		149.6, C		149.9, C		149.8, C	
12	134.1, C		134.6, C		136.2, C		138.1, C	
12a	128.6, C		124.3, C*		122.0, C		123.7, C	
13	42.0, CH <sub>2</sub>	H <sub>a</sub> 2.63, d (12.0) H <sub>b</sub> 3.51, d (12.0)	34.9, CH <sub>2</sub>	H <sub>a</sub> 3.22, d (11.6) H <sub>b</sub> 4.03, d (11.6)	46.5, CH <sub>2</sub>	H <sub>a</sub> 1.84, d (13.6) H <sub>b</sub> 2.94, d (13.6)	44.5, CH <sub>2</sub>	H <sub>a</sub> 1.72, d (13.1) H <sub>b</sub> 2.97, d (13.1)
14	78.9, C		145.0, C		80.7, C		79.8, C	

15	61.7, CH	3.44, s	134.5, C		58.4, CH	3.83, s	58.1, CH	3.83, s
16	27.1, CH <sub>3</sub>	1.70, s	20.9, CH <sub>3</sub>	2.37, s	26.9, CH <sub>3</sub>	0.88, s	32.5, CH <sub>3</sub>	1.80, s
17	207.6, C		200.4, C		86.1, C		84.6, C	
18	30.3, CH <sub>3</sub>	1.89, s	29.6, CH <sub>3</sub>	1.84, s	21.1, CH <sub>3</sub>	1.25, s	22.0, CH <sub>3</sub>	1.22, s
CH <sub>3</sub> O-2	60.9 or 62.2	4.10, s	61.5	4.14, s	60.9	3.91, s	60.9	3.87, s
CH <sub>3</sub> O-6	62.2 or 60.9	4.10, s	56.7 or 56.6	4.04 or 4.05, s	56.6	4.07, s	56.6	4.05, s
CH <sub>3</sub> O-7	56.7 or 56.6	4.07, s	56.6 or 56.7	4.05 or 4.04, s	56.5	4.09, s	56.4	4.09, s
CH <sub>3</sub> O-11	56.6 or 56.7	4.07, s	61.3	4.08, s	61.2	4.13, s	61.4	4.05, s
HO-3		15.95, s		16.00, s				
HO-4						12.71, s		12.71, s
HO-9						15.19, s		15.20, s
HO-10		15.91, s		16.02, s				
HO-14		4.91, s				4.81, s		
HO-17						5.59 (s)		4.96 (s)

\*Assignments could be interchanged due to lack of HMBC correlations.

<sup>a</sup>Recorded at 400 MHz for <sup>1</sup>H and 100 MHz for <sup>13</sup>C.

<sup>b</sup>Recorded at 500 MHz for <sup>1</sup>H and 125 MHz for <sup>13</sup>C.

## CHAPTER V: THIELAVINS: TUNED BIOSYNTHESIS AND LR-HSQMBC FOR STRUCTURE ELUCIDATION

Zeinab Y. Al Subeh, Huzefa A. Raja, Amanda Maldonado, Joanna E. Burdette, Cedric J. Pearce, Nicholas H. Oberlies. *The Journal of Antibiotics* 2021. DOI: <https://doi.org/10.1038/s41429-021-00405-6>.

A series of thielavins I, V, and Q (**1-3**) and the previously undescribed thielavin Z<sub>8</sub> (**4**) were isolated from cultures of a fungal *Shiraia*-like sp. (strain MSX60519) that were grown under a suite of media and light conditions, with enhanced biosynthesis noted using rice as a substrate with 12:12 h light:dark cycles. Conversely, oatmeal medium and continuous white LED light exposure negatively affected the production of these compounds, at least by strain MSX60519. The structure of **4** was determined using NMR spectroscopic data and mass fragmentation patterns. Of note, the utility of LR-HSQMBC and NOESY NMR experiments in the structural elucidation of these hydrogen-deficient natural products was demonstrated. Compounds **1-4** exhibited cytotoxic activity at the micromolar level against human breast, ovarian, and melanoma cancer cell lines.

### Introduction

Recently, we evaluated the effect of different fermentation conditions, including varying both culture media and light exposure, on the biosynthesis of perylenequinones, specifically hypocrellins and hypomycins, by the fungus *Shiraia*-like sp. (strain MSX60519).<sup>58, 238</sup> We showed that the production of these fungal metabolites could be tuned based on media and light exposure. For instance, continuous LED exposure led to enhanced production of hypocrellins on rice medium vs hypomycins on oatmeal medium.<sup>58</sup> Previously, those classes of secondary metabolites had not been reported from the same fungus, and it was interesting to see how their biosynthesis could be modulated.

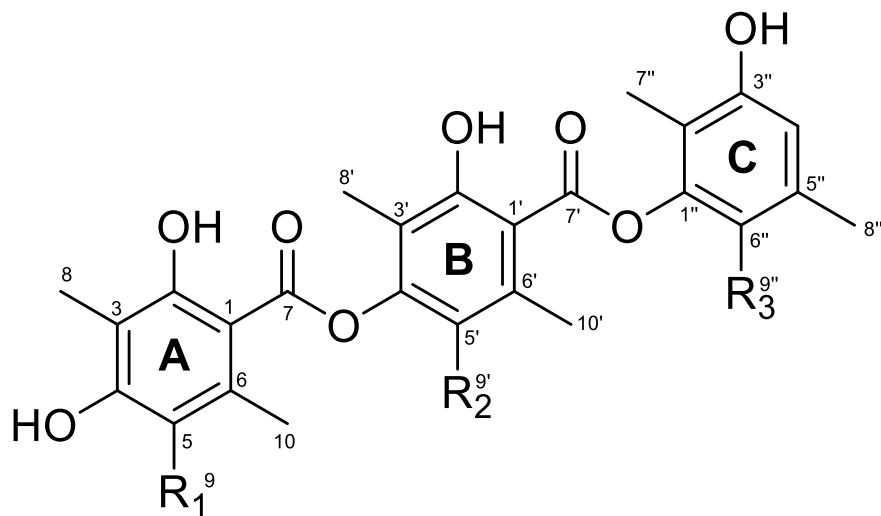
As part of follow-up work, the production of non-perylenequinone secondary metabolites by cultures grown on rice and incubated under 12:12 h light:dark cycles was observed. As described herein, these minor constituents were identified as thielavins I (**1**), V (**2**), and Q (**3**), along with the previously undescribed thielavin Z<sub>8</sub> (**4**). Thielavins are a group of polyphenolic fungal secondary metabolites composed of two or more monocyclic aromatic units linked by ester bonds. A wide-range of biological properties have been reported for thielavins, and these include antimicrobial,<sup>239, 240</sup> antihyperglycemic,<sup>241, 242</sup> antifouling,<sup>243</sup> cytotoxic,<sup>50, 244, 245</sup> and herbicidal activities,<sup>246</sup> inhibition of prostaglandin biosynthesis,<sup>247, 248</sup> and inhibition of indoleamine 2,3-dioxygenase.<sup>249</sup> Given the distinct conditions used to generate **1-4** and the broad range of biological activities, we felt compelled to explore these compounds further.

Despite the description of many thielavins and thielavin-like secondary metabolites since their discovery in 1981,<sup>247, 250</sup> various challenges are associated with their structure elucidation. This is due to the sparsity of <sup>1</sup>H-<sup>1</sup>H coupling, the low hydrogen to carbon ratio, and the abundance of fully-substituted carbons (e.g., ranging from 16 to 19 in **1-4**). Data derived from standard COSY and HMBC NMR experiments may not be enough to derive the full structural assignments of these compounds, leading to at least some incorrect assignments in the literature.<sup>239, 251</sup> As such, the sequence of aromatic units in thielavins have been assigned based on MS fragmentation patterns,<sup>243, 244, 252</sup> and the chemical shifts of ester carbonyls were arbitrarily assigned for most thielavins.<sup>241, 243, 244</sup> Given the prominence of NMR spectroscopy for establishing molecular connectivity,<sup>253, 254</sup> the isolated thielavins (**1-4**) were used to test the power of a relatively new NMR experiment, i.e. long-range heteronuclear single quantum multiple bond correlation (LR-HSQMBC), coupled with NOESY experiments, to assign the full structures of these hydrogen-deficient compounds.

## Results and Discussion

There were a few key goals with these studies. First, we were intrigued with the ability to tune the biosynthesis of distinct fungal metabolites by varying the media and the light source when fermenting *Shiraia*-like sp. (strain MSX60519). In addition, while thielavins are known in the literature, their structure elucidation by NMR can be challenging, especially due to the relatively low number of hydrogens. As such, we strove to evaluate the usefulness of LR-HSQMBC NMR

experiments, coupled with NOESY experiments, to fully assign the structures of these molecules. Finally, the biological activity of **1-4** was evaluated against a suite of human cancer cell lines.



Compound	R <sub>1</sub>	R <sub>2</sub>	R <sub>3</sub>
<b>1</b>	H	CH <sub>3</sub>	CH <sub>3</sub>
<b>2</b>	H	CH <sub>3</sub>	H
<b>3</b>	H	H	H
<b>4</b>	CH <sub>3</sub>	CH <sub>3</sub>	CH <sub>3</sub>

**Figure 5.1.** Structures of compounds **1-4**.

**The Effect of Growth Medium and Light on the Production of Thielavins.** The *Shiraia*-like sp. (strain MSX60519) was grown on three different grain-based media: rice, Cheerios,<sup>184</sup> and breakfast oatmeal (old fashioned Quaker oats). As previously described,<sup>58</sup> these cultures were incubated under three different light conditions in triplicates: 12:12 h light:dark cycles, continuous LED light, and complete darkness. The relative abundance of **1-4** (Fig. 5.1) were evaluated using UPLC-HRESIMS data from the resulting extracts. Cultures grown on rice medium under 12:12 h light:dark cycles showed the highest abundance of **1-4** (Fig. 5.2), suggesting rice as the best medium for the production of thielavins, while oatmeal medium showed the lowest abundance of these compounds. On the other hand, exposure to continuous LED light negatively affected the biosynthesis of thielavins, regardless of culture media (Fig.

5.2). Interestingly, the production of three distinct classes of compounds (i.e., hypocrellins, hypomyces, and thielavins) from *Shiraia*-like sp. was affected differently by the culture medium and light exposure.<sup>58</sup> Enhanced production of hypocrellins was observed in cultures grown on rice and incubated under light:dark cycles or continuous LED light, while hypomyces preferred oatmeal medium and LED light incubation.<sup>58</sup> The optimal growth conditions for enhanced production of thielavins have not been reported extensively in the literature, and with this study, thielavins showed higher abundance in rice-fermentation cultures incubated with regular light:dark cycles. While it is well appreciated that secondary metabolite production in fungi is sensitive to fermentation conditions,<sup>224</sup> biosynthesis experiments with strain MSX60519 were particularly notable in this regard.

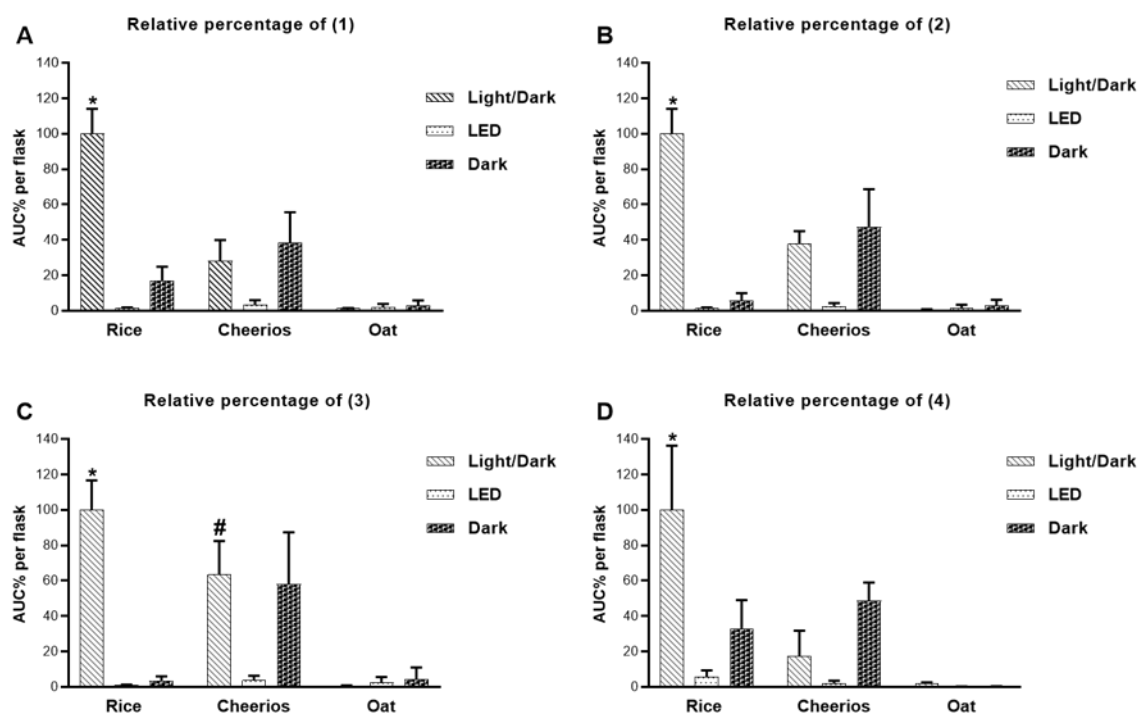


**Figure 5.2.** Panels A-D show the relative percentages of 1-4, respectively, across cultures grown on rice, Cheerios, and oatmeal media under 12:12 h light:dark cycles, continuous LED, or in darkness. The relative percentages were measured by LC-HRMS in three biological replicates and multiplied by the extract weight, and then normalized according to the extract with highest abundance. \* Indicates significantly higher productions of 1-4 by cultures grown on rice under 12:12 h light:dark cycles as compared to other growth conditions ( $p < 0.05$ ). # Indicates statistically no difference in thielavin production as compared to culture grown rice under 12:12 h light:dark cycles. Data are presented as mean  $\pm$  SD.

**Structure Elucidation of 1-4.** Compound **1** was obtained as white amorphous powder. The HRESIMS and NMR data of **1** suggested that it belonged to the thielavin class of natural products (Figs. 5.6-5.7 and Table 5.3), which our team had studied previously.<sup>244</sup> For instance, key features apparent in the <sup>13</sup>C NMR spectrum included the presence of two ester carbonyl moieties, 18 aromatic carbons, and 8 aryl methyls. In addition, the HMBC correlations exhibited by methyl groups and aromatic hydrogens (Fig. 5.8) suggested that **1** was thielavin I, which was reported previously from the fungus *Chaetomium carinthiacum*.<sup>241</sup> However, the collected and reported <sup>1</sup>H and <sup>13</sup>C NMR data did not align perfectly (Table 5.4), possibly due to differences in referencing based on residual solvent signals. Moreover, as discussed below, we were able to more fully assign the structure, and those data are reported in comparison to the literature, to facilitate the identification of this compound in the future (see Tables 5.3 and 5.4).

While these oligomeric molecules may appear relatively simple, there are several challenges to assigning their structures completely. To start, the structural similarities between the aromatic units within and/or between thielavins results in only subtle differences, typically the presence, absence, or variable position of a methyl moiety. This is compounded by the fact that they are hydrogen deficient, and this renders the COSY NMR spectrum (and even coupling constants from the <sup>1</sup>H NMR spectrum) of limited value due to the lack of <sup>1</sup>H-<sup>1</sup>H coupling. Moreover, even with typical heteronuclear experiments, insufficient HMBC correlations could lead to erroneous structural assignments, as was the case with thielavins Q and R.<sup>239, 251</sup>

To address these challenges, the usefulness of the LR-HSQMBC NMR experiment was evaluated. As the name indicates, LR-HSQMBC is a recently developed NMR experiment that provides long-range correlation data across 4-, 5-, and even 6-bond heteronuclear couplings,<sup>255</sup> and it has been used to enhance the structure elucidation of hydrogen-deficient molecules.<sup>256-258</sup> The LR-HSQMBC spectrum of **1** (Fig. 5.9) showed correlations of H-5, H<sub>3</sub>-10, H<sub>3</sub>-8', and H<sub>3</sub>-9' with the carbonyl at C-7 ( $\delta_c$  171.2), which confirmed the connection between rings A and B (Fig. 5.3). The connection between rings B and C was supported by the LR-HSQMBC correlations of H<sub>3</sub>-10', H<sub>3</sub>-7'', and H<sub>3</sub>-9'' with the carbonyl at C-7' ( $\delta_c$  169.5). Thus, the LR-HSQMBC experiment of **1** confirmed the sequence of the rings and the assignment of the two separate carbonyl moieties (i.e., C-7 and C-7') (Table 5.3); this was further evidence that the assignments for this compound reported previously could be improved (Table 5.4).<sup>241</sup>

Additionally, the HRESIMS fragmentation data of **1** were supportive of the sequence of the rings (Fig. 5.19).

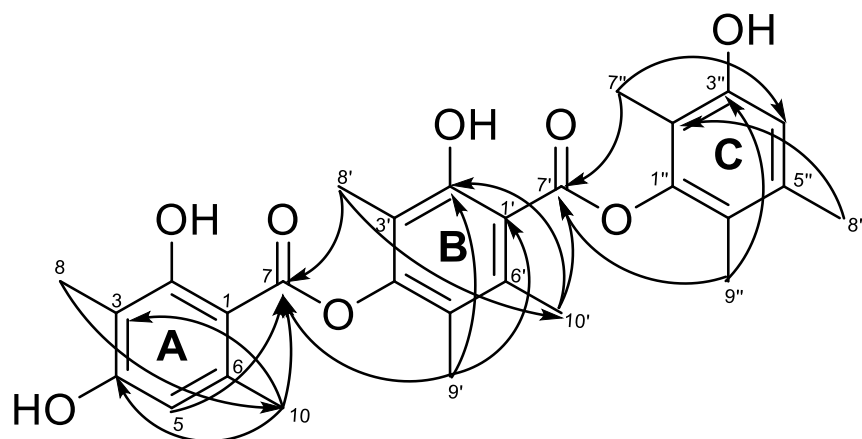


**Figure 5.3.** Key LR-HSQC correlations of compound **1**.

Compound **2** was a white powder with a molecular formula  $C_{27}H_{28}O_8$  as deduced by HRESIMS (Fig. 5.6).  $^1H$  and  $^{13}C$  NMR spectra collected in  $CD_3OD$ , identified **2** as thielavin V (Fig. 5.10), which was reported previously from a *Setophoma* sp.<sup>252</sup> Thielavin V (**2**) differs from **1** by the lack of a  $9''$ - $CH_3$  and the presence of an extra aromatic hydrogen at the  $6''$  position. Table 5.5 compares the collected and literature NMR data of **2**, and the HRESIMS fragmentation data of **2** were supportive of this structural assignment (Fig. 5.19).

Compound **3** was isolated as a white amorphous powder. The molecular formula of **3** was deduced by HRESIMS data (Fig. 5.6) and 1D and 2D NMR data (Figs. 5.11-5.13), indicating that **3** matched the structure of thielavin Q. This was first reported in 2011, and the structure was later revised in 2013 based on new HMBC correlations.<sup>239, 251</sup> The previously reported  $^1H$  and  $^{13}C$  NMR data of thielavin Q (**3**) were measured in two different solvents ( $CD_3OD$  for  $^1H$  and a 9.75 to 0.25 mixture of  $CDCl_3/CD_3OD$  for  $^{13}C$ ). Herein, we report the  $^1H$  and  $^{13}C$  NMR data for **3** in  $CDCl_3$  for more convenient identification of this compound in the future (Table 5.3). In addition, the HRESIMS fragmentation data of **1** were supportive of this structural assignment (Fig. 5.19).

The molecular formula of **4** was deduced as  $C_{29}H_{32}O_8$  by HRESIMS data (Fig. 5.6), suggesting the same index of hydrogen deficiency (i.e., 14) as observed for **1-3**. The  $^1H$  and  $^{13}C$  NMR data

of **4** indicated nine aryl methyls, one aromatic hydrogen, and four hydroxy groups (Table 5.1 and Fig. 5.14). The two chelated and exchangeable hydrogens at  $\delta_{\text{H}}$  11.59 (2-OH) and 11.42 (2'-OH) suggested a hydroxy group  $\beta$  to each ester (i.e., C-7 and C-7'). The HMBC correlations of three methyl groups [H<sub>3</sub>-8 ( $\delta_{\text{H}}$  2.18) to C-2, C-3, and C-4; H<sub>3</sub>-9 ( $\delta_{\text{H}}$  2.23) to C-4, C-5, and C-6; and H<sub>3</sub>-10 ( $\delta_{\text{H}}$  2.67) to C-1, C-5, and C-6] and the two hydroxys [2-OH ( $\delta_{\text{H}}$  11.59) to C-1, C-2, and C-3; and 4-OH ( $\delta_{\text{H}}$  5.30) to C-3, C-4, and C-5] indicated the presence of a 2,4-dioxygenated-3,5,6-trimethylbenzoyl ring (i.e., ring A). Similarly, the HMBC correlations of three methyl groups [H<sub>3</sub>-8' ( $\delta_{\text{H}}$  2.13) to C-2', C-3', and C-4'; H<sub>3</sub>-9' ( $\delta_{\text{H}}$  2.14) to C-4', C-5', and C-6'; and H<sub>3</sub>-10' ( $\delta_{\text{H}}$  2.70) to C-1', C-5', and C-6'] and a chelated hydroxy [2'-OH ( $\delta_{\text{H}}$  11.42) to C-1', C-2', and C-3'] confirmed the structure of ring B as a 2',4'-dioxygenated-3',5',6'-trimethylbenzoyl moiety (Figs. 5.4 and 5.16). The third aromatic ring (i.e., ring C) was found to have three methyl groups attached to C-2'', C-5'', and C-6'' based on HMBC correlations (Fig. 5.4), in addition to the oxygenated carbon at C-1'' and a hydroxylated carbon at C-3''. The oxygenated C-4' in ring B was linked with C-1 in ring A through an ester linkage, while another ester bond formed the connection of ring B at C-1' with ring C at C-1''. The LR-HSQMBC spectrum of **4** showed four-bond heteronuclear couplings of H<sub>3</sub>-10 and H<sub>3</sub>-10' with the C-7 and C-7' carbonyls, respectively (Figs. 5.17-5.18). However, the correlations of CH<sub>3</sub>-8', -9', -7'', and -9'' with the ester linkages was not very clear, which might be attributed to the paucity of sample, relative to what was used for the same experiment on **1**. Compound **4** was ascribed the trivial name thielavin Z<sub>8</sub>.

**Table 5.1.** <sup>1</sup>H (700 MHz) and <sup>13</sup>C (175 MHz) NMR data of **4** in CDCl<sub>3</sub>.

no.	Ring A		no.	Ring B		no.	Ring C	
	$\delta_{\text{C}}$ , type	$\delta_{\text{H}}$		$\delta_{\text{C}}$ , type	$\delta_{\text{H}}$		$\delta_{\text{C}}$ , type	$\delta_{\text{H}}$
1	104.6, C		1'	110.3, C		1''	148.4, C	
2	161.5, C		2'	160.7, C		2''	114.0, C	
3	107.8, C		3'	117.0, C		3''	152.0, C	
4	158.0, C		4'	152.9, C		4''	115.0, C	6.61, s
5	115.7, C		5'	138.4 or 138.5		5''	120.8, C	
6	138.4 or 138.5, C		6'	121.4, C		6''	136.0, C	
7	170.5, C		7'	170.5, C		7''	9.8, CH <sub>3</sub>	2.07, s
8	8.2, CH <sub>3</sub>	2.18, s	8'	10.0, CH <sub>3</sub>	2.13, s	8''	20.1, CH <sub>3</sub>	2.26, s
9	12.2, CH <sub>3</sub>	2.23, s	9'	13.7, CH <sub>3</sub>	2.14, s	9''	12.8, CH <sub>3</sub>	2.03, s

10	19.5, CH <sub>3</sub>	2.67, s	10'	19.6, CH <sub>3</sub>	2.70, s	3''-OH	4.62, s
2-OH		11.59, s	2'-OH		11.42, s		
4-OH		5.30, s					

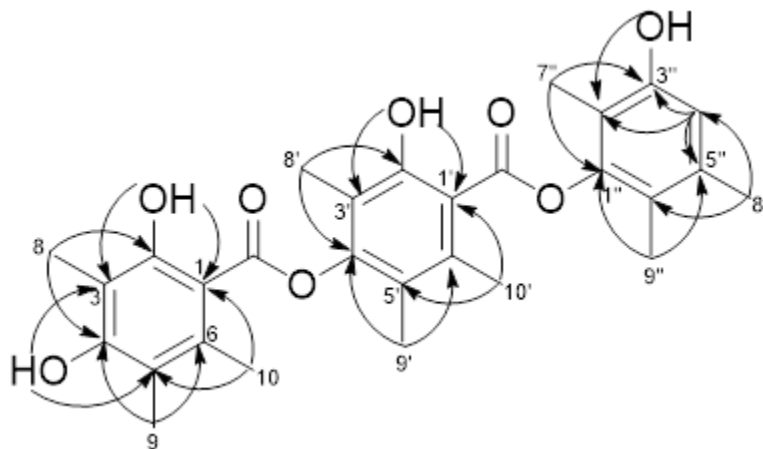


**Figure 5.4.** Key HMBC correlations of compound **4**.

In the literature, NOESY NMR data were not typically collected for thielavins, probably because these molecules lack asymmetric centers. However, NOESY experiments can be used to facilitate the structure elucidation of these compounds, as shown for **3** and **4** (Fig. 5.5). The NOESY spectra of these two compounds showed intra-ring and inter-ring correlations among the methyl groups, aromatic hydrogens, and/or hydroxy groups attached to rings A, B, and C (Figs. 5.20 and 5.21), confirming the positions of the aromatic substituents in **3** and **4** (Fig. 5.5). Compound **4**, for instance, showed NOESY correlations between 2-OH/H<sub>3</sub>-8, H<sub>3</sub>-8/4-OH, 4-OH/H<sub>3</sub>-9, and H<sub>3</sub>-9/H<sub>3</sub>-10 in ring A. Similar correlations were exhibited by the substituents attached to rings B and C (Fig. 5.5). On the other hand, inter-ring NOESY correlations between H<sub>3</sub>-10/H<sub>3</sub>-8' and H<sub>3</sub>-10'/H<sub>3</sub>-7'' in **4** confirmed the sequence of rings A, B, and C, and these conclusions were confirmed via MS fragmentation patterns (Fig. 5.19). Overall, while somewhat non-traditional, NOESY correlations can be used as an orthogonal means for confirming the structures of thielavins.

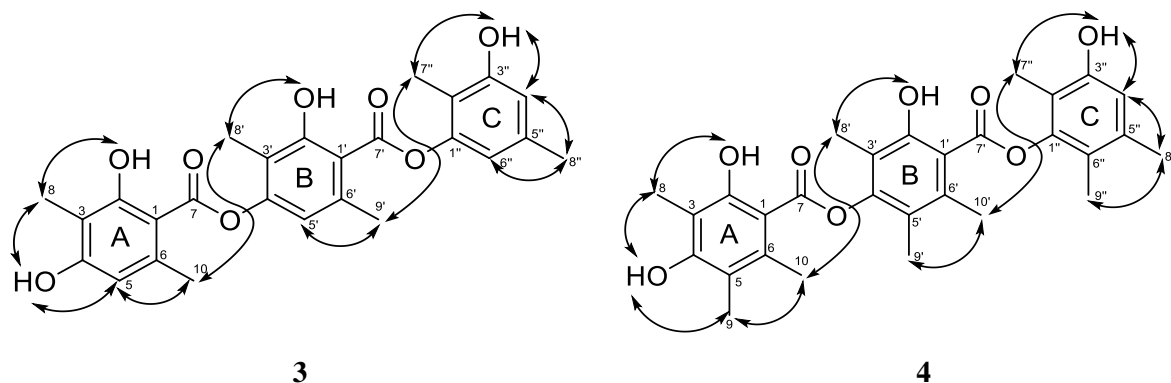


**Figure 5.5.** Intra- and inter-ring NOESY correlations for **3** and **4**.

**Cytotoxic Activities of Thielavins 1-4.** The cytotoxic activities of **1-4** were evaluated against three cancer cell lines, including MDA-MB-231 (human breast cancer), OVCAR3 (human ovarian cancer), and MDA-MB-435 (human melanoma cancer). Compounds **1-4** exhibited moderate cytotoxic activities, ranging between 8-24  $\mu\text{M}$  (Table 5.2). The difference between **1** and **2** is only a single methyl group in ring C, suggesting this may improve cytotoxicity in the latter, albeit only slightly.

**Table 5.2.**  $\text{IC}_{50}$  ( $\mu\text{M}$ ) values of **1-4** against three human cancer cell lines

Compound	MDA-MB-231	OVCAR3	MDA-MB-435
1	24.1	10.6	12.4
2	8.9	4.5	7.8
3	13.8	14.7	18.6
4	14.3	8.2	18.1
taxol	0.6	1.8	0.3

## Conclusion

This study brought to light three new aspects to the thielavin literature. First, we showed the effect of culture medium and light exposure on the production of thielavins by *Shiraia*-like sp., suggesting that fermentation on rice under 12:12 h light:dark cycles enhanced biosynthesis of these compounds. We also expanded the number of thielavins by the identification of thielavin **Z<sub>8</sub>** (**4**). Perhaps more importantly, we showed how LR-HSQMBC and NOESY NMR experiments can be used in a mutually supportive manner to enhance the structural assignments of these hydrogen deficient molecules.

## Materials and Methods

**General Experimental Procedures.** Ultraviolet (UV) spectra were measured using a Varian Cary 100 Bio UV–Vis spectrophotometer (Varian Inc.). 1D and 2D NMR data were obtained using an Agilent 700 MHz NMR spectrometer equipped with a cryoprobe, or a JEOL ECA-500 NMR spectrometer operating at 500 MHz, or a JEOL ECS-400 spectrometer operating at 400 MHz that is equipped with a high-sensitivity JEOL Royal probe and a 24-slot autosampler. Residual solvent signals were used for referencing the NMR spectra. UPLC-HRESIMS data for the culture extracts and the pure compounds **1-4** were collected via a Thermo Fisher Scientific Q Exactive Plus mass spectrometer equipped with an electrospray ionization source (ESI) and connected to a Waters Acquity UPLC system with a BEH Shield RP18 column (Waters, 1.7  $\mu\text{m}$ ; 50  $\times$  2.1 mm) that was heated to 40 °C. The mobile phase consisted of CH<sub>3</sub>CN-H<sub>2</sub>O (0.1% formic acid) using a gradient system of 15:85 to 100:0 over 10 min at a flow rate of 0.3 mL/min. MS data were collected from  $m/z$  150 to 2000, while alternating between positive and negative modes. Analytical and preparative HPLC experiments were carried out using a Varian Prostar HPLC system equipped with ProStar 210 pumps and a Prostar 335 photodiode array detector (PDA). Flash chromatography was carried out using a Teledyne ISCO CombiFlash Rf 200 that was equipped with UV and evaporative light-scattering detectors and using Silica Gold columns.

**Fungal Identification, Fermentation, and Isolation.** Fungal strain MSX60519 was previously identified as a *Shiraia*-like sp. in the family Shiraiaceae, Pleosporales, Dothideomycetes, Ascomycota, as detailed recently.<sup>58</sup> A live culture of this strain is accessioned at Mycosynthetix, Inc. (Hillsborough, NC, USA). The ITS sequences were deposited in GenBank under accession numbers: MN970609 and MN970610.

The media and fermentation studies were described recently.<sup>58</sup> In brief, cultures of strain MSX60519 were grown on three different grain-based media [i.e., rice, Cheerios,<sup>184</sup> and breakfast oatmeal (old fashioned Quaker oats)] using nine cultures per medium, where three were incubated under 12:12 h light:dark cycles, three were placed under white light-emitting diode (LED) lamps (Ustellar, flexible LED strip lights; 24W) to provide continuous light exposure, and three cultures were incubated in complete darkness. Statistical analysis was carried

out using GraphPad Prism (GraphPad Software, La Jolla, CA), and comparisons were made using one-way ANOVA followed by Tukey post-test.

The organic extracts of rice-fermentation cultures incubated under 12:12 h light:dark cycles were defatted and then subjected to fractionation via normal-phase flash chromatography to afford four fractions. The second flash chromatography fraction of each extract was subjected to preparative HPLC over a Phenomenex Synergi C<sub>12</sub> preparative column using an isocratic system of 60:40 of CH<sub>3</sub>CN-H<sub>2</sub>O (0.1% formic acid) for 45 min at a flow rate of 21.2 mL/min to yield thielavin V (**2**, 1.3 mg), thielavin Q (**3**, 1.1 mg), thielavin I (**1**, 10.8 mg), and thielavin Z<sub>8</sub> (**4**, 1.1 mg).

*Thielavin I (1)*: White amorphous powder; <sup>1</sup>H NMR (500 MHz, pyridine-*d*<sub>5</sub>) and <sup>13</sup>C NMR (125 MHz, pyridine-*d*<sub>5</sub>) (see Table 5.3); HRESIMS *m/z* 495.1999 [M + H]<sup>+</sup> (calcd. for C<sub>28</sub>H<sub>31</sub>O<sub>8</sub>, 495.2019).

*Thielavin V (2)*: White amorphous powder; <sup>1</sup>H NMR (500 MHz, CD<sub>3</sub>OD) and <sup>13</sup>C NMR (125 MHz, CD<sub>3</sub>OD) (see Table 5.3); HRESIMS *m/z* 481.1844 [M + H]<sup>+</sup> (calcd. for C<sub>27</sub>H<sub>29</sub>O<sub>8</sub>, 481.1862).

Thielavin Q (**3**): White amorphous powder; UV (MeOH) λ<sub>max</sub> (log ε) 315 (3.69), 276 (4.13), 217 (4.44), 211 (4.38) nm; <sup>1</sup>H NMR (CDCl<sub>3</sub>, 700 MHz) and <sup>13</sup>C NMR (CDCl<sub>3</sub>, 175 MHz) (see Table 5.3); HRESIMS *m/z* 467.1691 [M + H]<sup>+</sup> (calcd. for C<sub>26</sub>H<sub>27</sub>O<sub>8</sub>, 467.1706).

*Thielavin Z<sub>8</sub> (4)*: White amorphous powder; UV (MeOH) λ<sub>max</sub> (log ε) 320 (3.75), 278 (4.16), 217 (4.55) nm; <sup>1</sup>H NMR (CDCl<sub>3</sub>, 700 MHz) and <sup>13</sup>C NMR (CDCl<sub>3</sub>, 175 MHz) (see Table 5.1); HRESIMS *m/z* 509.2156 [M + H]<sup>+</sup> (calcd. for C<sub>29</sub>H<sub>33</sub>O<sub>8</sub>, 509.2175).

**Cytotoxicity Assay.** To evaluate the cytotoxic activity of **1-4**, human melanoma cancer cells MDA-MB-435, human breast cancer cells MDA-MB-231, and human ovarian cancer cells OVCAR3, were purchased from the American Type Culture Collection (Manassas, VA). The cell line was propagated at 37 °C in 5% CO<sub>2</sub> in RPMI 1640 medium, supplemented with fetal bovine serum (10%), penicillin (100 units/mL), and streptomycin (100 μg/mL). Cells in log phase growth were harvested by trypsinization followed by two washes to remove all traces of enzyme. A total of 5,000 cells were seeded per well of a 96-well clear, flat-bottom plate

(Microtest 96, Falcon) and incubated overnight (37 °C in 5% CO<sub>2</sub>). Samples dissolved in DMSO were then diluted and added to the appropriate wells. The cells were incubated in the presence of test substance for 72 h at 37 °C and evaluated for viability with a commercial absorbance assay (CellTiter-Blue Cell Viability Assay, Promega Corp, Madison, WI) that measured viable cells. IC<sub>50</sub> values are expressed in μM relative to the solvent (DMSO) control; taxol (paclitaxel) was used as a positive control.

### **Funding**

This research was supported by the National Institutes of Health via the National Cancer Institute (P01 CA125066).

## Supplementary Data

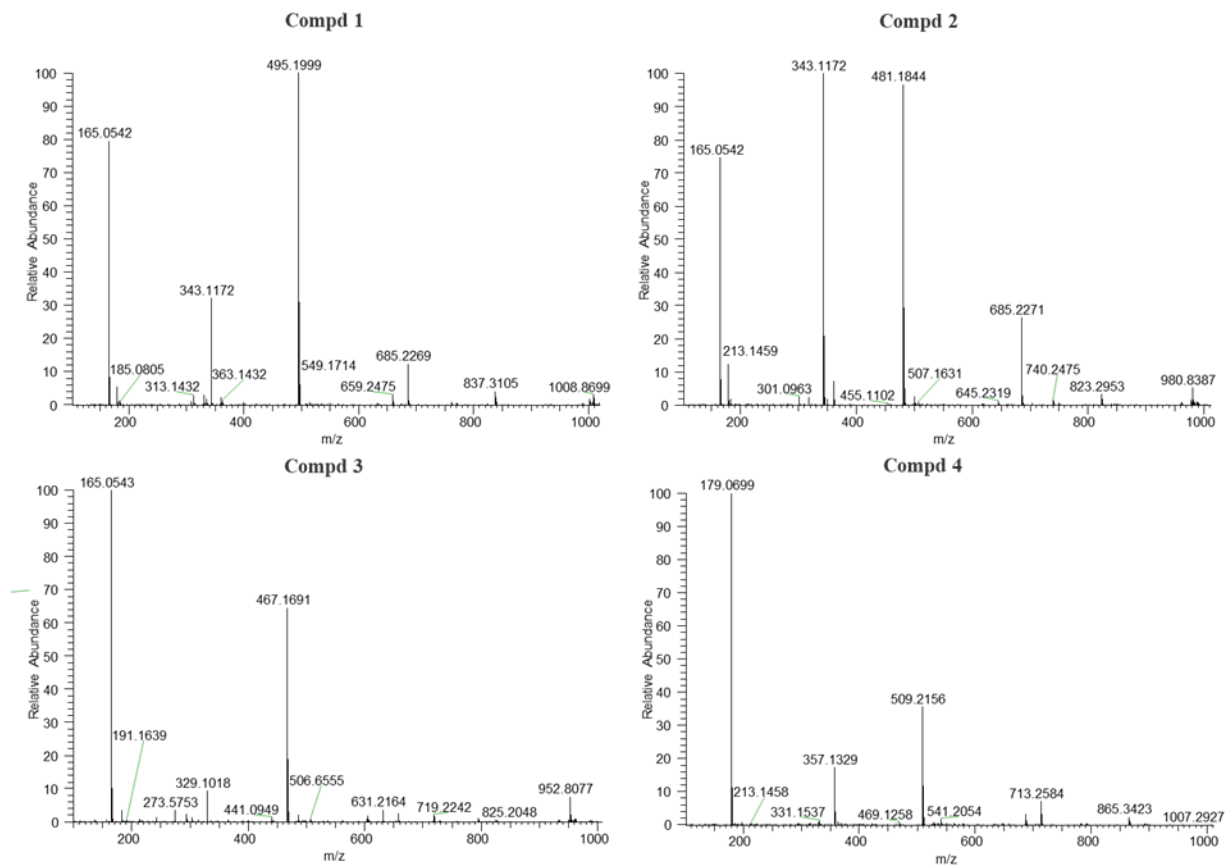


**Figure 5.6.** (+)-HRESIMS data of compounds 1-4.

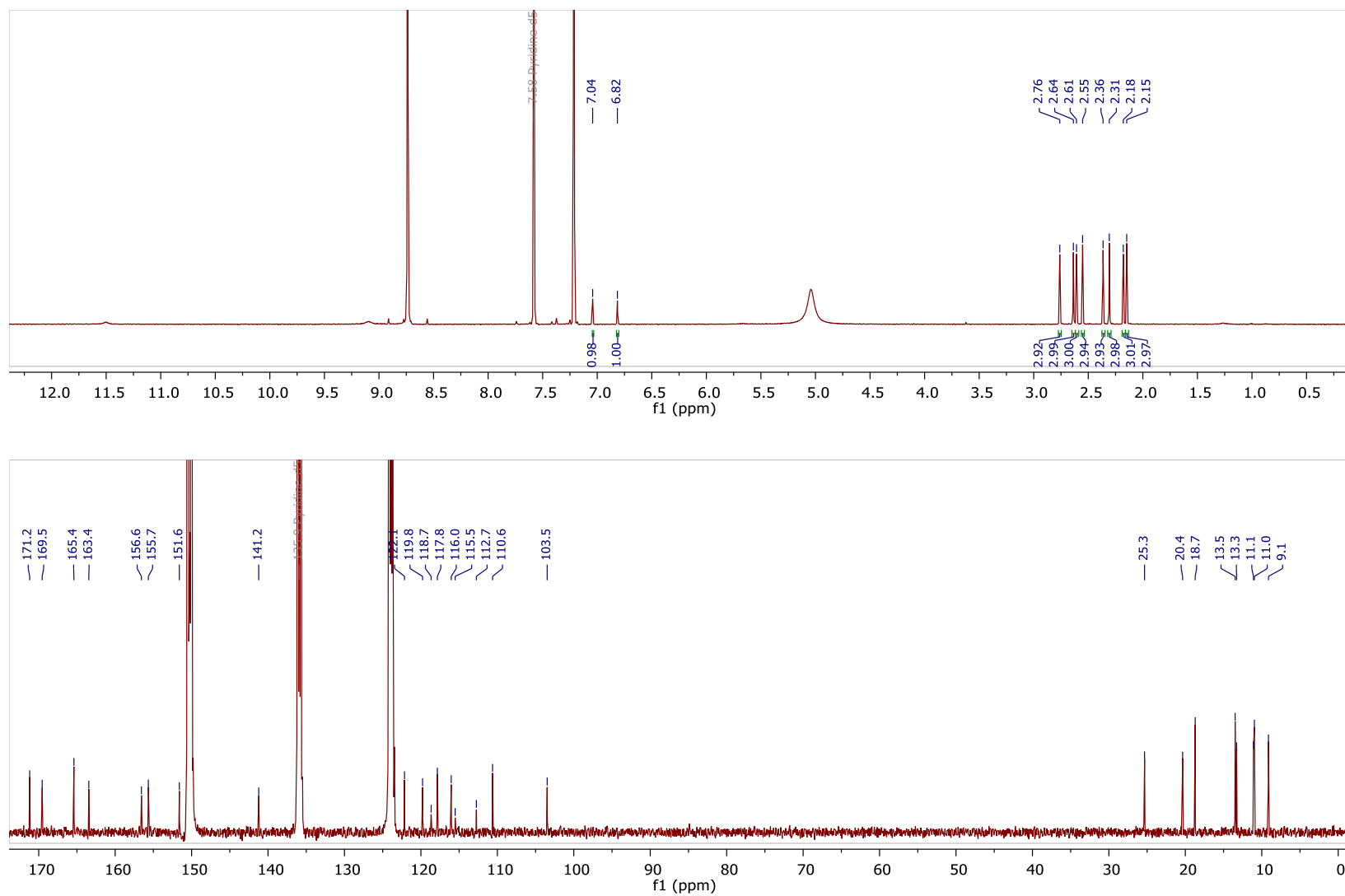


**Figure 5.7.**  $^1\text{H}$  and  $^{13}\text{C}$  NMR spectra of compound **1** [500 MHz for  $^1\text{H}$  and 125 MHz for  $^{13}\text{C}$ , Pyridine- $d_5$ ].

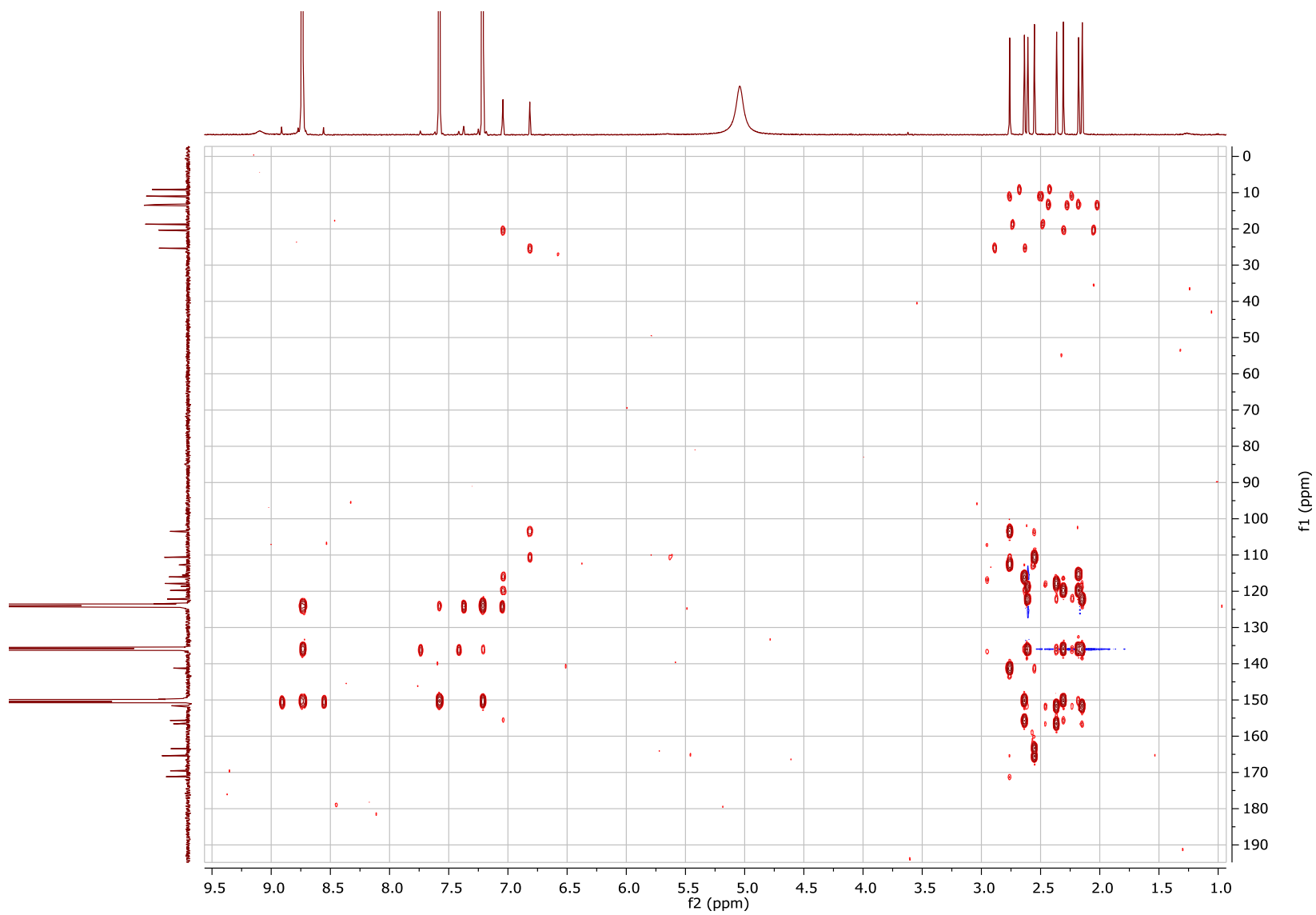


**Figure 5.8.** HMBC NMR spectrum of compound **1** [500 MHz,  $\text{Pyridine-}d_5$ ].

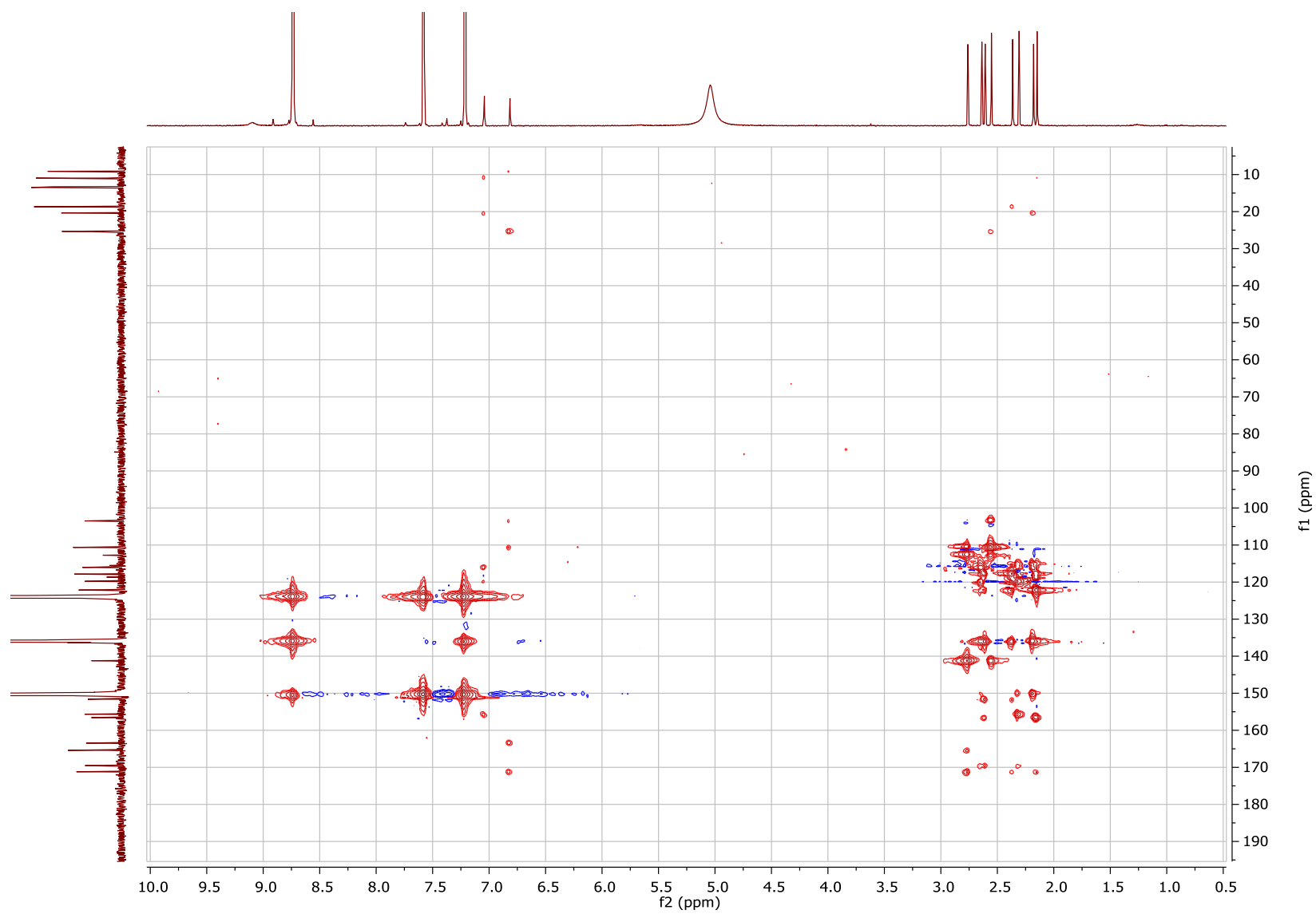


**Figure 5.9.** LR-HSQC NMR spectrum of compound **1** [500 MHz, Pyridine- $d_5$ ].

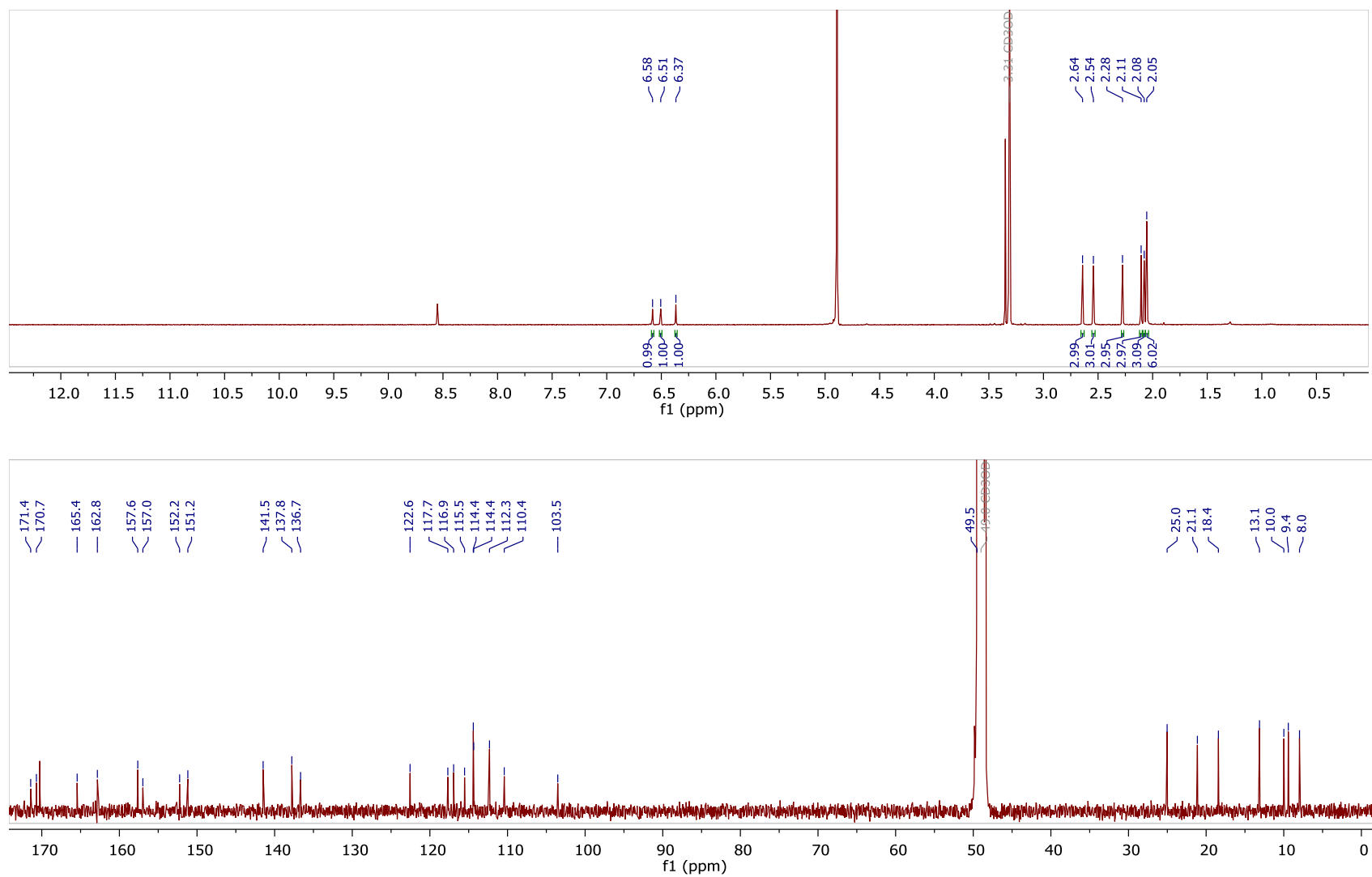


**Figure 5.10.** <sup>1</sup>H and <sup>13</sup>C NMR spectra of compound 2 [500 MHz for <sup>1</sup>H and 125 MHz for <sup>13</sup>C, CD<sub>3</sub>OD].

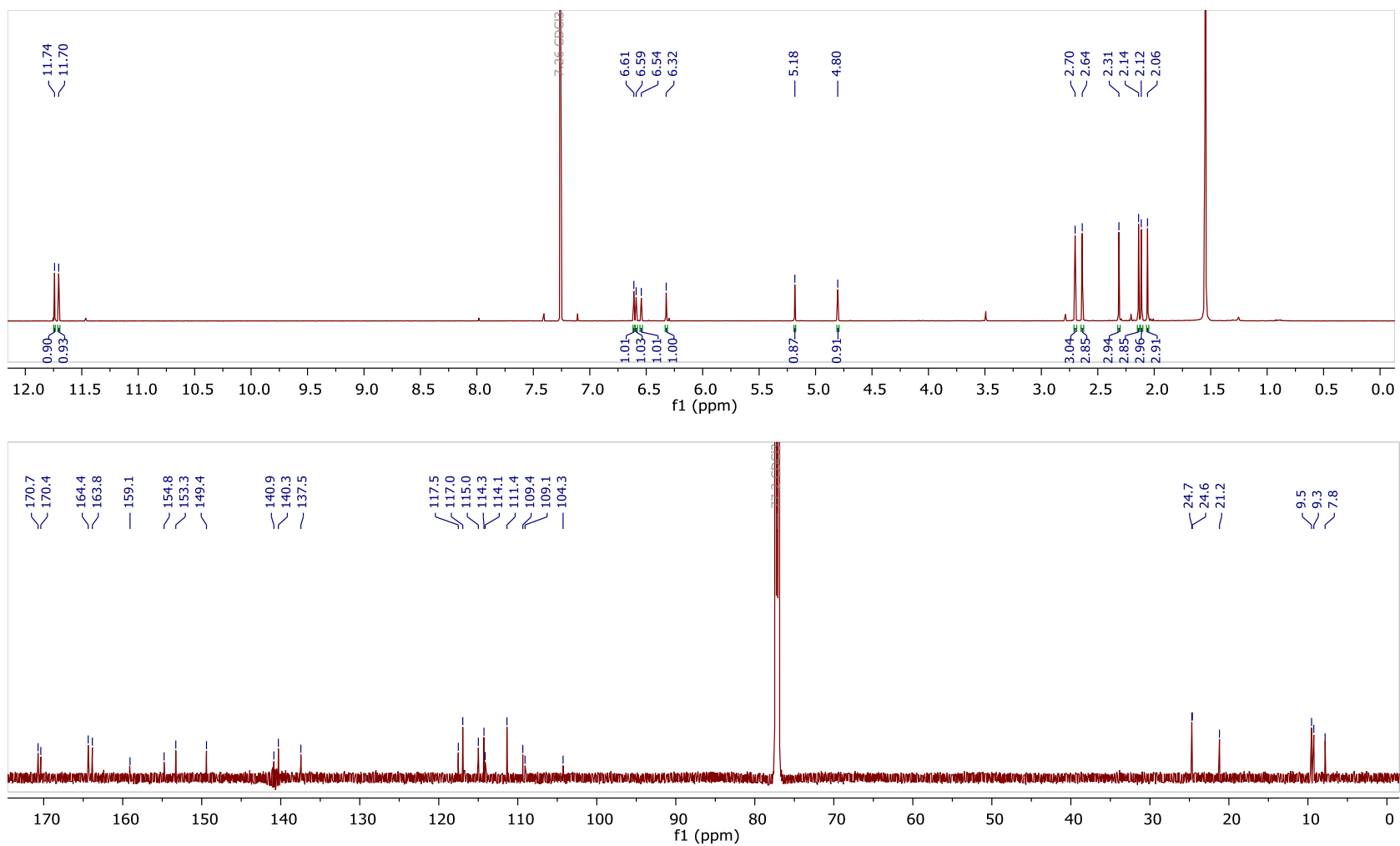


**Figure 5.11.**  $^1\text{H}$  and  $^{13}\text{C}$  NMR spectra of compound **3** [700 MHz for  $^1\text{H}$  and 175 MHz for  $^{13}\text{C}$ ,  $\text{CDCl}_3$ ].

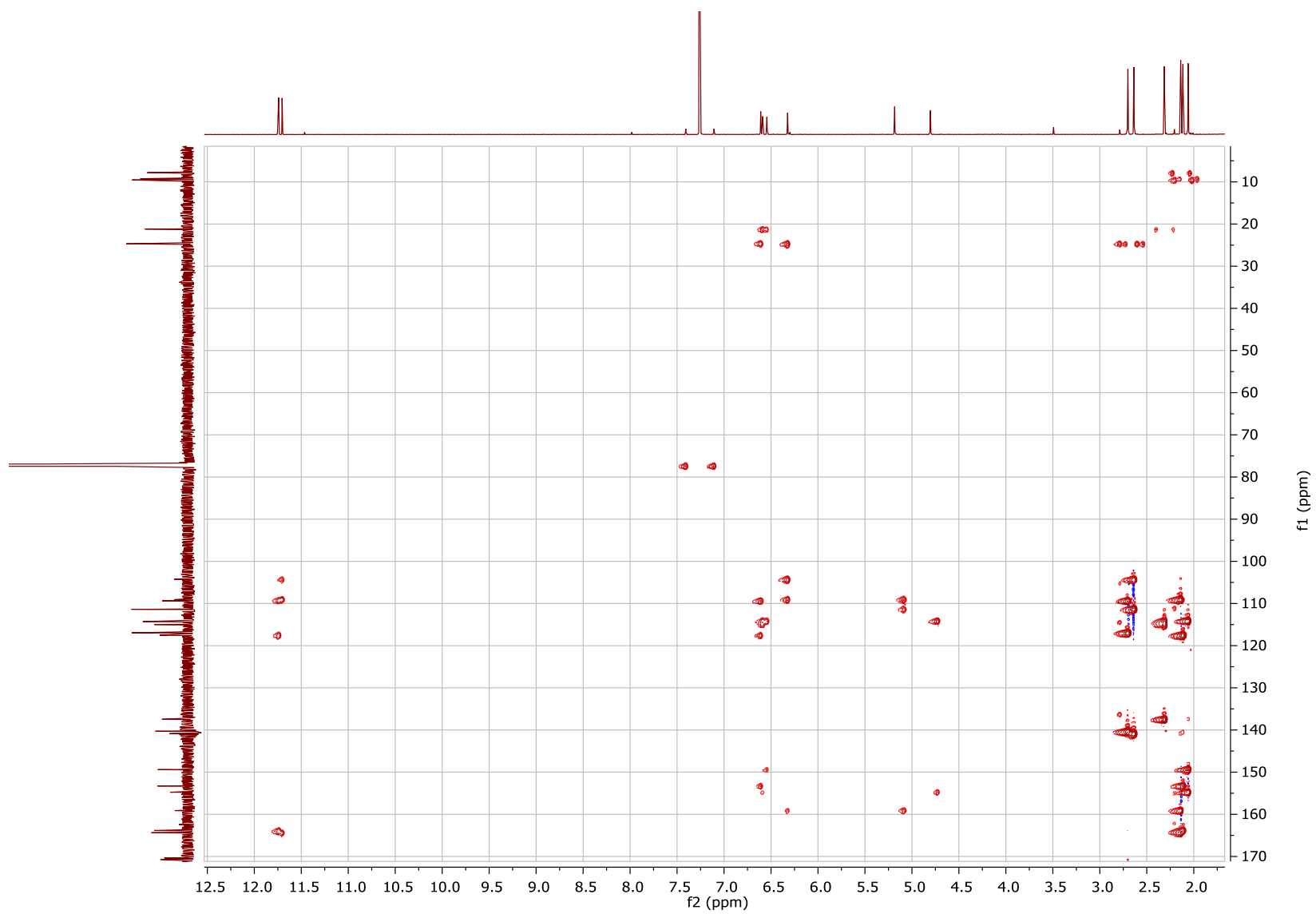


**Figure 5.12.** HMBC NMR spectrum of compound **3** [700 MHz, CDCl<sub>3</sub>].

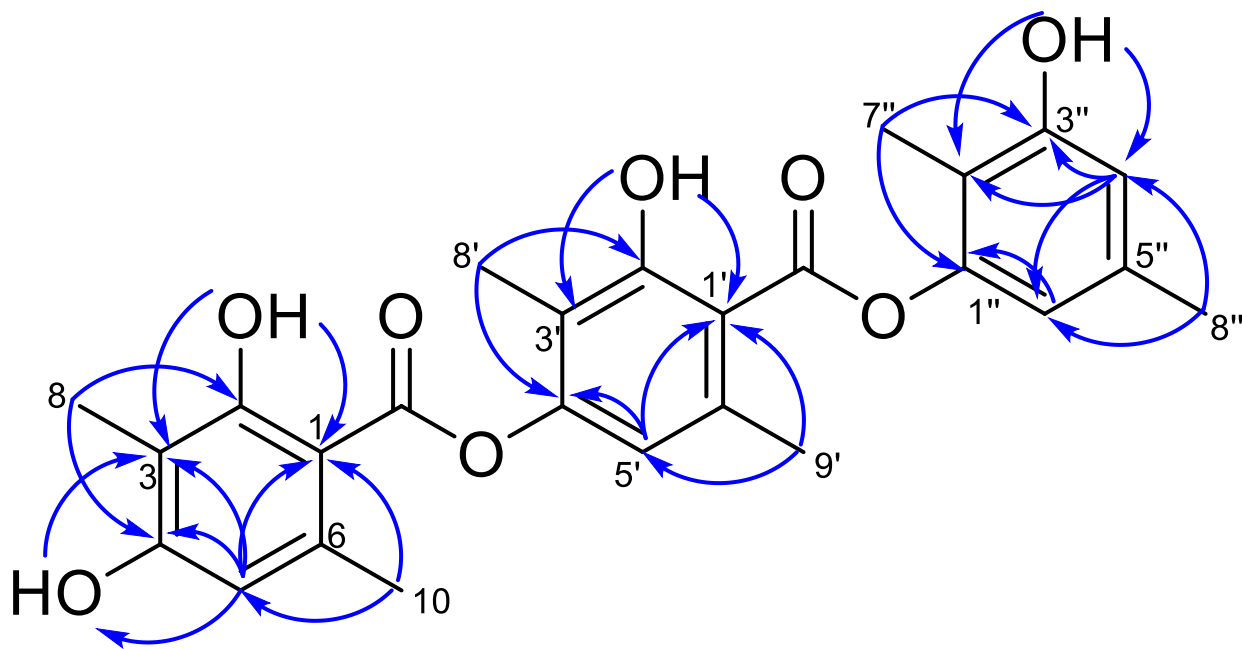


**Figure 5.13.** Key HMBC correlations of compound 3.

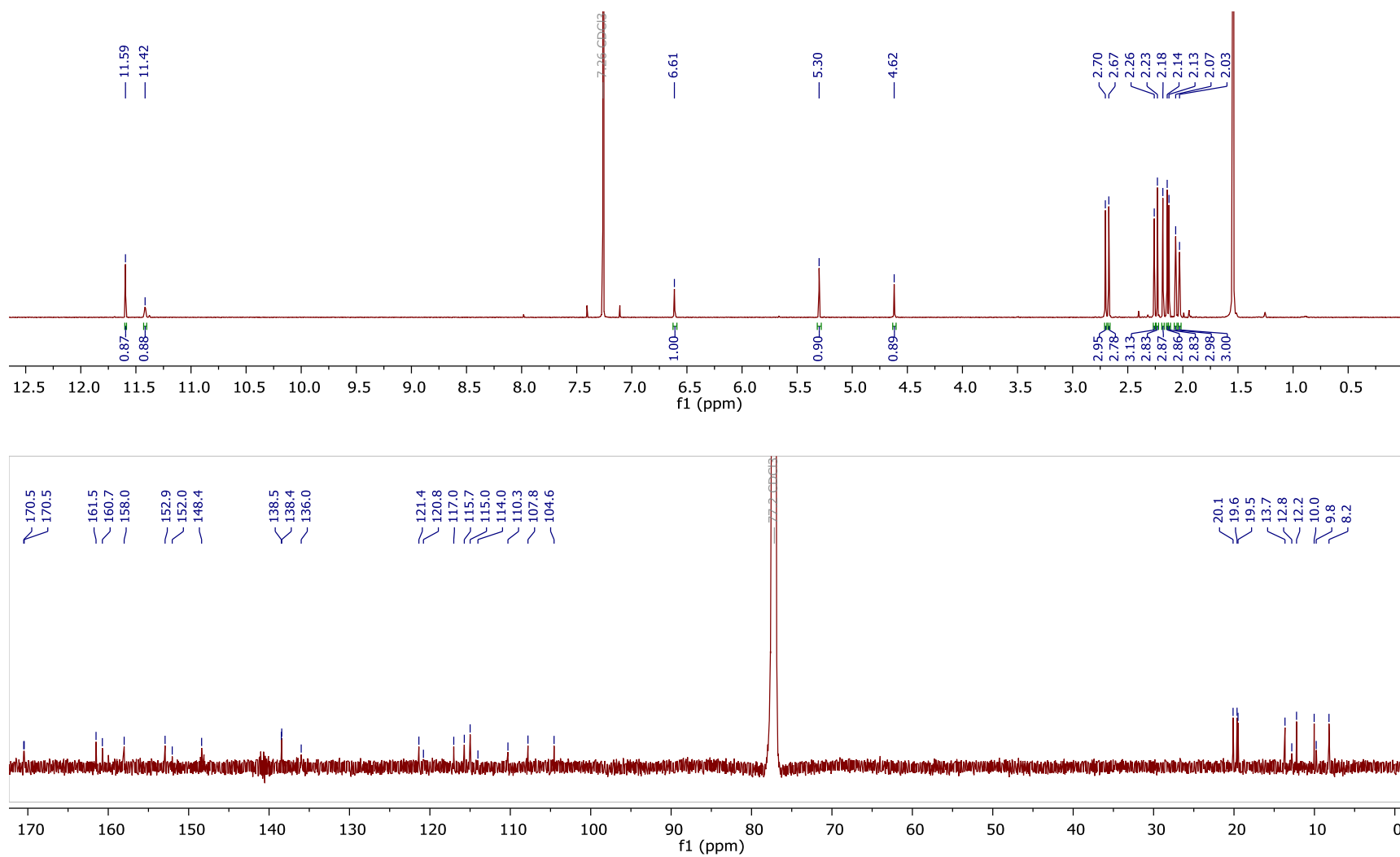


**Figure 5.14.** <sup>1</sup>H and <sup>13</sup>C NMR spectra of compound **4** [700 MHz for <sup>1</sup>H and 175 MHz for <sup>13</sup>C, CDCl<sub>3</sub>].

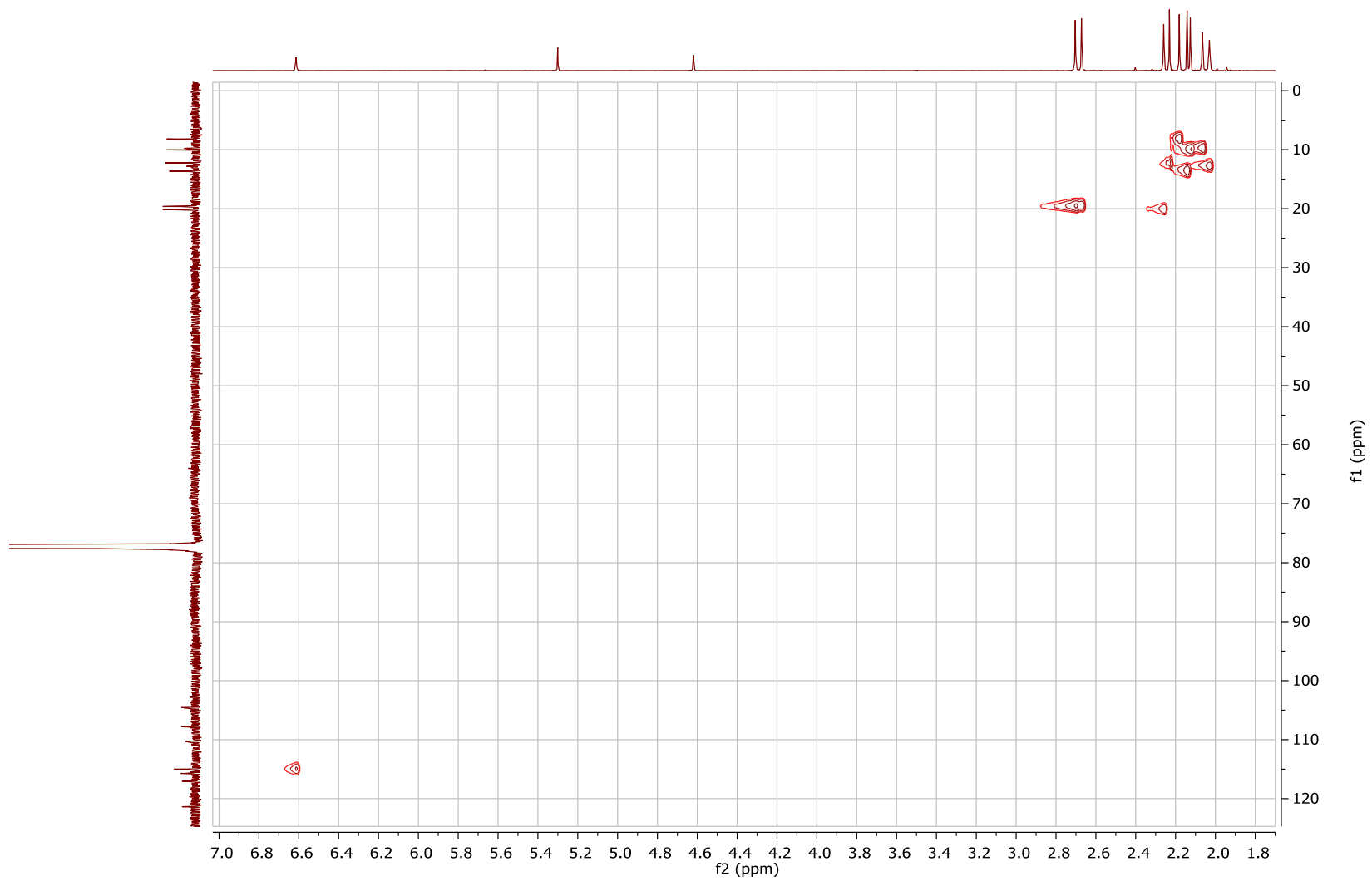


**Figure 5.15.** Edited-HSQC NMR spectrum of compound 4 [700 MHz,  $\text{CDCl}_3$ ].

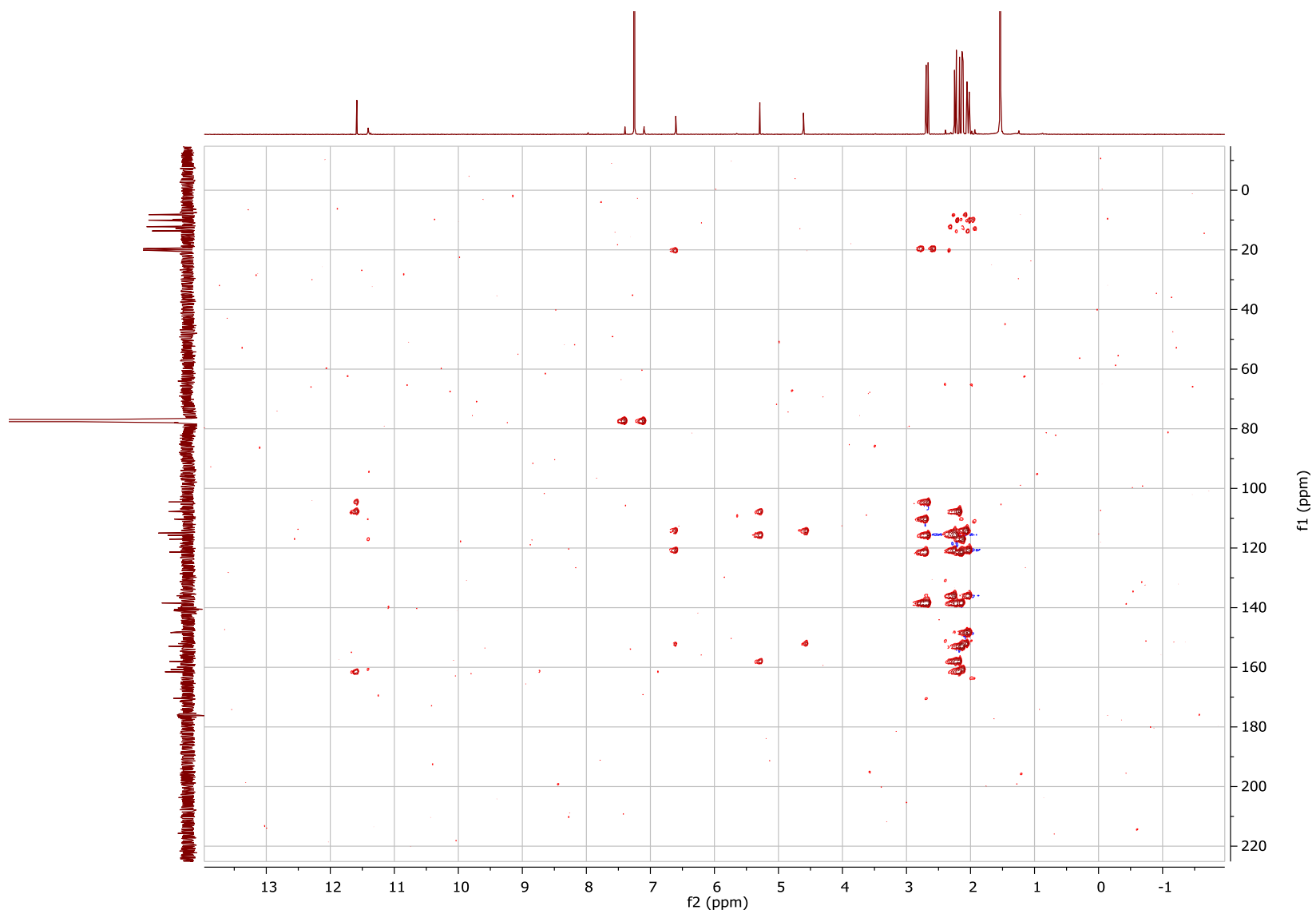


**Figure 5.16.** HMBC NMR spectrum of compound **4** [700 MHz,  $\text{CDCl}_3$ ].

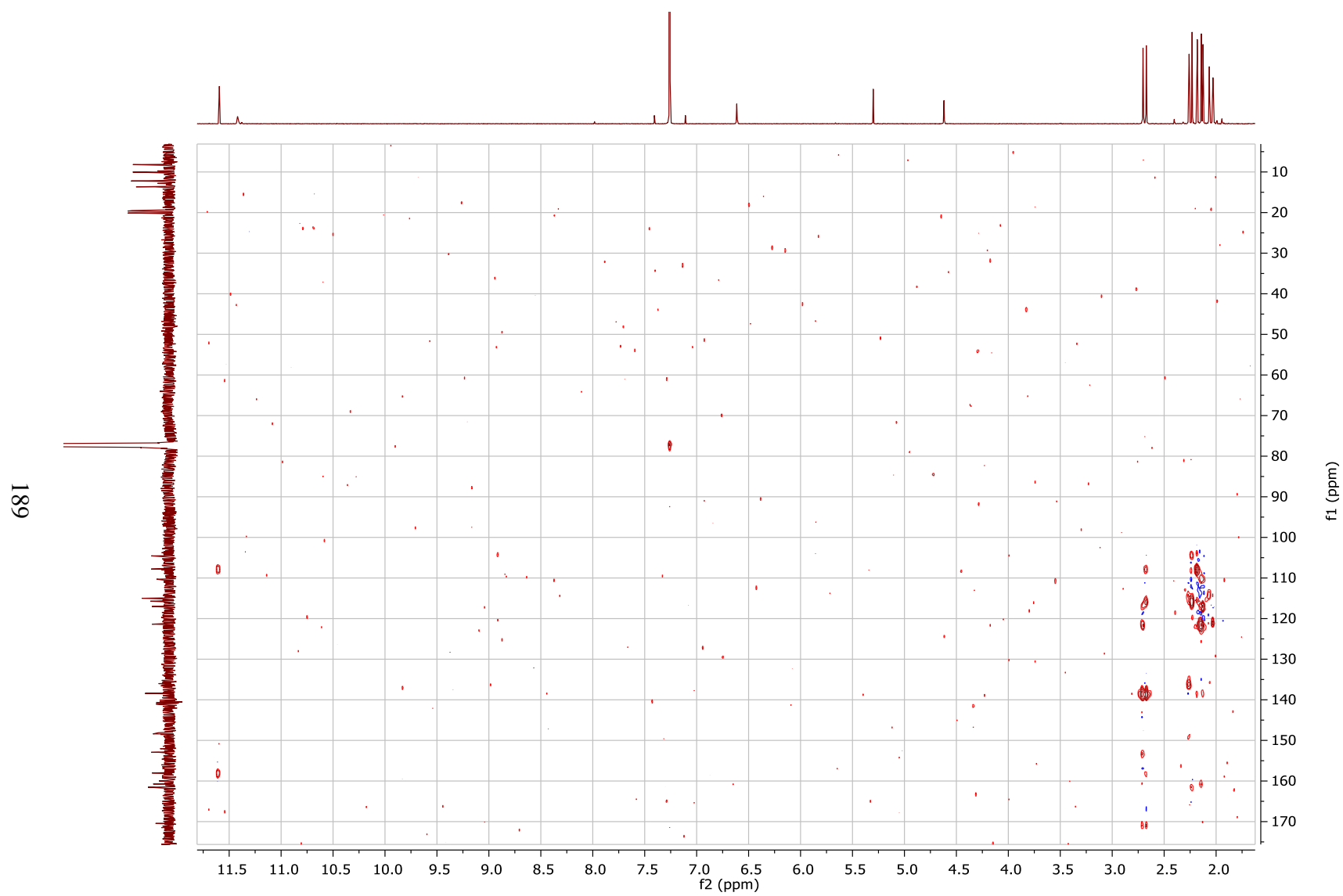


**Figure 5.17.** LR-HSQC NMR spectrum of compound **4** [400 MHz,  $\text{CDCl}_3$ ].

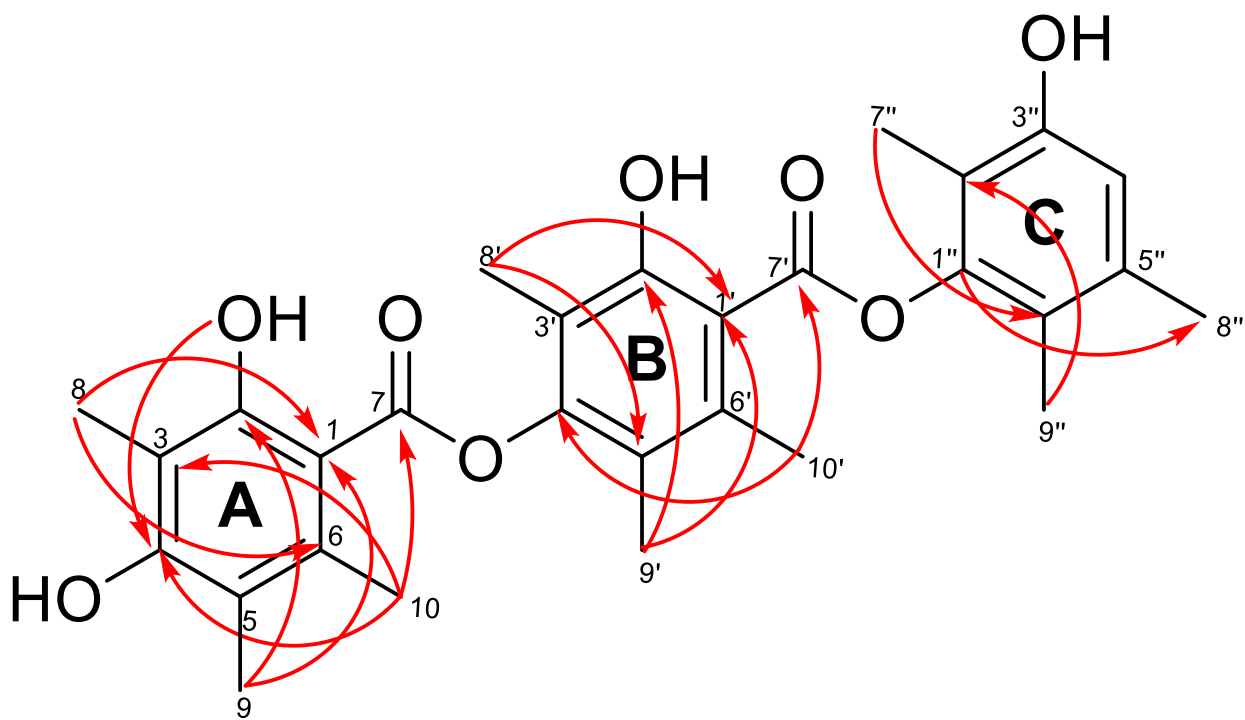
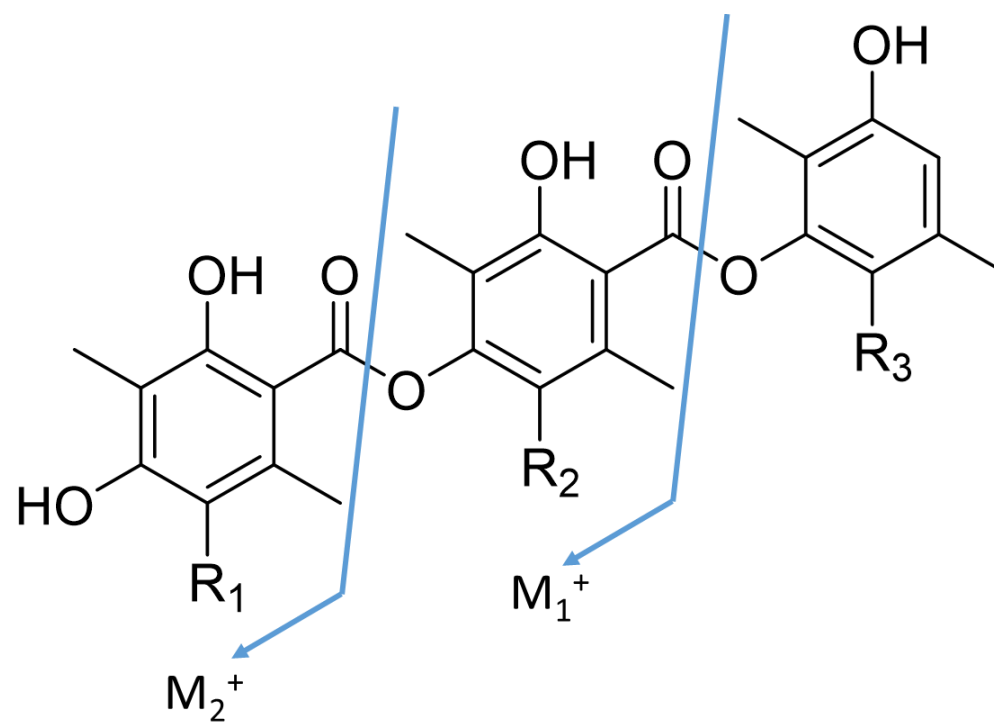


**Figure 5.18.** Key LR-HSQC correlations of compound 4.



Compd	$R_1$	$R_2$	$R_3$	$M_1^+$	$M_2^+$
1	H	CH <sub>3</sub>	CH <sub>3</sub>	343.1172	165.0542
2	H	CH <sub>3</sub>	H	343.1172	165.0542
3	H	H	H	329.1018	165.0543
4	CH <sub>3</sub>	CH <sub>3</sub>	CH <sub>3</sub>	357.1329	179.0699

**Figure 5.19.** (+)-HRESIMS fragmentation of 1-4.

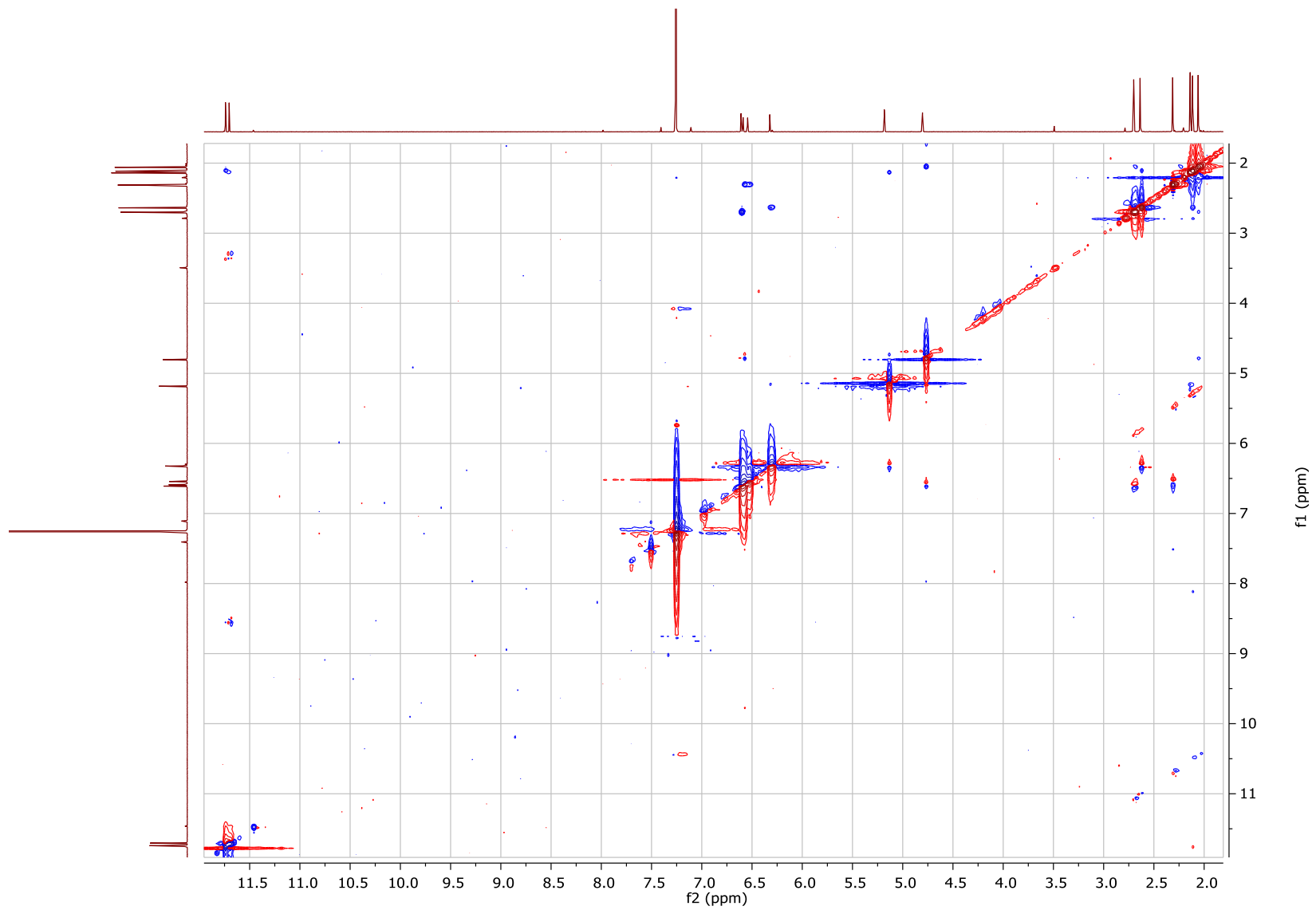


**Figure 5.20.** NOESY NMR spectrum of compound **3** [400 MHz, CDCl<sub>3</sub>].

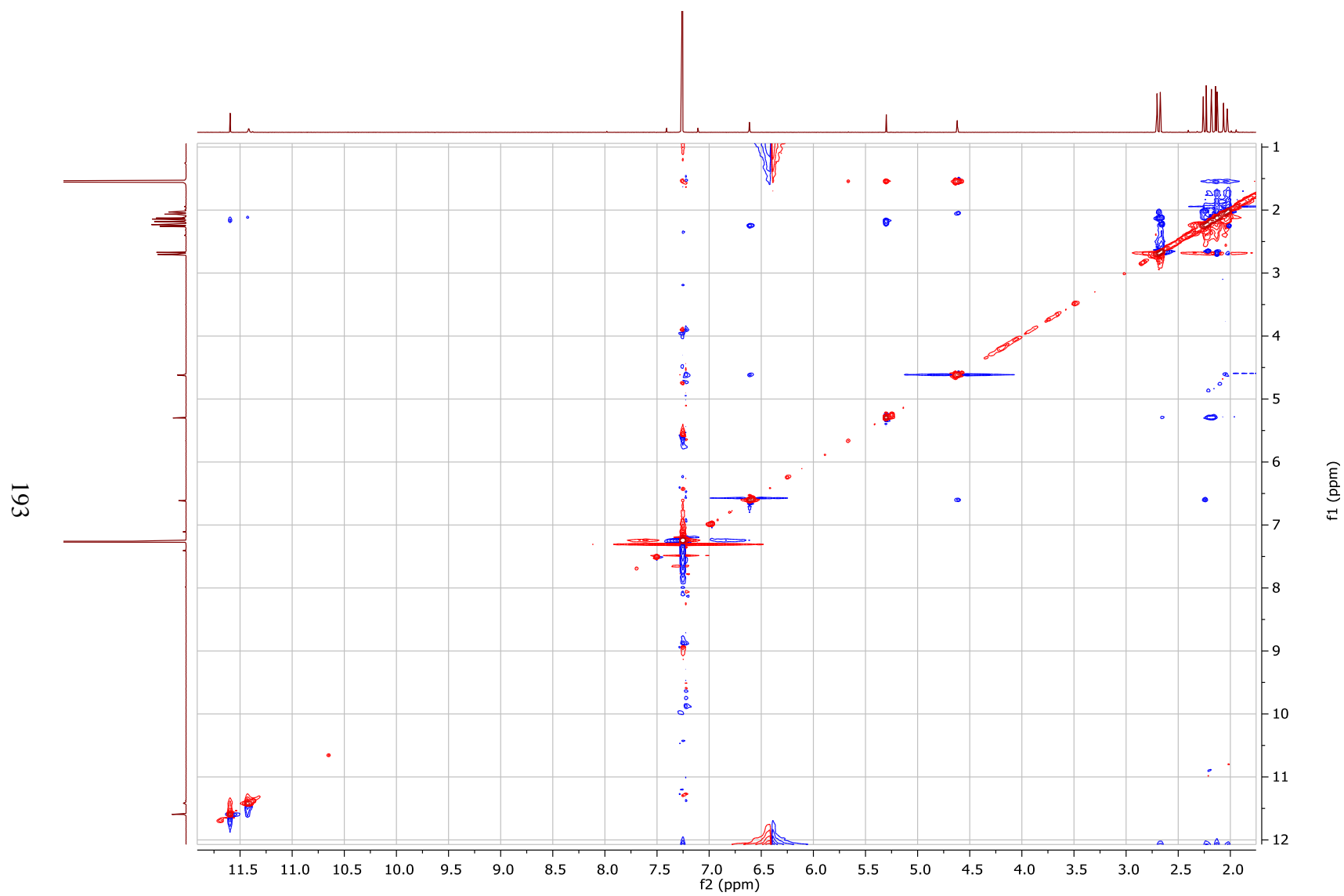


**Figure 5.21.** NOESY NMR spectrum of compound **4** [400 MHz, CDCl<sub>3</sub>].

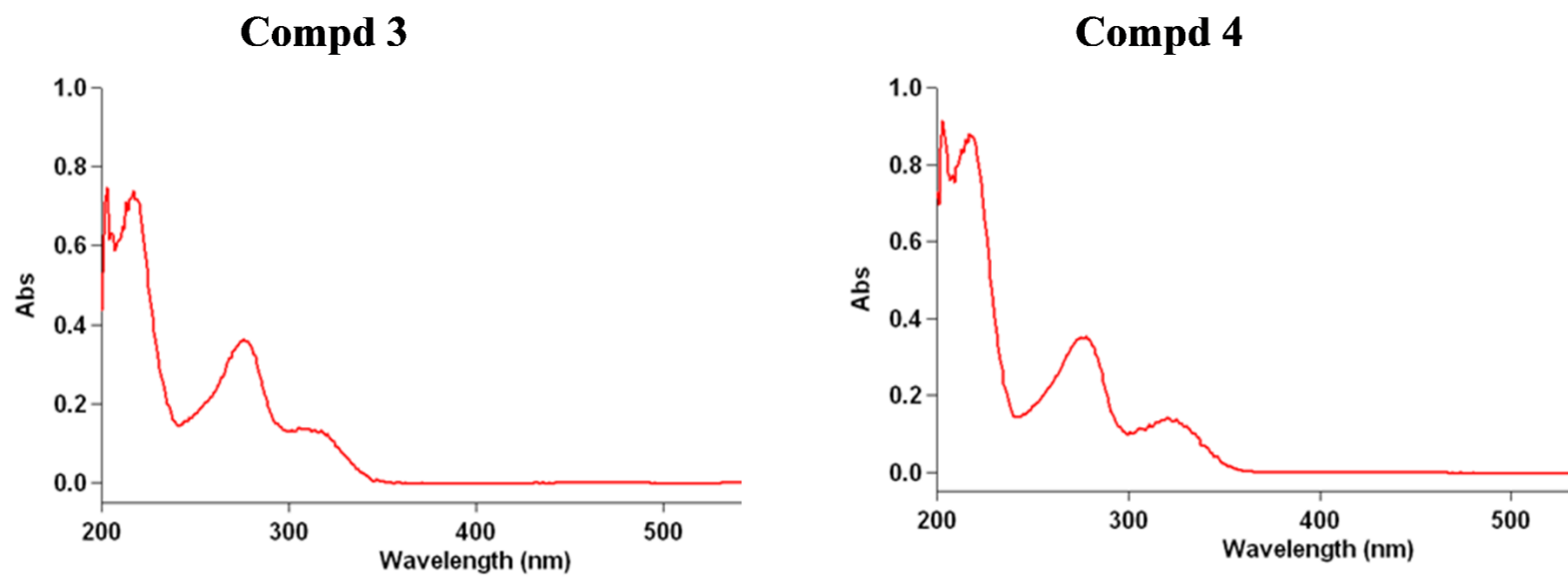


**Figure 5.22.** UV spectra of compounds **3** and **4** analyzed in CH<sub>3</sub>OH (0.0125 mg/mL).

**Table 5.3.**  $^1\text{H}$  and  $^{13}\text{C}$  NMR data of compounds **1-3**.

no.	<b>1<sup>a</sup></b>		<b>2<sup>b</sup></b>		<b>3<sup>c</sup></b>	
	$\delta_{\text{C}}$ , type	$\delta_{\text{H}}$	$\delta_{\text{C}}$ , type	$\delta_{\text{H}}$	$\delta_{\text{C}}$ , type	$\delta_{\text{H}}$
1	103.5, C		103.5, C		104.3, C	
2	165.4, C		165.4, C		164.4, C	
3	110.6, C		110.4, C		109.1, C	
4	163.4, C		162.8, C		159.1, C	
5	112.7, C	6.82, s	112.3, C	6.37, s	111.4, C	6.32, s
6	141.2, C		141.5, C		140.9, C	
7	171.2, C		171.4, C*		170.4, C*	
8	9.1, CH <sub>3</sub>	2.55, s	9.4, CH <sub>3</sub>	2.05, s	7.8, CH <sub>3</sub>	2.14, s
10	25.3, CH <sub>3</sub>	2.76, s	25.0, CH <sub>3</sub>	2.64, s	24.7, CH <sub>3</sub>	2.64, s
1'	118.7, C		116.9, C		109.4, C	
2'	156.6, C		157.0, C		163.8, C	
3'	117.8, C		117.7, C		117.5, C	
4'	151.6, C		152.2, C		153.3, C	
5'	122.1, C		122.6, C		117.0, C	6.61, s
6'	136.0, C		136.7, C		140.3, C	
7'	169.5, C		170.7, C*		170.7, C*	
8'	11.0, CH <sub>3</sub>	2.36, s	10.0, CH <sub>3</sub>	2.08, s	9.5, CH <sub>3</sub>	2.12, s
9'	13.5, CH <sub>3</sub>	2.15, s	13.1, CH <sub>3</sub>	2.11, s	24.6, CH <sub>3</sub>	2.70, s
10'	18.7, CH <sub>3</sub>	2.61, s	18.4, CH <sub>3</sub>	2.54, s		
1''	150.1, C		151.2, C		149.4, C	
2''	116.0, C		115.5, C		114.1, C	
3''	155.7, C		157.6, C		154.8, C	
4''	115.5, C	7.04, s	114.4, C	6.58, s	114.3, C	6.59, s
5''	136.0, C		137.8, C		137.5, C	
6''	119.8, C		114.4, C	6.51, s	115.0, C	6.54, s
7''	11.1, CH <sub>3</sub>	2.64, s	8.0, CH <sub>3</sub>	2.05, s	9.3, CH <sub>3</sub>	2.06, s
8''	20.4, CH <sub>3</sub>	2.18, s	21.1, CH <sub>3</sub>	2.28, s	21.2, CH <sub>3</sub>	2.31, s
9''	13.3, CH <sub>3</sub>	2.31, s				
2-OH						11.70, s
4-OH						5.18, s
2'-OH						11.74, s
3''-OH						4.80, s

\*Assignments could be interchanged.

<sup>a</sup>Recorded at 500 MHz for  $^1\text{H}$  and 125 MHz for  $^{13}\text{C}$  in pyridine- $d_5$ .<sup>b</sup>Recorded at 500 MHz for  $^1\text{H}$  and 125 MHz for  $^{13}\text{C}$  in  $\text{CD}_3\text{OD}$ .<sup>c</sup>Recorded at 700 MHz for  $^1\text{H}$  and 175 MHz for  $^{13}\text{C}$  in  $\text{CDCl}_3$ .

**Table 5.4.** Collected  $^1\text{H}$  and  $^{13}\text{C}$  NMR data of **1** in pyridine- $d_5$  as compared to the literature.

no.	<b>1</b> <sup>a</sup>		<b>1</b> <sup>b</sup>	
	$\delta_{\text{C}}$ , type	$\delta_{\text{H}}$	$\delta_{\text{C}}$ , type	$\delta_{\text{H}}$
1	103.5, C		103.2, C	
2	165.4, C		165.0, C	
3	110.6, C		110.3, C	
4	163.4, C		163.1, C	
5	112.7, C	6.82, s	112.4, C	6.64, s
6	141.2, C		140.9, C	
7	171.2, C		170.8, C*	
8	9.1, CH <sub>3</sub>	2.55, s	8.7, CH <sub>3</sub>	2.37, s
10	25.3, CH <sub>3</sub>	2.76, s	25.0, CH <sub>3</sub>	2.59, s
1'	118.7, C		117.5, C	
2'	156.6, C		156.5, C	
3'	117.8, C		117.8, C	
4'	151.6, C		151.4, C	
5'	122.1, C		121.8, C	
6'	136.0, C		135.6, C	
7'	169.5, C		169.2, C*	
8'	11.0, CH <sub>3</sub>	2.36, s	19.7, CH <sub>3</sub>	2.19, s
9'	13.5, CH <sub>3</sub>	2.15, s	13.1, CH <sub>3</sub>	1.98, s
10'	18.7, CH <sub>3</sub>	2.61, s	10.5, CH <sub>3</sub>	2.44, s
1''	150.1, C		149.7, C	
2''	116.0, C		115.7, C	
3''	155.7, C		155.3, C	
4''	115.5, C	7.04, s	115.2, C	6.86, s
5''	136.0, C		135.6, C	
6''	119.8, C		119.4, C	
7''	11.1, CH <sub>3</sub>	2.64, s	18.4, CH <sub>3</sub>	2.44, s
8''	20.4, CH <sub>3</sub>	2.18, s	20.0, CH <sub>3</sub>	2.01, s
9''	13.3, CH <sub>3</sub>	2.31, s	12.9, CH <sub>3</sub>	2.12, s

\*Assignments could be interchanged.

<sup>a</sup>Collected NMR data

<sup>b</sup>NMR data as reported by Sakemi et al., 2002.<sup>241</sup>

**Table 5.5.** Collected  $^1\text{H}$  and  $^{13}\text{C}$  NMR data of **2** in  $\text{CD}_3\text{OD}$  as compared to the literature.

no.	<b>2</b> <sup>a</sup>		<b>2</b> <sup>b</sup>	
	$\delta_{\text{C}}$ , type	$\delta_{\text{H}}$	$\delta_{\text{C}}$ , type	$\delta_{\text{H}}$
1	103.5, C		103.5, C	
2	165.4, C		165.6, C	
3	110.4, C		110.6, C	
4	162.8, C		163.4, C	
5	112.3, C	6.37, s	112.7, C	6.36, s
6	141.5, C		141.6, C	
7	171.4, C*		171.6, C*	
8	9.4, CH <sub>3</sub>	2.05, s	9.5, CH <sub>3</sub>	2.05, s
10	25.0, CH <sub>3</sub>	2.64, s	25.2, CH <sub>3</sub>	2.63, s
1'	116.9, C		117.0, C	
2'	157.0, C		157.1, C	
3'	117.7, C		117.8, C	
4'	152.2, C		152.4, C	
5'	122.6, C		122.7, C	
6'	136.7, C		136.8, C	
7'	170.7, C*		170.8, C*	
8'	10.0, CH <sub>3</sub>	2.08, s	10.1, CH <sub>3</sub>	2.07, s
9'	13.1, CH <sub>3</sub>	2.11, s	13.2, CH <sub>3</sub>	2.10, s
10'	18.4, CH <sub>3</sub>	2.54, s	18.5, CH <sub>3</sub>	2.54, s
1''	151.2, C		151.3, C	
2''	115.5, C		115.7, C	
3''	157.6, C		157.8, C	
4''	114.4, C	6.58, s	114.5, C	6.58, s
5''	137.8, C		137.9, C	
6''	114.4, C	6.51, s	114.6, C	6.50, s
7''	8.0, CH <sub>3</sub>	2.05, s	8.10, CH <sub>3</sub>	2.05, s
8''	21.1, CH <sub>3</sub>	2.28, s	21.3, CH <sub>3</sub>	2.27, s

\*Assignments could be interchanged.

<sup>a</sup>Collected NMR data

<sup>b</sup>NMR data as reported by de Medeiros et al., 2015.<sup>252</sup>

## CHAPTER VI: REDOX BEHAVIORS OF PERYLENEQUINONES DRIVE THEIR STRUCTURAL DIVERSITY

Zeinab Y. Al Subeh, Amy Waldbusser, Huzefa A. Raja, Cedric J. Pearce, Kin Lok Ho, Michael J. Hall, Michael R. Probert, Nicholas H. Oberlies, and Shabnam Hematian. To be submitted to *the Journal of the American Chemical Society*.

Hypocrellins and hypomyces are two sub-classes of fungal perylenequinones with unique phototoxic properties. Of these, more is known about hypocrellins, which were reported to have phototoxic activity against a variety of cancer cell lines and microbial diseases; only limited pharmacological studies have been reported on hypomyces. With the growing interest in these compounds as naturally-occurring photosensitizers, more studies were needed to better understand the structural relationships between these two subclasses of perylenequinones. In this study, the biosynthetic precursor (**7**) of class B fungal perylenequinones was isolated and characterized from *Shiraiia*-like sp. (strain MSX60519). Furthermore, the electrochemical and chemical redox behaviors of hypocrellins and hypomyces were investigated under aerobic and anaerobic conditions, suggesting the ability of hypocrellins-producing fungi to defend themselves against their own toxins by reducing these photosensitizers. These studies also served to build the structural relationship between hypocrellins (**1-3**), and between hypocrellins and hypomyces (**4-6**). Chemical reductions of hypocrellins under anaerobic conditions identified the origin of hypomyces A (**4**), hypomyces C (**5**), and hypomyces E (**6**), serving to confirm (**4**) and revise (**5** and **6**) absolute configurations. Overall, hypocrellins were shown to possess a fully reversible reduction process, and this may serve to impart self-protection from the toxicity of these molecules.

### **Introduction**

Hypocrellins, a sub-class of perylenequinones, have gained interest in photodynamic therapy as naturally-occurring photosensitizers,<sup>190, 191, 193, 194</sup> with hypocrellin, its enantiomer (hypocrellin A), hypocrellin B, and shiraiachrome A as the main members of this class of fungal metabolites.<sup>221</sup> We recently reported the first isolation of shiraiachrome A enantiomer (*ent*-shiraiachrome A, **1**) as a major constituent in the extract of *Shiraiia*-like sp. (strain

MSX60519).<sup>58, 238</sup> In addition, hypocrellin (**2**), hypocrellin B (**3**) and three hypomyces- specifically hypomycesin A (**4**), C (**5**), and E (**6**)- were isolated from the same fungal strain (Fig. 6.1).<sup>58, 238</sup> Hypomycesins are structurally similar to hypocrellins but with an additional six-membered ring and a less extended conjugated  $\pi$ -system, which is due to the absence of the  $\Delta 1(2)$  double bond (Fig. 6.1).<sup>226, 227</sup> The biosynthetic gene clusters responsible for the biosynthesis of some fungal perylenequinones, i.e., cercosporin, hypocrellin A, and elsinochrome C, have been identified.<sup>259-262</sup> However, the key biosynthetic steps involved in generation of hypocrellins, such as the formation of the seven-membered ring, are still unresolved. Moreover, the biosynthesis of hypomycesins has never been reported.

In previous work, we reported the first isolation of these two classes, hypocrellins and hypomycesins, from the same fungal species (i.e., strain MSX60519). Furthermore, we showed that exposure to light was important for the biosynthesis of both hypocrellins and hypomycesins, with approximately 70- and 20-fold improvement in the production of hypocrellins (**1-2**) and hypomycesins (**4-6**), respectively, when the fungi were grown under either continuous exposure to LED light or under 12/12 h light/dark cycles as compared to complete darkness.<sup>58</sup> Additionally, these two structural classes (i.e, hypocrellins and hypomycesins) displayed potent cytotoxic activity against human skin melanoma cancer cells (SK-MEL-28) when exposed to light,<sup>58</sup> and they are known to exhibit a broad-range of toxicities against both bacteria and fungi.<sup>193, 194, 216, 263</sup> These interesting properties and findings have raised many questions, especially with respect to the biosynthesis of these perylenequinones. For instance, how does exposure to light facilitate the biosynthesis of these compounds without negatively impacting the growth of the fungus? In other words, how do hypocrellin-producing fungi protect themselves against their own phototoxins? In addition, is it possible that hypocrellins serve as the biosynthetic precursors for hypomycesins, and what are the reaction conditions or requirements for converting hypocrellins into hypomycesins?

The mechanism used by hypocrellin-producing fungi to avoid self-toxicity has not been reported; however, evidence from fungi that produce the structurally related compound, cercosporin, suggested the ability of fungi to reduce and detoxify this photosensitizer.<sup>218, 264, 265</sup> The reduced form of cercosporin has been shown to be a species with little photosensitizing capacity, resulting in less toxicity compared to the parent cercosporin.<sup>215, 266, 267</sup> Given the structural

similarities between hypocrellins and cercosporin (Fig. 6.10), it is conceivable that hypocrellin-producing fungi adapt similar mechanisms to defend themselves against these photosensitizers.

The goals of this study were to better understand the biosynthesis of hypocrellins and hypomyces, specifically to examine the origins of structural diversity of these two sub-classes of perylenequinones. We investigated their redox activity to probe the ability of hypocrellin-producing fungi to reduce, and hence, detoxify these perylenequinones. Here, we present the isolation and characterization of the proposed naturally-occurring biosynthetic precursor of hypocrellins. Furthermore, our electrochemical measurements revealed that the reduction of hypocrellins can take place at milder reducing conditions relative to hypomyces. We also report the results for the chemical reduction of hypocrellins using sodium dithionite ( $\text{Na}_2\text{S}_2\text{O}_4$ ) as a reducing agent under both aerobic and anaerobic conditions. Surprisingly, anaerobic reduction of hypocrellins led to the formation of hypomyces, suggesting a means for hypocrellins-producing fungi to ameliorate the toxicity of these compounds.

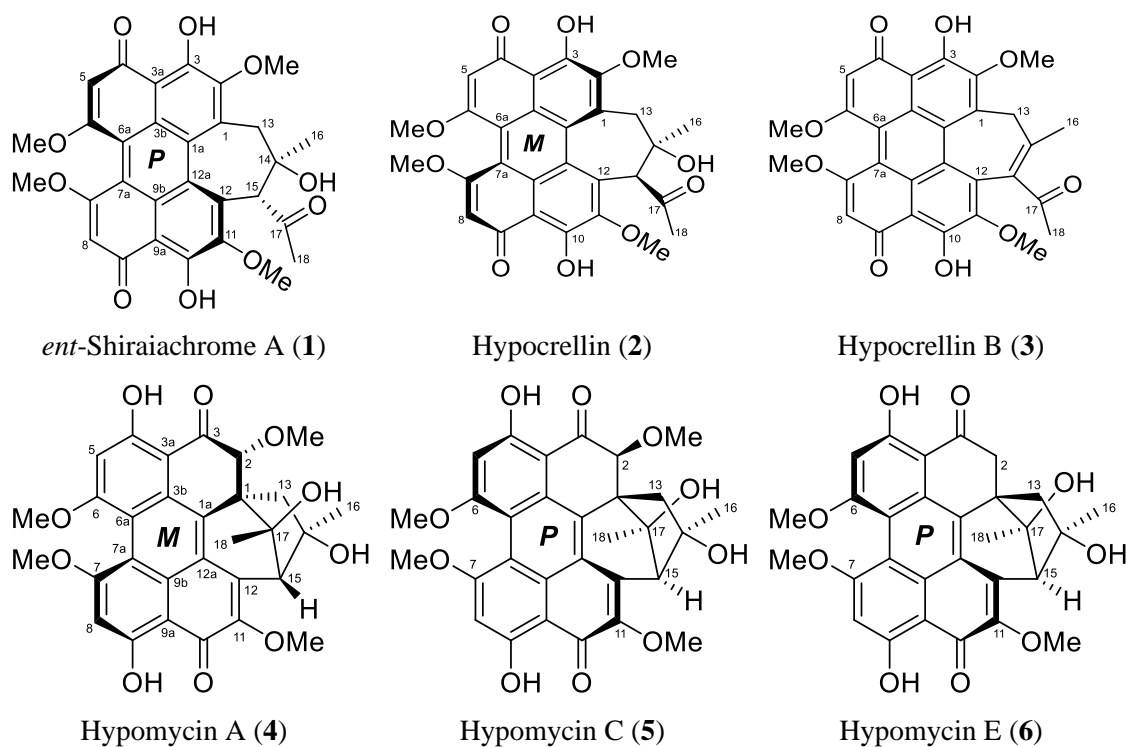


**Figure 6.1.** Structures of the hypocrellins (1-3) and hypomyces (4-6) discussed in this study. Note that the absolute configurations of 5 and 6 are revised relative to what was proposed originally.<sup>58</sup>

## Results and Discussion

The questions of this study were probed via three interconnected phases. Initially, a scaled-up culture of strain MSX60519 led to the isolation and elucidation of the suggested biosynthetic precursor of hypocrellins. Next, cyclic voltammetry and UV–vis spectroelectrochemistry were used to examine the electrochemical reversibility of the reduction process of hypocrellins and the UV–vis spectra of the semiquinone (i.e., one-electron reduced) and hydroquinone (i.e., two-electron reduced) forms of *ent*-shiraiachrome A (**1**). In addition, chemical reduction of hypocrellins under aerobic condition led to a suite of demethylated derivatives. Interestingly, a series of demethoxylated derivatives along with the conversion of hypocrellins into hypomycins were observed under anaerobic reduction conditions. Finally, this study led to a structural revision of hypomycin C and E as supported by our redox data and <sup>1</sup>H-NMR characterization of the intramolecular hydrogen bonds (i.e., H-bonds).

**Identification of the Potential Precursor of Hypocrellins.** To secure larger quantities of hypocrellins, particularly *ent*-shiarachrome A (**1**), cultures of strain MSX60519 were grown on rice medium with exposure to white LED light, replicating conditions reported recently.<sup>58</sup> The resulting extract (1.7 g) yielded 580 mg of **1**, 23 mg of **2**, and 0.5-2 milligrams of **3-6**. In addition, a benefit of scaling the biosynthesis of fungal metabolites is the identification of other minor constituents,<sup>116</sup> and in this case a new hypocrellin-like compound (**7**, 1.5 mg) was identified through high resolution electrospray ionization mass spectrometry (HRESIMS) and UV-vis absorption spectroscopy (Figs 6.11 & 6.12). The molecular formula of **7**, as deduced from the HRESIMS data (measured  $m/z$  547.1583 [M + H]<sup>+</sup> vs. calculated 547.1604), was similar to that reported for **1** and **2** (C<sub>30</sub>H<sub>26</sub>O<sub>10</sub>). However, the <sup>1</sup>H- and <sup>13</sup>C-NMR spectra revealed only 13 proton and 15 carbon signals, suggesting the symmetrical nature for this compound (Table 6.1 and Fig. 6.13). Examination of the 1D and 2D NMR spectra confirmed the same conjugated pentacyclic core in **7** as other perylenequinones (Figs 6.13-6.17). However, the unsymmetrical seven-membered carbocyclic ring was missing in **7**, being replaced by 2-propanone side chains attached at C-1 and C-12 of the pentacyclic core (Figure 6.2A). Compound **7** was ascribed the trivial name prehypocrellin.

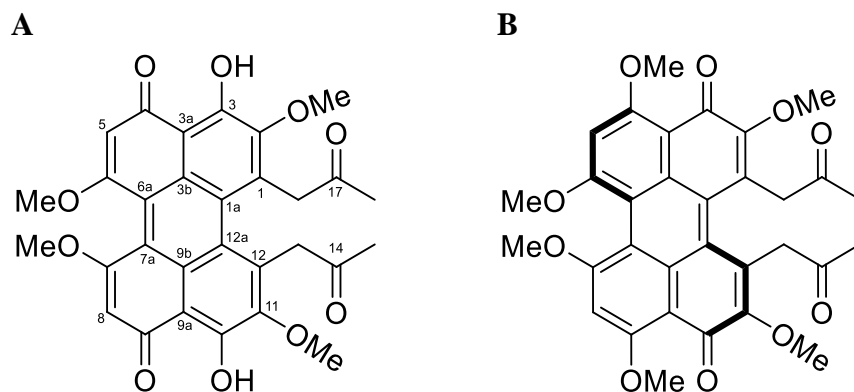


**Figure 6.2.** Structure of compound **7** (A) as compared to the synthetic precursor used in the total synthesis of hypocrellin A (B) as reported by O'Brien *et al.*<sup>204</sup>

**Table 6.1.** NMR Spectroscopic Data for **7** in CDCl<sub>3</sub> (700 MHz for <sup>1</sup>H and 175 MHz for <sup>13</sup>C,  $\delta$  in ppm).

position	<b>5</b>	
	$\delta_C$ , type	$\delta_H$ (J, Hz)
1, 12	132.5, C	
1a, 12a	125.6, C	
2, 11	151.1, C	
3, 10	171.3, C	
3a, 9a	107.1, C	
3b, 9b	126.3, C	
4, 9	179.7, C	
5, 8	102.5, CH	6.53, s
6, 7	165.8, C	
6a, 7a	119.2, C	
13, 16	47.7, CH <sub>2</sub>	3.61, d (17.4) 4.06, d (17.4)
14, 17	204.6, C	
15, 18	30.0, CH <sub>3</sub>	2.26, s
CH <sub>3</sub> O-2, CH <sub>3</sub> O-11	60.6, CH <sub>3</sub>	4.12, s
CH <sub>3</sub> O-6, CH <sub>3</sub> O-7	56.7, CH <sub>3</sub>	3.92, s
HO-3, HO-10		15.93, s

We propose that compound **7** represents a common intermediate in the biosynthetic pathway of compounds in the hypocrellin family. The structural similarity between **7** and the synthetic

precursor used in the total synthesis of hypocrellin A, as described by O'Brien *et al.* (Fig. 6.2B),<sup>204</sup> further supports this conclusion. In fact, the structure of **7** was suggested as a plausible biosynthetic intermediate for a variety of fungal perylenequinones,<sup>204, 228, 268</sup> although it has never been isolated from perylenequinone-producing fungi. In this context, compound **7** may follow a variety of biotransformation paths to yield the structural diversity seen with perylenequinones, and the isolation of this biosynthetic intermediate supports what had been hypothesized in the literature, that a common biosynthetic intermediate is responsible for the pentacyclic core and the common substituents for compounds in class B perylenequinones, including cercosporin-like compounds, elsinochromes, and hypocrellins.<sup>228</sup> For instance, reduction of the ketone moieties at C-14 and C-17 give rise to compounds like calphostins, phleichromes, and cercosporin (Fig. 6.3). Alternatively, oxidative enol coupling could generate elsinochromes products (Fig. 6.3), while diastereoselective aldol cyclization may generate hypocrellin derivatives (Fig. 6.3). Interestingly, compound **7** is optically inactive as it showed no activity on Electronic Circular Dichroism (ECD). This could be attributed to the presence of a racemic mixture of two atropisomeric enantiomers; a similar observation was reported previously for hypocrellin B (**3**).<sup>58, 186, 201</sup> The isolation of only a relatively small amount of **7** (1.5 mg), even from a scaled up fungal culture, can be attributed to the high reactivity of this biosynthetic intermediate and its facile conversion into other perylenequinone derivatives.

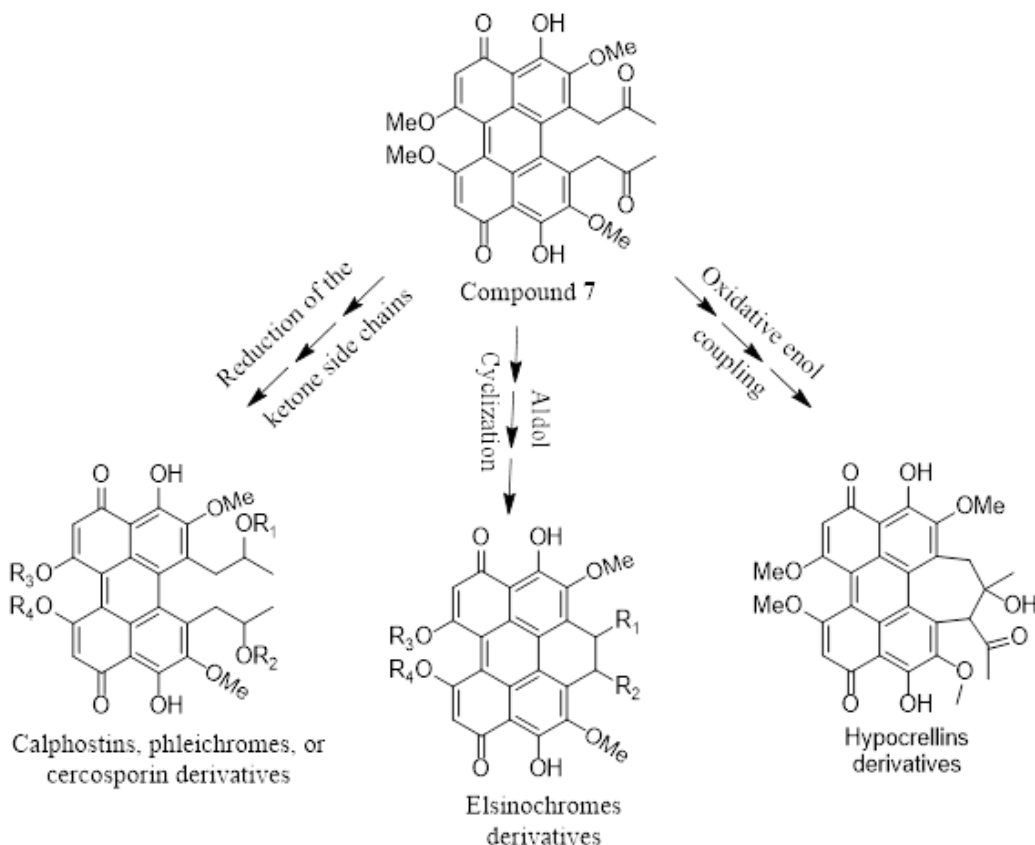


**Figure 6.3.** Compound 7 as a common precursor for class B perylenequinone derivatives.

**Electrochemical Study of Hypocrellins and Hypomycins.** To study the redox behavior of both hypocrellins (**1-3**) and hypomycins (**4-6**), cyclic voltammetry measurements were conducted in acetonitrile containing 100 mM of *tetra-n*-butylammonium hexafluorophosphate,  $[(n\text{Bu})_4\text{N}][\text{PF}_6]$ , as the supporting electrolyte and under rigorous air-free conditions (Fig. 6.4). All potential values are reported against the silver/silver chloride (Ag/AgCl) reference electrode. The voltammograms of the hypocrellin molecules (i.e., **1-3**) showed two reversible one-electron reduction processes. The first reduction event represents the formation of the semiquinone radical anion form ( $\text{SQ}^{\cdot-}$ ) of hypocrellins with half-wave potentials ( $E_{1/2}$ ) ranging from  $-0.46$  V to  $-0.51$  V (Table 6.2). The second reduction event gave rise to hypocrellins in the dianion ( $\text{Q}^{2-}$ ) state with  $E_{1/2}$  ranging from  $-0.71$  V to  $-0.76$  V (Fig. 6.4 and Table 6.2). The presence of the additional  $\pi$ -bond at C-14 and C-15 in hypocrellin B (**3**), which is in conjugation with the  $\text{sp}^2$ -hybridized perylenequinone core, led to easier first- and second-electron reduction processes, as **3** has the least negative values of the  $E_{1/2}$ , followed by **1** and **2**. Hypomycins (i.e., **4-6**) also

showed two one-electron reversible reduction events, and as expected, their  $E_{1/2}$  values were more negative – ranging from  $-0.96$  V to  $-1.05$  V and  $-1.29$  V to  $-1.36$  V for the first and second reduction events, respectively (Fig. 6.4 and Table 6.2). Here, the less extended conjugated  $\pi$ -system in the pentacyclic core of **4-6** was responsible for their more difficult reduction processes. Additionally, the absence of the inductive electron-withdrawing effect of a methoxy group at C-2 in hypomycin E (**6**) resulted in more difficult first- and second-electron reduction processes, as **6** had the most negative  $E_{1/2}$  values, followed by **4** and **5** (Fig. 6.4)

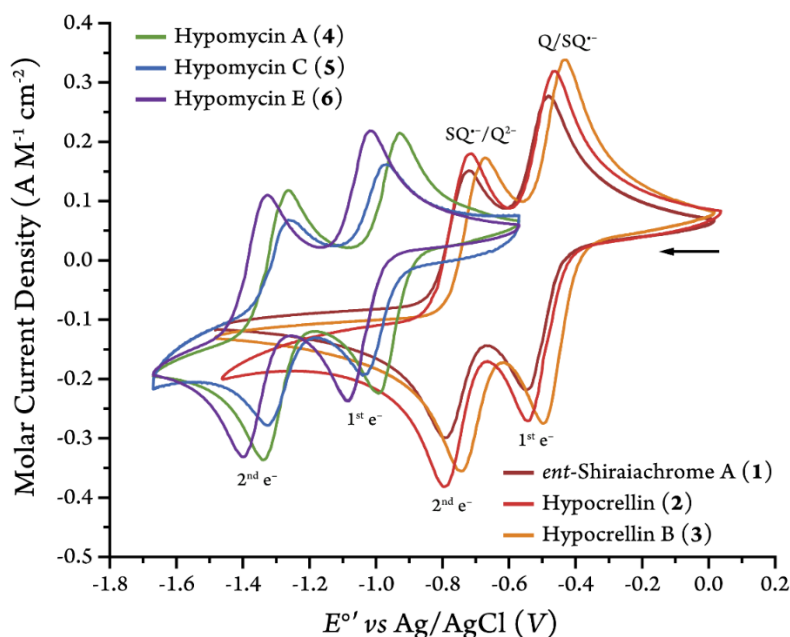


**Figure 4.** Normalized cyclic voltammograms of hypocrellins (**1-3**) and hypomycons (**4-6**) in acetonitrile with 100 mM of  $[(n\text{Bu}_4)\text{N}][\text{PF}_6]$  as the supporting electrolyte. **Q**: quinone form.  $\text{SQ}^{\bullet-}$ : semiquinone radical anion form.  $\text{Q}^{2-}$ : hydroquinone dianion form.

Further characterization for the semiquinone radical anion and hydroquinone dianion forms of *ent*-shiraiachrome A (**1**) was performed using the UV–vis spectroelectrochemistry. Initially, the UV–vis spectrum was collected for **1** in its starting quinone form, showing maximum absorption in the blue region ( $\lambda_{\text{max}} = 430$  nm) along with two weaker electronic absorptions at 540 and 580 nm (Fig. 6.5). At  $-650$  mV, where the semiquinone radical anion form of **1** would be the most dominant species, the UV-vis spectrum showed a more extended absorption profile in the visible and near IR (vis-NIR) regions with the maxima in the red region ( $\lambda_{\text{max}} = 640$  nm). The dianion form of **1** was dominant at  $-850$  mV, which showed two strong electronic absorptions at 500 and

530 nm. The reduced forms of *ent*-shiraiachrome A (**1**) absorb blue light with lower intensities as compared to the starting quinone from (Fig. 6.5) and their photochemical behaviors (i.e., the nature of the excited electronic states and relaxation mechanisms) are remarkably different. Accordingly, unlike the photoactivated (i.e., excited electronic state) *ent*-shiraiachrome A which reacts with dioxygen ( $^3\text{O}_2$ ) through direct energy transfer to generate singlet dioxygen ( $^1\text{O}_2$ ),<sup>58</sup> the reduced form of **1** is expected to react with dioxygen in its ground electronic state through an electron transfer process, in the absence of proton transfer, producing superoxide ( $\text{O}_2^{\cdot-}$ ) or peroxide ( $\text{O}_2^{2-}$ ) species. Therefore, a significantly lower phototoxicity of the reduced form of **1**, as compared to the starting quinone form is expected. Similar observations were reported for the reduced derivatives of cercosporin,<sup>264, 267</sup> suggesting that this could be a universal trait for these perylenequinones.

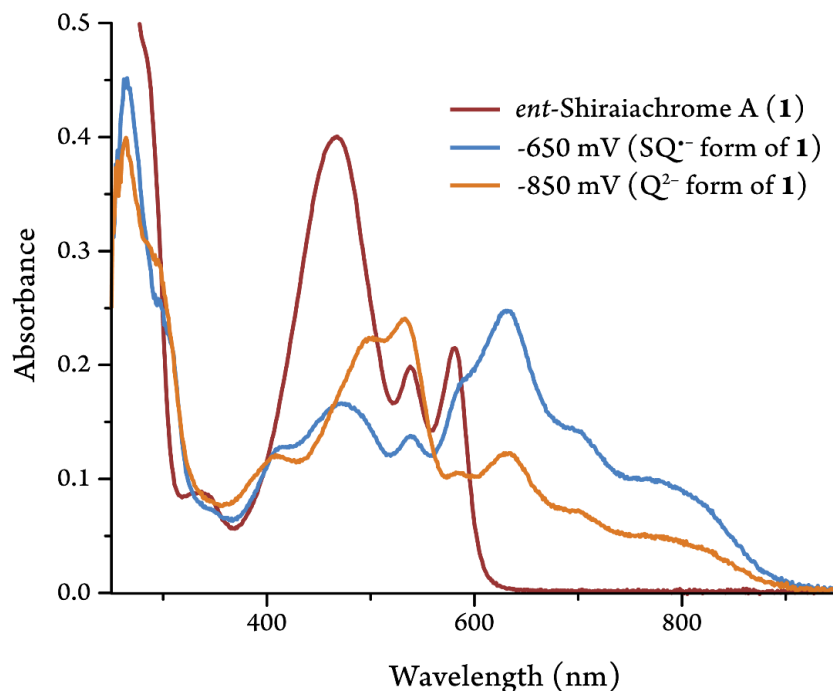


**Figure 5.** UV–vis spectroelectrochemistry spectra of the first (semiquinone radical anion form, SQ $^{\cdot-}$ ) and second (hydroquinone form, Q $^{2-}$ ) reductions of *ent*-shiraiachrome A (**1**) (248  $\mu\text{M}$ ) in acetonitrile with 0.1 M [(*n*Bu) $_4$ N][PF $_6$ ] as the supporting electrolyte.

**Chemical Reduction of Hypocrellins and Hypomycins under Aerobic Conditions.** Since the cyclic voltammograms of hypocrellins (**1-3**) showed full electrochemical reversibility of their reduction process, chemical reductions of these three compounds were performed using sodium

dithionite ( $\text{Na}_2\text{S}_2\text{O}_4$ ) as a reducing agent. As a start, these reactions were conducted at a small scale ( $\sim 1$  mg of each compound) under ambient conditions to maintain an adequate supply of  $\text{O}_2$ . Treating the deep red solutions of **1-3** individually with excess amounts of  $\text{Na}_2\text{S}_2\text{O}_4$  aqueous solution resulted in an immediate color change from deep red to yellow (Figs 6.18A & B) representing the formation of the reduced hydroquinone (HQ) forms of **1-3**. Subsequently, the reversible reaction of HQ forms with  $\text{O}_2$  was observed *via* the development of the red color as air diffused in the solutions. (Fig. 6.18C). This indicated that compounds **1-3** were spontaneously reduced to the yellow hydroquinone form in the presence of the appropriate reducing agent and then were readily oxidized back to the quinone form (red color) through reaction with  $\text{O}_2$ . The UPLC-HRESIMS data for the reaction mixtures of **1-3** confirmed the recovery of the original compounds in the quinone form, rather than the hydroquinone form (Figs 6.19-6.21). In addition, a series of other side products were produced by this redox reaction. The molecular formula of these products, as deduced by HRESIMS, indicated the loss of one and/or two of the methyl groups in the structures of **1-3** (Figs 6.19-6.21). To further characterize these derivatives, scaled-up reduction reactions of 10 mg of *ent*-shiraiachrome A (**1**) with  $\text{Na}_2\text{S}_2\text{O}_4$  were conducted in four replicates (total of 40 mg). After that, the reaction mixtures were subjected to UPLC-HRESIMS, where the four reactions showed the same side products observed in the small-scale reduction reaction of **1** (Fig 6.22). The reaction mixtures were then combined and subjected to preparative HPLC to obtain compounds **8-10**, in addition to the recovery of **1** in the quinone form (Fig. 6.6). The structures of **8-10** were characterized by analyzing their HRESIMS data and 1D and 2D NMR spectra (Table 6.3 and Figs 6.23-6.26). Accordingly, the methoxy groups attached to C-11 in **8** and to C-2 in **9** were replaced with hydroxy moieties (Fig. 6.6). On the other hand, both methoxy groups attached to C-2 and C-11 were replaced with hydroxy groups in **10**. The compounds, **8**, **9**, and **10**, were generated in approximately a 3:3:1 ratio, respectively (Fig. 6.6). The replacement of one or both methoxy groups at these positions (i.e., C-2 and C-11) by hydroxyl groups confirmed that these positions were susceptible to nucleophilic substitution, as reported in simpler quinone systems.<sup>269</sup> Compounds **8-10** exhibited the characteristic electronic absorption profile of perylenequinones (Fig. 6.27) and maintained the same axial chirality of *ent*-shiraiachrome A (**1**), as noted by their ECD spectra (Fig. 6.28).

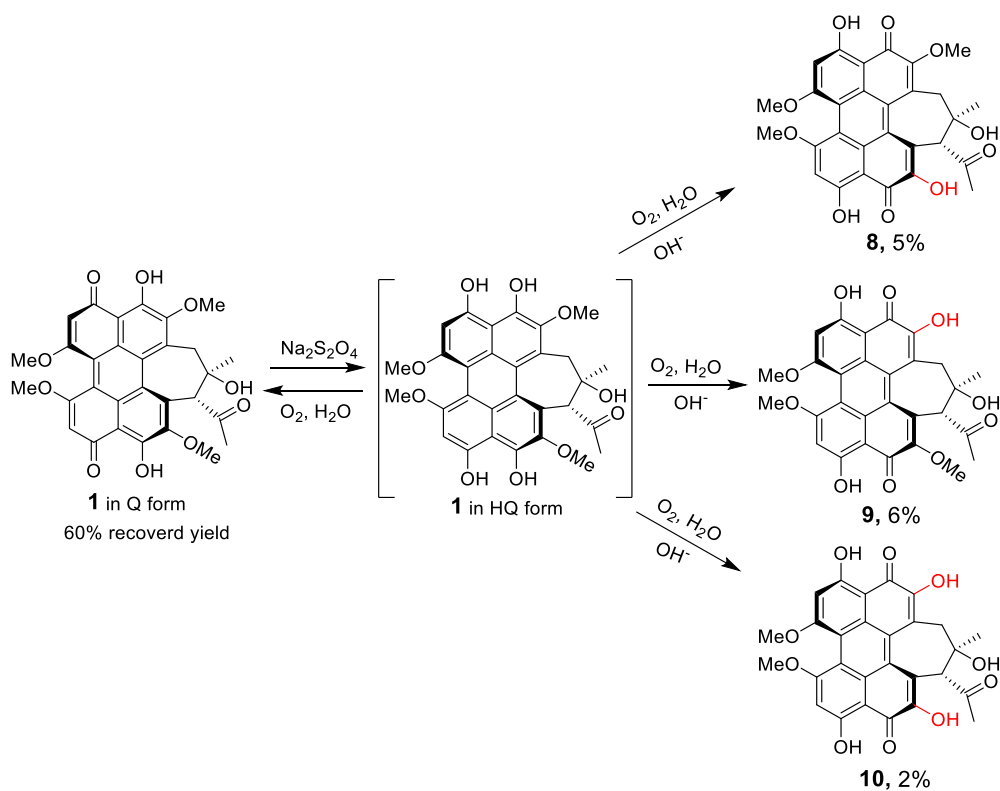


**Figure 6.6.** Generation of **8-10** via reduction of *ent*-shiraiachrome A (**1**) under aerobic conditions.

Similar experiments with the hypomycins (i.e., **4-6**) resulted in no detectable substitution of the methoxy groups, one of which is attached to a sp<sup>3</sup> carbon in hypomycins (i.e., C-2). Here, aerobic reduction with Na<sub>2</sub>S<sub>2</sub>O<sub>4</sub> led to the full recovery of the original hypomycins compounds in their quinone forms (Figs. 6.29-6.31). As expected, no apparent color change was observed during the reduction process (Fig. 6.32). Indeed, the electronic absorption profiles of hypomycins in the visible region are significantly different than hypocrellins, in that the former are yellow to orange-colored fungal metabolites, as opposed to the deep red-colored hypocrellins (Figs. 6.18-6.32).

**Chemical Reduction of Hypocrellins under Anaerobic Conditions.** As the chemical reduction of hypocrellins (**1-3**) resulted in a series of demethylated analogues as minor products, we were intrigued to investigate this reaction under anaerobic condition. *Ent*-shiraiachrome A (**1**, 10 mg) was treated with excess Na<sub>2</sub>S<sub>2</sub>O<sub>4</sub> under argon in triplicate (total of 30 mg of **1**). UPLC-HRESIMS data of the reaction mixtures confirmed the recovery of **1** in the quinone form as a

major product (64%) (Fig. 6.33). Surprisingly, eight other derivatives were also detected, and this was observed consistently across triplicate reactions (Figs. 6.7A & 6.33). Based on matching the UPLC retention time and HRESIMS data, these products were identified as hypocrellin (2), hypocrellin B (3), hypomyacin A (4), hypomyacin C (5), and hypomyacin E (6) (Fig. 6.34). Three new products were also identified (i.e., 11-13) with molecular formulae of  $C_{29}H_{24}O_9$  for both 11 and 12 and  $C_{28}H_{22}O_8$  for 13 as deduced by HRESIMS data (Fig. 6.7A). Accordingly, these compounds were missing either one (as in 11 and 12) or two methoxy groups (as in 13) relative to the starting compound 1. The generation of these natural (2-6) and un-natural (11-13) analogues through the anaerobic reduction of 1 reveal that the structural diversity of fungal hypocrellins and hypomycins drives from their redox activities.

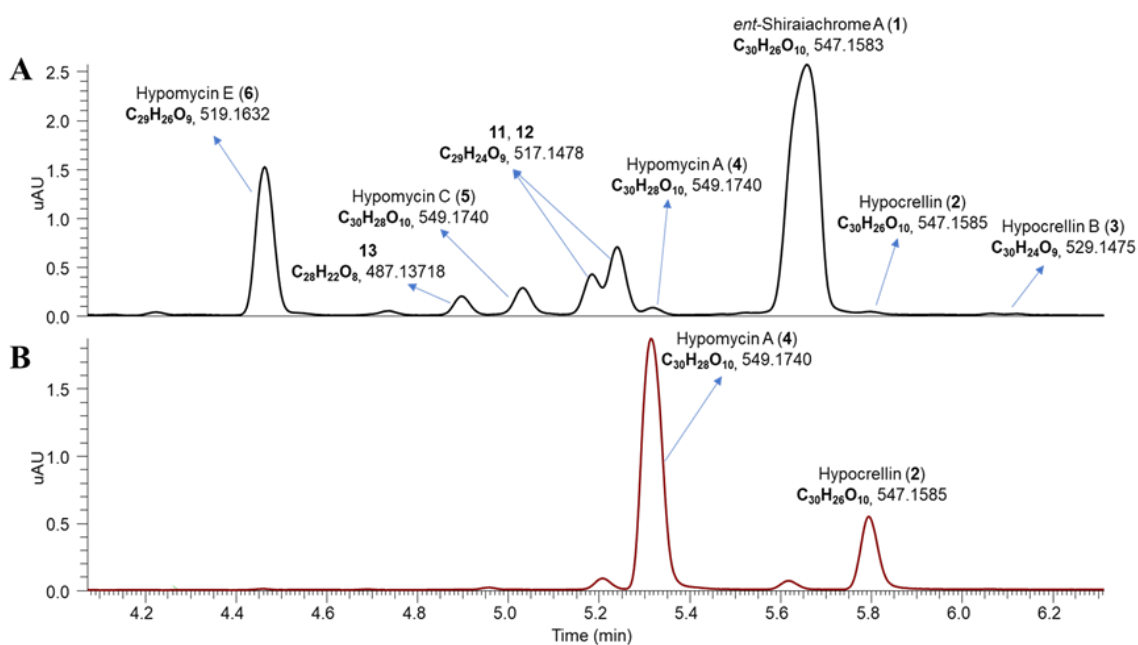


**Figure 6.7.** UPLC-PDA-HRESIMS chromatogram of anaerobic reduction reaction of A) *ent*-shiraiachrome A (1) and B) hypocrellin (2). HRESIMS data are reported as  $[M + H]^+$ .

To facilitate the isolation of the products, the same anaerobic reaction was conducted using 50 mg of 1 followed by preparative HPLC to obtain 1-6, and 11-12 (Fig. 6.8). The structures were confirmed by ECD spectra as compared to those reported previously (Fig. 6.35).<sup>58, 238</sup> Aside from the recovered *ent*-shiraiachrome A, hypomyacin E (6) provided the highest yield among these derivatives (~11%) followed by hypomyacin C (~5%). Hypomyacin A (4) was isolated in low yield (~0.5%) from the anaerobic reduction of 1 (Fig. 6.8). This was surprising as hypomyacin A (4)

showed the highest abundance in the extract of strain MSX60519 as compared to **5** or **6**.<sup>58</sup> This led us to propose that hypomycin A (**4**) is a derivative of hypocrellin (**2**) rather than *ent*-shiraiachrome A (**1**), particularly since the axial chirality of **4** matches that of **2** (i.e., *M*) rather than that of **1** (i.e., *P*; Fig. 6.1). In this context, the reduction reaction of **1** led to the generation of **2**, which in turn underwent anaerobic reduction to provide hypomycin A (**4**).

To test this hypothesis, 4.6 mg of pure hypocrellin (**2**) was reduced using Na<sub>2</sub>S<sub>2</sub>O<sub>4</sub> under anaerobic conditions, and the UPLC-HRESIMS data of the reaction mixture showed the production of hypomycin A (**4**) in a relatively high yield (65%), in addition to the recovery of **2** in quinone form (11%) (Fig. 6.7B & 6.36). Interestingly, the yield of intramolecular cyclization to produce hypomycin A (**4**) from the anaerobic reduction of hypocrellin (**2**) was remarkably higher as compared to the relatively low yield of hypomycin C (**5**) and E (**6**) from the anaerobic reduction of *ent*-shiraiachrome A (**1**) (i.e., 5% and 11%, respectively). This might be attributed to the stronger intramolecular hydrogen bonding present between HO-14 and the C-17 carbonyl in **2** as evidenced by the donor-acceptor distance of 2.70 Å as compared to 2.79 Å in **1** (Fig. 6.37). This would increase the electrophilicity, and hence the reactivity, of the C-17 carbonyl in **2** to produce **4** in such a high yield. These data correlated well with our previous findings, where the isolated amount of hypomycin A (**4**) was significantly higher than those of hypomycin C (**5**) and E (**6**) from fungal strain MSX60519 grown on oatmeal medium under continuous LED light exposure.<sup>58</sup> Therefore, the hypomyces (**4-6**) likely derive from the hypocrellin class, and their production requires the reduction of the appropriate hypocrellins under anaerobic conditions. Indirectly, this indicates the ability of fungi to reduce different hypocrellins under oxygen-free condition to provide a variety of hypomyces. Other evidence from the literature that supports this conclusion is the recent discovery of hypomycin A enantiomer, (*P*)-hypomycin A, from the stromata extract of *Hypocrella bambusae*, where hypocrellin A (i.e., the hypocrellin enantiomer) was the major constituent in the extract.<sup>263</sup> Accordingly, to satisfy the stereochemical requirements, hypomycin A (**4**) with absolute configuration of *M(R)*, 1*S*, 2*R*, 14*R*, 15*S*, 17*R* would derive from hypocrellin (**2**) with absolute configuration of *M(R)*, 14*R*, 15*S*, while (*P*)-hypomycin A (enantiomer of **4**) with absolute configuration *P(S)*, 1*R*, 2*S*, 14*S*, 15*R*, 17*S* would derive from hypocrellin A (enantiomer of **2**) with an absolute configuration of *P(S)*, 14*S*, 15*R*.<sup>58</sup>  
<sup>263</sup> The conversion process of *ent*-shiraiachrome A (**1**) into the other derivatives of hypocrellins (**2-3**) and hypomyces (**5-6**) is discussed below in more details.

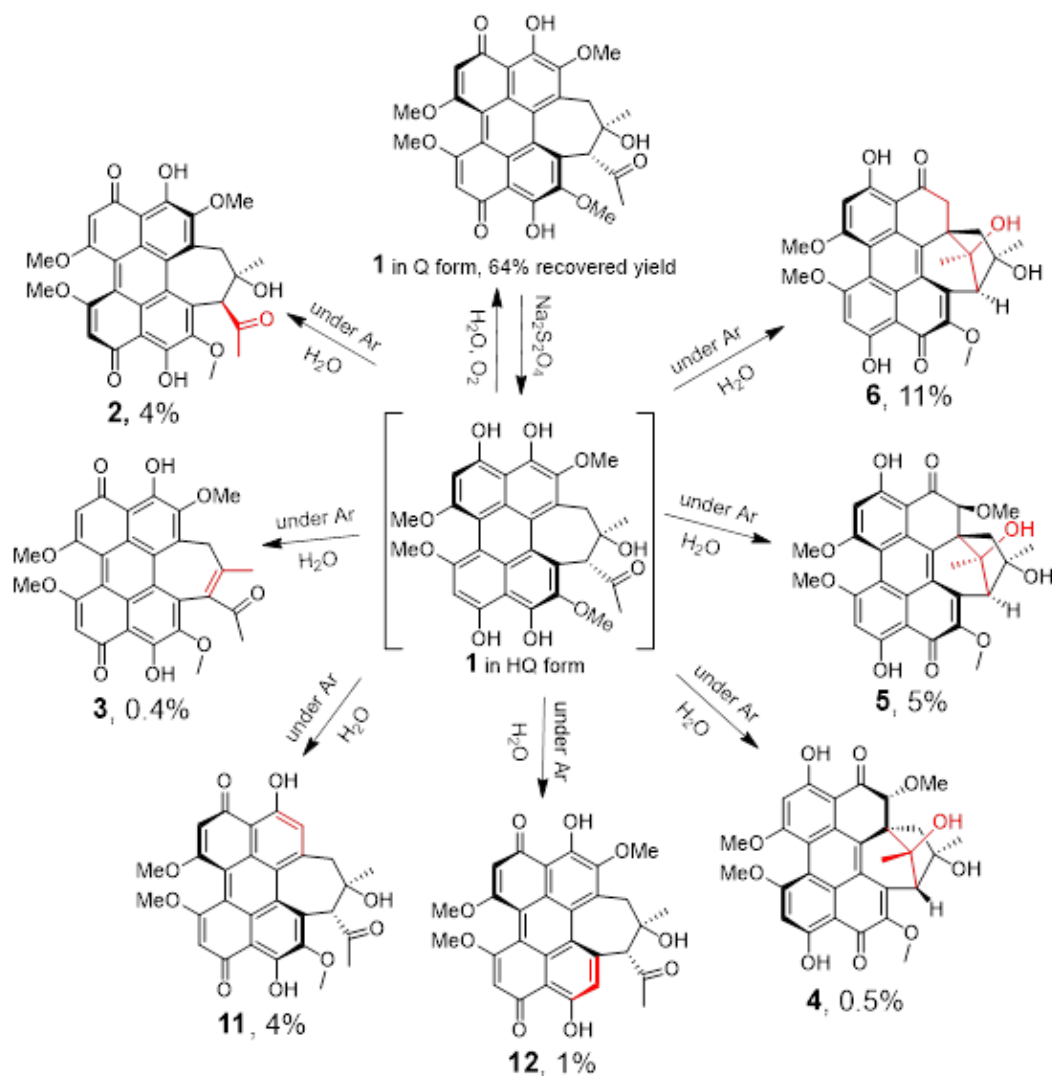


**Figure 6.8.** Derivatives obtained by chemical reduction of *ent*-shiraiachrome A (**1**) with  $\text{Na}_2\text{S}_2\text{O}_4$  under anaerobic condition.

It was interesting to observe the conversion of *ent*-shiraiachrome A (**1**) to hypocrellin (**2**) as this requires flipping the axial chirality from *P(S)* in **1** to *M(R)* in **2**, besides switching the stereochemistry at C-15 from  $15R$  in **1** to  $15S$  in **2**. We believe that the intramolecular hydrogen bonding between C-17 carbonyl and HO-14 maintains the structures of **1** and **2** in the keto form at C-17 (Fig. 6.38). This hydrogen bonding was previously reported in the X-ray crystal structure of **2**.<sup>185</sup> Furthermore, the orientation of this acetyl group determines the axial chirality of **1** and **2** to facilitate the formation of this intramolecular hydrogen-bonding. Accordingly,  $15R$  configuration goes with *P(S)* chirality as in **1** while  $15S$  configuration facilitates *M(R)* chirality as in **2**. In theory, conversion of **1** into **2** can be achieved through keto-enol tauomerism at C-17

carbonyl (Fig. 6.38). The enol form of **1** could be favored if the hydrogen bonding between C-17 carbonyl and HO-14 was disturbed, where the double bond in the enol form would be stabilized by the conjugated system of the pentacyclic core (Fig. 6.38). Therefore, the keto-enol tautomerism process at C-17 in **1** allows the formation of 15*R* stereocenter along with *P(S)* chirality as in *ent*-shiraiachrome A (**1**) or the formation of 15*S* stereocenter along with *M(R)* chirality as in hypocrellin (**2**). To investigate this possibility, we used deuterated DMSO as hydrogen bond acceptor to dissolve a pure sample of *ent*-shiraiachrome A (**1**). <sup>1</sup>H NMR of **1** in DMSO-*d*<sub>6</sub> showed unclear broadened signals indicating the presence of equilibrium between the keto- and the enol-forms (Fig. 6.39). After drying the sample and re-collecting the <sup>1</sup>H NMR in CDCl<sub>3</sub>, two sets of hydrogen signals appeared in the spectrum. One set matches that of *ent*-shiraiachrome A (**1**), while the second set matches the <sup>1</sup>H NMR of hypocrellin (**2**) (Fig. 6.40). This proves that hypocrellin (**2**) can derivatize from **1** simply by exposure to a hydrogen bond acceptor solvent (such as DMSO) to facilitate the keto-enol tautomerism at C-17 carbonyl, and the reduction of **1** is not an essential step in the conversion of **1** into **2**. Moreover, we suggest the same phenomenon of keto-enol tautomerism at C-17 between hypocrellin A (the enantiomer of **2**) and shiraiachrome A (the enantiomer of **1**) as evidenced by their concurrent isolations from various fungal strains.<sup>186, 201, 221, 263, 270</sup>

Despite the isolation of hypocrellin B (**3**) from different fungal species as a naturally-occurring perylenequinone, it is also known to be a dehydrated product of other hypocrellins. Hypocrellin B (**3**) can readily be produced by a simple dehydration of either hypocrellin (**2**), hypocrellin A, shiraiachrome A, or *ent*-shiraiachrome A (**1**).<sup>58, 186, 201</sup> The absence of ECD activity for **3** was suggested to be a result of its planar structure or more likely a racemic mixture of the *M(R)* and *P(S)* enantiomers of **3**.<sup>58, 204</sup> Herein, we report the first X-ray crystallography of **3**, where a racemic mixture of both *M(R)* and *P(S)* enantiomers of **3** was observed (Fig. 6.9). Accordingly, compound **3** exhibits a low barrier of atropisomerization which can be observed at room temperature. The fact that hypocrellin B (**3**) exists as a racemic mixture of the two possible atropisomers further supports our theory that the stereochemistry at C-15 is a major factor in determining the favored axial chirality of *ent*-shiraiachrome A (**1**) and hypocrellin (**2**) and losing the stereochemistry at C-15, as in **3**, leads to a racemic mixture of the two atropisomers.

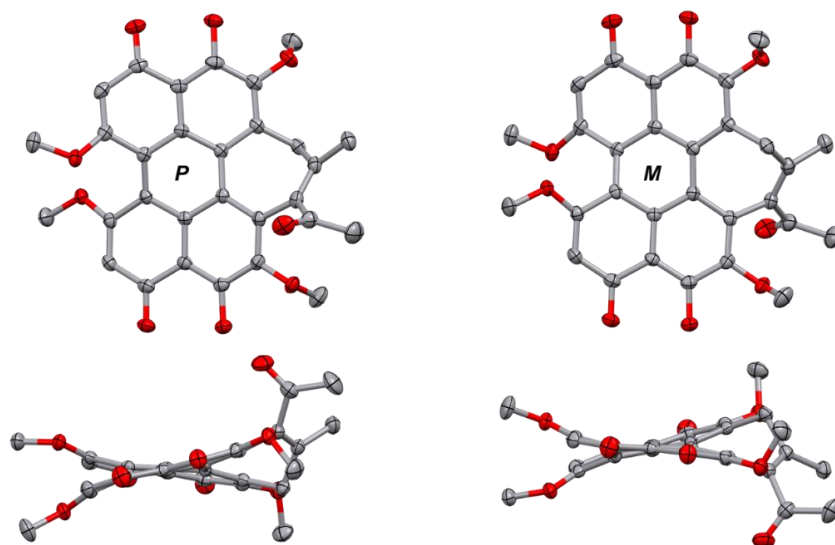


**Figure 6.9.** X-ray crystallography of hypocrellin B (**3**).

The conversion of hypocrellins (**1** or **2**) into hypomycins (**4-6**) requires the reduction of hypocrellins under oxygen-free environment. Hypomycins production was not observed under any other conditions, i.e. DMSO exposure, dehydration reaction, or reduction under aerobic condition. A question that comes to mind is whether hypomycins formed before or after exposing the reaction mixture to oxygen. Although the reduction reaction was conducted in oxygen-free settings, UPLC-MS data and products purification were performed after drying the reaction mixture under anaerobic environment and then expose it to normal room condition. To answer this question,  $^1\text{H}$  NMR for the reaction mixtures of **1** and **2** were collected in deuterated acetonitrile before any oxygen exposure (Figs. 6.41-6.42). Interestingly, the main set of peaks observed in the reduction reaction of *ent*-shiraiachrome A (**1**) matches those of hypomycin E (**6**) (Fig. 6.33), while the anaerobic reduction reaction of hypocrellin (**2**) showed peaks that match those of hypomycin A (**4**) (Fig. 6.42). Accordingly, rearrangement of hypocrellins structures to produce hypomycins occurs before exposure to any source of oxygen and occurs under complete anaerobic condition.

In our previous work, the absolute configuration of *P(S)*, *1S*, *2R*, *14S*, *15S*, *17R* for hypomycin C (**5**) and *P(S)*, *1S*, *14S*, *15S*, *17R* for hypomycin E (**6**) were suggested based on their ECD spectra, NOESY analyses, and their structural similarity to hypomycin A (**4**) (Fig. 6.43). These studies

suggested that **5** and **4** differed in the configuration at C-14 stereogenic center and their axial chirality, and **6** is a demethoxylated derivative of **5**.<sup>58, 227</sup> However, the anaerobic reduction reactions of **1** and **2** revealed that hypomycin A (**4**) originates from hypocrellin (**2**), while hypomycin C (**5**) and E (**6**) derive from *ent*-shiraiachrome A (**1**). This new information caused us to revisit the structure elucidations of **4-6**. The absolute configurations of hypomycin A (**4**) and hypocrellin (**2**) were in good agreement (Fig. 6.1), where both exhibit *M(R)* chirality and 14*R* configuration at C-14. However, the previously proposed 14*S* configuration in **5** and **6** do not match with the 14*R* configuration in **1** (Fig. 6.43). As the absolute configuration of **1** was reported to be *P(S)*, 14*R*, 15*R*,<sup>58</sup> compounds **5** and **6** should exhibit 14*R* configuration at C-14 and their NOESY spectra were re-analyzed to revise the structures of **5** and **6** (Fig. 6.44). As suggested by the NOESY correlations of **5** and **6** (Fig. 6.44), the order of the six-membered ring and the seven-membered ring in **5** and **6** is flipped as compared to **4** (Fig. 6.1). The orientation of these two rings and their substituents were further confirmed by examining the observed exchangeable hydroxy protons in <sup>1</sup>H NMR and the presence of intra-molecular hydrogen bonding in **4-6** structures (Fig. 6.45). The <sup>1</sup>H NMR of hypomycin A (**4**) collected in CDCl<sub>3</sub> showed the two exchangeable hydrogens at HO-14 (δ<sub>H</sub> 4.81) and HO-17 (δ<sub>H</sub> 5.59),<sup>58</sup> which suggests that these two hydrogens are stabilized by forming intramolecular hydrogen bonding (Fig. 6.46). The 3D structure of **4** confirms the presence of hydrogen bonding between HO-14 and HO-17 (2.69 Å) (Fig. 6.46). On the other hand, HO-17 (δ<sub>H</sub> 4.96), but not HO-14, was observed in the <sup>1</sup>H NMR of hypomycin C (**5**) in CDCl<sub>3</sub> (Fig. 6.47),<sup>58</sup> which indicates that only HO-17 is stabilized by hydrogen bonding with CH<sub>3</sub>O-2 (Fig. 6.45). Such hydrogen bonding between HO-17 and CH<sub>3</sub>O-2 is not possible with the previously suggested structure as the donor-acceptor distance would be 3.86 Å. Using DMSO-*d*<sub>6</sub> solvent as hydrogen bond acceptor allowed for observing the two exchangeable protons at HO-14 (δ<sub>H</sub> 4.25) and HO-17 (δ<sub>H</sub> 4.76) in **5** (Fig. 6.48). The absence of CH<sub>3</sub>O-2 in **6** results in losing the hydrogen bonding with HO-17 (Figs 6.49 & 6.45). Therefore, neither of exchangeable hydrogens at HO-14 and HO-17 were observed in the <sup>1</sup>H NMR of **6** in CDCl<sub>3</sub>.<sup>58</sup> Accordingly, the absolute configurations of **5** and **6** were revised to *P(S)*, 1*R*, 2*S*, 14*R*, 15*R*, 17*S* and *P(S)*, 1*R*, 14*R*, 15*R*, 17*S* respectively (Fig. 6.1).

Compounds **11** and **12** represent demethoxylated derivatives of **1**, where one of the four methoxy groups of **1** is missing as deduced by their HRESIMS data (Fig. 6.7A). Analysis of 1D and 2D NMR of **11** confirmed the loss of the methoxy group at C-2 as compared to **1** (Table 6.4 and

Figs. 6.50 & 6.52). The extra aromatic proton signal at  $\delta_{\text{H}}$  7.25 showed HMBC correlations with C-3, C-3a, C-1a, and C-13, which support the position of this proton at C-2 in place of the methoxy group (Fig. 6.50). On the other hand, the isolated amount of **12** was small (0.49 mg) with relatively low purity (Figure S44). However, the HMBC correlations exhibited by the extra aromatic proton at  $\delta_{\text{H}}$  7.31 with C-9a, C-10, C-12a, and C-15 support the loss of the methoxy group at C-11 in **12** as compared to **1** (Table 6.4 and Figs. 6.51-6.52). Although compound **13** was not isolated in significant amount to allow its full characterization, its HRESIMS data indicated the loss of two methoxy groups as compared to **1**. These are suggested to be the methoxy groups at C-2 and C-11. The axial chirality of **11-13** derivatives is suggested to be similar to that of the original compound (**1**) as the ECD spectrum of **11** correlates with *P(S)* chirality (Fig. 6.35).

## Conclusion

This study expanded our knowledge on the biosynthesis and the redox behavior of hypocrellins and hypomyces. The results of this study brought to light four new aspects to the literature. First, the biosynthetic precursor of hypocrellins were isolated and characterized. Second, the cyclic voltammograms of hypocrellins and hypomyces proved their reversible reduction process. Third, hypomyces were shown to derivatize from reduced hypocrellins under anaerobic condition, which suggests the ability of hypocrellin-producing fungi to reduce these compounds as a defense mechanism to detoxify these photosensitizers. Finally, the aerobic and the anaerobic reduction reactions of hypocrellins allowed to better understand the relationship between these compounds and their derivatives, which were successfully used to revise the structures of hypomyces C (**5**) and E (**6**). Moreover, X-ray crystal structures of *ent*-shiraiachrome A (**1**) and hypocrellin B (**3**) were reported for the first time.

## Materials and Methods

**General Experimental Procedure.** ECD was measured using an Olis DSM 17 ECD spectrophotometer (Olis, Inc.). UV–vis absorption spectroscopic data were collected using a Cary-60 spectrophotometer (Agilent). Electrochemical data was collected using a Bio-Logic SP-200 potentiostat. 1D and 2D NMR spectra were recorded in either CDCl<sub>3</sub>, CD<sub>3</sub>CN, or DMSO-*d*<sub>6</sub> using an Agilent 700 MHz spectrometer equipped with a cryoprobe, a JEOL ECA–500

spectrometer, or a JEOL ECS-400 spectrometer equipped with a high sensitivity JEOL Royal probe and a 24-slot autosampler. Residual solvent signals were used for referencing the NMR spectra. UPLC-HRESIMS data were collected via an LTQ-Orbitrap XL mass spectrometry system (Thermo Finnigan, San Jose, CA, USA) connected to a Waters Acquity UPLC system. A BEH Shield RP18 column (Waters, 1.7  $\mu\text{m}$ ; 50  $\times$  2.1 mm) heated to 40  $^{\circ}\text{C}$  was used. The mobile phase consisted of  $\text{CH}_3\text{CN-H}_2\text{O}$  (0.1% formic acid) in a gradient system of 15:85 to 100:0 over 10 min at a flow rate of 0.3 mL/min. MS data were collected from  $m/z$  150 to 2000 in the positive mode. All analytical and preparative HPLC experiments were carried out using a Varian Prostar HPLC system equipped with ProStar 210 pumps and a Prostar 335 photodiode array detector (PDA). HPLC data were collected and analyzed using Galaxie Chromatography Workstation software (version 1.9.3.2, Varian Inc.). For preparative HPLC, a Synergi  $\text{C}_{12}$  column (Waters, 5  $\mu\text{m}$ ; 250  $\times$  21.2 mm) was used. Flash chromatography was carried out using a Teledyne ISCO CombiFlash Rf 200 that was equipped with both UV and evaporative light-scattering detectors and using Silica Gold columns (from Teledyne Isco).

**Media and Fermentations.** The culture of fungal strain MSX60519 was maintained on potato dextrose agar (PDA; Difco) and was transferred periodically to fresh PDA Petri plates. An agar plug from the leading edge of the PDA culture was transferred to a sterile tube with 10 mL of YESD (2% soy peptone, 2% dextrose, and 1% yeast extract). The YESD culture was grown for 7 days on an orbital shaker (100 rpm) at room temperature ( $\sim 23^{\circ}\text{C}$ ) and then used to inoculate solid fermentation media.

Twelve cultures of strain MSX60519 were grown over rice medium in 250 mL Erlenmeyer flasks as previously described.<sup>58</sup> To prepare rice medium, 10 g of rice were added to each flask with 20 mL of deionized water. After autoclaving, the flasks were inoculated with YESD seed cultures (described above) and incubated at room temperature for 15 days under continuous LED light exposure. These conditions were found to enhance the production of ent-shiraiachrome A (**1**) and hypocrellin (**2**) from fungal strain MSX60519.

**Extraction, Fractionation, and Isolation.** Extraction of the solid cultures was performed as previously described.<sup>58</sup> Shortly, each culture was chopped and shaken overnight in 90 mL of 1:2  $\text{CH}_3\text{OH-CHCl}_3$ . The extract was vacuum filtered and 90 mL of  $\text{CHCl}_3$  and 100 mL of DI  $\text{H}_2\text{O}$

were added were added to the filtrate. The mixture was stirred for 30 min and then transferred into a separatory funnel. The bottom layer was drawn off, evaporated to dryness, and then, reconstituted in 100 mL of 1:1 CH<sub>3</sub>OH-CH<sub>3</sub>CN and 100 mL of hexanes. The biphasic solution was shaken vigorously and transferred into a separatory funnel. The CH<sub>3</sub>OH/CH<sub>3</sub>CN layer was drawn off and evaporated under vacuum.

The organic extracts collected from the twelve cultures were combined to provide a total of 2.2 g. These were dissolved in CHCl<sub>3</sub>, adsorbed onto Celite 545, and subdivided into five fractions via normal-phase flash chromatography using a gradient solvent system of hexanes-CHCl<sub>3</sub>-CH<sub>3</sub>OH at a 35 mL/min flow rate and 41 column volumes over 40 min. The first and the second flash chromatography fraction of the extract were subjected to preparative HPLC over a Phenomenex Synergi C<sub>12</sub> preparative column using an isocratic system of 60:40 of CH<sub>3</sub>CN-H<sub>2</sub>O (0.1% formic acid) over 45 min at a flow rate of 21.24 mL/min to yield *ent*-shiraiachrome A (**1**, 580 mg), hypocrellin (**2**, 23 mg), hypocrellin B (**3**, 1.4 mg), and hypomycin A (**4**, 4.6 mg). The third flash chromatography fraction was subjected to prep-HPLC using the same protocol to obtain hypomycin C (**5**, 1.3 mg), hypomycin E (**6**, 0.5 mg), and compound **7** (1.5 mg).

Prehypocrellin (**7**): Dark red amorphous powder; UV (CH<sub>3</sub>OH)  $\lambda_{\max}$  (log  $\epsilon$ ) 576 (3.74), 470 (4.02), 254 (4.31), 213 (4.46) nm; <sup>1</sup>H NMR (CDCl<sub>3</sub>, 700 MHz) and <sup>13</sup>C NMR (CDCl<sub>3</sub>, 175 MHz) (see Table 6.1); HRESIMS  $m/z$  547.1583 [M + H]<sup>+</sup> (calcd. for C<sub>30</sub>H<sub>27</sub>O<sub>10</sub>, 547.1604).

**Cyclic Voltammetry Measurements.** A three-electrode setup was used for all voltammetry experiments with a 3.0-mm glassy carbon disk working electrode, a carbon rod counter electrode, and a leak-free Ag/AgCl reference electrode (3.4 M KCl) inside an OMNI-Lab inert atmosphere (< 0.5 ppm of O<sub>2</sub> and H<sub>2</sub>O) glovebox filled with nitrogen. The potentials were referenced to the Ag/AgCl electrode. All electrodes were cleaned with acetone and nanopure water before and after use. Acetonitrile was further deoxygenated by bubbling with argon for 45-60 minutes followed by storage over 3 Å molecular sieves for at least 72 hours prior to use.

**Spectroelectrochemistry.** A three-electrode setup was used for spectroelectrochemistry experiments with a platinum mesh working electrode, a platinum wire counter electrode, and a leak-free Ag/AgCl reference electrode (3.4 M KCl). The solutions were made inside the glovebox and transferred into a custom made 1 mm Schlenk cuvette designed specifically for

spectroelectrochemistry experiments. The cuvette was then sealed and brought outside of the glovebox to the UV-vis instrument. First, a blank was recorded which consisted of 100 mM of the supporting electrolyte,  $[(n\text{Bu})_4\text{N}][\text{PF}_6]$ , in solution without the electrodes present. Then, a solution containing both the electrolyte (100 mM) and compound **1** (248  $\mu\text{M}$ ) was added to the cuvette and the UV-vis spectrum was recorded. The electrodes were then inserted into the solution, connected to the potentiostat, and another spectrum was recorded, demonstrating a slight increase in the baseline due to the blockage of the working electrode. This solution was then used for a blank, and subsequent UV-vis measurements were recorded as a negative potential was applied to the solution. The starting potential was -0.3 V, and was decreased by 0.05 V when the UV-vis spectra was unchanging. The final potential applied was -0.850 V.

**Small-scale Chemical Reduction of Hypocrellins (1-3) and Hypomyces (4-6) with Sodium Dithionite.** Chemical reductions of compounds **1-6** using sodium dithionite ( $\text{Na}_2\text{S}_2\text{O}_4$ ) as a reducing agent was first conducted at a small scale where 1 mg material of *ent*-shiraiachrome A (**1**), hypocrellin (**2**) and hypocrellin B (**3**) was placed in a scintillation vial and dissolved separately in 1 mL acetonitrile. Each solution was then treated with excess amount of  $\text{Na}_2\text{S}_2\text{O}_4$  by adding 0.6 mL of aqueous sodium dithionite solution (480 mM) and mix thoroughly. Similar procedure was followed for the chemical reduction of hypomycesin A (**4**), C (**5**), and E (**6**), but using 0.5 mg of each compound. The six reaction vials were left open at room condition overnight to provide regular oxygen supply. After 24 h, UPLC-HRESIMS data were collected for the reaction mixtures of **1-6** as well as for the starting materials, i.e., pure samples of **1-6** dissolved in acetonitrile.

**Scaled-up Chemical Reduction of *ent*-Shiraiachrome A (1) under Aerobic Condition.** The scaled up aerobic reduction of *ent*-shiraiachrome A (**1**) was conducted in four replicates. For each reaction, 10 mg of **1** was dissolved in 2.5 mL of acetonitrile and then treated with 3 mL of sodium dithionite solution (960 mM). The reaction mixtures were stirred for 3 h and then left open overnight. After 24 h, the four reaction mixtures were dried out and subjected to UPLC-HRESIMS system.

To purify the resulting products, the four reactions were combined and subjected to a preparative reverse-phase HPLC separation using a Phenomenex Synergi  $\text{C}_{12}$  preparative column and a

gradient system of 50:50 to 60:40 CH<sub>3</sub>CN-H<sub>2</sub>O (0.1% formic acid) over 15 min at a flow rate of 21 mL/min to obtain compounds **1** (23.6 mg), **8** (1.8 mg), **9** (2.5 mg), and **10** (0.6 mg).

11-O-Demethyl-*ent*-shiraiachrome A (**8**): Dark red amorphous powder; <sup>1</sup>H NMR (CDCl<sub>3</sub>, 400 MHz) and <sup>13</sup>C NMR (CDCl<sub>3</sub>, 100 MHz) (see Table 6.3); HRESIMS *m/z* 533.1424 [M + H]<sup>+</sup> (calcd. for C<sub>29</sub>H<sub>25</sub>O<sub>10</sub>, 533.1447).

2-O-Demethyl-*ent*-shiraiachrome A (**9**): Dark red amorphous powder; <sup>1</sup>H NMR (CDCl<sub>3</sub>, 500 MHz) and <sup>13</sup>C NMR (CDCl<sub>3</sub>, 125 MHz) (see Table 6.3); HRESIMS *m/z* 533.1424 [M + H]<sup>+</sup> (calcd. for C<sub>29</sub>H<sub>25</sub>O<sub>10</sub>, 533.1447).

2,11-O-Demethyl-*ent*-shiraiachrome A (**10**): Dark red amorphous powder; <sup>1</sup>H NMR (CDCl<sub>3</sub>, 700 MHz) and <sup>13</sup>C NMR (CDCl<sub>3</sub>, 175 MHz) (see Table 6.3); HRESIMS *m/z* 519.1298 [M + H]<sup>+</sup> (calcd. for C<sub>28</sub>H<sub>23</sub>O<sub>10</sub>, 519.1291).

#### **Chemical Reduction of *ent*-Shiraiachrome A (**1**) and Hypocrellin (**2**) under Anaerobic**

**Condition.** Anaerobic reduction of **1** was performed in triplicates, where 10 mg of **1** was used in each reaction (total of 30 mg). Under a dry oxygen-free argon atmosphere using standard Schlenk techniques, each sample of **1** was dissolved in 2.5 mL of acetonitrile and then treated with 3 mL of aqueous sodium dithionite solution (960 mM). The reactions were left stirring for 30 min before drying them out under vacuum and oxygen free condition. After 24 hr, NMR sample of each reaction was prepared under oxygen-free cabinet and used to collect <sup>1</sup>H NMR data. Afterward, UPLC-HRESIMS data were collected for each reaction. Standard pure samples of **1-6** were concurrently subjected to UPLC-HRESIMS system and used to identify the reaction products by matching their molecular ion peak and retention time. For the purpose of purifying the observed products, i.e., compounds **2-12** in fig. 6.8, the anaerobic reduction reaction of **1** was scaled up by reacting 50 mg of **1** following the same procedure. The reaction mixture was then subjected to a preparative reverse-phase HPLC separation using a Phenomenex Synergi C<sub>12</sub> preparative column and an isocratic system of 60:40 CH<sub>3</sub>CN-H<sub>2</sub>O (0.1% formic acid) for 30 min at a flow rate of 21 mL/min to obtain compounds **1** (31.8 mg), **2** (2.1 mg), **3** (0.18 mg), **5** (2.26 mg), **6** (5.3 mg), **11** (1.6 mg), and **12** (0.5 mg).

Anaerobic reduction of hypocrellin (**2**, 4.6 mg) was conducted following the same protocol described for *ent*-shiraiachrome A (**1**). Hypocrellin sample was dissolved in 2 mL of acetonitrile and then treated with 1.5 mL of aqueous sodium dithionate solution (960 mM). After drying out the reaction mixture,  $^1\text{H}$  NMR data was collected under anaerobic condition. After that, the reaction mixture was subjected to UPLC-HRESIMS and then purified via preparative reverse-phase HPLC system using a Phenomenex Synergi  $\text{C}_{12}$  semi-preparative column and an isocratic system of 60:40  $\text{CH}_3\text{CN-H}_2\text{O}$  (0.1% formic acid) for 30 min at a flow rate of 4.7 mL/min to obtain compounds **2** (0.5 mg) and **4** (2.97 mg).

2-Demethoxy-*ent*-shiraiachrome A (**11**): Dark red amorphous powder;  $^1\text{H}$  NMR ( $\text{CDCl}_3$ , 400 MHz) and  $^{13}\text{C}$  NMR ( $\text{CDCl}_3$ , 100 MHz) (see Table 6.4); HRESIMS  $m/z$  517.1478  $[\text{M} + \text{H}]^+$  (calcd. for  $\text{C}_{29}\text{H}_{25}\text{O}_9$ , 517.1498).

11-Demethoxy-*ent*-shiraiachrome A (**12**): Dark red amorphous powder;  $^1\text{H}$  NMR ( $\text{CDCl}_3$ , 700 MHz) and  $^{13}\text{C}$  NMR ( $\text{CDCl}_3$ , 175 MHz) (see Table 6.4); HRESIMS  $m/z$  517.1478  $[\text{M} + \text{H}]^+$  (calcd. for  $\text{C}_{29}\text{H}_{25}\text{O}_9$ , 517.1498).

## Supplementary Data

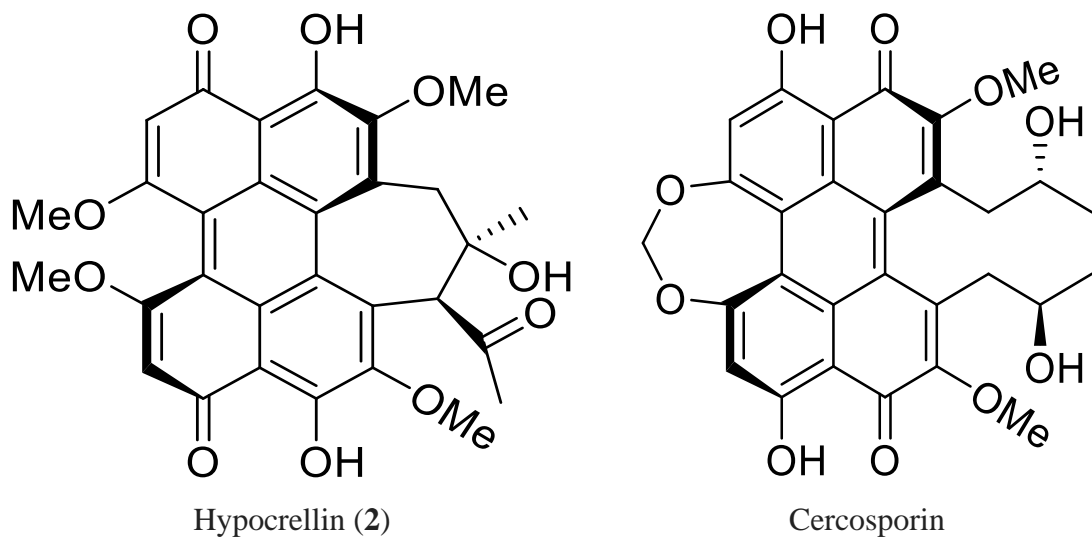


**Figure 6.10.** Structural similarity between hypocrellin (2) and cercosporin.

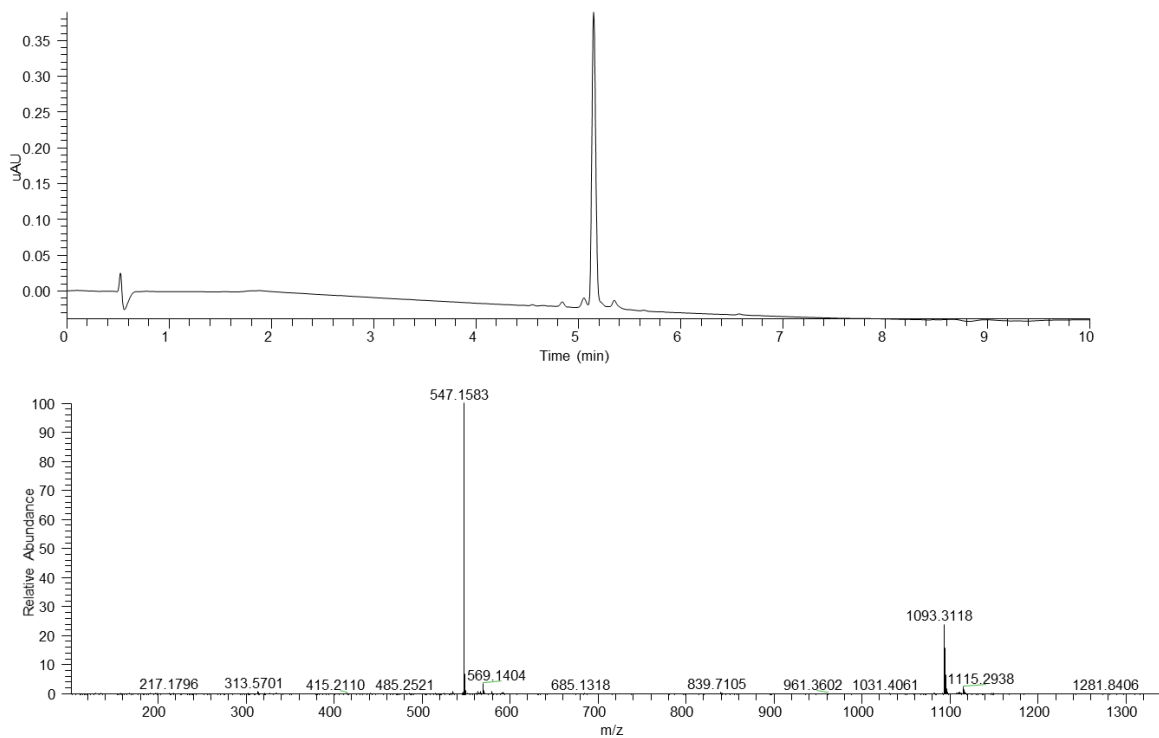


**Figure 6.11.** UPLC-(+)-HRESIMS chromatogram of 7.

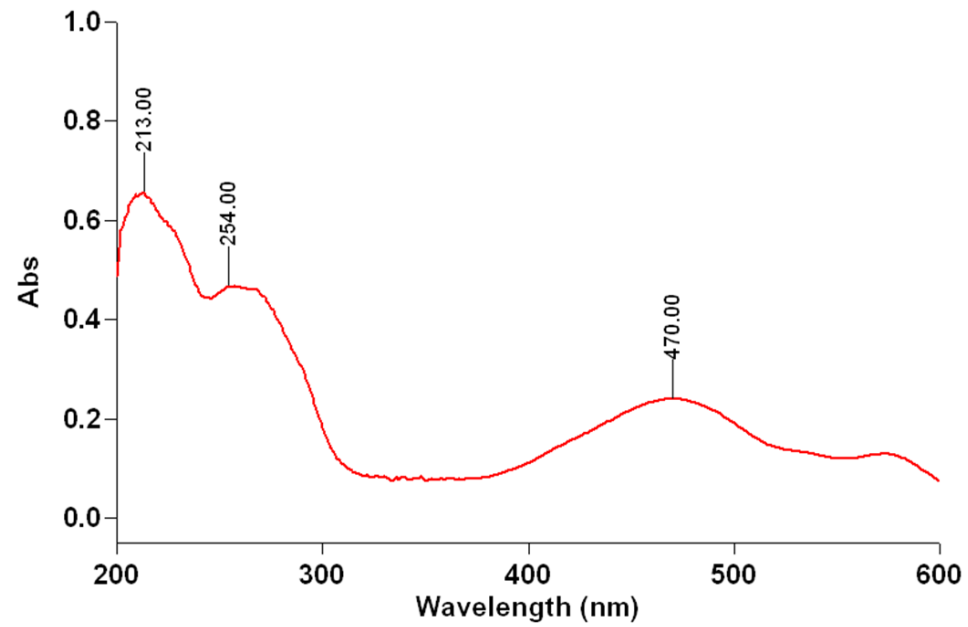


**Figure 6.12.** UV spectrum of **7** in methanol at concentration of 0.0125 mg/mL.

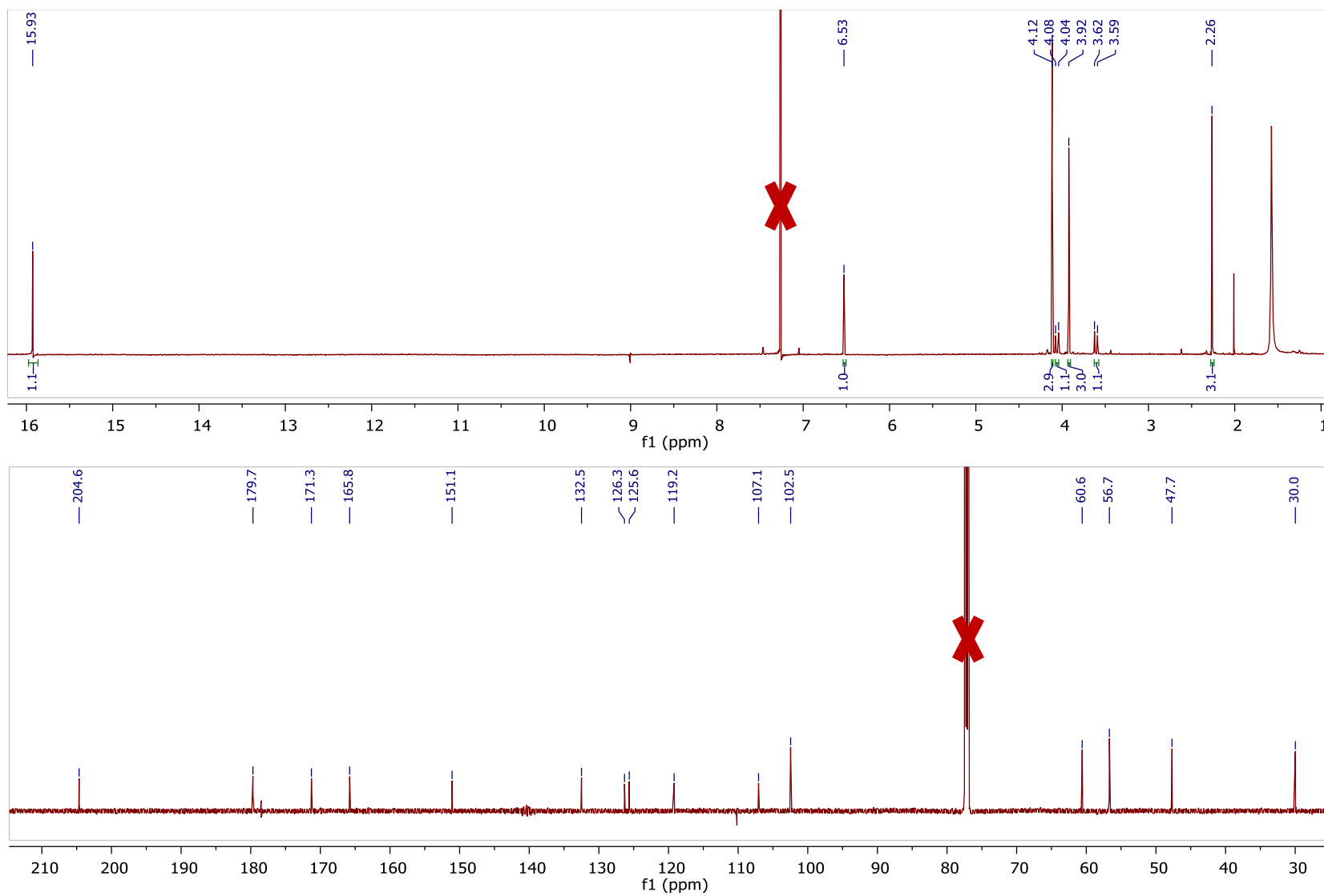


**Figure 6.13.**  $^1\text{H}$  and  $^{13}\text{C}$  NMR spectra of **7** [700 MHz for  $^1\text{H}$  and 175 MHz for  $^{13}\text{C}$ ,  $\text{CDCl}_3$ ].

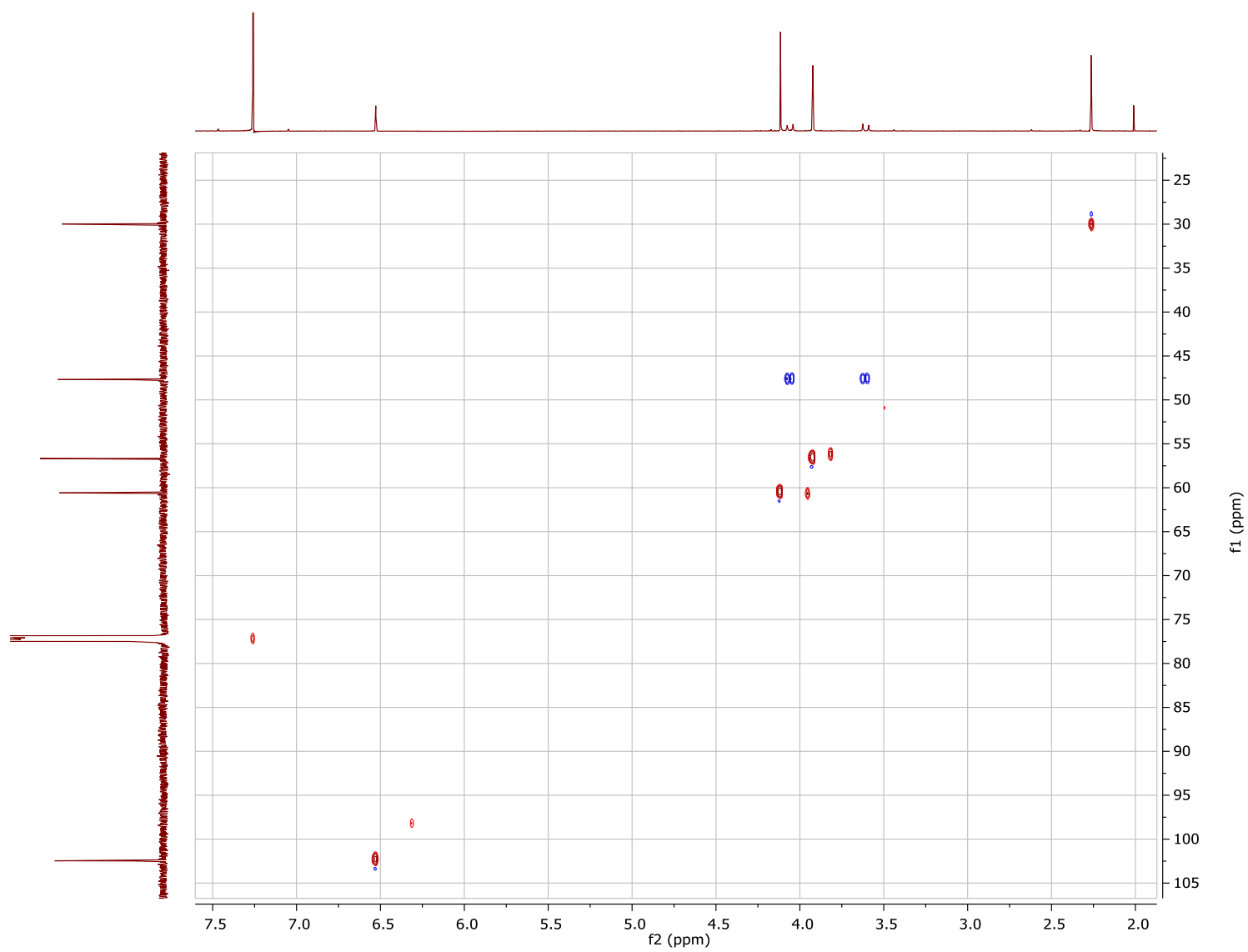


**Figure 6.14.** Edited-HSQC NMR spectrum of **7** [700 MHz,  $\text{CDCl}_3$ ].

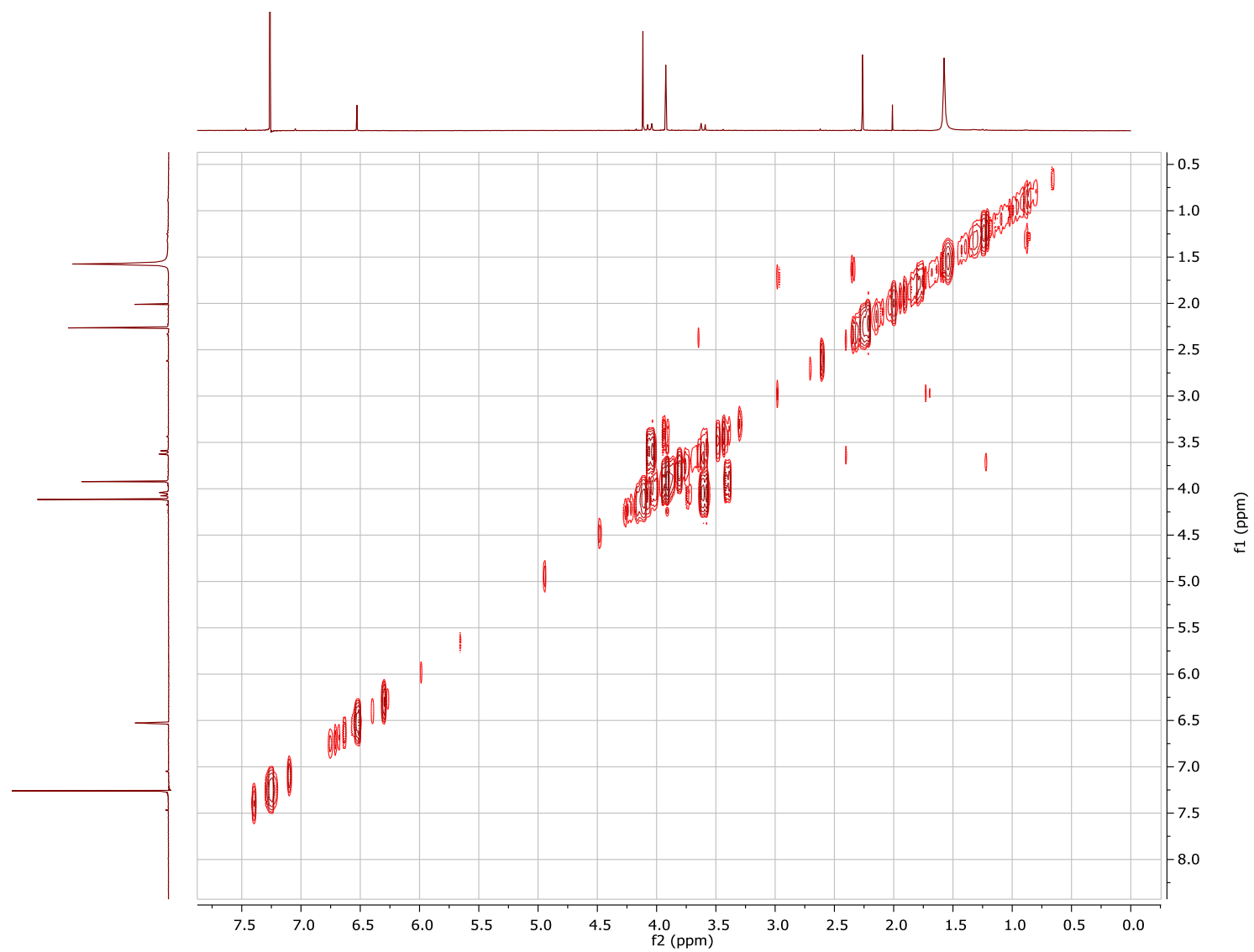


**Figure 6.15.** COSY NMR spectrum of **7** [700 MHz, CDCl<sub>3</sub>].

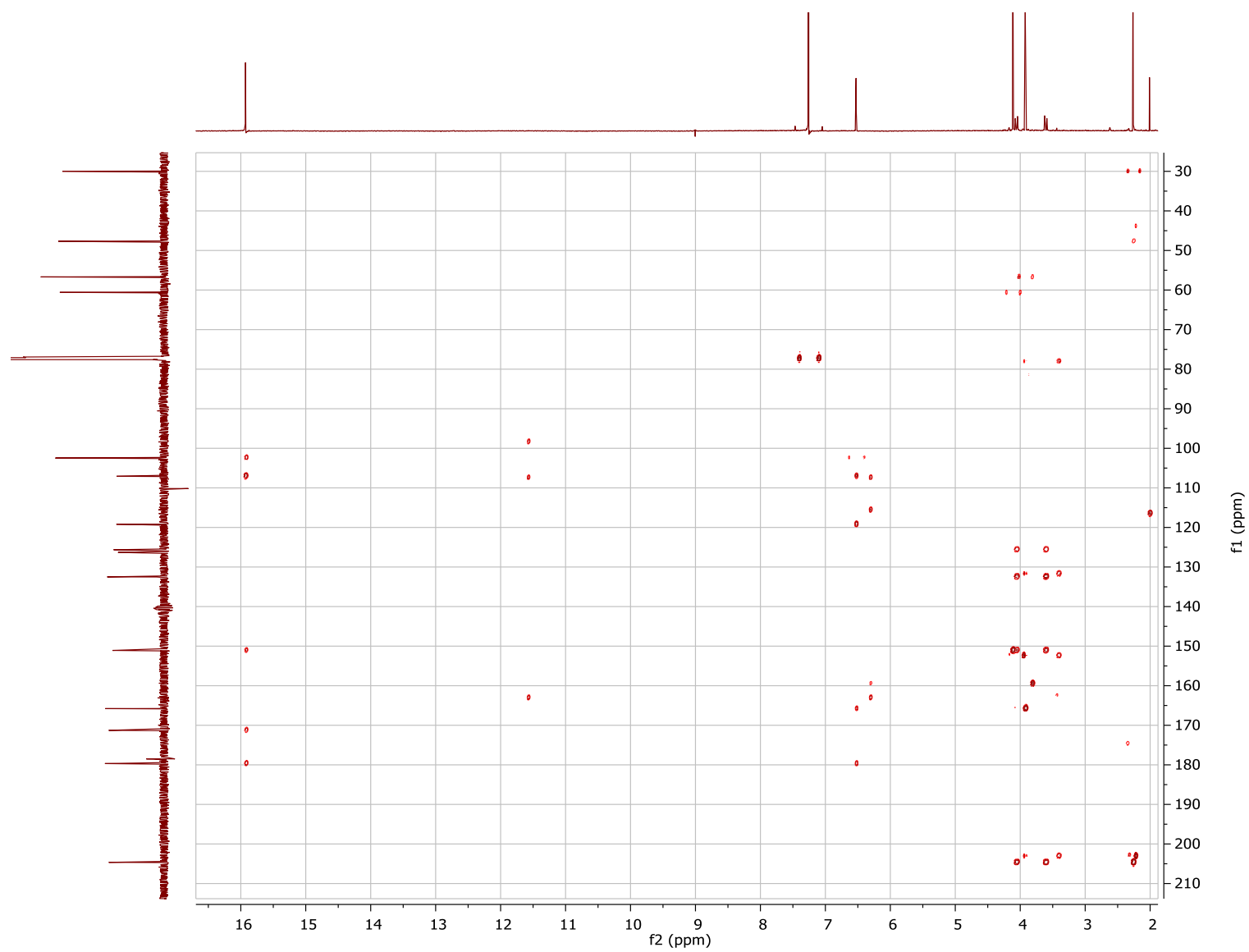


**Figure 6.16.** HMBC NMR spectrum of **7** [700 MHz, CDCl<sub>3</sub>].

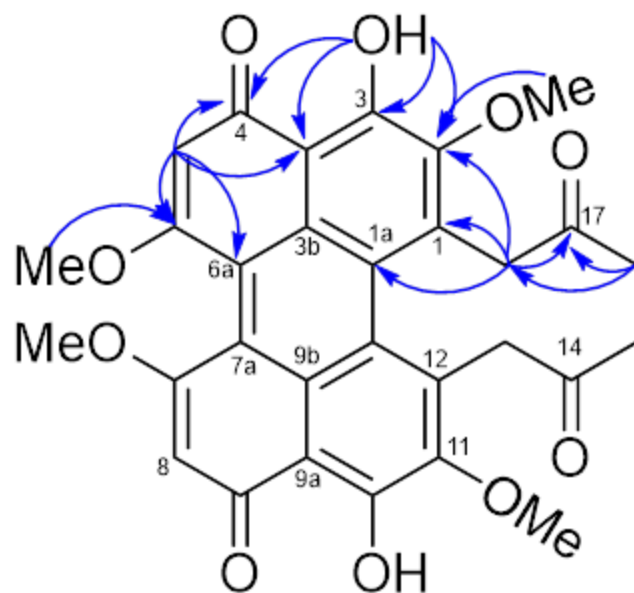


**Figure 6.17.** Key HMBC correlations of **7**.

**Table 6.2.**  $E_{1/2}$ ,  $\Delta E_{1/2}$ , and  $i_{pa}/i_{pc}$  values for the cyclic voltammograms of **1-6** in MeCN with 100mM of [(nBu)<sub>4</sub>N][PF<sub>6</sub>] as the supporting electrolyte.

	$E_{1/2}$ (V vs Ag/AgCl)	
	1 <sup>st</sup> Reduction	2 <sup>nd</sup> Reduction
<i>ent</i> -Shiraiachrome A ( <b>1</b> )	-0.514	-0.756
Hypocrellin ( <b>2</b> )	-0.503	-0.756
Hypocrellin B ( <b>3</b> )	-0.464	-0.709
Hypomycin A ( <b>4</b> )	-0.960	-1.302
Hypomycin C ( <b>5</b> )	-1.001	-1.290
Hypomycin E ( <b>6</b> )	-1.050	-1.364

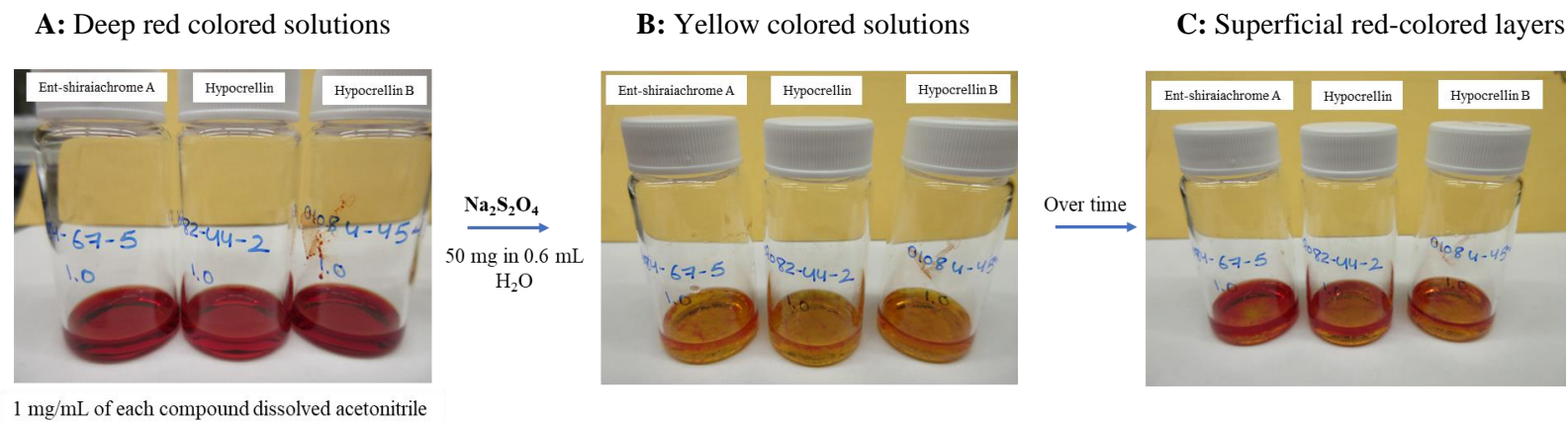


**Figure 6.18.** Small scale reduction reactions of ent-shiraiachrome A (1), hypocrellin (2), and hypocrellin B (3) with Na<sub>2</sub>S<sub>2</sub>O<sub>4</sub> under aerobic condition.

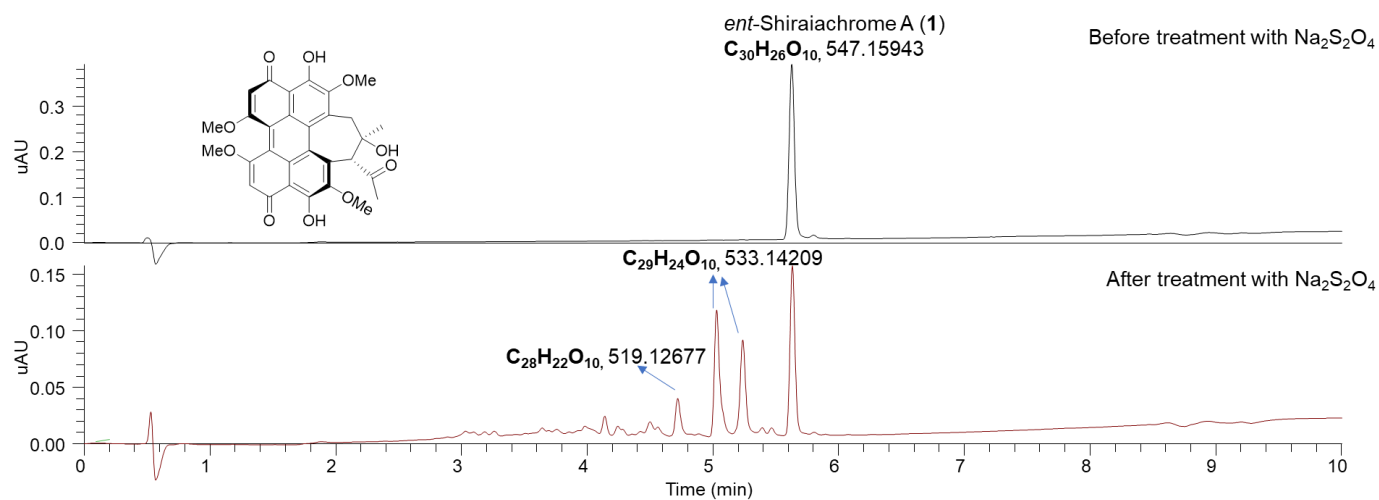


**Figure 6.19.** UPLC-PDA-HRESIMS chromatogram of ent-shiraiachrome A (1) before and after treatment with Na<sub>2</sub>S<sub>2</sub>O<sub>4</sub> as a reducing agent overnight.

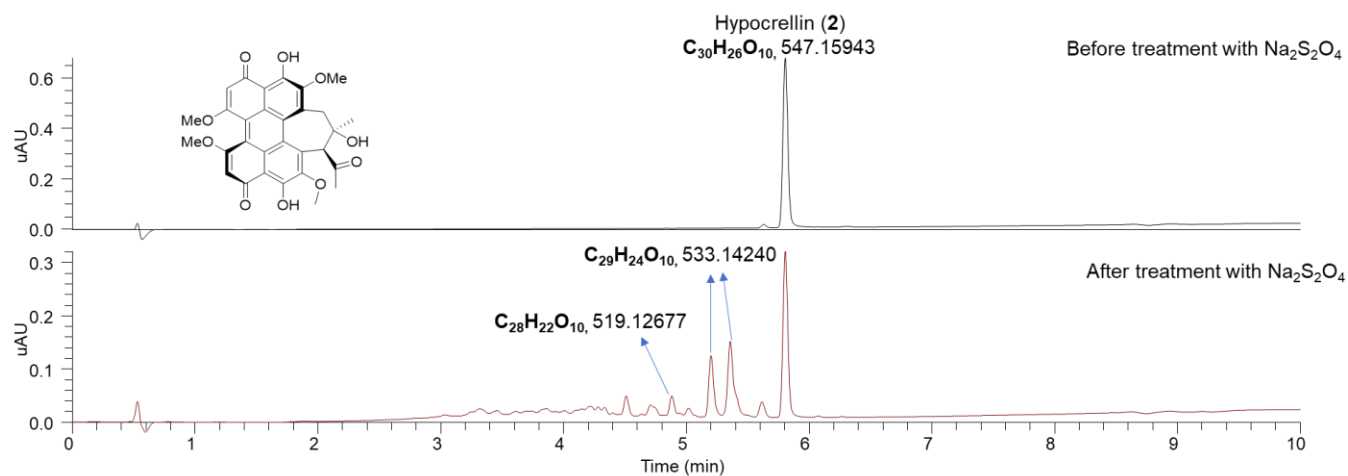


**Figure 6.20.** UPLC-PDA-HRESIMS chromatogram of hypocrellin (**2**) before and after treatment with Na<sub>2</sub>S<sub>2</sub>O<sub>4</sub> as a reducing agent overnight.

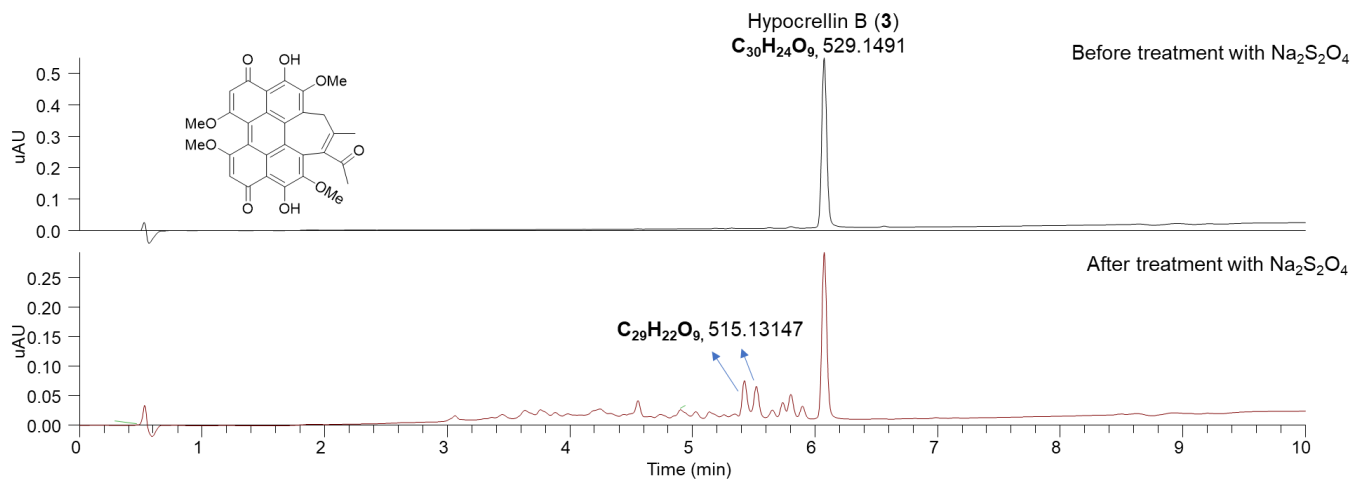


**Figure 6.21.** UPLC-PDA-HRESIMS chromatogram of hypocrellin B (**3**) before and after treatment with Na<sub>2</sub>S<sub>2</sub>O<sub>4</sub> as a reducing agent overnight.

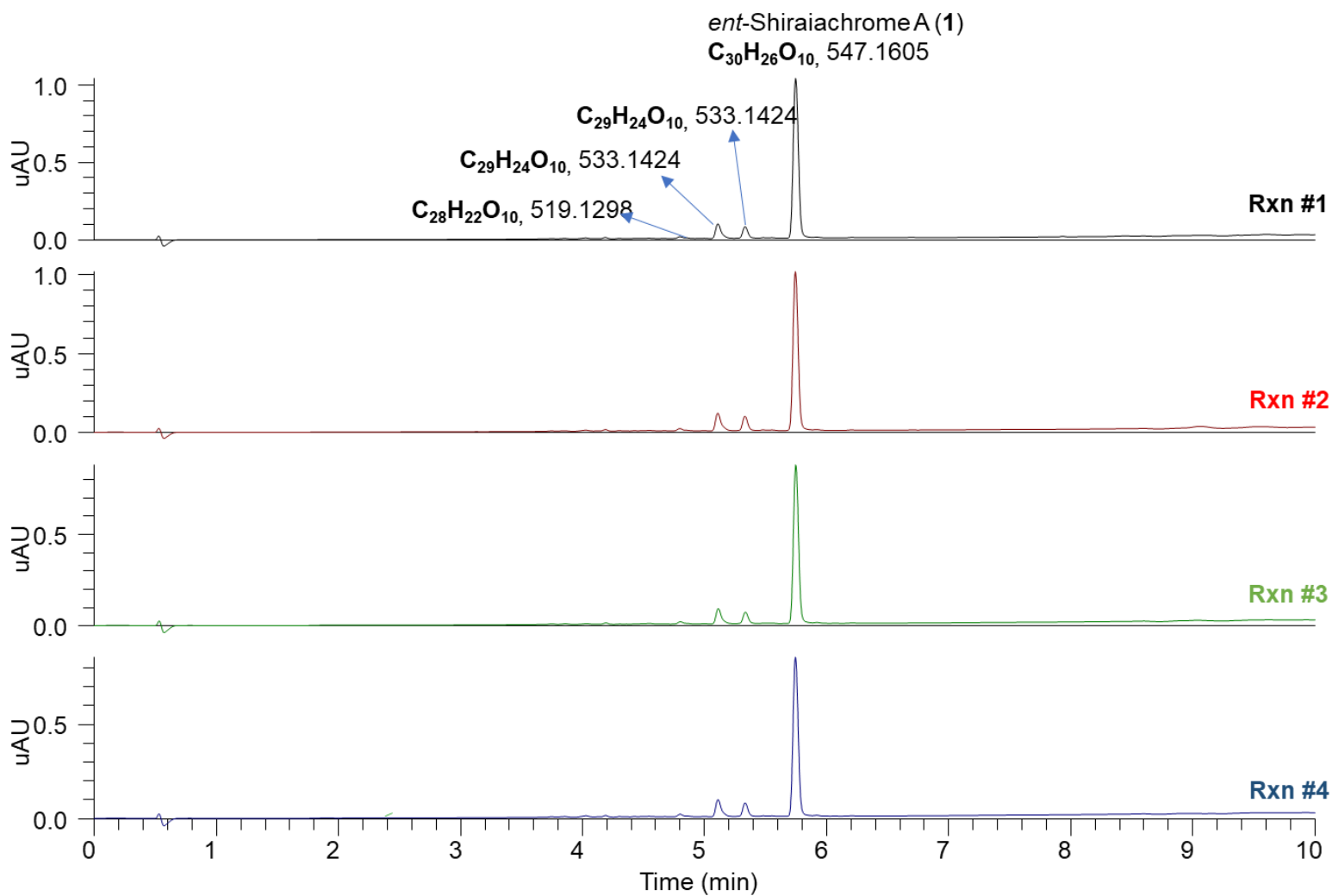


**Figure 6.22.** UPLC-PDA-HRESIMS chromatograms for the four replicates aerobic reduction reactions of *ent*-shiraiachrome A (**1**) with  $Na_2S_2O_4$  (10 mg of **1** was used in each reaction).

**Table 6.3.** NMR Spectroscopic Data for **8-10** in CDCl<sub>3</sub> ( $\delta$  in ppm).

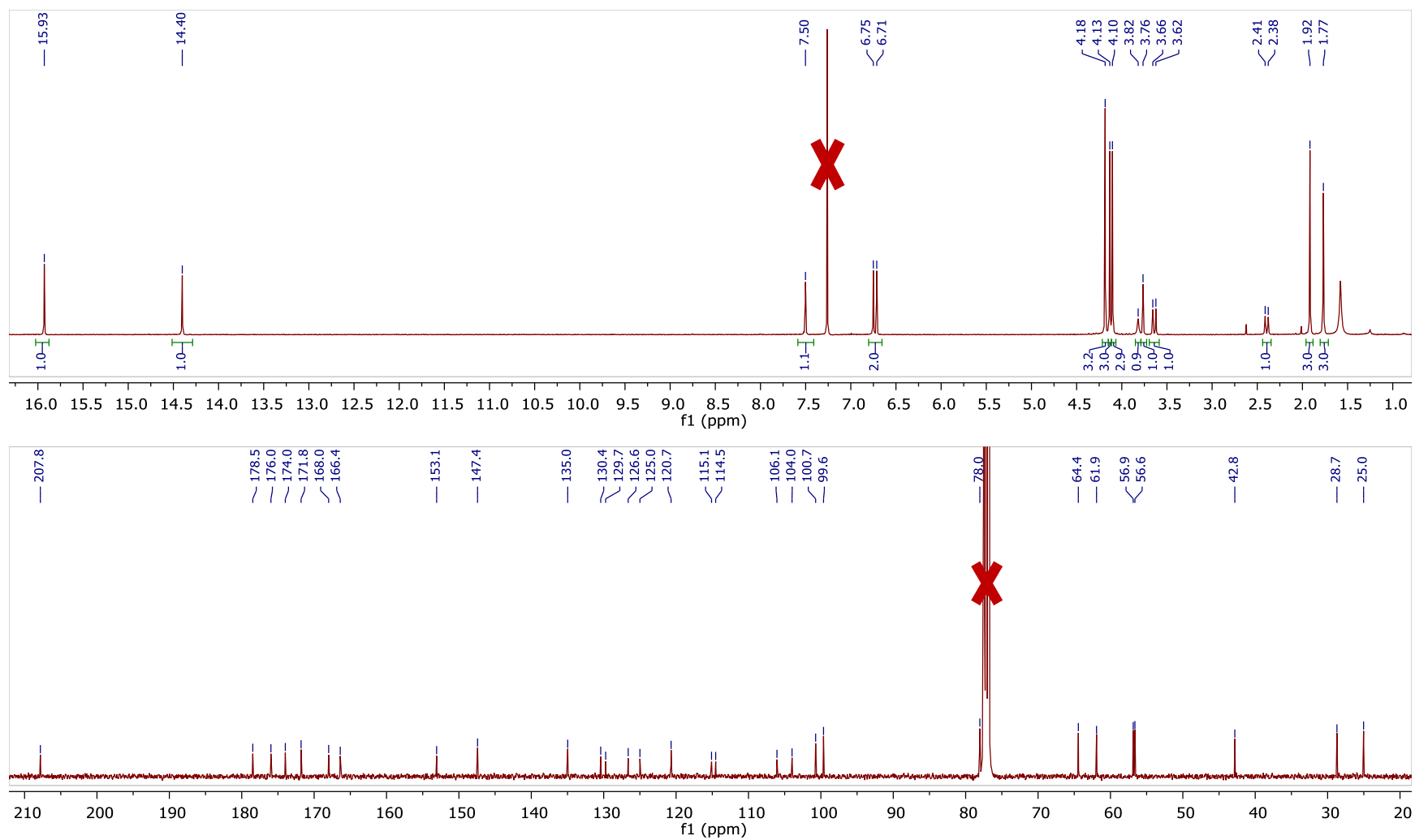
position	<b>8<sup>a</sup></b>		<b>9<sup>b</sup></b>		<b>10<sup>c</sup></b>	
	$\delta_C$ , type	$\delta_H$ (J, Hz)	$\delta_C$ , type	$\delta_H$ (J, Hz)	$\delta_C$ , type	$\delta_H$ (J, Hz)
1	135.0, C		121.9, C		121.9, C	
1a	129.7, C		130.8, C		130.9, C	
2	153.1, C		149.4, C		149.5, C	
3	178.5, C		176.5, C		177.6, C	
3a	106.1, C		103.9, C		103.9, C	
3b	125.5, C or 126.6, C		125.6, C or 125.9, C		125.8, C or 126.2, C	
4	174.0, C		171.7, C		170.5, C	
5	100.7, CH	6.71, s	99.8, CH	6.74, s	99.5, CH	6.77, s
6	166.4, C		167.5, C		167.1, C	
6a	114.5, C		115.0, C		113.8, C or 114.1, C	
7	168.0, C		166.7, C		167.6, C	
7a	115.1, C		113.9, C		113.8, C or 114.1, C	
8	99.6, CH	6.75, s	100.2, CH	6.72, s	99.3, CH	6.77, s
9	171.8, C		173.3, C		170.5, C	
9a	104.0, C		106.4, C		104.0, C	
9b	125.5, C or 126.6, C		125.6, C or 125.9, C		125.8, C or 126.2, C	
10	176.0, C		178.8, C		177.1, C	
11	147.4, C		150.2, C		147.4, C	
12	120.7, C		129.4, C		120.7, C	
12a	130.4, C		131.3, C		130.0, C	
13	42.8, CH <sub>2</sub>	2.40, d (13.6)	42.5, CH <sub>2</sub>	2.42, d (14.0)	42.6, CH <sub>2</sub>	2.47, d (14.2)

		3.64, d (13.6)		3.54, d (14.0)		3.54, d (14.2)
14	78.0, C		78.3, C		78.7, C	
15	64.4, CH	3.76, s	64.6, CH	3.78, s	64.6, CH	3.84, s
16	25.0, CH <sub>3</sub>	1.77, s	24.8, CH <sub>3</sub>	1.78, s	25.0, CH <sub>3</sub>	1.79, s
17	207.8, C		206.7, C		207.8, C	
18	28.7, CH <sub>3</sub>	1.92, s	28.4, CH <sub>3</sub>	1.85, s	28.6, CH <sub>3</sub>	1.91, s
CH <sub>3</sub> O-2	61.9, CH <sub>3</sub>	4.18, s				
CH <sub>3</sub> O-6	56.6, CH <sub>3</sub>	4.10, s	56.7, CH <sub>3</sub>	4.12, s	56.7, CH <sub>3</sub> or 56.8, CH <sub>3</sub>	4.13, s
CH <sub>3</sub> O-7	56.9, CH <sub>3</sub>	4.13, s	56.7, CH <sub>3</sub>	4.10, s	56.7, CH <sub>3</sub> or 56.8, CH <sub>3</sub>	4.13, s
CH <sub>3</sub> O-11			61.0, CH <sub>3</sub>	4.27, s		
HO-2						7.46, s
HO-4		15.93, s		14.49, s		14.30, s
HO-9		14.40, s		15.77, s		14.16
HO-11		7.50, s				7.50, s
HO-14		3.82, brs				

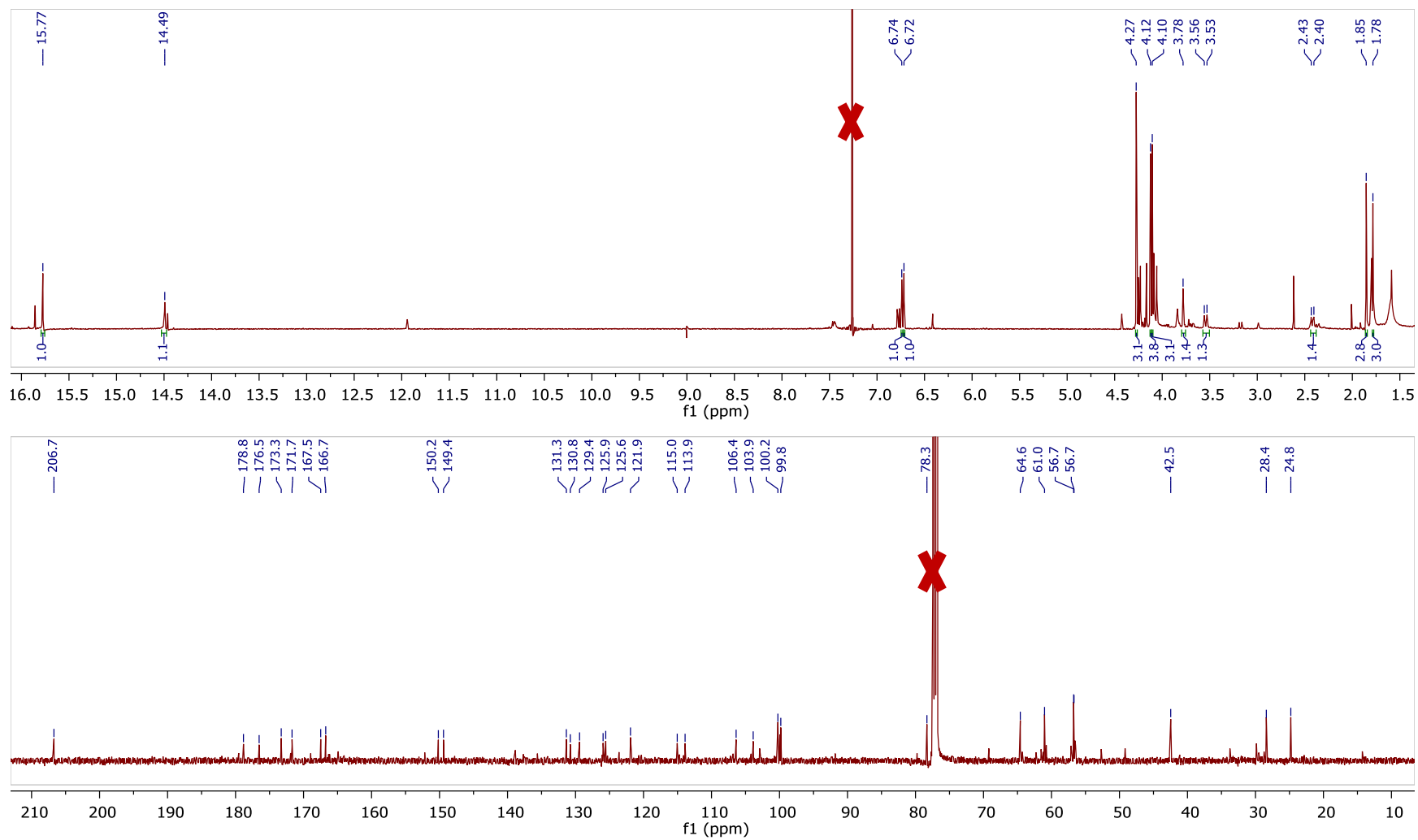
<sup>a</sup>Recorded at 400 MHz for <sup>1</sup>H and 100 MHz for <sup>13</sup>C.

<sup>b</sup>Recorded at 500 MHz for <sup>1</sup>H and 125 MHz for <sup>13</sup>C.

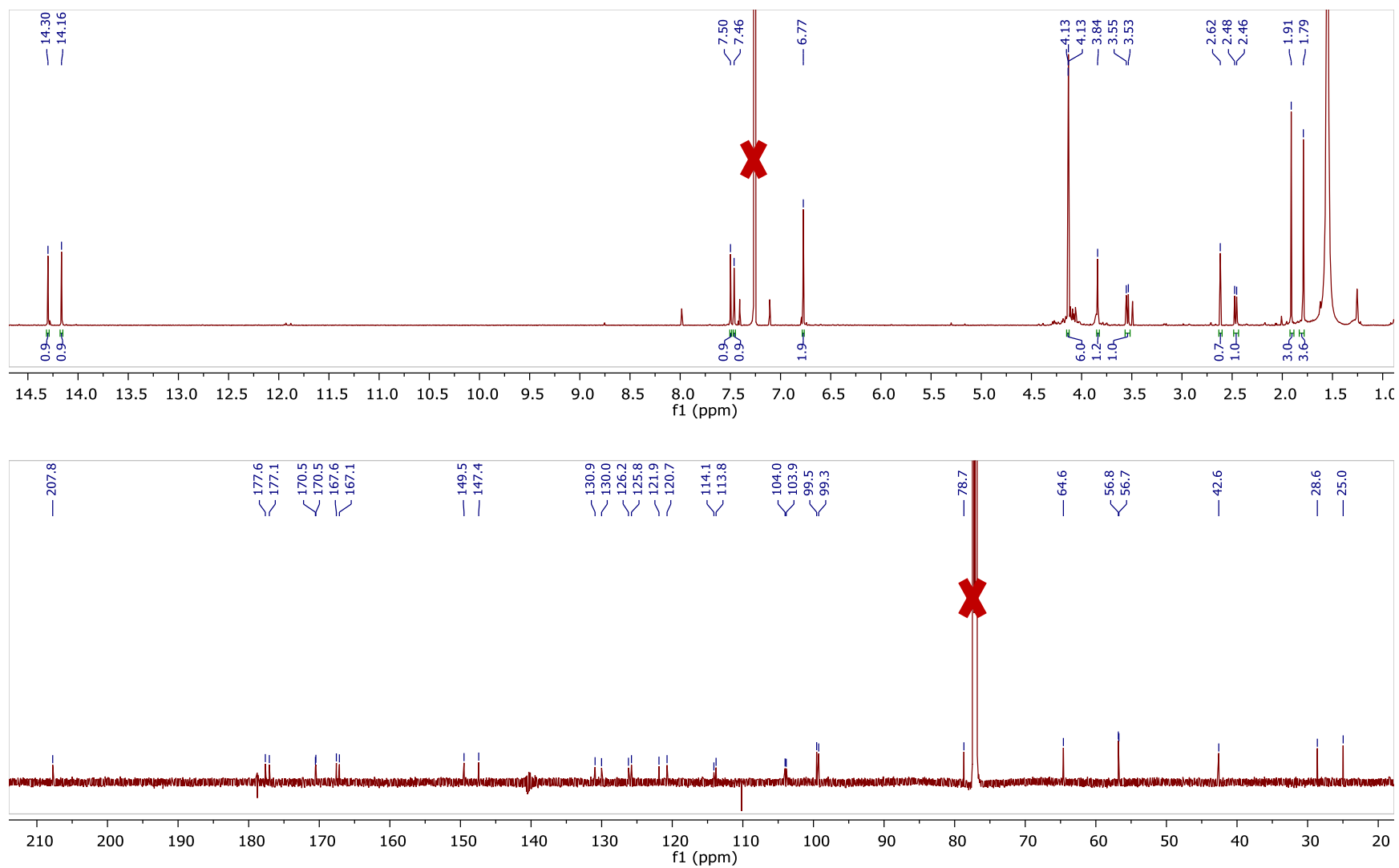
<sup>c</sup>Recorded at 700 MHz for <sup>1</sup>H and 175 MHz for <sup>13</sup>C.



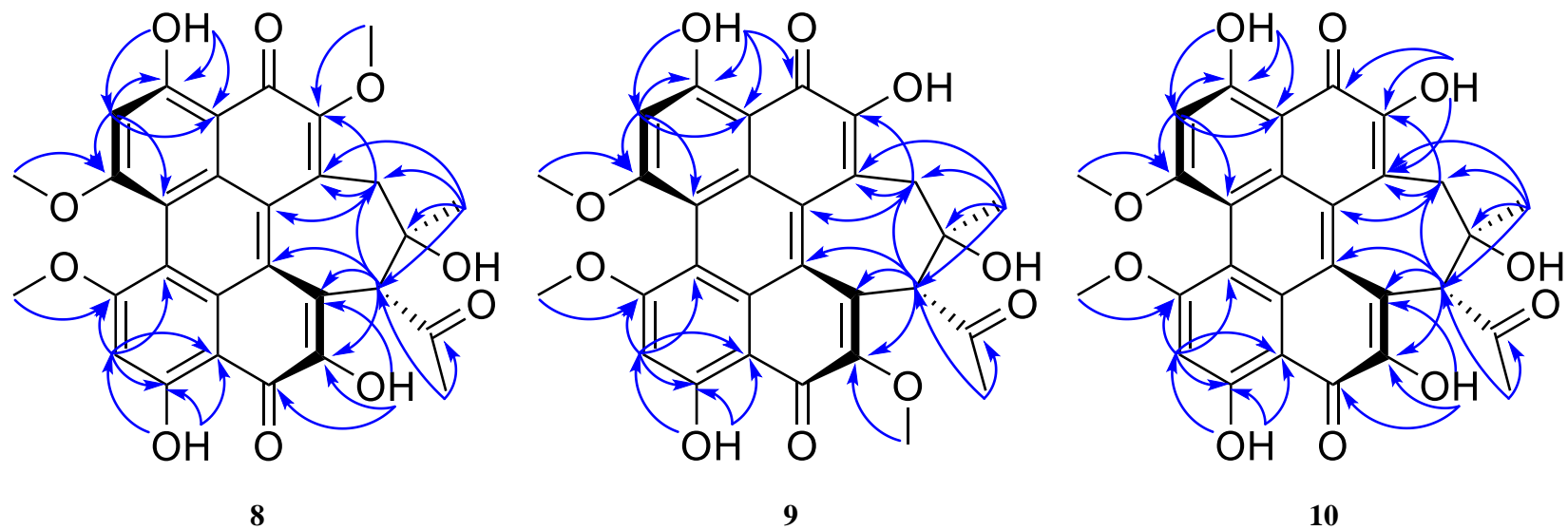
**Figure 6.23.**  $^1\text{H}$  and  $^{13}\text{C}$  NMR spectra of **8** [400 MHz for  $^1\text{H}$  and 100 MHz for  $^{13}\text{C}$ ,  $\text{CDCl}_3$ ].



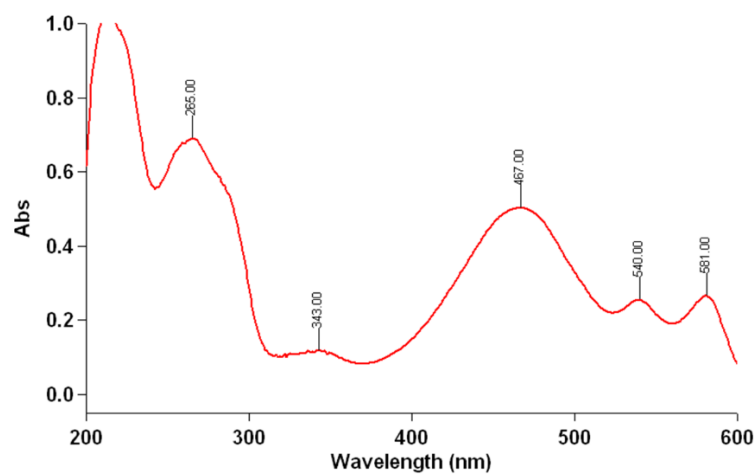
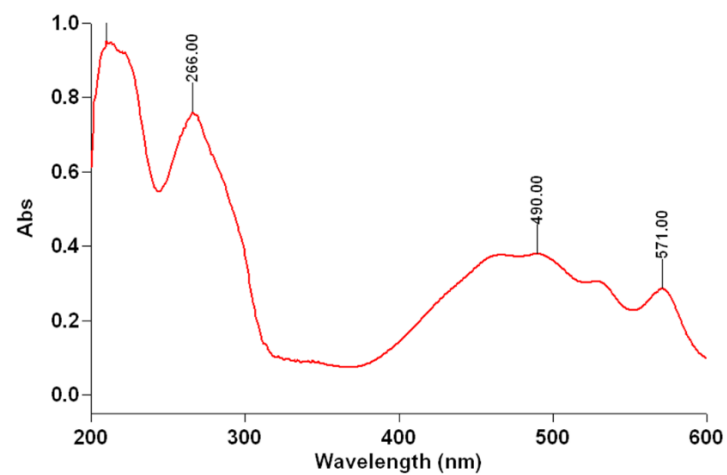
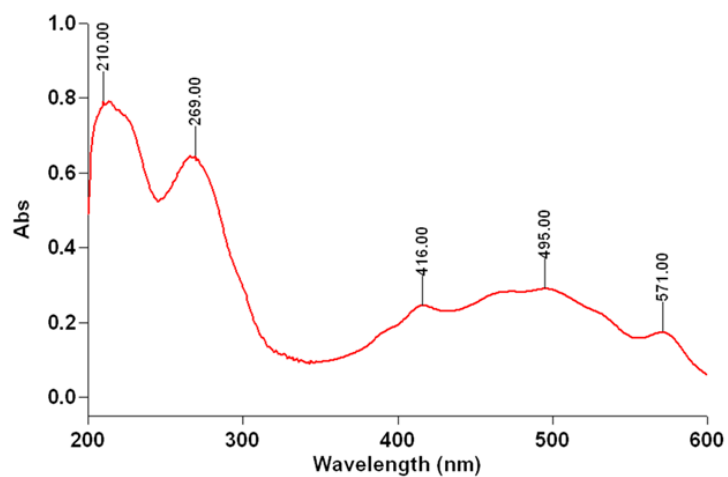
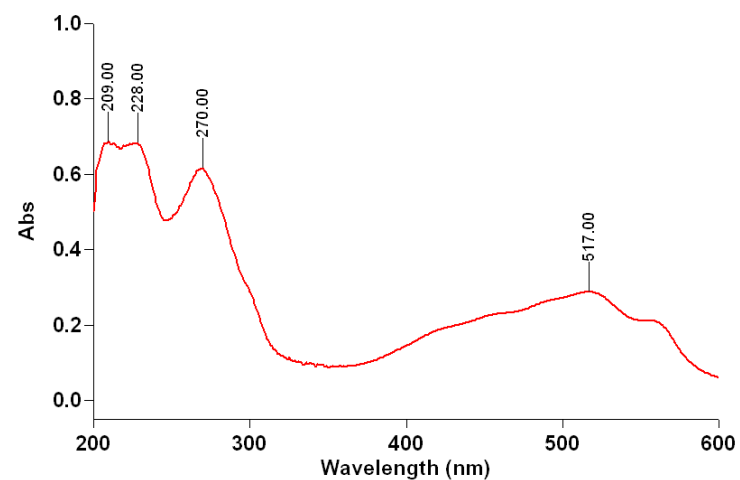
**Figure 6.24.**  $^1\text{H}$  and  $^{13}\text{C}$  NMR spectra of **9** [500 MHz for  $^1\text{H}$  and 125 MHz for  $^{13}\text{C}$ ,  $\text{CDCl}_3$ ].



**Figure 6.25.**  $^1\text{H}$  and  $^{13}\text{C}$  NMR spectra of **10** [700 MHz for  $^1\text{H}$  and 175 MHz for  $^{13}\text{C}$ ,  $\text{CDCl}_3$ ].



**Figure 6.26.** Key HMBC correlations for compounds 8-10.

**1****8****9****10**

**Figure 6.27.** UV spectrum of compounds **8-10** in methanol at concentration of 0.0125 mg/mL as compared to *ent*-shiraiachrome A (**1**).

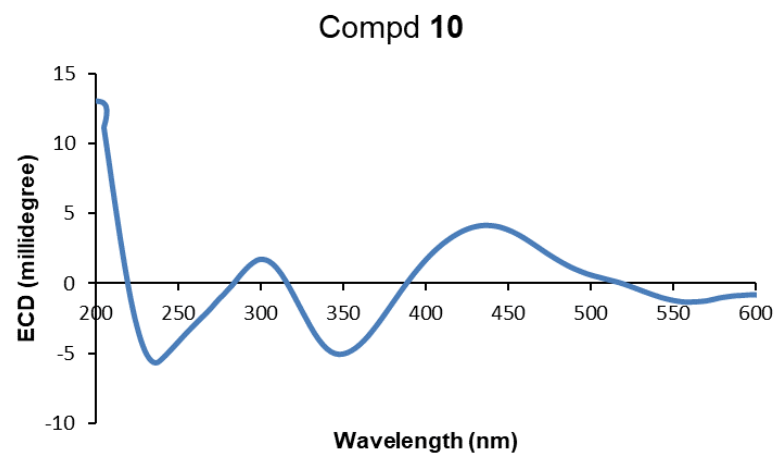
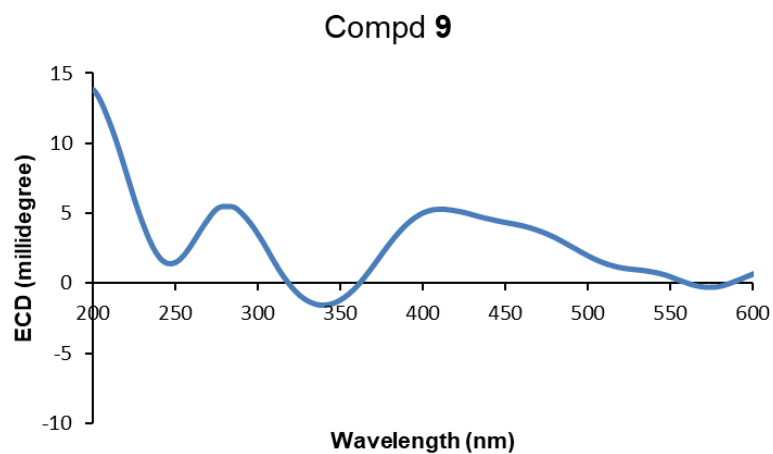
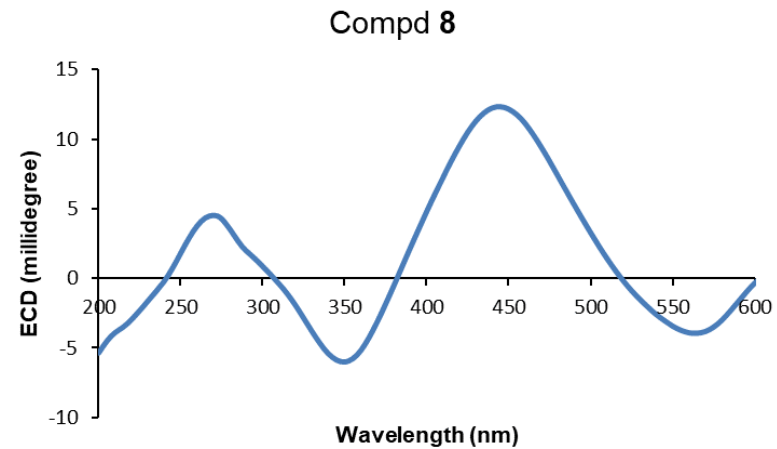
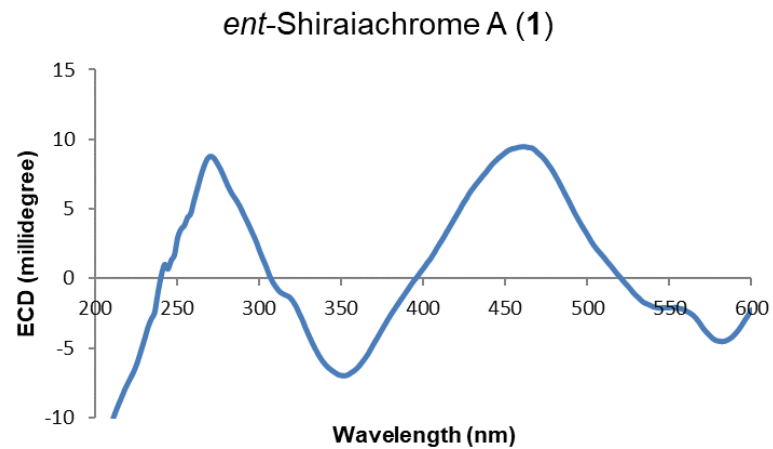


**Figure 6.28.** ECD spectra for compounds **8-10** as compared to *ent*-shiraiachrome A (**1**) in CH<sub>3</sub>OH at a concentration of 0.2 mg/mL.

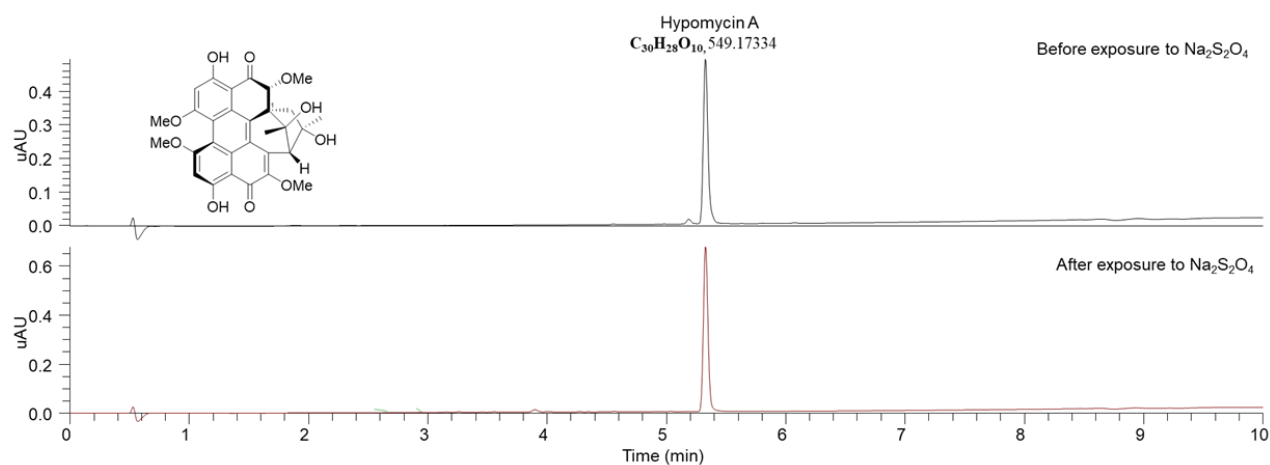


**Figure 6.29.** UPLC-PDA-HRESIMS chromatogram of hypomycin A (**4**) before and after treatment with Na<sub>2</sub>S<sub>2</sub>O<sub>4</sub> as a reducing agent overnight.

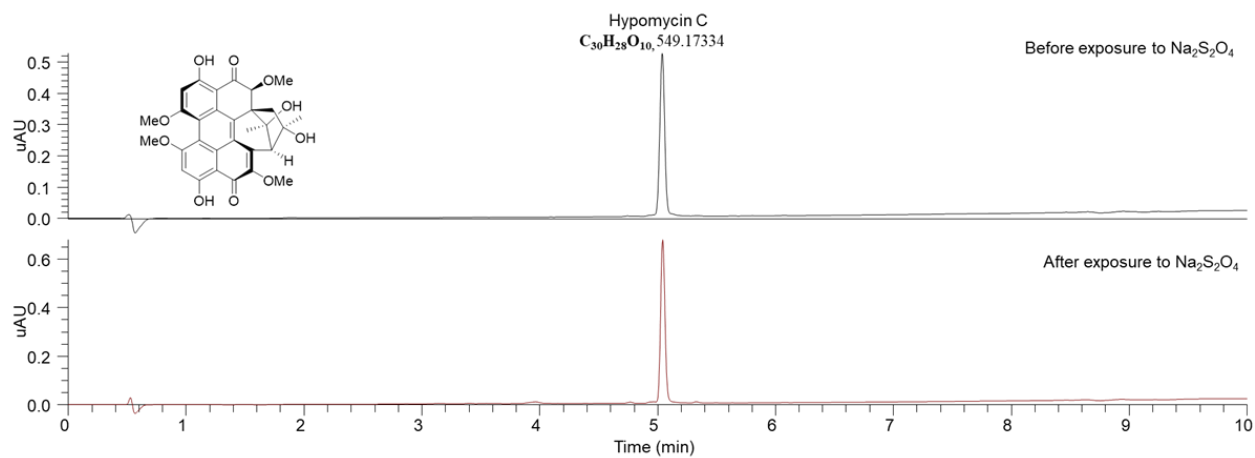


**Figure 6.30.** UPLC-PDA-HRESIMS chromatogram of hypomycin C (**5**) before and after treatment with Na<sub>2</sub>S<sub>2</sub>O<sub>4</sub> as a reducing agent overnight.

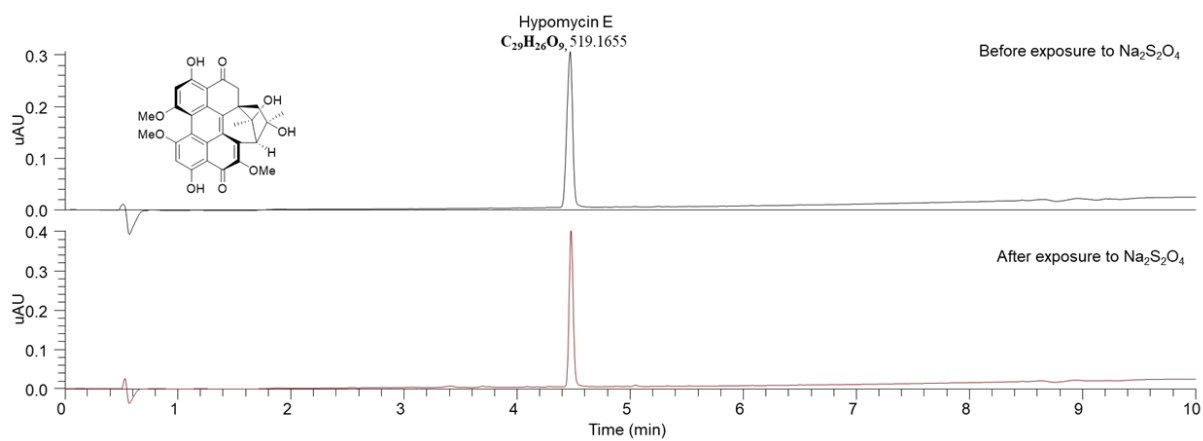


**Figure 6.31.** UPLC-PDA-HRESIMS chromatogram of hypomycin E (6) before and after treatment with  $\text{Na}_2\text{S}_2\text{O}_4$  as a reducing agent overnight.

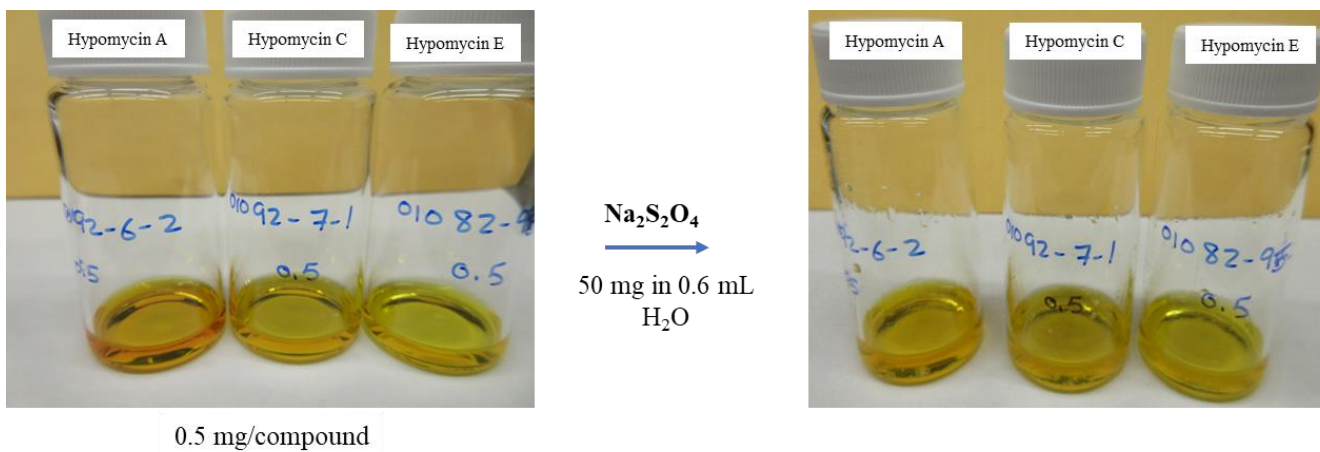


**Figure 6.32.** Small scale reduction reactions of hypomycin A (4), C (5), and E (6) with  $\text{Na}_2\text{S}_2\text{O}_4$  under aerobic conditions. Note the absence of a color change, relative to what was observed for 1-3 (Figure S9).

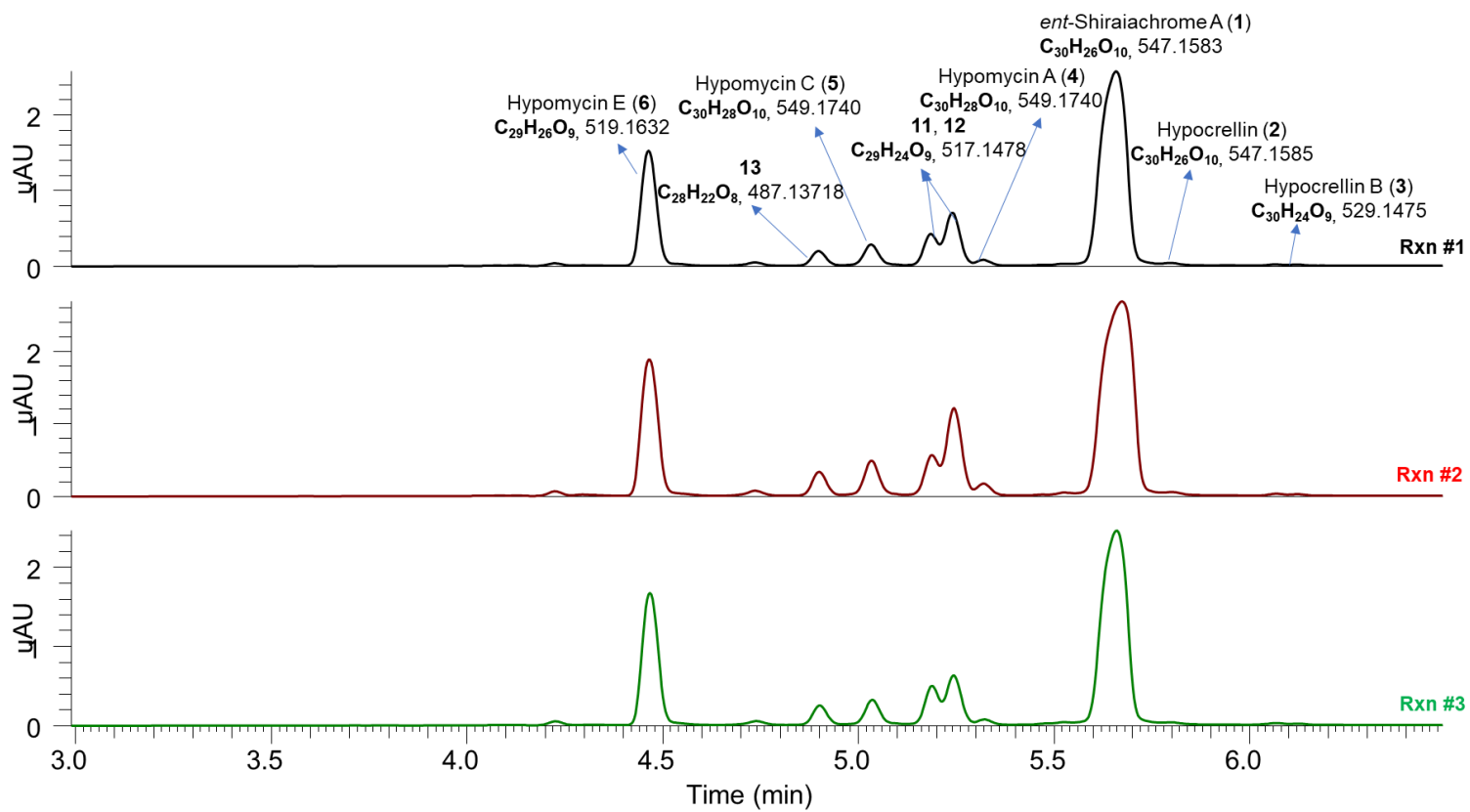


**Figure 6.33.** UPLC-PDA-HRESIMS chromatograms for the triplicate anaerobic reduction reactions of *ent*-shiraiachrome A (1) with  $Na_2S_2O_4$ . HRESIMS data are reported as  $[M + H]^+$ .

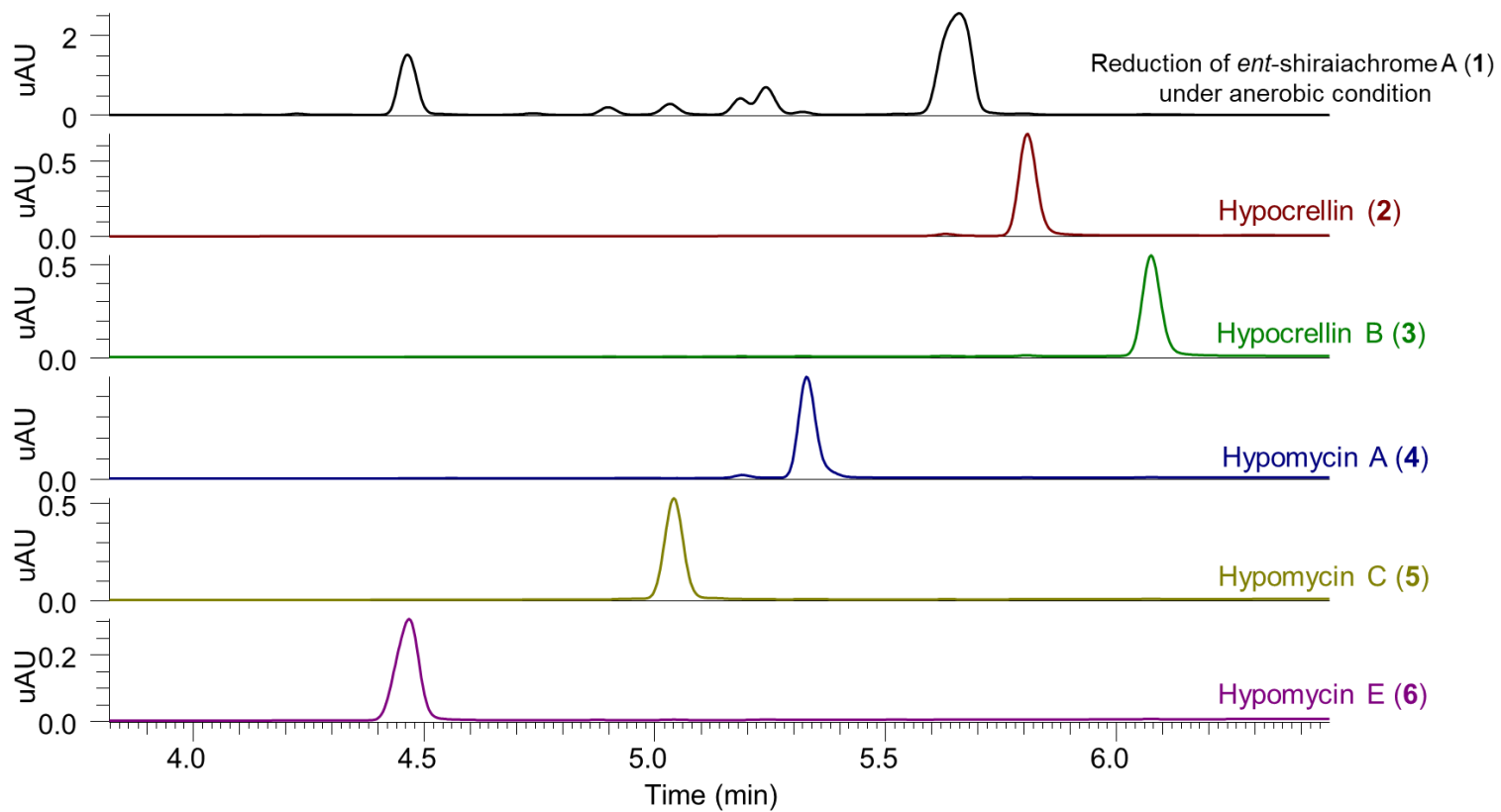


**Figure 6.34.** UPLC-PDA-HRESIMS chromatograms for the anaerobic reduction reactions of *ent*-shiraiachrome A (1) as compared to UPLC-HRESIMS chromatograms of pure standards of 2-6.

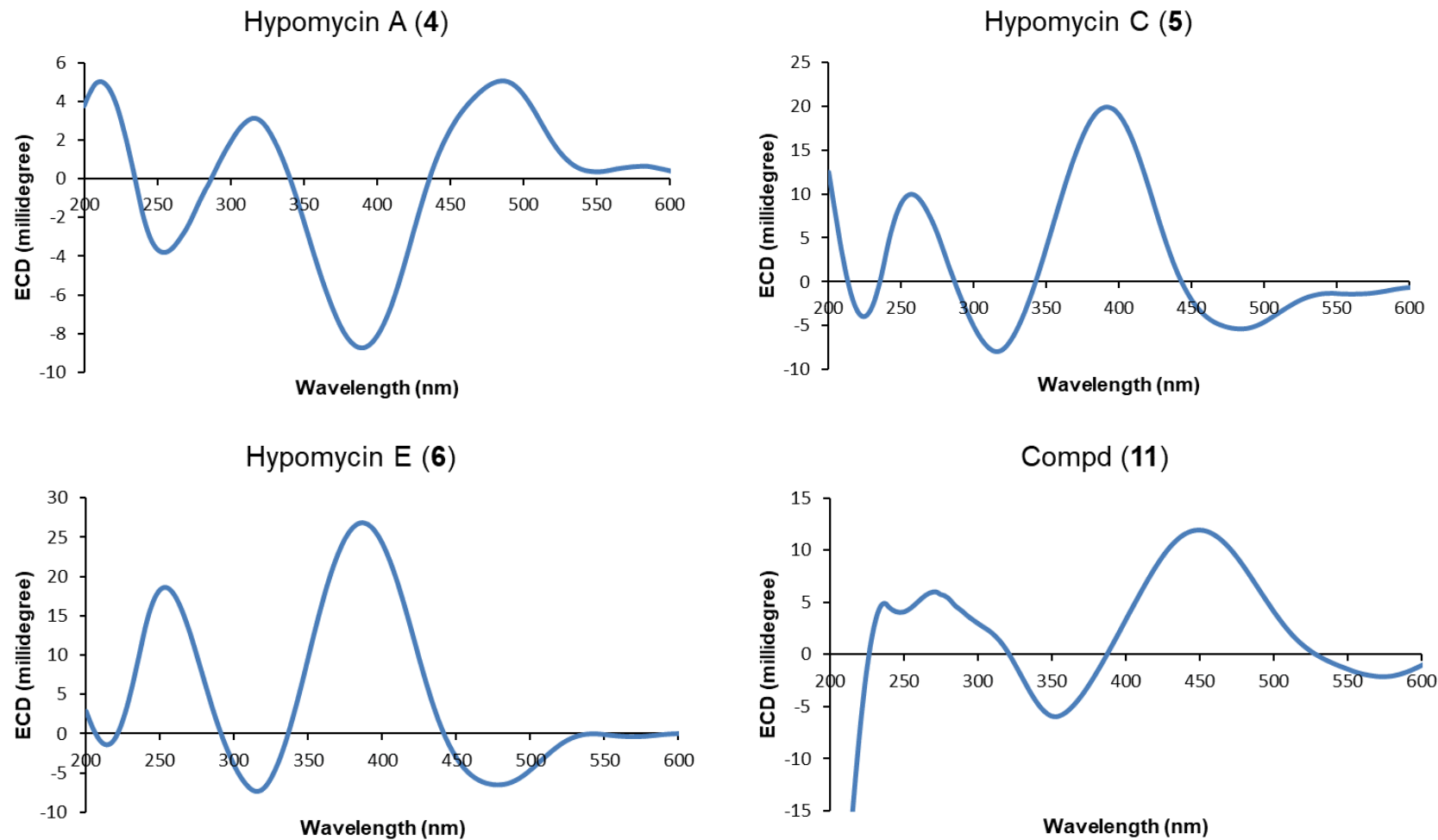


**Figure 6.35.** ECD spectra in CH<sub>3</sub>OH for compounds **4-6** and **11** which were isolated from the anaerobic reduction reaction of **1** and **2**.

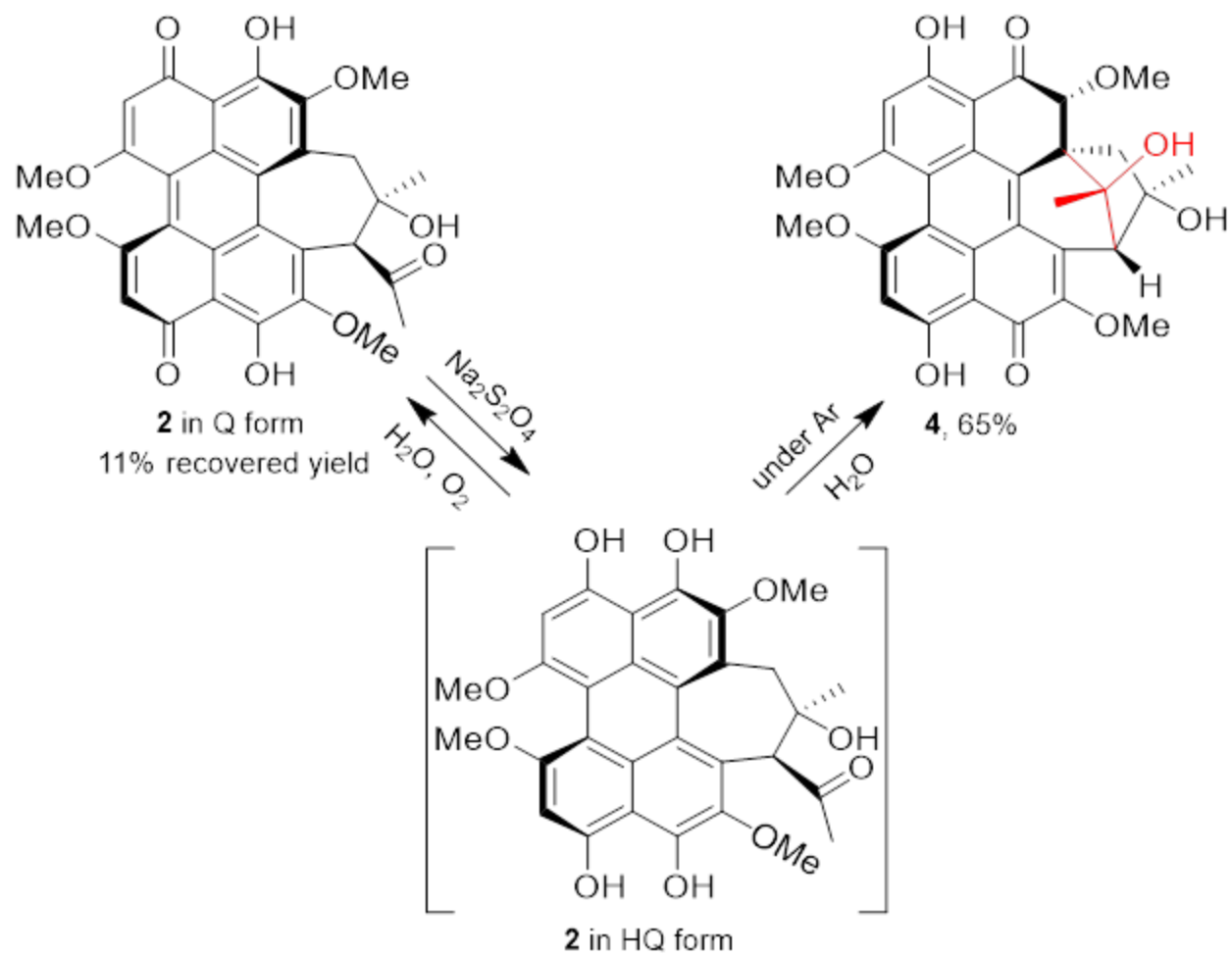


**Figure 6.36.** Hypomycin A (**4**) obtained by chemical reduction of hypocrellin (**2**) with  $\text{Na}_2\text{S}_2\text{O}_4$  under anaerobic condition.

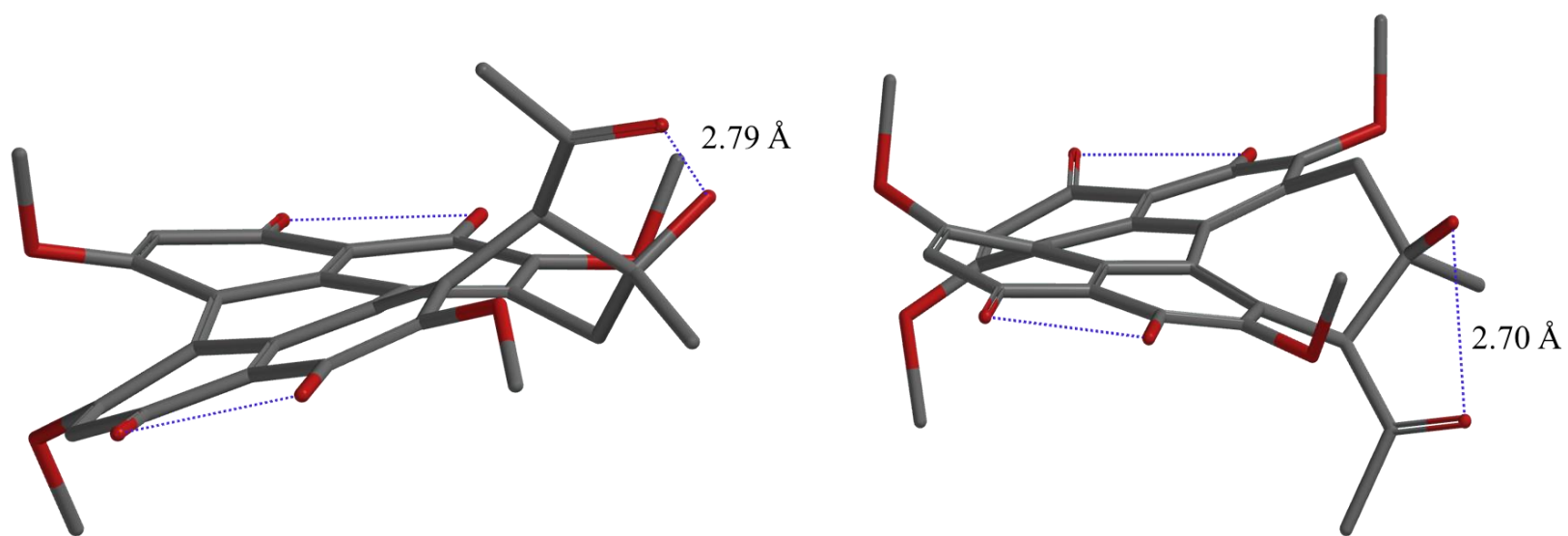


**Figure 6.37.** Intramolecular hydrogen-bonding between HO-14 and the C-17 carbonyl in the 3D structures of *ent*-shiraiachrome A (**1**) and hypocrellin (**2**). The donor-acceptor distance of 2.70 Å in **2** and 2.79 Å in **1** indicates stronger hydrogen-bonding in hypocrellin (**2**).

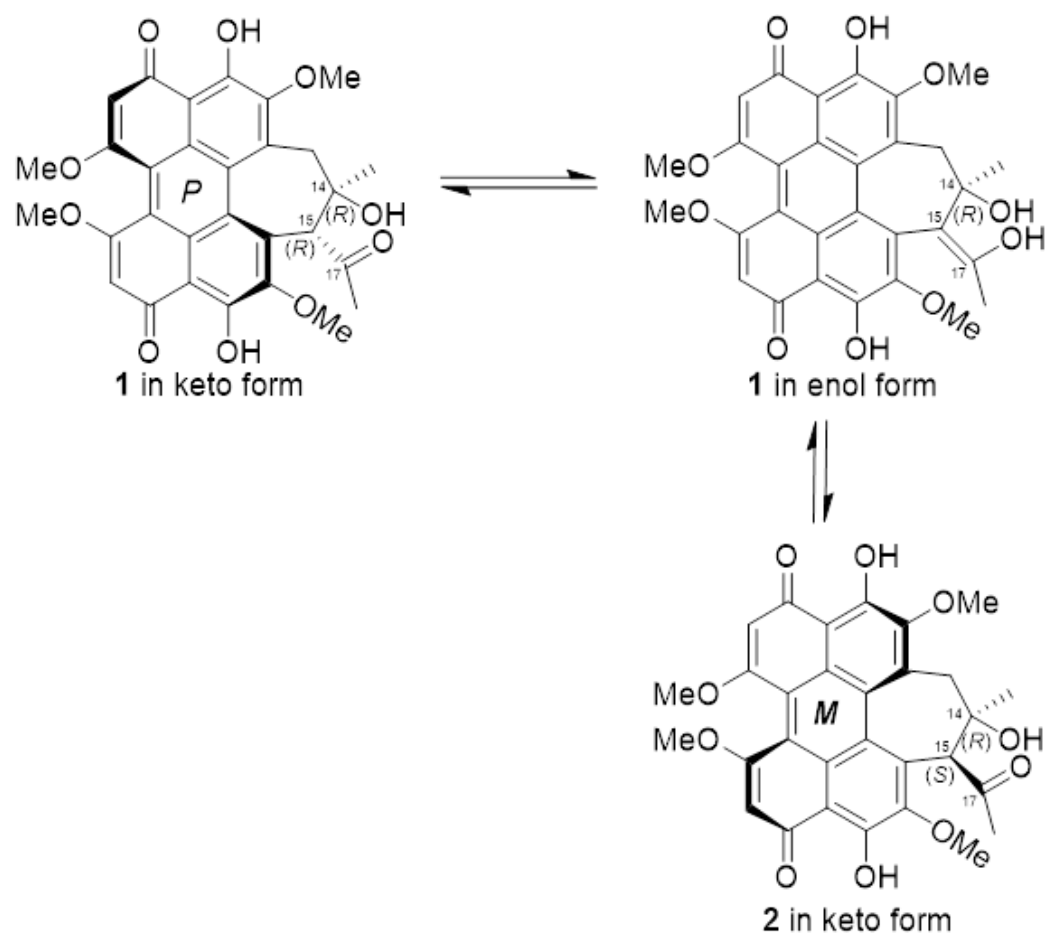


**Figure 6.38.** Keto-enol tautomerism of *ent*-shiraiachrome A (**1**) at C-17 carbonyl intermediates the conversion process of **1** into **2**.

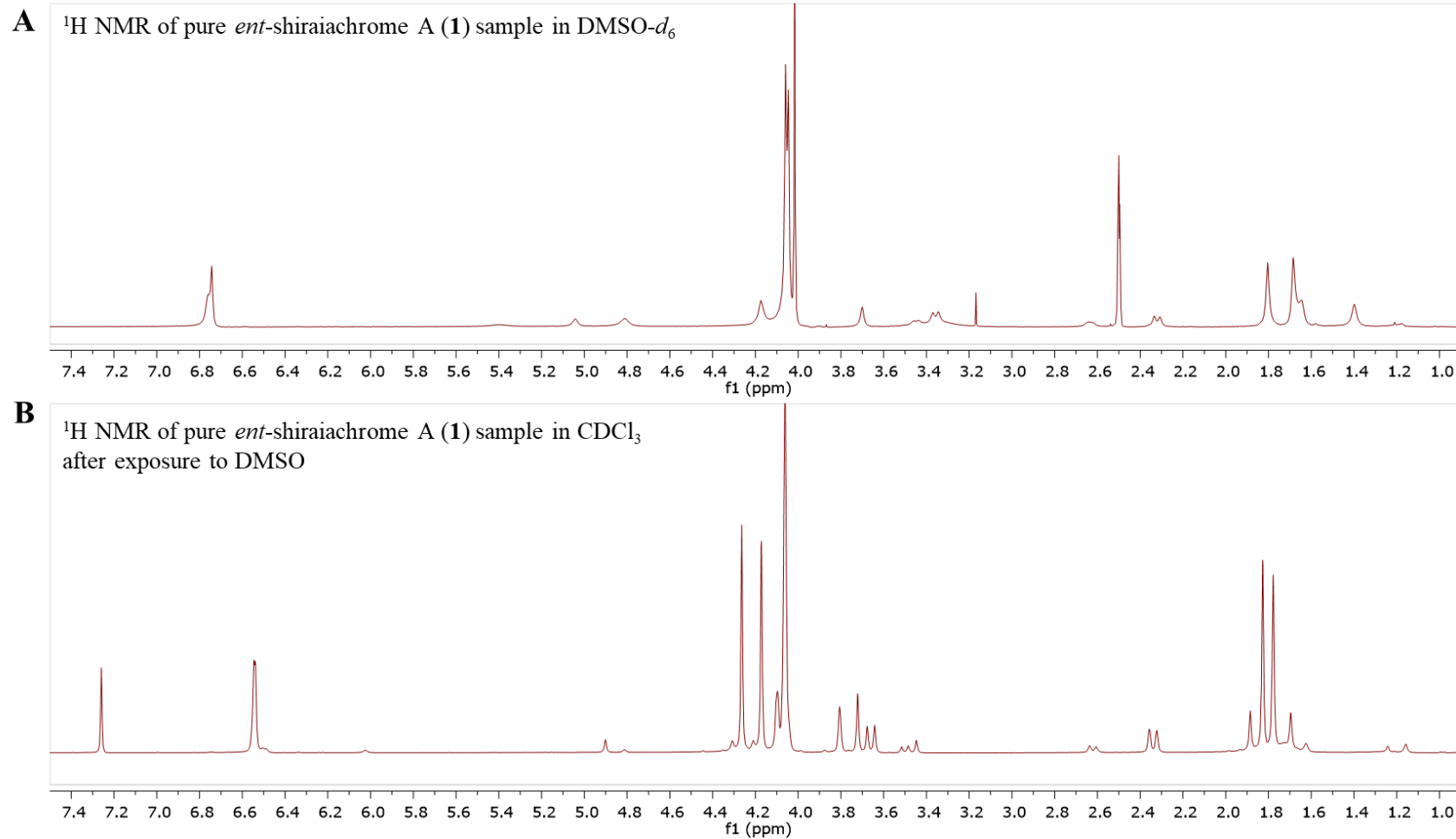


**Figure 6.39.**  $^1\text{H}$  NMR of pure *ent*-shiraiachrome A (**1**) in  $\text{DMSO-}d_6$  (**A**) and  $^1\text{H}$  NMR of **1** in  $\text{CDCl}_3$  after exposure to DMSO (**B**).

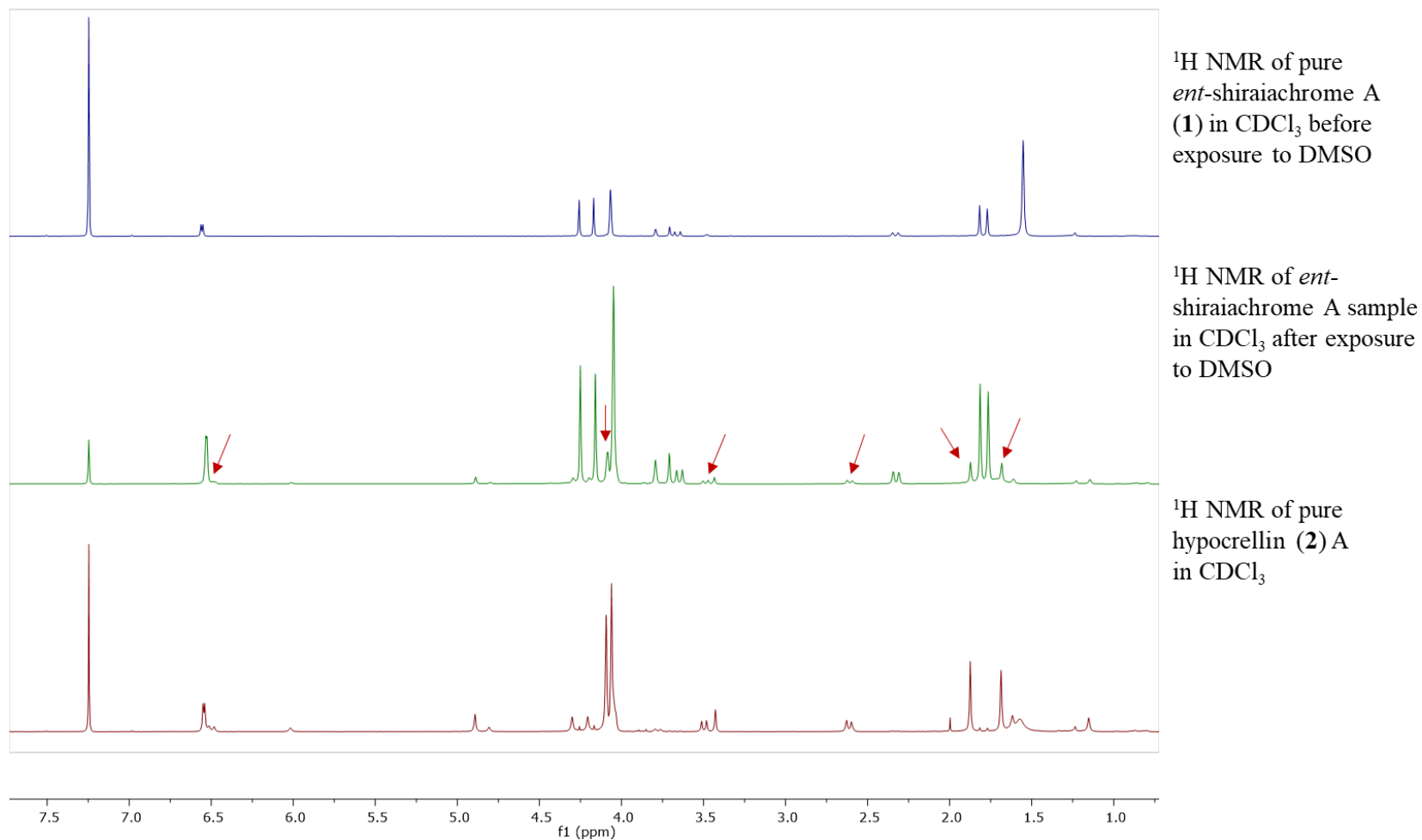
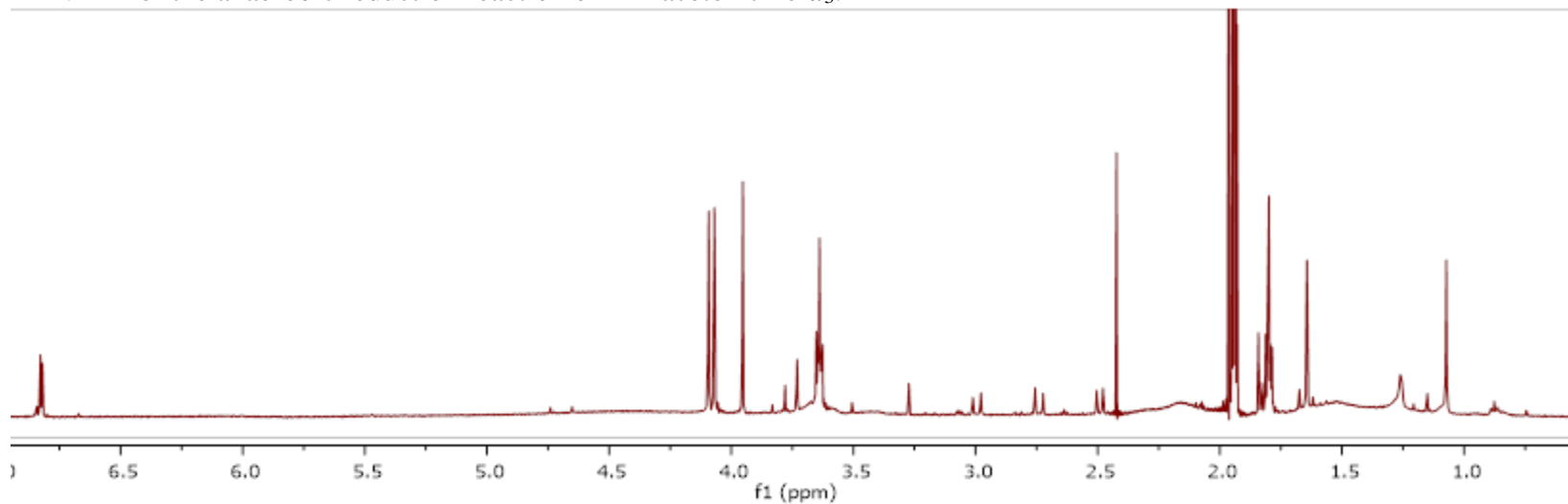


**Figure 6.40.**  $^1\text{H}$  NMR of pure *ent*-shiraiachrome A (1) in  $\text{CDCl}_3$  before and after exposure to DMSO vs  $^1\text{H}$  NMR of hypocrellin (2) in  $\text{CDCl}_3$ . Red arrows show the new set on peaks formed in *ent*-shiraiachrome A (1) sample after exposure to DMSO, which matches the  $^1\text{H}$  NMR of hypocrellin (2).

$^1\text{H}$  NMR for the anaerobic reduction reaction of **1** in acetonitrile- $d_3$ .



$^1\text{H}$  NMR for hypomycin E (**6**) in acetonitrile- $d_3$ .

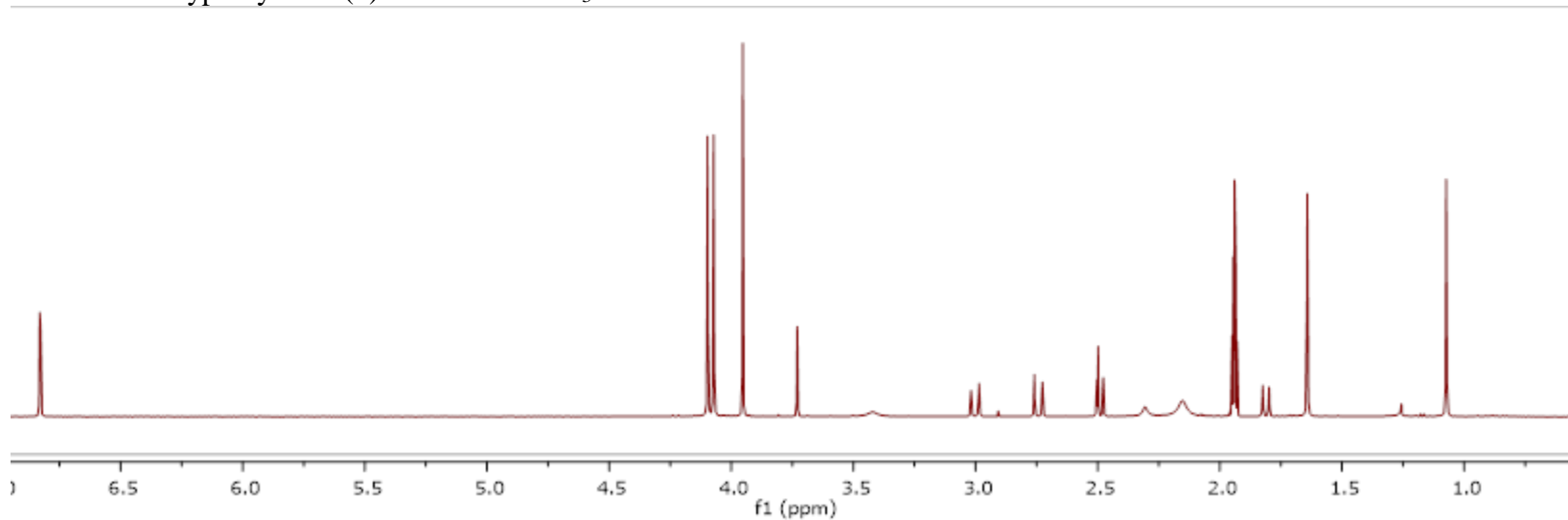
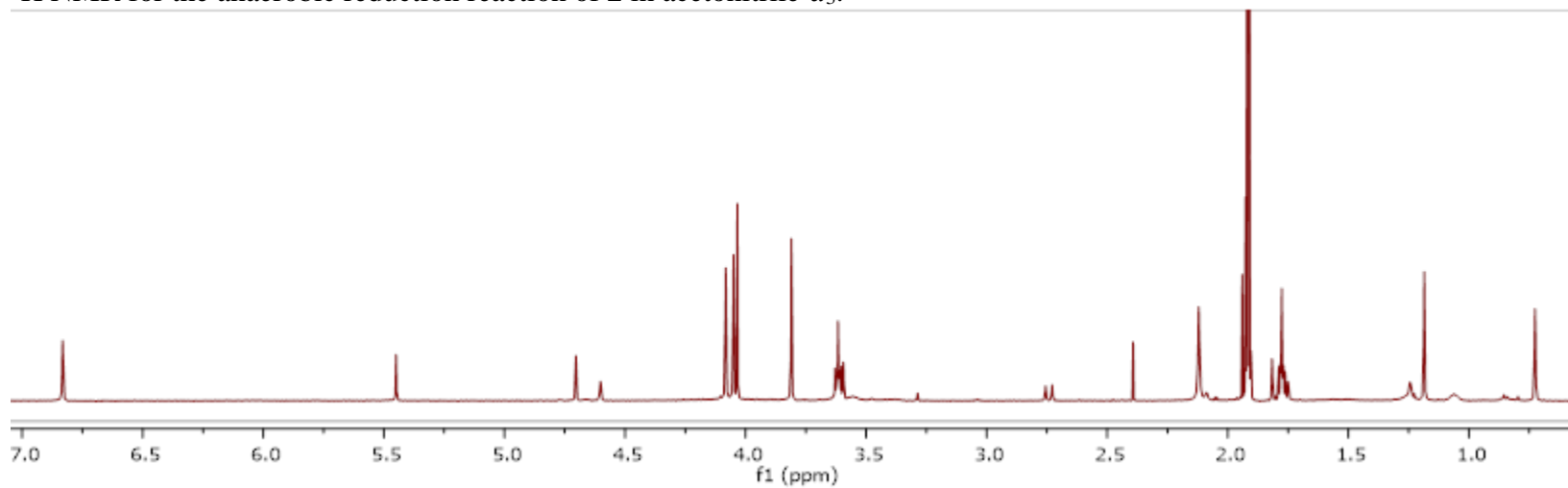


**Figure 6.41.**  $^1\text{H}$  NMR for the anaerobic reduction reaction mixture of *ent*-shiraiachrome A (**1**) as compared to hypomycin E (**6**) in acetonitrile- $d_3$ .

$^1\text{H}$  NMR for the anaerobic reduction reaction of **2** in acetonitrile- $d_3$ .



$^1\text{H}$  NMR for hypomycin A (**4**) in acetonitrile- $d_3$ .

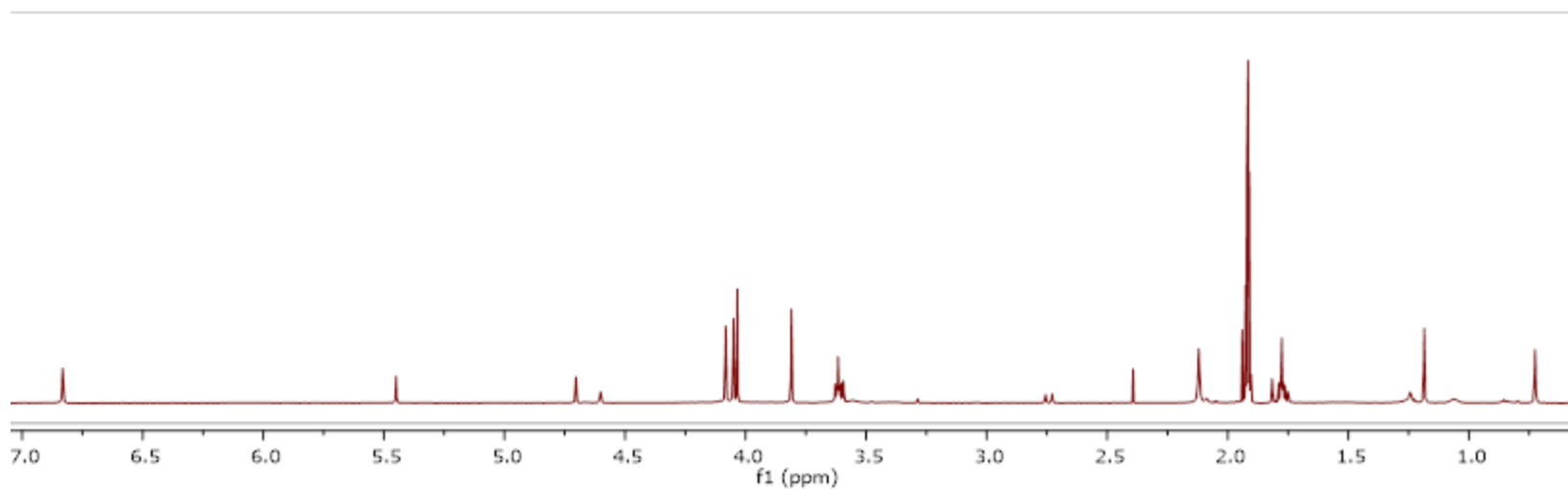
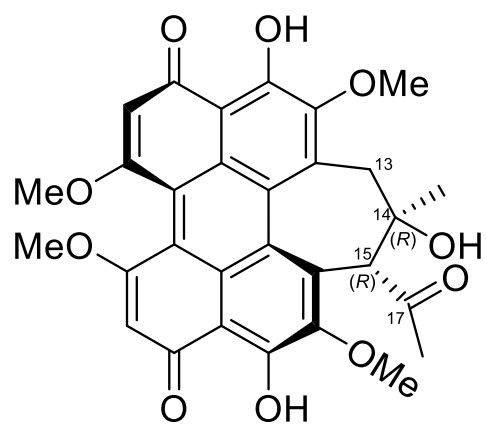
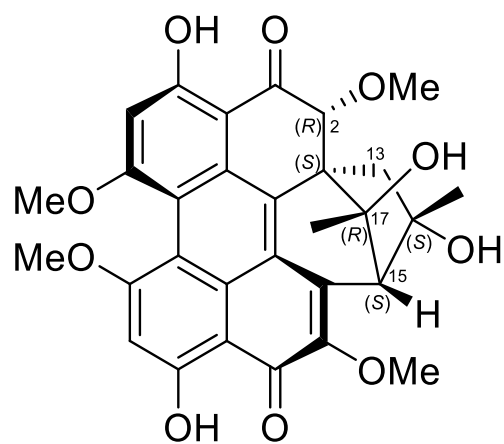


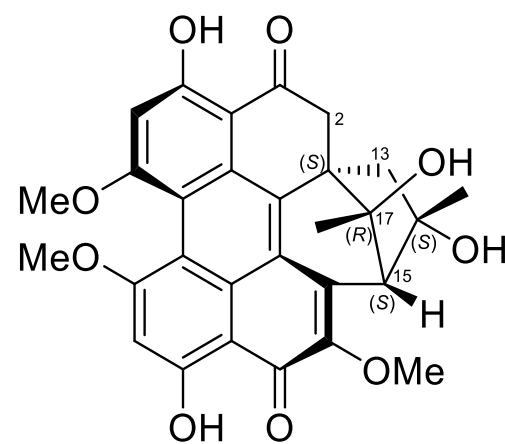
**Figure 6.42.**  $^1\text{H}$  NMR for the anaerobic reduction reaction mixture of hypocrellin (**2**) as compared to hypomycin A (**4**) in acetonitrile- $d_3$ .



*ent*-Shiraiachrome A (1)



Hypomycin C (5)



Hypomycin E (6)

**Figure 6.43.** Previously reported structures of hypomycin C (5) and E (6) as compared to *ent*-shiraiachrome A (1).<sup>6</sup>

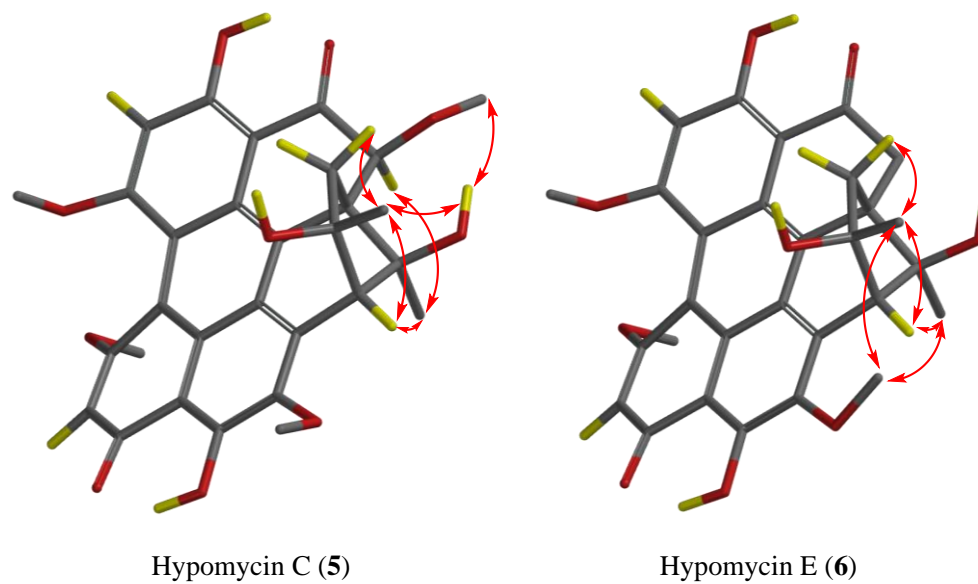


**Figure 6.44.** Key NOESY correlations of hypomycin C (5) and hypomycin E (6).

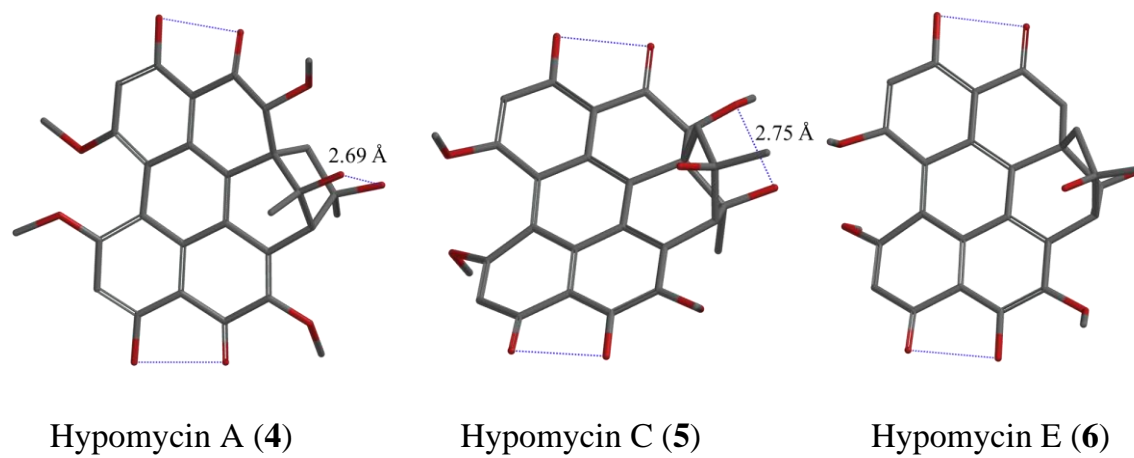


**Figure 6.45.** The observed intramolecular hydrogen-bonding of the exchangeable protons in hypomycin A (4), C (5), and E (6).

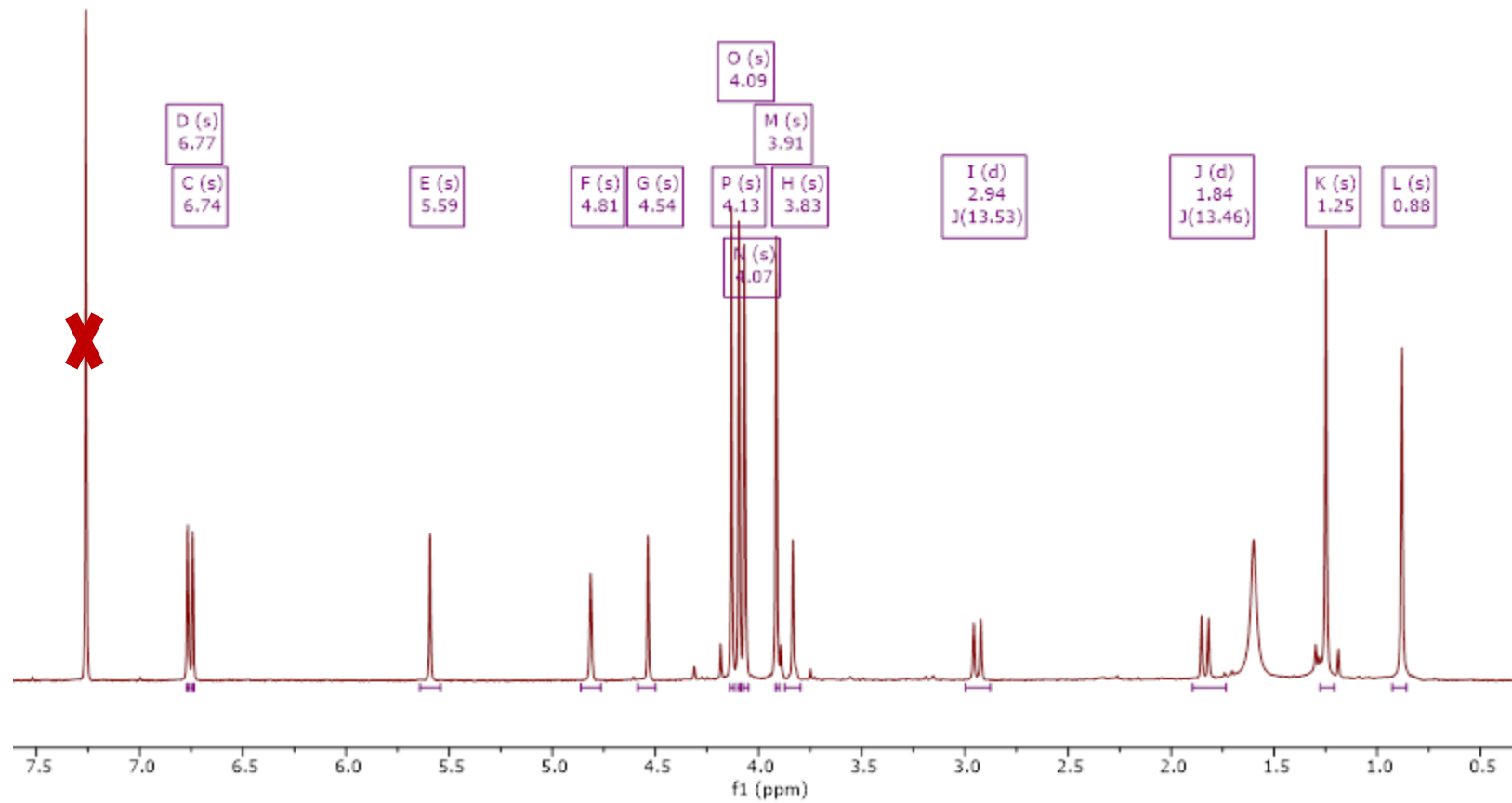


**Figure 6.46.**  $^1\text{H}$  NMR of hypomycin A (4) [400 MHz,  $\text{CDCl}_3$ ].

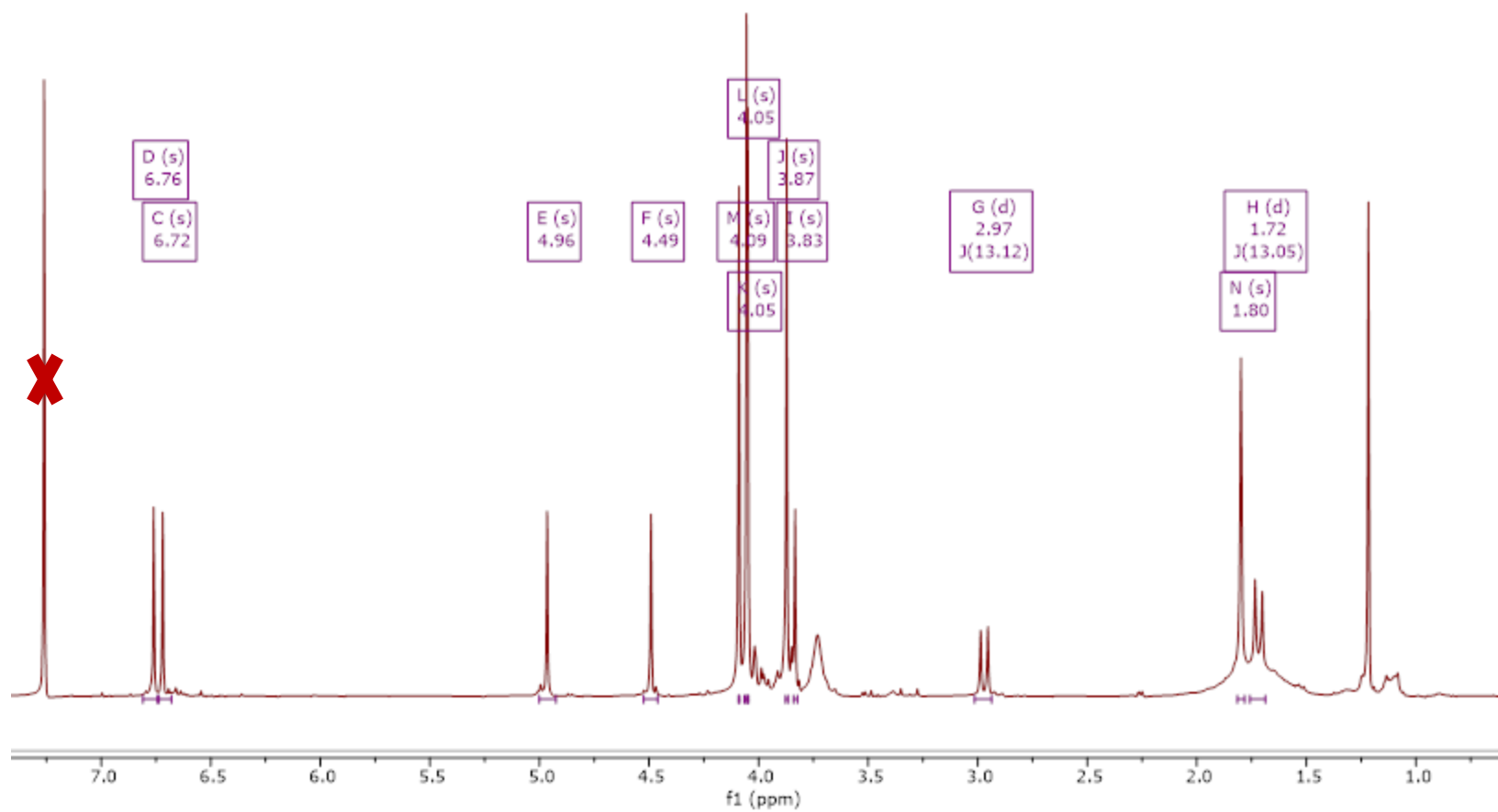


**Figure 6.47.**  $^1\text{H}$  NMR of hypomycin C (**5**) [400 MHz,  $\text{CDCl}_3$ ].

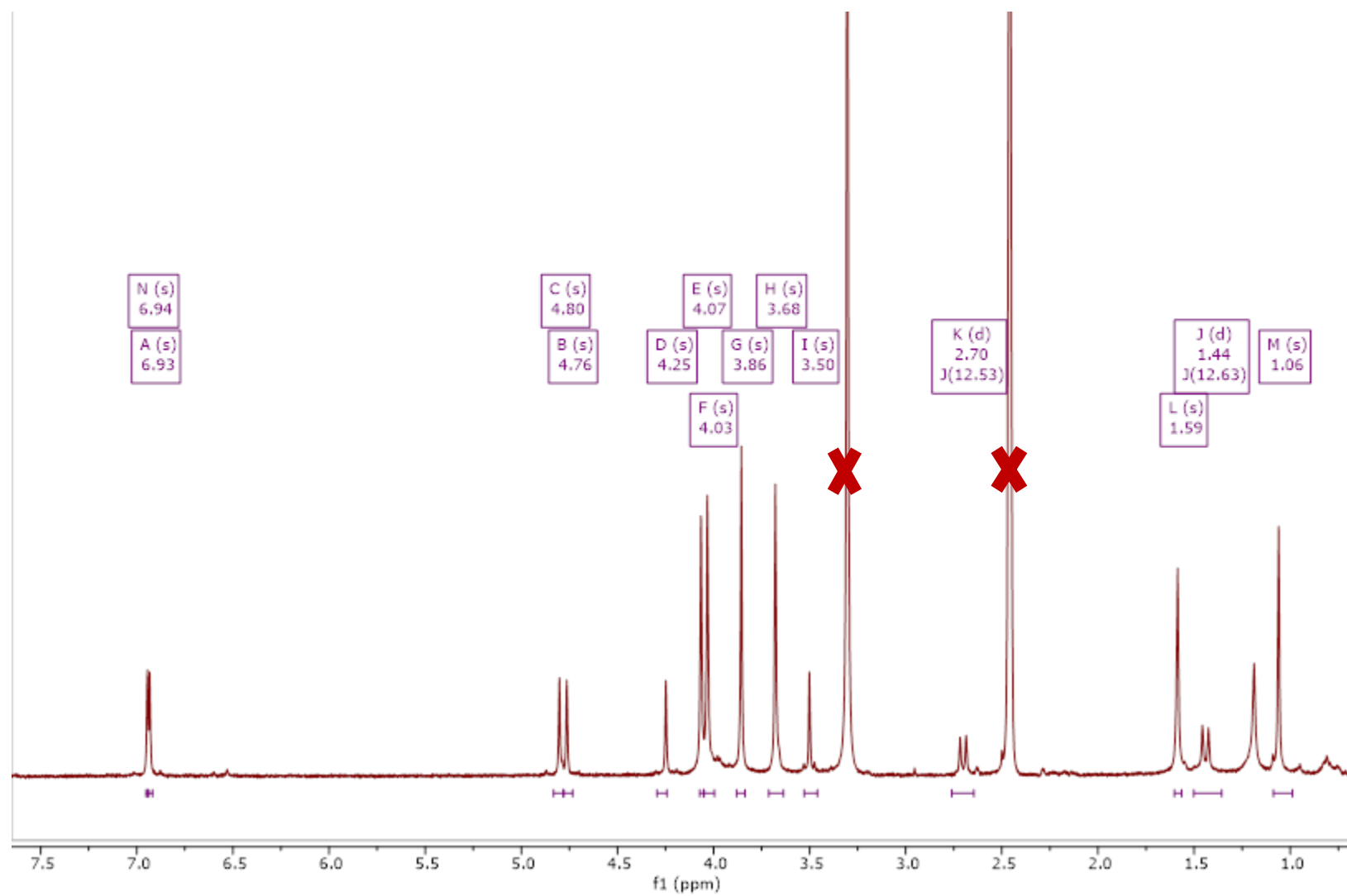
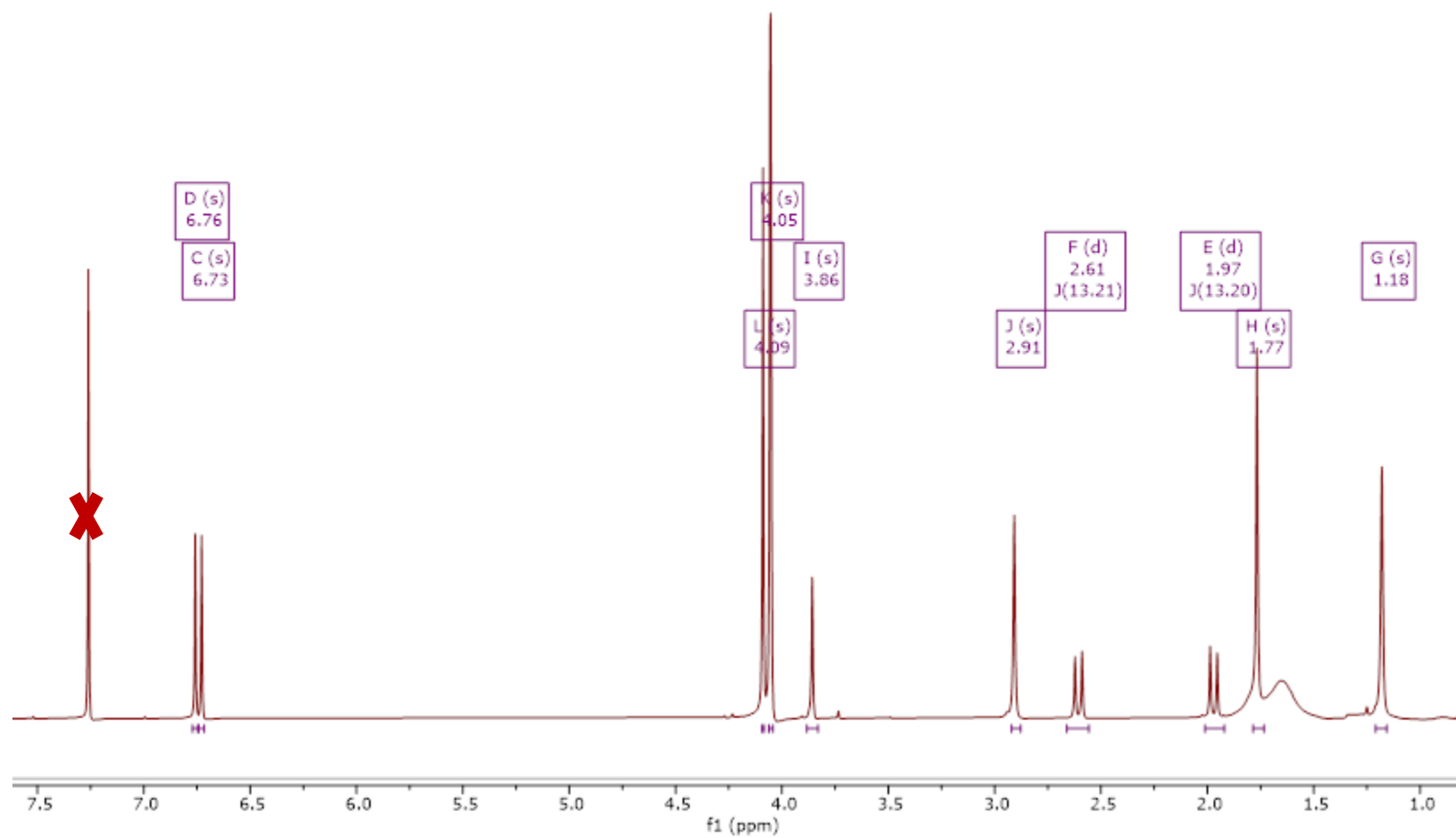


Figure 6.48.  $^1\text{H}$  NMR of hypomycin C (5) [400 MHz,  $\text{DMSO}-d_6$ ].



**Figure 6.49.**  $^1\text{H}$  NMR of hypomycin E (6) [400 MHz,  $\text{CDCl}_3$ ].

**Table 6.4.** NMR Spectroscopic Data for **11-12** in CDCl<sub>3</sub> ( $\delta$  in ppm).

position	<b>11<sup>a</sup></b>		<b>12<sup>b</sup></b>	
	$\delta_C$ , type	$\delta_H$ (J, Hz)	$\delta_C$ , type	$\delta_H$ (J, Hz)
1	146.1, C		134.5, C	
1a	125.4, C		124.3 or 126.8, C	
2	125.5, CH	7.25, s	151.0, C	
3	170.5, C		165.8, C	
3a	106.5, C		107.6, C	
3b	123.6, C		124.3, C or 126.8, C	
4	185.2, C		185.3, C	
5	103.7, CH	6.45, s	103.7, CH or 103.8, CH	6.45, s
6	167.6, C		168.1, C	
6a	120.7, C		121.9, C	
7	168.3, C		167.9, C	
7a	120.7, C		120.8, C	
8	103.2, CH	6.48, s	103.7, CH or 103.8, CH	6.43, s
9	184.2, C		185.6, C	
9a	107.8, C		106.9, C	
9b	128.0, C		127.6, C	
10	166.8, C		169.3, C	
11	148.9, C		122.3, CH	7.31, s
12	131.0, C		134.0, C	
12a	127.6, C		126.0, C	
13	50.9, CH <sub>2</sub>	2.78, d (14.0)	43.3, CH <sub>2</sub>	2.42, d (13.6)
		3.00, d (14.0)		3.62, d (13.6)

14	79.4, C		80.5, C	
15	63.9, CH	3.77, s	66.1, CH	4.25, s
16	24.8, CH <sub>3</sub>	1.77, s	24.3, CH <sub>3</sub>	1.77, s
17	206.8, C		207.4, C	
18	28.6, CH <sub>3</sub>	1.81, s	32.2, CH <sub>3</sub>	1.97, s
CH <sub>3</sub> O-2			61.9, CH <sub>3</sub>	4.19, s
CH <sub>3</sub> O-6	56.5, CH <sub>3</sub>	4.05, s	56.6, CH <sub>3</sub> or 56.7, CH <sub>3</sub>	4.06, s
CH <sub>3</sub> O-7	56.7, CH <sub>3</sub>	4.07, s	56.7, CH <sub>3</sub> or 56.6, CH <sub>3</sub>	4.05, s
CH <sub>3</sub> O-11	61.3, CH <sub>3</sub>	4.28, s		
HO-3		15.47, s		
HO-10		16.10, s		

---

<sup>a</sup>Recorded at 400 MHz for <sup>1</sup>H and 100 MHz for <sup>13</sup>C.

<sup>b</sup>Recorded at 700 MHz for <sup>1</sup>H and 175 MHz for <sup>13</sup>C.

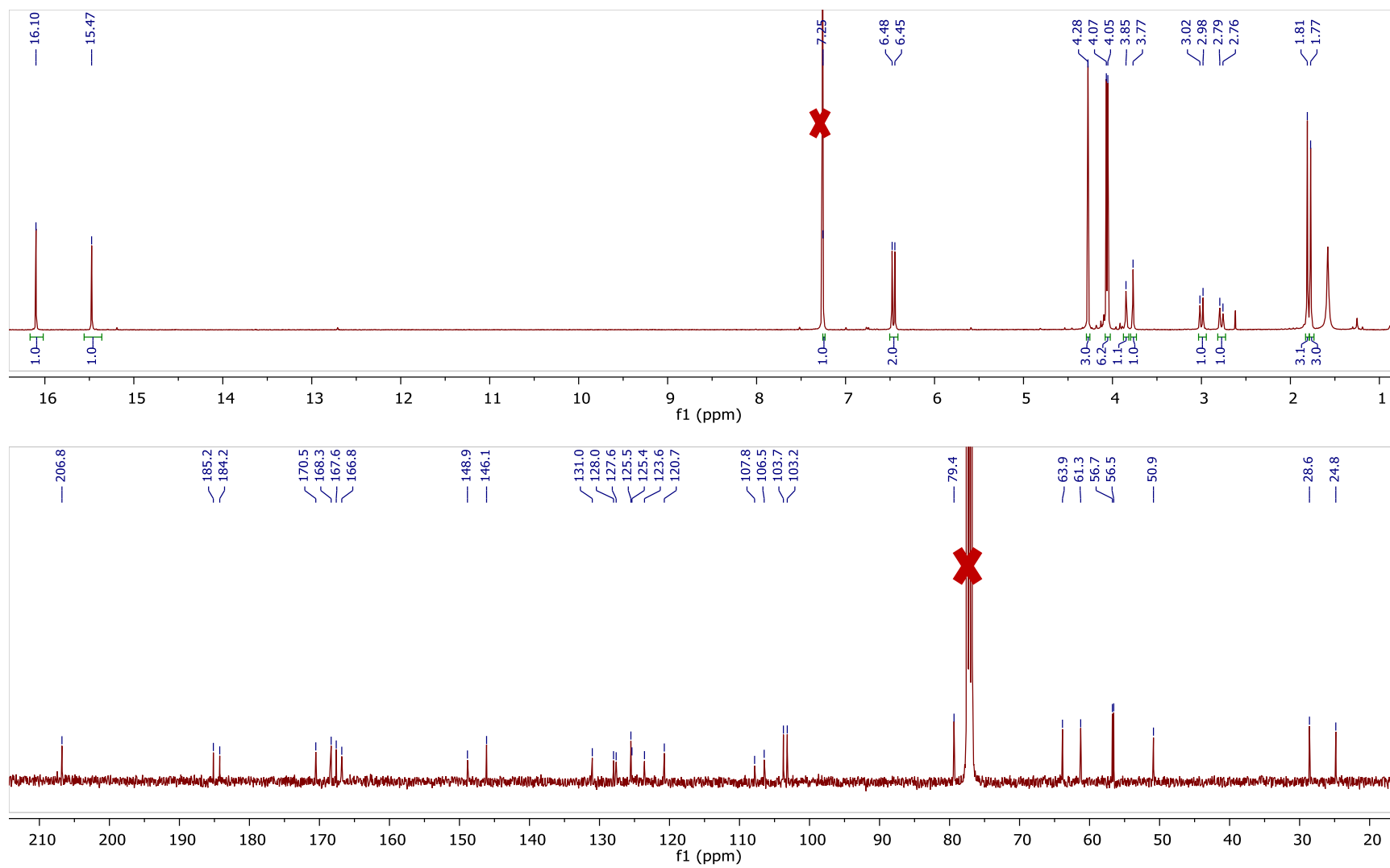


**Figure 6.50.**  $^1\text{H}$  and  $^{13}\text{C}$  NMR spectra of **11** [400 MHz for  $^1\text{H}$  and 100 MHz for  $^{13}\text{C}$ ,  $\text{CDCl}_3$ ].

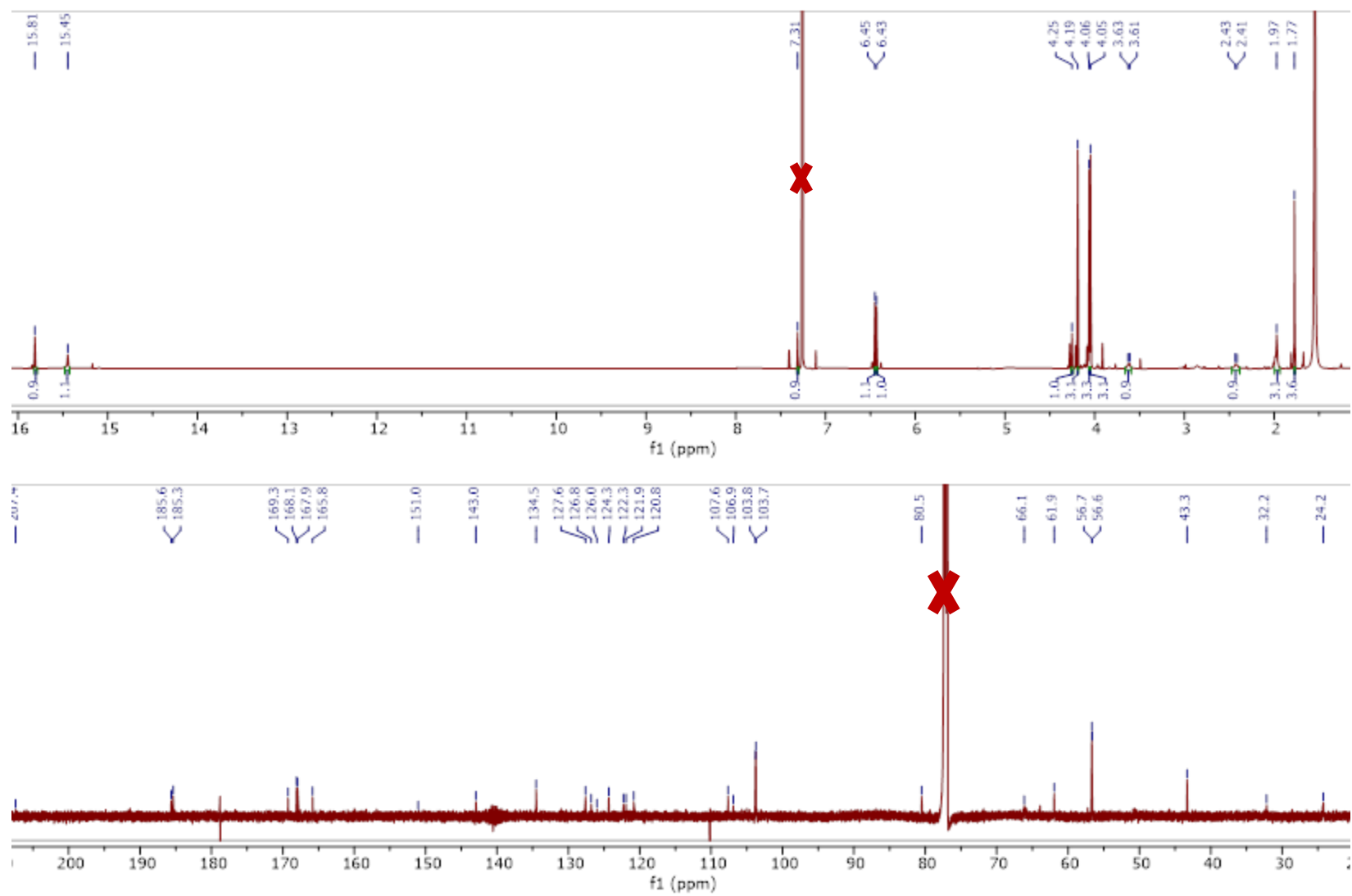


**Figure 6.51.**  $^1\text{H}$  and  $^{13}\text{C}$  NMR spectra of **12** [700 MHz for  $^1\text{H}$  and 175 MHz for  $^{13}\text{C}$ ,  $\text{CDCl}_3$ ].

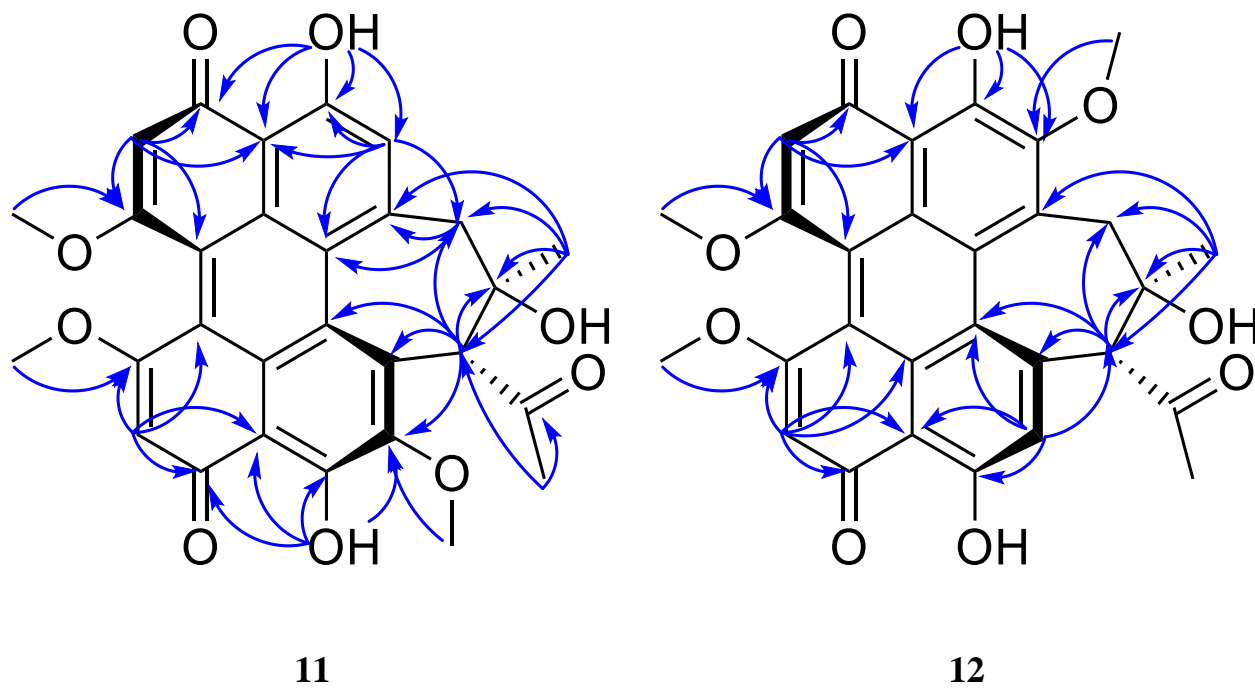


Figure 6.52. Key HMBC correlations for compounds 11 and 12.

## CHAPTER VII: THREE DIKETOMORPHOLINES FROM A *PENICILLIUM* SP. (STRAIN G1071)

Zeinab Y. Al Subeh, Huzefa A. Raja, Joanna E. Burdette, Joseph O. Falkinham, Scott E. Hemby, and Nicholas H. Oberlies. *Phytochemistry* 2021, 189, 112830.

Three previously undescribed diketomorpholine natural products, along with the known phenalenones, herqueinone (**5**) and norherqueinone (**6**), were isolated from the mycoparasitic fungal strain G1071, which was identified as a *Penicillium* sp. in the section *Sclerotiora*. The chemical structures were established by analyzing NMR data and mass spectrometry fragmentation patterns. The absolute configurations of deacetyl-javanicunine A (**1**), javanicunine C (**2**), and javanicunine D (**3**), were assigned by examining ECD spectra and Marfey's analysis. The structural diversity generated by this fungal strain was interesting, as only a few diketomorpholines (~17) have been reported from nature.

### Introduction

Pyrrolidinoindolines are a family of alkaloids isolated from fungi and plants <sup>271, 272</sup>. These specialised metabolites have been shown to exhibit a variety of biological properties, including anti-inflammatory <sup>273</sup>, P-glycoprotein inhibition <sup>274, 275</sup>, plant growth regulation <sup>276, 277</sup>, and cytotoxicity <sup>278</sup>. While the pyrrolidinoindolines include those with both diketopiperazine and diketomorpholine moieties, the majority are made up of the former. Diketopiperazines are usually derived from two amino acids, which can vary to give structural diversity to this class of compounds <sup>279</sup>. For instance, Trp and Leu were reported as key building blocks in fructigenine B and brevicompanine B <sup>277, 280</sup>, Trp and Pro in verruculogen and brevianamide F <sup>281, 282</sup>, and Phe and His in phenylahistin <sup>283</sup>. Moreover, diketopiperazines have served as the inspiration for clinical drugs, such as tadalafil for erectile dysfunction <sup>284</sup>, retosiban for preterm labor <sup>285</sup>, and aplaviroc for human immunodeficiency viruses <sup>279</sup>.

Compared to diketopiperazines, only a few diketomorpholines have been reported from nature. For example, the Dictionary of Natural Products reports > 1300 specialised metabolites with a diketopiperazine moiety, yet only 17 natural products have been reported in the diketomorpholine

class. Diketomorpholines are usually derived from an amino acid that forms an amide and ester linkage with another  $\alpha$ -hydroxy acid moiety (i.e., an amino acid analogue in which the amine group was replaced with a hydroxy group)<sup>286</sup>. A fungal artificial chromosomes and metabolomic scoring (FAC-MS) technology and stable isotope feeding experiments were utilized to identify the biosynthetic pathway of dioxomorpholines<sup>287</sup>. As suggested for acu-dioxomorpholine, which is derived from Trp and Phe, the biosynthesis of dioxomorpholines involves transamination of the second amino acid, followed by reduction to produce an  $\alpha$ -hydroxy acid. The condensation of this  $\alpha$ -hydroxy acid with the first amino acid is facilitated by a nonribosomal peptide synthetase gene that features a new type of condensation domain proposed to use an unusual arginine active site for ester bond formation<sup>287</sup>. Mollenines A and B were the first diketomorpholines to be isolated from a fungus, *Eupenicillium molle* (strain NRRL 13062), and they had moderate cytotoxic and antibacterial activities<sup>278</sup>. These were followed by the discovery of javanicunine A and B from *E. javanicum*<sup>288</sup>. More recently, P-glycoprotein inhibitory effects were reported in some diketomorpholines<sup>274, 289</sup>. Due to our interest in exploring the chemical diversity of fungi,<sup>290-292</sup> we were intrigued that the majority of these diketomorpholine analogues, 15 out of 17, were isolated from fungi.

## Results and Discussion

In the course of examining fungi from freshwater habitats, which are an under investigated ecological niche of microorganisms for both taxonomic and chemical diversity<sup>60</sup>, a fungal culture was collected from submerged wood in a stream in Connecticut, USA. This sample [*Penicillium* sp. (strain G1071)] was flagged for further investigation, since dereplication did not yield any hits compared to an in-house database of over 625 fungal metabolites<sup>151, 293</sup>. Interestingly, strain G1071 was isolated from a minute mushroom fruiting on submerged wood and should be considered an immigrant to freshwater<sup>60, 294, 295</sup>. Fungal strain G1071 was grown over two weeks on rice medium, and the extract was purified via flash chromatography and HPLC to yield compounds **1-3** and **5-6**. The structures of **1-3** were determined by NMR spectroscopic data, and their absolute configurations were assigned by examining ECD spectra, in addition to acid hydrolysis and Marfey's analysis. Compounds **5** and **6** were herqueinone and norherqueinone, respectively, based on agreement with characterization data in the literature<sup>296, 297</sup>. Compounds **1-3** were also tested in suite of biological assays, including those for cytotoxicity, antimicrobial, *mu*

opioid receptor, and cathepsin K assays, but unfortunately, we could not ascribe biological activities to these interesting fungal metabolites.

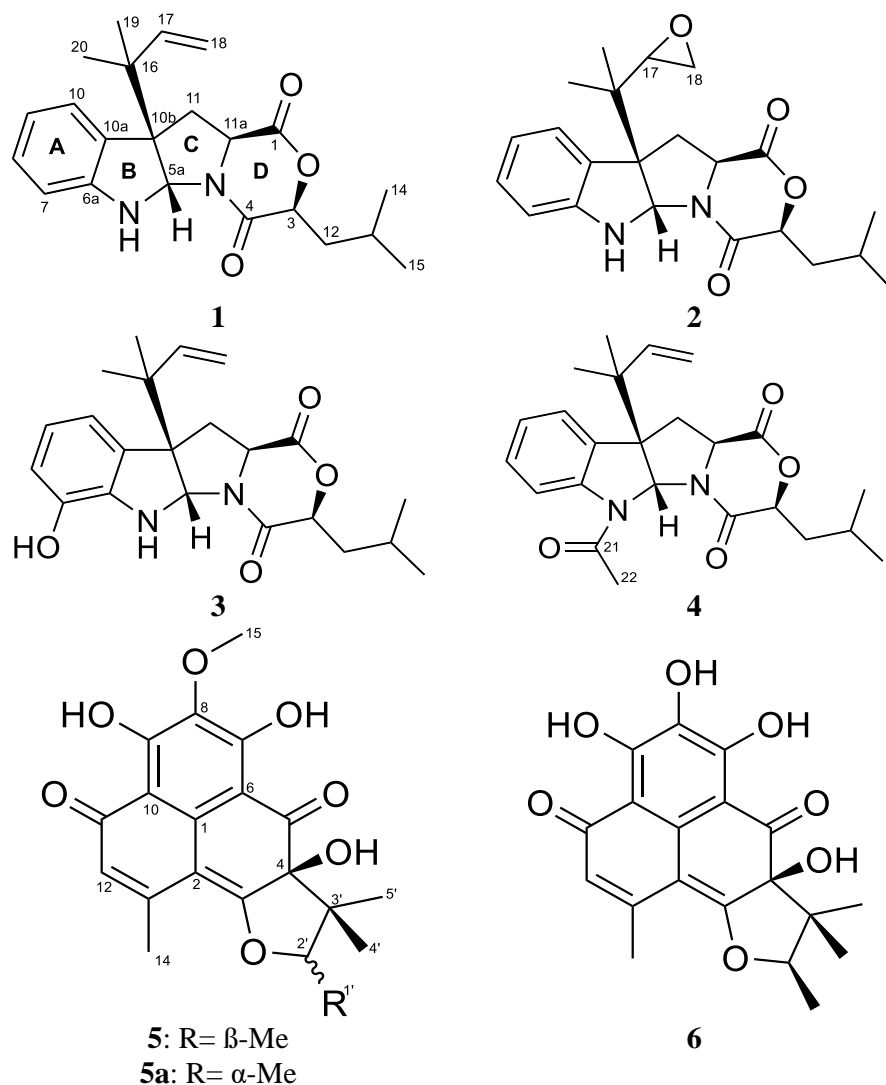


**Figure 7.1.** Chemical structures of compounds **1-6**.

Compound **1** was obtained as a yellow oil with a molecular formula of  $C_{22}H_{28}N_2O_3$  as deduced by HRESIMS (Fig. 7.7), indicating an index of hydrogen deficiency of 10. An examination of the  $^1H$  and  $^{13}C$  NMR data (Table 7.1) indicated the presence of a disubstituted aromatic ring, a terminal double bond, two carbonyls, and four methyl groups. The tryptophan core was suggested by the COSY spin system from H-7 to H-10, the HMBC correlations of H-5a with C-6a, C-10a, C-10b, and C-11, and the HMBC correlations of H<sub>2</sub>-11 and H-11a with the C-1 carbonyl (Fig. 7.2). The

1,1-dimethyl-2-propenyl group attached to C-10b was confirmed by the HMBC correlations of H<sub>3</sub>-19 and H<sub>3</sub>-20 with C-16, C-17, and C-18. This side chain includes a characteristic terminal double bond and has been observed in various compounds with diketopiperazine and diketomorpholine moieties<sup>273, 277, 280, 298</sup>, and our data corresponded well with the literature. A 2-hydroxy-4-methylpentanoate unit was suggested by the <sup>1</sup>H-<sup>1</sup>H spin system from H-3 to H<sub>3</sub>-15, along with the HMBC correlation of H-3 with the C-4 carbonyl. This unit represents an α-hydroxy leucine-like moiety, where the amine group in Leu is replaced with a hydroxy. This α-hydroxy acid contributes to ring D by forming an ester linkage with the carboxylic acid of a Trp building block from one side and an amide linkage with the same Trp from the other side. Searching the literature for compounds with structural similarities showed that the NMR spectra of **1** matched those for the immediate synthetic precursor of javanicunine A (**4**), which was reported recently<sup>299</sup> (Table 7.2). Therefore, compound **1** is the deacetylated derivative of javanicunine A (**4**) and is reported for the first time as a fungal metabolite, which we have ascribed the trivial name, deacetyl-javanicunine A. NOESY cross peaks of H-5a with H<sub>3</sub>-19, H<sub>3</sub>-20, H-17, and H<sub>2</sub>-18 suggested the same orientation of the H-5a proton and the dimethyl-2-propenyl unit (Fig. 7.3). Additionally, NOESY correlations of H-3 with H-11a supported the co-facial orientation of these two protons (Fig. 7.3). Based on the match in the 1D and 2D NMR spectra (Table 7.2 and Figs. 7.8-7.12), UV maxima, and specific rotation data (measured in CH<sub>2</sub>Cl<sub>2</sub> [ $\alpha$ ]<sub>D</sub><sup>20</sup> = -394 vs reported in CH<sub>2</sub>Cl<sub>2</sub> [ $\alpha$ ]<sub>D</sub><sup>20</sup> = -361) with those reported for the synthetic precursor of javanicunine A, the absolute configuration of **1** was assigned as 3*S*, 5*aS*, 10*bR*, 11*aS*<sup>299</sup>.

**Table 7.1.** <sup>1</sup>H and <sup>13</sup>C NMR data in CDCl<sub>3</sub> for **1** and CD<sub>3</sub>CN for **2** and **3**.

No.	<b>1</b> <sup>a</sup>		<b>2</b> <sup>a</sup>		<b>3</b> <sup>b</sup>	
	$\delta_C$ , type	$\delta_H$ , (J in Hz)	$\delta_C$ , (type)	$\delta_H$ , (J in Hz)	$\delta_C$ , (type)	$\delta_H$ , (J in Hz)
1	169.0, C		170.0, C		170.1, C	
3	77.7, CH	4.69, dd (10.0, 2.4)	78.0, CH	4.83, dd (9.9, 2.8)	78.1, CH	4.82, dd (9.8, 3.1)
4	166.0, C		166.3, C		166.6, C	
5a	77.9, CH	5.48, s	78.0, CH	5.54, s	78.6, CH	5.45, s
6		5.06, brs		5.42, brs		5.00, brs
6a	149.7, C		151.4, C		138.9, C	
7	109.7, CH	6.59, d (7.7)	110.5, CH	6.65, d (7.8)	142.6, C	
8	129.3, CH	7.12, t (8.0)	129.8, CH	7.11, t (7.6)	120.6 or 116.1, CH	6.66, d (4.2)

9	119.2, CH	6.78, t (7.5)	119.5, CH	6.76, t (7.5)	117.8, CH	6.81, t (4.3)
10	125.1, CH	7.17, d (7.5)	126.1, CH	7.26, d (7.5)	116.1 or 120.6, CH	6.66, d (4.3)
10a	128.8, C		129.8, C		131.9, C	
10b	61.9, C		62.5, C		63.4, C	
11	36.2, CH <sub>2</sub>	2.56, m	36.2, CH <sub>2</sub>	2.60, dd (12.8, 10.5)	36.7, CH <sub>2</sub>	2.47, dd (12.8, 10.6)
		2.62, m		2.65, dd (12.9, 7.1)		2.54, dd (12.8, 6.8)
11a	57.8, CH	4.06, dd (10.3, 7.0)	58.3, CH	4.09, dd (10.3, 7.0)	58.4, CH	4.06, dd (10.6, 6.9)
12	37.9, CH <sub>2</sub>	1.81, m	38.4, CH <sub>2</sub>	1.66, ddd (13.6, 10.2, 3.5)	38.4, CH <sub>2</sub>	1.66, ddd (14.2, 9.9, 4.3)
		1.93, m		1.87, m		1.87, m
13	24.1, CH	1.91, m	25.0, CH <sub>2</sub>	1.83, m	25.0, CH	1.83, m
14	23.4, CH <sub>3</sub>	0.97, d (6.2)	21.4, CH <sub>3</sub>	0.90, d (6.2)	21.5, CH <sub>3</sub>	0.90, d (6.4)
15	21.3, CH <sub>3</sub>	0.90, d (6.1)	23.4, CH <sub>3</sub>	0.96, d (6.4)	23.4, CH <sub>3</sub>	0.96, d (6.5)
16	41.0, C		38.9, C		41.6, C	
17	143.3, CH	5.96, dd (17.4, 10.8)	56.5, CH	2.94, t (3.5)	145.2, CH	6.06, dd (17.0, 11.2)
18	115.0, CH <sub>2</sub>	5.09, d (17.4)	43.8, CH <sub>2</sub>	2.45, m	114.3, CH <sub>2</sub>	5.07, dd (17.0, 1.2)
		5.15, d (10.8)				5.08, dd (11.0, 1.2)
19	22.9, CH <sub>3</sub>	1.00, s	19.0, CH <sub>3</sub>	0.83, s	23.3, CH <sub>3</sub>	0.97, s
20	22.6, CH <sub>3</sub>	1.12, s	19.5, CH <sub>3</sub>	0.93, s	23.1, CH <sub>3</sub>	1.09, s

<sup>a</sup> Data collected at 400 MHz (<sup>1</sup>H) and 100 MHz (<sup>13</sup>C).

<sup>b</sup> Data collected at 700 MHz (<sup>1</sup>H) and 175 MHz (<sup>13</sup>C).

To further confirm that **1** represented the deacetylated analogue of javanicunine A (**4**), acetylation of **1** at *N*-6 was performed to afford **4**. The addition of the acetyl group was confirmed by the molecular formula of **4** (C<sub>24</sub>H<sub>30</sub>N<sub>2</sub>O<sub>4</sub>), as deduced by HRESIMS data (Fig. 7.13), and the new methyl (i.e.,  $\delta_{\text{H}}/\delta_{\text{C}}$  2.63/23.7) and carbonyl (i.e.,  $\delta_{\text{C}}$  170.0) signals (Table 7.3 & Fig. 7.14). The NMR (Table 7.3) and specific rotation data (measured in CH<sub>2</sub>Cl<sub>2</sub> [ $\alpha$ ]<sub>20</sub><sup>D</sup> = -196 vs reported in CH<sub>2</sub>Cl<sub>2</sub> [ $\alpha$ ]<sub>20</sub><sup>D</sup> = -152) of **4** matched those reported for javanicunine A<sup>288, 299</sup>. The absolute configuration of **4** was determined previously by acid hydrolysis, which showed that **4** was derived from L-tryptophan (L-Trp)<sup>288</sup>, further supporting the 3*S*, 5*aS*, 10*bR*, 11*aS* assignment of **1**.

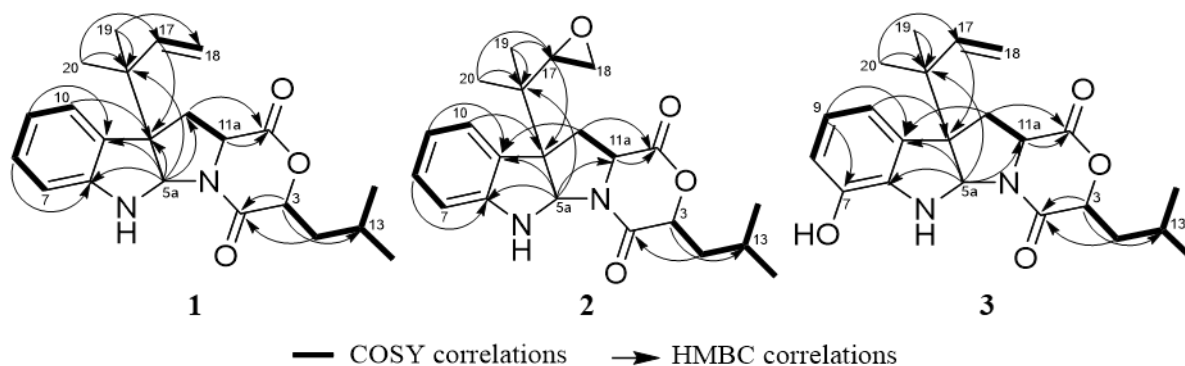


**Figure 7.2.** Key COSY and HMBC correlations of **1-3**.

Finally, the ECD spectra of **1** and **4** revealed an interesting observation. Specifically, the ECD of **1** exhibited a negative Cotton effect at 245 nm, while the *N*-acetylated derivative (**4**) exhibited a positive Cotton effect at this range of wavelengths (Fig. 7.4). Similar behavior was reported previously for diketopiperazines and their *N*-acetylated derivatives with the same absolute configurations at the B-C ring junction (i.e. positions 5a and 10b), position C-3, and position C-11a as compounds **1** and **4**<sup>280, 300, 301</sup>. This further confirmed the absolute configuration of these two compounds as 3*S*, 5a*S*, 10b*R*, 11a*S*.

The molecular formula of compound **2** was identified as C<sub>22</sub>H<sub>28</sub>N<sub>2</sub>O<sub>4</sub> as deduced by HRESIMS (Fig. 7.15). <sup>1</sup>H and <sup>13</sup>C NMR data suggested structural similarity with **1** (Table 7.1), however, compound **2** was missing the three olefinic protons at C-17 and C-18, indicating a loss of the terminal double bond. The two new sets of signals (i.e.  $\delta_{\text{H}}/\delta_{\text{C}}$  2.94/56.5 and  $\delta_{\text{H}}/\delta_{\text{C}}$  2.45/43.8) for positions C-17 and C-18, respectively, suggested the presence of an oxirane ring. The fact that compounds **1** and **2** shared the same index of hydrogen deficiency supported this conclusion. The position of the oxirane ring was confirmed by the HMBC correlations of H-17 with C-10b, C-19, and C-20 carbons (Fig. 7.2). Therefore, compound **2** differed from **1** by having a 2-isopropylloxirane side chain attached to C-10b instead of the 1,1-dimethyl-2-propenyl group. The NOESY spectrum of **2** suggested a similar relative configuration as that observed in **1** (Fig. 7.3), where H-5a correlated with H<sub>3</sub>-19 and H<sub>3</sub>-20, while H-3 correlated with H-11a. Due to free rotation, the configuration of the oxirane ring could not be defined despite the observed NOESY cross peak between H-17 and H-5a. The ECD spectrum of **2** was nearly identical to that for **1**, suggesting the same configuration for positions 3, 5a, 10b, and 11a in **1** and **2** (Fig.7.4). Furthermore, acid hydrolysis and Marfey's analysis of **2** revealed the presence of L-Trp, also in

accord with the data for compounds **1** and **4** (Figs. 7.21 and 7.22)<sup>288</sup>. Accordingly, compound **2** has the absolute configuration of 3*S*, 5*aS*, 10*bS*, and 11*aS*, and was named as javanicunine C.

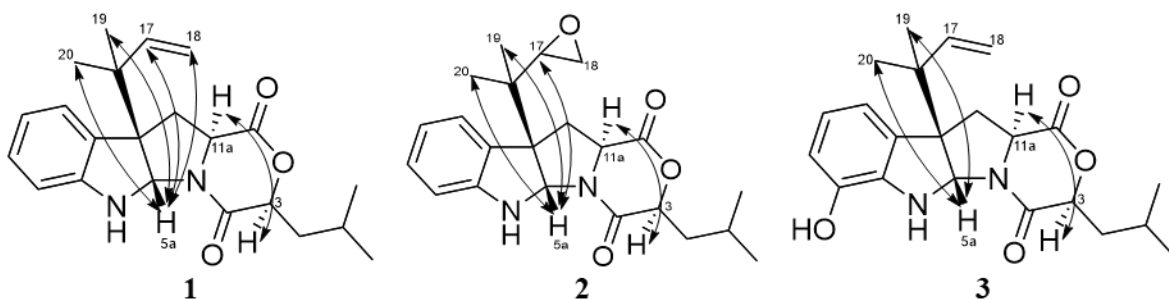


**Figure 7.3.** Key NOESY correlations of compounds **1-3**.

As determined by the HRESIMS data (Fig. 7.23), compound **3** shared the same molecular formula as **2** (C<sub>22</sub>H<sub>28</sub>N<sub>2</sub>O<sub>4</sub>). However, **3** maintained the terminal double bond between C-17 and C-18, as noted by the two sets of signals (i.e.  $\delta_{\text{H}}/\delta_{\text{C}}$  6.06/ 145.2 and  $\delta_{\text{H}}/\delta_{\text{C}}$  5.07 & 5.08/114.3) for positions C-17 and C-18, respectively. Unlike **1** and **2**, the NMR data of **3** (Table 7.1) showed only three aromatic protons in the indole core, suggesting hydroxylation of this aromatic ring, which was supported by the deshielded carbon at  $\delta_{\text{C}}$  142.6 (C-7). The position of the hydroxy group was assigned based on the -CH-CH-CH- proton spin system observed from H-8 to H-10, along with the HMBC correlations of H-9 with C-7, and H-10 with C-10*b*. As with **1** and **2**, the NOESY spectrum of **3** showed correlations of H-5*a* with H<sub>3</sub>-19 and H<sub>3</sub>-20, while H-3 correlated with H-11*a* (Fig. 7.3). The similar ECD spectra (Fig. 7.4) and specific rotation of **1** and **3** ( $[\alpha]_{\text{D}}^{20} = -356$  for **1** in CH<sub>3</sub>CN and -345 for **3** in CH<sub>3</sub>CN) suggested that **3** represented the 7-hydroxy analogue of **1** with an absolute configuration of 3*S*, 5*aS*, 10*bR*, 11*aS*. Compound **3** was assigned the name javanicunine D. Interestingly, compound **3** was structurally similar to javanicunine B, where they share the same molecular formula<sup>288</sup>. However, javanicunine B has the hydroxy group attached to C-11*a*.

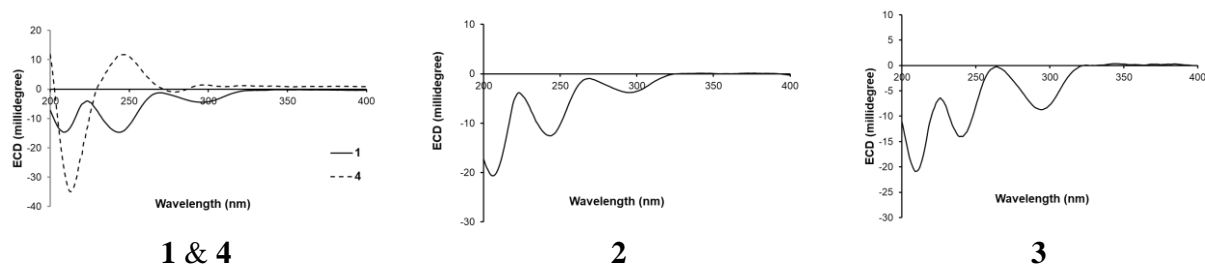


**Figure 7.4.** ECD spectra of compounds **1-4** in CH<sub>3</sub>CN.

The structures of **1-3** were also supported by their HRESIMS fragmentation patterns (Fig. 7.29). Fragment A, which represents the loss of the side chain attached to C-10b, was the same in compounds **1** and **2** ( $m/z$  301) (Fig. 7.5), which confirmed the presence of the epoxide group in place of the terminal double bond in **2**. On the other hand, fragment A was 16 Da higher in **3** ( $m/z$  317), supporting the presence of the same dimethyl-2-propenyl side chain attached to C-10b as in **1**. The presence of the hydroxy group attached to the indoline ring of **3** was supported by its  $m/z$  for fragment B ( $m/z$  146), which is 16 units higher than that for **1** and **2**.

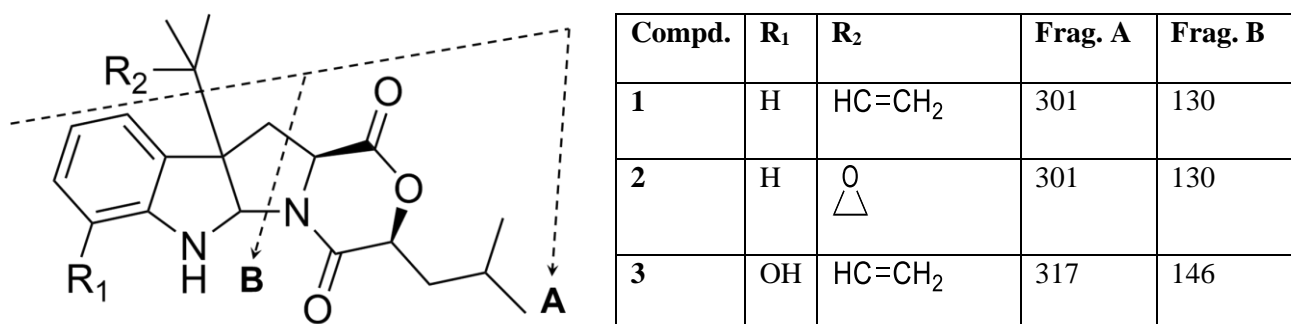


**Figure 7.5.** (+)-HRESIMS fragmentation patterns of **1-3**.

Based on the identified biosynthesis pathway of acu-dioxomorpholine<sup>287</sup>, compounds **1-3** likely derive from Trp and Leu. Transamination of Leu to replace the amino group with a ketone, followed by reduction to an alcohol via NAD(P)H-dependent reductase, allows for the conversion of the Leu to  $\alpha$ -hydroxy leucine. A nonribosomal peptide synthetase gene that features a new type of condensation domain, as reported for acu-dioxomorpholine, could be responsible for condensation of Trp with  $\alpha$ -hydroxy leucine.

It is well established that some natural products are chemically reactive and prone to transformation by environmental stimuli, such as pH, temperature, light, air, or solvent exposure, and understanding of the possible transformations that could be induced is important to differentiate between natural products and their possible artifacts<sup>274, 302</sup>. Solvolysis was suggested previously for several diketomorpholines after exposure to protic solvents (e.g., MeOH or EtOH)<sup>274, 278</sup>. To investigate this, MeOH solutions of **1-4** were prepared at a concentration of 0.2 mg/mL and subjected to UPLC-HRESIMS after 48 h. An ion peak corresponding to  $[M + H]^+ + \text{MeOH}$  was obtained for each compound (Fig. 7.30), suggesting an opening of ring D and formation of a methyl ester (Fig. 7.6). Although Khalil et al. suggested that solvolytically unstable diketomorpholines can be stabilized by the alkylation of *N*-5<sup>274</sup>, compounds **1-4** are all *N*-alkylated diketomorpholines and are still susceptible to partial solvolysis. Interestingly, while we could generate these artifacts by treating the isolated fungal metabolites, none of the methanolysis products were isolated from the original extract despite the use of MeOH in the extraction process. It is possible that in the context of the multicomponent extract, with only limited exposure to methanol, and with the *N*-alkylation noted by Khalil et al.<sup>274</sup> that such methanolysis reactions are minimized.

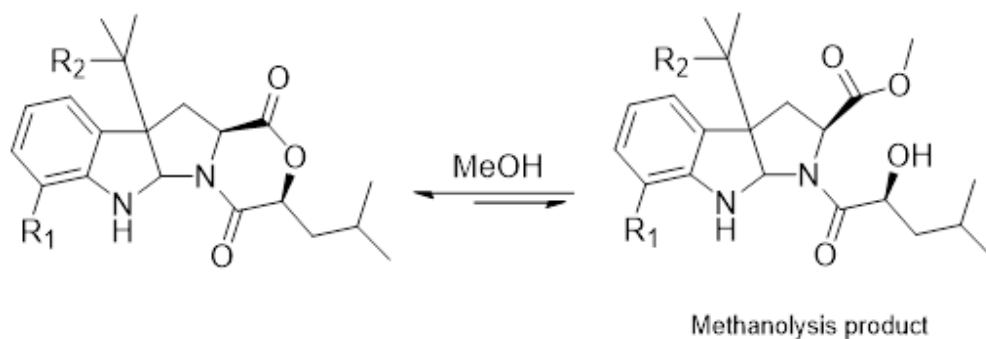


**Figure 7.6.** Proposed methanolysis products of **1-4**.  $R_1$  and  $R_2$  groups for compounds **1-4** are as noted in Fig. 7.5.

Compound **5** was the major constituent of the fungal extract and was identified as herqueinone by comparing its MS and NMR data (Figs. 7.31 and 7.32) with those reported in the literature<sup>296, 297</sup>. Epimerization of herqueinone to produce a mixture of herqueinone (**5**)/isoherqueinone (**5a**) was also observed (Fig. 7.33), and this phenomenon was reported previously for herqueinone<sup>303</sup>. Compound **6** was identified as a desmethoxylated derivative of **5** by examining its HRESIMS spectrum and 1D, and 2D NMR data (Figs. 7.34-7.35). The 1D structure of **6** matched those

reported for norherqueinone and its epimer, isonorherqueinone<sup>296</sup>. However, the specific rotation of **6** (measured in pyridine  $[\alpha]_{20}^D = +847$ ) allowed its identification as norherqueinone (reported in pyridine  $[\alpha]_{20}^D = +1080$ ) rather than isonorherqueinone (reported in pyridine  $[\alpha]_{20}^D = -730$ )<sup>304</sup>. As the NMR data of norherqueinone (**6**) have never been published, <sup>1</sup>H and <sup>13</sup>C NMR spectra of **6** are reported in the supporting information (Fig. 7.35). Both **5** and **6** belong to the phenalenone family. Various *Penicillium* species in section *Sclerotiora* had been reported to produce phenalenones, such as *P. herquei* strain PSU-RSPG93 and strain P14190<sup>297, 305</sup>.

The biological activity of these fungal metabolites (**1-3**) were elusive, as they were neither cytotoxic against a panel of cancer cell lines ( $IC_{50} > 25 \mu\text{M}$ , Table 7.4) nor antimicrobial against a broad series of pathogenic microorganisms ( $MIC > 60 \mu\text{g/mL}$ , Table 7.5). Minimal inhibitory concentrations (MICs) of these compounds were measured by broth microdilution against various pathogenic microorganisms as outlined in Table 7.5. STarFish, which is a computational target fishing model for natural products, was utilized to identify possible protein targets for **1-4**<sup>306</sup>. The *Mu*-type opioid receptor for **1** and cathepsin K for **1**, **2**, and **4** were suggested by STarFish as possible targets for these compounds (score range between 0.06-0.1). These two proteins play a vital role in pain management and the bone resorption process, respectively. Unfortunately, testing of compounds **1-3** against cAMP accumulation assay and compounds **2**, **3**, **5**, and **6** for cathepsin K inhibition showed negative results.

## Conclusion

This project expanded the natural diketomorpholines family with the identification of three undescribed fungal metabolites. The structures and absolute configurations of **1-3** were determined by examining 1D and 2D NMR data, mass spectrometry fragmentation patterns, ECD spectra, and Marfey's analysis. Despite testing against a suite of cytotoxicity, antimicrobial, protease and second messenger assays, we were unable to ascribe biological properties for these structurally interesting fungal metabolites. Given the preponderance of diketopiperazines reported in the literature, and the relative lack of diketomorpholines from nature, further studies to probe and compare the biosynthesis of these metabolites seems warranted.

## Materials and Methods

**General Experimental Procedure.** Optical rotation data were collected using a Rudolph Research Autopol III polarimeter (Rudolph Research Analytical). ECD and UV spectra were measured using an Olis DSM 17 ECD spectrophotometer (Olis, Inc.) and a Varian Cary 100 Bio UV–Vis spectrophotometer (Varian Inc.), respectively. 1D and 2D NMR spectra were recorded in either CDCl<sub>3</sub> or CD<sub>3</sub>CN using an Agilent 700 MHz spectrometer equipped with a cryoprobe, a JEOL ECA–500 spectrometer, or a JEOL ECS-400 spectrometer equipped with a high sensitivity JEOL Royal probe and a 24-slot autosampler. Residual solvent signals were used for referencing the NMR spectra. UPLC-HRESIMS data were collected via an LTQ-Orbitrap XL mass spectrometry system (Thermo Finnigan, San Jose, CA, USA) connected to a Waters Acquity UPLC system. A BEH Shield RP C<sub>18</sub> column (Waters, 1.7 μm; 50 × 2.1 mm) heated to 40 °C was used. The mobile phase consisted of CH<sub>3</sub>CN–H<sub>2</sub>O (0.1% formic acid) in a gradient system of 15:85 to 100:0 over 10 min at a flow rate of 0.3 mL/min. MS data were collected from *m/z* 150 to 2000 in the positive mode. All analytical and preparative HPLC experiments were carried out using a Varian Prostar HPLC system equipped with ProStar 210 pumps and a Prostar 335 photodiode array detector (PDA). HPLC data were collected and analyzed using Galaxie Chromatography Workstation software (version 1.9.3.2, Varian Inc.). For preparative HPLC, an Atlantis T3 column (Waters, 5 μm; 250 × 19 mm) was used. Flash chromatography was carried out using a Teledyne ISCO CombiFlash Rf 200 that was equipped with both UV and evaporative light–scattering detectors and using Silica Gold columns (from Teledyne Isco).

**Fungal Strain Isolation and Identification.** Strain G1071 was isolated from a minute mushroom fruiting body, which was growing out of submerged wood collected in January 2019 from a freshwater stream in Hebron, Connecticut (N41 41.26776, W72 26.52564). Placing the entire mushroom fruiting body on antibiotic water agar (AWA, agar 20 g, streptomycin sulfate 250 mg/L, penicillin G 250 mg/L, distilled water 1L; antibiotics were added to the molten agar immediately after autoclaving) followed by incubating the Petri plate at room temperature encouraged growth of fungal hyphae. A small portion of hyphae along with the agar was excised and placed on potato dextrose agar (PDA, Difco) to obtain a pure culture of strain G1071. The fungus produced a yellow to yellow-green to light olivaceous green colony with a dark yellow-

green reverse within 14 days when incubated at 25 °C. Morphological characteristics of the fungal strain on PDA indicated the strain could be identified as a *Penicillium* sp.<sup>307</sup>.

For molecular identification, the ITS rDNA region was amplified to confirm whether the fungus belongs to the genus *Penicillium*; this was accomplished with the primer combination ITS1F and ITS4<sup>171, 233</sup> using DNA extraction, PCR, and sequencing methods outlined previously<sup>170</sup>. In addition, to obtain more specific information about species level identification by Maximum Likelihood analysis using RAxML<sup>308</sup> run on the CIPRES server<sup>309</sup>, the second largest (*RPB2*) subunit of RNA polymerase was studied using the primer combination RPB2-5f and RPB2-7Cr<sup>310</sup>. The *RPB2* region was utilized, since it is an important secondary marker utilized for phylogenetic analysis of *Penicillium* spp.<sup>307</sup>. The *RPB2* region has the added advantage of lacking introns in the amplicon, which permits constructing robust and easy alignments when used for phylogenetic analysis<sup>307</sup>.

Based on BLAST searches of the ITS region with both the RefSeq database<sup>173</sup> as well as with pairwise sequence identification from CBS Database - Westerdijk Fungal Biodiversity Institute – KNAW, strain G1071 showed  $\geq 99\%$  sequence similarity with *Penicillium* sp. including *P. herquei*. Similar results were obtained upon a BLAST search using *RPB2*. Since *P. herquei* is a member of the section *Sclerotiora*,<sup>311,312</sup> all species showing high sequence homology with strain G1071 based on the *RPB2* region were downloaded and aligned using MUSCLE<sup>313</sup>. Maximum Likelihood (RAxML) analysis showed that strain G1071 was nested in a unique clade with strong ML bootstrap support (100%), and was related to *P. herquei*, *P. verrucisporum*, and *P. choerospondiatis* with  $\geq 98\%$  bootstrap support (Fig. 7.36). Based on the morphology of the culture, BLAST search results, and ML analysis, we identify strain G1071 as belonging to *Penicillium* sp. in the section *Sclerotiora*, Aspergillaceae, Eurotiomycetes, Ascomycota. Additional micromorphological and molecular phylogenetic analysis using *CaM*, *BenA* and *RPB2* data are warranted to verify if strain G1071 might be a novel species. From an ecological perspective, strain G1071 is not truly a freshwater species because *Penicillium* spp. are ubiquitous fast-growing molds that do not have adaptations to live and reproduce in fresh water, but rather occur fortuitously in aquatic habitats<sup>60</sup>. The sequences obtained in this study were deposited in GenBank (ITS: MW341222; RPB2:MW349119, MW349120).

**Fermentation, Extraction, and Isolation.** A culture of strain G1071 was maintained on a malt extract slant and was transferred periodically. A fresh culture was grown on PDA media, subsequently; an agar plug from the PDA culture was transferred to a sterile falcon tube with 10 mL of YESD (2% soy peptone, 2% dextrose, and 1% yeast extract). The YESD cultures were grown for 7 days on an orbital shaker (100 rpm) at room temperature (~23°C) and then used to inoculate five small-scale flasks of solid fermentation media. Each solid-state fermentation was prepared in a 250 mL Erlenmeyer flask using 10 g of autoclaved rice that was moistened with 20 mL of deionized water. The cultures were then incubated at room temperature for two weeks.

To each small-scale solid fermentation culture of G1071, 60 mL of 1:1 MeOH:CHCl<sub>3</sub> was added. The cultures were chopped with a spatula and shaken for 12 h at 100 rpm at rt. followed by vacuum filtration. The filtrate from the five small-scale cultures were combined, and then 900 mL of CHCl<sub>3</sub> and 1000 mL of deionized water were added and stirred for 30 min before being transferred to a separatory funnel. The bottom layer was drawn off and evaporated to dryness. The dried organic extract was re-constituted in 500 mL of 1:1 MeOH:CH<sub>3</sub>CN and 500 mL hexanes. The biphasic solution was shaken vigorously and then transferred to a separatory funnel. The MeOH:CH<sub>3</sub>CN layer was separated and evaporated to dryness under vacuum. This defatted extract material (490 mg) was dissolved in CHCl<sub>3</sub>, adsorbed onto Celite 545, and fractionated into four fractions via normal-phase flash chromatography using a gradient solvent system of hexanes-CHCl<sub>3</sub>-MeOH at a 30 mL/min flow rate and 80 column volumes over 45 min. The first fraction from the flash chromatography was subjected to a preparative reverse-phase HPLC separation (Atlantis T3) using an isocratic system of 60:40 CH<sub>3</sub>CN-H<sub>2</sub>O (0.1% formic acid) for 35 min at a flow rate of 17.0 mL/min to yield five subfractions. Subfractions 1, 2, and 5 were identified as compounds **2** (3.9 mg), **3** (1.0 mg), and **1** (4.0 mg), respectively. The third fraction from the flash chromatography was subjected to a preparative reverse-phase HPLC separation (Atlantis T3) using an isocratic system of 50:50 CH<sub>3</sub>CN-H<sub>2</sub>O (0.1% formic acid) for 45 min at a flow rate of 17.0 mL/min to afford compounds **5** (85.0 mg) and **6** (3.5 mg).

Deacetyl-javanicunine A (**1**): Yellow oil;  $[\alpha]_{20}^D = -356$  (c = 0.1, CH<sub>3</sub>CN); UV (CH<sub>3</sub>CN)  $\lambda_{max}$  (log  $\epsilon$ ) 298 (3.4), 243 (3.8), 206 (4.5) nm. <sup>1</sup>H NMR (CDCl<sub>3</sub>, 400 MHz) and <sup>13</sup>C NMR (CDCl<sub>3</sub>, 100 MHz) (see Table 7.1); HRESIMS  $m/z$  369.2173 [M + H]<sup>+</sup> (calcd. for C<sub>22</sub>H<sub>29</sub>N<sub>2</sub>O<sub>3</sub>, 369.2172).

Javanicunine C (**2**): Yellow oil;  $[\alpha]_{20}^D = -346$  ( $c = 0.1$ ,  $\text{CH}_3\text{CN}$ ); UV ( $\text{CH}_3\text{CN}$ )  $\lambda_{\text{max}}$  ( $\log \epsilon$ ) 298 (3.4), 242 (3.8), 205 (4.4) nm.  $^1\text{H}$  NMR ( $\text{CD}_3\text{CN}$ , 400 MHz) and  $^{13}\text{C}$  NMR ( $\text{CD}_3\text{CN}$ , 100 MHz) (see Table 7.1); HRESIMS  $m/z$  385.2130  $[\text{M} + \text{H}]^+$  (calcd. for  $\text{C}_{22}\text{H}_{29}\text{N}_2\text{O}_4$ , 385.2121).

Javanicunine D (**3**): Yellow oil;  $[\alpha]_{20}^D = -345$  ( $c = 0.1$ ,  $\text{CH}_3\text{CN}$ ); UV ( $\text{CH}_3\text{CN}$ )  $\lambda_{\text{max}}$  ( $\log \epsilon$ ) 295 (3.4), 212 (4.5) nm.  $^1\text{H}$  NMR ( $\text{CD}_3\text{CN}$ , 700 MHz) and  $^{13}\text{C}$  NMR ( $\text{CD}_3\text{CN}$ , 176 MHz) (see Table 7.1); HRESIMS  $m/z$  385.2119  $[\text{M} + \text{H}]^+$  (calcd. for  $\text{C}_{22}\text{H}_{29}\text{N}_2\text{O}_4$ , 385.2121).

Javanicunine A (**4**): Colorless amorphous solid;  $[\alpha]_{20}^D = -196$  ( $c = 0.1$ ,  $\text{CH}_2\text{Cl}_2$ ).  $^1\text{H}$  NMR ( $\text{CDCl}_3$ , 500 MHz) and  $^{13}\text{C}$  NMR ( $\text{CDCl}_3$ , 125 MHz) (see Table 7.3); HRESIMS  $m/z$  411.2263  $[\text{M} + \text{H}]^+$  (calcd. for  $\text{C}_{24}\text{H}_{31}\text{N}_2\text{O}_4$ , 411.2278).

Herqueinone (**5**) and isoherqueinone (**5a**): Orange amorphous powder.  $^1\text{H}$  NMR (400 MHz,  $\text{DMSO-d}_6$ ) **5**,  $\delta$  15.75 (s, 1H, 9-OH), 13.18 (s, 1H, 7-OH), 7.57 (s, 1H, 4-OH), 6.36 (s, 1H, 12-H), 4.86 (q,  $J = 6.7$  Hz, 1H, 2'-H), 3.77 (s, 3H, 15-H), 2.50 (s, 3H, 14-H), 1.55 (d,  $J = 6.7$  Hz, 3H, 1'-H), 1.37 (s, 3H, 4'-H), 0.98 (s, 3H, 5'-H); **5a**,  $\delta$  15.73 (s, 1H, 9-OH), 13.26 (s, 1H, 7-OH), 7.52 (s, 1H, 4-OH), 6.36 (s, 1H, 12-H), 4.98 (q,  $J = 6.5$  Hz, 1H, 2'-H), 3.76 (s, 3H, 15-H), 2.47 (s, 3H, 14-H), 1.37 (d,  $J = 6.6$  Hz, 3H, 1'-H), 1.31 (s, 3H, 4'-H), 0.78 (s, 3H, 5'-H);  $^{13}\text{C}$  NMR (100 MHz,  $\text{DMSO-d}_6$ ) **5**,  $\delta$  197.0 (C-5), 186.3 (C-11), 178.9 (C-3), 162.9 (C-9), 162.0 (C-7), 151.0 (C-13), 138.9 (C-1), 131.2 (C-8), 122.7 (C-12), 109.1 (C-10), 103.1 (C-2), 102.6 (C-6), 96.0 (C-2'), 78.9 (C-4), 60.0 (C-15), 43.0 (C-3'), 23.9 (C-14), 23.7 (C-5'), 18.7 (C-1'), 16.0 (C-4'); **5a**,  $\delta$  197.7 (C-5), 186.4 (C-11), 178.1 (C-3), 163.0 (C-9), 161.9 (C-7), 150.8 (C-13), 139.0 (C-1), 131.2 (C-8), 122.8 (C-12), 109.2 (C-10), 103.0 (C-6), 102.6 (C-2), 90.5 (C-2'), 78.5 (C-4), 59.9 (C-15), 46.0 (C-3'), 23.8 (C-14), 16.1 (C-4'), 15.9 (C-5'), 12.9 (C-1'); HRESIMS  $m/z$  373.1275  $[\text{M} + \text{H}]^+$  (calcd. for  $\text{C}_{20}\text{H}_{21}\text{O}_7$ , 373.1281).

Norherqueinone (**6**): Orange amorphous powder;  $[\alpha]_{20}^D = +847$  ( $c = 0.1$ , pyridine).  $^1\text{H}$  NMR (500 MHz,  $\text{DMSO-d}_6$ )  $\delta$  15.32 (s, 1H, 9-OH), 12.99 (s, 1H, 7-OH), 7.49 (s, 1H, 4-OH), 6.32 (s, 1H, 12-H), 4.81 (q,  $J = 6.7$  Hz, 1H, 2'-H), 2.48 (s, 3H, 14-H), 1.53 (d,  $J = 6.7$  Hz, 3H, 1'-H), 1.36 (s, 3H, 4'-H), 0.96 (s, 3H, 5'-H);  $^{13}\text{C}$  NMR (125 MHz,  $\text{DMSO-d}_6$ )  $\delta$  197.2 (C-5), 186.4 (C-11), 177.4 (C-3), 157.5 (C-9), 157.3 (C-7), 150.4 (C-13), 135.1 (C-1), 129.5 (C-8), 122.8 (C-12), 109.0 (C-10), 103.2 (C-2), 102.5 (C-6), 95.6 (C-2'), 78.8 (C-4), 43.0 (C-3'), 23.8 (C-14), 23.8 (C-5'), 18.7 (C-1'), 16.1 (C-4'); HRESIMS  $m/z$  359.1120  $[\text{M} + \text{H}]^+$  (calcd. for  $\text{C}_{19}\text{H}_{19}\text{O}_7$ , 359.1125).

**Acetylation of Deacetyl-Javanicunine A (1).** Acetylation of compound **1** was carried out as described previously <sup>299</sup>. In brief, 2.5 mg of **1** were dissolved in 500  $\mu\text{L}$  of *N,N*-diisopropylethylamine (DIPEA). Then, 150  $\mu\text{L}$  of acetic anhydride was added gradually. The reaction mixture was kept at 60 °C for 15 hrs. The mixture was evaporated to dryness and then subjected to semi-preparative HPLC over a Phenomenex PFP column using a gradient system of 50:50 to 60:40 of  $\text{CH}_3\text{CN-H}_2\text{O}$  (0.1% formic acid) over 15 min at a flow rate of 4.72 mL/min to yield 1.0 mg of javanicunine A (**4**).

**Acid Hydrolysis and Marfey's Analysis of Javanicunine C (2).** Acid hydrolysis and Marfey's analysis were performed according to Helaly et al. <sup>314</sup> and Capon et al. <sup>315</sup> with slight modification. Briefly, 500  $\mu\text{L}$  of 6 M HCl was added to 1.5 mg of javanicunine C (**2**). The resulting solution was kept in a sealed vial after being flushed with nitrogen and left stirring at 110 °C for 24 h. The reaction mixture was then neutralized with 500  $\mu\text{L}$  of 6 M NaOH and allowed to dry completely. The resulting sample was subjected to UPLC-HRMS to confirm the production of Trp (Fig. 7.21). For the Marfey's analysis, the hydrolysate mixture was re-dissolved in deionized water (250  $\mu\text{L}$ ) before adding 100  $\mu\text{L}$  of sodium bicarbonate (1 M) and 500  $\mu\text{L}$  of 1-fluoro-2-4-dinitrophenyl-5-L-alanine amide (L-FDAA) (1% in acetone). The resulting solution was kept stirring at 37 °C for 1 h and then neutralized with 100  $\mu\text{L}$  of 1 M HCl. Similarly, L-Trp and D-Trp were dissolved in water and treated with L-FDAA as described for the acid hydrolysate to afford L-FDAA standards. UPLC-HRMS analysis of the Marfey's derivatives of compound **2**, L-Trp, and D-Trp was performed using an LTQ-Orbitrap XL mass spectrometer connected to a Waters Acquity UPLC system (Fig. 7.22).

**Cytotoxicity and Antimicrobial Assays.** To evaluate the cytotoxic activity of **1-3** against human melanoma cancer cells (MDA-MB-435), human breast cancer cells (MDA-MB-231), and human ovarian cancer cells (OVCAR3), the previously described protocol was followed <sup>59</sup>. In brief, a total of 5,000 cells were seeded per well of a 96-well clear, flat-bottom plate (Microtest 96, Falcon) and incubated overnight (37 °C in 5%  $\text{CO}_2$ ). Samples dissolved in DMSO were then diluted and added to the appropriate wells. The cells were incubated in the presence of test substance for 72 h at 37 °C and evaluated for viability with a commercial absorbance assay.

Testing for antibacterial and antifungal activities included tests against Gram-negative *Escherichia coli* and *Pseudomonas aeruginosa*, Gram-positive *Staphylococcus aureus*, methicillin-resistant *Staphylococcus aureus* (MRSA), *Bacillus subtilis*, *Mycobacterium smegmatis*, and *Bacillus anthracis*, and the fungi *Saccharomyces cerevisiae*, *Candida albicans*, and *Aspergillus niger*. Minimal inhibitory concentrations (MICs) of compounds **1–3** were measured by broth microdilution antimicrobial assays. The antimicrobial assay protocol is previously described<sup>316</sup>.

**STarFish Analysis.** The full details for how to use STarFish to probe the potential biological activity of a compound have been detailed recently<sup>306</sup>, and these directions were followed to upload the compounds into the software and analyze for potential activities (Software download link: <https://github.com/ntcockroft/STarFish>).

**cAMP Accumulation Assay.** The cAMP Hunter eXpress OPRM1 CHO-K1 GPCR assay (Eurofins DiscoverX Corporation) was performed according to manufacturer's instructions. Briefly, cells were seeded in 100  $\mu$ L cell plating reagent in 96 well plates and allowed to incubate at 37 °C (5% CO<sub>2</sub>, 95% relative humidity) for 24 hr. Media was removed from cells, and cells were washed with 30  $\mu$ L of cell assay buffer. Compounds **1–3** were assessed using an 11 point 5-fold serial dilution with a starting concentration of 10 mM. Aliquots of compound/forskolin solution were added to cells (final concentrations were 20  $\mu$ M forskolin, and 0.4% DMSO) and incubated at 37 °C and 5% CO<sub>2</sub> for 30 min. Next, cAMP antibody reagent detection solution was added to each well according to manufacturer's instructions at room temperature protected from light for one hr. Next, enzyme acceptor solution was added, and the solution allowed to incubate at RT protected from light overnight. Luminescence was quantified using an iD5 multimode microplate reader plate reader with SoftMax® Pro software (Molecular Devices, San Jose, CA). Data were normalized to vehicle and forskolin only control values and analyzed using three parameter nonlinear regression with GraphPad Prism 8.0.

**Screening for Cathepsin K Inhibition.** Cathepsin K Inhibitor Screening kit (Sigma, #MAK-201K) was purchased and used to investigate cathepsin K inhibitory activity of compounds **2, 3, 5, and 6**. Fluorescence (FLU,  $\lambda_{ex}$ = 400/  $\lambda_{em}$ = 505nm) was quantified using a iD5 multimode microplate reader plate reader in kinetic mode for 60 minutes at 37 °C (SoftMax® Pro software;

Molecular Devices, San Jose, CA). Data were normalized to Enzyme Control values and analyzed using GraphPad Prism 8.0.

### **Funding**

This research was supported in part by the National Cancer Institute/NIH via grant P01 CA125066. This work was performed in part at the Joint School of Nanoscience and Nanoengineering, a member of the Southeastern Nanotechnology Infrastructure Corridor (SENIC) and National Nanotechnology Coordinated Infrastructure (NNCI), which is supported by the National Science Foundation (Grant ECCS-1542174).

### **Supplementary Data**

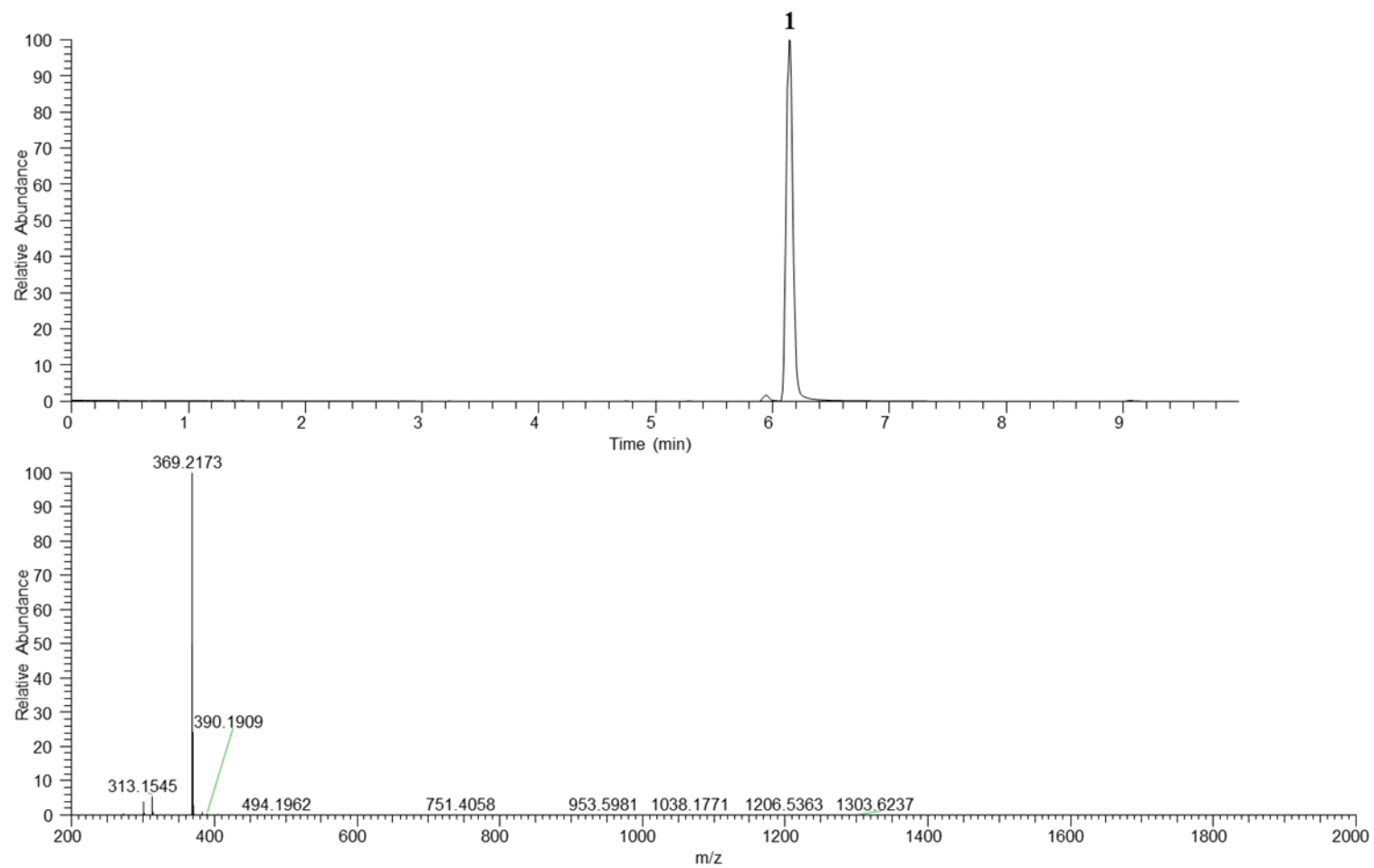


**Figure 7.7.** UPLC-(+)-HRESIMS spectrum of **1**.

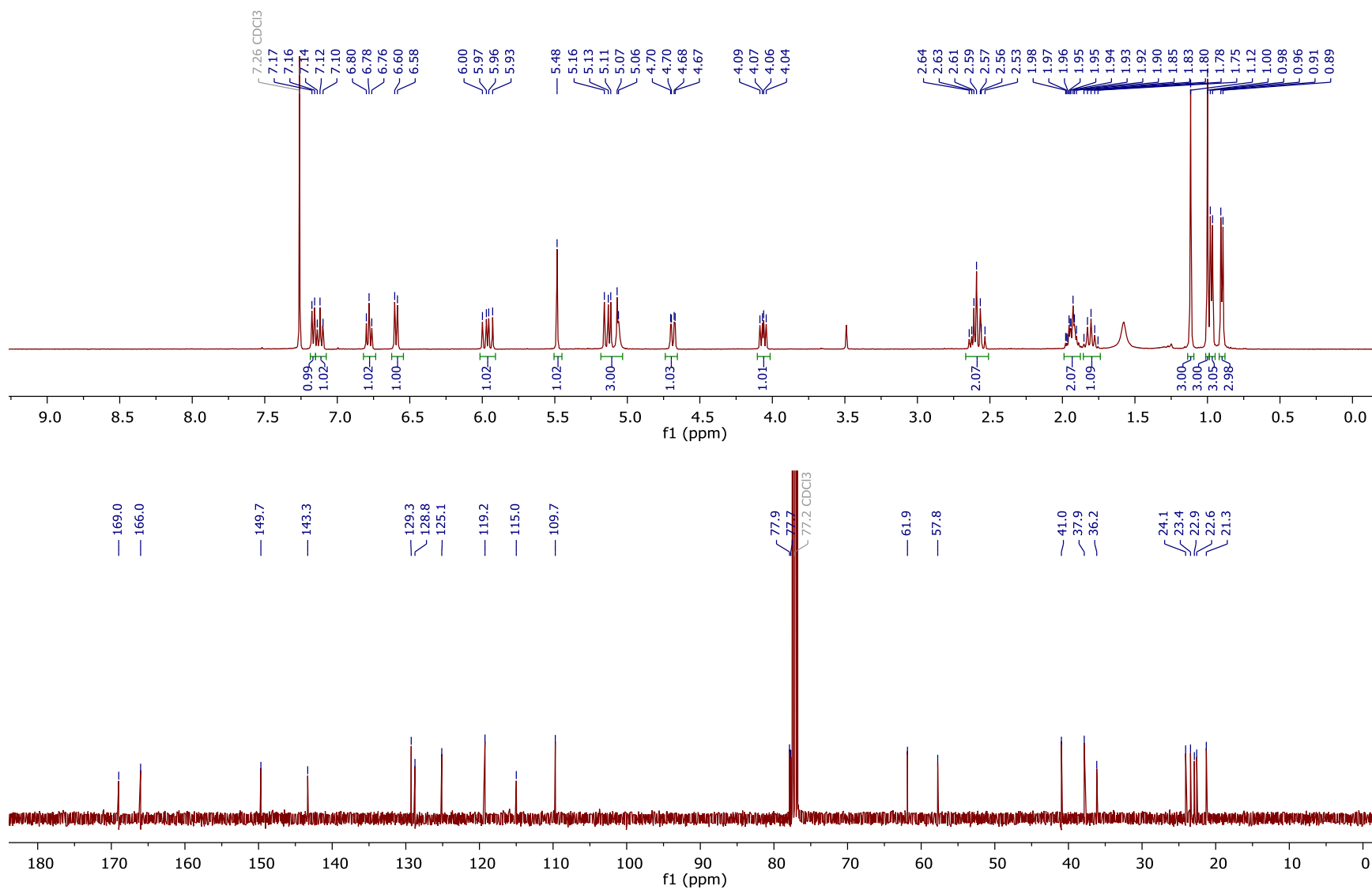


**Figure 7.8.**  $^1\text{H}$  and  $^{13}\text{C}$  NMR spectra of **1** [400 MHz for  $^1\text{H}$  and 100 MHz for  $^{13}\text{C}$ ,  $\text{CDCl}_3$ ].

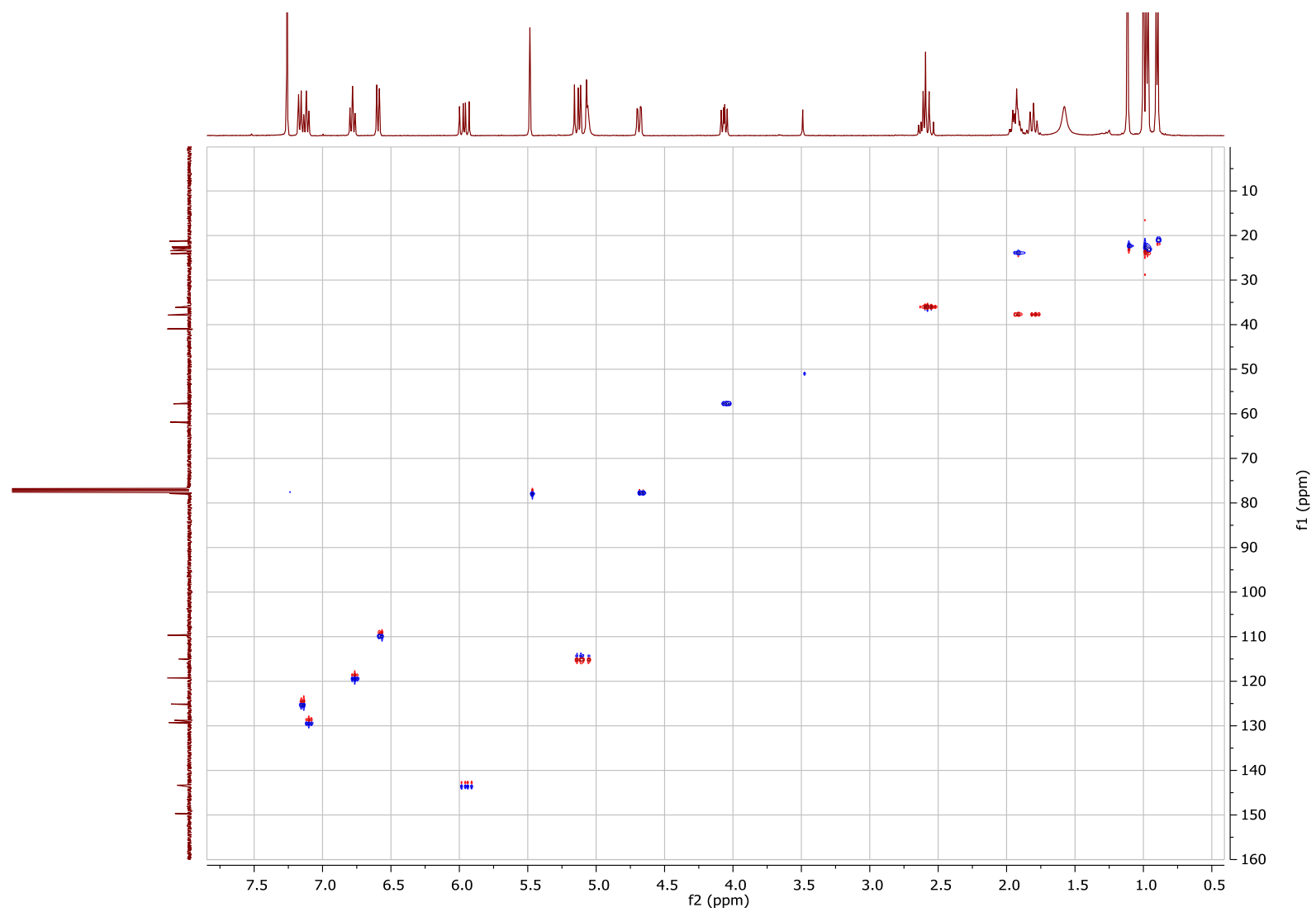


**Figure 7.9.** Edited-HSQC NMR spectrum of **1** [400 MHz, CDCl<sub>3</sub>].

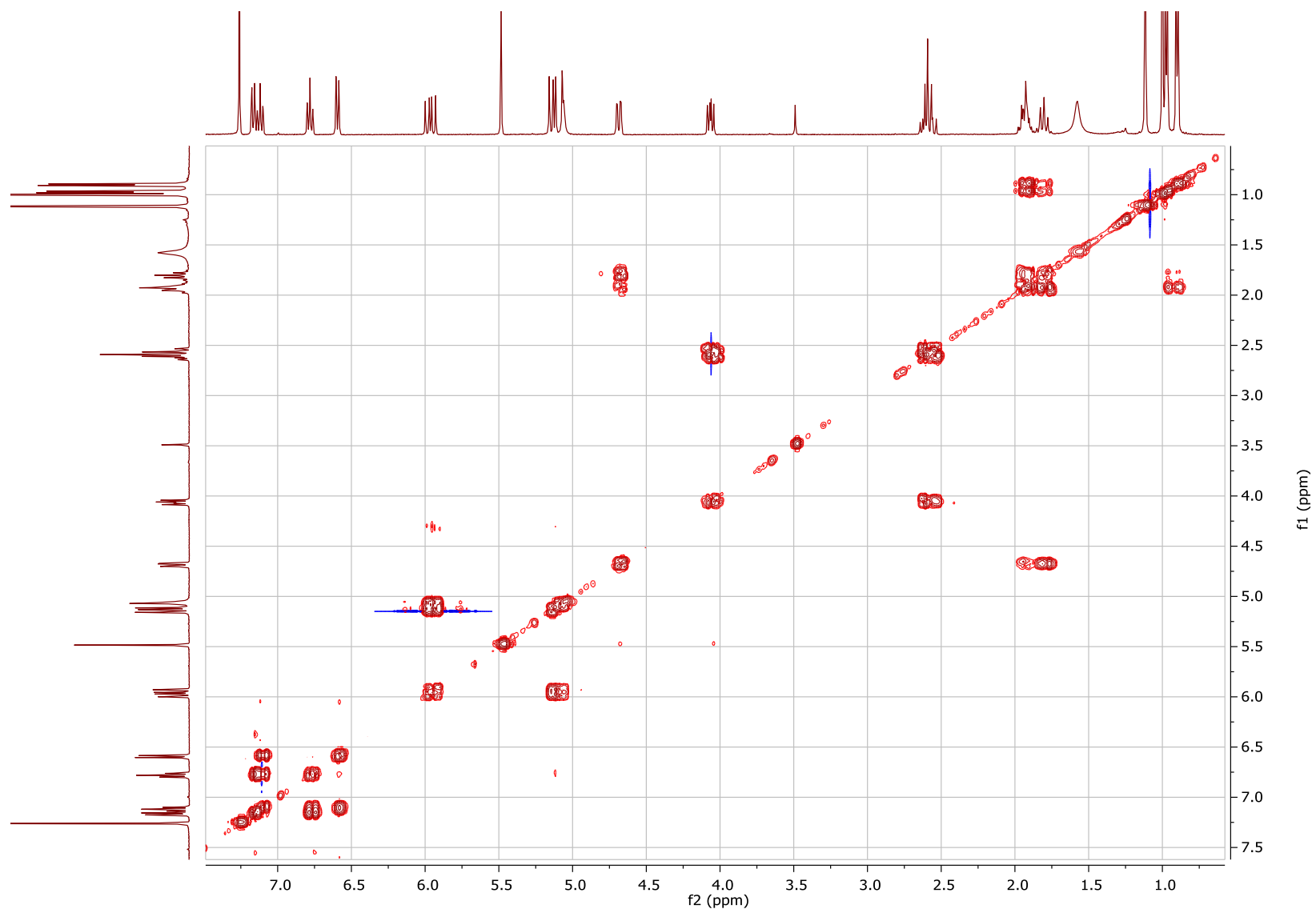


**Figure 7.10.** COSY NMR spectrum of **1** [400 MHz, CDCl<sub>3</sub>].

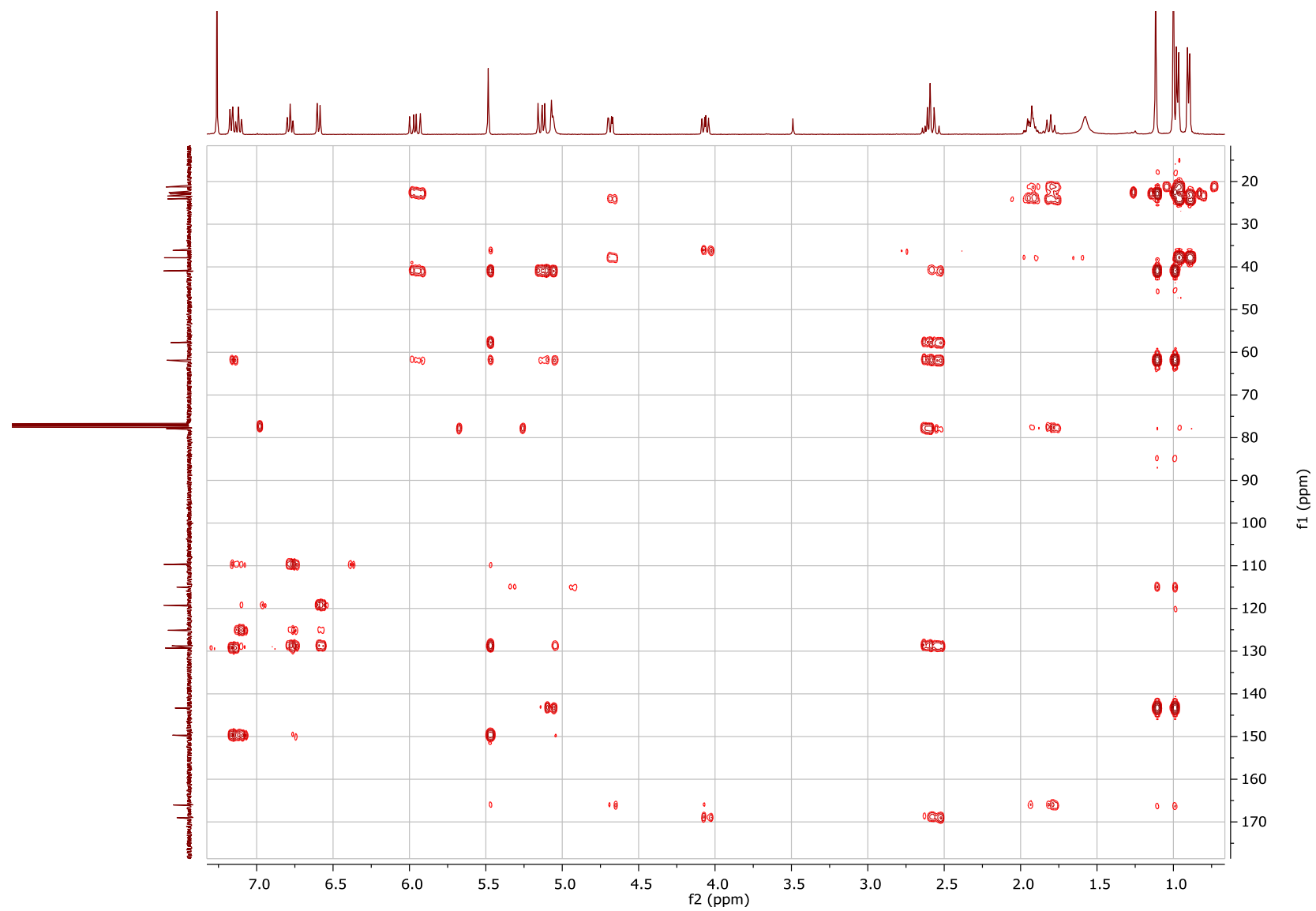
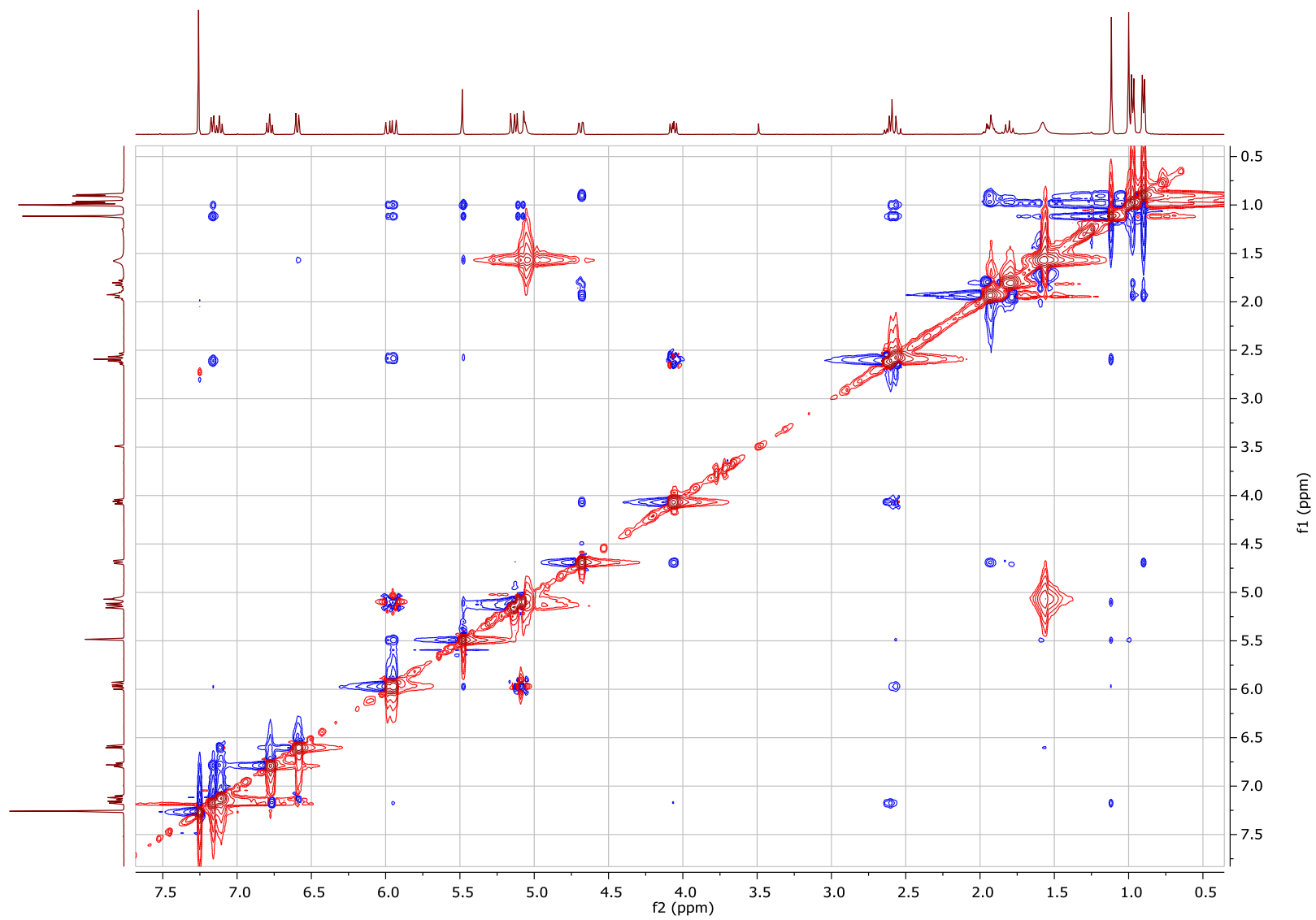


Figure 7.11. HMBC NMR spectrum of 1 [400 MHz, CDCl<sub>3</sub>].



**Figure 7.12.** NOESY NMR spectrum of **1** [500 MHz,  $\text{CDCl}_3$ ].

**Table 7.2.** Collected  $^1\text{H}$  and  $^{13}\text{C}$  NMR data of **1** in  $\text{CDCl}_3$  as compared to the literature.

no.	<b>1<sup>a</sup></b>		<b>Reported for 1<sup>b</sup></b>	
	$\delta_{\text{C}}$ , type	$\delta_{\text{H}}$ , (J in Hz)	$\delta_{\text{C}}$ (type)	$\delta_{\text{H}}$ , (J in Hz)
1	169.0, C		168.9, C	
3	77.7, CH	4.69, dd (10.0, 2.5)	77.6, CH	4.69, dd (9.6, 2.4)
4	166.0, C		165.9, C	
5a	77.9, CH	5.48, s	77.8, CH	5.49, s
6		5.06, brs		5.05-5.16, m
6a	149.7, C		149.6, C	
7	109.7, CH	6.59, d (7.7)	109.6, CH	6.58, d (7.6)
8	129.3, CH	7.12, t (8.0)	129.1, CH	7.11, td (7.6, 1.2)
9	119.2, CH	6.78, t (7.5)	119.1, CH	6.77, td (7.2, 2.0)
10	125.1, CH	7.17, d (7.5)	124.9, CH	7.16, d (7.6)
10a	128.8, C		128.6, C	
10b	61.9, C		61.8, C	
11	36.2, CH <sub>2</sub>	2.55, m 2.62, m	36.0, CH <sub>2</sub>	2.53-2.66, m
11a	57.8, CH	4.06, dd (10.3, 7.0)	57.6, CH	4.06, dd (10.0, 7.2)
12	37.9, CH <sub>2</sub>	1.81, m 1.93, m	37.8, CH <sub>2</sub>	1.79, t (9.6) 1.88-1.97, m
13	24.1, CH	1.91, m	23.9, CH	1.88-1.97, m
14	23.4, CH <sub>3</sub>	0.97, d (6.2)	23.3, CH <sub>3</sub>	0.97, d (6.4)
15	21.3, CH <sub>3</sub>	0.90, d (6.1)	21.2, CH <sub>3</sub>	0.90, d (6.4)
16	41.0, C		40.8, C	
17	143.3, CH	5.96, dd (17.4, 10.8)	143.2, CH	5.97, dd (17.2, 10.8)
18	115.0, CH <sub>2</sub>	5.09, d (17.4)	114.9, CH <sub>2</sub>	5.05-5.16, m
		5.15, d (10.8)		5.05-5.16, m
19	22.9, CH <sub>3</sub>	1.00, s	22.8, CH <sub>3</sub>	1.00, s
20	22.6, CH <sub>3</sub>	1.12, s	22.5, CH <sub>3</sub>	1.12, s

<sup>a</sup> Collected NMR data<sup>b</sup> NMR data as reported by Wang et al., 2019

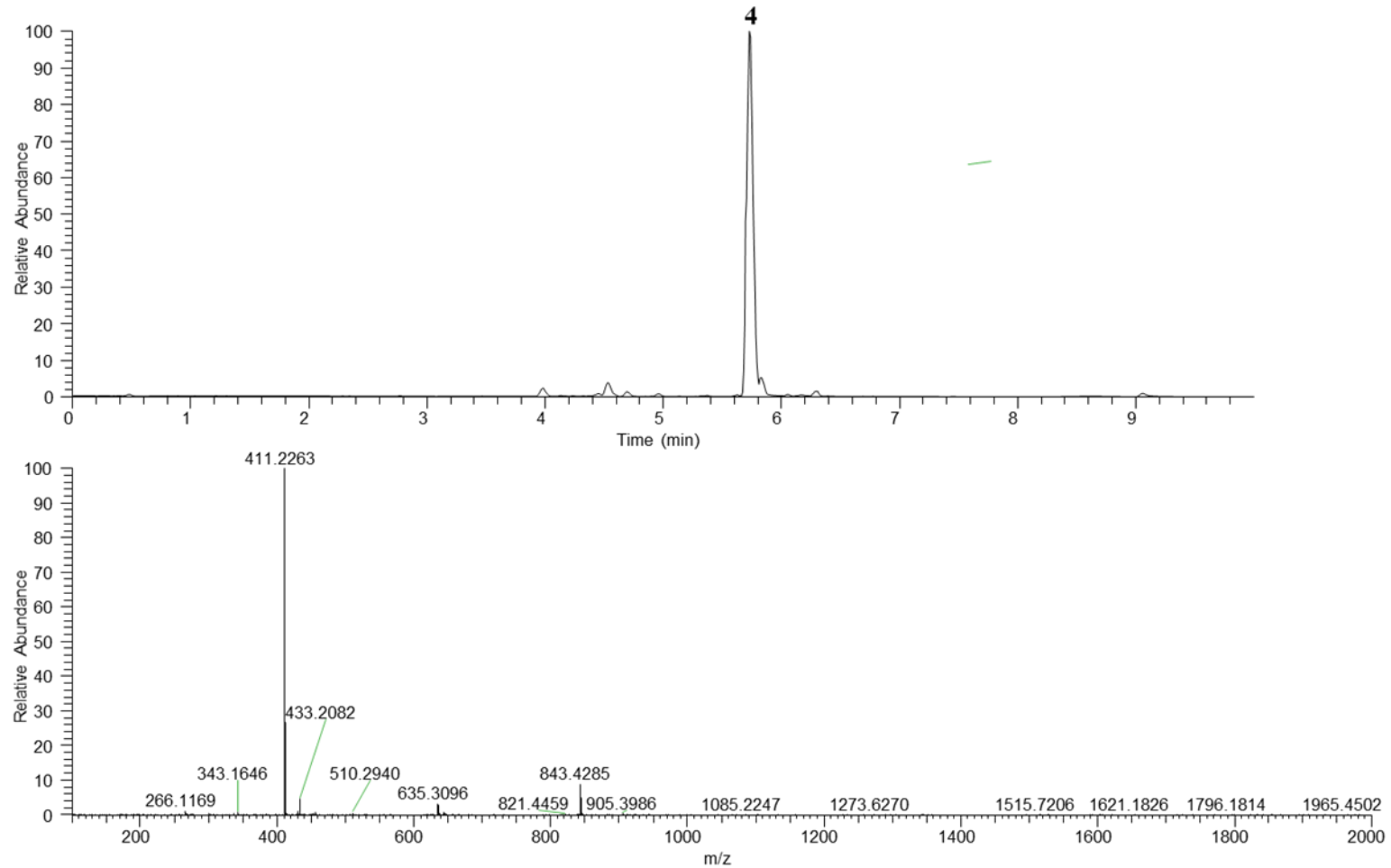


**Figure 7.13.** UPLC-(+)-HRESIMS spectrum of **4**.

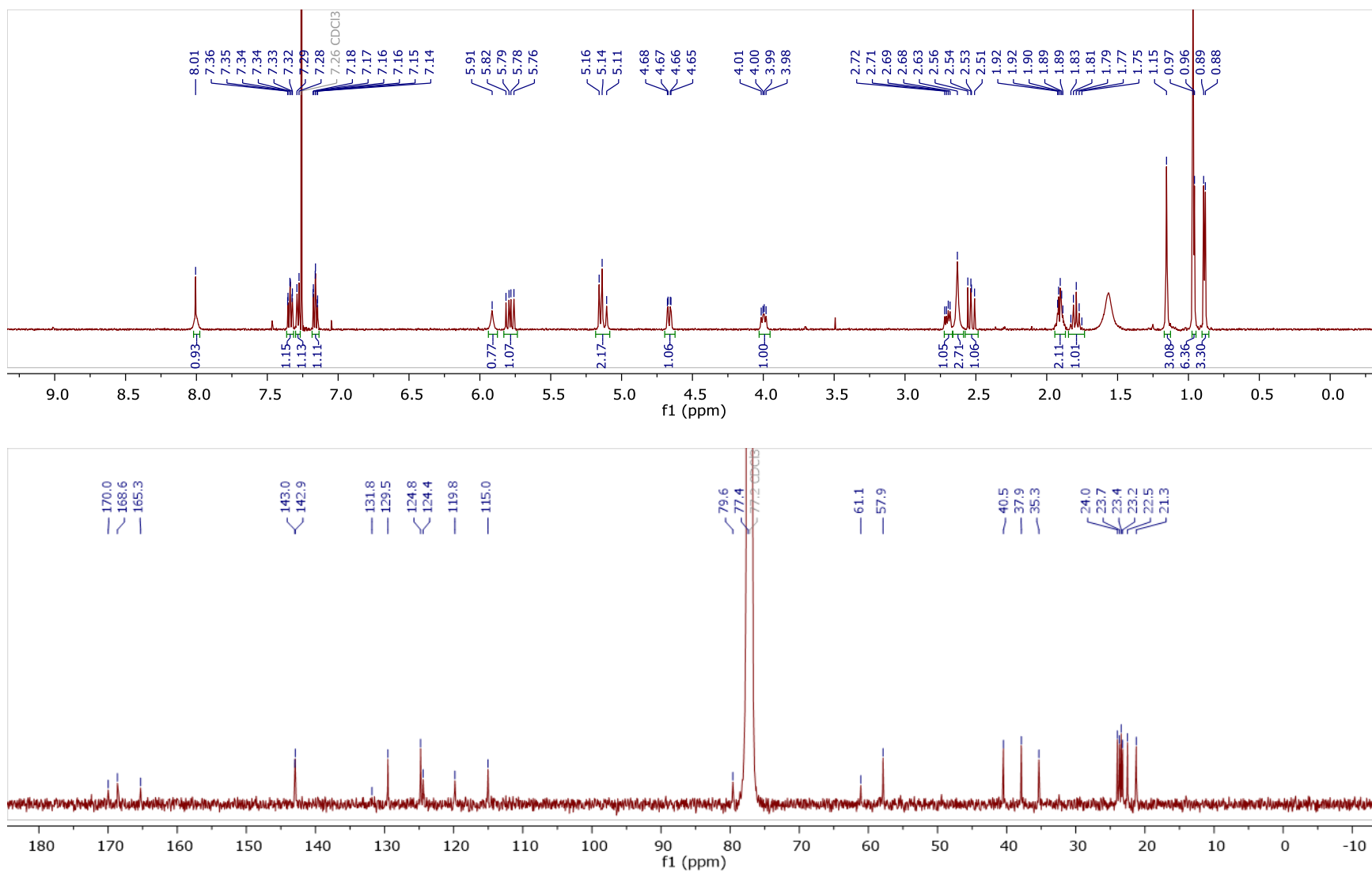


**Figure 7.14.**  $^1\text{H}$  and  $^{13}\text{C}$  NMR spectra of **4** [500 MHz for  $^1\text{H}$  and 125 MHz for  $^{13}\text{C}$ ,  $\text{CDCl}_3$ ].

**Table 7.3.** Collected  $^1\text{H}$  and  $^{13}\text{C}$  NMR data of **4** in  $\text{CDCl}_3$  as compared to the literature.

no	<b>4<sup>a</sup></b>		<b>Reported for 4<sup>b</sup></b>	
	$\delta_{\text{C}}$ , type	$\delta_{\text{H}}$ , (J in Hz)	$\delta_{\text{C}}$ (type)	$\delta_{\text{H}}$ , (J in Hz)
1	168.6, C		168.5, C	
3	77.4, CH	4.66, dd (10.1, 2.3)	77.2, CH	4.66, dd (9.6, 2.8)
4	165.3, C		165.1, C	
5a	79.6, CH	5.91, br s	79.4, CH	5.92, br s
6a	143.0, C		142.8, C	
7	119.8, CH	8.01, brs	119.6, CH	7.99, br d
8	129.5, CH	7.34, td (7.3, 1.2)	129.3, CH	7.34, td (7.2, 1.5)
9	124.8, CH	7.16, td (7.6, 1.0)	124.6, CH	7.16, td (7.5, 1.0)
10	124.4, CH	7.28, br d (7.5)	124.3, CH	7.28, br d (7.7)
10a	131.8, C		132.0, C	
10b	61.1, C		60.9, C	
11	35.3, CH <sub>2</sub>	2.53, dd (12.9, 10.9)	35.2, CH <sub>2</sub>	2.53, dd (13.0, 10.8)
		2.70, dd (12.7, 6.4)		2.70, dd (13.0, 6.4)
11a	57.9, CH	4.00, dd (10.8, 6.4)	57.7, CH	4.00, dd (10.8, 6.4)
12	37.9, CH <sub>2</sub>	1.79, m	37.7, CH <sub>2</sub>	1.82, m
		1.89, m		1.89, m
13	24.0, CH	1.90, m	23.8, CH	1.90, m
14	21.3, CH <sub>3</sub>	0.89, d (6.1)	21.1, CH <sub>3</sub>	0.89, d (6.1)
15	23.4, CH <sub>3</sub>	0.96, d (4.4)	23.2, CH <sub>3</sub>	0.97, d (4.4)
16	40.5, C		40.4, C	
17	143.0, CH	5.79, dd (17.4, 10.8)	142.8, CH	5.79, dd (17.4, 10.8)
18	115.0, CH <sub>2</sub>	5.12, d (17.4)	114.8, CH <sub>2</sub>	5.12, d (17.4)
		5.15, d (10.8)		5.15, d (10.8)
19	22.5, CH <sub>3</sub>	1.15, s	22.4, CH <sub>3</sub>	1.16, s
20	23.2, CH <sub>3</sub>	0.97, s	23.0, CH <sub>3</sub>	0.97, s
21	170.0, C		169.8, C	
22	23.7, CH <sub>3</sub>	2.63, br s	23.5, CH <sub>3</sub>	2.63, br s

<sup>a</sup> Collected NMR data<sup>b</sup> NMR data as reported by Shou et al., 2006

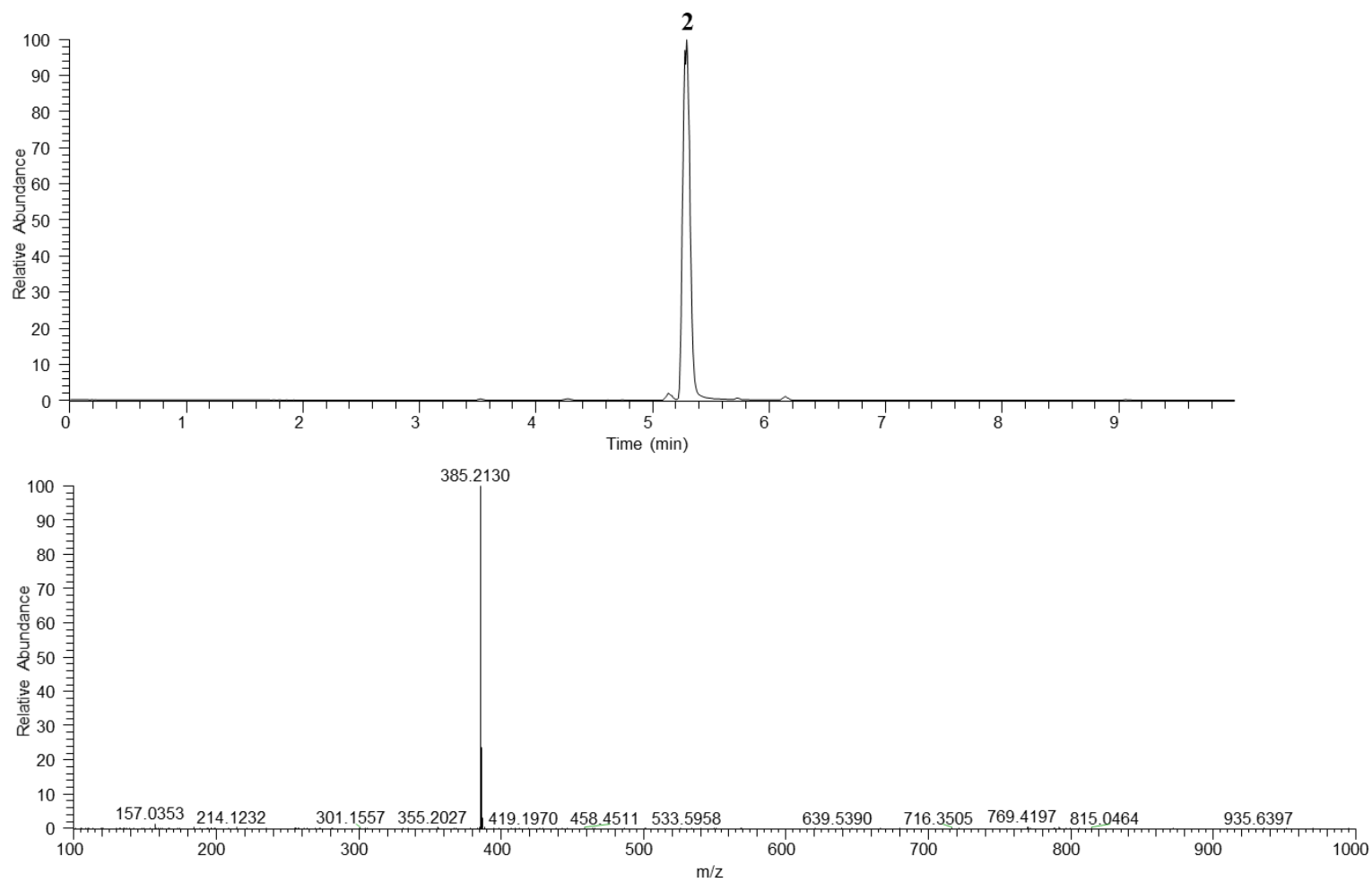


**Figure 7.15.** UPLC-(+)-HRESIMS spectrum of **2**.

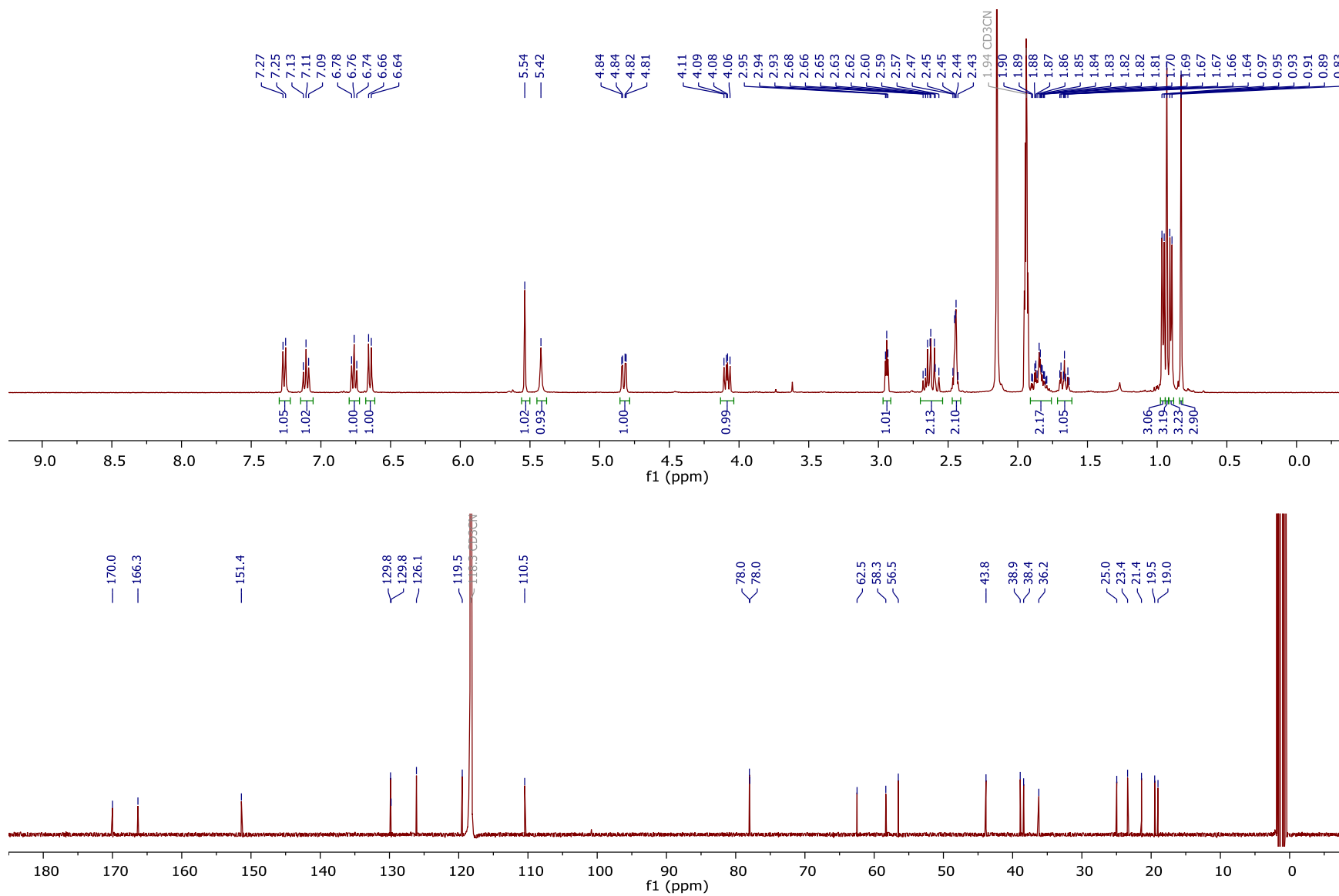


**Figure 7.16.** <sup>1</sup>H and <sup>13</sup>C NMR spectra of **2** [400 MHz for <sup>1</sup>H and 100 MHz for <sup>13</sup>C, CD<sub>3</sub>CN].

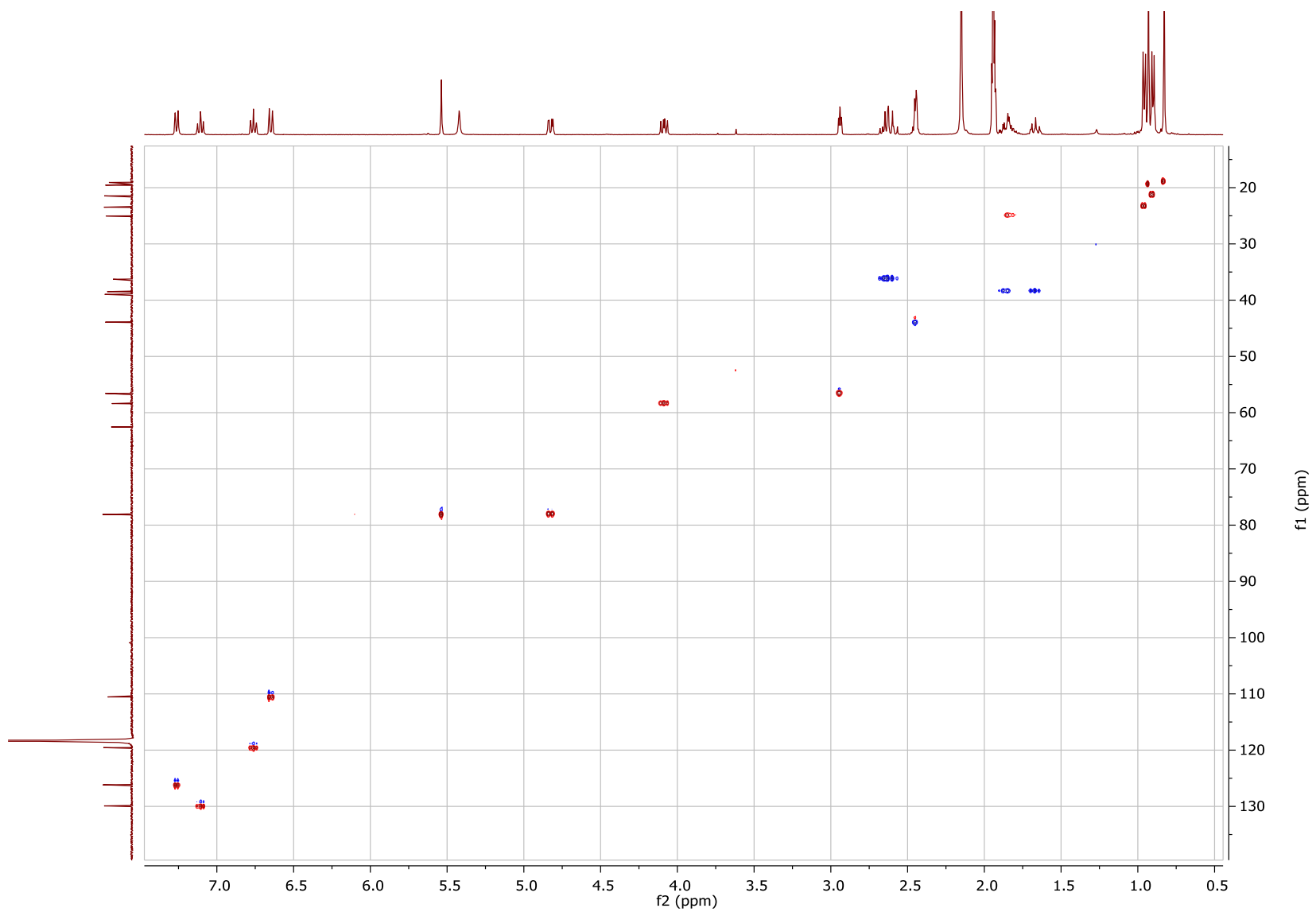


**Figure 7.17.** Edited-HSQC NMR spectrum of **2** [400 MHz, CD<sub>3</sub>CN].

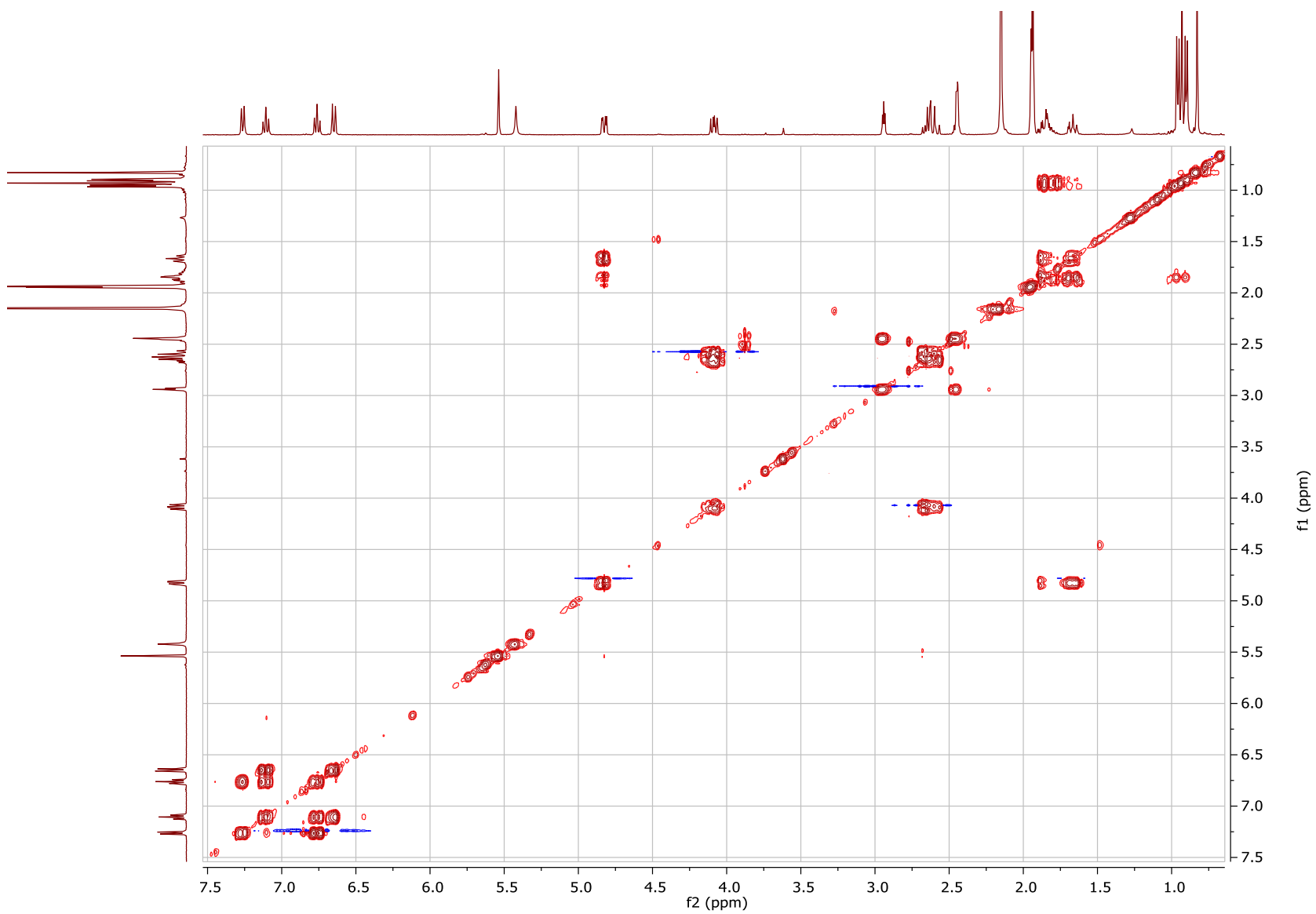


**Figure 7.18.** COSY NMR spectrum of **2** [400 MHz, CD<sub>3</sub>CN].

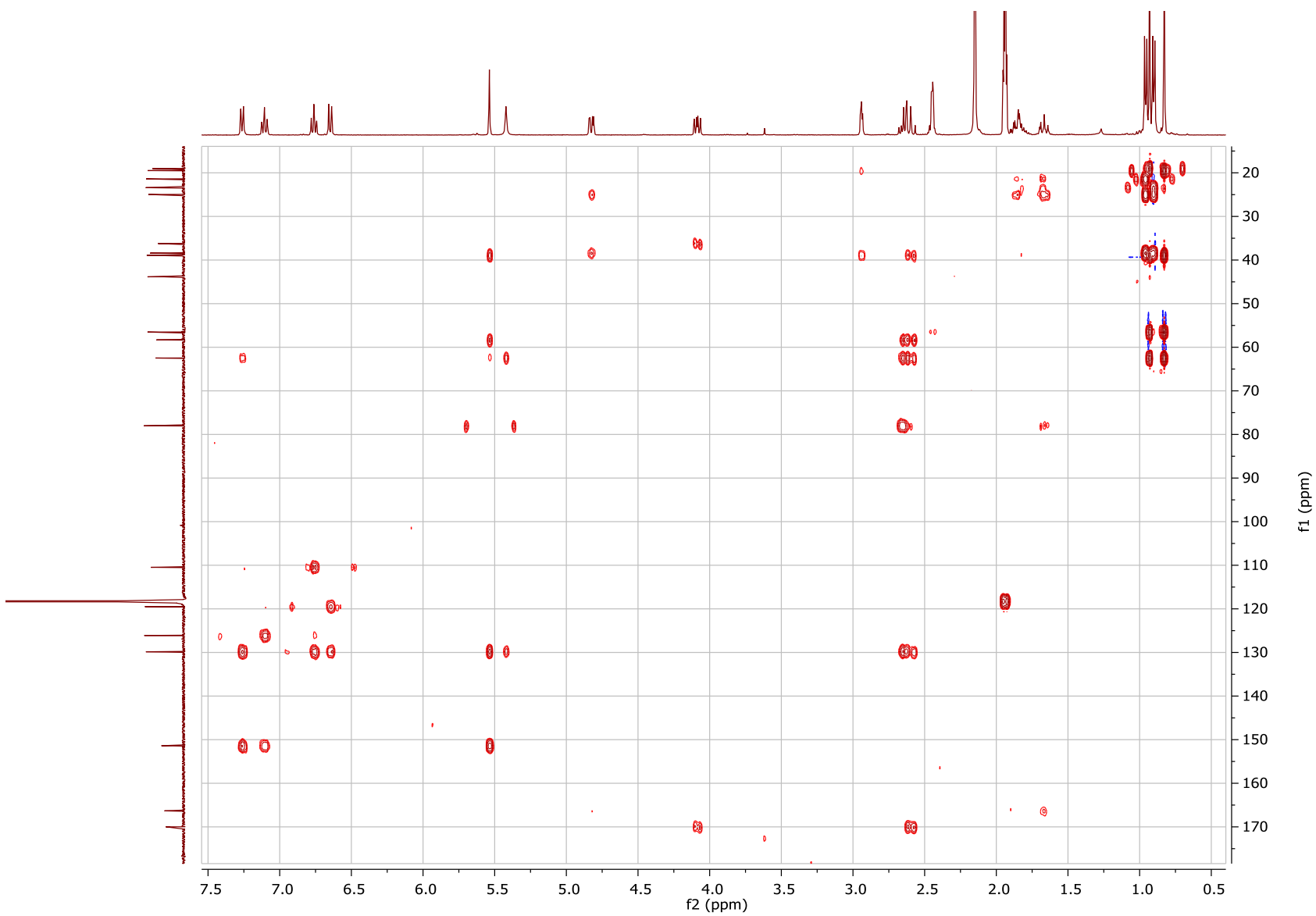


**Figure 7.19.** HMBC NMR spectrum of **2** [400 MHz,  $\text{CD}_3\text{CN}$ ].

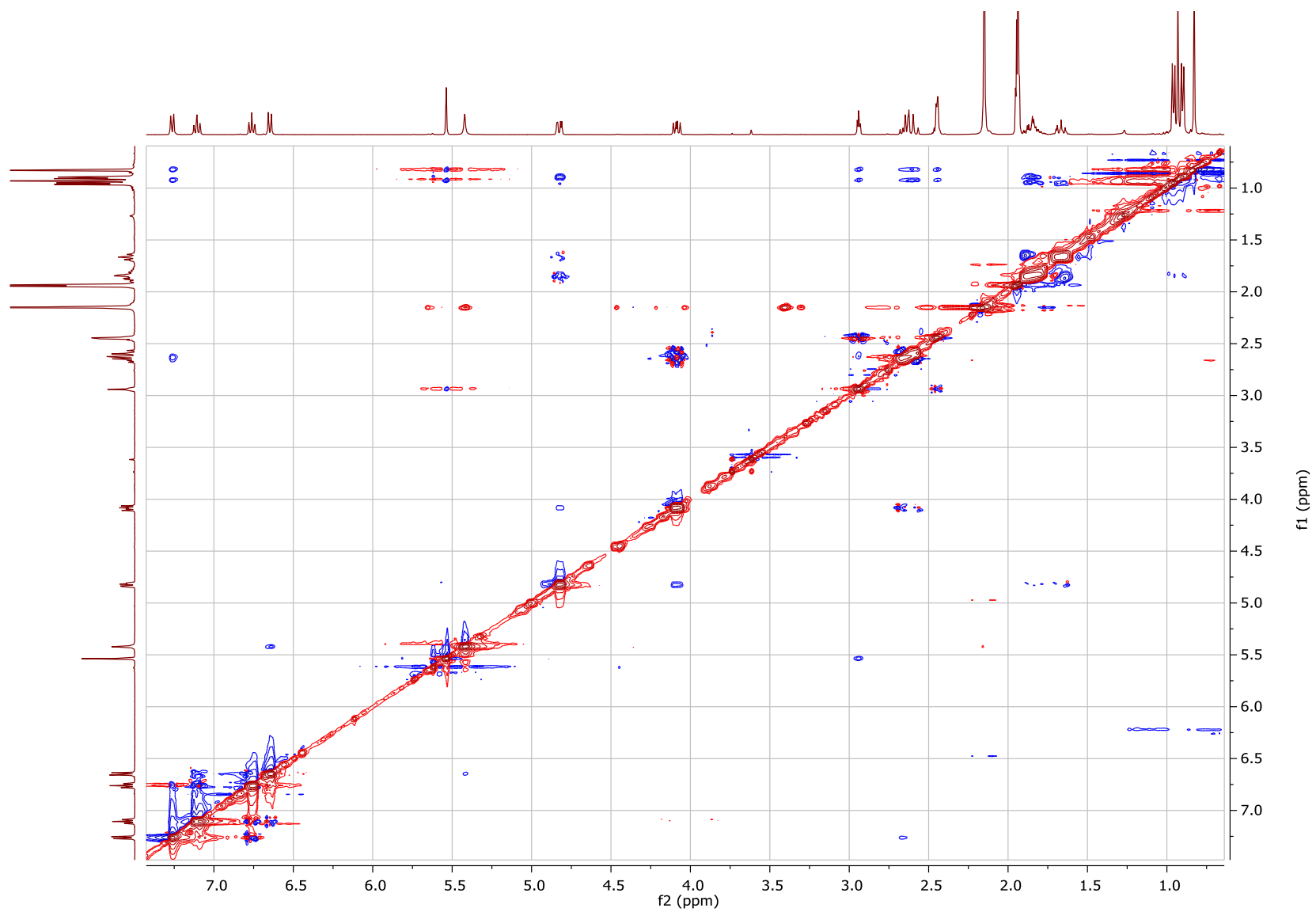
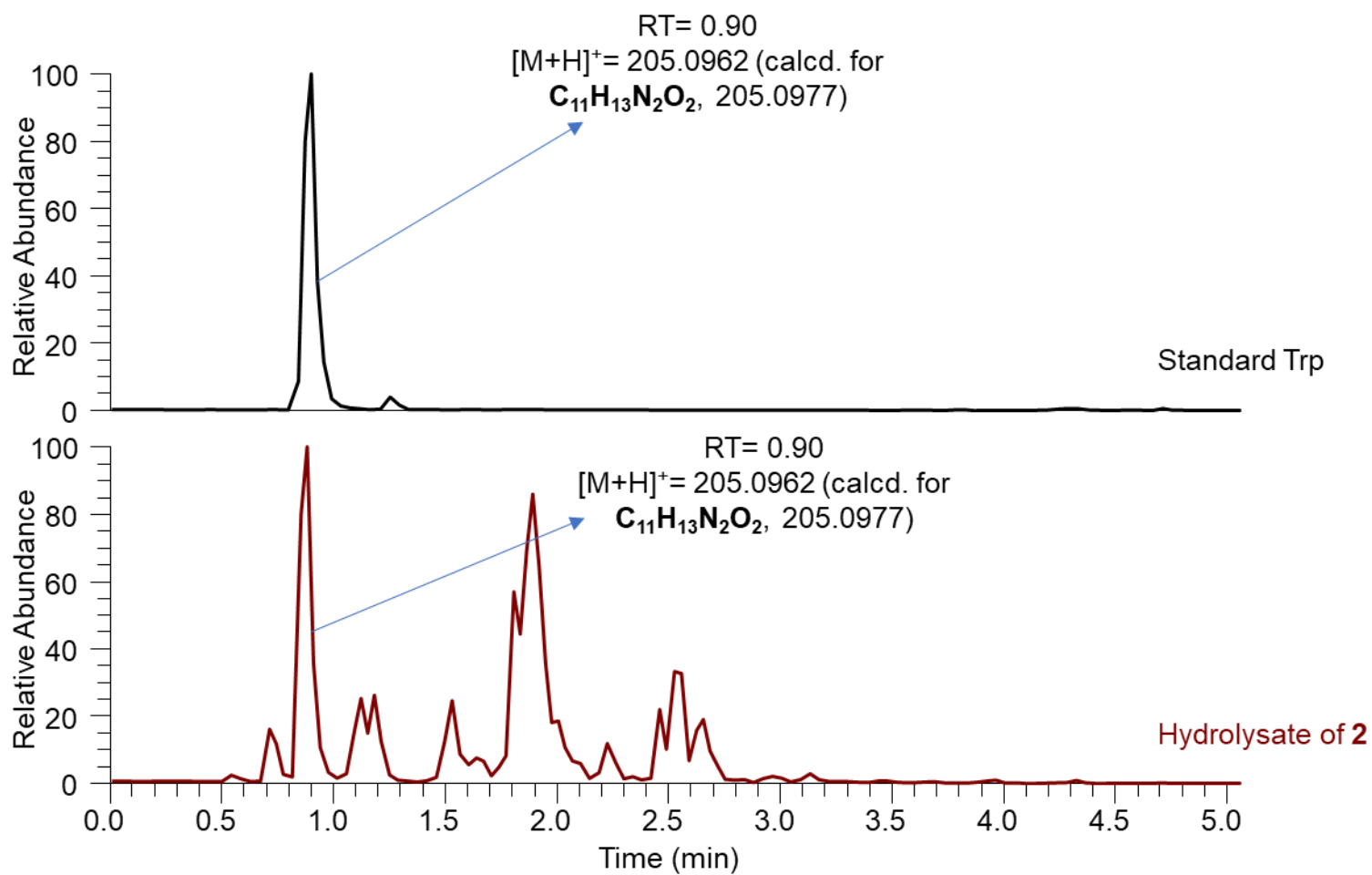
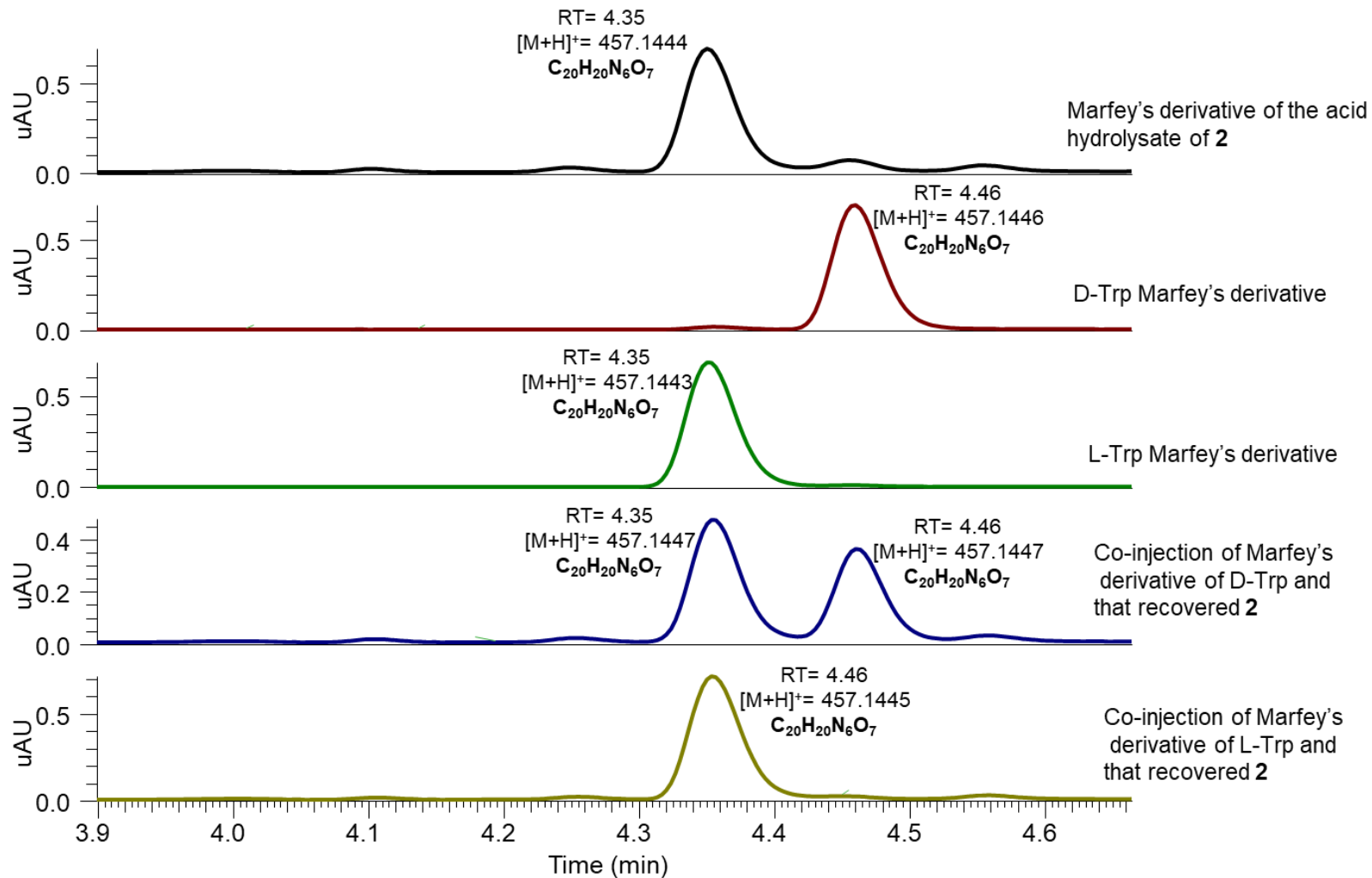


Figure 7.20. NOESY NMR spectrum of **2** [400 MHz, CD<sub>3</sub>CN].



**Fig. 7.21.** UPLC-HRESIMS chromatograms of the hydrolysate sample of **2** and standard tryptophan sample showing the release to Trp by acid hydrolysis.



**Figure 7.22.** UPLC-PDA chromatograms of tryptophan Marfey's derivative of **2**. (a) Injection of Trp Marfey's derivative recovered from the acid hydrolysate of javanicunine D (**2**), (b) Injection of D-Trp Marfey's derivative, (c) Injection of L-Trp Marfey's derivative, (d) Co-injection of Marfey's derivative of D-Trp with the Marfey's derivative of Trp recovered from hydrolysis of **2**, (e) Co-injection of Marfey's derivative of L-Trp with the Marfey's derivative of Trp recovered from hydrolysis of **2**.

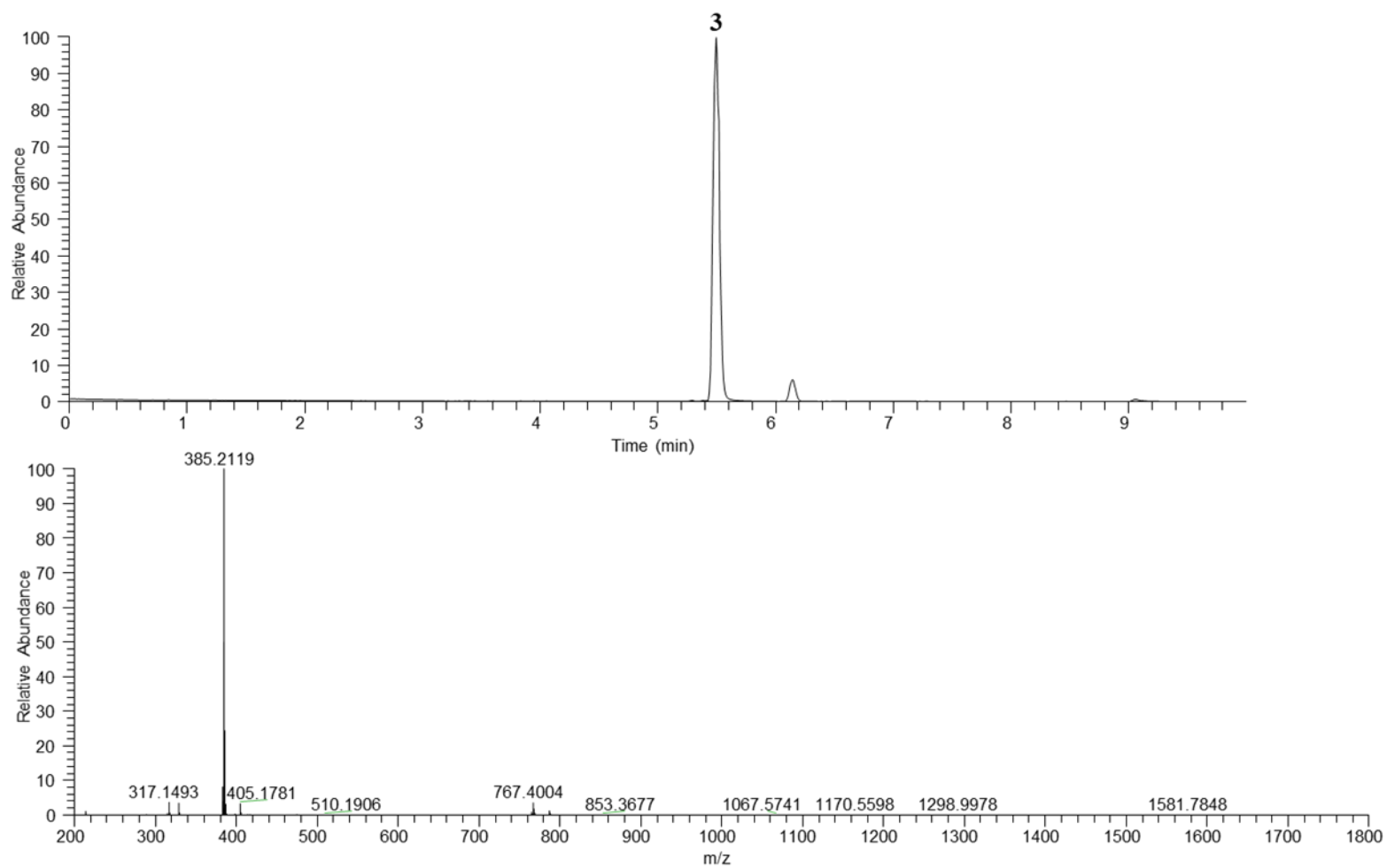


**Figure 7.23.** UPLC-(+)-HRESIMS spectrum of **3**.

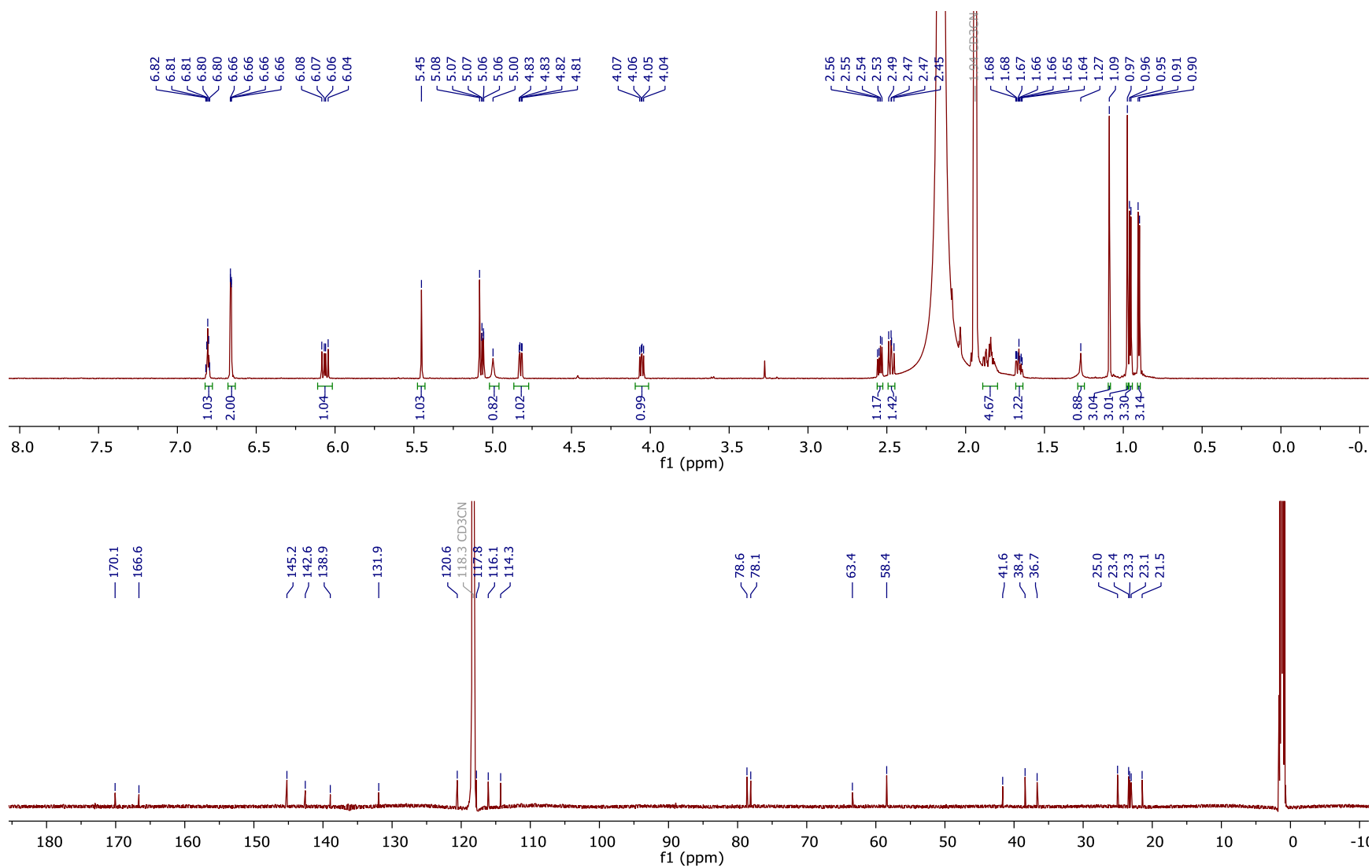
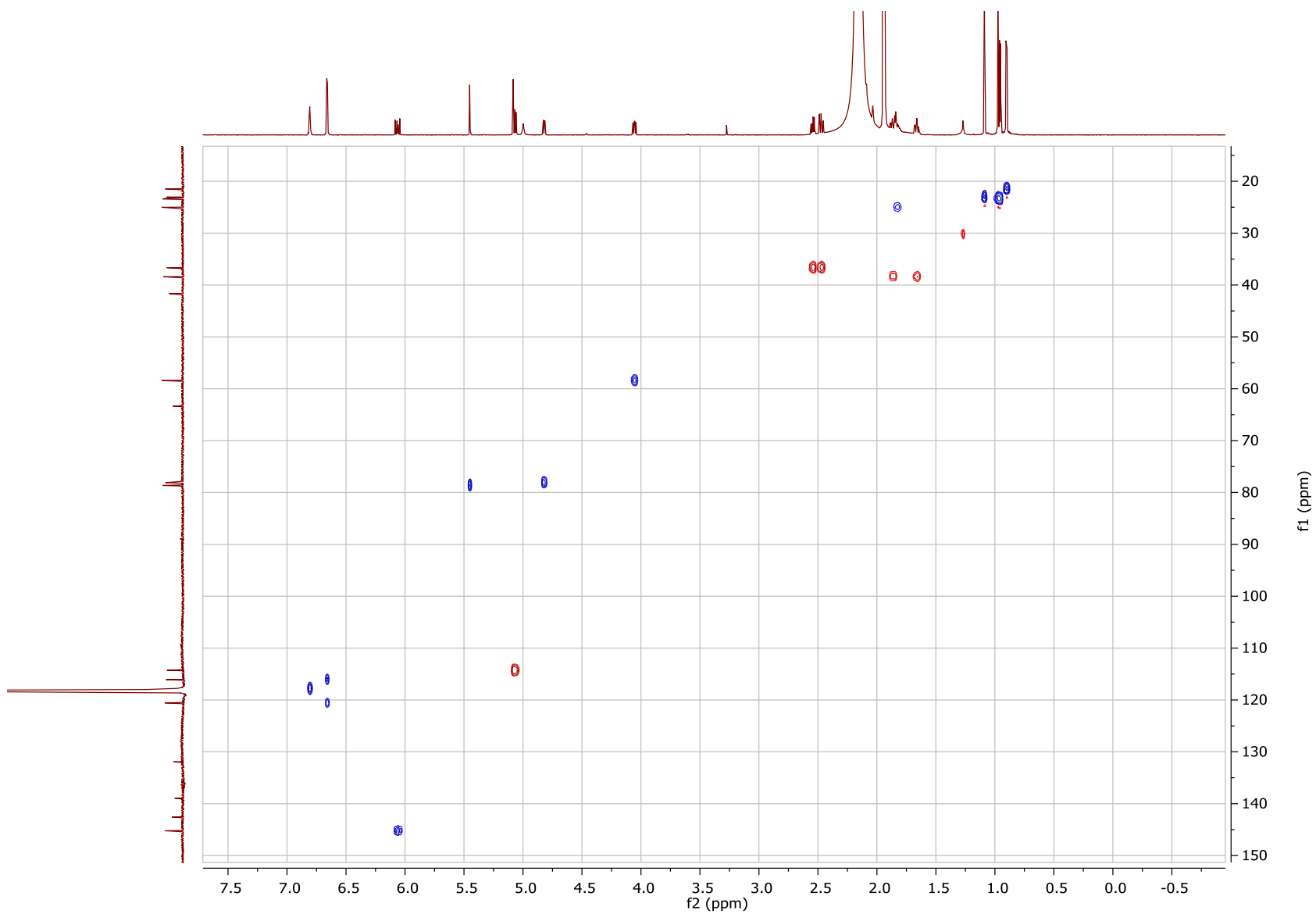
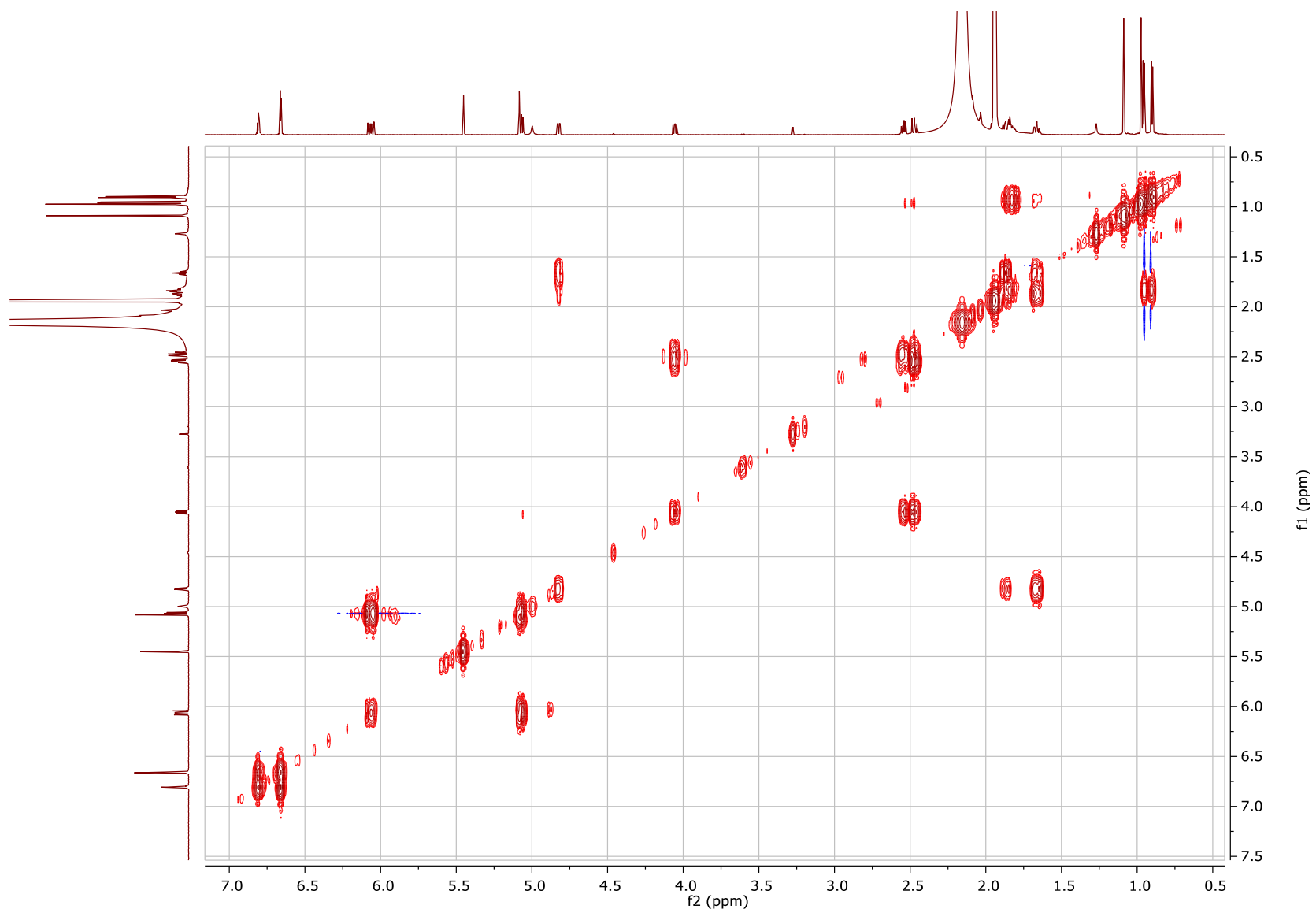


Figure 7.24.  $^1\text{H}$  and  $^{13}\text{C}$  NMR spectra of **3** [700 MHz for  $^1\text{H}$  and 175 MHz for  $^{13}\text{C}$ ,  $\text{CD}_3\text{CN}$ ]



**Figure 7.25.** Edited-HSQC NMR spectrum of **3** [700 MHz,  $\text{CD}_3\text{CN}$ ].

300



**Figure 7.26.** COSY NMR spectrum of **3** [700 MHz, CD<sub>3</sub>CN].

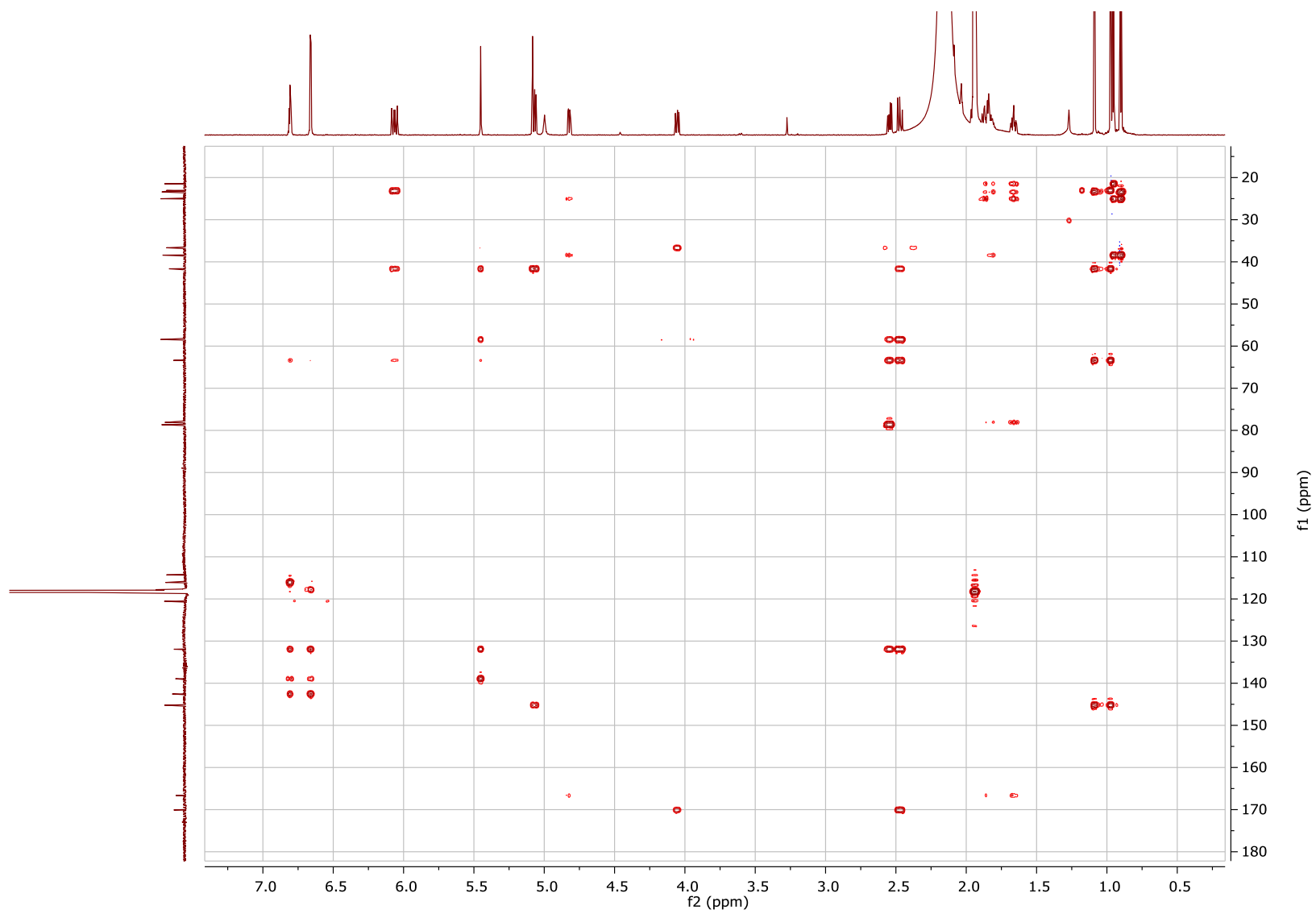


**Figure 7.27.** HMBC NMR spectrum of **3** [700 MHz, CD<sub>3</sub>CN].

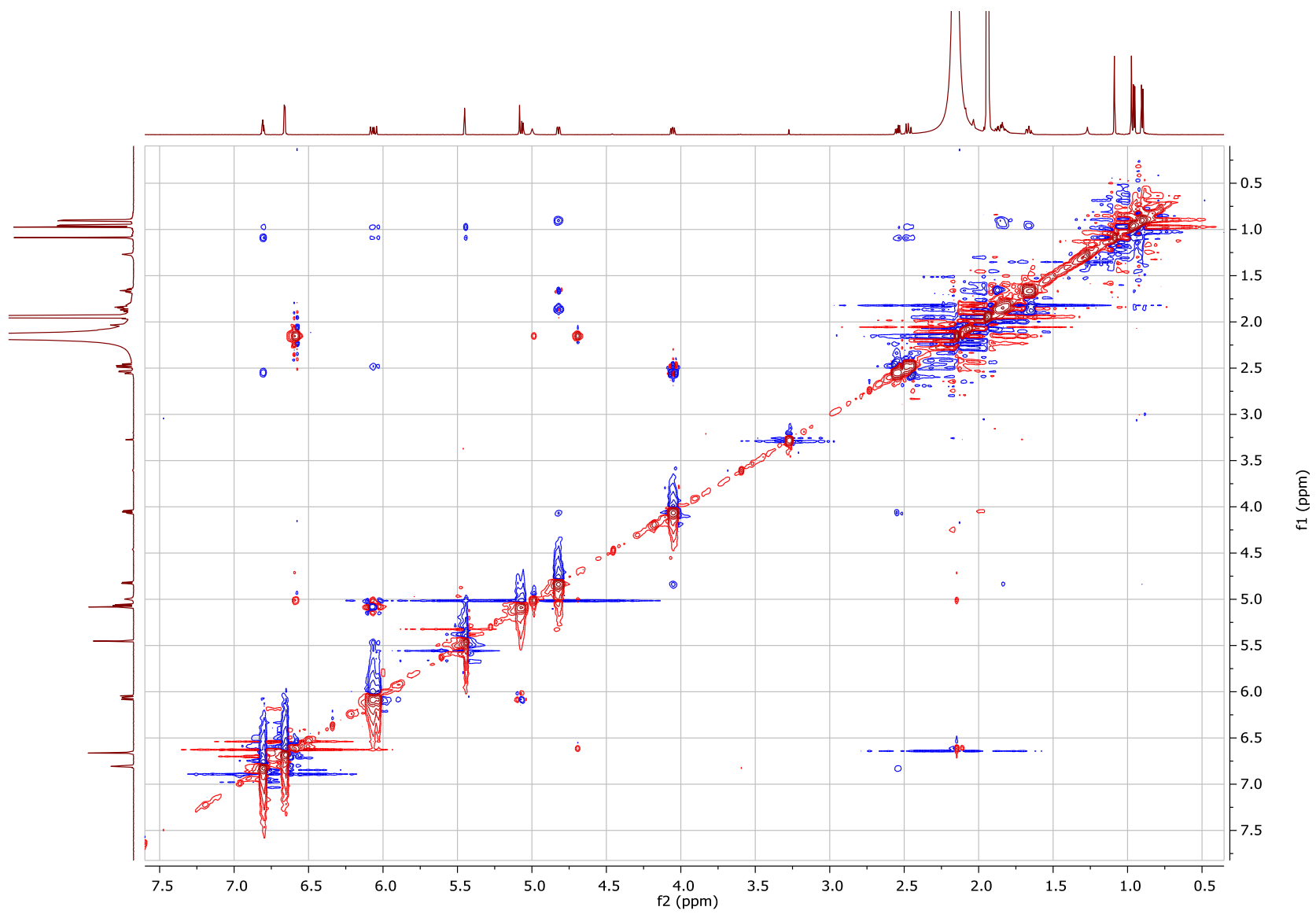


**Figure 7.28.** NOESY NMR spectrum of **3** [500 MHz, CD<sub>3</sub>CN].

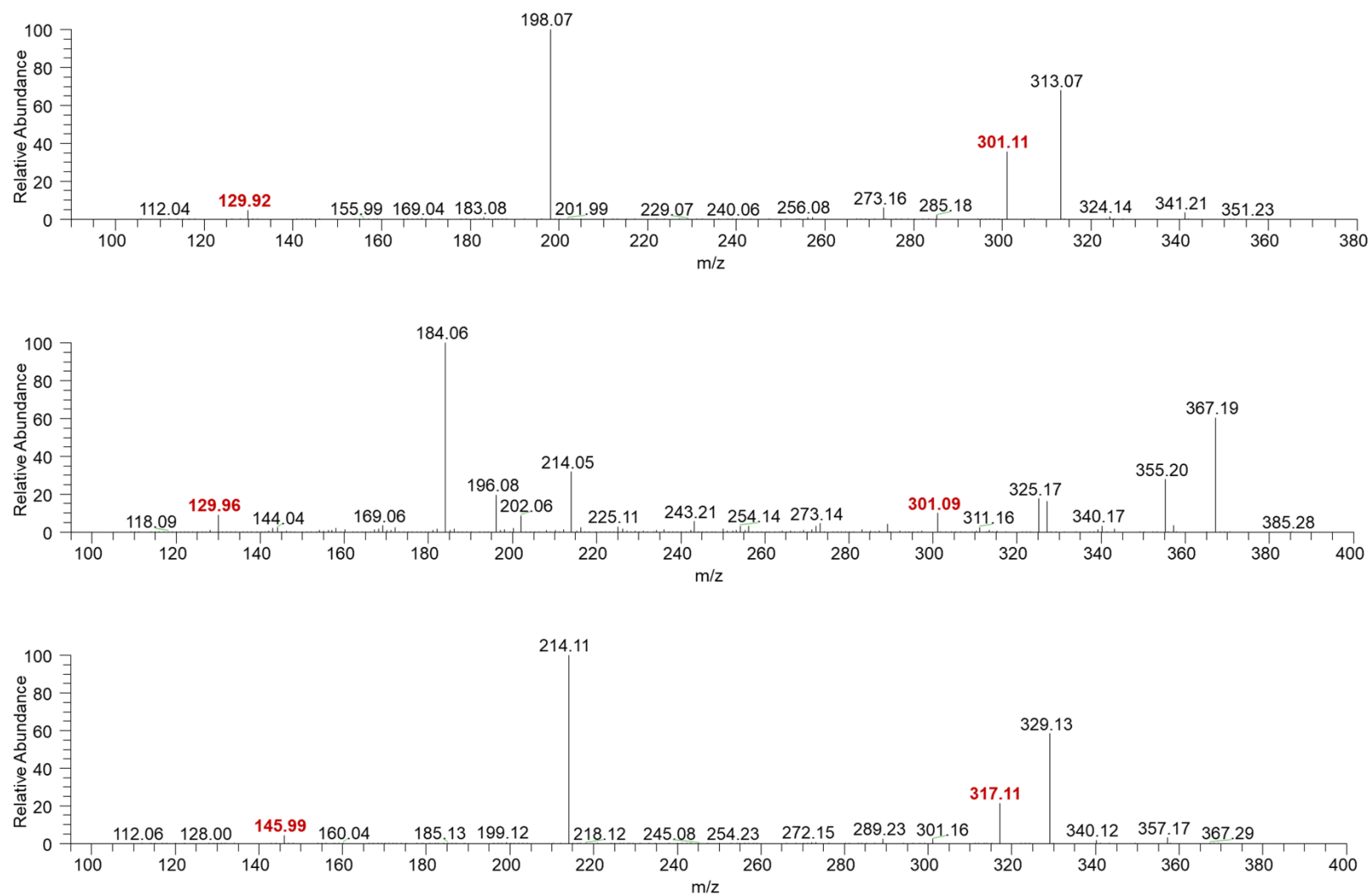


**Figure 7.29.** MS2 fragmentation patterns of compounds 1-3.

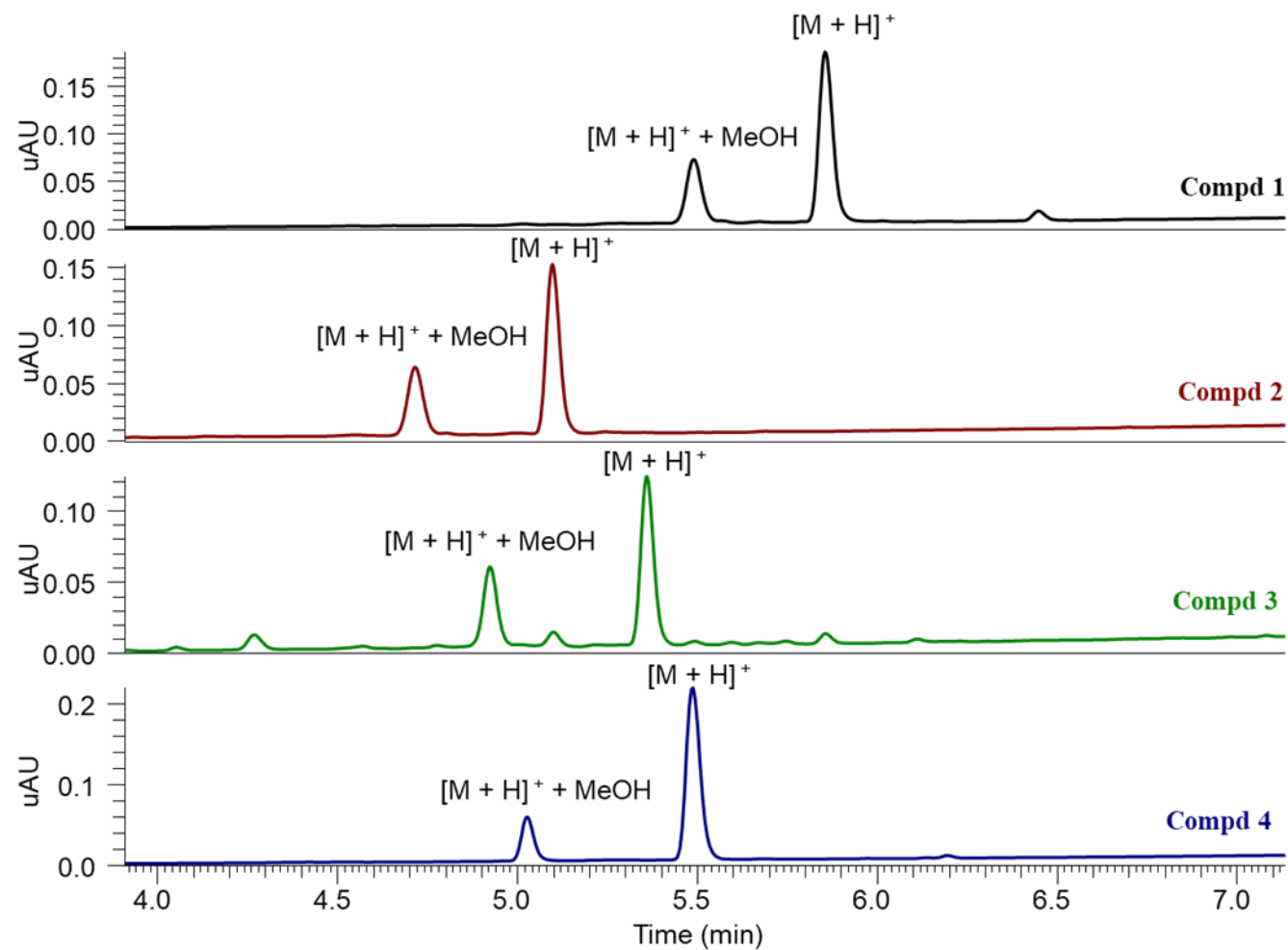


**Figure 7.30.** UPLC-PDA chromatograms of compounds **1-4** after exposure to methanol for 48 hours at a concentration of 0.2 mg/mL.

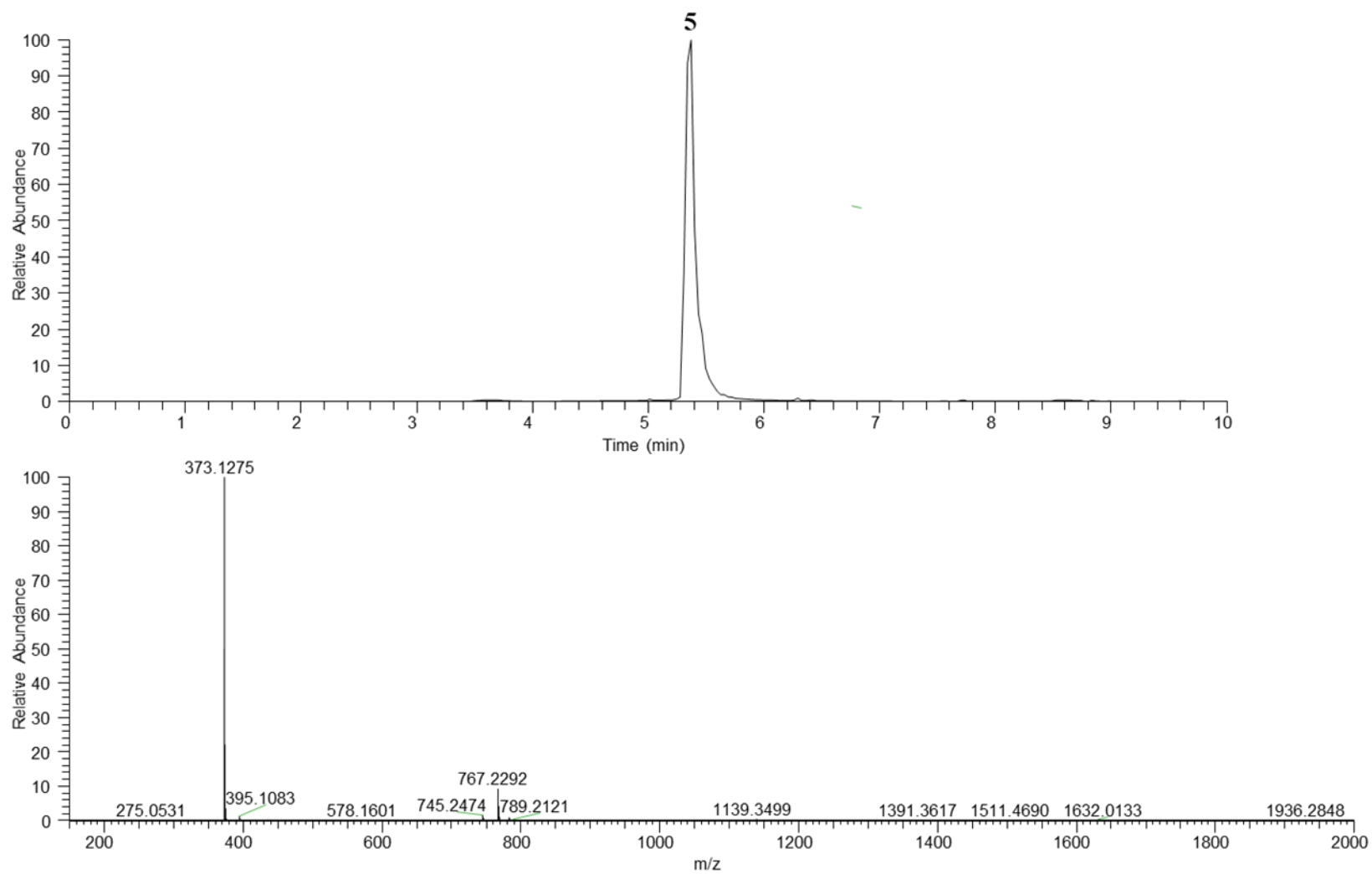


**Figure 7.31.** UPLC-(+)-HRESIMS spectrum of **5**.

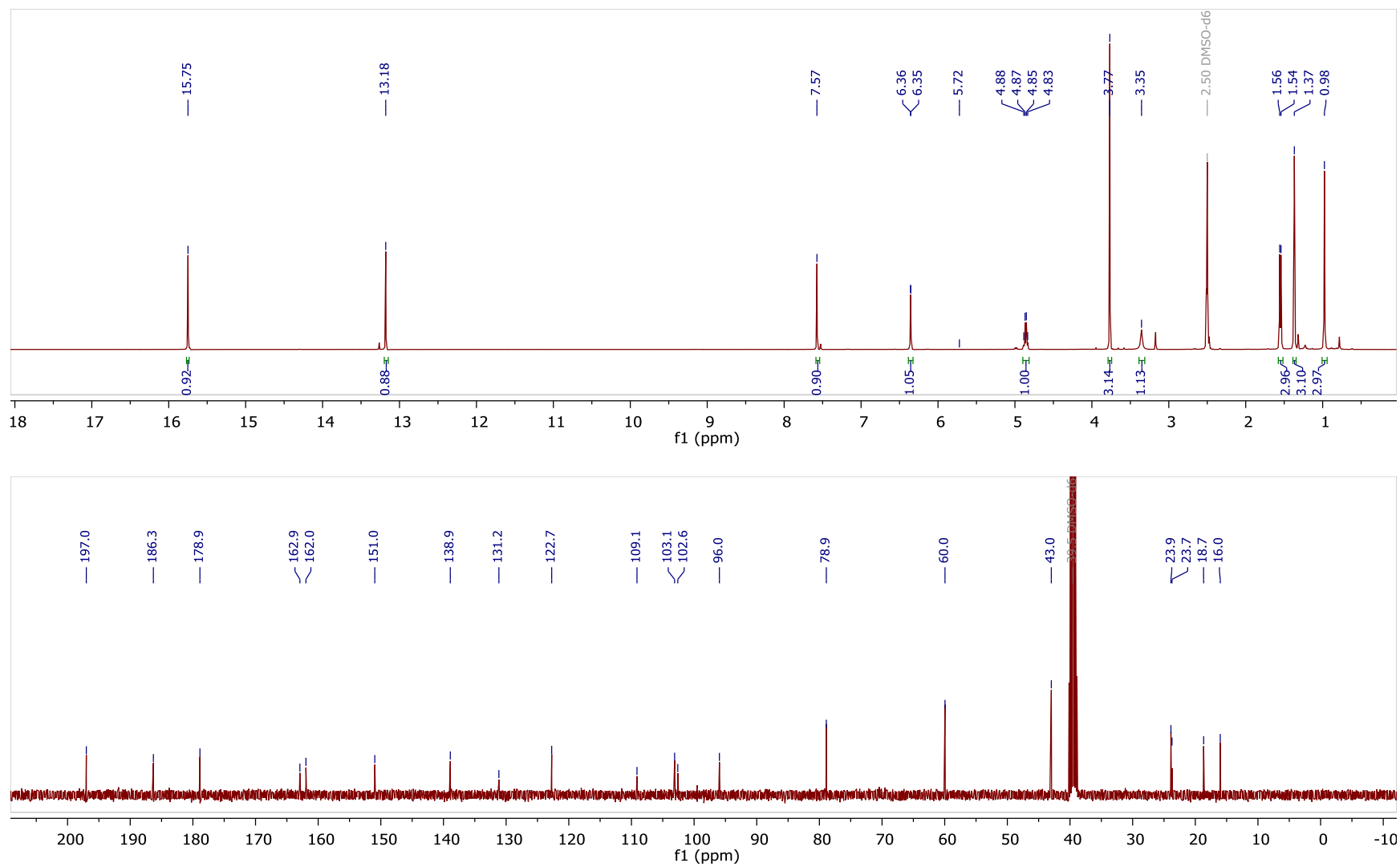
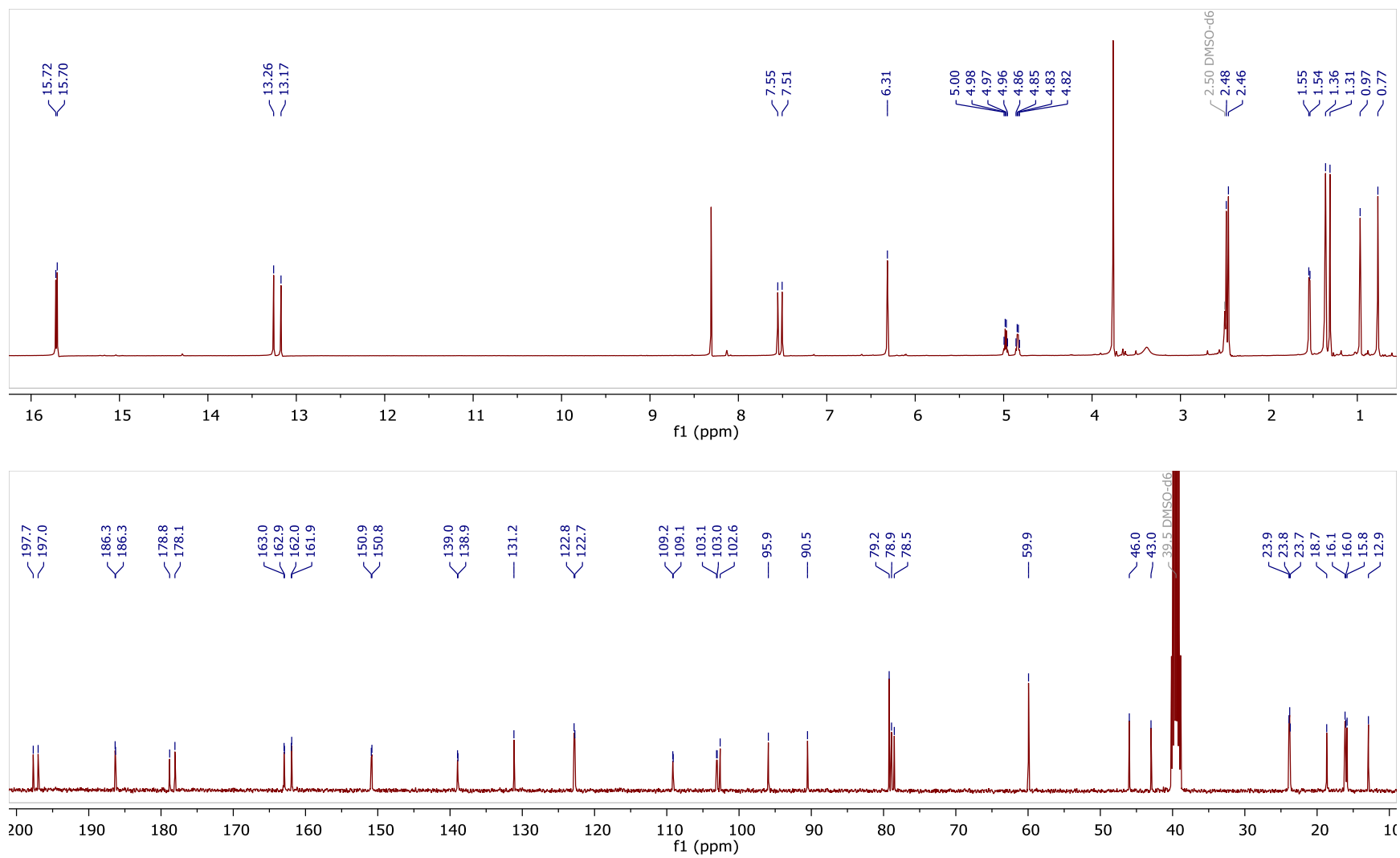
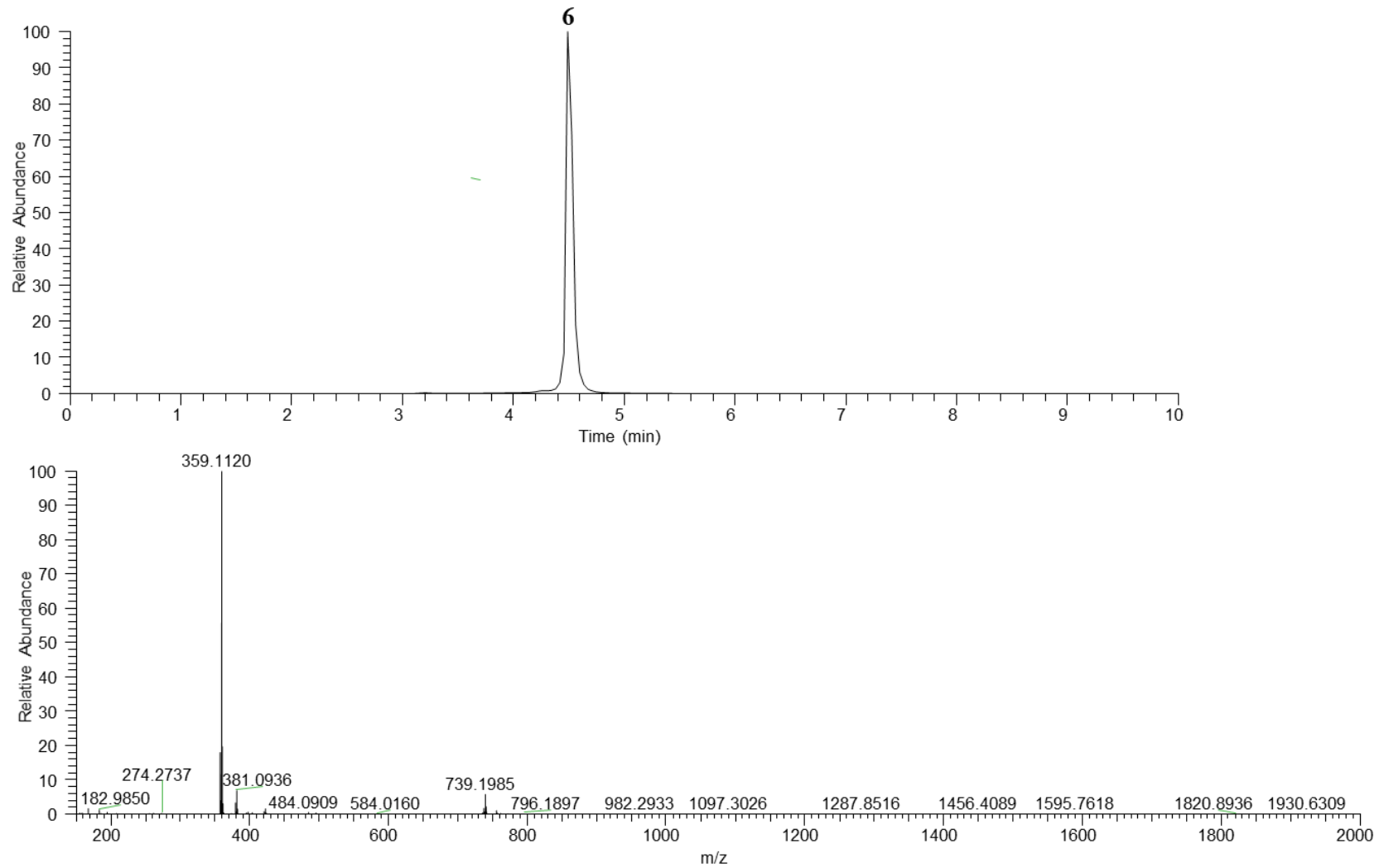


Figure 7.32. <sup>1</sup>H and <sup>13</sup>C NMR spectra of 5 [400 MHz for <sup>1</sup>H and 100 MHz for <sup>13</sup>C, DMSO-d<sub>6</sub>].



**Figure 7.33.** <sup>1</sup>H and <sup>13</sup>C NMR spectra of **5:5a** mixture [400 MHz for <sup>1</sup>H and 100 MHz for <sup>13</sup>C, DMSO-d<sub>6</sub>].



**Figure 7.34.** UPLC-(+)-HRESIMS spectrum of **6**.

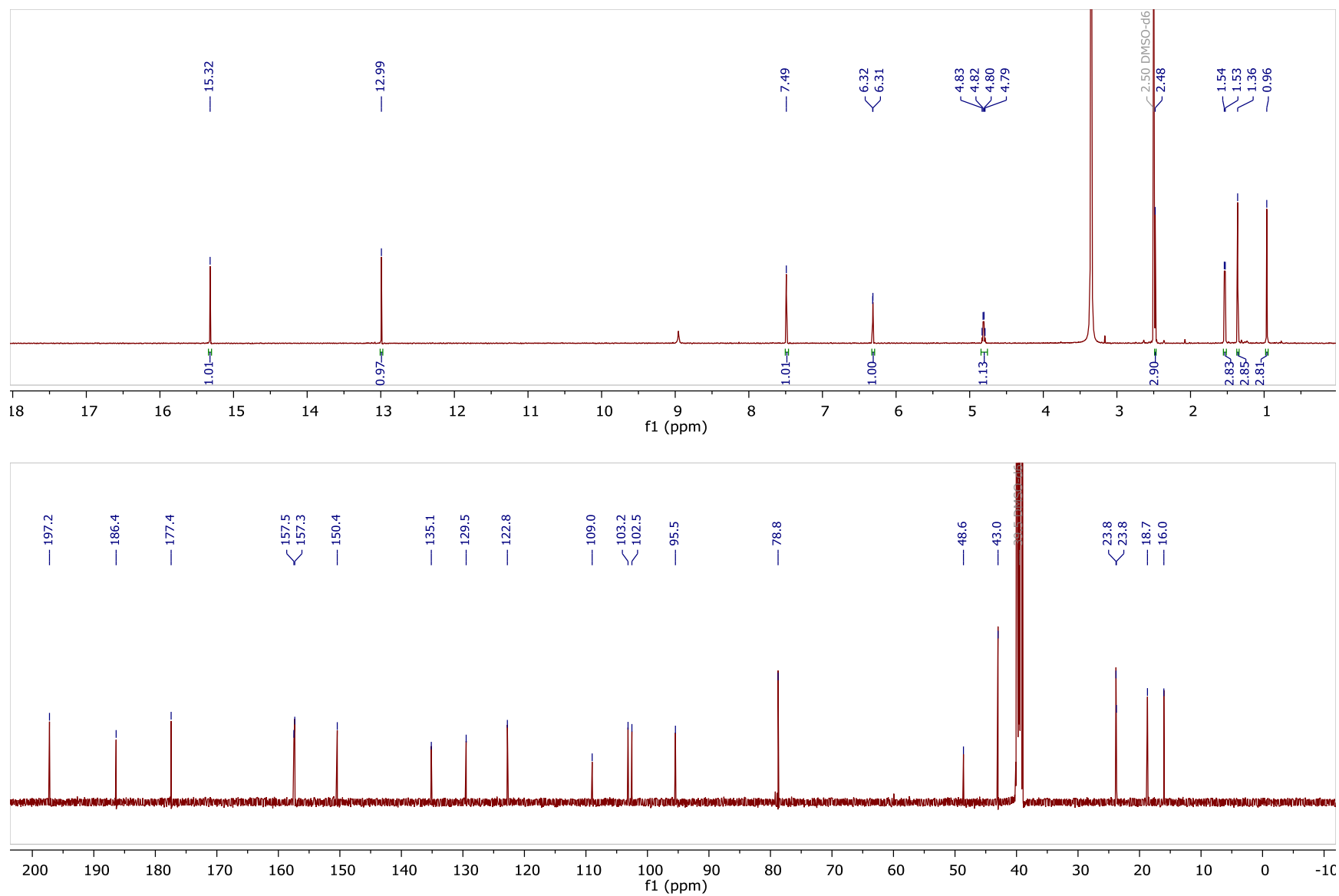


**Figure 7.35.** <sup>1</sup>H and <sup>13</sup>C NMR spectra of **6** [500 MHz for <sup>1</sup>H and 125 MHz for <sup>13</sup>C, DMSO-d<sub>6</sub>]

**Table 7.4.** Cytotoxic activities of compounds **1** & **2** (IC<sub>50</sub> in  $\mu\text{M}$ ) against three cancer cell lines.

<b>Compound</b>	<b>MDA-MB-231</b>	<b>OVCAR3</b>	<b>MDA-MB-435</b>
<b>1</b>	>25	>25	>25
<b>2</b>	>25	>25	>25
Taxol*	0.6	1.8	0.3

\*IC<sub>50</sub> values are reported in nM.

**Table 7.5.** Minimal Inhibitory Concentrations (MICs) in  $\mu\text{g/mL}$  for compounds **1-3** against a series of pathogenic microorganisms.

<b>Compd #</b>	<b><i>E. coli</i></b>	<b><i>S. aureus</i></b>	<b><i>MRSA</i></b>	<b><i>P. aeruginosa</i></b>	<b><i>M. smegmatis</i></b>	<b><i>B. subtilis</i></b>	<b><i>B. anthracis</i></b>	<b><i>S. cerevisiae</i></b>	<b><i>C. albicans</i></b>	<b><i>A. niger</i></b>
<b>1</b>	> 138	> 125	> 125	> 125	> 125	> 125	> 125	> 125	> 125	> 125
<b>2</b>	115	125	> 125	63	> 125	> 125	> 125	> 125	> 125	> 125
<b>3</b>	113	125	> 125	125	> 125	> 125	> 125	> 125	> 125	> 125

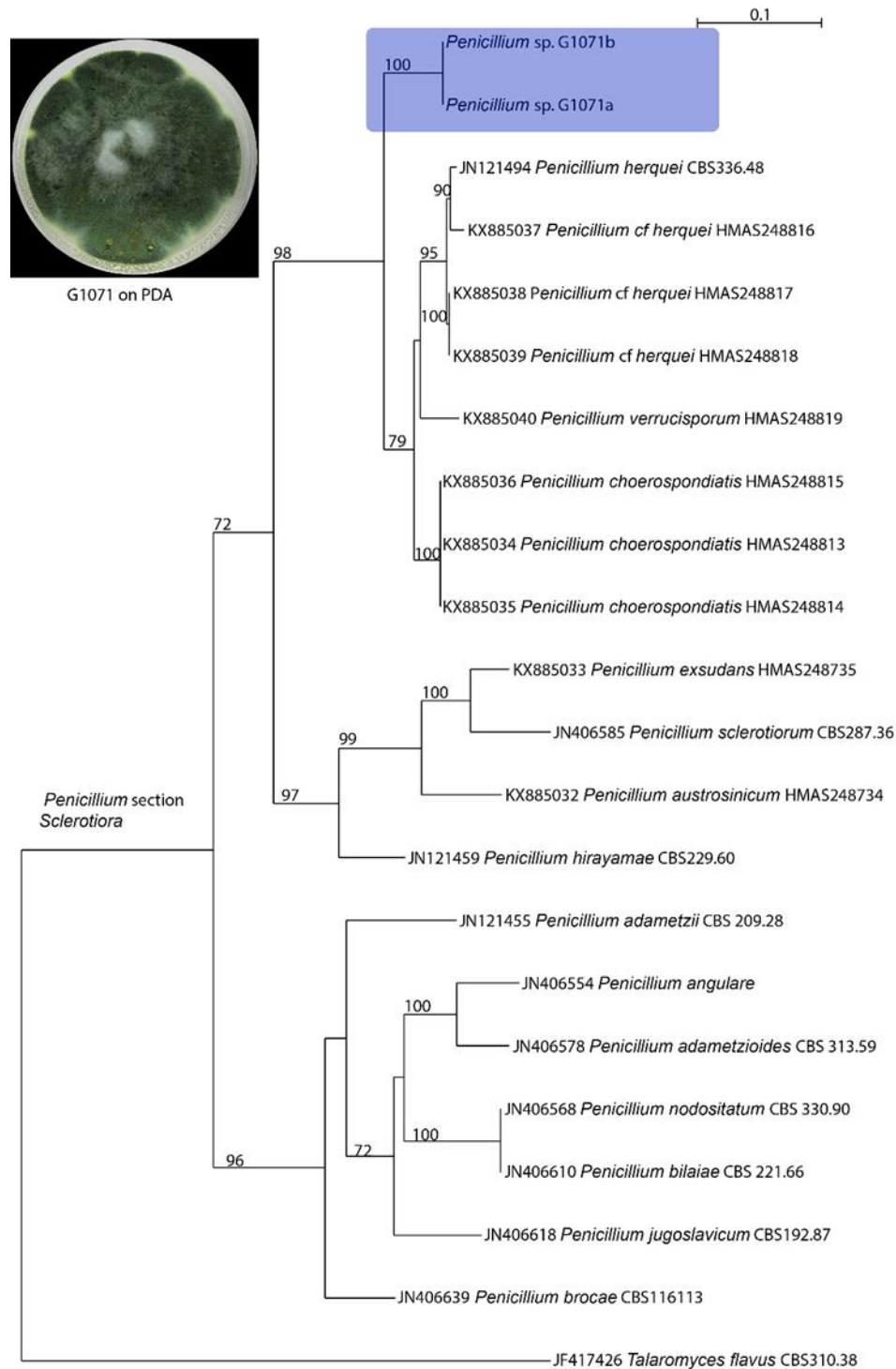


**Figure 7.36.** Phylogram of the most likely tree ( $-\ln L = 5734.34$ ) from a RAxML analysis of 22 taxa based on *RPB2* sequences (974 bp) from several *Penicillium* strains belonging to the section *Sclerotiora*. Numbers refer to RAxML bootstrap support values  $\geq 70\%$  based on 1000 replicates. Strain G1071 is identified as *Penicillium* sp. section *Sclerotiora* (highlighted in purple). A three-week culture of strain G1071 is shown to the left. Bar indicates nucleotide substitutions per site.

## REFERENCES

- (1) Cancer Statistics; National Cancer Institute: 2020.
- (2) Cancer; World Health Organization: 2021.
- (3) Sung, H.; Ferlay, J.; Siegel, R. L.; Laversanne, M.; Soerjomataram, I.; Jemal, A.; Bray, F. *CA. Cancer J. Clin.* **2021**, DOI: 10.3322/caac.21660.
- (4) Siegel, R. L.; Miller, K. D.; Fuchs, H. E.; Jemal, A. *CA. Cancer J. Clin.* **2021**, *71*, 7-33.
- (5) Yabroff, K. R.; Lund, J.; Kepka, D.; Mariotto, A. *Cancer Epidemiol. Biomarkers Prev.* **2011**, *20*, 2006-2014.
- (6) Luengo-Fernandez, R.; Leal, J.; Gray, A.; Sullivan, R. *Lancet Oncol.* **2013**, *14*, 1165-1174.
- (7) Stewart, B. W.; Wild, C. *World Health Organization* **2014**.
- (8) Angela, B. M.; Yabroff, K. R.; Yongwu, S.; Eric, J. F.; Martin, L. B. *J. Natl. Cancer Inst.* **2011**, *103*, 117-128.
- (9) Types of Cancer Treatment. <https://www.cancer.gov/about-cancer/treatment/types> (April 25, 2020),
- (10) Apuri, S. *South Med. J.* **2017**, *110*, 638-642.
- (11) Dagogo-Jack, I.; Shaw, A. T. *Nat. Rev. Clin. Oncol.* **2018**, *15*, 81-94.
- (12) Pucci, C.; Martinelli, C.; Ciofani, G.; Ciofani, G. *Ecancermedicalscience.* **2019**, *13*, 961.
- (13) Alfarouk, K. O.; Bashir, A. H. H.; Ibrahim, M. E.; Stock, C. M.; Taylor, S.; Walsh, M.; Rauch, C.; Muddathir, A. K.; Verduzco, D.; Mohammed, O. Y.; Elhassan, G. O.; Elhassan, G. O.; Harguindey, S.; Reshkin, S. J. *Cancer Cell Int.* **2015**, *15*, 71.
- (14) Kinghorn, A. D.; Chin, Y.-W.; Swanson, S. M. *Curr. Opin. Drug Discov. Devel.* **2009**, *12*, 189-196.
- (15) Newman, D. J.; Cragg, G. M. *J. Nat. Prod.* **2020**, *83*, 770-803.
- (16) Greenwell, M.; Rahman, P. K. S. M. *Int. J. Pharm. Sci. Res.* **2015**, *6*, 4103-4112.
- (17) Moudi, M.; Go, R.; Yien, C. Y. S.; Nazre, M. *Int J Prev Med* **2013**, *4*, 1231-1235.
- (18) Ojima, I.; Lichtenthal, B.; Lee, S.; Wang, C.; Wang, X. *Expert. Opin. Ther. Pat.* **2016**, *26*, 1-20.
- (19) Lorence, A.; Nessler, C. L. *Phytochemistry* **2004**, *65*, 2735-2749.

- (20) Ardalani, H.; Avan, A.; Ghayour-Mobarhan, M. *Avicenna J. Phytomed.* **2017**, *7*, 285-294.
- (21) Arnold, L. D.; Sergio, S. *J. Antibiot.* **2009**, *62*, 5-16.
- (22) Minotti, G.; Menna, P.; Salvatorelli, E.; Cairo, G.; Gianni, L. *Pharmacol. Rev.* **2004**, *56*, 185-229.
- (23) Kornienko, A.; Evidente, A.; Vurro, M.; Mathieu, V.; Cimmino, A.; Evidente, M.; van Otterlo, W. A. L.; Dasari, R.; Lefranc, F.; Kiss, R. *Med. Res. Rev.* **2015**, *35*, 937-967.
- (24) Manzoni, M.; Rollini, M. *Appl. Microbiol. Biotechnol.* **2002**, *58*, 555-64.
- (25) Aharonowitz, Y.; Cohen, G.; Martín, J. F.; Annual Reviews, I. *Ann. Rev. Microb.* **1992**, *46*, 461-95.
- (26) Strader, C. R.; Pearce, C. J.; Oberlies, N. H. *J. Nat. Prod.* **2011**, *74*, 900-7.
- (27) De Carli, L.; Larizza, L. *Mutat. Res.* **1988**, *195*, 91-126.
- (28) Chen, L.; Yue, Q.; Zhang, X.; Xiang, M.; Wang, C.; Li, S.; Che, Y.; Ortiz-López, F. J.; Bills, G. F.; Liu, X.; An, Z. *BMC Genomics* **2013**, *14*, 339.
- (29) Anjum, T.; Azam, A.; Irum, W. *Indian J. Pharm. Sci.* **2012**, *74*, 372-374.
- (30) Patel, G.; Patil, M. D.; Soni, S.; Khobragade, T. P.; Chisti, Y.; Banerjee, U. C. *Biotechnol. Rep. (Amst)* **2016**, *11*, 77-85.
- (31) Panaccione, D. G. *FEMS Microbiol. Lett.* **2005**, *251*, 9-17.
- (32) Gonzalez-Medina, M.; Figueroa, M.; Medina-Franco, J. L.; Owen, J. R.; El-Elimat, T.; Pearce, C. J.; Oberlies, N. H. *Front. Pharmacol.* **2017**, *8*, 180.
- (33) Mousa, W. K.; Raizada, M. N. *Front. Microbiol.* **2013**, *4*, 65.
- (34) Keller, N. P. *Nat Rev Microbiol* **2019**, *17*, 167-180.
- (35) Evidente, A.; Kornienko, A.; Cimmino, A.; Andolfi, A.; Lefranc, F.; Mathieu, V.; Kiss, R. *Nat. Prod. Rep.* **2014**, *31*, 617-627.
- (36) Gomes, N.; Lefranc, F.; Kijjoo, A.; Kiss, R. *Mar. Drugs* **2015**, *13*, 3950-3991.
- (37) Greve, H.; Mohamed, I. E.; Pontius, A.; Kehraus, S.; Gross, H.; König, G. M. *Phytochem. Rev.* **2010**, *9*, 537-545.
- (38) Stierle, A. A.; Stierle, D. B. *Nat. Prod. Commun.* **2015**, *10*, 1671-1682.
- (39) Wani, M. C.; Taylor, H. L.; Wall, M. E.; Coggon, P.; McPhail, A. T. *J. Am. Chem. Soc.* **1971**, *93*, 2325-2327.

- (40) Horwitz, S. B. *Ann. Oncol.* **1994**, *5*, 3-6.
- (41) Strobel, G.; Stierle, A.; Stierle, D.; Hess, W. W. *Mycotaxon.* **1993**, *47*, 71.
- (42) Eyberger, A. L.; Dondapati, R.; Porter, J. R. *J. Nat. Prod.* **2006**, *69*, 1121-4.
- (43) Kour, A.; Shawl, A. S.; Rehman, S.; Sultan, P.; Qazi, P. H.; Suden, P.; Khajuria, R. K.; Verma, V. *World J. Microbiol. Biotechnol.* **2008**, *24*, 1115-1121.
- (44) Kusari, S.; Lamshöft, M.; Spitteller, M. *J. Appl. Microbiol.* **2009**, *107*, 1019-1030.
- (45) Uzma, F.; Mohan, C. D.; Hashem, A.; Konappa, N. M.; Rangappa, S.; Kamath, P. V.; Singh, B. P.; Mudili, V.; Gupta, V. K.; Siddaiah, C. N.; Chowdappa, S.; Alqarawi, A. A.; Abd\_Allah, E. F. *Front. Pharmacol.* **2018**, *9*, 309.
- (46) Seenivasan, A.; Subhagar, S.; Aravindan, R.; Viruthagiri, T. *Indian J. Pharm. Sci.* **2008**, *70*, 701-709.
- (47) Kumar, P.; Singh, B.; Thakur, V.; Thakur, A.; Thakur, N.; Pandey, D.; Chand, D. *Biotechnol. Rep. (Amst)* **2019**, *24*, e00395.
- (48) Martin, V. *Semin. Oncol. Nurs.* **1993**, *9*, 2-5.
- (49) Silva, C. G.; Rocha, M. P.; de Almeida, V. L.; Campana, P. R. V. *Ref. Ser. Phytochem.* **2017**, 67-102.
- (50) Kinghorn, A. D.; Carache de Blanco, E. J.; Lucas, D. M.; Rakotondraibe, H. L.; Orjala, J.; Soejarto, D. D.; Oberlies, N. H.; Pearce, C. J.; Wani, M. C.; Stockwell, B. R.; Burdette, J. E.; Swanson, S. M.; Fuchs, J. R.; Phelps, M. A.; Xu, L.; Zhang, X.; Shen, Y. Y. *Anticancer Res.* **2016**, *36*, 5623-5637.
- (51) Bérdy, J. *J. Antibiot.* **2005**, *58*, 1-26.
- (52) Hawksworth, D. L.; Lücking, R. *Microbiol. Spectr.* **2017**, *5*, FUNK-0052-2016.
- (53) Singh, S.; Sharma, B.; Kanwar, S. S.; Kumar, A. *Front. Plant. Sci.* **2016**, *7*, 1667-1667.
- (54) Xiao, Z.; Morris-Natschke, S. L.; Lee, K.-H. *Med. Res. Rev.* **2016**, *36*, 32-91.
- (55) Wolinsky, J. B.; Colson, Y. L.; Grinstaff, M. W. *J. Control. Release* **2012**, *159*, 14-26.
- (56) Al Subeh, Z. Y.; Chu, N. Q.; Korunes-Miller, J. T.; Tsai, L. L.; Graf, T. N.; Hung, Y. P.; Pearce, C. J.; Grinstaff, M. W.; Colby, A. H.; Colson, Y. L.; Oberlies, N. H. *J. Control. Release* **2021**, *331*, 260-269.
- (57) Nielsen, J. C.; Nielsen, J. *Synth. Syst. Biotechnol.* **2017**, *2*, 5-12.
- (58) Al Subeh, Z. Y.; Raja, H. A.; Monro, S.; Flores-Bocanegra, L.; El-Elimat, T.; Pearce, C. J.; McFarland, S. A.; Oberlies, N. H. *J. Nat. Prod.* **2020**, *83*, 2490-2500.

- (59) Al Subeh, Z. Y.; Raja, H. A.; Maldonado, A.; Burdette, J. E.; Pearce, C. J.; Oberlies, N. H. *J. Antibiot.* **2021**, *74*, 300-306.
- (60) El-Elimat, T.; Raja, H. A.; Figueroa, M.; Al Sharie, A. H.; Bunch, R. L.; Oberlies, N. H. *J. Nat. Prod.* **2021**, *84*, 898-916.
- (61) Expected new cancer cases and deaths in 2020; Centers for Disease Control and Prevention: 2020.
- (62) Siegel, R. L.; Miller, K. D.; Jemal, A. *CA. Cancer J. Clin.* **2020**, *70*, 7-30.
- (63) Bray, F.; Ferlay, J.; Soerjomataram, I.; Siegel, R. L.; Torre, L. A.; Jemal, A. *CA. Cancer J. Clin.* **2018**, *68*, 394-424.
- (64) SEER cancer statistics review (CSR) 1975-2016.; National Cancer Institute: 2019.
- (65) Zappa, C.; Mousa, S. A. *Transl. Lung Cancer Res.* **2016**, *5*, 288-300.
- (66) Goldstraw, P.; Chansky, K.; Crowley, J.; Mitchell, A.; Bolejack, V.; Giroux, D.; Kingsbury, L.; Shemanski, L.; Stratton, K.; Rami-Porta, R.; Asamura, H.; Eberhardt, W. E. E.; Nicholson, A. G.; Groome, P.; Goldstraw, P.; Rami-Porta, R.; Serra Mitjans, M.; Asamura, H.; Ball, D.; Beer, D. G.; Beyruti, R.; Detterbeck, F.; Edwards, J.; Galateau-Salle, F.; Gleeson, F.; Huang, J.; Rusch, V.; Travis, W.; Krug, L.; Kennedy, C.; McCaughan, B.; Kim, J.; Park, J. S.; Kim, Y. T.; Kondo, H.; Krasnik, M.; Kubota, K.; Lerut, A.; Vansteenkiste, J.; Nackaerts, K.; Lyons, G.; Marino, M.; Marom, E. M.; Erasmus, J.; Rice, D.; Swisher, S.; Van Meerbeeck, J.; Van Schil, P.; Nakano, T.; Hasegawa, S.; Nicholson, A. G.; Nowak, A.; Peake, M.; Rice, T.; Blackstone, E.; Rosenzweig, K.; Ruffini, E.; Saijo, N.; Sculier, J. P.; Suzuki, K.; Tachimori, Y.; Thomas, C. F.; Tsao, M. S.; Turrisi, A.; Watanabe, H.; Wu, Y. L.; Wu, Y. L.; Baas, P.; Inai, K.; Kernstine, K.; Kindler, H.; Pass, H.; Falkson, C.; Filosso, P. L.; Giaccone, G.; Kondo, K.; Lucchi, M.; Okumura, M.; Abad Cavaco, F.; Ansotegui Barrera, E.; Abal Arca, J.; Parente Lamelas, I.; Arnau Obrer, A.; Guijarro Jorge, R.; Bascom, G. K.; Blanco Orozco, A. I.; Gonzalez Castro, M.; Blum, M. G.; Chimondeguy, D.; Cvijanovic, V.; Defranchi, S.; De Olaiz Navarro, B.; Escobar Campuzano, I.; Macia Vidueira, I.; Fernandez Araujo, E.; Andreo Garcia, F.; Fong, K. M.; Francisco Corral, G.; Cerezo Gonzalez, S.; Freixinet Gilart, J.; Garcia Aranguena, L.; Garcia Barajas, S.; Girard, P.; Goksel, T.; Gonzalez Budino, M. T.; Gonzalez Casaurran, G.; Gullon Blanco, J. A.; Hernandez Hernandez, J.; Iglesias Heras, M.; Hernandez Rodriguez, H.; Herrero Collantes, J.; Izquierdo Elena, J. M.; Jakobsen, E.; Kostas, S.; Leon Atance, P.; Nunez Ares, A.; Liao, M.; Losanovscky, M.; Lyons, G.; Magaroles, R.; De Esteban Julvez, L.; Marinan Gorospe, M.; Melchor Iniguez, R.; Miravet Sorribes, L.; Naranjo Gozalo, S.; Alvarez De Arriba, C.; Nunez Delgado, M.; Padilla Alarcon, J.; Penalver Cuesta, J. C.; Pass, H.; Pavon Fernandez, M. J.; Rosenberg, M.; Sanchez De Cos Escuin, J. S.; Saura Vinuesa, A.; Strand, T. E.; Subotic, D.; Terra, R.; Thomas, C.; Tournoy, K.; Velasquez, M.; Yokoi, K. *J. Thorac. Oncol.* **2016**, *11*, 39-51.
- (67) Sawabata, N.; Ohta, M.; Matsumura, A.; Nakagawa, K.; Hirano, H.; Maeda, H.; Matsuda, H. *Ann. Thorac. Surg.* **2004**, *77*, 415-420.
- (68) Predina, J. D.; Keating, J.; Patel, N.; Nims, S.; Singhal, S. *J. Surg. Oncol.* **2016**, *113*, 264-9.

- (69) Sawabata, N.; Maeda, H.; Matsumura, A.; Ohta, M.; Okumura, M. *Surg. Today*. **2012**, *42*, 238-244.
- (70) Sasaki, H.; Suzuki, A.; Tatematsu, T.; Shitara, M.; Hikosaka, Y. U.; Okuda, K.; Moriyama, S.; Yano, M.; Fujii, Y. *Oncol. Lett.* **2014**, *7*, 1300.
- (71) Arriagada, R.; Bergman, B.; Dunant, A.; Le Chevalier, T.; Pignon, J. P.; Vansteenkiste, J.; International Adjuvant Lung Cancer Trial Collaborative, G. *N. Engl. J. Med.* **2004**, *350*, 351-60.
- (72) Winton, T.; Livingston, R.; Johnson, D.; Rigas, J.; Johnston, M.; Butts, C.; Cormier, Y.; Goss, G.; Inculet, R.; Vallieres, E.; Fry, W.; Bethune, D.; Ayoub, J.; Ding, K.; Seymour, L.; Graham, B.; Tsao, M.-S.; Gandara, D.; Kesler, K.; Demmy, T.; Shepherd, F. *N. Engl. J. Med.* **2005**, *352*, 2589-97.
- (73) *Br. Med. J.* **1995**, *311*, 899-909.
- (74) Scagliotti, G. V. *Clin. Cancer Res.* **2005**, *11*, 5011s-5016s.
- (75) Marcucci, F.; Berenson, R.; Corti, A. *Front. Oncol.* **2013**, *3*, 161.
- (76) Su, J.; Chen, F.; Cryns, V. L.; Messersmith, P. B. *Journal of the American Chemical Society*. **2011**, *133*, 11850-3.
- (77) Colby, A. H.; Oberlies, N. H.; Pearce, C. J.; Herrera, V. L.; Colson, Y. L.; Grinstaff, M. W. *Wiley Interdiscip. Rev. Nanomed. Nanobiotechnol.* **2017**, *9*, doi:10.1002/wnan.1451.
- (78) Griset, A. P.; Walpole, J.; Liu, R.; Gaffey, A.; Colson, Y. L.; Grinstaff, M. W. *Journal of the American Chemical Society*. **2009**, *131*, 2469-71.
- (79) Perry, J.; Chambers, A.; Spithoff, K.; Laperriere, N. *Curr. Oncol.* **2007**, *14*, 189-94.
- (80) Mo, R.; Jiang, T.; Gu, Z. *Nanomedicine (Lond)*. **2014**, *9*, 1117-1120.
- (81) Dong, Y.; Eltoukhy, A. A.; Alabi, C. A.; Khan, O. F.; Veiseh, O.; Dorkin, J. R.; Sirirungruang, S.; Yin, H.; Tang, B. C.; Pelet, J. M.; Chen, D.; Gu, Z.; Xue, Y.; Langer, R.; Anderson, D. G. *Adv. Healthc. Mater.* **2014**, *3*, 1392-7.
- (82) Gu, F. X.; Karnik, R.; Wang, A. Z.; Alexis, F.; Levy-Nissenbaum, E.; Hong, S.; Langer, R. S.; Farokhzad, O. C. *Nano Today*. **2007**, *2*, 14-21.
- (83) Ueda, K. *J. Thorac. Dis.* **2019**, *11*, 1229.
- (84) Attenello, F. J.; Mukherjee, D.; Dato, G.; McGirt, M. J.; Bohan, E.; Weingart, J. D.; Olivi, A.; Quinones-hinojosa, A.; Brem, H. *Ann. Surg. Oncol.* **2008**, *15*, 2887-93.
- (85) Walter, K. A.; Cahan, M. A.; Gur, A.; Tyler, B. *Cancer Res.* **1994**, *54*, 2207.

- (86) Sonvico, F.; Barbieri, S.; Colombo, P.; Mucchino, C.; Barocelli, E.; Cantoni, A. M.; Cavazzoni, A.; Petronini, P. G.; Rusca, M.; Carbognani, P.; Ampollini, L. *J. Thorac. Dis.* **2018**, *10*, 194.
- (87) Kaplan, J. A.; Liu, R.; Freedman, J. D.; Padera, R.; Schwartz, J.; Colson, Y. L.; Grinstaff, M. W. *Biomaterials* **2016**, *76*, 273-81.
- (88) Mayerl, F.; Gao, Q.; Huang, S.; Klohr, S. E.; Matson, J. A.; Gustavson, D. R.; Pirnik, D. M.; Berry, R. L.; Fairchild, C.; Rose, W. C. *J. Antibiot.* **1993**, *46*, 1082-8.
- (89) El-Elimat, T.; Raja, H. A.; Ayers, S.; Kurina, S. J.; Burdette, J. E.; Mattes, Z.; Sabatelle, R.; Bacon, J. W.; Colby, A. H.; Grinstaff, M. W.; Pearce, C. J.; Oberlies, N. H. *Org. Lett.* **2019**, *21*, 529-534.
- (90) Wolinsky, J. B.; Ray, W. C.; Colson, Y. L.; Grinstaff, M. W. *Macromolecules* **2007**, *40*, 7065-7068.
- (91) A. Cipurković; E. Horozić; N. Đonlagić; S. Marić; M. Saletović; Ademović, Z. *Technologica Acta* **2018**, *11*, 25-35.
- (92) Manavitehrani, I.; Fathi, A.; Badr, H.; Daly, S.; Negahi Shirazi, A.; Dehghani, F. *Polymers* **2016**, *8*, 20.
- (93) Gang, S.; Charles, F. B.; Christopher, W. B.; Brian, D. A.; Fan, M. *BMC Bioinformatics* **2011**, *12*, S36.
- (94) Wolinsky, J. B.; Liu, R.; Walpole, J.; Chirieac, L. R.; Colson, Y. L.; Grinstaff, M. W. *J. Control. Release* **2010**, *144*, 280-287.
- (95) Lackey, A.; Donington, J. S. *Semin. Intervent. Radiol.* **2013**, *30*, 133-40.
- (96) Dare, A. J.; Anderson, B. O.; Sullivan, R.; Pramesh, C. S.; Yip, C.-H.; Ilbawi, A.; Adewole, I. F.; Badwe, R. A.; Gauvreau, C. L., *Surgical services for cancer care*. World Bank Publications: Washington, 2015; Vol. 3, p 223-238.
- (97) Allen, M. S.; Darling, G. E.; Pechet, T. T. V.; Mitchell, J. D.; Herndon, J. E.; Landreneau, R. J.; Inculet, R. I.; Jones, D. R.; Meyers, B. F.; Harpole, D. H.; Putnam, J. B.; Rusch, V. W. *Ann. Thorac. Surg.* **2006**, *81*, 1013-1020.
- (98) El-Sherif, A.; Fernando, H. C.; Santos, R.; Pettiford, B.; Luketich, J. D.; Close, J. M.; Landreneau, R. J. *Ann. Surg. Oncol.* **2007**, *14*, 2400-2405.
- (99) Ginsberg, R. J.; Rubinstein, L. V. *Ann. Thorac. Surg.* **1995**, *60*, 615-22.
- (100) Ma, L.; Qiu, B.; Zhang, J.; Li, Q. W.; Wang, B.; Zhang, X. H.; Qiang, M. Y.; Chen, Z. L.; Guo, S. P.; Liu, H. *Chin. J. Cancer* **2017**, *36*, 93.

- (101) Guggino, G.; Doddoli, C.; Barlesi, F.; Acri, P.; Chetaille, B.; Thomas, P.; Giudicelli, R.; Fuentes, P. *Eur. J. Cardiothorac. Surg.* **2004**, *25*, 449-55.
- (102) Mahvi, D. A.; Liu, R.; Grinstaff, M. W.; Colson, Y. L.; Raut, C. P. *CA. Cancer J. Clin.* **2018**, *68*, 488-505.
- (103) Seca, A. M. L.; Pinto, D. *Int. J. Mol. Sci.* **2018**, *19*, 263.
- (104) Narvekar, M.; Xue, H. Y.; Eoh, J. Y.; Wong, H. L. *AAPS PharmSciTech* **2014**, *15*, 822-33.
- (105) Liu, R.; Wolinsky, J. B.; Walpole, J.; Southard, E.; Chirieac, L. R.; Grinstaff, M. W.; Colson, Y. L. *Ann. Surg. Oncol.* **2010**, *17*, 1203-13.
- (106) Liu, R.; Wolinsky, J. B.; Catalano, P. J.; Chirieac, L. R.; Wagner, A. J.; Grinstaff, M. W.; Colson, Y. L.; Raut, C. P. *Ann. Surg. Oncol.* **2012**, *19*, 199-206.
- (107) Middleton, J. C.; Tipton, A. J. *Biomaterials* **2000**, *21*, 2335-2346.
- (108) Kellar, A.; Egan, C.; Morris, D. *Biomed. Res. Int.* **2015**, *2015*, 1-17.
- (109) Ampollini, L.; Sonvico, F.; Barocelli, E.; Cavazzoni, A.; Bilancia, R.; Mucchino, C.; Cantoni, A. M.; Carbognani, P. *Eur. J. Cardiothorac. Surg.* **2010**, *37*, 557-65.
- (110) Lardinois, D.; Jung, F. J.; Opitz, I.; Rentsch, K.; Latkoczy, C.; Vuong, V.; Varga, Z.; Rousson, V.; Günther, D.; Bodis, S.; Stahel, R.; Weder, W. *J. Thorac. Cardiovasc. Surg.* **2006**, *131*, 697-703.
- (111) Chiu, B.; Coburn, J.; Pilichowska, M.; Holcroft, C.; Seib, F. P.; Charest, A.; Kaplan, D. L. *Br. J. Cancer* **2014**, *111*, 708-15.
- (112) Oberlies, N. H.; Kroll, D. J. *J. Nat. Prod.* **2004**, *67*, 129-135.
- (113) Blackwell, M. *Am. J. Bot.* **2011**, *98*, 426-38.
- (114) Pan, R.; Bai, X.; Chen, J.; Zhang, H.; Wang, H. *Front. Microbiol.* **2019**, *10*, 294.
- (115) Höfs, R.; Walker, M.; Zeeck, A. *Angew. Chem. Int. Ed. Engl.* **2000**, *39*, 3258-3261.
- (116) Amrine, C. S. M.; Raja, H. A.; Darveaux, B. A.; Pearce, C. J.; Oberlies, N. H. *J. Ind. Microbiol. Biotechnol.* **2018**, *45*, 1053-1065.
- (117) Sica, V. P.; Figueroa, M.; Raja, H. A.; El-Elimat, T.; Darveaux, B. A.; Pearce, C. J.; Oberlies, N. H. *J. Ind. Microbiol. Biotechnol.* **2016**, *43*, 1149-1157.
- (118) Vandermolen, K. M.; Oberlies, N. H.; Darveaux, B. A.; Pearce, C. J.; Chen, W. L.; Swanson, S. M. *RSC Adv.* **2014**, *4*, 18329-18335.
- (119) Graf, T. N.; Kao, D.; Rivera-Chávez, J.; Gallagher, J. M.; Raja, H. A.; Oberlies, N. H. *Planta Med.* **2020**, *86*, 988-996.

- (120) Bode, H. B.; Bethe, B.; Höfs, R.; Zeeck, A. *ChemBiochem.* **2002**, *3*, 619-27.
- (121) Amrine, C. S. M.; Huntsman, A. C.; Doyle, M. G.; Burdette, J. E.; Pearce, C. J.; Fuchs, J. R.; Oberlies, N. H. *ACS Med. Chem. Lett.* **2021**, *12*, 625-630.
- (122) Shen, W.; Mao, H.; Huang, Q.; Dong, J. *Eur. J. Med. Chem.* **2015**, *97*, 747-77.
- (123) Jana, N.; Nanda, S. *New J. Chem.* **2018**, *42*, 17803-17873.
- (124) Gao, Y.; Duan, F.-F.; Liu, L.; Peng, X.-G.; Meng, X.-G.; Ruan, H.-L. *J. Nat. Prod.* **2021**, *84*, 483-494.
- (125) Tanaka, H.; Nishida, K.; Sugita, K.; Yoshioka, T. *Jpn. J. Cancer Res.* **1999**, *90*, 1139-45.
- (126) Schirmer, A.; Kennedy, J.; Murli, S.; Reid, R.; Santi, D. V. *Proc. Natl. Acad. Sci.* **2006**, *103*, 4234-9.
- (127) Ninomiya-Tsuji, J.; Kajino, T.; Ono, K.; Ohtomo, T.; Matsumoto, M.; Shiina, M.; Mihara, M.; Tsuchiya, M.; Matsumoto, K. *J. Biol. Chem.* **2003**, *278*, 18485-18490.
- (128) Wu, J.; Powell, F.; Larsen, N. A.; Lai, Z.; Byth, K. F.; Read, J.; Gu, R. F.; Roth, M.; Toader, D.; Saeh, J. C.; Chen, H. *ACS Chem. Biol.* **2013**, *8*, 643-50.
- (129) Liu, Q.; Sabnis, Y.; Zhao, Z.; Zhang, T.; Buhrlage, S. J.; Jones, L. H.; Gray, N. S. *Chem. Biol.* **2013**, *20*, 146-159.
- (130) Fakhouri, L.; El-Elimat, T.; Hurst, D. P.; Reggio, P. H.; Pearce, C. J.; Oberlies, N. H.; Croatt, M. P. *Bioorg. Med. Chem.* **2015**, *23*, 6993-9.
- (131) Napolitano, C.; Murphy, P. V.; Natoni, A.; Santocanale, C.; Evensen, L.; Lorens, J. B. *Bioorg. Med. Chem. Lett.* **2011**, *21*, 1167-1170.
- (132) Liniger, M.; Neuhaus, C.; Hofmann, T.; Fransioli-Ignazio, L.; Jordi, M.; Drueckes, P.; Trappe, J.; Fabbro, D.; Altmann, K.-H. *ACS Med. Chem. Lett.* **2010**, *2*, 22-27.
- (133) Jogireddy, R.; Barluenga, S.; Winssinger, N. *ChemMedChem.* **2010**, *5*, 670-673.
- (134) Hearn, B.; Sundermann, K.; Cannoy, J.; Santi, D. *ChemMedChem.* **2007**, *2*, 1598-1600.
- (135) Althagafy, H. S.; Graf, T. N.; Sy-Cordero, A. A.; Gufford, B. T.; Paine, M. F.; Wagoner, J.; Polyak, S. J.; Croatt, M. P.; Oberlies, N. H. *Bioorg. Med. Chem.* **2013**, *21*, 3919-3926.
- (136) Paguigan, N. D.; Al-Huniti, M. H.; Raja, H. A.; Czarnecki, A.; Burdette, J. E.; González-Medina, M.; Medina-Franco, J. L.; Polyak, S. J.; Pearce, C. J.; Croatt, M. P.; Oberlies, N. H. *Bioorg. Med. Chem.* **2017**, *25*, 5238-5246.
- (137) Al-Huniti, M. H.; Rivera-Chávez, J.; Colón, K. L.; Stanley, J. L.; Burdette, J. E.; Pearce, C. J.; Oberlies, N. H.; Croatt, M. P. *Org. Lett.* **2018**, *20*, 6046-6050.

- (138) El-Elimat, T.; Raja, H.; Day, C. S.; Chen, W.-L.; Swanson, S. M.; Oberlies, N. H. *J. Nat. Prod.* **2014**, *77*, 2088-2098.
- (139) Ayers, S.; Graf, T. N.; Adcock, A. F.; Kroll, D. J.; Matthew, S.; Carcache de Blanco, E. J.; Shen, Q.; Swanson, S. M.; Wani, M. C.; Pearce, C. J.; Oberlies, N. H. *J. Nat. Prod.* **2011**, *74*, 1126-1131.
- (140) El-Elimat, T.; Figueroa, M.; Raja, H. A.; Graf, T. N.; Swanson, S. M.; Falkinham, J. O., 3rd; Wani, M. C.; Pearce, C. J.; Oberlies, N. H. *European. J. Org. Chem.* **2015**, *2015*, 109-121.
- (141) Acuña, U. M.; Wittwer, J.; Ayers, S.; Pearce, C. J.; Oberlies, N. H.; EJ, D. E. B. *Anticancer Res.* **2012**, *32*, 2665-71.
- (142) Acuña, U. M.; Wittwer, J.; Ayers, S.; Pearce, C. J.; Oberlies, N. H.; Carcache De Blanco, E. J. *Anticancer Res.* **2012**, *32*, 2415-2421.
- (143) Janecki, T. **2014**.
- (144) Dakas, P. Y.; Jogireddy, R.; Valot, G.; Barluenga, S.; Winssinger, N. *Chemistry* **2009**, *15*, 11490-7.
- (145) Majhi, S.; Das, D. *Tetrahedron* **2021**, *78*, 131801.
- (146) Yñiguez-Gutierrez, A. E.; Bachmann, B. O. *J. Med. Chem.* **2019**, *62*, 8412-8428.
- (147) Truax, N. J.; Romo, D. *Nat. Prod. Rep.* **2020**, *37*, 1436-1453.
- (148) Schwan, J.; Christmann, M. *Chem. Soc. Rev.* **2018**, *47*, 7985-7995.
- (149) Wender, P. A.; Verma, V. A.; Paxton, T. J.; Pillow, T. H. *Acc. Chem. Res.* **2008**, *41*, 40-9.
- (150) Sigma-Aldrich: Analytical, Biology, Chemistry & Materials. <https://www.sigmaaldrich.com/united-states.html> (April 13, 2021),
- (151) El-Elimat, T.; Figueroa, M.; Ehrmann, B. M.; Cech, N. B.; Pearce, C. J.; Oberlies, N. H. *J. Nat. Prod.* **2013**, *76*, 1709-1716.
- (152) Paguigan, N. D.; El-Elimat, T.; Kao, D.; Raja, H. A.; Pearce, C. J.; Oberlies, N. H. *J. Antibiot.* **2017**, *70*, 553-561.
- (153) Agatsuma, T.; Takahashi, A.; Kabuto, C.; Nozoe, S. *Chem. Pharm. Bull. (Tokyo)* **1993**, *41*, 373.
- (154) Tatsuta, K.; Takano, S.; Sato, T.; Nakano, S. *Chem. Lett.* **2001**, 172-173.
- (155) Isaka, M.; Suyarnsestakorn, C.; Tanticharoen, M.; Kongsaree, P.; Thebtaranonth, Y. *J. Org. Chem.* **2002**, *67*, 1561-6.
- (156) Xu, L.; He, Z.; Xue, J.; Chen, X.; Wei, X. *J. Nat. Prod.* **2010**, *73*, 885-889.

- (157) Wee, J. L.; Sundermann, K.; Licari, P.; Galazzo, J. *J. Nat. Prod.* **2006**, *69*, 1456-9.
- (158) Sugawara, F.; Kim, K.-W.; Kobayashi, K.; Uzawa, J.; Yoshida, S.; Murofushi, N.; Takahashi, N.; Strobel, G. A. *Phytochemistry* **1992**, *31*, 1987-1990.
- (159) Jana, N.; Nanda, S. *European. J. Org. Chem.* **2012**, *2012*, 4313-4320.
- (160) Liu, Q. A.; Shao, C. L.; Wang, K. L.; Chen, M.; Wang, C. Y.; Gu, Y. C.; Blum, M.; Gan, L. S. *J. Agric. Food Chem.* **2014**, *62*, 3183-3191.
- (161) Nakajima, H.; Ishida, T.; Otsuka, Y.; Hamasaki, T.; Ichinoe, M. *Phytochemistry* **1997**, *45*, 41-45.
- (162) Aldrich, T. J.; Rolshausen, P. E.; Roper, M. C.; Reader, J. M.; Steinhaus, M. J.; Rapicavoli, J.; Vosburg, D. A.; Maloney, K. N. *Phytochemistry* **2015**, *116*, 130-137.
- (163) Stinson, E. E.; Wise, W. B.; Moreau, R. A.; Jurewicz, A. J.; Pfeffer, P. E. *Can. J. Chem.* **1986**, *64*, 1590-1594.
- (164) Meng, X.; Mao, Z.; Lou, J.; Xu, L.; Zhong, L.; Peng, Y.; Zhou, L.; Wang, M. *Molecules* **2012**, *17*, 11303-11314.
- (165) Lai, D.; Wang, A.; Cao, Y.; Zhou, K.; Mao, Z.; Dong, X.; Tian, J.; Xu, D.; Dai, J.; Peng, Y.; Zhou, L.; Liu, Y. *J. Nat. Prod.* **2016**, *79*, 2022-2031.
- (166) Shigemori, H.; Hosoya, T.; Matsumoto, T. *Heterocycles* **2010**, *81*, 1231.
- (167) Kocharin, K.; Supothina, S.; Prathumpa, W. *Adv. Biosci. Biotechnol.* **2013**, *04*, 1049-1056.
- (168) Latif, Z.; Sarker, S. D. *Methods Mol. Biol.* **2012**, *864*, 255-74.
- (169) Schoch, C. L.; Seifert, K. A.; Huhndorf, S.; Robert, V.; Spouge, J. L.; Levesque, C. A.; Chen, W.; Fungal Barcoding, C.; Fungal Barcoding Consortium Author, L. *Proc Natl Acad Sci USA* **2012**, *109*, 6241-6246.
- (170) Raja, H. A.; Miller, A. N.; Pearce, C. J.; Oberlies, N. H. *J. Nat. Prod.* **2017**, *80*, 756-770.
- (171) Gardes, M.; White, T. J.; Fortin, J. A.; Bruns, T. D.; Taylor, J. W. *Can. J. Bot.* **1991**, *69*, 180-190.
- (172) White TJ; Bruns T; Lee SH; Taylor JW **1991**.
- (173) Schoch, C. L.; Robbertse, B.; Robert, V.; Vu, D.; Cardinali, G.; Irinyi, L.; Meyer, W.; Nilsson, R. H.; Hughes, K.; Miller, A. N.; Kirk, P. M.; Abarenkov, K.; Aime, M. C.; Ariyawansa, H. A.; Bidartondo, M.; Boekhout, T.; Buyck, B.; Cai, Q.; Chen, J.; Crespo, A.; Crous, P. W.; Damm, U.; De Beer, Z. W.; Dentinger, B. T. M.; Divakar, P. K.; Dueñas, M.; Feau, N.; Fliiegerova, K.; García, M. A.; Ge, Z.-W.; Griffith, G. W.; Groenewald, J. Z.; Groenewald, M.; Grube, M.; Gryzenhout, M.; Gueidan, C.; Guo, L.; Hambleton, S.; Hamelin, R.; Hansen, K.; Hofstetter, V.; Hong, S.-B.; Houbraken, J.; Hyde, K. D.; Inderbitzin, P.; Johnston, P.

R.; Karunaratna, S. C.; Kõljalg, U.; Kovács, G. M.; Kraichak, E.; Krizsan, K.; Kurtzman, C. P.; Larsson, K.-H.; Leavitt, S.; Letcher, P. M.; Liimatainen, K.; Liu, J.-K.; Lodge, D. J.; Luangsaard, J. J.; Lumbsch, H. T.; Maharachchikumbura, S. S. N.; Manamgoda, D.; Martín, M. P.; Minnis, A. M.; Moncalvo, J.-M.; Mulè, G.; Nakasone, K. K.; Niskanen, T.; Olariaga, I.; Papp, T.; Petkovits, T.; Pino-Bodas, R.; Powell, M. J.; Raja, H. A.; Redecker, D.; Sarmiento-Ramirez, J. M.; Seifert, K. A.; Shrestha, B.; Stenroos, S.; Stielow, B.; Suh, S.-O.; Tanaka, K.; Tedersoo, L.; Telleria, M. T.; Udayanga, D.; Untereiner, W. A.; Diéguez Uribeondo, J.; Subbarao, K. V.; Vágvölgyi, C.; Visagie, C.; Voigt, K.; Walker, D. M.; Weir, B. S.; Weiß, M.; Wijayawardene, N. N.; Wingfield, M. J.; Xu, J. P.; Yang, Z. L.; Zhang, N.; Zhuang, W.-Y.; Federhen, S. *Database (Oxford)* **2014**, 2014, bau061.

(174) Marin-Felix, Y.; Hernández-Restrepo, M.; Iturrieta-González, I.; García, D.; Gené, J.; Groenewald, J.; Cai, L.; Chen, Q.; Quaedvlieg, W.; Schumacher, R. *Stud Mycol* **2019**, 94, 1-124.

(175) Liu, F.; Wang, J.; Li, H.; Wang, W.; Cai, L. *Fungal. Syst. Evol.* **2019**, 4, 43-57.

(176) Phookamsak, R.; Mortimer, P. E.; Hyde, K. D.; Phookamsak, R.; Mortimer, P. E.; Hyde, K. D.; Phookamsak, R.; Liu, J. K.; Manamgoda, D. S.; Chukeatirote, E.; Hyde, K. D.; Phookamsak, R.; Liu, J. K.; Manamgoda, D. S.; Chukeatirote, E.; Hyde, K. D.; Phookamsak, R.; Hyde, K. D.; McKenzie, E. H. C. *Phytotaxa*. **2014**, 176, 260-269.

(177) Quaedvlieg, W.; Verkley, G. J. M.; Shin, H. D.; Barreto, R. W.; Alfenas, A. C.; Swart, W. J.; Groenewald, J. Z.; Crous, P. W. *Stud. Mycol.* **2013**, 75, 307-390.

(178) de Gruyter, J.; Woudenberg, J. H.; Aveskamp, M. M.; Verkley, G. J.; Groenewald, J. Z.; Crous, P. W. *Mycologia* **2010**, 102, 1066-81.

(179) Gouy, M.; Guindon, S.; Gascuel, O. *Mol. Biol. Evol.* **2010**, 27, 221-4.

(180) Talavera, G.; Castresana, J. *Syst Biol* **2007**, 56, 564-577.

(181) Kalyaanamoorthy, S.; Minh, B. Q.; Wong, T. K. F.; von Haeseler, A.; Jermiin, L. S. *Nat. Methods* **2017**, 14, 587-589.

(182) Zhang, D.; Gao, F.; Jakovlić, I.; Zou, H.; Zhang, J.; Li, W. X.; Wang, G. T. *Mol Ecol Resour* **2020**, 20, 348-355.

(183) Nguyen, L.-T.; Schmidt, H. A.; Von Haeseler, A.; Minh, B. Q. *Mol Biol Evol* **2015**, 32, 268-274.

(184) Du, L.; King, J. B.; Cichewicz, R. H. *J. Nat. Prod.* **2014**, 77, 2454-8.

(185) Wei-Shin, C.; Yuan-Teng, C.; Xiang-Yi, W.; Friedrichs, E.; Puff, H.; Breitmaier, E. *Liebigs Ann. Chem.* **1981**, 1981, 1880-1885.

(186) Wu, H.; Lao, X.-F.; Wang, Q.-W.; Lu, R.-R.; Shen, C.; Zhang, F.; Liu, M.; Jia, L. *J. Nat. Prod.* **1989**, 52, 948-951.

- (187) Morakotkarn, D.; Kawasaki, H.; Seki, T.; Okane, I.; Tanaka, K. *Mycoscience* **2008**, *49*, 258-265.
- (188) Dai, D. Q.; Wijayawardene, N. N.; Tang, L. Z.; Liu, C.; Han, L. H.; Chu, H. L.; Wang, H. B.; Liao, C. F.; Yang, E. F.; Xu, R. F.; Li, Y. M.; Hyde, K. D.; Bhat, D. J.; Cannon, P. F. *MycKeys* **2019**, *58*, 1-26.
- (189) Diwu, Z. *Photochem. Photobiol.* **1995**, *61*, 529-539.
- (190) Jiang, Y.; Leung, A. W.; Wang, X.; Zhang, H.; Xu, C. *Int. J. Radiat. Biol.* **2014**, *90*, 575-579.
- (191) Qi, S.; Guo, L.; Yan, S.; Lee, R. J.; Yu, S.; Chen, S. *Acta. Pharm. Sin. B* **2019**, *9*, 279-293.
- (192) Du, W.; Sun, C.; Liang, Z.; Han, Y.; Yu, J. *World J. Microbiol. Biotechnol.* **2012**, *28*, 3151-3157.
- (193) Yang, Y.; Wang, C.; Zhuge, Y.; Zhang, J.; Xu, K.; Zhang, Q.; Zhang, H.; Chen, H.; Chu, M.; Jia, C. *Front. Microbiol.* **2019**, *10*, 1810.
- (194) Su, Y.; Sun, J.; Rao, S.; Cai, Y.; Yang, Y. *J. Photochem. Photobiol. B, Biol.* **2011**, *103*, 29-34.
- (195) Hudson, J. B.; Zhou, J.; Chen, J.; Harris, L. *Photochem. Photobiol.* **1994**, *60*, 253.
- (196) Donohoe, C.; Senge, M. O.; Arnaut, L. G.; Gomes-da-Silva, L. C. *Biochim. Biophys. Acta. Rev. Cancer.* **2019**, *1872*, 188308.
- (197) Zang, L. Y.; Zhang, Z. Y.; Misra, H. P. *Photochem. Photobiol.* **1990**, *52*, 677-83.
- (198) Ali, S.; Olivo, M. *Int. J. Oncol.* **2002**, *21*, 1229-1237.
- (199) Ma, G.; Khan, S. I.; Jacob, M. R.; Tekwani, B. L.; Li, Z.; Pasco, D. S.; Walker, L. A.; Khan, I. A. *Antimicrob. Agents Chemother.* **2004**, *48*, 4450-4452.
- (200) Ma, F.; Huang, H.; Ge, X.; Yang, X.; Yang, C.; Han, L.; Zhou, J.; Zhou, L. *Bioorg. Med. Chem. Lett.* **2013**, *23*, 1689-1692.
- (201) Kishi, T.; Tahara, S.; Taniguchi, N.; Tsuda, M.; Tanaka, C.; Takahashi, S. *Planta Med.* **1991**, *57*, 376-9.
- (202) Liu, X.; Xie, J.; Zhang, L.; Chen, H.; Gu, Y.; Zhao, J. *J. Photochem. Photobiol. B, Biol.* **2009**, *94*, 171-178.
- (203) Ma, J.-H.; Zhao, J.-Q.; Jiang, L.-J. *Free Radic. Res.* **2001**, *35*, 607-617.
- (204) O'Brien, E. M.; Morgan, B. J.; Mulrooney, C. A.; Carroll, P. J.; Kozlowski, M. C. *J. Org. Chem.* **2010**, *75*, 57-68.

- (205) Lei, X. Y.; Zhang, M. Y.; Ma, Y. J.; Wang, J. W. *J. Ind. Microbiol. Biotechnol.* **2017**, *44*, 1415-1429.
- (206) Ma, Y. J.; Zheng, L. P.; Wang, J. W. *Microb. Cell Fact.* **2019**, *18*, 121.
- (207) Ma, Y. J.; Zheng, L. P.; Wang, J. W. *Front. Microbiol.* **2019**, *10*, 2023.
- (208) Cai, Y.; Liang, X.; Liao, X.; Ding, Y.; Sun, J.; Li, X. *Appl. Biochem. Biotechnol.* **2010**, *160*, 2275-86.
- (209) Sun, C. X.; Ma, Y. J.; Wang, J. W. *Ultrason. Sonochem.* **2017**, *38*, 214-224.
- (210) Tisch, D.; Schmoll, M. *Appl. Biochem. Biotechnol.* **2010**, *85*, 1259-1277.
- (211) Ma, Y. J.; Sun, C. X.; Wang, J. W. *Photochem. Photobiol.* **2019**, *95*, 812-822.
- (212) Sun, C. X.; Ma, Y. J.; Wang, J. W. *J. Photochem. Photobiol. B, Biol.* **2018**, *182*, 100-107.
- (213) Gao, R.; Xu, Z.; Deng, H.; Guan, Z.; Liao, X.; Zhao, Y.; Zheng, X.; Cai, Y. *Arch. Microbiol.* **2018**, *200*, 1217-1225.
- (214) Bills, G.; Martin, J.; Collado, J.; Platas, G.; Overy, D.; Ruben Tormo, J.; Vicente, F.; Verkley, G. J. M.; Crous, P. W. *SIMB News* **2009**, 133-147.
- (215) Daub, M. E.; Ehrenshaft, M. *Physiol. Plant.* **1993**, *89*, 227-236.
- (216) Leung, A. W.; Ip, M.; Xu, C. S.; Wang, X. N.; Yung, P. T.; Hua, H. Y. *Hong Kong Med. J.* **2017**, *23*, 36-37.
- (217) Wang, Z.-J.; He, Y.-Y.; Huang, C.-G.; Huang, J.-S.; Huang, Y.-C.; An, J.-Y.; Gu, Y.; Jiang, L.-J. *Photochem. Photobiol.* **1999**, *70*, 773-780.
- (218) Sollod, C. C.; Jenns, A. E.; Daub, M. E. *Appl. Environ. Microbiol.* **1992**, *58*, 444-9.
- (219) Lynch, F. J.; Geoghegan, M. J. *Trans. Br. Mycol. Soc.* **1979**, *73*, 311-327.
- (220) Ehrenshaft, M.; Upchurch, R. G. *Appl. Environ. Microbiol.* **1991**, *57*, 2671-6.
- (221) Mazzini, S.; Merlini, L.; Mondelli, R.; Scaglioni, L. *J. Chem. Soc., Perkin Trans. 2* **2001**, 409-416.
- (222) Smirnov, A.; Fulton, D. B.; Andreotti, A.; Petrich, J. W. *J. Am. Chem. Soc.* **1999**, *121*, 7979-7988.
- (223) Elias, B. C.; Said, S.; de Albuquerque, S.; Pupo, M. T. *Mycol. Res.* **2006**, *161*, 273-280.
- (224) Bills, G. F.; Gloer, J. B. *Microbiol. Spectr.* **2016**, *4*, FUNK-0009-2016.
- (225) Frisvad, J. C. *Methods Mol. Biol.* **2012**, *944*, 47-58.

- (226) Liu, W. Z.; Shen, Y. X.; Liu, X. F.; Chen, Y. T.; Xie, J. L. *Chin. Chem. Lett.* **2001**, *12*, 431-432.
- (227) Shen, Y. X.; Liu, W. Z.; Rong, X. G.; Sun, Y. H. *Acta. Pharm. Sin.* **2003**, *38*, 834-7.
- (228) Hu, J.; Sarrami, F.; Li, H.; Zhang, G.; Stubbs, K. A.; Lacey, E.; Stewart, S. G.; Karton, A.; Piggott, Andrew M.; Chooi, Y.-H. *Chem. Sci.* **2019**, *10*, 1457-1465.
- (229) Mulrooney, C. A.; O'Brien, E. M.; Morgan, B. J.; Kozlowski, M. C. *European. J. Org. Chem.* **2012**, *2012*, 3887-3904.
- (230) Zhou, Z.; Liu, Y.; Qin, M.; Sheng, W.; Wang, X.; Li, Z.; Zhong, R. *J. Photochem. Photobiol. B, Biol.* **2014**, *134*, 1-8.
- (231) Cao, E. H.; Xin, S. M.; Cheng, L. S. *Int. J. Radiat. Biol.* **1992**, *61*, 213-9.
- (232) Shi, R.; Li, C.; Jiang, Z.; Li, W.; Wang, A.; Wei, J. *Molecules* **2017**, *22*, 112.
- (233) Innis, M. A.; Gelfand, D. H.; Sninsky, J. J.; White, T. J., *PCR Protocols : a Guide to Methods and Applications*. Elsevier Science: St. Louis, 2014.
- (234) Gazis, R.; Chaverri, P. *Fungal Ecol.* **2010**, *3*, 240-254.
- (235) Bruhn, T.; Schaumlöffel, A.; Hemberger, Y.; Bringmann, G. *Chirality* **2013**, *25*, 243-9.
- (236) Monroe, S.; Yin, H.; McFarland, S. A.; Colon, K. L.; Roque, J.; Cameron, C. G.; McFarland, S. A.; Konda, P.; Gujar, S.; Gujar, S.; McFarland, S. A.; Gujar, S.; Gujar, S.; Thummel, R. P.; Lilje, L. *Chem. Rev.* **2019**, *119*, 797-828.
- (237) McCain, J.; Colón, K. L.; Barrett, P. C.; Monroe, S. M. A.; Sainuddin, T.; Roque Iii, J.; Pinto, M.; Yin, H.; Cameron, C. G.; McFarland, S. A. *Inorg. Chem.* **2019**, *58*, 10778-10790.
- (238) Al Subeh, Z. Y.; Raja, H. A.; Monroe, S.; Flores-Bocanegra, L.; El-Elimat, T.; Pearce, C. J.; McFarland, S. A.; Oberlies, N. H. *J. Nat. Prod.* **2020**, *83*, 3765-3766.
- (239) de Medeiros, L. S.; Murgu, M.; deSouza, A. Q. L.; Rodrigues-Fo, E. *Helv. Chim. Acta* **2011**, *94*, 1077-1084.
- (240) Take, Y.; Inouye, Y.; Nakamura, S.; Allaudeen, H. S.; Kubo, A. *J. Antibiot.* **1989**, *42*, 107-15.
- (241) Sakemi, S.; Hirai, H.; Ichiba, T.; Inagaki, T.; Kato, Y.; Kojima, N.; Nishida, H.; Parker, J. C.; Saito, T.; Tonai-Kachi, H.; VanVolkenburg, M. A.; Yoshikawa, N.; Kojima, Y. *J. Antibiot.* **2002**, *55*, 941-51.
- (242) Rivera-Chávez, J.; González-Andrade, M.; del Carmen González, M.; Glenn, A. E.; Mata, R. *Planta Med.* **2013**, *79*, 198-205.

- (243) Han, Z.; Li, Y. X.; Liu, L. L.; Lu, L.; Guo, X. R.; Zhang, X. X.; Zhang, X. Y.; Qi, S. H.; Xu, Y.; Qian, P. Y. *Mar. Drugs* **2017**, *15*, 128.
- (244) Ayers, S.; Ehrmann, B. M.; Adcock, A. F.; Kroll, D. J.; Wani, M. C.; Pearce, C. J.; Oberlies, N. H. *Tetrahedron Lett.* **2011**, *52*, 5733-5735.
- (245) Togashi, K.; Ko, H. R.; Ahn, J. S.; Osada, H. *Biosci. Biotechnol. Biochem.* **2001**, *65*, 651-3.
- (246) Rojas, I. S.; Lotina-Hennsen, B.; Mata, R. *J. Nat. Prod.* **2000**, *63*, 1396-1399.
- (247) Kitahara, N.; Endo, A.; Furuya, K.; Takahashi, S. *J. Antibiot.* **1981**, *34*, 1562-8.
- (248) Kitahara, N.; Haruyama, H.; Hata, T.; Takahashi, S. *J. Antibiot.* **1983**, *36*, 599-600.
- (249) Jang, J.-P.; Jang, J.-H.; Oh, M.; Son, S.; Kim, S. M.; Kim, H.-M.; Shin, K.-S.; Oh, H.; Soung, N. K.; Hong, Y.-S.; Kim, B. Y.; Ahn, J. S. *J. Antibiot.* **2014**, *67*, 331-333.
- (250) Matsumoto, K.; Tanaka, K.; Matsutani, S.; Sakazaki, R.; Hino, H.; Uotani, N.; Tanimoto, T.; Kawamura, Y.; Nakamoto, S.; Yoshida, T. *J. Antibiot.* **1995**, *48*, 106-12.
- (251) de Medeiros, L. S.; Murgu, M.; de-Souza, A. Q.; Rodrigues-Fo, E. *Helv. Chim. Acta* **2013**, *96*, 1406-1407.
- (252) de Medeiros, L. S.; Abreu, L. M.; Nielsen, A.; Ingmer, H.; Larsen, T. O.; Nielsen, K. F.; Rodrigues-Filho, E. *Phytochemistry* **2015**, *111*, 154-162.
- (253) Elyashberg, M. *Trends Analyt. Chem.* **2015**, *69*, 88-97.
- (254) Keifer, P. A. *Prog. Drug Res.* **2000**, *55*, 137.
- (255) Williamson, R. T.; Buevich, A. V.; Martin, G. E.; Parella, T. *J. Org. Chem.* **2014**, *79*, 3887-94.
- (256) Tran, T. D.; Cartner, L. K.; Bokesch, H. R.; Henrich, C. J.; Wang, X. W.; Mahidol, C.; Ruchirawat, S.; Kittakoop, P.; O'Keefe, B. R.; Gustafson, K. R. *Magn. Reson. Chem.* **2019**, DOI: 10.1002/mrc.4932.
- (257) Chan, S. T. S.; Nani, R. R.; Schauer, E. A.; Martin, G. E.; Williamson, R. T.; Saurí, J.; Buevich, A. V.; Schafer, W. A.; Joyce, L. A.; Goey, A. K. L.; Figg, W. D.; Ransom, T. T.; Henrich, C. J.; McKee, T. C.; Moser, A.; MacDonald, S. A.; Khan, S.; McMahon, J. B.; Schnermann, M. J.; Gustafson, K. R. *J. Org. Chem.* **2016**, *81*, 10631-10640.
- (258) Motiram-Corral, K.; Nolis, P.; Parella, T.; Sauri, J. *J. Nat. Prod.* **2020**, *83*, 1275-1282.
- (259) Newman, A. G.; Townsend, C. A. *J. Am. Chem. Soc.* **2016**, *138*, 4219-28.
- (260) Chen, H. Q.; Lee, M. H.; Chung, K. R. *Microbiology* **2007**, *153*, 2781-2790.

- (261) Deng, H.; Gao, R.; Liao, X.; Cai, Y. *J. Biotechnol.* **2017**, *259*, 228-234.
- (262) Chooi, Y. H.; Zhang, G.; Hu, J.; Muria-Gonzalez, M. J.; Tran, P. N.; Pettitt, A.; Maier, A. G.; Barrow, R. A.; Solomon, P. S. *Environ. Microbiol.* **2017**, *19*, 1975-1986.
- (263) Li, Y.-T.; Yang, C.; Wu, Y.; Lv, J.-J.; Feng, X.; Tian, X.; Zhou, Z.; Pan, X.; Liu, S.; Tian, L.-W. *J. Nat. Prod.* **2021**, *84*, 436-443.
- (264) Daub, M. E.; Leisman, G. B.; Clark, R. A.; Bowden, E. F. *Proc. Natl. Acad. Sci.* **1992**, *89*, 9588-92.
- (265) Daub, M. E.; Herrero, S.; Chung, K.-R. *FEMS Microbiol. Lett.* **2005**, *252*, 197-206.
- (266) Daub, M. E.; Li, M.; Bilski, P.; Chignell, C. F. *Photochem. Photobiol.* **2000**, *71*, 135-40.
- (267) Leisman, G. B.; Daub, M. E. *Photochem. Photobiol.* **1992**, *55*, 373-379.
- (268) O'Brien, E. M.; Li, J.; Carroll, P. J.; Kozlowski, M. C. *J. Org. Chem.* **2010**, *75*, 69-73.
- (269) Bogeski, I.; Gulaboski, R.; Kappl, R.; Mirceski, V.; Stefova, M.; Petreska, J.; Hoth, M. *J. Am. Chem. Soc.* **2011**, *133*, 9293-303.
- (270) Fang, L. Z.; Qing, C.; Shao, H. J.; Yang, Y. D.; Dong, Z. J.; Wang, F.; Zhao, W.; Yang, W. Q.; Liu, J. K. *J. Antibiot.* **2006**, *59*, 351-4.
- (271) Wang, Y.-H.; Long, C.-L.; Yang, F.-M.; Wang, X.; Sun, Q.-Y.; Wang, H.-S.; Shi, Y.-N.; Tang, G.-H. *J. Nat. Prod.* **2009**, *72*, 1151-1154.
- (272) Li, Y.; Sun, K. L.; Wang, Y.; Fu, P.; Liu, P. P.; Wang, C.; Zhu, W. M. *Chin. Chem. Lett.* **2013**, *24*, 1049-1052.
- (273) Lin, D.; Xinying, Y.; Tianjiao, Z. *Chem. Pharm. Bull.* **2009**, *57*, 873-876.
- (274) Khalil, Z. G.; Huang, X. c.; Raju, R.; Piggott, A. M.; Capon, R. J. *J. Org. Chem.* **2014**, *79*, 8700-8705.
- (275) Raju, R.; Piggott, A. M.; Huang, X.-C.; Capon, R. J. *Org. Lett.* **2011**, *13*, 2770-2773.
- (276) de Montaigu, A.; Oeljeklaus, J.; Krahn, J. H.; Suliman, M. N. S.; Halder, V.; de Ansorena, E.; Nickel, S.; Schlicht, M.; Plíhal, O.; Kubiasová, K.; Radová, L.; Kracher, B.; Tóth, R.; Kaschani, F.; Coupland, G.; Kombrink, E.; Kaiser, M. *ACS Chem. Biol.* **2017**, *12*, 1466-1471.
- (277) Kusano, M.; Sotoma, G.; Koshino, H.; Uzawa, J. *J. Chem. Soc. Perkin Trans. I* **1998**, 2823-2826.
- (278) Wang, H. J.; Gloer, J. B.; Wicklow, D. T.; Dowd, P. F. *J. Nat. Prod.* **1998**, *61*, 804-807.
- (279) Borthwick, A. D. *Chem. Rev.* **2012**, *112*, 3641-3716.

- (280) Arai, K.; Kimura, K.; Mushiroda, T.; Yamamoto, Y. *Chem. Pharm. Bull.* **1989**, *37*, 2937-2939.
- (281) Afiyatullo, S. S.; Kalinovskii, A. I.; Pivkin, M. V.; Dmitrenok, P. S.; Kuznetsova, T. A. *Chem. Nat. Compd.* **2004**, *40*, 615-617.
- (282) Ben Ameer Mehdi, R.; Shaaban, K. A.; Rebai, I. K.; Smaoui, S.; Bejar, S.; Mellouli, L. *J. Nat. Prod.* **2009**, *23*, 1095-1107.
- (283) Kanoh, K.; Kohno, S.; Asari, T.; Harada, T.; Katada, J.; Muramatsu, M.; Kawashima, H.; Sekiya, H.; Uno, I. *Bioorg. Med. Chem. Lett.* **1997**, *7*, 2847-2852.
- (284) Daugan, A.; Grondin, P.; Ruault, C.; Le Monnier de Gouville, A. C.; Coste, H.; Linget, J. M.; Kirilovsky, J.; Hyafil, F.; Labaudiniere, R. *J. Med. Chem.* **2003**, *46*, 4533.
- (285) Borthwick, A. D.; Liddle, J. *Med. Res. Rev.* **2011**, *31*, 576-604.
- (286) Berthet, M.; Legrand, B.; Martinez, J.; Parrot, I. *Org. Lett.* **2017**, *19*, 492-495.
- (287) Robey, M. T.; Ye, R.; Bok, J. W.; Clevenger, K. D.; Islam, M. N.; Chen, C.; Gupta, R.; Swyers, M.; Wu, E.; Gao, P.; Thomas, P. M.; Wu, C. C.; Keller, N. P.; Kelleher, N. L. *ACS Chem. Biol.* **2018**, *13*, 1142-1147.
- (288) Shou, N.; Koohei, N.; Hitoshi, H.; Nakadate, S.; Nozawa, K.; Horie, H. *Heterocycles* **2006**, *68*, 1969-1972.
- (289) Aparicio-Cuevas, M. A.; Rivero-Cruz, I.; Sánchez-Castellanos, M.; Menéndez, D.; Raja, H. A.; Joseph-Nathan, P.; González, M. d. C.; Figueroa, M. *J. Nat. Prod.* **2017**, *80*, 2311-2318.
- (290) El-Elimat, T.; Zhang, X.; Jarjoura, D.; Moy, F. J.; Orjala, J.; Kinghorn, A. D.; Pearce, C. J.; Oberlies, N. H. *ACS Med. Chem. Lett.* **2012**, *3*, 645-649.
- (291) González-Medina, M.; Prieto-Martínez, F. D.; Naveja, J. J.; Méndez-Lucio, O.; El-Elimat, T.; Pearce, C. J.; Oberlies, N. H.; Figueroa, M.; Medina-Franco, J. L. *Future Med. Chem.* **2016**, *8*, 1399-412.
- (292) González-Medina, M.; Owen, J. R.; El-Elimat, T.; Pearce, C. J.; Oberlies, N. H.; Figueroa, M.; Medina-Franco, J. L. *Front. Pharmacol.* **2017**, *8*.
- (293) Paguigan, N. D.; El-Elimat, T.; Kao, D.; Raja, H. A.; Pearce, C. J.; Oberlies, N. H. *J. Antibiot.* **2017**, *70*, 553-561.
- (294) Shearer, C. A. *Nova Hedwigia* **1993**, *56*, 1-33.
- (295) Park, D. *Trans. Br. Mycol. Soc.* **1972**, *58*, 291-299.
- (296) Quick, A.; Thomas, R.; Williams, D. J. *J. Chem. Soc. Chem. Commun.* **1980**, 1051-1053.

- (297) Nishikori, S.; Takemoto, K.; Kamisuki, S.; Nakajima, S.; Kuramochi, K.; Tsukuda, S.; Iwamoto, M.; Katayama, Y.; Suzuki, T.; Kobayashi, S.; Watashi, K.; Sugawara, F. *J. Nat. Prod.* **2016**, *79*, 442-446.
- (298) Yang, S. Q.; Li, X. M.; Li, X.; Chi, L. P.; Wang, B. G. *Mar. Drugs* **2018**, *16*, 114.
- (299) Wang, M. Z.; Si, T. X.; Ku, C. F.; Zhang, H. J.; Li, Z. M.; Chan, A. S. C. *J. Org. Chem.* **2019**, *84*, 831-839.
- (300) Takase, S.; Kawai, Y.; Uchida, I.; Tanaka, H.; Aoki, H. *Tetrahedron* **1985**, *41*, 3037-3048.
- (301) Hino, T.; Taniguchi, M.; Yamamoto, I.; Yannaguchi, K.; Nakagawa, M. *Tetrahedron Lett.* **1981**, *22*, 2565-2568.
- (302) Capon, R. J. *Nat. Prod. Rep.* **2020**, *37*, 55-79.
- (303) Cason, J.; Koch, C. W.; Correia, J. S. *J. Org. Chem.* **1970**, *35*, 179-186.
- (304) Galarraga, J. A.; Neill, K. G.; Raistrick, H. *Biochem. J.* **1955**, *61*, 456-464.
- (305) Tansakul, C.; Rukachaisirikul, V.; Maha, A.; Kongprapan, T.; Phongpaichit, S.; Hutadilok-Towatana, N.; Borwornwiriyan, K.; Sakayaroj, J. *Nat. Prod. Res.* **2014**, *28*, 1718-24.
- (306) Cockroft, N. T.; Cheng, X.; Fuchs, J. R. *J. Chem. Inf. Model.* **2019**, *59*, 4906-4920.
- (307) Visagie, C. M.; Houbraken, J.; Frisvad, J. C.; Hong, S. B.; Klaassen, C. H. W.; Perrone, G.; Seifert, K. A.; Varga, J.; Yaguchi, T.; Samson, R. A. *Stud. Mycol.* **2014**, *78*, 343-371.
- (308) Stamatakis, A. *Bioinformatics* **2006**, *22*, 2688-90.
- (309) Miller, M. A.; Pfeiffer, W.; Schwartz, T., Creating the CIPRES Science Gateway for Inference of large phylogenetic trees. In *In Proceedings of the Gateway Computing Environments Workshop (GCE)*, 2010; pp 1-8.
- (310) Liu, Y. J.; Whelen, S.; Hall, B. D. *Mol. Biol. Evol.* **1999**, *16*, 1799-808.
- (311) Visagie, C. M.; Houbraken, J.; Rodrigues, C.; Silva Pereira, C.; Dijksterhuis, J.; Seifert, K. A.; Jacobs, K.; Samson, R. A. *Persoonia* **2013**, *31*, 42-62.
- (312) Wang, X.-C.; Chen, K.; Zeng, Z.-Q.; Zhuang, W.-Y. *Sci. Rep.* **2017**, *7*, 1-14.
- (313) Edgar, R. C. *Nucleic Acids Res.* **2004**, *32*, 1792-7.
- (314) Helaly, S. E.; Teponno, R. B.; Bernecker, S.; Stadler, M.; Helaly, S. E.; Ashrafi, S.; Maier, W.; Teponno, R. B.; Dababat, A. A. *J. Nat. Prod.* **2018**, *81*, 2228-2234.
- (315) Capon, R. J.; Skene, C.; Stewart, M.; Ford, J.; O'Hair, R. A. J.; Williams, L.; Lacey, E.; Gill, J. H.; Heiland, K.; Friedel, T. *Org. Biomol. Chem.* **2003**, *1*, 1856-1862.

(316) Ayers, S.; Ehrmann, B. M.; Adcock, A. F.; Kroll, D. J.; Carcache de Blanco, E. J.; Shen, Q.; Swanson, S. M.; Falkinham, J. O., 3rd; Wani, M. C.; Mitchell, S. M.; Pearce, C. J.; Oberlies, N. H. *J. Pept. Sci.* **2012**, *18*, 500-10.